

**CASE FILE
COPY**

SD72-SH-0046

FINAL REPORT**ESTABLISHMENT OF DESIGN CRITERIA
FOR ACCEPTABLE FAILURE MODES AND
FAIL SAFE CONSIDERATIONS FOR THE
SPACE SHUTTLE STRUCTURAL SYSTEM**

JUNE 1, 1972

Contract NAS8-27269

Prepared for
George C. Marshall Space Flight Center
Marshall Space Flight Center, Alabama 35812

Prepared by: *R. W. Westrup*
R. W. Westrup
System Design

Approved by: *S. M. Treman*
S. M. Treman, Director
System Design



Space Division
North American Rockwell
12214 Lakewood Boulevard
Downey, California 90241



SD72-SH-0046

FINAL REPORT

ESTABLISHMENT OF DESIGN CRITERIA
FOR ACCEPTABLE FAILURE MODES AND
FAIL SAFE CONSIDERATIONS FOR THE
SPACE SHUTTLE STRUCTURAL SYSTEM

JUNE 1, 1972

Contract NAS8-27269

Prepared for
George C. Marshall Space Flight Center
Marshall Space Flight Center, Alabama 35812

Prepared by: *R. W. Westrup*
R. W. Westrup
System Design

Approved by: *S. M. Treman*
S. M. Treman, Director
System Design



Space Division
North American Rockwell
12214 Lakewood Boulevard
Downey, California 90241

TECHNICAL REPORT INDEX ABSTRACT

ACCESSION NUMBER				DOCUMENT SECURITY CLASSIFICATION Unclassified			
TITLE OF DOCUMENT FINAL REPORT - ESTABLISHMENT OF DESIGN CRITERIA FOR ACCEPTABLE FAILURE MODES AND FAIL SAFE CONSIDERATIONS FOR THE SPACE SHUTTLE STRUCTURAL SYSTEM						LIBRARY USE ONLY	
AUTHOR(S) Westrup, Robert W.							
CODE QNO 85282		ORIGINATING AGENCY AND OTHER SOURCES Space Division of North American Rockwell Corp. Downey, California			DOCUMENT NUMBER SD72-SH-0046		
PUBLICATION DATE 1 June 1972			CONTRACT NUMBER NAS8-27269				

<p>DESCRIPTIVE TERMS</p> <p>SAFE-LIFE, FAIL-SAFE, FRACTURE, FATIGUE, CRACK GROWTH, RESIDUAL STRENGTH, STRUCTURAL DESIGN CRITERIA</p>
--

<p>ABSTRACT</p> <p>Investigations of fatigue life, and safe-life and fail-safe design concepts as applied to Space Shuttle structure are summarized. The results are evaluated to select recommended structural design criteria to provide assurance that premature failure due to propagation of undetected crack-like defects will not occur during shuttle operational service.</p> <p>The Space Shuttle booster, GDC configuration B-9U, is selected as the reference vehicle. Structural elements used as basis of detail analyses include wing spar caps, vertical stabilizer skins, crew compartment skin, orbiter support frame, propellant tank shell structure. Fatigue life analyses of structural elements are performed to define potential problem areas and establish upper limits of operating stresses. Flaw growth analyses are summarized in parametric form over a range of initial flaw types and sizes, operating stresses and service life requirements. Service life of 100 to 500 missions is considered. Design provisions to satisfy crack arrest and residual strength requirements under fail-safe approach are determined for selected elements. A parametric range of residual strength from 1.0 to 1.2 times limit load is investigated. An estimate is made of capabilities of various inspection methods to detect crack-like defects. This estimate is used as the basis to evaluate effects of applying candidate safe-life criteria to the reference vehicle. Effects considered include structural weight, required inspection methods, and in-service inspection frequency. Relative merits of safe-life and fail-safe design approaches are compared for applicable structural elements.</p>
--

FOREWORD

This report summarizes the results of the studies conducted under contract NAS8-27269, Establishment of Design Criteria for Acceptable Failure Modes and Fail Safe Considerations for the Space Shuttle Structural System. The study was conducted by the Space Division of North American Rockwell Corporation for the Marshall Space Flight Center of the National Aeronautics and Space Administration. The work was performed over the period of June 15, 1971, to May 15, 1972.

The numerical results and comparisons given in this report are expressed in the International System of Units as the primary system. In most cases, the customary English units are also indicated. The customary units were used in the engineering analyses conducted under this study.

North American Rockwell personnel who participated in the investigation include: R. W. Westrup, study manager and principal investigator; J. P. Sanders, fatigue and fracture analysis; J. E. Collipriest and R. M. Ehret, fracture properties data and two-dimensional crack growth analysis methods; and J. Mamon, inspection methods and flaw detection capabilities.

CONTENTS

Section	Page
1.0 INTRODUCTION	1-1
1.1 BACKGROUND	1-1
1.2 STUDY APPROACH	1-3
1.3 STUDY OBJECTIVES	1-4
2.0 BASELINE VEHICLE MISSION AND CONFIGURATION	2-1
2.1 PROGRAM OBJECTIVE	2-1
2.2 MISSION PROFILES	2-1
2.2.1 Operational Mission	2-1
2.2.2 Ferry Mission	2-8
2.3 BOOSTER CONFIGURATION	2-11
2.3.1 General Arrangement	2-11
2.3.2 Body Structure	2-17
2.3.3 Aerodynamic Surfaces	2-27
2.3.4 Body Thermal Protection System	2-30
2.3.5 Weight Summary	2-33
3.0 STRUCTURAL DESIGN LOADS AND CRITERIA FOR BASELINE VEHICLE	3-1
3.1 STRUCTURAL DESIGN CRITERIA	3-1
3.1.1 Design Philosophy	3-1
3.1.2 Design Requirements	3-2
3.1.3 Design Conditions	3-3
3.1.4 Loads and Pressures	3-5
3.1.5 Design Factors	3-6
3.1.6 Service Life	3-7
3.1.7 Design Thickness	3-9
3.2 DESIGN LOADS	3-10
3.2.1 Aerodynamic Surfaces	3-10
3.2.2 Body Loads	3-10
3.2.3 Propellant Tank Pressures	3-21
3.3 SERVICE LOAD SPECTRA	3-21
3.3.1 Wing Load Spectra	3-21
3.3.2 Vertical Stabilizer Load Spectra	3-21
3.3.3 Body Load Spectra	3-21
3.4 STRUCTURAL TEMPERATURES	3-29

Section	Page	
4.0	SELECTED STRUCTURAL ELEMENTS	4-1
4.1	SELECTION SUMMARY	4-1
4.2	SELECTION RATIONALE	4-1
5.0	FATIGUE AND FRACTURE PROPERTIES	5-1
5.1	FATIGUE PROPERTIES	5-1
	5.1.1 2219 Aluminum Alloy	5-1
	5.1.2 6Al-4V Titanium Alloy	5-1
5.2	FRACTURE PROPERTIES	5-2
	5.2.1 Fracture Toughness	5-2
	5.2.2 Crack Growth Rate - Cyclic Load	5-7
	5.2.3 Empirical Fracture Data - 2219-T87 Welds	5-23
6.0	FATIGUE LIFE ANALYSIS	6-1
6.1	ANALYSIS METHODS AND SUMMARY OF RESULTS	6-1
6.2	FATIGUE ANALYSIS - WING	6-4
	6.2.1 Structural Configuration and Loading	6-4
	6.2.2 Damage Analysis	6-5
6.3	FATIGUE ANALYSIS - VERTICAL STABILIZER	6-18
	6.3.1 Structural Configuration and Loading	6-18
	6.3.2 Damage Analysis	6-18
6.4	FATIGUE ANALYSIS - INTERTANK ADAPTER	6-27
	6.4.1 Structural Configuration and Loading	6-27
	6.4.2 Damage Analysis	6-27
6.5	FATIGUE ANALYSIS - FUSELAGE STA. 2600	6-28
	6.5.1 Structural Configuration and Loading	6-28
	6.5.2 Damage Analysis - Membrane Loading	6-29
	6.5.3 Damage Analysis - Membrane Plus Discontinuity Loading	6-32
6.6	FATIGUE ANALYSIS - ORBITER AFT ATTACH SUPPORT FRAME	6-38
	6.6.1 Structural Configuration and Loading	6-38
	6.6.2 Damage Analysis	6-40
6.7	FATIGUE ANALYSIS - LOX TANK AFT BULKHEAD	6-42
	6.7.1 Structural Configuration and Loading	6-42
	6.7.2 Damage Analysis	6-42

Section	Page
6.8 FATIGUE ANALYSIS - CREW COMPARTMENT	6-46
6.8.1 Structural Configuration and Loading	6-46
6.8.2 Damage Analysis	6-46
6.9 FATIGUE ANALYSIS - WING - ALTERNATE MATERIAL	6-48
6.9.1 Structural Configuration and Loading	6-48
6.9.2 Damage Analysis	6-48
7.0 SAFE-LIFE ANALYSIS	7-1
7.1 ANALYSIS METHODS	7-1
7.1.1 Stress Intensity and Critical Flaw Size	7-1
7.1.2 Crack Growth Analysis	7-3
7.1.3 Retardation Effects	7-4
7.2 SAFE-LIFE ANALYSIS - WING	7-7
7.2.1 Structural Configuration and Loading	7-7
7.2.2 Crack Growth Analysis	7-7
7.2.3 Design Implications	7-11
7.3 SAFE-LIFE ANALYSIS - VERTICAL STABILIZER	7-31
7.3.1 Structural Configuration and Loading	7-31
7.3.2 Crack Growth Analysis	7-31
7.3.3 Design Implications	7-31
7.4 SAFE-LIFE ANALYSIS - CREW COMPARTMENT	7-35
7.4.1 Structural Configuration and Loading	7-35
7.4.2 Crack Growth Analysis	7-35
7.4.3 Design Implications	7-35
7.5 SAFE-LIFE ANALYSIS - ORBITER AFT ATTACH SUPPORT FRAME	7-37
7.5.1 Structural Configuration and Loading	7-37
7.5.2 Crack Growth Analysis	7-37
7.5.3 Design Implications	7-38
7.6 SAFE-LIFE ANALYSIS - FUSELAGE STA. 2600	7-45
7.6.1 Structural Configuration and Loading	7-45
7.6.2 Crack Growth Analysis	7-46
7.6.3 Design Implications	7-46
7.7 SAFE-LIFE ANALYSIS - PROPELLANT TANKS	7-50
7.7.1 Structural Configuration and Loading	7-50
7.7.2 Crack Growth Analysis	7-51
7.7.3 Design and Proof Test Implications	7-66
7.8 SAFE-LIFE ANALYSIS - WING SPAR CAPS - ALTERNATE MATERIAL	7-76
7.8.1 Structural Configuration and Loading	7-76
7.8.2 Crack Growth Analysis	7-76
7.8.3 Design Implications	7-76

Section	Page
7.9 SAFE-LIFE ANALYSIS - EXTERNAL TANK	7-81
7.9.1 Structural Configuration and Loading	7-81
7.9.2 Critical Flaw Sizes and Proof Test Requirements	7-81
8.0 FAIL-SAFE ANALYSIS	8-1
8.1 FAIL-SAFE ANALYSIS - WING	8-2
8.1.1 Structural Configuration and Loading	8-2
8.1.2 Residual Strength and Sizing Analysis - Monolithic Spar Cap	8-2
8.1.3 Residual Strength and Sizing Analysis - Multi-Element Spar Cap	8-6
8.1.4 Residual Fatigue Life	8-7
8.1.5 Design Evaluation	8-11
8.2 FAIL-SAFE ANALYSIS - VERTICAL STABILIZER	8-13
8.2.1 Structural Configuration and Loading	8-13
8.2.2 Inherent Residual Strength	8-13
8.2.3 Residual Strength of Planked Skins	8-19
8.2.4 Design Evaluation	8-25
8.3 FAIL-SAFE ANALYSIS - CREW COMPARTMENT	8-27
8.3.1 Structural Configuration and Loading	8-27
8.3.2 Residual Strength and Sizing Analysis	8-27
8.3.3 Cabin Atmosphere Leakage	8-33
8.3.4 Design Evaluation	8-37
8.4 FAIL-SAFE ANALYSIS - LH ₂ TANK	8-42
8.4.1 Cylindrical Shell	8-42
8.4.2 Circumferential Weld Loads	8-42
8.4.3 Design Evaluation	8-46
9.0 CRITERIA EVALUATION AND RECOMMENDATIONS	9-1
9.1 NDE TECHNIQUES AND CAPABILITIES	9-2
9.1.1 Basic NDE Techniques and Associated Equipment and Facility Requirements	9-2
9.1.2 Application of NDE Techniques to Reference Structural Elements	9-5
9.1.3 NDE Capabilities	9-7
9.2 EVALUATION OF DESIGN CRITERIA	9-10
9.2.1 Fatigue Life Criteria	9-10
9.2.2 Fail-Safe Design Criteria	9-11
9.2.3 Safe-Life Design Criteria	9-14
9.3 COMPARISON OF SAFE-LIFE VS. FAIL-SAFE DESIGN APPROACHES	9-29
9.4 SUMMARY OF RECOMMENDED DESIGN CRITERIA	9-32

Section	Page
APPENDIX	
SAMPLE COMPUTER PRINT-OUT FOR CRACK GROWTH ANALYSIS	A-1

ILLUSTRATIONS

Figure		Page
2-1	Typical Operational Mission Flight Profile	2-3
2-2	Ascent Trajectory Parameters	2-6
2-3	B-9U Booster Entry Trajectory Profile	2-6
2-4	Transcontinental Ferry Route	2-9
2-5	Typical Ferry Mission Profile	2-10
2-6	B-9U Booster Basic Configuration	2-13
2-7	Booster Structural Arrangement	2-15
2-8	Forward Skirt Structure	2-19
2-9	Liquid Oxygen Tank	2-21
2-10	Intertank Adapter Structure	2-22
2-11	Liquid Hydrogen Tank	2-24
2-12	Thrust Structure	2-25
2-13	Crew Compartment	2-26
2-14	Wing Arrangement and Support Points	2-28
2-15	Canard Structure	2-29
2-16	Vertical Stabilizer	2-31
2-17	Body TPS Shell Structure	2-32
3-1	Wing Bending Moment Distribution	3-13
3-2	Canard Bending Moment Distribution	3-14
3-3	Vertical Stabilizer Bending Moment Distribution	3-15
3-4	Body Loadings - Top ϕ	3-16
3-5	Body Loadings - Bottom ϕ	3-17

Figure	Page
3-6 Booster Main Engine Thrust vs. Time	3-20
3-7 B-9U Main LOX Tank Pressure Schedule	3-22
3-8 B-9U Main LH ₂ Tank Pressure Schedule	3-23
3-9 LOX Tank Limit Pressure Profiles	3-24
3-10 LH ₂ Tank Limit Pressure Profiles	3-25
3-11 B-9U Wing Load Spectra	3-26
3-12 B-9U Vertical Tail Load Spectra	3-27
3-13 B-9U Fuselage Sta. 2600 Load Spectra	3-28
3-14 Orbiter Aft Attach Load Spectra	3-30
3-15 B-9U Thrust Spectra	3-31
3-16 Wing Structure Transient Temperatures	3-32
3-17 Vertical Stabilizer Structure Transient Temperatures	3-33
5-1 S-N Curves for 2219 Aluminum	5-3
5-2 S-N Curves for Ti-6 Al-4V ($K_t = 3.0$)	5-4
5-3 S-N Curves for Ti-6 Al-4V ($K_t = 4.5$)	5-5
5-4 Modified Goodman Diagram for Ti-6 Al-4V (Annealed)	5-6
5-5 Orientation of Fracture Properties Test Specimens	5-8
5-6 Apparent Fracture Toughness vs. Thickness Ti-6 Al-4J Annealed - RW Orientation	5-11
5-7 Apparent Fracture Toughness vs. Thickness Ti-6 Al-4J Annealed - WR Orientation	5-12
5-8 Crack Growth Rate for Ti-6Al-4V Under Cyclic Loading	5-16
5-9 Crack Growth Rate for 2219-T87 Aluminum Alloy at 70 F - PTC Test Specimens	5-17
5-10 Crack Growth Rate for 2219-T87 Aluminum Alloy at 70 F - CT Test Specimens	5-18

Figure		Page
5-11	Crack Growth Rate for 2219-T87 Aluminum Alloy at -320 F - PTC Test Specimens	5-19
5-12	Deep Flaw Magnification Factor Used by NASA-MSFC	5-20
5-13	Generalized Crack Growth Rate Equation Compared to SD Experimental Data for 2024 and 2219 Aluminum	5-21
5-14	Generalized Crack Growth Rate Curves Used in Propellant Tank Analyses	5-22
5-15	Gross Stress for Fracture or Breakthrough of 2219-T87 Weld Specimens	5-25
5-16	Apparent Fracture Toughness for Fracture or Breakthrough of 2219-T87 Weld Specimens	5-26
5-17	Range of Apparent Fracture Toughness versus Thickness for 2219-T87 Weld Specimens	5-27
6-1	Wing Spar Cap Geometry	6-4
6-2	Vertical Stabilizer Planform	6-19
6-3	Vertical Stabilizer Cover Skin Sections	6-19
6-4	LH ₂ Tank Shell Model for Discontinuity Analysis	6-33
6-5	LH ₂ Tank Secondary Bending Moment Distribution	6-34
6-6	Orbiter Aft Attach Support Frame	6-38
7-1	Elementary Stress Intensity Solutions	7-2
7-2	Comparison of Predicted vs. Measured Crack Growth - Random Spectra Loading - B-1 Development Tests	7-6
7-3	Wing Spar Cap Cross Section	7-8
7-4	Wing Spar Cap Critical Flaw Sizes	7-10
7-5	Corner Crack Growth to Failure - Wing Spar Caps	7-12
7-6	Through Crack Growth to Failure - Wing Spar Caps	7-13
7-7	Part-Through Crack Growth to Failure - Wing Spar Caps	7-14
7-8	Corner Crack From Fastener Hole - Growth to Failure - Wing Spar Caps	7-15

Figure		Page
7-9	Missions to Failure - Corner Crack in Wing Spar Caps (Retardation not Considered)	7-16
7-10	Missions to Failure - Through Crack in Wing Spar Caps (Retardation not Considered)	7-17
7-11	Missions to Failure - Part-Through Crack in Wing Spar Caps (Retardation not Considered)	7-18
7-12	Missions to Failure - Corner Crack From Fastener Hole in Wing Spar Caps (Retardation not Considered)	7-19
7-13	Effect of Initial Flaw Size on Allowable Limit Stress for Safe-Life - Wing Spar Caps (Crack Growth Retardation not Considered)	7-20,21
7-14	Missions to Failure - Corner Crack in Wing Spar Caps (Retardation Included)	7-22
7-15	Missions to Failure - Through Crack in Wing Spar Caps (Retardation Included)	7-23
7-16	Missions to Failure - Part-Through Crack in Wing Spar Caps (Retardation Included)	7-24
7-17	Wing Spar Cap Iso-Stress Contours	7-26
7-18	Effect of Spar Cap Limit Design Stress on Wing Weight	7-27
7-19	Effect of Initial Flaw Size on Wing Weight for Safe-Life (Crack Growth Retardation not Considered)	7-28,29
7-20	Effect of Initial Flaw Size on Wing Weight for Safe-Life (Crack Growth Retardation Included)	7-30
7-21	Through Crack Growth to Failure - Vertical Stabilizer Skin	7-33
7-22	Missions to Failure - Through Crack in Vertical Stabilizer Skin	7-34
7-23	Through Crack Growth to Failure - Crew Compartment Skin	7-36
7-24	Frame Cap Configuration - Orbiter Aft Attach	7-39
7-25	Through Crack Growth to Failure - Orbiter Aft Attach Frame Cap	7-40
7-26	Missions to Failure - Through Crack in Orbiter Aft Attach Frame Cap	7-41

Figure		Page
7-27	Effect of Frame Cap Limit Stress on Weight of Orbiter Aft Attach Bulkhead	7-43
7-28	Effect of Initial Flaw Size on Structural Weight for Safe-Life - Orbiter Aft Attach Bulkhead	7-44
7-29	Part-Through Crack Growth to Failure - Fuselage Sta. 2600	7-48
7-30	Missions to Failure - Part-Through Crack on LH ₂ Tank Skin (Sta. 2600) - Circumferential Orientation	7-49
7-31	Predicted Two-Dimensional Growth for Part-Through Cracks	7-52
7-32	Comparison of Predicted Load Cycles to Leak With Experimental Results	7-53
7-33	Crack Growth to Failure - LH ₂ Tank Parent Metal ($\sigma_{lim} = 44.4$ ksi)	7-54
7-34	Crack Growth to Failure - LH ₂ Tank Parent Metal ($\sigma_{lim} = 40.0$ ksi)	7-55
7-35	Crack Growth to Failure - LH ₂ Tank Parent Metal ($\sigma_{lim} = 35.0$ ksi)	7-56
7-36	Crack Growth to Failure - LH ₂ Tank Welds ($\sigma_{lim} = 22.2$ ksi)	7-57
7-37	Crack Growth to Failure - LH ₂ Tank Welds ($\sigma_{lim} = 20.0$ ksi)	7-58
7-38	Crack Growth to Failure - LH ₂ Tank Welds ($\sigma_{lim} = 17.5$ ksi)	7-59
7-39	Crack Growth to Failure - LO ₂ Tank Parent Metal ($\sigma_{lim} = 53.0$ ksi)	7-60
7-40	Crack Growth to Failure - LO ₂ Tank Parent Metal ($\sigma_{lim} = 50.0$ ksi)	7-61
7-41	Crack Growth to Failure - LO ₂ Tank Parent Metal ($\sigma_{lim} = 45.0$ ksi)	7-62
7-42	Missions to Failure - Part-Through Crack in LH ₂ Tank Parent Metal	7-63
7-43	Missions to Failure - Part-Through Crack in LH ₂ Tank Welds	7-64
7-44	Missions to Failure - Part-Through Crack in LO ₂ Tank Parent Metal	7-65
7-45	Required Proof Test Stresses - LH ₂ Tank Parent Metal	7-69

Figure		Page
7-46	Required Proof Test Stresses - LO ₂ Tank Parent Metal	7-70
7-47	Required Proof Test Stresses - LH ₂ Tank Welds	7-71
7-48	Corner Crack From Fastener Hole - Growth to Failure - 2219-T87 Aluminum Wing Spar Caps	7-77
7-49	Missions to Failure - Corner Crack From Fastener Hole in 2219-T87 Aluminum Wing Spar Caps (Retardation Not Considered)	7-78
7-50	Summary Weight Comparison - Aluminum and Titanium Alloys for Wing Spar Caps	7-80
7-51	External Tank Configuration	7-82
7-52	External Tank LO ₂ Limit Pressure Profiles	7-83
7-53	External Tank LH ₂ Limit Pressure Profiles	7-84
8-1	Wing Spar Cap Multi-Element Fail-Safe Design Concept	8-3
8-2	Vertical Stabilizer Skin Plank Joint Configurations	8-14
8-3	Stress Intensity vs. Crack Length - Vertical Stabilizer Skins	8-20
8-4	Stress Intensity Coefficients for Cracked Panel with Riveted Reinforcing Straps	8-30
8-5	Stress Intensity Coefficient vs. Relative Stiffness of Reinforcing Member	8-31
8-6	Structure and System Weight Increase vs. Crack Arrest Strap Spacing - Crew Compartment	8-40
8-7	Applied and Allowable Hoop Stresses for Circumferential Welds - LH ₂ Tank	8-45
9-1	Estimated NDE Capabilities for Flaw Detection	9-9
9-2	Equivalent Depth of Detectable Cracks for Various NDE Techniques	9-9
9-3	Missions to Failure For Various Residual Strength Safety Factors - Part-Through Crack in Wing Spar Caps	9-19
9-4	Missions to Failure For Various Residual Strength Safety Factors - Through Crack in Orbiter Aft Attach Frame Cap	9-20

Figure		Page
9-5	Structural Weight Increase For Various Residual Strength Safety Factors and Initial Flaw Sizes - Part-Through Crack in Wing Spar Caps	9-21
9-6	Comparison of Nominal and Design Curves for Crack Growth Rate - 2219-T87 Aluminum Alloy	9-24

TABLES

Table	Page
2-1 Significant Events During the B-9U Entry Trajectory	2-7
2-2 B-9U Booster Weight Summary	2-34
2-3 B-9U Booster Wing Group Weight Breakdown	2-35
2-4 B-9U Booster Vertical Tail Group Weight Breakdown	2-37
2-5 B-9U Booster Body Group Weight Breakdown	2-38
3-1 Design Factors of Safety	3-8
3-2 Service Life Factors	3-8
3-3 Safe-Life Design Environments	3-11
3-4 Summary of Design Conditions	3-11
3-5 Design Loads for Aerodynamic Surfaces	3-12
3-6 Body Limit Design Loads	3-18
3-7 Booster/Orbiter Connection Loads	3-19
3-8 Estimated Range of Structural Temperatures	3-34
4-1 Matrix of Candidate Structural Elements - Shuttle Booster B-9U	4-3
5-1 Fracture Toughness Test Data for Ti-6Al-4V	5-9
5-2 Fracture Toughness Test Data for 2219 Aluminum Alloy	5-10
6-1 Fatigue Life of Selected Structural Elements	6-3
6-2 Wing Fatigue Damage ($K_T = 4.5$)	6-6,7,8,9
6-3 Wing Fatigue Damage ($K_T = 3.0$)	6-10,11,12,13
6-4 Wing Fatigue Damage ($K_T = 3.0, \sigma_{LIM} = 65$ ksi)	6-14,15,16,17
6-5 Vertical Stabilizer Fatigue Damage	6-22,23,24,25,26

Table	Page
6-6 Fuselage Sta. 2600 Fatigue Damage - Membrane Loading	6-30,31
6-7 LH ₂ Tank Secondary Bending Stresses	6-35
6-8 Fuselage Sta. 2600 Fatigue Damage - Membrane Plus Discontinuity Loading	6-36,37
6-9 Orbiter Aft Attach Frame Fatigue Damage	6-41
6-10 Wing Fatigue Damage - Aluminum Spar Caps (K _T = 3.0, σ _{lim} = 40 ksi)	6-49,50,51
6-11 Wing Fatigue Damage - Aluminum Spar Caps (K _T = 3.0, σ _{lim} = 35 ksi)	6-52,53,54
7-1 Wing Spar Cap Stress Spectrum	7-9
7-2 Vertical Stabilizer Stress Spectrum	7-32
7-3 Orbiter Aft Attach Frame Stress Spectrum	7-37
7-4 Cap Areas and Weight Increases - Orbiter Aft Attach Support Frame	7-42
7-5 Fuselage Sta. 2600 Stress Spectrum	7-45
7-6 Propellant Tank Stress Spectra	7-50
7-7 Summary of Characteristics of Allowable Initial Flaws in Propellant Tanks	7-67
7-8 Proof Factors and Associated Weight Increase for B-9U Propellant Tanks	7-74
7-9 Estimated Weight Increase of TPS to Accommodate Aluminum Wing Spar Caps	7-77
7-10 Summary of Critical Flaw Sizes for External Tank Components	7-85
7-11 External Tank Stresses and Wall Thicknesses for Flight Design and Proof Test Conditions	7-88
8-1 Limit Design Loads for Wing Lower Surface Spar Caps (Undamaged Structure) (kips)	8-5
8-2 Fail-Safe Design Loads for Wing Lower Surface Spar Caps (kips)	8-5
8-3 Wing Residual Fatigue Life (K _t = 3.0)	8-8

Table		Page
8-4	Stress Intensity vs. Crack Length - Vertical Stabilizer Skins	8-18
8-5	Crack-Arrest Strap Sizing and Structural Weight Increase - Crew Compartment	8-32
8-6	Normalized Flow Rates and Depressurization Time - Crew Compartment Atmosphere Leakage	8-38
8-7	Depressurization Time and Pressure System Weight - Crew Compartment Atmosphere Leakage	8-39
8-8	LH ₂ Tank Circumferential Weld Land Fail-Safe Requirements	8-46
9-1	Summary of Applicable NDE Techniques and Associated Equipment/Facility Requirements	9-3,4
9-2	Structural Weight Increases for Fail-Safe Design Approach	9-13
9-3	Structural Weight Increases for Safe-Life Design Approach and Various NDE Techniques	9-16
9-4	Structural Weight Increases for Various Residual Strength Safety Factors and Safe-Life Periods	9-25
9-5	Summary of Structural Weight Increases Resulting From Application of Proposed Safe-Life Design Criteria to the Reference Vehicle	9-27
9-6	Comparison of Safe-Life vs. Fail-Safe Design Approaches for Selected Structural Elements	9-30

REFERENCES

1. Anon., Space Shuttle Phase B Final Report; Vol. II, Technical Summary; Book 3, Booster Vehicle Definition, NR/SD Report SD 71-114-2 (25 June 1971).
2. Fletcher, D. A., and J. E. Jensen. A Study for Developing Safe-Life/Fail-Safe Criteria for the Space Shuttle, First Monthly Progress Report, General Dynamics Convair (19 April 1971).
3. Garrocq, C. A. Space Shuttle Booster Structural Design Criteria, General Dynamics Convair Report No. 76-549-30-007 (26 March 1971).
4. Kruse, G. Space Shuttle Booster B-9U Loads, General Dynamics Convair Report No. 76-549-30-008 (1 June 1971).
5. Jensen, J. E. A Study for Developing Safe-Life/Fail-Safe Criteria for the Space Shuttle, Second Monthly Progress Report, General Dynamics Convair (22 May 1971).
6. Diller, D. E. A Study for Developing Safe-Life/Fail-Safe Criteria for the Space Shuttle, Third Monthly Progress Report, General Dynamics Convair (22 June 1971).
7. Diller, D. E. A Study for Developing Safe-Life/Fail-Safe Design Criteria for the Space Shuttle, Fourth Monthly Progress Report, General Dynamics Convair (22 July 1971).
8. Preston, J. L. Compilation of S-N Fatigue Curves and Modified Goodman Diagrams Applicable to B-1 Structural Materials, North American Rockwell, Los Angeles Division Report TFD-71-845 (2 June 1971).
9. Kaufman, J. E., G. E. Nordmark and B. W. Lifka. Fracture Toughness, Fatigue and Corrosion Characteristics of 2020-T651, 2024-T851, 2219-T851, and 7001-T75 Aluminum Alloys, AFML-TR-66-291 (September 1966).
10. Hyler, W. S., and O. L. Deel. Summary of Fatigue Information on Ti-6Al-4V Alloy, DMIC Technical Note (5 October 1967).
11. Illg, Walter and Claude B. Castle. Fatigue of Four Stainless Steel Alloys and Three Titanium Alloys Before and After Exposure to 550 F, Up to 8000 Hours, NASA TN D-2899 (July 1965).
12. Dutko, T. R. Effect of Tapered Fasteners on the Fatigue Life of Titanium 6 Al-4V (Annealed) Joints, North American Rockwell, Los Angeles Division Report NA-67-822 (22 October 1968).

13. Campbell, J. E. Plane-Strain Fracture-Toughness Data for Selected Metals and Alloys, Battelle Memorial Institute, DMIC Report S-28 (June 1969).
14. Masters, J. N. Cyclic and Sustained Load Flaw Growth Characteristics of 6Al-4V Titanium, NASA CR-92231, The Boeing Company (July 1968).
15. Lorenz, P. M. Fracture Toughness and Subcritical Flaw Growth Characteristics of Saturn S-IC Tankage Materials, The Boeing Company Report D2-22802 (July 1964).
16. Tiffany, C. F., P. M. Lorenz and L. R. Hall. Investigation of Plane-Strain Flaw Growth in Thick-Walled Tanks, NASA CR-54837, The Boeing Company (February 1966).
17. Collipriest, J. E. Part-Through-Crack Fracture Mechanics Testing, NR/SD IR&D Report, SD 71-319.
18. Anon., F-111 Wing Carry-Through Structure Category J Structural-Material Tests, NR/LAD Report NA-70-451 (14 August 1970).
19. Zelus, B. P. and J. E. Bolton. Titanium Procurement Property Summary, NR/LAD Report TFD 71-1129 (13 September 1971).
20. Forman, R. G. Fatigue Flaw Growth Behaviour of 2219-T87 Aluminum at Cryogenic, Room, and Elevated Temperatures, NASA-MSC Materials Technology Branch Report 71-ES5-1 (2 September 1971).
21. Unpublished test data from NR/SD IR&D Fracture Properties Test Program on 2219-T87 Aluminum.
22. Substantiation Report - Baseline 39U Configuration Aerodynamic Surfaces, General Dynamics Convair (June 1971).
23. Wilhem, D. P. Fracture Mechanics Guidelines for Aircraft Structural Applications, AFFDL-TR-69-111 (February 1970).
24. Fracture Control of Metallic Pressure Vessels, NASA SP-8040 (May 1970).
25. Elber, W. "The Significance of Fatigue Crack Closure," Damage Tolerance in Aircraft Structures, ASTM STP 486 (May 1971).
26. Vroman, G. A. Correlation of PTC Specimen Crack Growth Characteristics to Compact Tension Specimen Data and Other Material Properties, Los Angeles Division, North American Rockwell Corporation, NA-71-879 (September 1971).
27. Strandlund, R. E. and D. E. Diller, A Study for Developing Safe-Life/Fail-Safe Design Criteria for the Space Shuttle, Seventh Monthly Progress Report, General Dynamics Convair (1 November 1971).

28. Poe, C. C., Jr. "Fatigue Crack Propagation in Stiffened Panels, Damage Tolerance in Aircraft Structures, ASTM STP 486 (May 1971).
29. Kuhn, Paul, Stresses in Aircraft and Shell Structures, New York: McGraw-Hill Book Company, Inc. (1956).
30. Poe, C. C., Jr.. "The Effect of Riveted and Uniformly Spaced Stringers on the Stress Intensity Factor of a Cracked Sheet," Proceedings of the Air Force Conference on Fatigue and Fracture of Aircraft Structures and Materials, AFFDL TR 70-144.
31. Strandlund, R. E., P.M. Nissley and J. E. Jensen, A Study for Developing Safe-Life/Fail-Safe Design Criteria for the Space Shuttle, Sixth Monthly Progress Report, General Dynamics Convair (29 September 1971).
32. Packman, P. F., H. S. Pearson, J. S. Owens and G. B. Marchese. The Applicability of a Fracture Mechanics - Nondestructive Testing Design Criterion, AFML-TR-68-32 (May 1968).
33. Sattler, Frank J. Nondestructive Flaw Definition Techniques for Critical Defect Determination, NASA CR-72602 (January 1970).
34. Kamm, H. W., and I. R. Kraska. A Review of Nondestructive Methods for the Detection of Concealed Cracks, AFML-TR-71-120 (July 1971).
35. Frederick, S. F. Service Life of Reusable Structures Based on NDT. McDonnell Douglas Corporation, Report MDC 62668 (December 1971).

1.0 INTRODUCTION

1.1 BACKGROUND

The space shuttle missions will subject structures to repeated sequences and combinations of loading and environmental conditions that are unprecedented in the history of aircraft and space vehicles. Although the total flight time associated with the design goal of 100 missions for the space shuttle operational life may be relatively small compared to that of contemporary commercial aircraft, the incidence of repeated high-stress load cycles may remain as a very significant consideration for structural design. This is due to several factors, including the presence of aerodynamic surfaces on booster and orbiter vehicles and the consequent response of the vehicle to wind shear and gust during ascent and entry, the asymmetric configuration and high thrust levels during boost, and the high maneuver load factors anticipated during entry. In addition, repeated cycles of large temperature excursions and, in some cases, associated thermal stresses will occur because of aerodynamic heating and the loading and depletion of cryogenic propellants.

Three general design approaches have evolved over the last two decades to prevent aerospace structures from failing catastrophically because of repeated load cycles: (1) fail-safe design, (2) safe-life design based on conventional fatigue considerations, and (3) safe-life design based on fracture mechanics considerations. The following brief discussion of these approaches includes a tentative evaluation of potential applicability to space shuttle structure.

The fail-safe design concept is based on the premise that a crack may develop and grow in the structure because of fatigue nucleation, material defects, or accidental damage; the growth of the crack will be eventually arrested, however, and a stable condition maintained by suitable design provisions. The residual strength of the structure in this weakened condition must be equal to or greater than a prescribed value, which is frequently taken as limit design load. It is presumed that the damage will be detected and repaired before catastrophic failure occurs during operation. This design philosophy has been extensively applied to the fuselage and main-wing structure of current jet transport aircraft. This basic approach may also have useful application to many of the structural elements of the space shuttle, excluding such areas as propellant tanks. However, before it can be determined that this is the most appropriate criteria for a given structural element, consideration must be given to the specific characteristics of the shuttle with respect to accessibility for thorough inspection, engineering and economic feasibility of damage detection and repair, potential impact on the two-week turnaround time, etc.

Safe-life design using conventional fatigue methods recognizes local stress concentrations due to detail design characteristics such as joints, fittings, section discontinuities, etc. However, it does not consider the potential of undetected crack-like defects existing in the structure before the start of operational service. The useful life of structural elements determined by fatigue test is comprised primarily of the number of cycles required to nucleate a crack, rather than cycles required for crack propagation to a critical value. This approach has also been widely applied to design of military and commercial aircraft over the last 15 years. Good results have been obtained in many cases, particularly for some of the current commercial jet transport aircraft which exhibit minimal structural maintenance problems in airline operation. However, the serious structural problems or failures encountered by some recent high-performance military aircraft after only limited operational service dramatically illustrate that conventional fatigue methods may not adequately guard against premature fracture. This is particularly true for structural designs involving higher operating stresses, lower toughness materials, and material forms or fabrication processes that involve a higher probability of inherent crack-like defects or reduced capability to detect such defects. It is apparent, therefore, that it would be dangerous to apply this approach to space shuttle structure without corollary application of safe-life criteria based on fracture mechanics considerations. However, it is desirable to survey cyclic stresses on typical structural elements of the space shuttle to determine the general magnitude of potential fatigue problems and appropriate criteria to assure a fatigue-resistant design.

Safe-life design based on fracture mechanics considerations is predicated on the assumption that crack-like defects may exist in the structure prior to operational service and the design must be developed so that such defects will not grow to critical dimensions during the operational life. This is accomplished by selecting materials and operating stresses such that (1) flaws of critical initial size are large enough to assure detection by non-destructive inspection or (2) it can be verified by proof test that no flaws of critical initial size exist in the structure. Some investigators in the field believe that no inspection program can be considered 100-percent reliable, and that proof-test verification is mandatory. The fracture mechanics approach to safe-life design has been applied rather extensively to space vehicle pressure tanks in recent years. Proof-test verification was accomplished on nearly all of the Apollo lunar module pressure vessels and on the propellant tanks of booster stages in the Saturn V vehicle. Unfortunately, serious difficulties appear to exist when rigorous proof-test verification criteria are applied directly to space shuttle structure. Proof testing of unpressurized structure, such as wings, fuselage shell, etc., may be impractical because of several factors, including schedule delay, cost, limited accuracy of load simulation, and scars to flight structure caused by attachment of test loading equipment. Valid proof testing of pressurized structure, such as main propellant tanks and crew compartment, will also be difficult and may be impractical. Integral tank design will produce complex load inputs much different than internal pressurization. Body bending and shear loadings on the shuttle vehicle will be much greater than for the Saturn V vehicle. Thus, it may be difficult to conduct a valid proof test by internal pressurization only. An additional problem is related to proof testing of the primary cryogenic propellant tanks.



A critical flaw over most of the surface of these tanks will involve a through-thickness crack rather than a surface crack for the materials and operating stresses currently being considered in space shuttle preliminary design. A leak-before-break characteristic is desirable for proof test, but may not be acceptable for operational service with cryogenic propellants. The proof-test levels required to verify that no initial flaws exist which could grow through the thickness of the tank walls (rather than to critical dimensions as a through crack) may impose unacceptable weight penalties on the shuttle design.

The preceding considerations illustrate that the design criteria for space shuttle structure must be carefully studied to achieve the basic program goals of minimum structural weight, minimum program costs, and demonstrated high reliability. It is further concluded that no single structural design approach will be adequate to achieve these primary goals. The most appropriate criteria will probably contain elements of the fail-safe design approach, fatigue resistant design, and fracture mechanics considerations which include both proof-test verification and nondestructive inspection as essential elements. In addition, it may be necessary to establish quality control criteria for material procurement and fabrication operations and quality assurance procedures for fabrication, checkout and test, and operational usage to assure effective fracture control of space shuttle structure over the entire life history, from raw material to the end of operational service. It is apparent, therefore, that the results of this study program will be an important element of the basic requirements and development approach for the space shuttle during final design, fabrication, and operational phases.

1.2 STUDY APPROACH

The Space Division will conduct this study using, as a point of departure, the space shuttle design definition and data that are available from the space shuttle Phase B study programs. It is believed that this study must be based on typical space shuttle requirements, missions, and structural configurations, rather than generalized concepts, for the following major reasons:

1. To assure that parametric studies cover applicable ranges of variables.
2. To provide realistic focus on problems or limitations associated with design, material characteristics, fabrication processes, nondestructive evaluation, verification tests, and flight and maintenance operations.
3. To make efficient use of analyses and data being developed on the space shuttle Phase B programs that support certain tasks of this study.
4. To permit realistic assessment of the impact of candidate design criteria on structural weight, vehicle performance, maintenance requirements, and program costs.

The booster vehicle and mission characteristics developed by Convair Division of General Dynamics during the space shuttle Phase B study program have been selected as the baseline for this study. This selection has been made in conjunction with the NASA/MSFC COR. The booster configuration is designated as B-9U; the characteristics of the vehicle and its associated mission are described in Reference 1. Typical mission characteristics are used to define reference spectra of structural loadings and environmental conditions that serve as the basis of safe-life, fail-safe, and fatigue assessments. Several major structural elements are selected that serve as the reference structural configurations. Selection is based on design, material, fabrication, and inspectability considerations so that a representative sample of all major structural systems is provided. Failure-mode characteristics of these selected structural elements under the reference loading/environment spectra are investigated by means of fracture mechanics and fatigue analysis methods and data. Parametric studies are performed to determine the effects of variation of load/environment spectra, design configuration, material combinations, and verification methods on structural weight, vehicle performance, maintenance requirements, etc., for the candidate criteria of each appropriate failure-mode approach. Results of the parametric studies are evaluated to determine the most promising criteria candidates, and recommendations are made for criteria selection.

1.3 STUDY OBJECTIVES

The study program has the following major objectives:

1. To develop rational design criteria to implement fail-safe and safe-life considerations of critical primary structure of the space shuttle.
2. To demonstrate that the recommended design approaches and associated criteria are appropriate, practical, and capable of providing the desired structural reliability and safety. This requires consideration of the following factors:
 - a. Mission requirements
 - b. Performance requirements
 - c. Service-life requirements
 - d. Maintenance requirements
 - e. Material selection
 - f. Weight control
 - g. Reliability

3. To develop parametric data for evaluation of the effect of changes in mission, configuration, material selection, and design approach or criteria on:
 - a. Performance
 - b. Service life
 - c. Maintenance requirements
 - d. Weight
 - e. Reliability

4. To bound the magnitude of potential fatigue problems on space shuttle primary structure and to determine the general level of attention and design verification criteria required to assure a fatigue-resistant structure.

2.0 BASELINE VEHICLE MISSION AND CONFIGURATION

2.1 PROGRAM OBJECTIVE

The objective of the Space Shuttle Program is to provide a low-cost space transportation system capable of placing and/or retrieving payloads in earth orbit. To achieve this objective, a fully reusable system capable of rapid turnaround and airline-type operation has been defined.

Three missions have been identified as representing the requirements for the definition of the Space Shuttle System. These missions are (A) "The design mission, 100 n. mi. due east circular orbit. The design mission insertion orbit shall be 50 x 100 n. mi. and for purposes of performance comparison calculations the vehicle shall be considered to be launched from a latitude of 28.5 degrees north; (B) the reference missions of major interest are: (1) 100 n. mi. south polar circular orbit; (2) 270 n. mi. at 55 inclination."

To achieve the objectives of the program, a two-stage vehicle capable of boost and earth entry with cruise-back to a designated landing site has been defined. This cycle is accomplished with reasonable acceleration levels, shirt-sleeve cabin environment, and quick, ground-turnaround time between flights. The significant elements of these missions are ground operations, mating of the orbiter and booster vehicles, and liftoff followed by staging of the two vehicles, with the first-stage booster returning to the launch area and the second-stage orbiter continuing on to the prescribed insertion orbit. Following a series of orbital maneuvers, the orbiter delivers and/or retrieves its payload and, at the appropriate orbital position, reenters the atmosphere, acquires the landing site, and completes the approach and landing. Following safing at the landing area, the vehicle enters a turnaround cycle consisting of thorough postflight inspection, a maintenance cycle, installation of a new payload, and mating with the booster vehicle. This mated system is checked out and returned to the launch area to begin a new mission cycle.

2.2 MISSION PROFILES

2.2.1 Operational Mission

Mission operations are summarized in Figure 2-1. Major phases of the operational mission are discussed below.

Ascent

The ascent phase is defined as beginning with engine ignition and ending with the initiation of separation. In the ignition/liftoff sequence, the thrust rises to 50 percent of full thrust and holds at that level until

main-stage in all engines can be verified and holddown release is verified. Upon verification, the thrust is increased at a controlled rate to 100 percent. The vehicle liftoff occurs when the thrust-to-weight ratio (T/W) is greater than 1.

During the ignition sequence the thrust vector control (TVG) is positioned to point at the vehicle center of gravity, and it maintains this position until the booster clears the holddown mechanism. Then the TVC controls the vehicle to required pitch, yaw, and roll attitudes until the vehicle clears the service towers. Commands to ensure tower clearance are either calculated by the onboard guidance, navigation, and control (GN&C) system or are programmed to a fixed time.

After the vehicle has cleared the service towers, the TVC is commanded by the GN&C system to provide roll, orienting the vehicle to the correct azimuth, and pitch, to provide the proper trajectory, such that the vehicle assumes a wing-level, pilot-side-up attitude and correct azimuth. TVC continues to control the vehicle to a preprogrammed pitch rate and fixed roll/yaw attitudes. During the period of 60 to 90 seconds, a yaw plane acceleration feedback system is switched in to reduce sideslip angle to minimize the induced roll.

At 125 seconds a closed loop guidance steering command is mixed with commanded pitch rate and the yaw attitude command to minimize trajectory dispersions and to steer the vehicle to the desired staging point. As propellant is depleted, along with increased thrust at altitude, the vehicle acceleration reaches 3g. At this point, approximately 160 seconds after launch, the main engines are throttled to maintain 3g for crew comfort and vehicle design loads. Ascent phase is terminated by initiation of separation based on indication of propellant depletion. Ascent trajectory parameters are given in Figure 2-2. The booster weight decreases from 4,188,000 lb at launch to about 806,000 lb at separation, while achieving a velocity of 10,800 fps at an altitude of 245,000 ft.

Separation

Near booster burnout, a signal from the booster LO₂ depletion sensor initiates the separation sequences. At depletion sensor signal, the booster engines are stepped to 50-percent thrust. Concurrently the orbiter engines are started and brought to 50-percent thrust. When both sets of engines are at 50-percent thrust and propellant depletion is imminent, the restraint mechanism between orbiter and booster is released, booster thrust decays to zero, and the orbiter rotates upwards and aft, relative to the booster, on separation system linkages until the orbiter is freed and accelerating under its own thrust. The control of all sequencing functions necessary for separation and maintaining control of both orbiter and booster is accomplished by software in the main computers of each vehicle.

After separation, the orbiter continues on its orbital mission and the booster positions itself for entry, using ACPS engines.

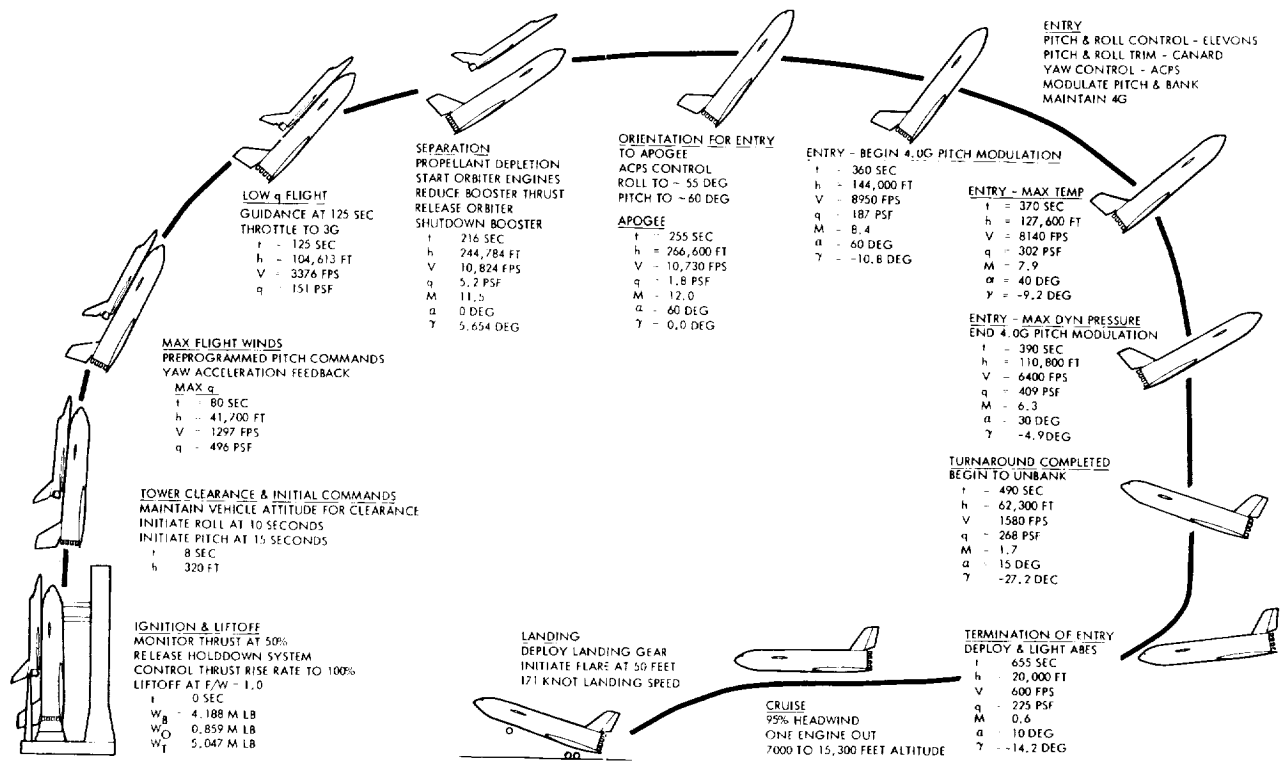


Figure 2-2. B-9U Booster Typical Operational Mission Profile

Entry

The booster entry phase starts at separation and terminates when the booster descends to 20,000 feet and deploys air-breathing engines for cruise back to the launch site. The entry mode for the B-9U booster is a supersonic transition. The angle of attack is reduced as Mach number is decreased; the angle of attack schedule is presented in Figure 2-3. Pitch and bank angle scheduling is used to minimize the flyback distance to the landing site with a 4.0g maximum load factor constraint. The entry phase is assumed to be concluded when the booster descends to an altitude of 20,000 feet.

The baseline entry trajectory is for a 100-n.mi. south polar circular orbit mission launched from the Western Test Range. Significant events during the booster entry are listed in Table 2-1. Staging occurs 216 seconds after launch. During the next 40 seconds the booster banks to a 55-degree angle and then pitches to a 60-degree angle of attack. That attitude is maintained until the load factor builds up to a maximum limit of 4.0g, which occurs 360 seconds after launch, at Mach 8.4. For the next 30 seconds the angle of attack is modulated downward. A peak dynamic pressure of 409 psf occurs at the end of the pitch modulation at Mach 6.3 and at an attitude of 30 degrees. Between Mach 6.3 and 2.5 the booster is kept at an angle of attack of 30 degrees and banked at 75 degrees. After 490 seconds, at Mach 1.7, the vehicle has turned around 180 degrees and is headed back to the launch site. The bank angle is reduced to 0 degree. From Mach 2.5 to 1.1 the angle of attack is reduced to 5 degrees, which is held through the transonic region. The subsonic attitude is 10 degrees. By 655 seconds after launch the booster has come down to an altitude of 20,000 feet, where the remaining flyback distance to the landing site is 399 n.mi. At the completion of the entry phase the gross weight of the booster has decreased slightly to 787,000 lb.

Cruise

The flyback profile is initiated at 20,000 feet, where the cruise engines are assumed to be fully deployed and operating normally; flyback range is determined from this point. An idle power descent is made to the optimum cruise altitude; this is the altitude for maximum specific range. The vehicle is then operated at the best cruise altitude for the duration of the cruise flight. For the mission with all engines operating in still air, the idle power descent is made to 14,500 feet, and a cruise climb at the optimum cruise altitude is performed between 14,500 feet and 18,500 feet. For the engine out case, the vehicle is operated at the optimum cruise altitudes between 5000 ft and 13,500 ft. An idle power descent is made from the end of cruise altitude to sea level for the completion of the flyback segment.

The flyback range requirement from the 20,000-foot altitude point is 399 n.mi.

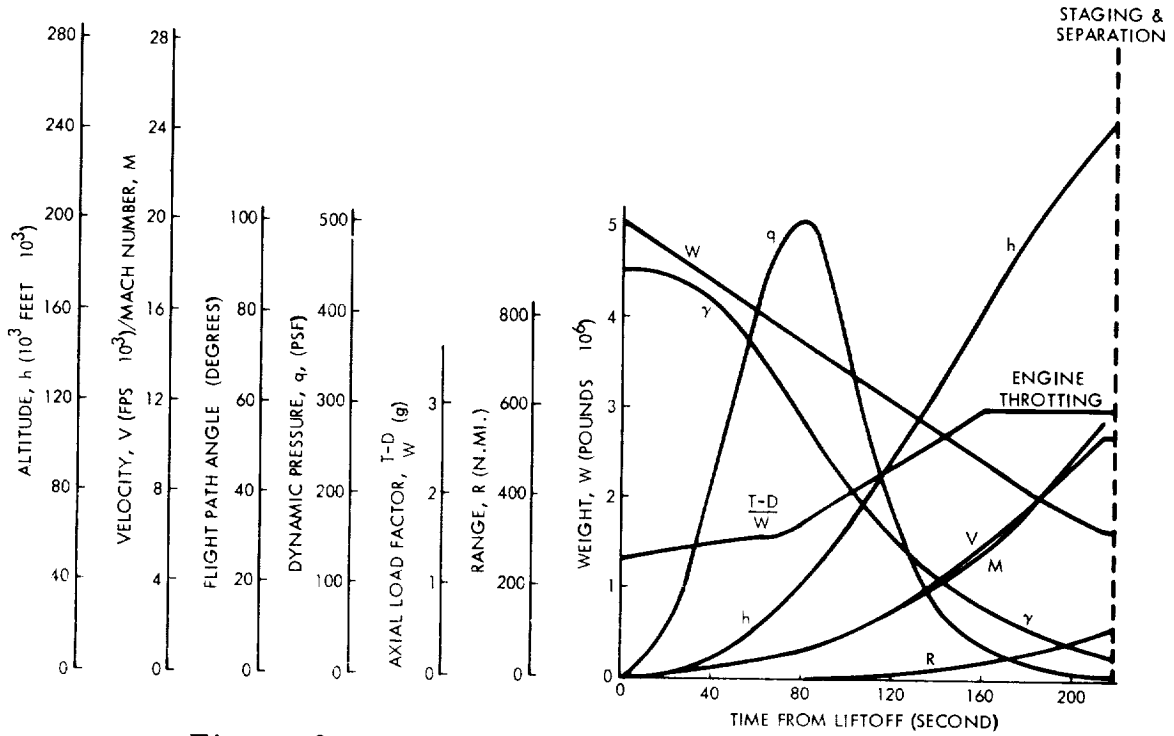


Figure 2-2. Ascent Trajectory Parameters

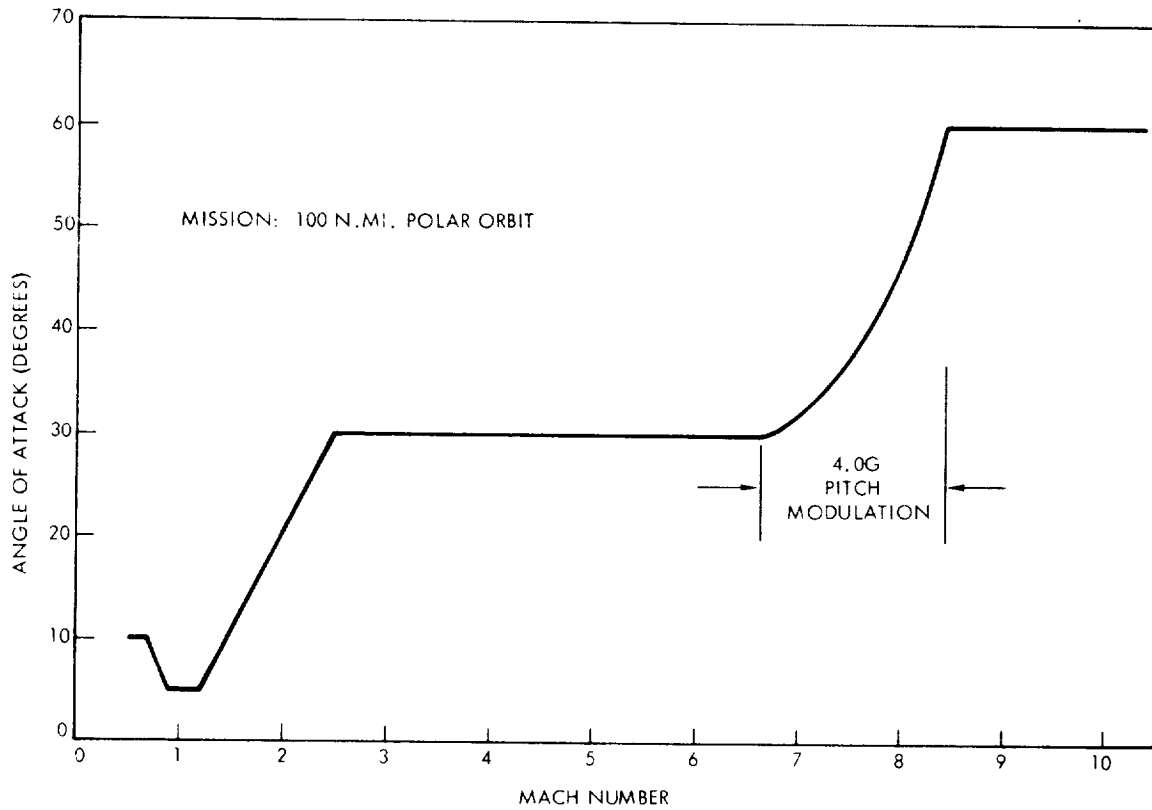


Figure 2-3. B-9U Booster Entry Trajectory Profile

Table 2-1. Significant Events During the B-9U Entry Trajectory

Event	Time (sec)	Altitude (feet)	Relative Velocity (fps)	Mach	Relative Gamma (deg)	Q (psf)	Load Factor	Alpha Angle (deg)	Bank Angle (deg)	Range (n.mi.)	Gross Weight (10^3 lb)
Staging	216	244,784	10,824	11.5	5.6	5.2	0.0	0	0	116	806
Apogee	255	266,600	10,730	12.0	0.0	1.8	0.0	60	55	186	
Begin 4.0g Pitch Modulation	360	144,000	8,950	8.4	-10.8	187	4.0	60	55	363	
Peak Supersonic q/End Pitch Mod.	390	110,800	6,400	6.3	-4.9	409	4.0	30	55	400	
Begin Pitchdown	455	84,000	2,420	2.5	-12.0	208	2.6	30	75	428	
Begin to Unbank	490	62,300	1,580	1.7	-27.2	268	1.9	15	75	423	
Peak Transonic q (1.2g)	590	24,700	915	0.9	-18.3	450	1.2	5	0	407	
Conclude Entry Phase	655	20,000	600	0.6	-14.2	225	0.9	10	0	399	787

Landing

The requirement for landing performance of the booster is that it land on a 10,000-foot runway on standard day conditions. This has been interpreted to include a 50-foot obstacle.

The basic landing technique for the B-9U booster is to approach from a 50-foot obstacle at a three degree glide slope and touchdown at 110 percent of the free air minimum velocity for the landing configuration. This results in a touchdown angle of attack of about 11.5 degrees. The booster has a 3 fps sink rate at touchdown, and there is a three second delay from touchdown until the nose gear is down and a one second delay from nose gear down until the brakes are applied. The baseline landing configuration is with 3 degree elevons, trimmed with the canard at 15 degrees. The entire landing is executed with the booster in this configuration.

2.2.2 Ferry Mission

Requirements and Criteria

Self-ferry performance requirements are defined as a selected flight route from KSC to Edwards AFB with several intermediate stops, as illustrated in Figure 2-4. Two segments from this route appear to require the greatest ferry capability, i.e.:

1. 300 n.mi. segment from KSC to Robbins AFB requiring takeoff capability from a 10,000-foot runway under sea level hot day conditions.
2. 235 n.mi. segment from Biggs AFB to Davis-Monthan AFB requiring takeoff capability from 13,600-foot runway at an elevation of 4000 feet under hot day conditions.

In determining self-ferry performance of the B-9U booster, the following mission profile was assumed:

1. Takeoff over a 35-foot obstacle utilizing the balanced field concept.
2. Climb to cruise altitude at maximum rate of climb against a 50-knot headwind.
3. Cruise at constant altitude at maximum specific range against a 50-knot headwind to the point of no return.
4. Continue cruise at constant altitude with one engine inoperative against a 50-knot headwind at maximum specific range from point of no return to beginning of descent.
5. Descend at L/D_{\max} at idle power with one engine inoperative against a 50-knot headwind.
6. Fuel reserves equal to 20 minutes at maximum endurance at sea level with all engines operating were included.

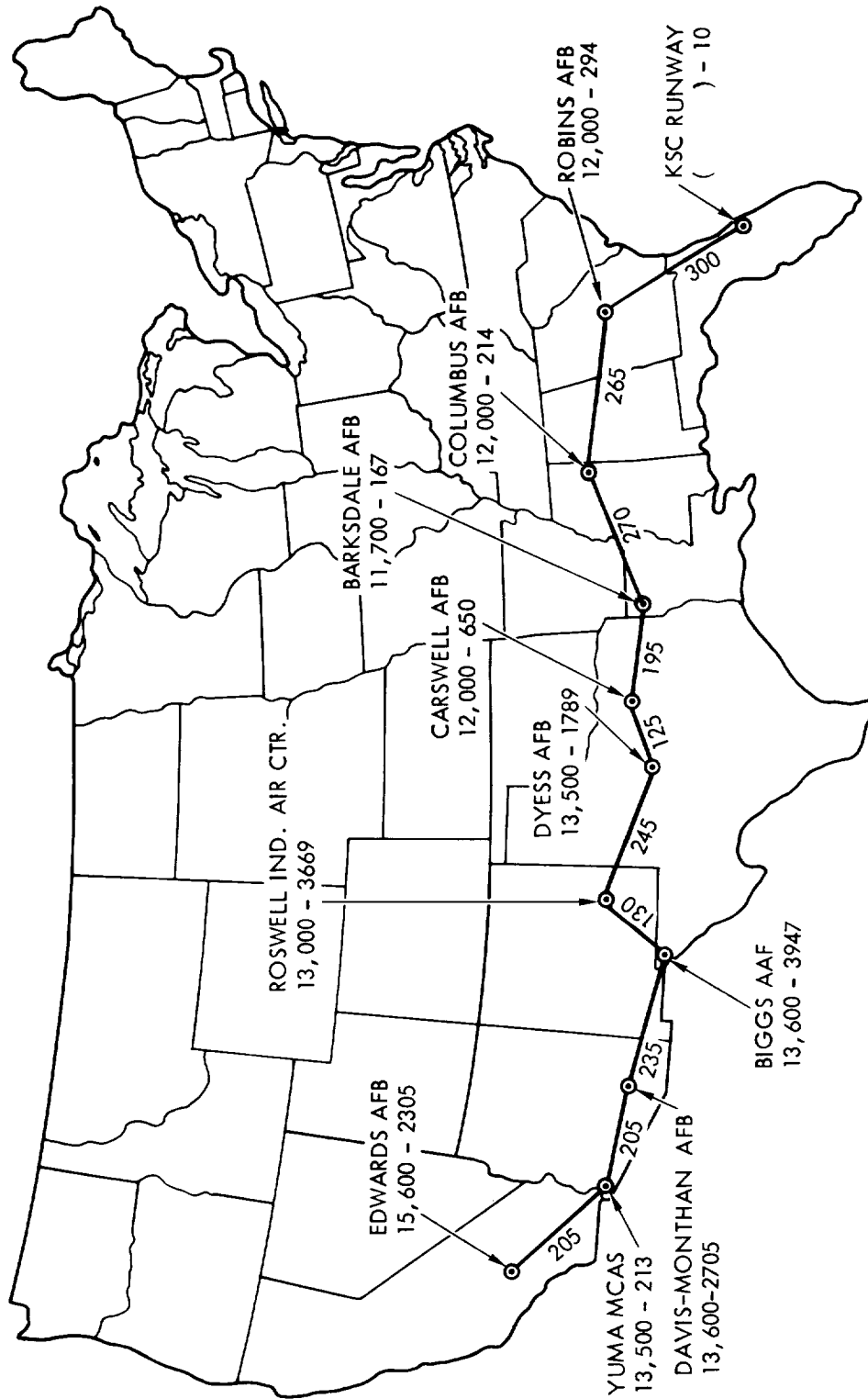
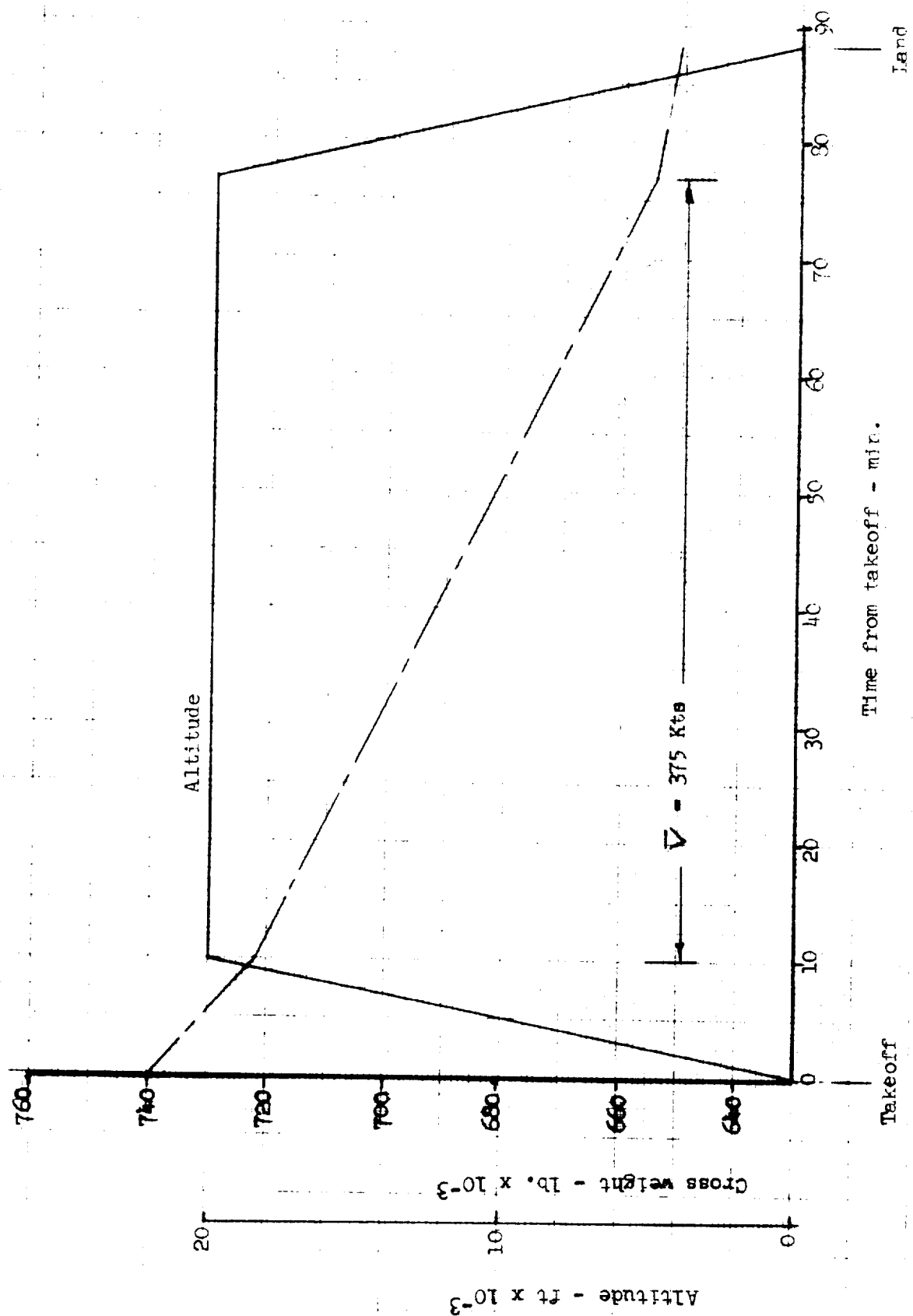


Figure 2-4. Transcontinental Ferry Route



Figure 2-5. Typical Ferry Mission Profile



B-9U Ferry Configuration

The B-9U ferry configuration is a modification of the baseline configuration that includes a tail cone which eliminates the blunt base region and improves the aerodynamic efficiency significantly.

Four rocket engines are removed for ferry operations to maintain the required balance. This results in an overall weight reduction of 8000 pounds. For ferry performance calculations, the following range of weights was used:

	Pounds
W_{\min}	= 631,828
W_{fuel}	= 143,786
W_{\max}	= 775,614

Typical Mission Profile

The characteristics of a typical ferry mission are given in Figure 2-5. These characteristics are based on the following operating modes.

For ferry takeoff the canard is set at $\delta_c = +10$ degrees and control is provided with the elevon. The ground roll attitude is equivalent to an angle of attack of $\alpha = -2.7$ degrees. At sea level under hot day conditions the maximum takeoff gross weight is limited to 724,000 lb for a 10,000-foot runway. At 4000 feet under hot day conditions, the maximum takeoff gross weight is limited to 765,000 lb for a 13,600-foot runway.

Climb performance is based on the air-breathing engines operating at maximum continuous power and the vehicle trimmed at an attitude that results in a maximum rate of climb at a given gross weight and altitude. A cruise altitude of 20,000 feet provides maximum specific ground range. Descent performance is based on operating at $(L/D)_{\max}$ with idle power.

2.3 BOOSTER CONFIGURATION

2.3.1 General Arrangement

The booster is shown in three view in Figure 2-6. The layout shows the external shape, major component arrangement, and the overall dimensions of the booster. A perspective cut-away drawing is given in Figure 2-7 which shows the general arrangement and structural configuration.

The B-9U booster is a low, delta wing vehicle with a single vertical tail and a small canard surface mounted forward above the body centerline. The body is basically a cylinder with fairings added to streamline the intersections with the aerodynamic surfaces.

Twelve main liquid-oxygen/liquid-hydrogen (LO_2/LH_2) high-chamber-pressure rocket engines of 550 thousand pounds sea level thrust each are installed in a cruciform pattern in the body base. These engines have an expansion ratio of 35:1 with ± 10 -degree gimbal provided for thrust vector control. Twelve turbofan engines, used for the subsonic flyback approach and landing, are shown in the extended position below the wing and body.

The landing gear is shown in the down position. The dual-wheel, steerable-nose-gear assembly and the two four-wheel-bogie main landing gear assemblies are of conventional design. The main gear retracts forward in a manner to avoid flow interference with the air-breathing engine inlets.

The crew compartment is conventionally located in the forebody. Visors are used to protect the forward windshields during the boost and entry flights.

Internally the booster is arranged with the LO_2 tank forward and the LH_2 tank aft. The tanks are of aluminum alloy, and they provide the primary load-carrying structure of the booster as well as functioning as pressure vessels. The tank diameter is 33 feet. The tanks are joined by a cylindrical intertank section that supports the canard pivot point and the forward attach links to the orbiter. The aft end of the LH_2 tank picks up the cylindrical thrust skirt, which is also 33 feet in diameter and includes truss-type thrust beams that intersect to form the main engine thrust pad/gimbal support points. The forward end of the LO_2 tank supports a tapered skirt that terminates in a bulkhead that supports the nose landing gear (Station 1339). The main landing gear is supported from trunnion points on external frames attached to the LH_2 tank. All the structural frames are external to the main tanks. The LH_2 tank is internally insulated. The orbiter forward attach points are at the aft LO_2 dome/intertank joint and take the axial loads as well as pitch and side loads, while the aft attach points, which take pitch and sideloads only, are at Station 2666 in the LH_2 tank region (Section C-C). The top of the booster is flat in the stage interface region to fair out the attach frames of the booster and to accommodate the booster linkage after separation.

The outer heat shield provides an aerodynamic surface for the body, which varies from a circular cross section at the nose gear station to a gradually flattening lower surface-transitioning into the wing fillet. The heat shield is also formed to provide the fairing to the fully pivoting canard at Station 2024, as well as the fairing for the orbiter interface. The heat shield is primarily of shallow corrugated frame stiffened panels utilizing Rene' 41 alloy principally, and titanium alloy in the regions of lower aerodynamic heating. The heat shield is supported via links from the primary structure to allow for expansion. The forebody ahead of Station 1479 is supported as an extension of the heat shield itself and moves with it, except for the nose gear that, as previously explained, is supported from an extension skirt on the primary load-carrying LO_2 tank.

The delta wing is mounted below the LH_2 tank. The wing carrythrough spars are reduced in depth in the center section to allow the wing to overlap the tank in the side view and thus minimize base area. The wing

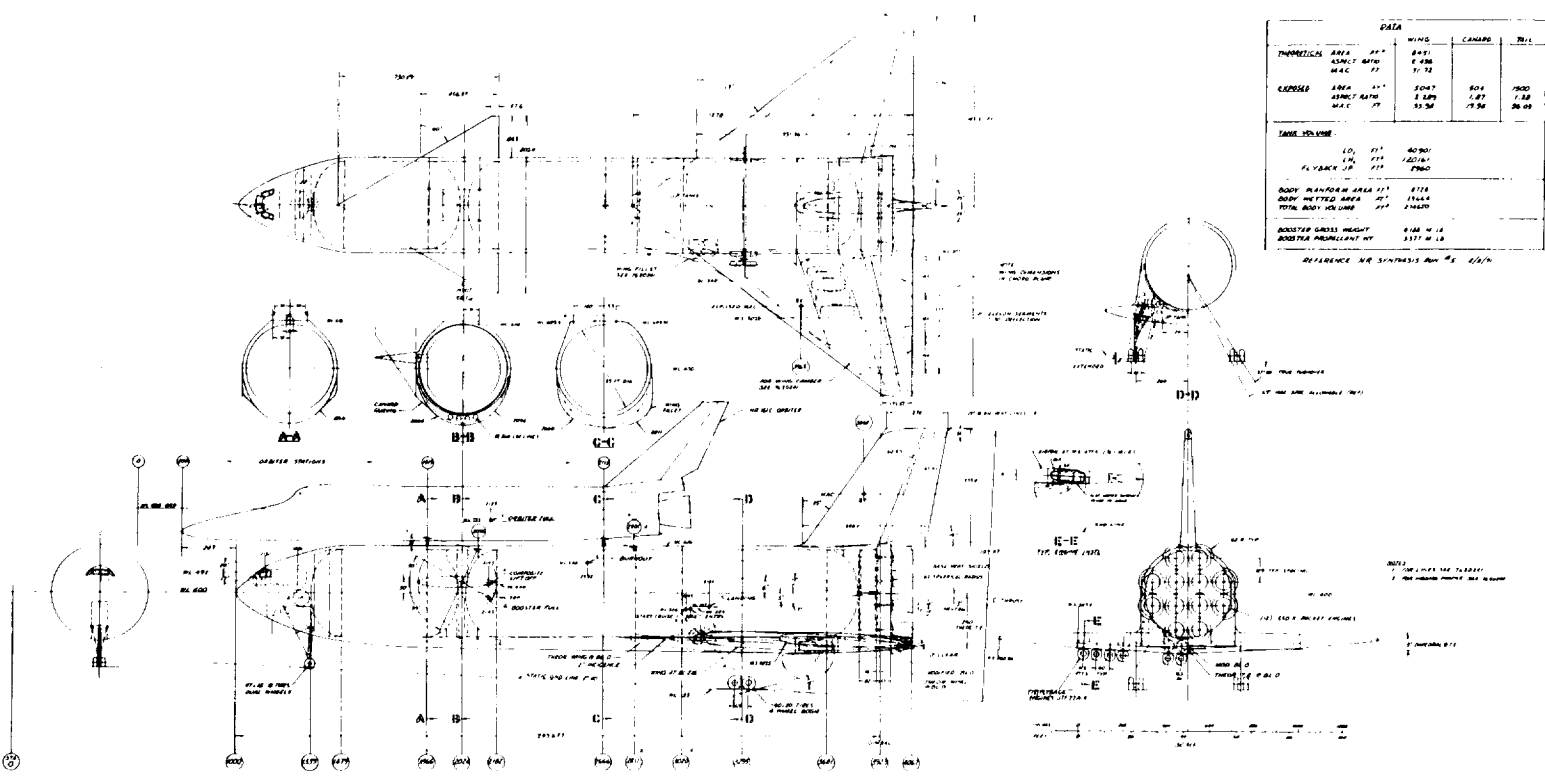


Figure 2-6. B-9U Booster Basic Configuration

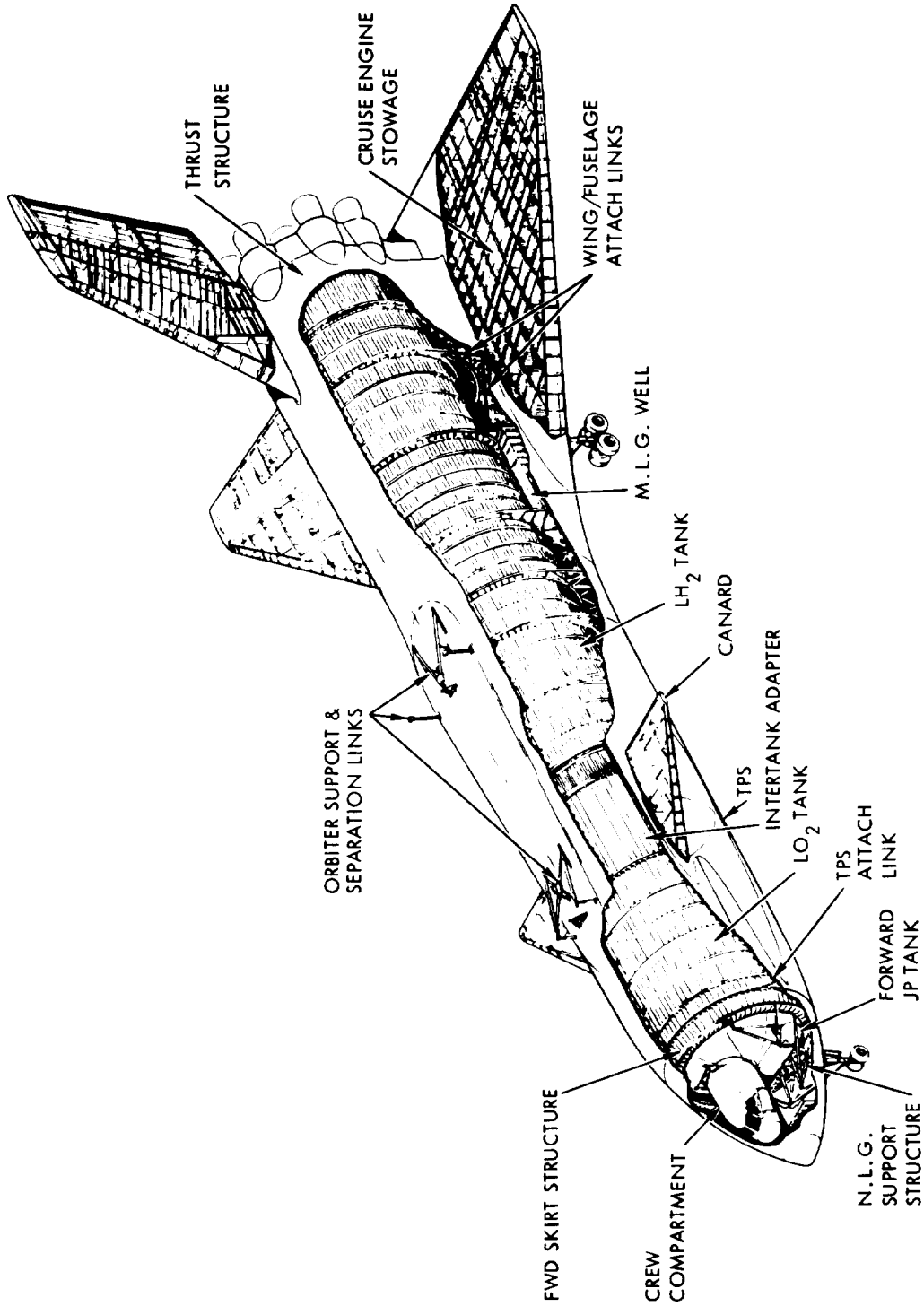


Figure 2-7. B-9U Booster Structural Arrangement

attaches to the hydrogen tank frames and to the thrust structure via a series of links designed to take out relative expansion differentials between the wing and the body.

The delta wing has a theoretical area of 8451 sq ft and an exposed area of 5047 sq ft installed at +2-degree angle of incidence to the body centerline to facilitate cruise and to reduce landing angle within the constraints of the boost loads on the wing. The leading edge sweep is 53 degrees. The installation of the JTF22A-4 air-breathing engines in the wing requires a maximum thickness chord ratio of 10.3 percent at wing Station 507.5 just outboard of the outboard engine. Installation of these engines below the body in the center section requires a 7.1-percent theoretical root thickness at the vehicle centerline. The airfoils are NASA four digit series with modifications to the leading edge radii and with conical camber at the tips to improve L/D. The trailing edge of the wing is perpendicular to the body centerline with elevons segmented into three spanwise parts for varying degrees of control. The wing structure is primarily titanium alloy with two main structural boxes. The forward box accommodates the airbreathing engines. The lower surface of the wing is thermally protected by a system of dynaflex insulation with metallic radiation cover panels.

The vertical tail is located on the body centerline. It has an area of 1500 sq ft with a leading edge sweep of 35 degrees to provide orbiter separation clearance consistent with weight and aerodynamic considerations. The tail thickness varies from 13 percent at the root to 11 percent at the tip. A 35-percent chord rudder is provided with ± 25 degrees of travel. The base of the rudder is cut off at 15 degrees to provide clearance for the upper rocket engines. Vent and exhaust lines are terminated at the fin tip trailing edge. The leading edge of the vertical tail has increased material thickness to act as a heat sink during the brief period of plume impingement during orbiter separation.

The canard provides a total exposed area of 504 sq ft. The leading edge sweep is 60 degrees and the thickness is 14 percent. The entire surface is pivoted at 56 percent of the root chord and moves 65 degrees nose down to decouple the effect of the surface during hypersonic entry. The surface wipes a body fairing to maintain a seal at all points along the down travel. This seal is to minimize entry heating. Upward travel of the leading edge of the canard is 30 degrees.

The main landing gear retracts forward into the wing fillet region. The main gear bogies incorporate 60-inch x 20-inch 40 PR tires. The nose gear has dual 47 x 18 tires.

Four main LO₂ lines are routed through the lower body main structure/heat shield interspace, past the main landing gear and aft to the vehicle base.

The outboard rocket engine powerhead packages are protected by local fairings tailored to keep the base area reduced to a minimum. A base heat shield is provided across the entire base station in the plane of the engine throats.

The crew compartment is conventionally located. Swivel seats adjustable for the vertical flight, entry, and cruise flight are provided for the captain and co-pilot, in conventional locations. The crew compartment is pressurized for shirtsleeve environment. Heat shields are provided over the windshields, which are sized for adequate landing visibility at the maximum 15-degree touchdown angle. Access with the booster in the vertical position is via a door to the left of the pilot seat. Access with the booster in the horizontal position is via a door in the compartment floor reached through the nose-gear wheel well. Aft of the crew compartment are the booster avionics systems installed in a controlled environment but separate from the crew compartment. Below the crew and avionics compartments is the nose-gear wheel well. The attitude control propulsion system (ACPS) engines are installed at Station 1300, eight on each side for yaw and four on top for pitchdown. (Pitchup and roll are provided by five engines on each wing.) The ACPS engines use LO_2/LH_2 propellants and deliver 2100 pounds of vacuum thrust each.

The flyback JP fuel is contained, as shown, in two compartments under the body between the main landing gears and in a tank in the nose. The fuel is fed to the four JTF22A-4 airbreathing engines under the body at Station 3560 and to the four similar engines in each wing.

Four auxiliary power units are installed in the wing root and ahead of the airbreathing engine bays and are accessible through doors in the wing upper surface.

The airbreathing engines are installed in podded configurations, pivoted at the aft support point. Each engine assembly has its own deployment rotary actuators. Longitudinal doors in the lower surface open to allow deployment of the airbreathing engines to the subsonic cruise position. The engines rotate through 180 degrees to the locked-extended position. Upon engine deployment the engine bay doors close to present a clean surface for cruise and landing.

2.3.2 Body Structure

The load-carrying body structure consists of five component assemblies which are bolted together to comprise the assembled structure. They are:

1. Forward skirt structure.
2. Liquid oxygen tank.
3. Intertank adapter.
4. Liquid hydrogen tank.
5. Thrust structure and base heat shield.

All of the components, except the thrust structure, are fabricated from aluminum alloy. The thrust structure is built of titanium and utilizes boron-aluminum composite materials for selected structural elements to

reduce weight and to increase stiffness. The base heat shield is coated columbium and Rene' 41. Its supporting structure uses titanium, Rene' 41 and tubular members of beryllium.

The wing (including the airbreathing engines), vertical stabilizer, canard surfaces, nose landing gear, rocket engines and the orbiter are attached to the basic body structure. The body is a "cold" structure while the aerodynamic surfaces are "hot" structure. Attachment method allows for thermal expansion of the hot structures with minimum restraint from the body. This is accomplished by the use of axially loaded links in correct number and orientation to carry all load combinations. All links contain mono-ball end fittings to preclude lateral restraint.

The enveloping body thermal protection system is a "hot" structure and is attached to the body structure by a series of fixed and linked connections. Air loads and inertia loads from the thermal protection system shells are applied to the body structure through these connections. The crew compartment is integrated with the forward segment of the body thermal protection system.

Forward Skirt

The forward skirt structure is shown in Figure 2-8. It consists of two stiffened aluminum alloy shells, one a short cylindrical section, the other a short conical section, and machined aluminum alloy frames. A circumferential pattern of tension bolts at the skirt's aft edge attaches it to the forward end of the liquid oxygen tank. The main trunnion of the nose landing gear is supported by the forward frame and a truss arrangement of tubes supports the upper end of the landing gear drag strut from the two frames. Vertical and side loads from the nose gear are introduced into the shell by the two frames. Longitudinal loads are introduced directly into the shell by back-up members behind the main trunnions. Sheet metal frames stabilize the skin/stringer shell between the machined load-introduction frames.

A cylindrical JP fuel tank is supported from the forward frame of the skirt. Vertical support loads are passed to the skirt shell through the deepened lower segment of the frame; longitudinal loads are carried to suitable stiffeners on the shell skin. Side load brace tubes are provided at each end of the tank.

The most forward attachment of the thermal protection system is also made through the skirt structure. Vertical links on each side and rollers, in tracks, at the top and bottom carry vertical and lateral reactions from the thermal protection system into the shell. There is no longitudinal restraint for the thermal protection system at this station.

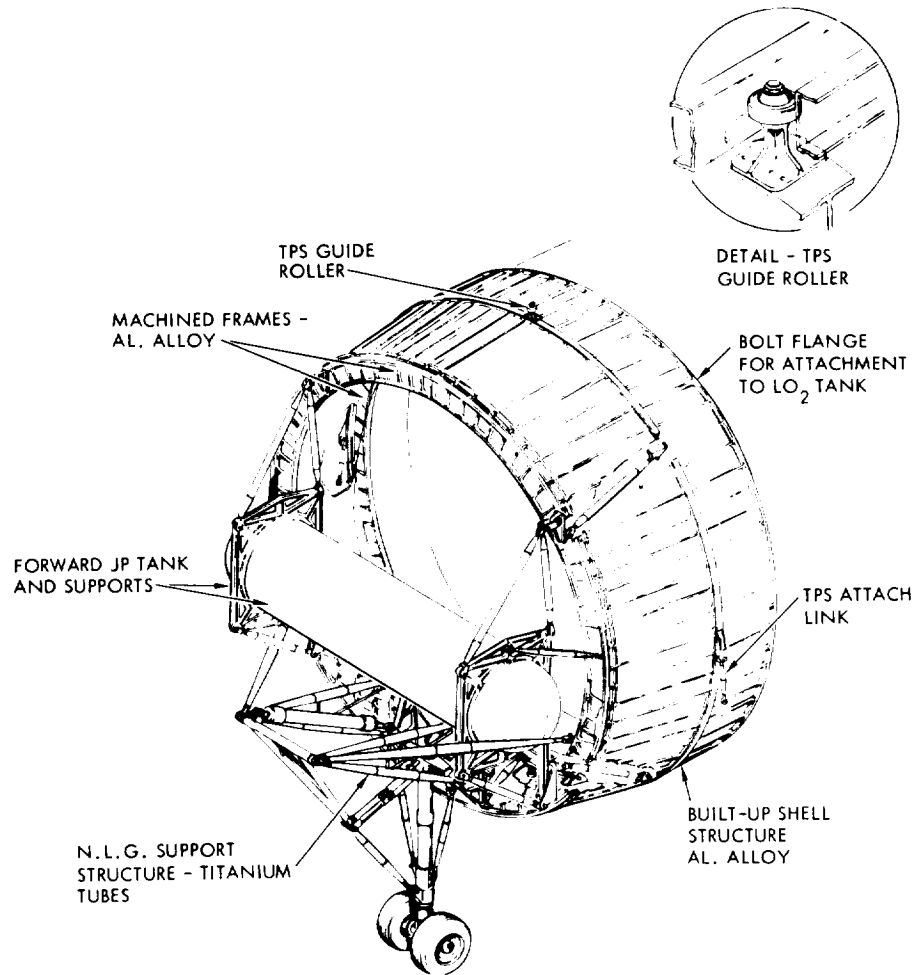


Figure 2-8. Forward Skirt Structure

LOX Tank

The liquid oxygen tank is designed largely by internal pressure resulting from the high density of the oxidizer and the axial accelerations of the vehicle. Bending moments are not as great as those further aft in the liquid hydrogen tank.

The oxygen tank is a welded assembly of 2219T87 aluminum alloy with forward and aft circumferential bolt patterns for joining it to the forward skirt and to the intertank adapter structures. Tank wall segments, with integral stringers, are milled from aluminum alloy plates, age formed to radius and butt welded together to make the cylindrical tank section.

End bulkheads are ellipsoidal ($\sqrt{2}$ diameter ratio) consisting of gores edge-welded together. The bulkheads are welded to the ends of the cylindrical section. Pressurization inlet and vent ports are provided. An access door is installed in the forward dome. A cylindrical sump, from which four liquid oxygen ducts lead to the main propulsion system, is incorporated in the aft dome.

Stabilizing frames, external to the tank, are spaced at 77-inch intervals. The frames are built up of a series of V forgings riveted between an outboard T flange and the longitudinal stringers of the tank. The V's, in conjunction with the outboard flange and the tank wall, form a truss-webbed stabilizing frame. The frame is shown in detail in Figure 2-9.

Since the temperature of liquid oxygen will not liquefy air on the tank's exterior, no cryogenic insulation is installed.

The forward orbiter attachment station is at the tangency of the ellipsoidal dome with the cylindrical section of the oxygen tank. A machined aluminum alloy internal/external bulkhead is integrated with the tank wall at this station. To achieve maximum bulkhead depth, part of the bulkhead extends beyond the tank skin to support the forward orbiter attachment links. A projecting section of bulkhead, on each side of the booster, provides for two attachments between the booster and the launch tower. The tower supports the booster during high wind conditions and reduces body bending.

Intertank Adapter Structure

The intertank adapter is a shell structure with a circumferential bolt pattern at each end to match those on the aft end of the oxygen tank and on the forward end of the hydrogen tank. It is of aluminum alloy construction consisting of integrally stiffened skins and six frames. It is a mechanically fastened structure since liquid containment is not required. In addition to carrying body bending loads, orbiter longitudinal loads are transmitted to the booster via the intertank adapter. See Figure 2-10.

The forward pair of orbiter launch links, which are also the orbiter attachment drag struts, are hinged to a longitudinal fitting on each side of the intertank structure. The forward and aft ends of the fitting are supported by frames approximately 144 inches apart.

A webbed external bulkhead extends from the intertank shell to the inboard side of the thermal protection system and forms one of the fixed supports for the TPS. In addition, the bulkhead serves as a purge system barrier in the annular space between the shell wall and the TPS.

Two independent canard surfaces are supported by the intertank structure. The canard spindle extends inboard through the adapter skin and is supported by a pair of large diameter bearings, one outboard and

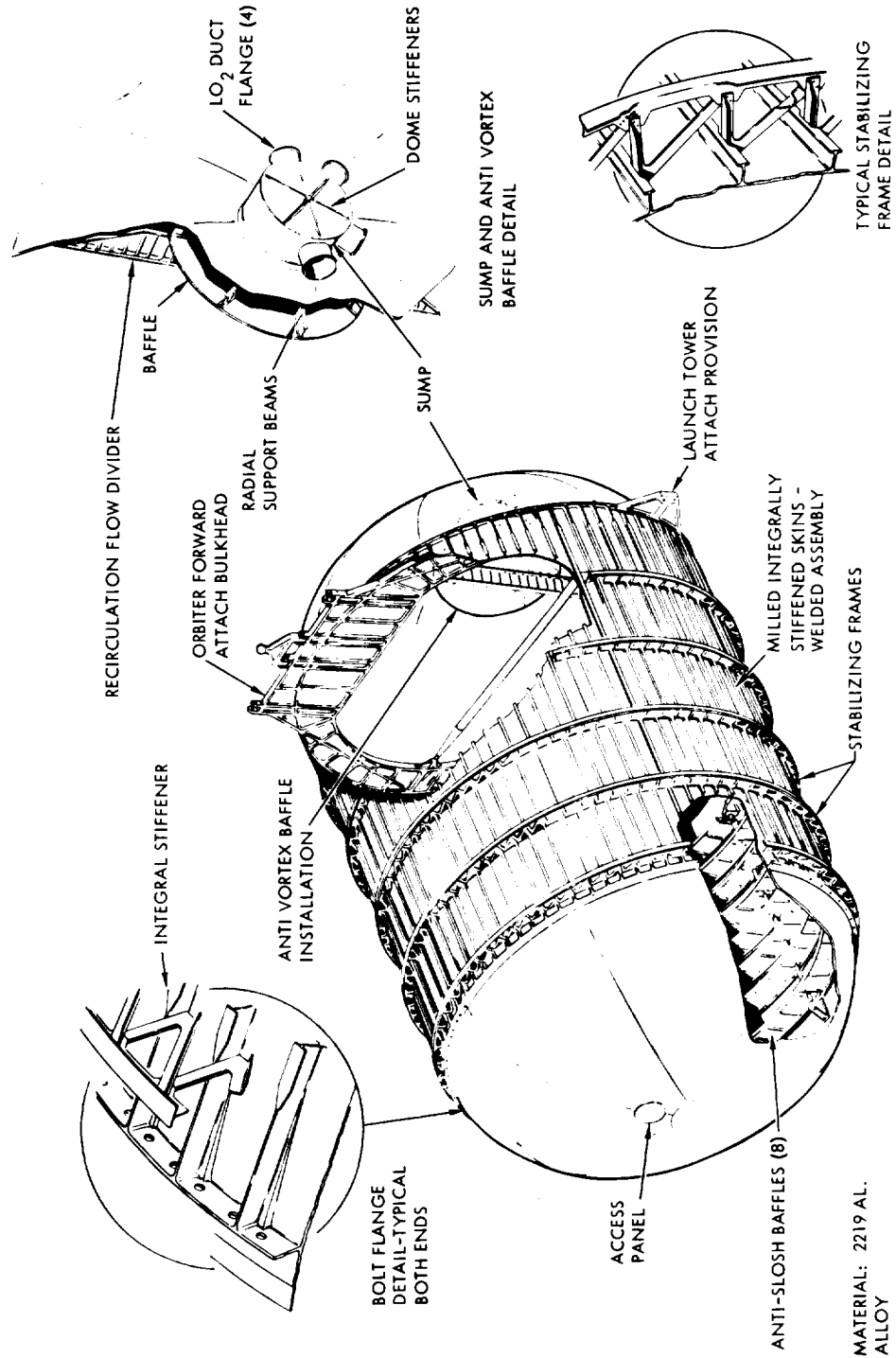


Figure 9. B-9U Liquid Oxygen Tank

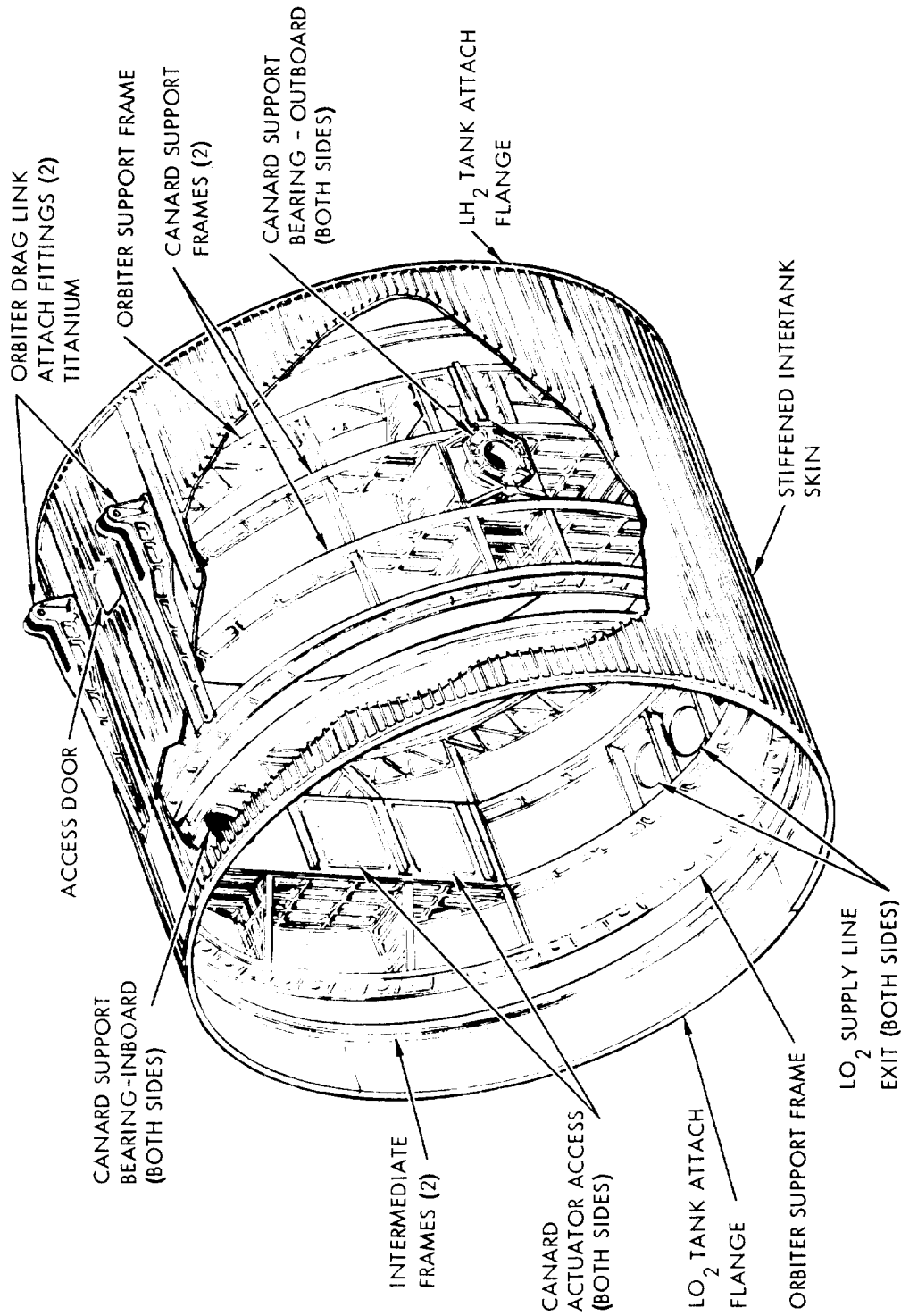


Figure 2-10. Intertank Adapter Structure

one inboard. The bearing housings are supported between a pair of frames inside the intertank structure. The hydraulic actuator cylinders are also supported by the frames.

The liquid oxygen ducts pass through the skin of the intertank adapter near the bottom of the vehicle and are routed aft between the body structure and the thermal protection system.

LH₂ Tank

The liquid hydrogen tank is shown in Figure 2-11. In construction it is similar to the liquid oxygen tank though the integral T-section stringers are more closely spaced to develop higher compression allowables. Polyphenylene oxide foam bonded to the inside of the tank wall provides cryogenic insulation and prevents condensation of liquid air on the exterior surface.

External tank stabilizing frames are of the built-up type described for the liquid oxygen tank.

An access door is provided in the forward bulkhead of the liquid hydrogen tank.

The orbiter aft support links and the aft separation system links are attached to the tank shell through two external frames machined from 2219 aluminum alloy plate. A circumferential band of thickened tank skin forms the inboard flange for each of these frames; the skin band also incorporates a vertical circumferential rib. A frame web/circumferential rib weld completes the frame installation. All tank frames for the introduction of concentrated loads into the tank shell are of similar construction.

Wing attachment is made by three vertical links and one longitudinal drag link on each side of the body. Three lateral load links also attach the wing to the tank and to the thrust structure. The links contain spherical bearings at each end and carry only axial loads. The wing is able to deflect under load and temperature gradients with minimal restraint from the fuselage.

Thrust Structure and Base Heat Shield

The thrust structure is a stiffened shell and is bolted to the aft end of the liquid hydrogen tank. It contains two transverse trussed-type bulkheads spaced 82 inches apart. These bulkheads distribute loads into the shell structure from the vertical stabilizer, the aft wing attachment struts, and the gimballed rocket engines. Trusses in longitudinal planes between the bulkheads comprise four thrust beams to which the rocket engines are attached. See Figure 2-12.

Intermediate circumferential frames stabilize the shell.

Four fittings, external to the thrust structure shell, support the booster/orbiter in the vertical launch position.

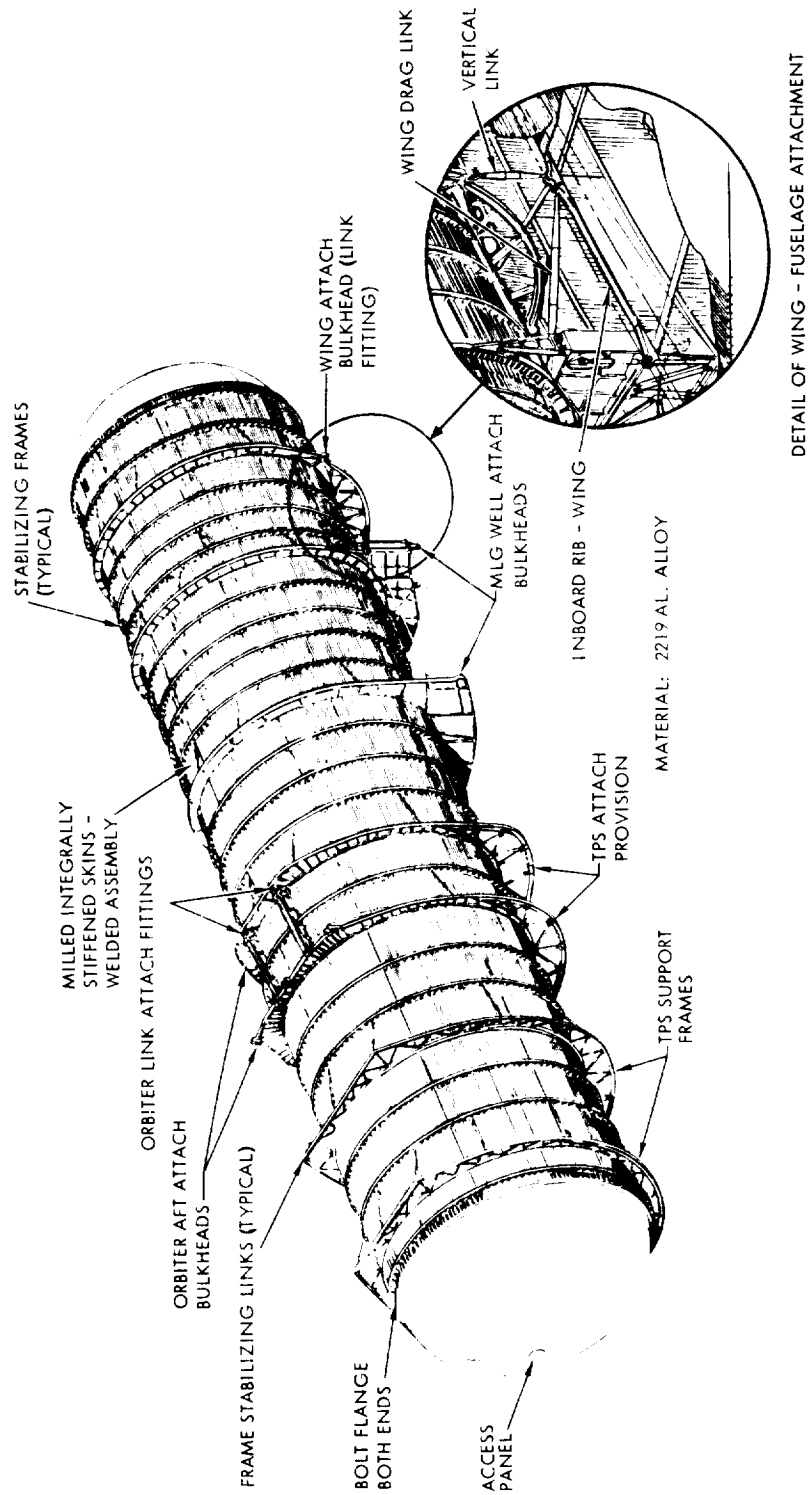


Figure 2-11. Liquid Hydrogen Tank

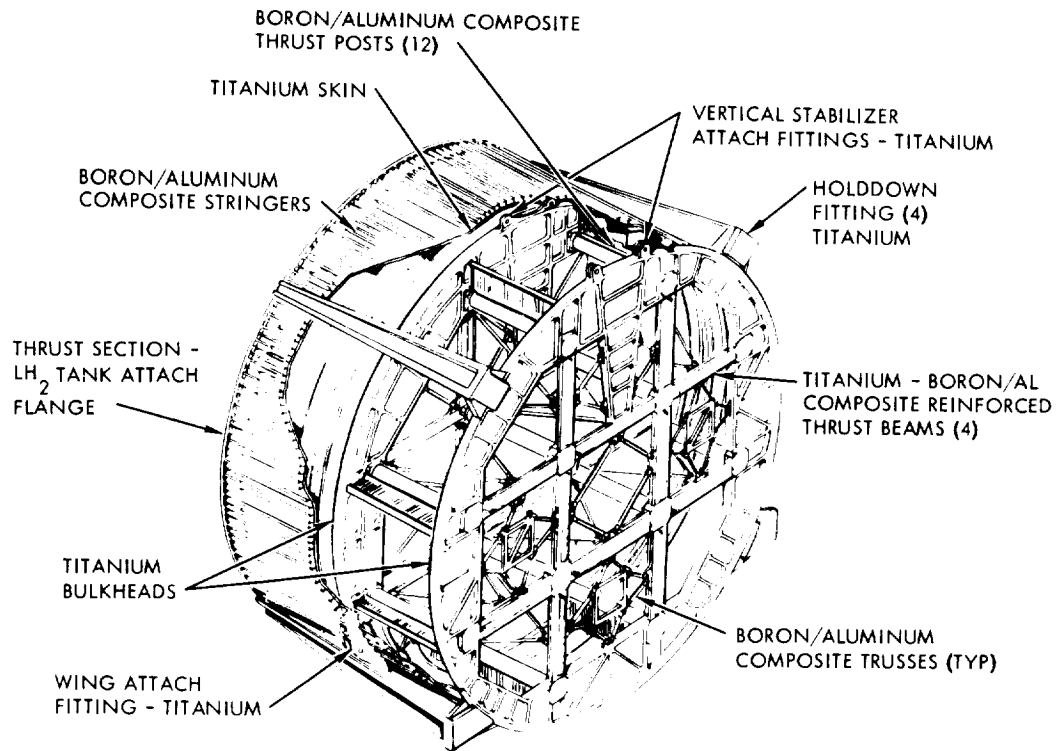


Figure 2-12. Thrust Structure

Spherical segments are installed on each rocket engine to provide a sealing surface for deflected engine positions. A mating ring and seal for each engine is supported from the aft structural bulkhead of the thrust structure. A heat shield consisting of corrugated panels and backed by insulation material is installed between and supported from the seal rings. The circumference of the base heat shield is defined by the rocket engine fairings. The skin extending forward of the base heat shield is part of the body thermal protection system.

Crew Compartment

Figure 2-13 illustrates the general structural arrangement of the crew compartment. It is a semi-monocoque structure incorporating rings and longitudinal stringers. Where possible, the structure is installed on the skin exterior. There are four openings in the structure: the windshield, the aft compartment access hatch, and two hatches opposite the pilots seats. The module consists of two compartments, the pilots station and the electronics compartment. These compartments are separated by an internal bulkhead. The aft end of the module is closed by an ellipsoidal bulkhead. The electronic compartment is cylindrical in section while the crew compartment is faired to maintain as much curvature as is compatible with the hot nose structure contour and internal furnishing envelope.

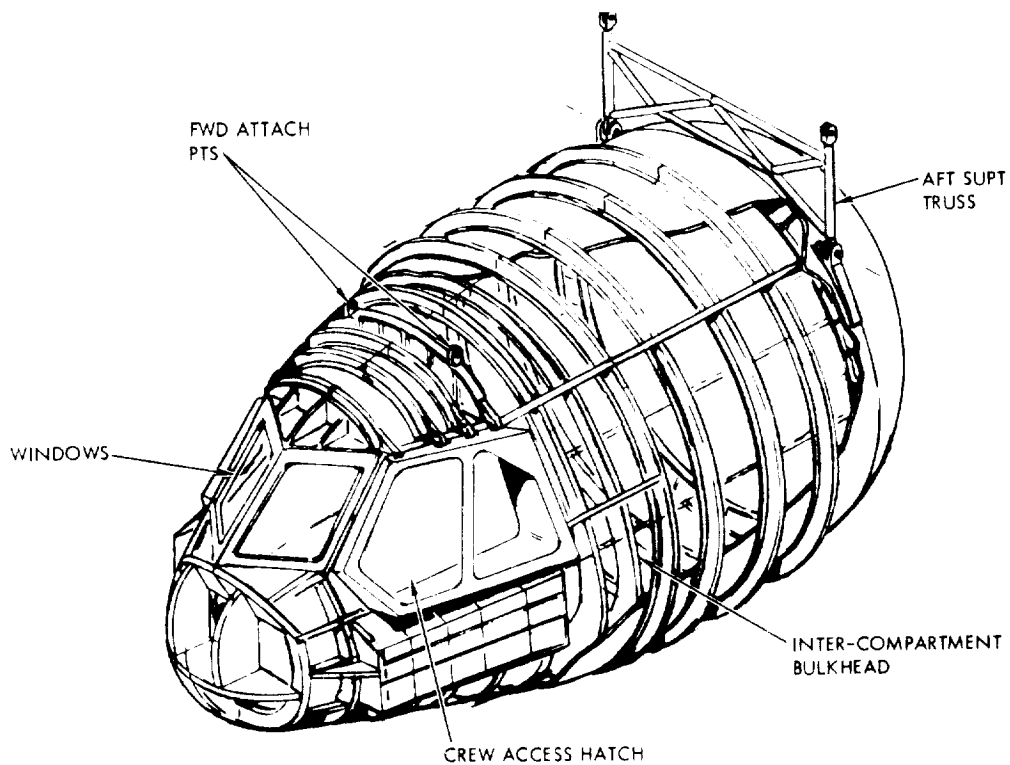


Figure 2-13. Crew Compartment

The compartment is supported by the hot nose shell structure at four points: at two points just aft of the crew compartment hatch and at two points on the frame at end of the electronics compartment. The gap between the nose structure and the crew compartment at the aft support is spanned by a pin ended truss. This truss will minimize thermal loads on both the nose structure and the compartment structure as the outer shell expands.

The structural material of the crew compartment is aluminum alloy except in those areas where the hot nose structure is in close proximity to the compartment structure. In these regions, such as the windshield frame and the pilot's hatches, the structure will be fabricated from 6 Al-4V titanium alloy. With the exception of the glazed areas the entire compartment is shrouded by a fibrous insulation blanket. The inner door windows are fabricated from heat tempered glass. The outer door windows are made from fused silica glass. The windshield is a laminated glass with an electrically conductive film for anti-icing. The floor and the bulkhead separating the electronics compartment from the crew station consist of aluminum alloy honeycomb panels backed up by a grid work of beams.

2.3.3 Aerodynamic Surfaces

Wing

The wing structure is shown in Figure 2-14. The wing structural arrangement is a fail-safe multi-spar, multi-rib configuration utilizing open corrugation cover panels on the upper surface and a thermally protected lower surface. The corrugations are positioned in a chordwise direction to minimize thermal stresses by accommodating skin expansion relative to the spar caps. The covers transmit air loads to the spars and reacts wing torsional loads. The wing has a hot leading edge, two primary structural boxes, an under-body carry-through and trailing edge elevons. Titanium alloy 6 Al-4V is used for the wing box structure. Boost phase venting is accommodated through the gap between the elevon and the fixed trailing edge upper surface. The wing inboard closing bulkhead redistributes spar shear loads to wing-to-body support fittings and the wing loads are reacted to the body through wing-to-body attach links. The corrugated bulkhead shear web allows for differential chordwise thermal expansion and the attach links accommodate wing deflection and relative thermal expansion between wing and body. Twelve flyback airbreathing engines are submerged in the wing structure during boost and recovery and are deployed for subsonic cruise and landing.

The main JP fuel tank is located just forward of the wing carry-through structure between the body TPS and the LH₂ tank. The JP tank is supported from the LH₂ tank and the MLG support structure and is protected by the TPS. The tank is constructed of aluminum alloy honeycomb sandwich panels with aluminum ribs and beams.

Canard

The canard structure is shown in Figure 2-15. The canard is a fully movable surface. The structural box is a multi-spar, multi-rib configuration

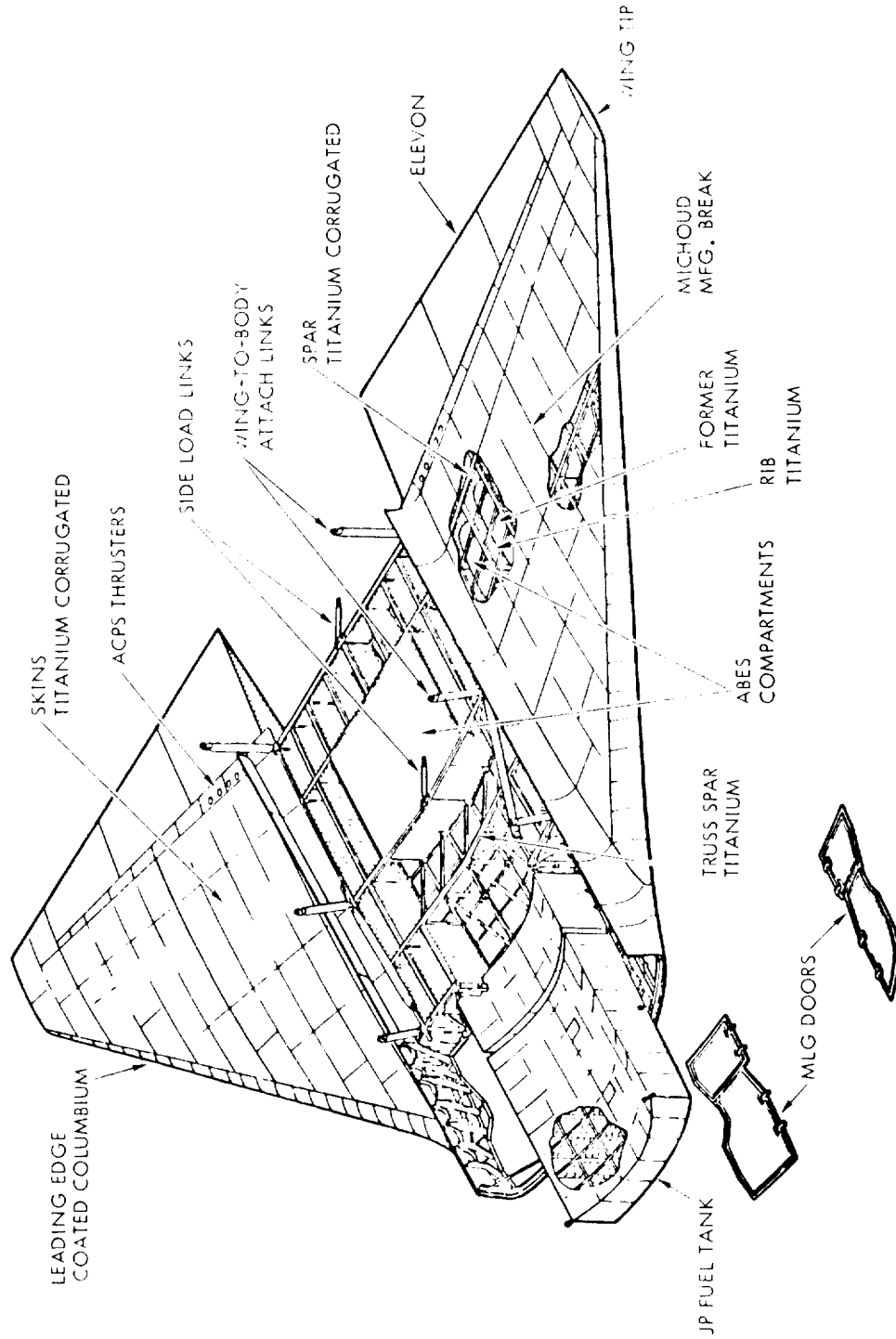


Figure 2-14. Wing Arrangement and Support Points

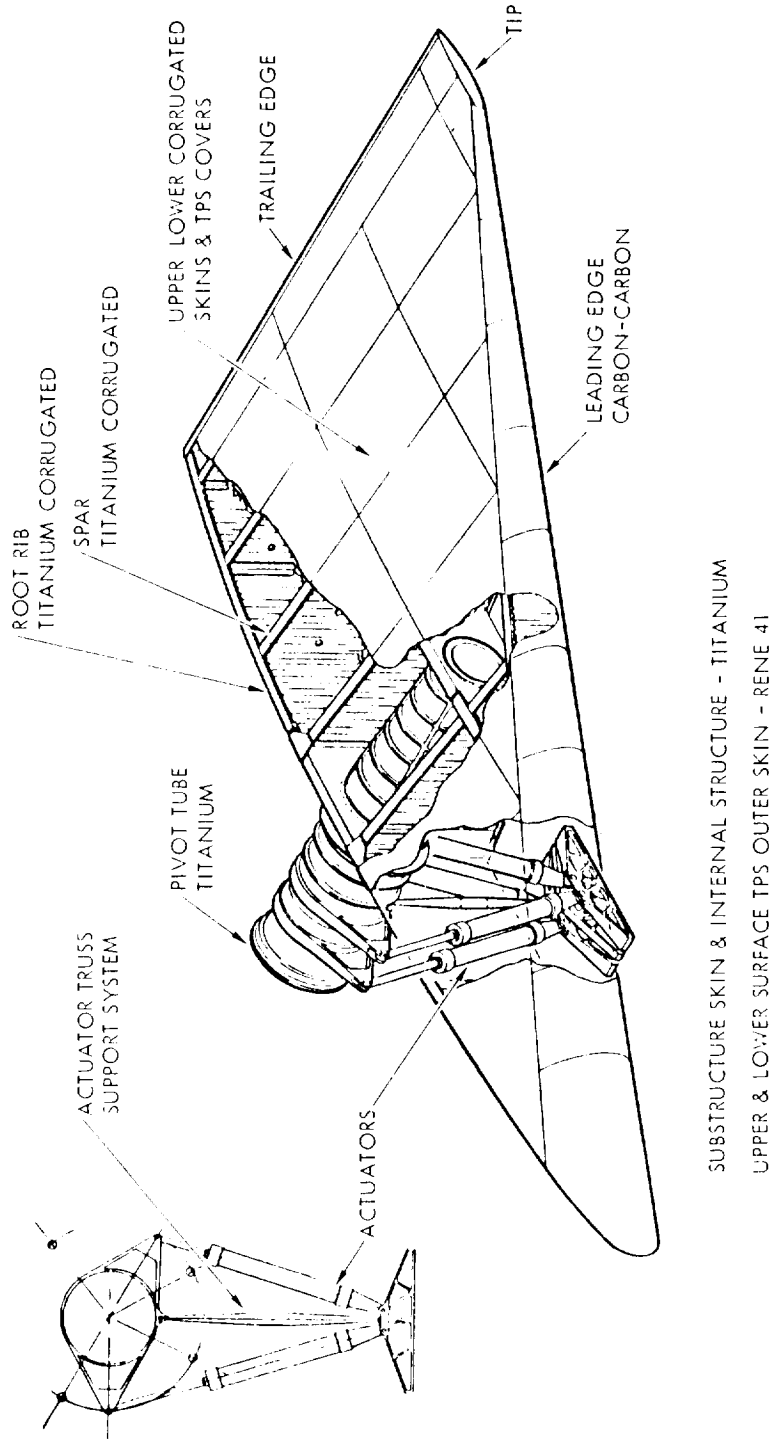


Figure 2-15. Canard Structure

with corrugated titanium structural skins supported on a welded, corrugated shear web substructure. The structural skins are protected with a TPS. The TPS consists of an insulation material and a semi-smooth outer skin supported from the structural skin by standoffs. The corrugated shear webs of the spars and ribs accommodate differential thermal expansion. A slotted-hinge leading edge is used to allow for spanwise thermal expansion relative to the front spar. The structural box is fixed to a pivot tube at the inboard rib. The outboard pivot tube/rib attachment is a sliding joint to accommodate differential thermal expansion between the pivot tube and the outer surfaces. Bending loads are carried through the pivot tube and reacted through two bearings supported in the intertank structure. Spherical self-aligning bearings are employed to allow for structural deflections. Venting is accommodated through the pivot tube into the intertank structure and then through the body vent ports.

Vertical Stabilizer

The vertical stabilizer structure is shown in Figure 2-16. The vertical stabilizer structural arrangement is a three-spar, multi-rib configuration with integrally stiffened skin/stringer panels. Spar and rib webs are of corrugated or trussed construction to allow for differential thermal expansion. The rudder is of similar construction. The entire structure is 6 Al-4V titanium except for the leading edge which is Rene' 41. The segment of leading edge that is subjected to the orbiter engine exhaust impingement is "heat sink" designed to withstand the increased temperature. Vertical stabilizer bending loads are reacted through spar-to-thrust-structure attach fittings at the center and rear spar. Torsional loads are reacted at the front spar pin joint and the rear spar attach fittings. The APU exhaust and the hydrogen vent lines are vented at the vertical stabilizer tip.

2.3.4 Body Thermal Protection System (TPS)

Figure 2-17 depicts an overall view of the baseline TPS adopted for the body of the booster. The TPS is a metallic radiative system which protects the load carrying primary structure to a peak temperature compatible with the aluminum structural material and the LH₂ tank insulation. No insulation is required to accomplish this. The TPS concept consists essentially of a separate stiffened shell that completely surrounds the basic primary structure. Support of the TPS shell from the primary structure is effected by two means. At each of three body stations, 2096, 2458, and 2811, the shell is rigidly attached around the periphery by mechanical fastening of the shell skin to the outer flanges of deep external primary structure frames. These attachments provide restraint of the TPS shell in all three axes. The restraint locations are selected to minimize thermal displacement of the shell relative to the canard pivot and the orbiter attachment fittings. The other method of support, in addition to the fixed supports, consists of a system of swinging links which attach the TPS shell to the primary structure and permit relative thermal growth longitudinally between these components. Forward of the fixed restraint at Station 2096, the entire forward section of the shell, including the hot nose structure, is free to expand longitudinally relative to the body primary structure. Support is provided by a link arrangement at Station 1423. The TPS shell

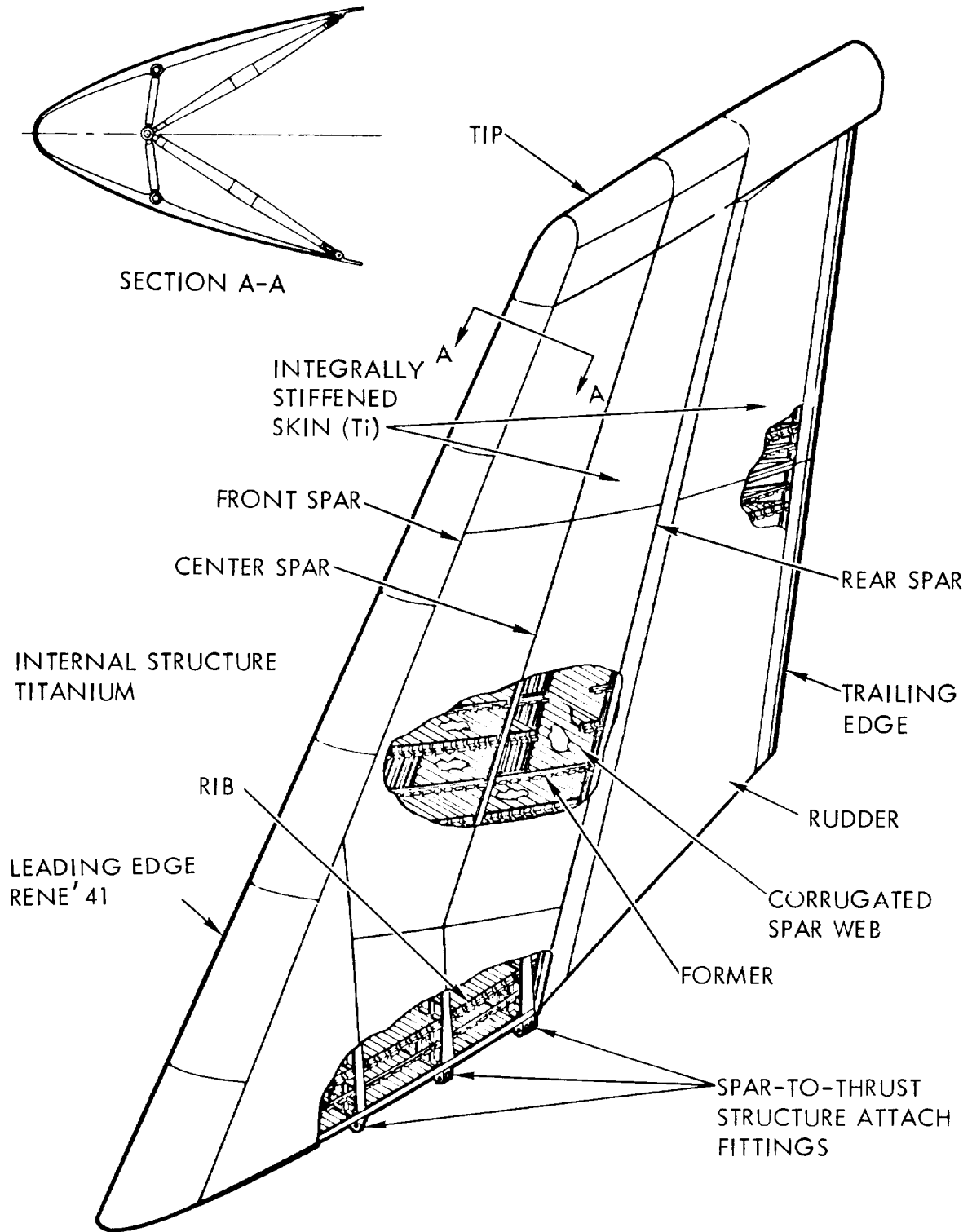


Figure 2-16. Vertical Stabilizer

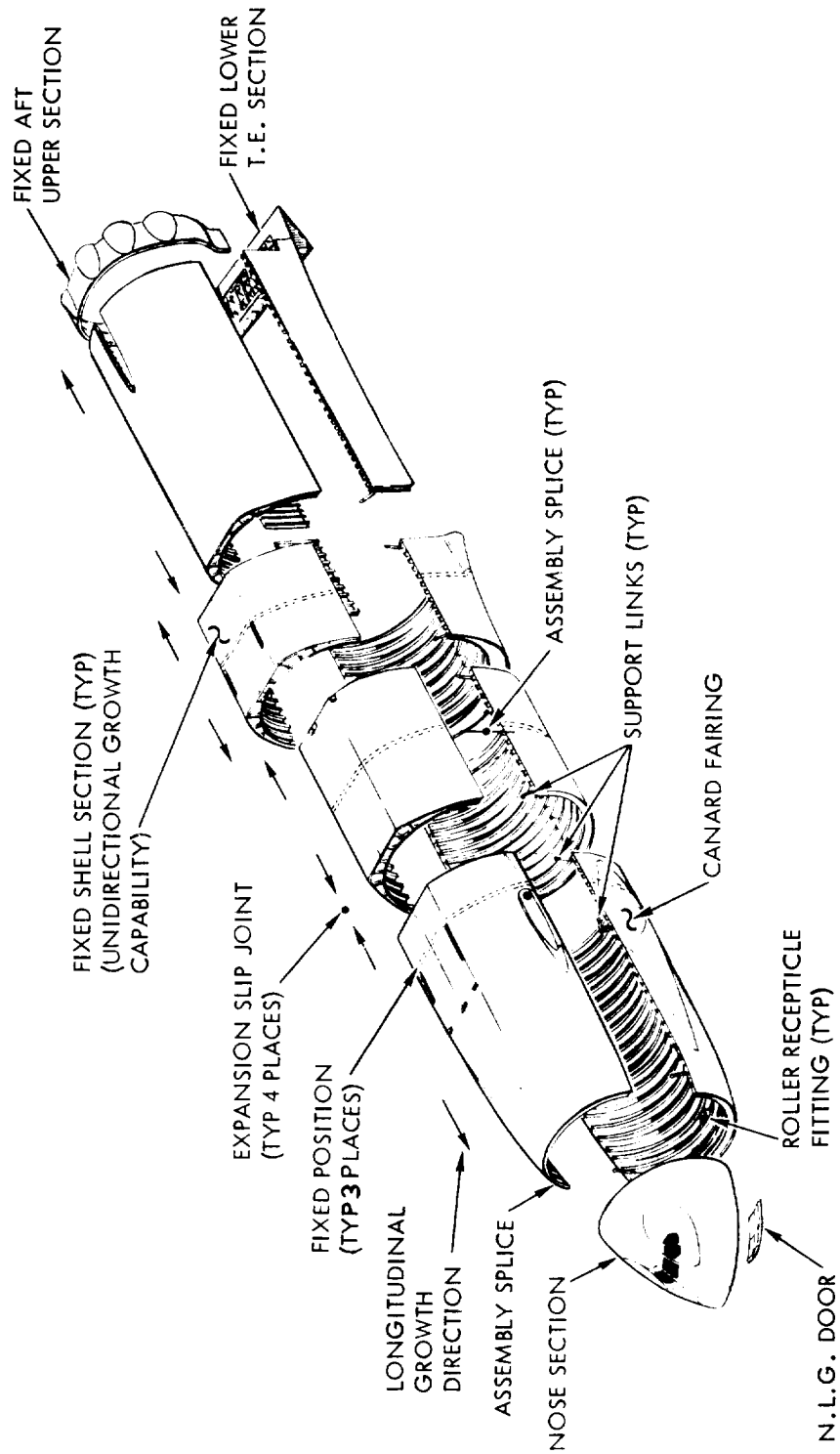


Figure 2-17. Body TPS Shell Structure



section over the wing is supported by the wing and is free to expand with the wing. Between the fixed stations, peripheral slip joints accommodate displacements due to the thermal expansion of the shell and the cryogenic contraction of the propellant tanks. Swinging links provide support for the free end of each section of the shell at each slip joint.

Each TPS shell section is essentially a frame-supported semimonocoque structure with open corrugation-stiffened skins. The primary loading on this shell structure is the lower surface air pressure induced by the hypersonic pull-out condition during booster recovery. The panel loads induced by this pressure are transmitted by the TPS frames to shear into the side walls of the shell and to be finally transmitted to the body primary structure by the system of fixed and link supports.

The TPS frames are stiffness critical since excessive in-plane deflection would cause interference with the propellant tank structure and subsystem components. A design that incorporates a material of high specific elastic modulus has therefore been adopted. The basic cross-section of the frame is an I section of aluminum, pocket milled to minimize web gages and to provide integral web stiffeners. To each cap of the aluminum section is attached a cap strip of beryllium to produce a frame design of high stiffness to weight ratio. The high specific heat of beryllium is also advantageous in that the beryllium strip adjacent to the hot outer skin provides a heat sink to absorb the "flash heating" effect characteristic of booster recovery and thereby create an acceptable temperature distribution through the frame.

The outer skin of the TPS shell features open corrugations to provide longitudinal stiffening and to accommodate circumferential thermal expansion relative to the cooler frames by flexing of the corrugations. Attachment of the corrugated skin to the frames is by mechanical fasteners in each of the "valleys" of the corrugation.

The TPS shell sections are further broken down into conveniently sized panel assemblies by the provision of bolted splices. This arrangement facilitates panel production, simplifies assembly, and allows periodic "in service" removal of individual panels for inspection and repair of the underlying structure and subsystems. As previously noted, individual skin panels within the panel assemblies are mechanically attached, a feature that will permit easy replacement or repair in service. In addition to these provisions, quick-open access panels will be located where required for the routine maintenance of subsystems.

2.3.5 Weight Summary

A summary weight statement for the B-9U booster is given in Table 2-2. Detail weight breakdowns for the wing group, vertical tail group, and body group are given in Tables 2-3, 2-4, and 2-5, respectively. All weight data are taken from Reference 2.

Table 2-2. B-9U Booster Weight Summary

	Weight (lbs)
Wing Group	70,875
Tail Group	20,634
Vertical Tail	13,121
Canard	7,513
Body Group	177,612
LH ₂ Tank	67,109
LO ₂ Tank	18,405
Thrust Structure	30,000
Other Body Structure	62,098
Induced Environmental Protection	72,031
Landing, Docking	27,361
Propulsion, Ascent	130,038
Propulsion, Cruise	46,404
Propulsion, Auxiliary	9,864
Prime Power	3,011
Electrical Conversion and Distribution	1,438
Hydraulic Conversion and Distribution	1,862
Surface Controls	7,889
Avionics	5,468
Environmental Control	1,475
Personnel Provision	985
Contingency	49,593
SUBTOTAL (DRY WEIGHT)	626,540
Personnel	476
Residual Fluids	11,534
SUBTOTAL (INERT WEIGHT)	638,550
Inflight Losses	22,080
Propellant - Ascent	3,382,307
Propellant - Cruise	143,786
Propellant - Maneuver and ACS	1,500
TOTAL BOOSTER WEIGHT AT LIFTOFF	4,188,223

Table 2-3. B-9U Booster Wing Group Weight Breakdown

	Weight (lbs)
Exposed Wing	54,203
<u>Structural Box</u>	29,469
Spars	14,550
Webs	4,176
Caps	6,868
Splices	3,506
Ribs	5,156
Webs	3,512
Caps	1,644
Upper Covers	5,360
Covers	4,378
Formers	982
Lower Covers	4,403
Covers	2,558
Formers	764
Engine Bay Formers	1,081
<u>Leading Edge</u>	3,996
<u>Trailing Edge</u>	681
<u>Secondary Structure</u>	11,678
Thermal Protection Skins, Insulation, and Standoffs	8,122
Fairings - Wing to Fuselage	1,000
Engine Bay Doors	2,108
Door Actuation	448
<u>Elevons</u>	8,379

Table 2-3. B-9U Booster Wing Group Weight Breakdown
(continued)

	Weight (lbs)	
Wing Carry-Through Structure		16,672
<u>Structural Box</u>		15,450
Spars		9,073
Webs	1,669	
Caps	7,404	
Ribs		4,333
Webs	2,498	
Caps	1,835	
Lower Covers		1,650
Covers	818	
Formers	292	
Engine Bay Formers	540	
Wing to Fuselage Attach Fittings		394
<u>Leading Edge</u>		622
<u>Secondary Structure</u>		600
Wing to Fuselage Attach Links		600
TOTAL WING GROUP WEIGHT		70,875
<p>NOTE: The wing carry-through lower surface coverings and doors blanked out by the fuselage act as body heat shield structure; therefore, their weights have been included under Induced Environmental Protection. The items allocated to Induced Environmental Protection include:</p>		
Belly Skins, Insulation, and Standoffs		3,765
Engine Bay Doors		1,054
Main Landing Gear Doors		<u>2,108</u>
	Total	6,927

Table 2-4. B-9U Booster Vertical Tail Group Weight Breakdown

	Weight (lbs)	
Structural Box		9,301
Spar Caps		779
Front	49	
Intermediate	351	
Rear	338	
Auxiliary	41	
Spar Webs		1,249
Front	146	
Intermediate	443	
Rear	464	
Auxiliary	196	
Ribs and Bulkheads		1,485
Root Rib	271	
Interspar Ribs	379	
Bulkheads	835	
Chordwise Stiffeners		567
Covers		4,517
Hinge Fittings (Integral with Spars)		168
Tail to Fuselage Attach Fittings and Fasteners		536
Leading Edge		866
Covers		292
Trusses and Supports		574
Trailing Edge		316
Covers		235
Stiffeners		30
Ribs		51
Tip		509
Rudder		2,129
TOTAL VERTICAL TAIL GROUP WEIGHT		13,121

Table 2-5. B-9U Booster Body Group Weight Breakdown

	Weight (lbs)
Main LH ₂ Tank	67,109
Forward Dome	1,947
Aft Dome	1,947
Barrel Section	57,290
Skin-Stiffeners	52,658
Frames	4,632
Baffles	575
Orbiter Attach Structure	5,350
Forward Bulkhead	1,650
Aft Bulkhead	800
Load Distribution (weight required for)	2,900
LH ₂ Tank Internal Insulation (PPO Foam)	7,168
Main LO ₂ Tank	18,405
Forward Dome	1,405
Aft Dome	2,902
Barrel Section	9,583
Skin-Stiffeners	9,138
Frames	445
Baffles	1,200
Orbiter Attach Structure	3,315
Forward Bulkhead	2,690
Load Distribution (weight required for)	625

Table 2-5. B-9U Booster Body Group Weight Breakdown
(Continued)

	Weight (lbs)
Nose Section	10,135
Forward Adapter Section	3,652
Intertank Basic Structure	14,141
Orbiter Bulkheads - Intertank Section	5,482
Thrust Structure	30,000
Skin Panels	9,579
Frames	2,470
Thrust Beams	6,284
Thrust Posts	3,060
Ground Fittings	1,332
Bulkheads	5,509
LO ₂ Line Backup	200
Tank Attach Bolts	250
Joints, Splices, and Fasteners	1,316
Other Miscellaneous and Secondary Structure	21,520
Crew and Avionics Compartment	1,800
Engine Heat Protection	5,235
Orbiter Attach and Separation Mechanism	3,655
Main Landing Gear and Wing Bulkheads	10,830
TOTAL BODY GROUP WEIGHT	177,612

3.0 STRUCTURAL DESIGN LOADS AND CRITERIA FOR BASELINE VEHICLE

3.1 STRUCTURAL DESIGN CRITERIA

Structural design criteria that are pertinent to the present study and are reflected in the characteristics of the baseline vehicle are summarized in the following sections. These criteria have been abstracted from Reference 3.

3.1.1 Design Philosophy

The basic structural design philosophy is that the structural components and elements shall be designed for minimum weight consistent with the required service life, degree of damage tolerance, and detail design requirements.

The intent of these requirements is to provide a structural system with the following characteristics:

1. Structures containing no defects or anomalies
 - a. Shall withstand ultimate loads and pressures in the expected operating environment without rupture or collapse
 - b. Shall withstand limit loads and pressures in the expected operating environments throughout its service life without detrimental deformations
 - c. Shall possess a nominal safe-life of 400 missions without fatigue crack initiation.
2. Structures containing defects or anomalies
 - a. If designed for safe life, it shall withstand the expected operating loads and pressures in the expected operating environment without rupture or collapse for a nominal safe life of 150 missions
 - b. If designed for fail safe, it shall withstand limit loads and pressures after the obvious partial failure of any principal structural element

The use of materials which are considered state of the art and are well characterized shall be the basic general rule.

When ground handling or test conditions are determined to be more critical than flight conditions, their effect should be minimized by investigating alternate ground handling or test methods.

3.1.2 Design Requirements

Program Requirements

The following program requirements shall be used in establishing structural design requirements:

1. Design service life shall be 100 missions and 10 years of operation.
2. The vehicle shall have intact abort capability after liftoff.
3. 550K thrust engines are baseline.
4. JP fuel is baseline for airbreathing engines.
5. The vehicle ascent trajectory load factors should not exceed 3g for passenger-carrying missions.

General Requirements

1. The structure shall be designed to survive the specified number of missions with a minimum of structural refurbishment, and in a manner that does not reduce the probability of the successful completion of any mission. Maximum consideration shall be given to the cumulative deteriorating effect of repeated exposure to the critical environmental conditions, such as temperature, creep, and fatigue.
2. The structure shall be designed by flight conditions wherever possible. The nonflight conditions and environment shall influence the design to the minimum extent possible.
3. The structure shall be designed to have sufficient strength to withstand simultaneously the limit loads, applied temperature and other accompanying environmental phenomena for each design condition without experiencing excessive deformation.
4. The structure shall be designed to withstand simultaneously the ultimate loads, applied temperature and other accompanying environmental phenomena without failure.
5. The vehicle shall be designed such that destructive flutter or other related dynamic instability or divergence phenomena shall not occur on the vehicle, or its components, at any condition along the design trajectories.
6. Structures designed only for positive pressure shall have provisions to prevent inadvertent depressurization.

7. Pressurized structure shall be designed so that any leakage occurring during a mission will permit successful completion of the mission. In no case shall leakage exceed levels stated in safety requirements for toxic and explosive fluids, or levels which might jeopardize system function or rated life.
8. Compartment vent and relief provisions shall be designed with sufficient vent capacity to prevent structural over-pressurization due to failure of pressurizing systems or components.
9. The effects of repeated loads and elevated temperatures shall be considered in the structural design. The design structural adequacy of the vehicle in flight shall not be impaired by fatigue damage resulting from exposure to non-flight and launch environments.
10. The effects of accumulative creep deformation shall be considered. The maximum permissible permanent deformation and creep cracks shall be defined based on the structural application and material behavior.
11. The effects of thermal stresses shall be combined with the appropriate ultimate load stresses when calculating required strength. Thermal stresses shall be based on limit temperatures.
12. If the protection against environments afforded by the overall vehicle design is not sufficient to limit detrimental effects to specified levels, provision shall be made for protection against these environments.
13. The structure shall not be designed to withstand loads, pressures, or environments due to malfunctions that would in themselves result in failure to accomplish the mission.

3.1.3 Design Conditions

The following phases and conditions in the service life of the shuttle vehicle shall be investigated for critical loads, temperatures, and structural response:

Ground Handling

Transportation
Proofing
Towing loads
Jacking loads
Hoisting, mating, erecting, and mooring

Prelaunch/Liftoff

Steady winds, wind shears, and gust
Vortex shedding



Prelaunch/Liftoff (continued)

Dampers, tower structure, and supports
Launcher system, holddown and release
Propellant loading and tank pressurization schedule
Ground thermal environment and thermal transients
Cargo loading conditions
Engine noise and vibration
Engine ignition transients and thrust buildup
Emergency engine shut-down and/or rebound
Purge system vent pressures

Boost/Ascent Flight

Steady winds, wind shears, and gusts
Control system characteristics/engine thrust scheduling
C.g. offsets
Thrust oscillations and engine vibration
Aerodynamic pressure distribution
Boundary layer noise
Buffet and separated flow
Aerodynamic heating

Staging/Separation

Booster engine shut-down
Orbiter engine start
Retro, ullage, and/or RCS engine operation
Separation mechanism activation
Plume impingement

Entry

Heat transfer from external flow field
Shock wave impingement
Aerodynamic loading and differential pressure loads
Steady winds, wind shear, gust
Tank ullage heating and pressurization

Transition and Atmospheric Cruise

Buffet and separated flow during transition
Aerodynamic pressure distribution
Steady winds, wind shears, and gusts
Control system characteristics/maneuvers
Cruise engine noise and vibration
Boundary layer noise
Transient thermal effects
Tank ullage heating and pressurization

Landing

Spin-up and spring back gear loads
Land impact
Symmetric and unsymmetric landing
Taxiing
Braking

Ferry Operations

Engine thrust buildup horizontal takeoff
Engine noise

3.1.4 Loads and Pressures

Loads

Limit loads shall be determined for the vehicle in the mated and unmated configurations for the conditions identified above.

The following effects shall be accounted for:

1. Vehicle external and internal geometry
2. Vehicle mass distribution, stiffness, and damping
3. Aerodynamic characteristics
4. Natural and specification environments
5. Interactions of propulsion, control, and other vehicle systems
6. Trajectory characteristics

The effects of transient loads shall be included in the determination of limit loads for all quasi-static and transient phenomena expected in each design environment. The dynamic loads shall account for the effects of vehicle structural flexibilities and damping, and coupling of structural dynamics with the control system and the external environment. The limit loads shall be calculated by multiplying quasi-static loads by appropriate dynamic load amplification factors. These dynamic factors can be derived by comparison to previous data in lieu of detailed dynamic response studies.

Pressures

Design-limit pressures shall be determined as follows:

1. Regulated pressure (i.e., main propellant tanks, personnel and cargo compartments, ACPS accumulators)
 - a. Limit pressure shall be based on the upper limit of the relief valve setting when the pressure is detrimental to the load-carrying capability of the structure.

- b. Limit pressure shall be based on the lower limit of the operating pressure when the pressure enhances the load-carrying capability of the structure.
2. Non-regulated pressure (i.e., vented compartments)
 - a. Upper and lower bounds of pressure shall be established in a rational manner when a range of pressure is possible for a particular structure.
 - b. Limit pressure shall be based on the upper bound when pressure decreases the load-carrying capability of the structure.
 - c. Limit pressure shall be based on the lower bound when pressure increases the load-carrying capability of the structure.
 3. Combined Loads and Pressures

Pressure vessels (including main propellant tanks) shall be capable of withstanding the following combinations of loads and pressures without rupture or collapse:

- a. Ultimate load and ultimate pressure when the pressure is destabilizing
- b. Ultimate load and limit pressure when the pressure is stabilizing
- c. Ultimate pressure alone

3.1.5 Design Factors

Design factors shall be used to account for structural analysis, environmental, and material uncertainties which are not amenable to rational approaches.

Factors of Safety

Table 3-1 shows the yield and ultimate factors of safety to be used in Phase B studies for various structural components.

Proof Factors

Table 3-1 shows the proof factors to be used in Phase B studies.

In addition to the above factors, when adequate fracture toughness data and sufficient knowledge of operating conditions are available to determine the required proof pressure from fracture mechanics principles, the required proof pressure will be determined from these data and used.

The methods and requirements are provided in the NASA design criteria monograph "Fracture Control of Metallic Pressure Vessels," NASA SP8040.

Service Life Factors and Environments

Table 3-2 shows factors to be used in relation to fatigue, flaw growth, and creep during Phase B studies.

Booster main propellant tanks, pressure vessels, and cabin structures shall be designed to preclude the occurrence of both functional failure (i.e., leakage of fluids and gasses) and structural failure (i.e., rupture). Flaw growth analyses for both types of phenomena shall be performed considering the complexity of structural details, environments, and loadings for each particular design. The factor 1.5 for flaw growth calculations during Phase B studies was selected on the basis of (1) the observation that flaw growth is a better behaved phenomenon than flaw initiation (i.e., fatigue) for which a life factor of 4 is traditionally used; and (2) the desire to maintain a realistic structural design approach with minimum weight impact. This life factor for flaw growth must be re-examined when sufficient flaw growth data for Space Shuttle materials become available.

Due to present uncertainties on (1) the behavior of materials under sustained and cyclic creep conditions, (2) temperature predictions due to lack of substantiating flight data, and (3) potential temperature overshoots due to presently undefined perturbations of nominal trajectories, a rather conservative approach was used in establishing life factors for creep evaluation during Phase B studies. These factors were a factor of four on design service life and, in addition, a factor of two on accumulated creep strain.

The design environments given in Table 3-3 are to be used for safe-life calculations.

Margins of Safety

The margin of safety shall be positive and shall be determined at ultimate allowable levels and at yield levels, when appropriate, at the temperatures expected for all critical conditions.

For minimum-weight design, the margin of safety should be as small as practicable.

3.1.6 Service Life

The combined effects of fatigue, thermal stress, and creep on general structure shall be evaluated.

Load spectra shall be defined to represent analytically the cumulative static, dynamic, and environmental loads and deflections anticipated for all major structural components during the service life of the vehicle.

Table 3-1. Design Factors of Safety

Component	Yield	Ultimate	Proof	Applied On
Main propellant tanks	{ 1.10	1.40	◁	Maximum relief valve pressure only
		1.10	-	Loads (+ limit pressure)
		1.00	-	Proof pressures
Personnel compartments, windows, doors, hatches	{ 1.10	1.50	-	Loads (+ limit pressure)
		1.50	1.50	Maximum operating pressure only
		1.00	-	Proof pressure
Airframe structure	{ 1.10	1.40	-	Boost + entry loads
		1.10	-	Aircraft mode loads
Pressure vessels	--	2.00	1.50	Maximum operating pressure
Pressurized lines fittings	--	2.50	1.50	Maximum operating pressure
Thermal stresses	{ 1.00	1.00		Thermal forces + flight loads
		1.00	1.25	Thermal forces alone
◁ Proof factor TBD based on Fracture Mechanics Analysis				

Table 3-2. Service Life Factors

ITEM	FACTOR	APPLIED ON
Fatigue initiation	4.0	Design service life
Flaw growth to leak	1.5	Design service life
Flaw growth to failure	1.5	Design service life
Creep	{ 4.0 and 2.0	Design service life
		Accumulated creep strain
NOTE: Design service life = 100 missions and 10 years of operation.		

Flaw growth shall not exceed the growth required to increase the maximum undetectable initial flaw to a size where the stress intensity under limit-stress levels exceeds the threshold stress-intensity values. The effects of short-time load excursions which result in stress intensities above the threshold (e.g., due to maneuver loads, vibratory loads, or gust loads) shall be accounted for in the fatigue-life predictions.

Safe-Life

Safe-life design concepts shall be applied to all structure vital to the integrity of the vehicle or the safety of personnel. The safe-life shall be determined using the factors given in Table 3-2.

The determination of structural safe-life shall take into consideration the effects of the following factors in combination with the expected operating environments:

Material properties and failure mechanisms

Load spectra

Cyclic-loads effects

Sustained-loads effects

Cumulative combined damage

Fail-Safe

Where practicable, fail-safe design concepts shall be applied. For all fail-safe structure, the failure of a single principal structural component shall not degrade the strength or stiffness of the structure below that necessary to carry limit load. All fail-safe structure shall be accessible for periodic inspection.

3.1.7 Design Thickness

The structural design thickness, t_d , for each metallic structural member other than mechanically or chemically milled pressure vessels shall be the minimum thickness obtained by either of the following calculations:

1. t_d = mean thickness based on equal plus and minus tolerances
2. t_d = N times the minimum thickness

where

N = 1.10 for strength design

N = 1.05 for stability design

The mean and minimum design thicknesses, as used above, shall include allowances for cumulative material damage or loss resulting from repeated exposure to the design environment. The design thickness for mechanically or chemically milled pressure vessels shall be the minimum thickness (i.e., mean minus the lower tolerance).

3.2 DESIGN LOADS

Design conditions listed in 3.1.3 were evaluated by GDC to determine critical conditions and resulting external loads on booster primary structure. These limit design loadings are summarized in the following sections; data are abstracted from Reference 4. A summary of characteristics for critical design conditions is given in Table 3-4.

3.2.1 Aerodynamic Surfaces

A summary of design loadings at the root of aerodynamic surfaces is given in Table 3-5. The spanwise distribution of bending moment is given in Figures 3-1, 3-2 and 3-3 for the wing, canard, and vertical stabilizer, respectively.

3.2.2 Body Loads

Body Shell Loads

Internal loads consisting of axial and shear loads and bending and torsion moments were determined along the body length for 25 different load conditions by GDC as part of their Phase B study effort. The results of this analysis are documented in Reference 4. These data have been reviewed and ten loading conditions identified as being of potential interest for the present study. The resulting distributed longitudinal loading (N_x) on the body shell at the top and bottom centerlines is plotted versus body station in Figures 3-4 and 3-5. These loadings are based on limit external loads and limit nominal compartment ullage pressures. The identifying numbers for design conditions are the same as employed in Reference 4.

The body bending moment, axial force, and compartment pressure for these selected design conditions and three body stations of potential interest for the present study are summarized in Table 3-6.

Orbiter Attachment Loads

Design limit loads for the connection between booster and orbiter vehicles are summarized in Table 3-7.

Thrust Loads

The variation of total booster main engine thrust over the boost period is plotted in Figure 3-6.

Table 3-3. Safe-life Design Environments

COMPONENT	DESIGN ENVIRONMENT
LO ₂ Tank	LO ₂ @ -320°F or GO ₂ @ 70°F Air at 70°F Air at 70°F } 3 1/2% salt solution with alternate drying
LH ₂ Tank	
Intertank Adapter	
TPS, Wing, Canard	
Empenage, Thrust	
Structure, and Orbiter	
Attachments	

Table 3-4. Summary of Design Conditions

Condition	Axial Load Factor (g)	Lateral Load Factor (g)	Wind Speed at 60 Feet or αq (βq)	Remarks
Two-week standby	1.0	-	72.1 knots	Unfueled, unpressurized
One-day hold	1.0	-	48 knots	Fueled, pressurized
One-hour to launch	1.0	-	34.4 knots	Fueled, unpressurized
Liftoff				
LO ₂ mass	1.31 ±0.15	TBD		
LH ₂ mass	1.31 ±0.25	TBD		
Orbiter & other	1.31 ±0.21	TBD		
Maximum dynamic pressure				
αq	1.71	+0.62, -0.20	±2800 deg-psf	
βq	1.71	±0.15	±2400 deg-psf	
Maximum thrust	3.0 ±0.30	TBD	±480 deg-psf	
Booster burnout	3.0 ±0.30	TBD	±100 deg-psf	
Booster recovery		4.0		
Subsonic gust		2.05		
Subsonic maneuver		2.50		
Landing		2.0		
		±.35		

Table 3-5. Design Loads for Aerodynamic Surfaces

Surface	Design Condition	Shear		Bending Moment		Torque	
		(lb x 10 ³)	MN	(in-lbx10 ⁶)	NM-m	(in-lbx10 ⁶)	MN-m
Wing	Max α -q	646.7	2.90	173.9	1.98	25.7	.293
	Entry	650.6	2.92	163.1	1.86	30.0	.342
	2.5g Man.	518.9	2.33	150.3	1.71	77.1	.880
	Subsonic gust	508.5	2.28	146.3	1.67	74.5	.850
Canard	2.5g Man.	64.0	.287	4.76	.0544	1.55	.0177
	Max α -q	43.9	.197	3.66	.0418	-1.26	-.0144
Vertical Stabilizer	Subsonic side gust	272	1.22	63.0	.719	77.0	.879
	Subsonic rudder kick	204	.915	50.9	.580	45.3	.516
	Max β -q	187	.839	43.2	.492	61.0	.695
NOTE: (1) All loads are limit (2) Loads are at root of aerodynamic surface (3) Loads are per panel							

TSU 13A
MODEL 101 X 101
REVISED 10/74
PAGE 11 OF 11

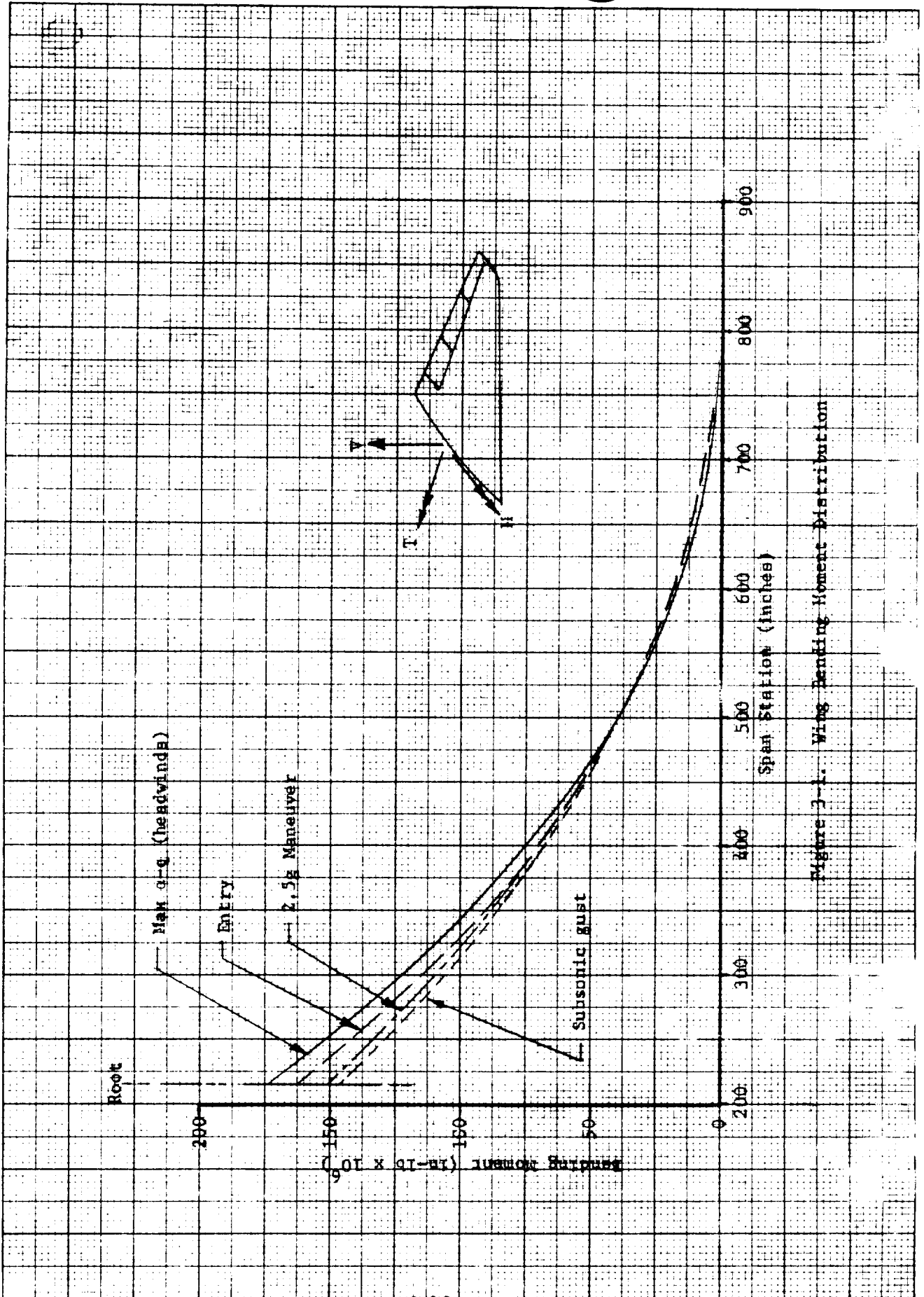


Figure 3-1. Wing Bending Moment Distribution

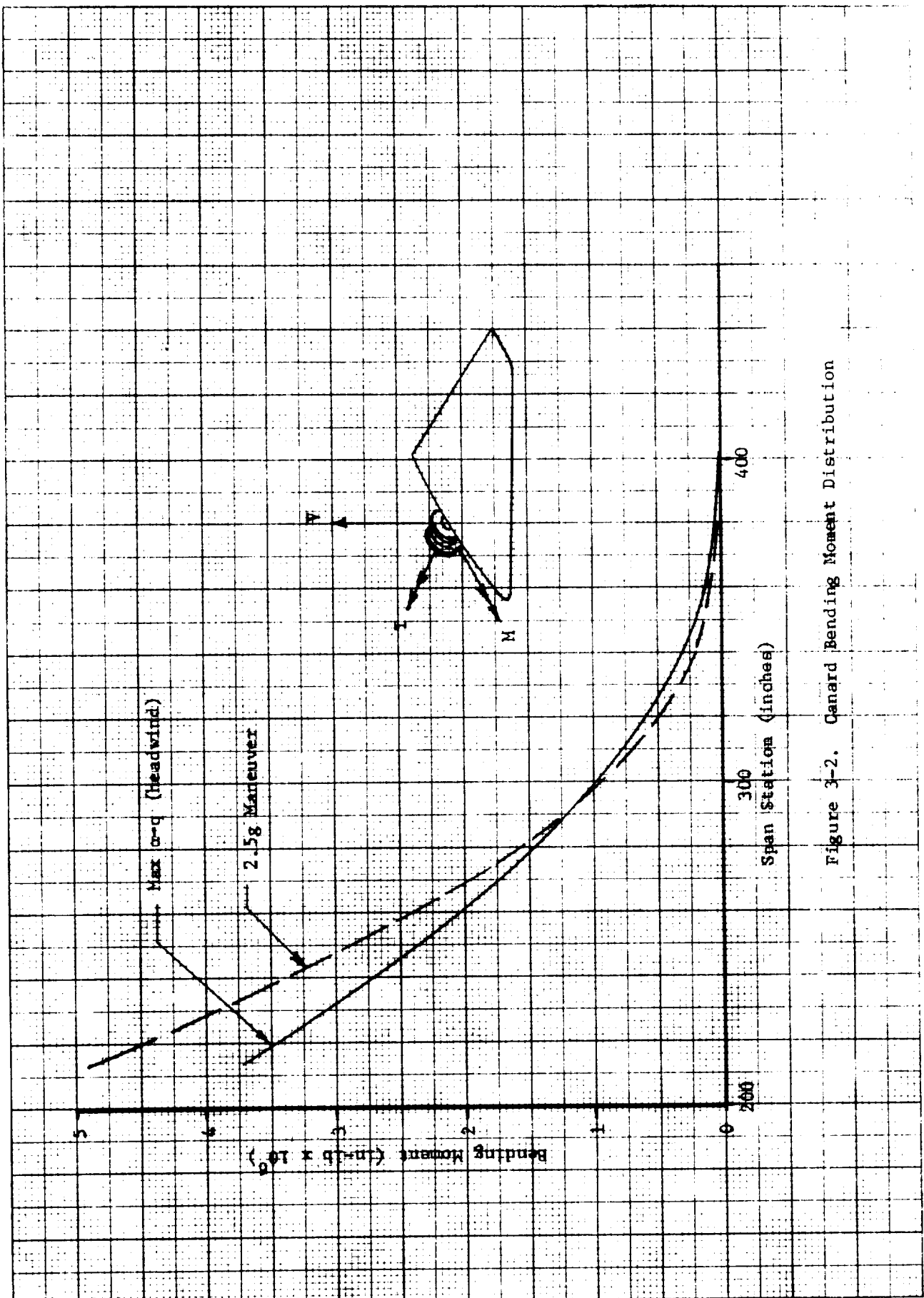


Figure 3-2. Canard Bending Moment Distribution

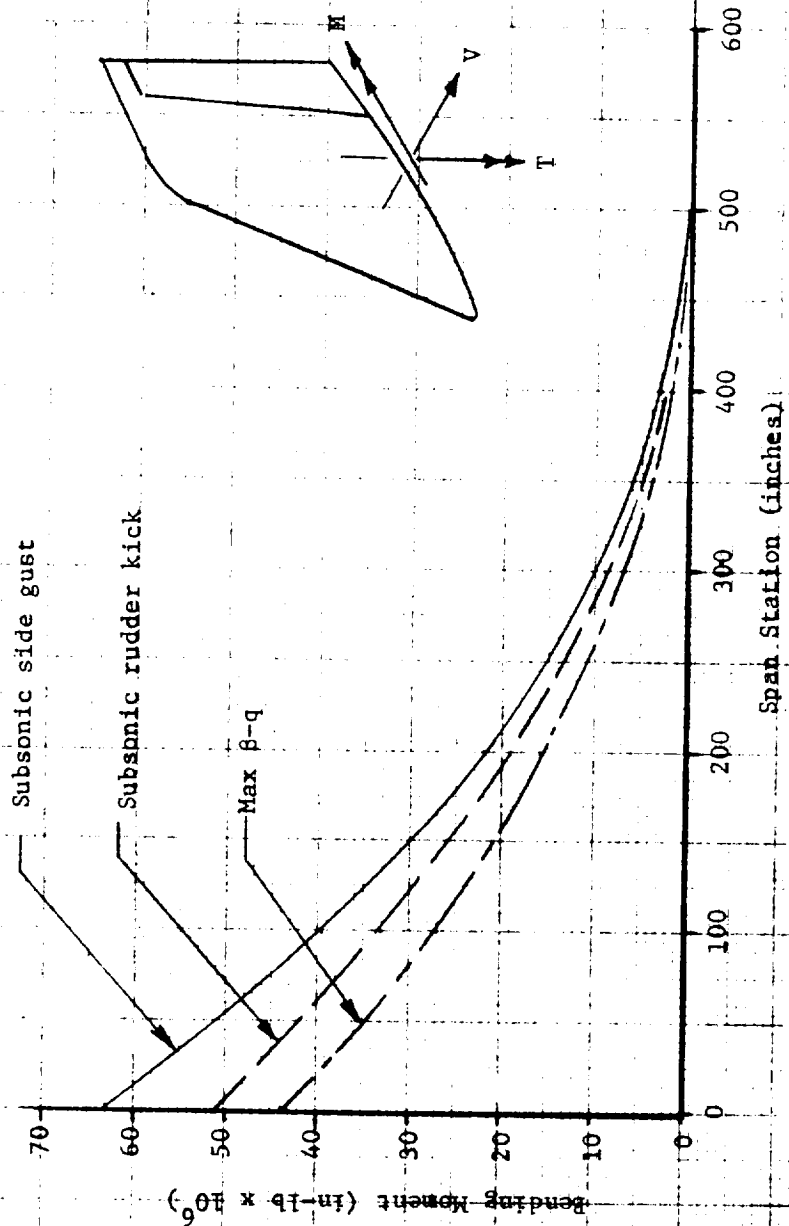
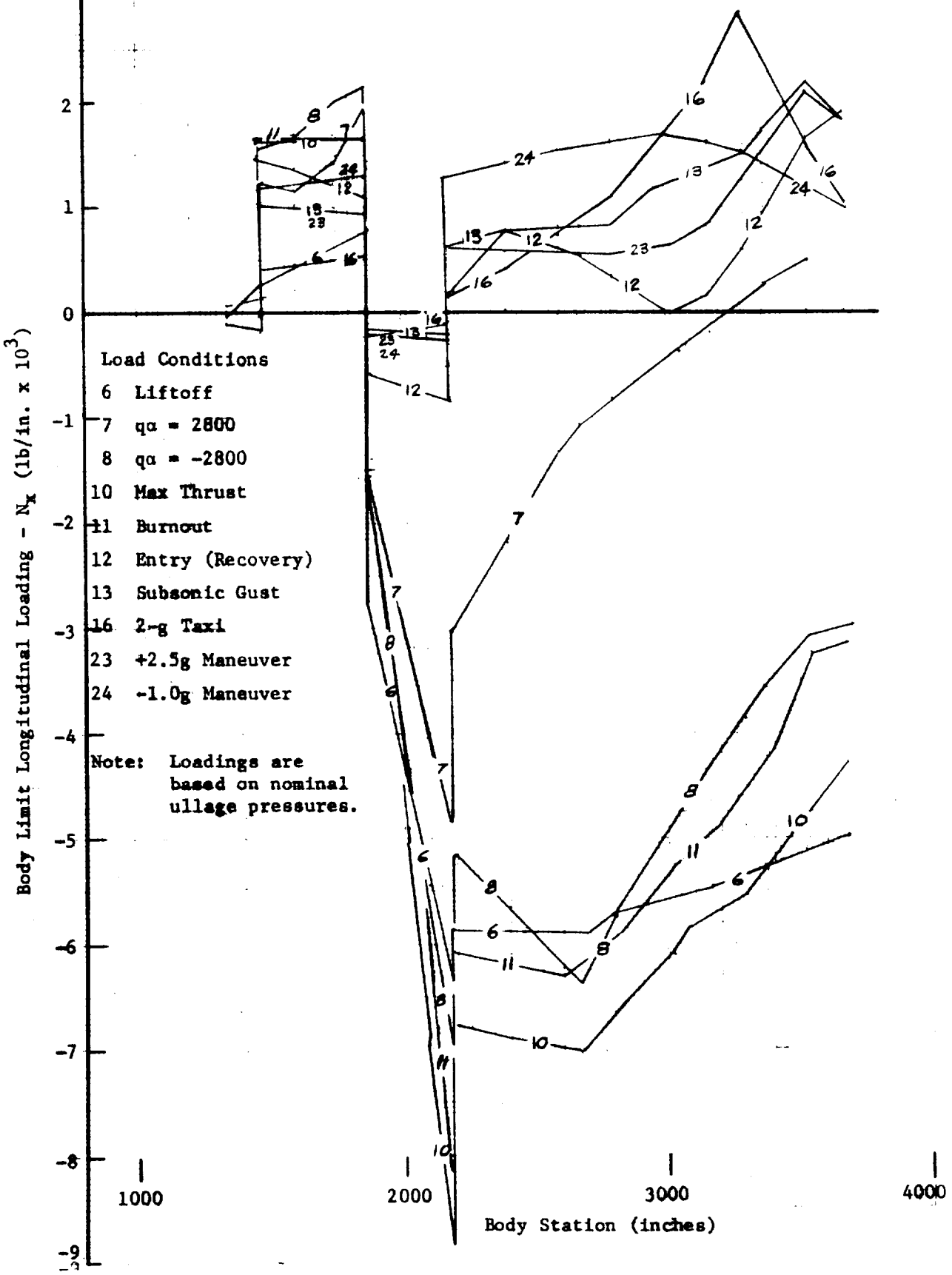


Figure 3-3. Vertical Stabilizer Bending Moment Distribution

PREPARED BY: RWW	SPACE DIVISION NORTH AMERICAN ROCKWELL CORPORATION 12214 LAKEWOOD BOULEVARD • DOWNEY, CALIFORNIA 90241	3-16
CHECKED BY:		PAGE NO. OF
DATE: 8-9-71	Figure 3-4. Body Loadings - Top Q.	REPORT NO. SD72-SH-0046
		MODEL NO. B-9U



PREPARED BY: RWV	SPACE DIVISION NORTH AMERICAN ROCKWELL CORPORATION 12214 LAKEWOOD BOULEVARD • DOWNEY, CALIFORNIA 90241	PAGE NO. 3-17 OF
CHECKED BY:		REPORT NO. SD72-SH-0046
DATE: 8-9-71	Figure 3-5. Body Loadings - Bottom G	MODEL NO. B-9U

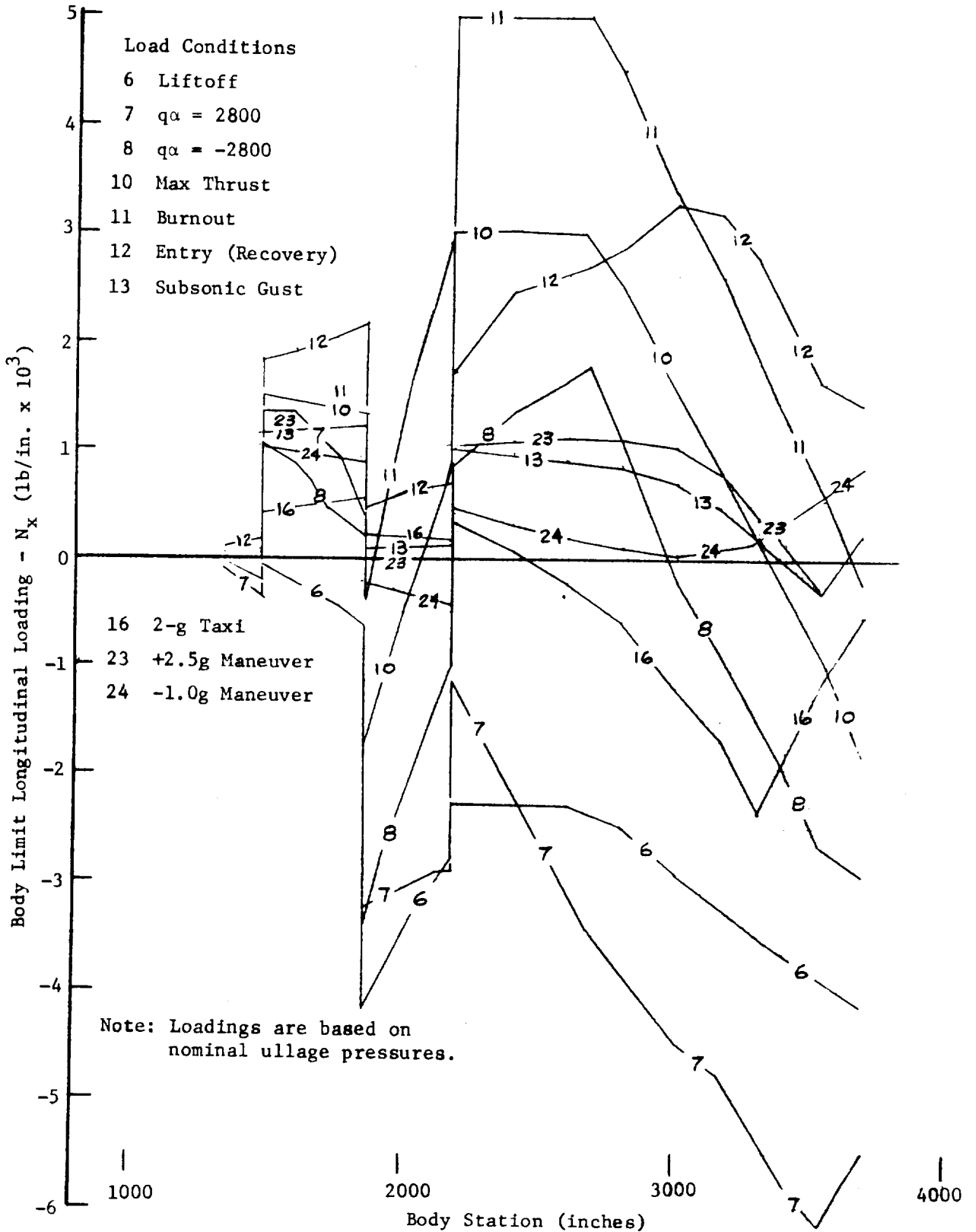


Table 3-6. Body Limit Design Loads

Cond. No.	Condition	Bending Moment (1) (in-lb x 10 ⁶)			Axial Force (2) (lb x 10 ³)			Internal Pressure (3) (psig)		
		Sta. 1864	Sta. 2180	Sta. 2600	Sta. 1864	Sta. 2180	Sta. 2600	Sta. 1864	Sta. 2180	Sta. 2600
6	Liftoff	86.0	-220	-223	104	5660	5730	2.2	0	5.1
7	α -q = 2800	97.2	-118	109	312	4830	5030	14.0	0	18.2
8	α -q = -2800	117	-370	-486	283	4910	5090	14.0	0	18.2
10	Maximum thrust	17.5	-602	-616	226	4880	5050	16.8	0	20.8
11	Burnout	24.6	-679	-695	225	3230	3400	16.8	0	20.8
12	Entry (Recovery)	-64.9	-92.9	-124	56.3	93.5	124	15.0	0	17.2
13	Subsonic gust	-15.9	-16.9	-4.9	26	42.8	58.8	11.0	0	9.0
16	2-g Taxi	-26.4	-9.4	59.5	0	0	0	3.3	0	2.5
23	+2.5g Maneuver	-12.0	-24.2	-33.4	25.6	63.1	78.8	11.0	0	9.0
24	-1.0g Maneuver	24.6	50.1	83.6	12.6	23.6	30.7	11.0	0	9.0

(1) Positive bending moment is tension on upper surface

(2) Positive axial force is compression

(3) Compartment nominal ullage pressure with respect to free-stream ambient

Table 3-7. Booster/Orbiter Connection Loads

CONDITION		WIND	F _x (KIPS)	F _y (KIPS)	F _z (KIPS)	A _y (KIPS)	A _z (KIPS)	M _x (X 10 ⁶ IN-LB)	
TWO-WEEK GROUND WINDS, UNFUELED, WITH TOWER SUPPORT		HEAD	268	0	56.9	0	-33.0	0	
		TAIL	268	0	-119.0	0	149.0	0	
		SIDE	268	±98.5	28.8	±30.2	34.9	∓17.1	
ONE-DAY GROUND WINDS, FUELED, WITH TOWER SUPPORT		HEAD	859	0	95.2	0	62.7	0	
		TAIL	859	0	-0.1	0	161.0	0	
		SIDE	859	±53.3	80.0	±16.3	99.5	∓9.28	
ONE-HOUR GROUND WINDS, FUELED, UNSUPPORTED		HEAD	859	0	89.5	0	76.5	0	
		TAIL	859	0	30.0	0	138.0	0	
		SIDE	859	±33.3	80.0	±10.2	99.5	∓5.80	
DYNAMIC LIFTOFF PLUS ONE-HOUR GROUND WINDS		HEAD	1296	0	119.0	0	134.0	0	
		TAIL	1295	0	82.2	0	182.0	0	
		SIDE	1296	±20.5	121.0	±2.92	150.0	∓4.14	
MAX α-q α-q = 2800 α-q = -2800		HEAD	1798	0	224.8	0	234.8	0	
		TAIL	1804	0	83.0	0	950.3	0	
		NO WIND	1808	0	137.4	0	625.6	0	
MAX β-q ±2400		SIDE	1802	±81.2	128.8	±166.8	653.7	∓72.3	
3g MAX THRUST		N _x = 3.3 N _y = 0 N _z = -0.35		2849	0	135.2	0	424.5	0
		N _x = 3.3 N _y = +0.1 N _z = -0.25		2849	±55.4	179.3	±30.7	394.5	∓7.6
BOOSTER BURNOUT		N _x = 3.3 N _y = 0 N _z = -0.46		2841	0	62.9	0	459.0	0
		N _x = 3.3 N _y = +0.1 N _z = -0.36		2841	±55.4	118.3	±30.7	428.0	∓7.6

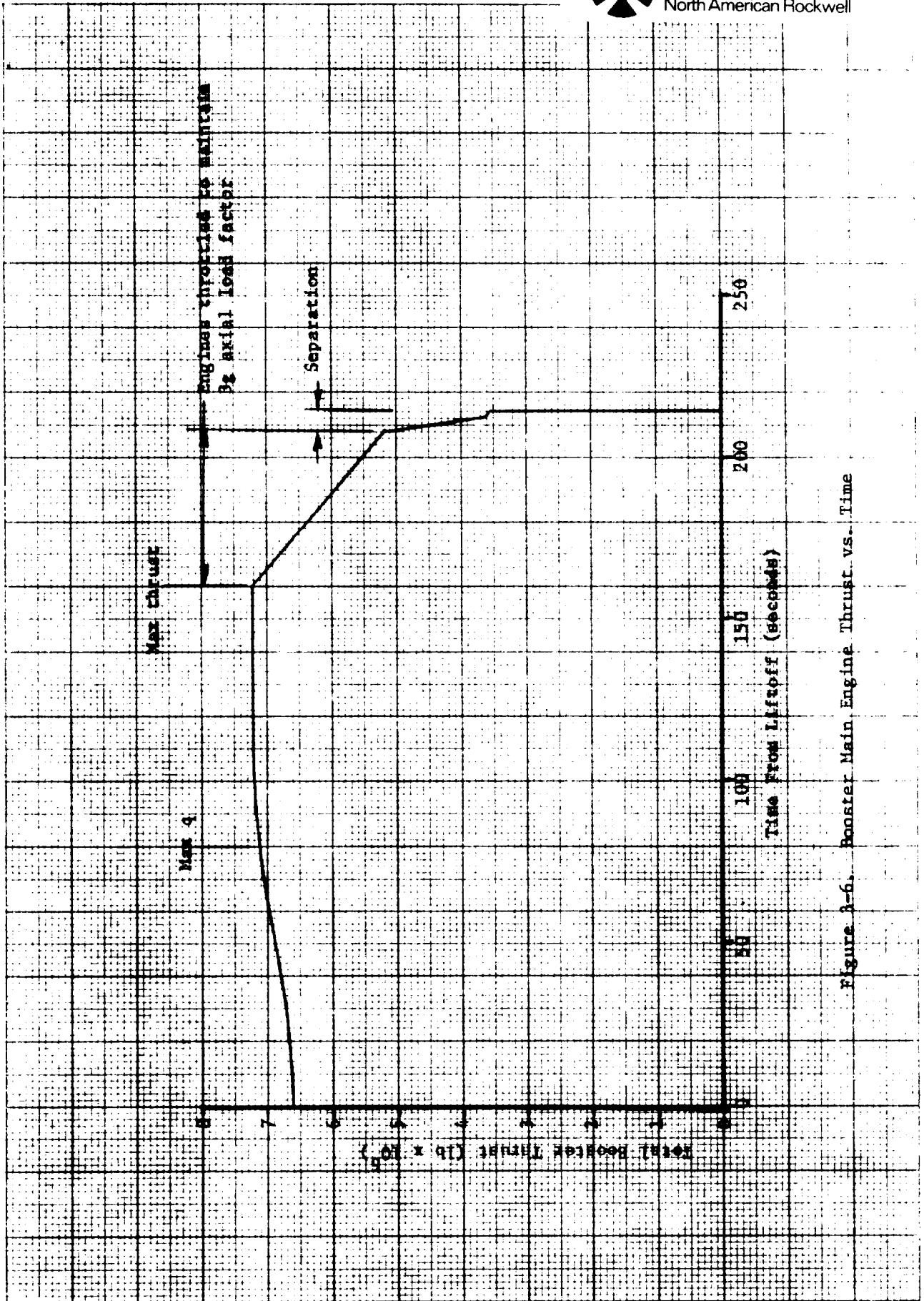


Figure 3-6. Booster Main Engine Thrust vs. Time

3.2.3 Propellant Tank Pressures

The ullage pressure schedule over the complete mission is plotted in Figures 3-7 and 3-8 for the LOX and LH₂ tanks respectively. Also indicated on these curves is the variation of total pressure (ullage plus head) at the bottom of the tanks.

The resulting design pressure profiles over the length of the tanks are plotted in Figures 3-9 and 3-10.

3.3 SERVICE LOAD SPECTRA

Service load spectra for major structural elements of the B-9U booster have been determined by GDC in support of other contracted studies. Data summarized in this section is taken from References 5, 6, and 7. The data is presented in the form of curves giving number of exceedances versus load magnitude for key loading parameters. The number of exceedances are based on a total of 100 operational missions. Ferry missions are not included in these curves, but their effect can be approximated by doubling the number of exceedances indicated for cruise, landing, and taxi flight phases.

3.3.1. Wing Load Spectra

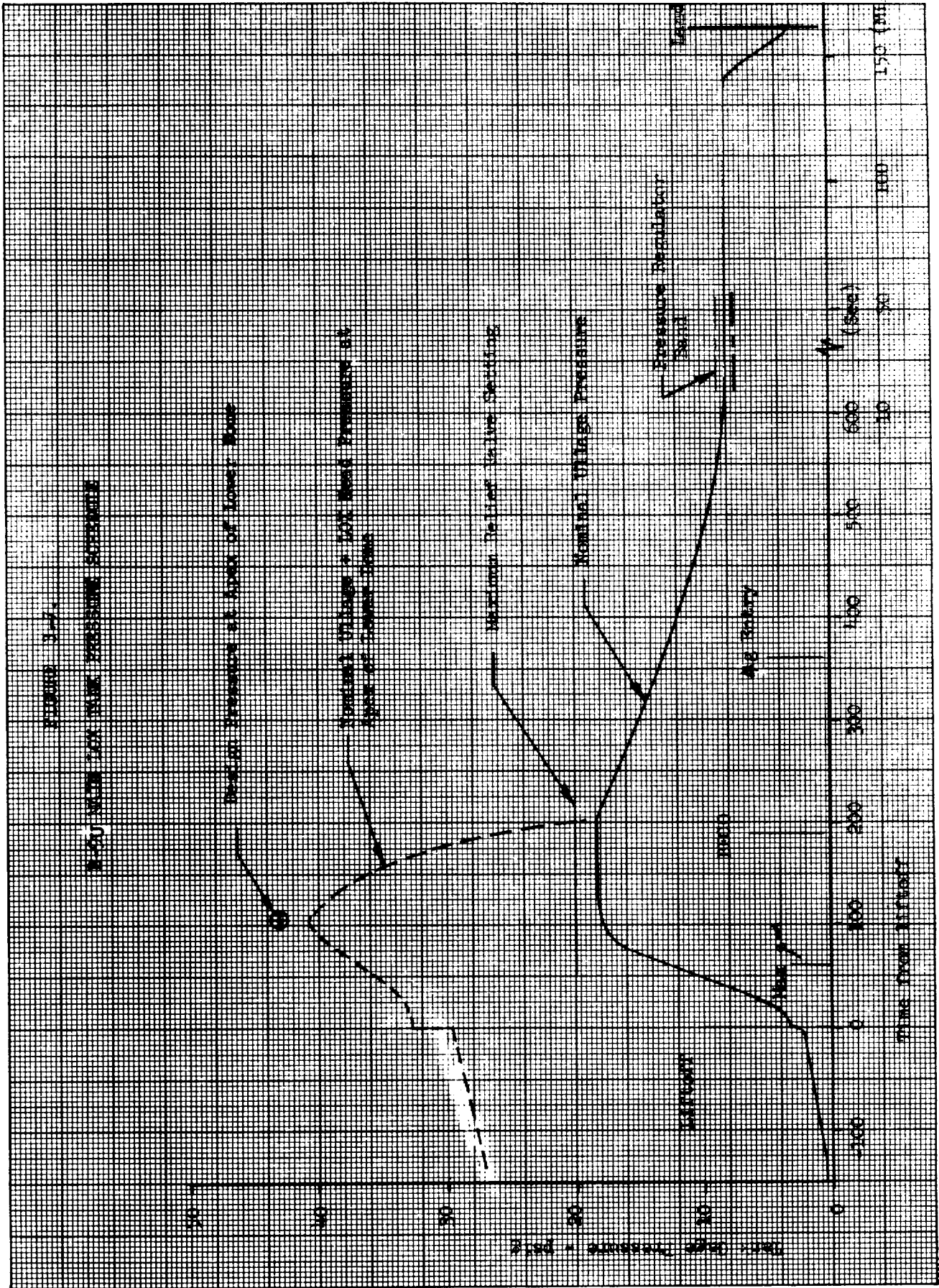
Load spectra for the wing are given in Figure 3-11 in terms of mean and alternating bending moment at the wing root. The bending moments are expressed as a percentage of maximum design bending moment. The ascent phase has been divided into segments, and a series of curves are plotted which give exceedances of alternating bending moment for various values of mean bending moment. Wing bending moment for the entry phase is assumed to increase from zero to a positive maximum; the load magnitude shown for this flight phase refers to the maximum value of this one-sided bending moment distribution.

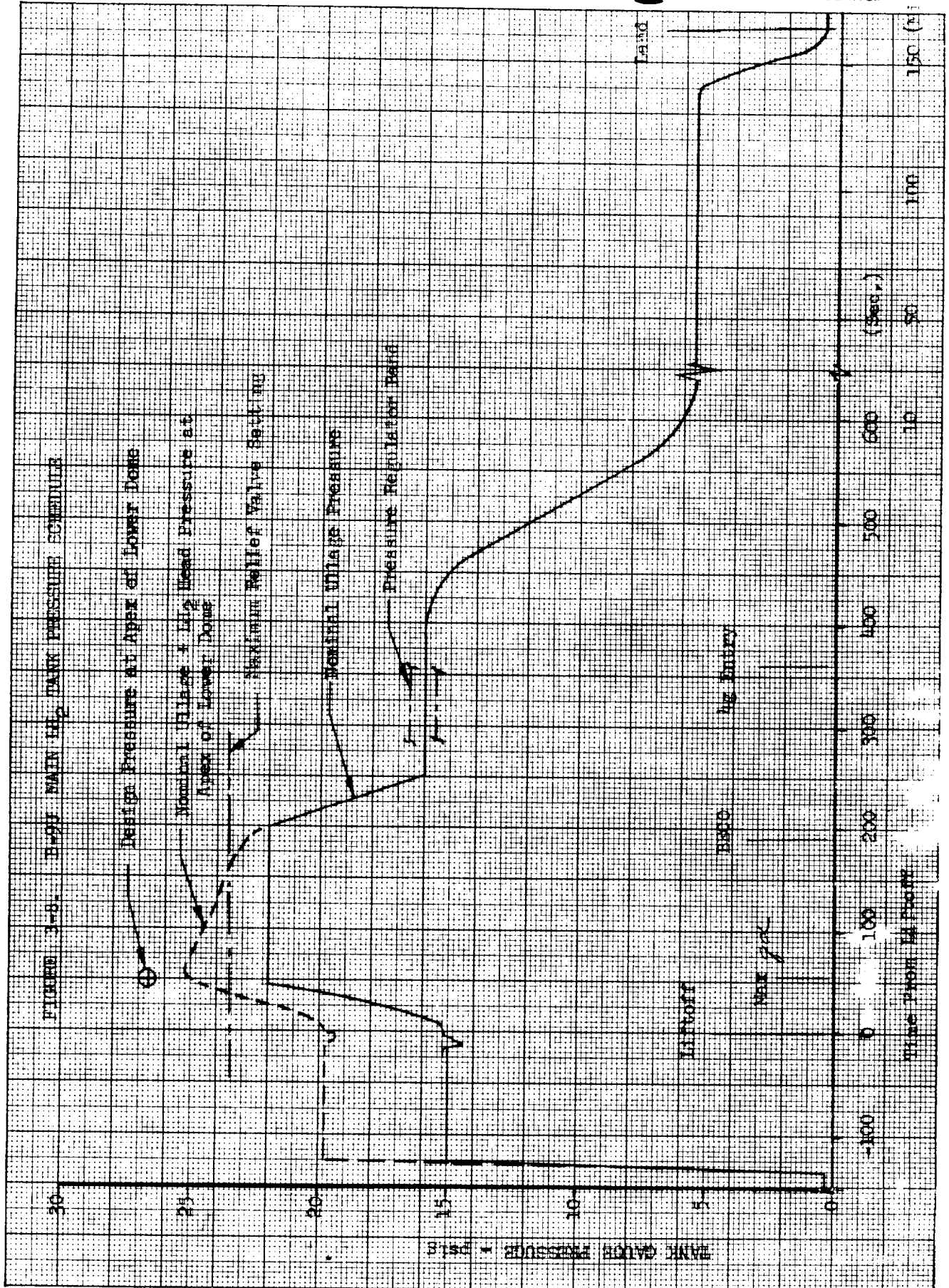
3.3.2 Vertical Stabilizer Load Spectra

Load spectra for the vertical stabilizer are given in Figure 3-12. The data is presented in the same form as for the wing; the ascent phase is divided into segments and a series of curves are plotted which give exceedance of alternating bending moment at the root of the vertical stabilizer. The alternating bending moment is again expressed as a percentage of maximum design value. The mean bending moment is zero for all flight conditions.

3.3.3 Body Load Spectra

Service load spectra are given in Figure 3-13 for fuselage station 2600; this station is in the region of maximum bending moment on the body. The data is plotted as exceedance of alternating bending moment at Sta. 2600 in conjunction with a prescribed mean bending moment. Two types of loading variation are represented on this figure. The bending moment for maximum thrust and entry conditions increases from zero to a positive or negative peak; this peak value is defined by the load exceedance curves. Transient bending moments due to atmospheric disturbances will alternate about some





KE 10 X 10 TO THE CENTIMETER 46 1517
1 1/2 X 1 1/2 CM. • ALBANY, N.Y.
MADE IN U.S.A.
KEUFFEL & ESSER CO.

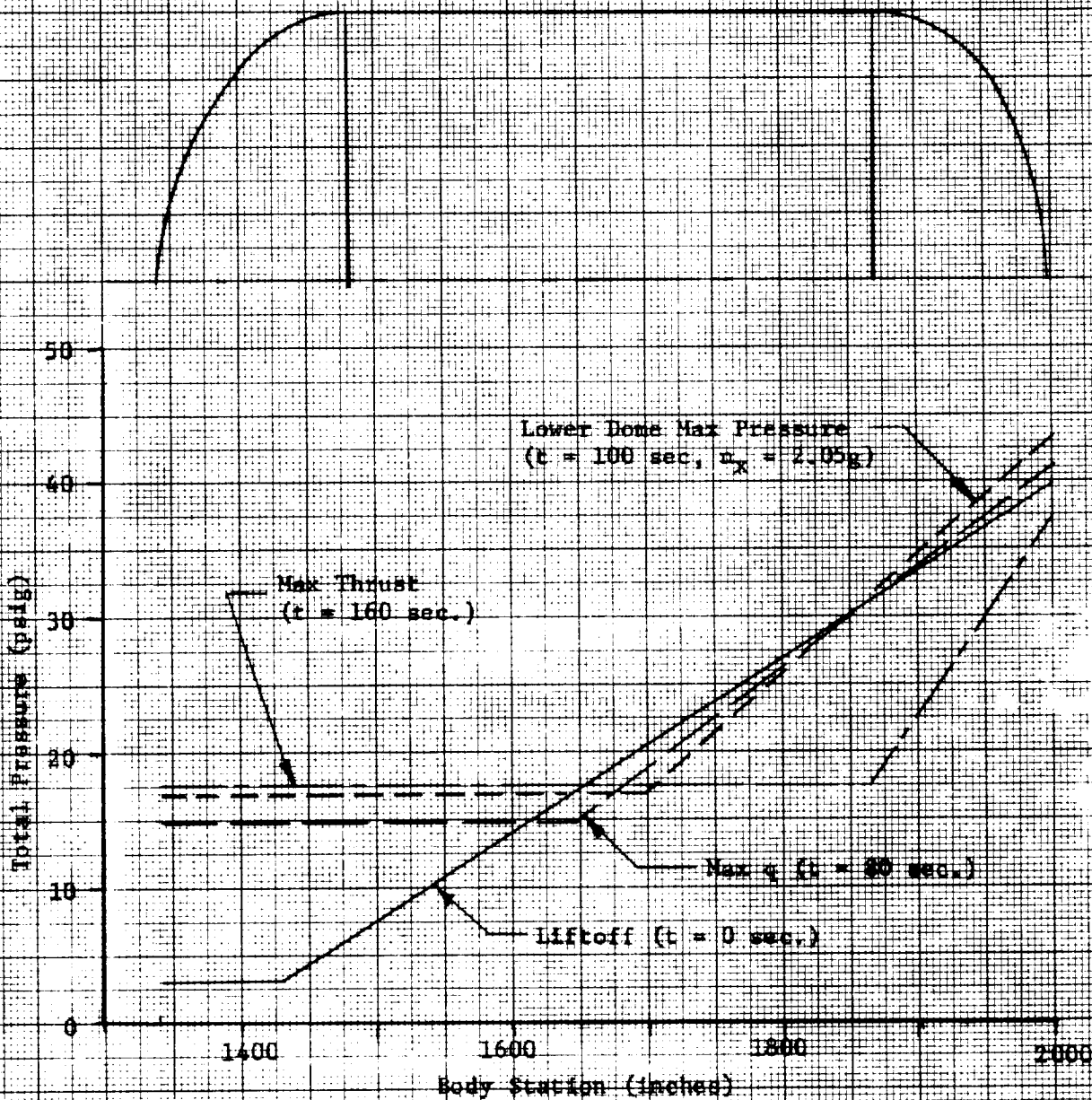


Figure 3-9. LOX Tank Limit Pressure Profiles



FIGURE 3-11
B-50 WING LOAD SPECTRA

Vehicle Life = 100 Missions

Mean Load = 0
(Entry Condition)

Mean Bending Moment
(Percent of Design Value)

Number of Exceedances (N_e) = Cycles

± Alternating Bending Moment - Percent of Design Value

EUGENE DIETZGEN CO.
MADE IN U. S. A.
NO. 340-L510 DIETZGEN GRAPH PAPER
SEMI-LOGARITHMIC
5 CYCLES X 10 DIVISIONS PER INCH

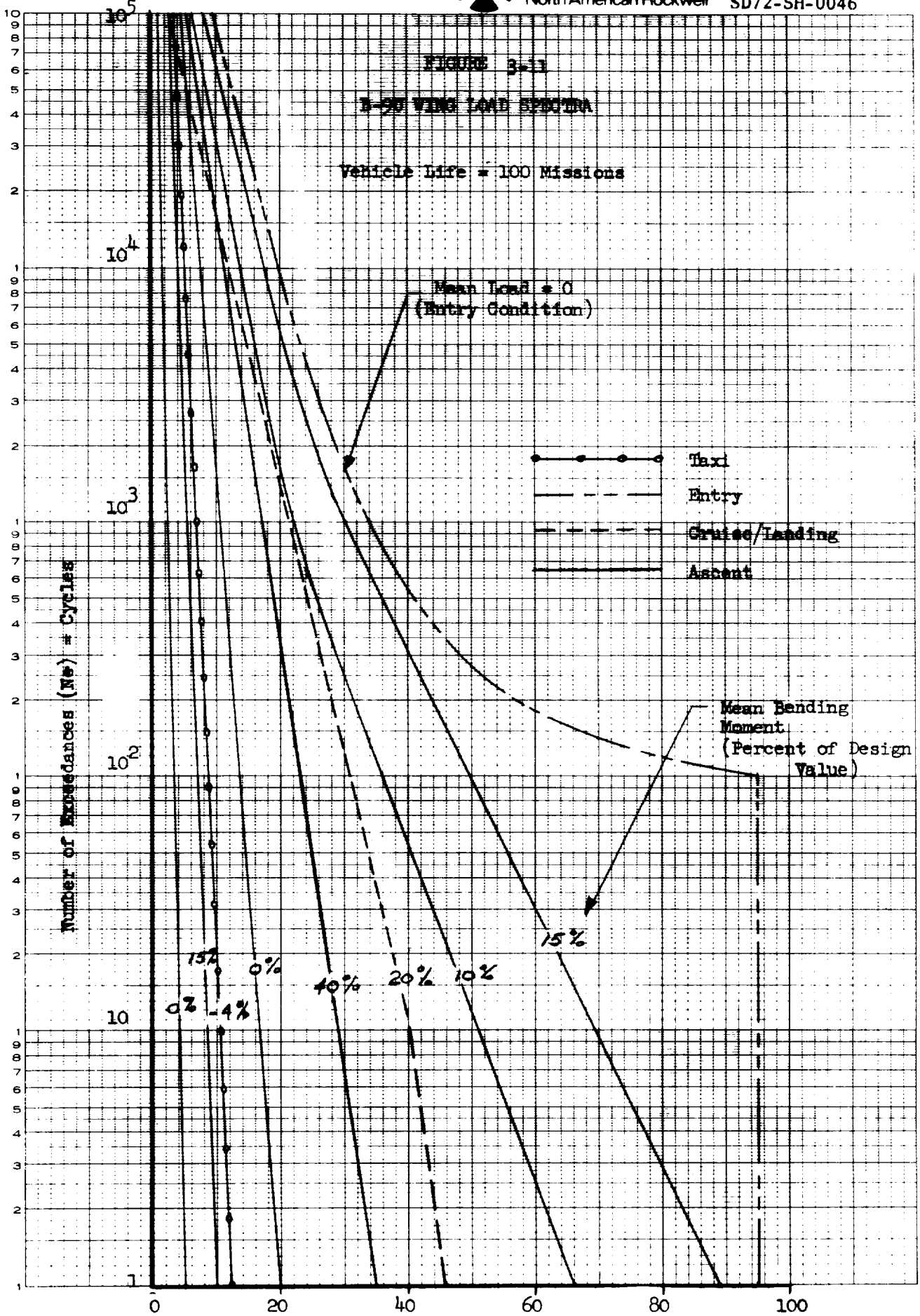
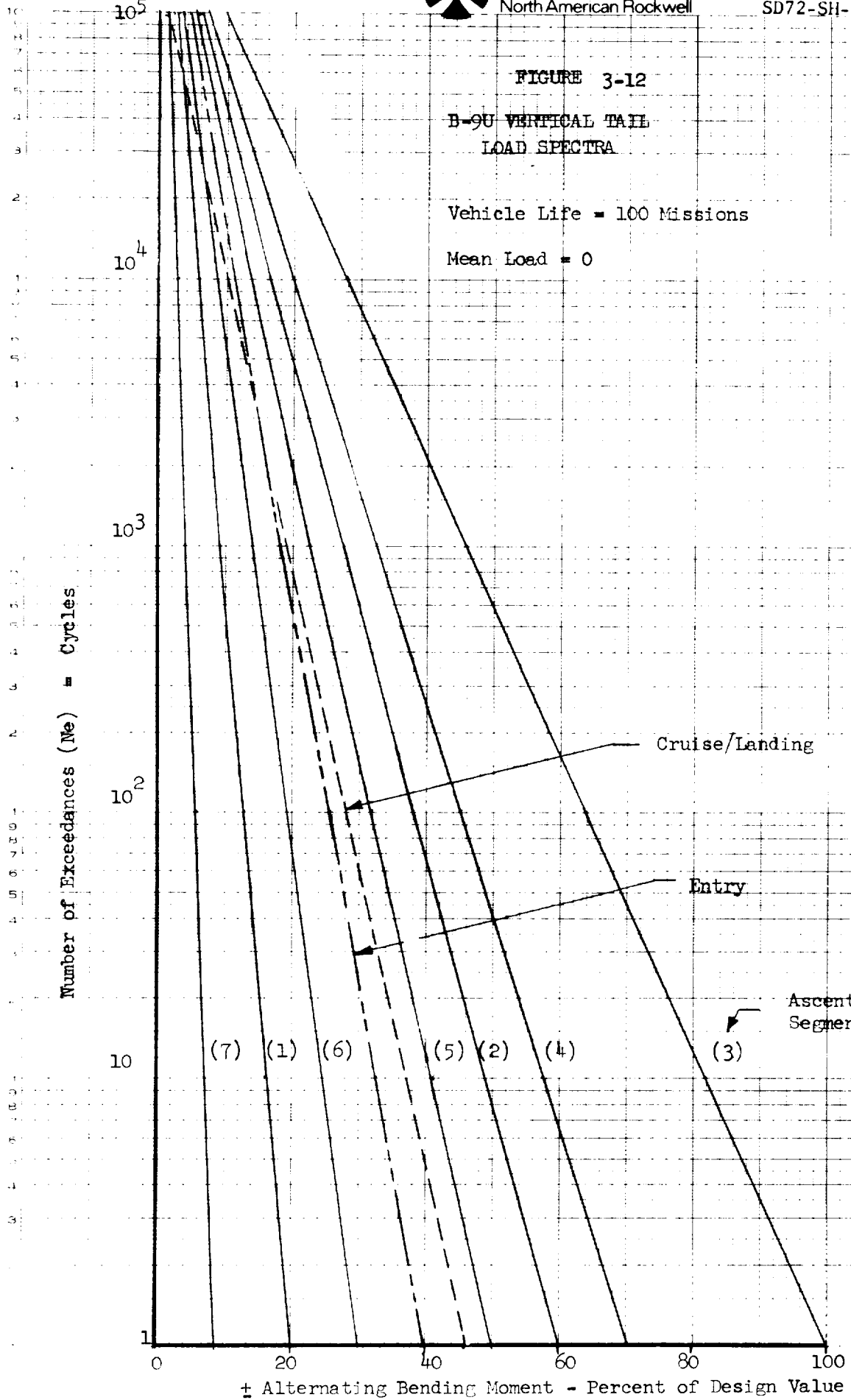




FIGURE 3-12
B-90 VERTICAL TAIL
LOAD SPECTRA

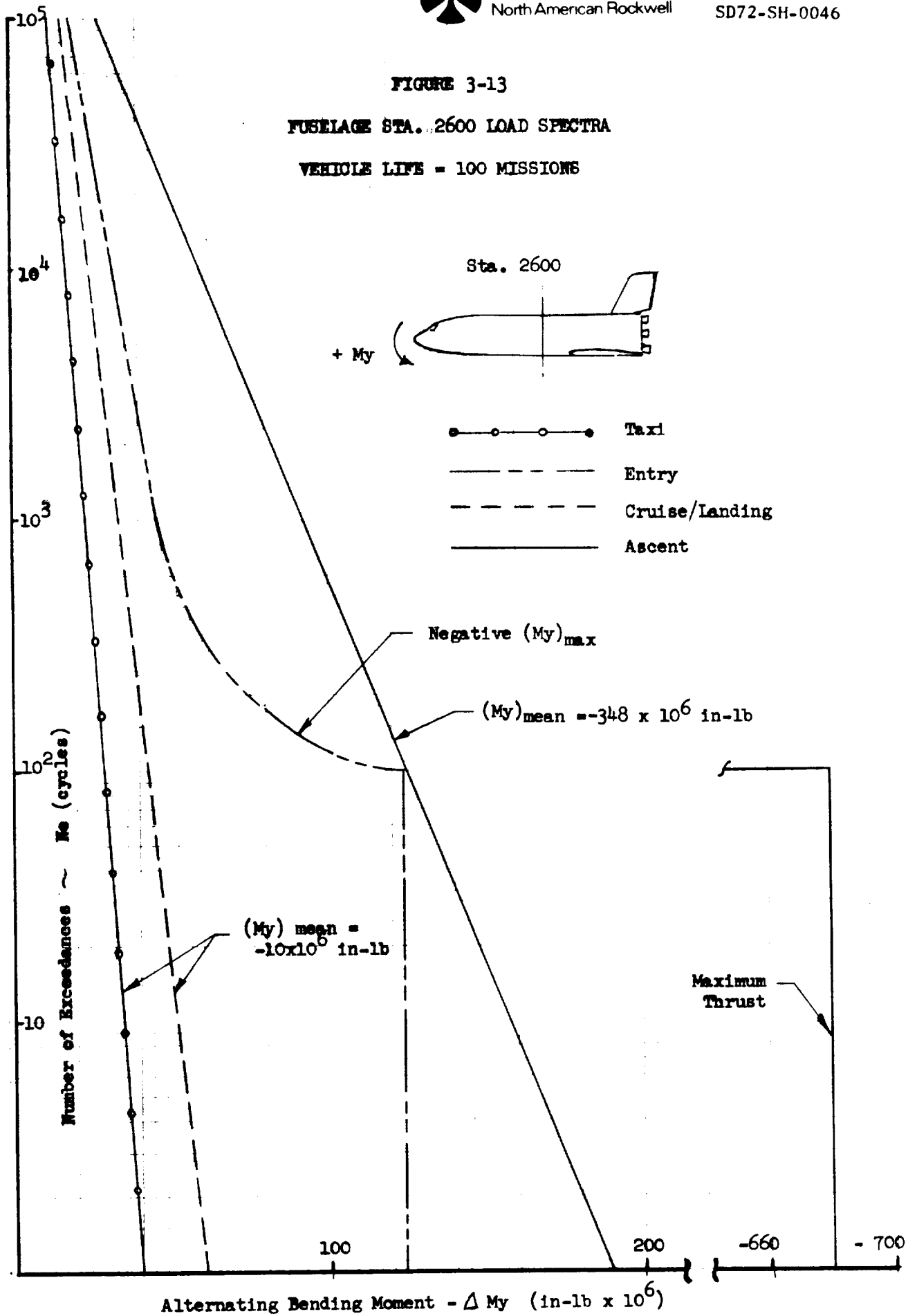
Vehicle Life = 100 Missions
Mean Load = 0

Number of Exceedances (Ne) = Cycles



EUGENE DIETZGEN CO.
340-0510 DIETZGEN GRAPH PAPER
SEMI-LOGARITHMIC
5 CYCLES X 10 DIVISIONS PER INCH

± Alternating Bending Moment - Percent of Design Value



mean value which is the result of steady-state aerodynamic and thrust forces. Major aerodynamic transients will occur in the maximum α - β regime during ascent, so a mean bending moment applicable to this condition is used for the ascent flight phase. The effect of axial load and tank ullage pressure must also be considered, of course.

Service load spectra are given in Figure 3-14 for the orbiter aft attachment. The exceedance of alternating loads in the normal and lateral directions are given, expressed as a percentage of maximum design values.

The exceedance of main engine thrust variation for one flight is given in Figure 3-15.

3.4 STRUCTURAL TEMPERATURES

Detailed thermal analysis has not been performed in the Phase B study on all structural elements of present interest. However, typical transient temperature histories on the wing and vertical stabilizer are illustrated in Figures 3-16 and 3-17, respectively. The wing lower surface has a thermal protection system (TPS) over the primary structure. Primary structure of the wing upper surface and the vertical stabilizer main box is exposed to direct aerodynamic heating. The vertical stabilizer is also subjected to heating from plume impingement of the orbiter main engines during the separation phase.

A summary of the estimated range of temperature on each of the selected structural elements for the major mission phases is given in Table 3-8. These estimates are based on the specific data and general trends indicated in Figures 3-16 and 3-17, and consideration of the following factors:

1. The TPS is designed to protect the primary structure by limiting the maximum temperatures to approximately 300F for aluminum sub-structure and 650F for titanium sub-structure.
2. Primary structure covered by TPS will experience thermal lag compared to outer surface temperatures. Peak temperatures will occur at a later time and decay more slowly than for the outer surface.
3. Primary structure involving thick sections, such as wing spar caps and orbiter aft attachment bulkhead, will have significant heat sink capability. Peak temperatures on these members will be much less than for thin skins, and the peak temperature will decay more slowly.
4. Internal insulation is employed in the LH₂ tank; the resulting minimum temperature expected on the structural wall is approximately -200F.
5. The crew compartment will be environmentally controlled for crew habitability.

FIGURE 3-14

ORBITER AFT ATTACH LOAD SPECTRA

Vehicle Life = 100 Missions

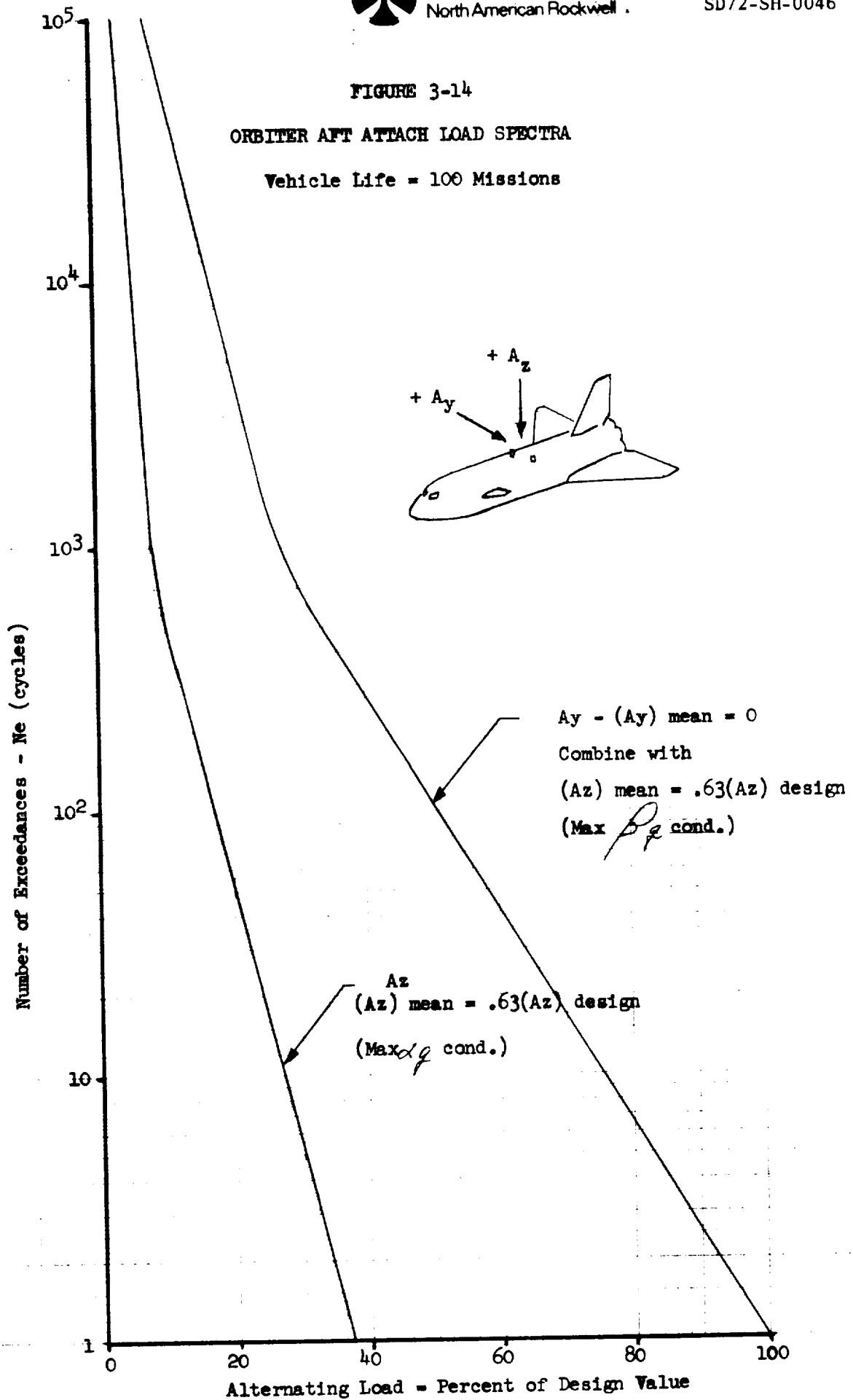
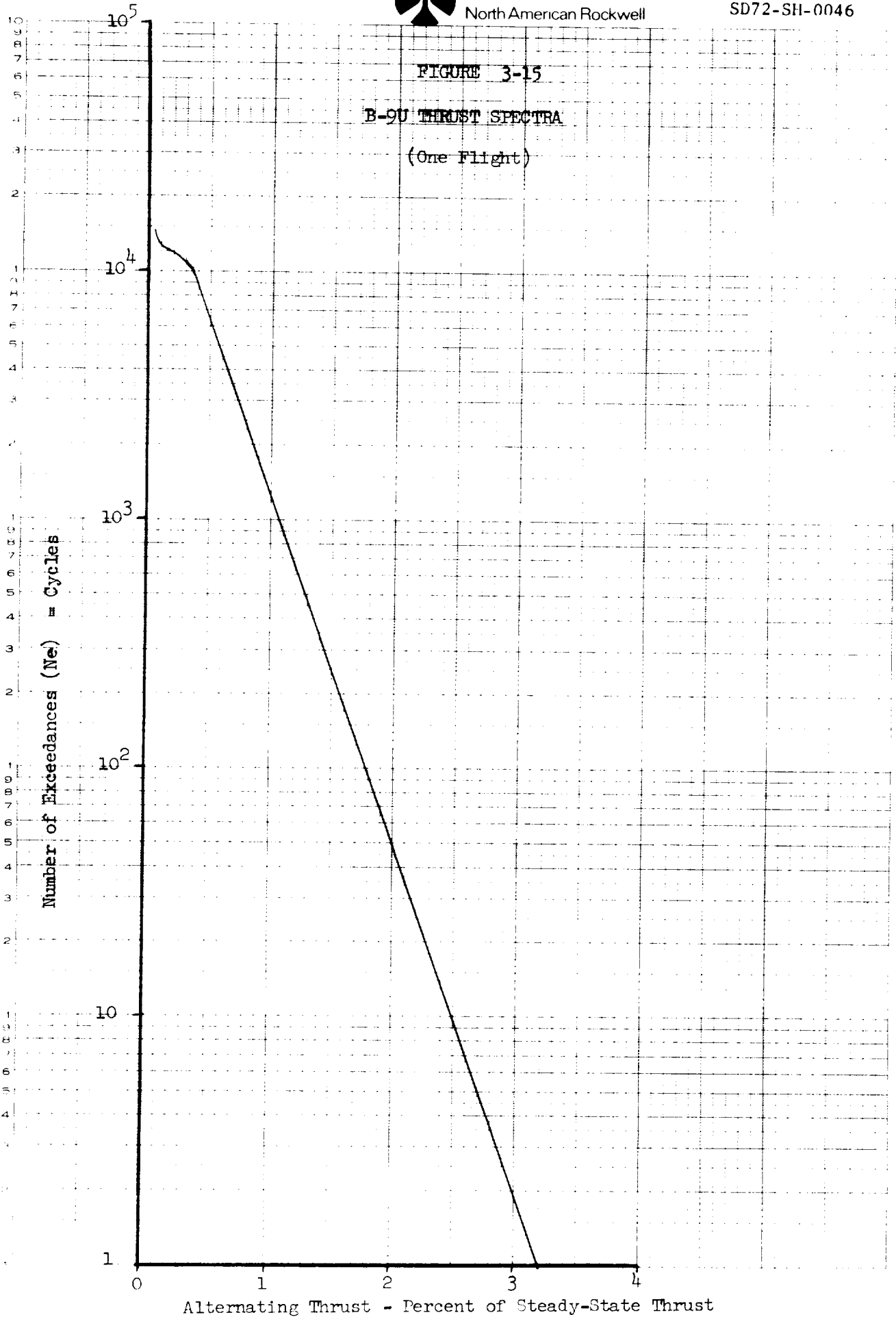




FIGURE 3-15
B-9U THRUST SPECTRA
(One Flight)



EUGENE DIETZGEN CO.
MADE IN U.S.A.

NO. 34D-LS10 DIETZGEN GRAPH PAPER
SEMI-LOGARITHMIC
5 CYCLES X 10 DIVISIONS PER INCH

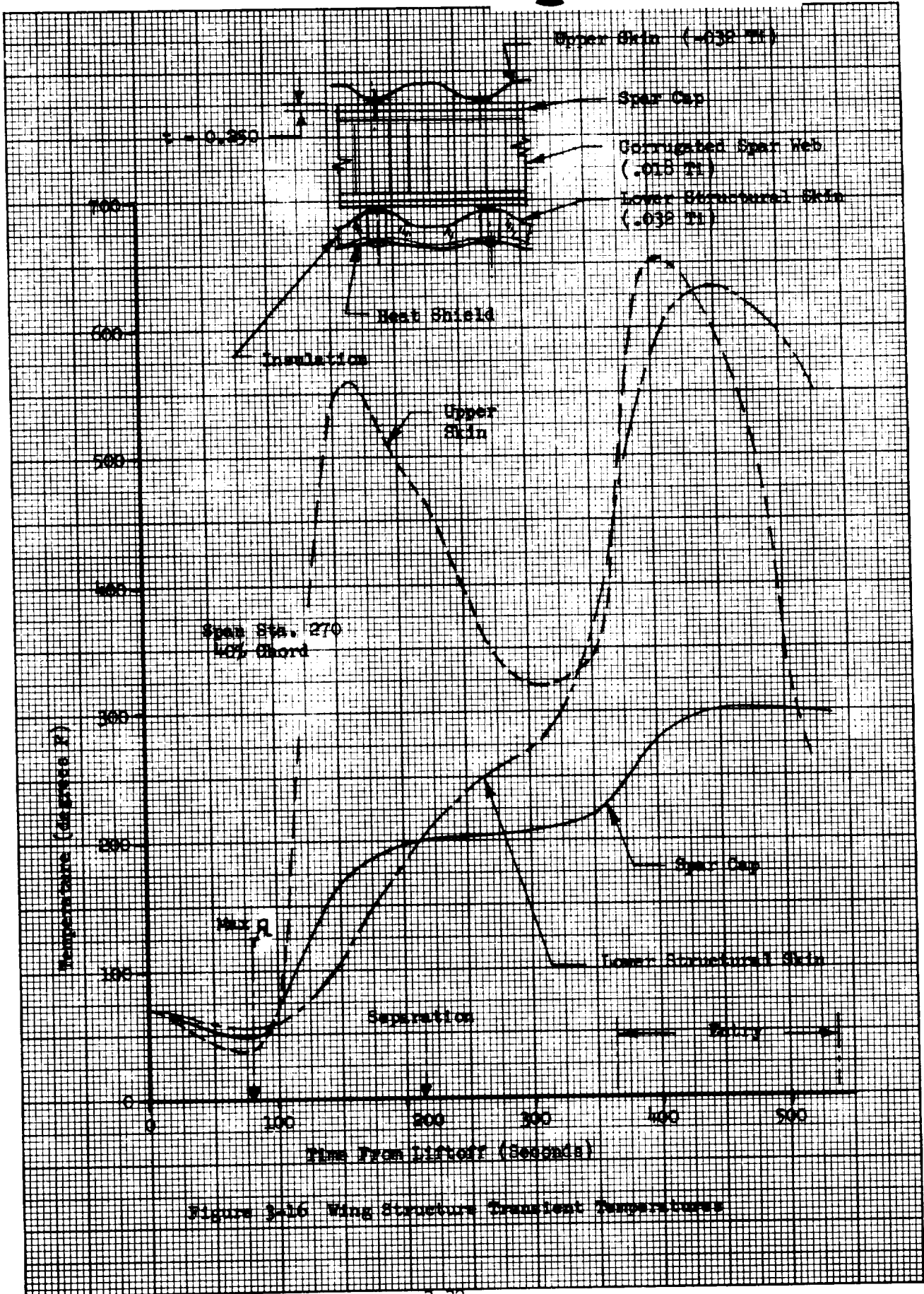


Figure 3-16 Wing Structure Transient Temperatures

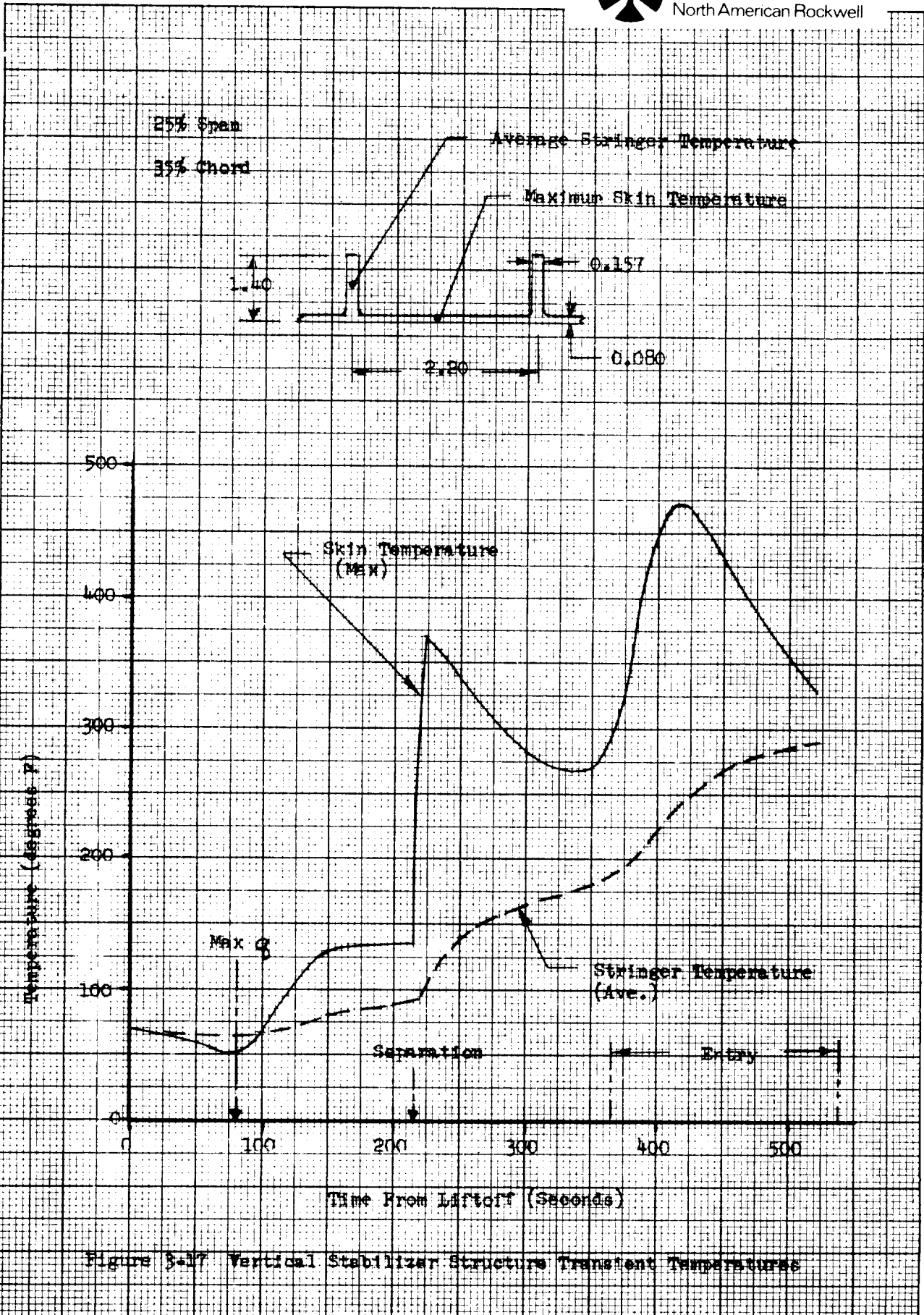


Figure 3-17 Vertical Stabilizer Structure Transient Temperatures

K&E 10 X 10 TO THE 1/2 INCH 359T-11
 KEUFFEL & ESSER CO. MADE IN U.S.A.
 ALBANY, NY

Table 3-8 Estimated Range of Structural Temperatures

Structural Element	Flight Phase				
	Ascent	Entry	Cruise	Landing/ Taxi	Ferry
LH ₂ Tank Cyl. Shell	-200F to -100F	100F to 300F	100F to 300F	100F to 300F	-65F to 130F
LOX Tank Cyl. Shell	-297F to OF	100F to 300F	100F to 300F	100F to 300F	↑
LOX Tank Aft. Bulkhead	-297F	-297F to 100F	100F to 200F	100F to 200F	
Wing Spars	OF to 130F	200F to 300F	200F to 300F	100F to 300F	↓
Vert. Stab. Main Box Skins (Root)	OF to 130F	300F to 480F	100F 300F	OF to 130F	
Intertank Adapter Cyl. Shell	-250F to 130F	200F to 300F	200F to 300F	200F to 300F	↓
Orbiter Aft Attach Bulkhead	-200F to OF	OF to 200F	100F to 200F	100F to 200F	
Crew Compartment Cyl. Shell	60F to 100F	←—————→			60F to 100F



4.0 SELECTED STRUCTURAL ELEMENTS

4.1 SELECTION SUMMARY

To provide an efficient and effective basis to conduct the study, it is necessary to select discrete structural elements and associated critical sections for detailed strength, fatigue, and fracture mechanics investigations. The elements should be selected to provide a representative sample covering the range of materials, operating environments, design approach, and failure modes expected for the shuttle booster structure. In general, they should also represent structural areas which are a significant portion of the structural weight, so that the influence of different criteria and approaches on vehicle weight and performance will be determined on a realistic basis.

A matrix of candidate structural elements of the B-9U booster is presented in Table 4-1. This table also summarizes the type of structural configuration, selected material, operating stress and temperature environment, weight of similar structure, and proof test and inspection considerations as determined in the Space Shuttle Phase B Study. Review and evaluation of this matrix led to the following selection; reasons for selection are discussed below.

The following structural elements are of primary interest and are selected as the principal basis for detailed investigations:

1. LH₂ tank cylindrical shell-mid region (Sta. 2600)
2. LOX tank cylindrical shell-forward region
3. LOX tank cylindrical shell-aft region
4. LOX tank aft bulkhead
5. Wing spars (lower surface)-root region
6. Vertical stabilizer main box-root region
7. Crew compartment cylindrical shell

The following structural elements are of secondary interest and will be investigated to an extent appropriate to date availability and study scope.

1. Orbiter aft support bulkhead
2. Intertank adapter cylindrical shell.

4.2 SELECTION RATIONALE

The main propellant tanks of the booster are obviously primary elements for investigation because of their susceptibility to fracture, the catastrophic consequences of failure, and the large amount of structural weight involved. Because of the low density of liquid hydrogen, the pressure gradient from forward to aft end of the LH₂ tank is relatively small. Therefore, a single section at Sta. 2600 has been selected for analysis. This is in the region of the maximum body bending moment and should therefore



provide a good basis to evaluate the influence of flight loads on fatigue and fracture characteristics of the tank. The evaluation of behavior under hoop stresses due to internal pressure determined at this station should be representative of the entire LH₂ tank. A large pressure gradient exists over the length of the LOX tank, so sections at both the forward and aft ends of the cylindrical shell are selected for analysis. The aft bulkhead of the LOX tank is subjected to a maximum design pressure, so it is selected for evaluation as an example of pressure vessel membrane structure. The general results and trends determined for this member should also be applicable to the other propellant tank bulkheads.

The wing spars are selected as the most appropriate elements of the wing structural assembly for investigation. They represent a significant portion of the structural weight and are loaded by axial tension and compression stresses. In-service accessibility and inspection limitations exist because of attachment of cover skins and thermal protection system; the effects of these limitations should be investigated. Spars on the wing upper and lower surfaces are of similar configuration; however, the lower surface operates at higher tensile stress levels, so it is selected for analysis.

The main box of the vertical stabilizer is also selected for analysis because of the different nature of the aerodynamic loading and because it is of different structural configuration from the wing. Integral-stiffened skin planks resist the spanwise bending loads rather than concentrated spar members.

Although the crew compartment represents only a relatively small portion of the structural weight, it is selected for evaluation in this study because of special problems related to crew safety. The current design approach applied to almost all aircraft pressurized fuselage structure provides a high fail-safe capability such that a skin crack can extend completely between frame members without causing catastrophic rupture. However, this concept may not be practical for space shuttle, considering the loss of cabin atmosphere that will occur before the crew can descend to a safe attitude or don pressure suits. Therefore, it is considered desirable to evaluate the crew compartment cylindrical shell, with special attention to crew safety provisions.

The orbiter aft support bulkhead is of interest as an example of a heavy forged member subjected to repeated load cycles. The same type of structure is also found at the orbiter forward attachment and at wing support frames. However, the basic design and stress analysis data is less well developed for these members than for the other structural elements considered. Also, the total weight involved is a relatively small percentage of the vehicle structural weight, so that fracture mechanics and fatigue design considerations applied to these members should not have a major impact on the total vehicle weight and performance.

The intertank adapter is also of interest as an example of unpressurized fuselage structure. However, because of thrust and inertia loadings during boost, the compression design stresses are much higher than the maximum tension stresses encountered. Therefore, it is unlikely that fracture considerations would cause a significant change in the design approach or the structural weight of this assembly.

Structural Element	Type of Structure	Material	Total Weight of Similar Structure	Percent ⁽¹⁾ Vehicle Structural Weight	Limit Stress (tension)	Potential Failure Modes	Criticality Level	Candidate Design Approach	Type of Loading	Temperature Cycles	Potential for Initial Flaws	Proof Test Feasible
① LH ₂ tank cylinder shell, mid region ▶ (Sta. 2600)	Integral stiffened, welded panels	2219-T87 aluminum alloy plate	23,800 kg (52,600 lb)	23.0	310 MN/m ² (45 ksi)	Leakage	Deferred critical	Safe life	Biaxial tension (discrete spectral) plus body bending (random spectral)	143 K (-200 F) to 422 K (300 F)	Parent metal, moderate Welds, high	Yes ⁽⁴⁾
						Rupture	Immediate catastrophic					
② LO ₂ tank cylinder shell, forward region ③ LO ₂ tank, cylinder shell, aft region	Integral stiffened, welded panels	2219-T87 aluminum alloy plate	4100 kg (9100 lb)	3.7	270 MN/m ² (39 ksi) 345 MN/m ² (50 ksi)	Leakage	To be determined	Safe life	Biaxial tension (discrete spectral) plus body bending (random spectral)	91 K (-297 F) to 422 K (300 F)	Parent metal, moderate Welds, high	Yes ⁽⁴⁾
						Rupture	Immediate catastrophic					
④ LO ₂ tank aft bulkhead	Unstiffened, welded gore panels	2219-T87 aluminum alloy sheet	3700 kg ⁽²⁾ (8200 lb)	3.3	345 MN/m ² (50 ksi)	Leakage	To be determined	Safe life	Biaxial tension (discrete spectral)	91 K (-297 F) to 366 K (200 F)	Parent metal, low Welds, high	Yes ⁽⁴⁾
						Rupture	Immediate catastrophic					
⑤ Crew compartment cylinder shell	Skin, stringer, frame	2124 aluminum alloy sheet	680 kg (1500 lb)	0.6		Leakage	Mission abort	Safe life and fail safe	Biaxial tension (discrete spectral)	289 K (60 F) to 311 K (100 F)	Low	Yes
						Rupture	Immediate catastrophic					
⑥ Wing spars, lower surface	Machined extrusion	6AL-4V titanium (annealed)	7000 kg (15,400 lb)	6.2	620 MN/m ² (90 ksi)	Tensile fracture	Deferred critical	Fail safe	Axial tension/compression (random spectral)	273 K (0 F) to 422 K (300 F)	Low	No
⑦ Wing spars, upper surface					440 MN/m ² (64 ksi)	Tensile fracture, compression buckling	Deferred critical					
⑧ Orbiter support bulkhead (aft)	Machined forging	2219-T851 aluminum alloy	1200 kg (2700 lb)	1.1	250 MN/m ² (36 ksi)	Fracture under tension and bending	Immediate catastrophic	Safe life	Bending plus axial load (random spectral)	143 K (-200 F) to 366 K (200 F)	Moderate	Very difficult
⑨ Vertical stabilizer main box	3-spar box, integral stiffened skin planks	6AL-4V titanium (annealed)	2000 kg (4500 lb)	1.8	210 MN/m ² (30 ksi)	Tensile fracture, compression buckling	Immediate critical (loss of vehicle, possible crew survival)	Fail safe	Axial tension/compression (random spectral)	273 K (0 F) to 522 K (480 F)	Moderate	Very difficult
⑩ Intertank adapter, cylinder shell	Integral stiffened skin riveted to frames	7075 aluminum alloy plate	3400 kg (7600 lb)	3.1	90 MN/m ² (13 ksi)	Tensile fracture, compression buckling	Immediate catastrophic	Safe life	Axial tension/compression (random spectral)	111 K (-250 F) to 422 K (300 F)	Moderate	Yes

NOTES

- (1) Total weight of structural system (excluding TWS, landing, docking) = (247,000 lb)
(2) Total weight of LO₂ and LH₂ tank bulkheads
(3) Estimated, based on skin temperature and heat-sink capacity of substructure
(4) Validity of proof test to verify no leakage during service life is questionable
(5) Interior surface of LH₂ tank bulkheads not accessible because of foam insulation

Recommended selection code:

- ▶ Primary elements for study
▷ Secondary elements for study

FOLDOUT FRAME

1

10/10/10

Table 4-1. Matrix of Candidate Structural Elements and Characteristics - B-9U Booster

Type of Loading	Temperature Cycles	Potential for Initial Flaws	Proof Test Feasible	Accessibility		Applicable NDE Methods			
				Fabrication and Proof Test	Operational Service	Detail	Assembly	Post-Proof	Operational
Biaxial tension (discrete spectra) plus body bending (random spectra)	143 k (-200 F) to 422 k (300 F)	Parent metal, moderate Welds, high	Yes ⁽⁴⁾	Completely accessible	Interior surface not accessible Exterior surface accessible by removal of TPS	Visual, penetrant (both sides) Ultrasonic (raw material)	Visual, X-ray, penetrant (welds)	Visual, X-ray (welds), penetrant (welds and local parent metal) Acoustic emission (during proof)	Visual, leak detection, pressure decay, penetrant and X-ray (local areas)
Biaxial tension (discrete spectra) plus body bending (random spectra)	91 k (-297 F) to 422 k (300 F)	Parent metal, moderate Welds, high	Yes ⁽⁴⁾	Completely accessible	Interior surface accessible ⁽⁵⁾ Exterior surface accessible by removal of TPS	Same as ①	Same as ①	Same as ①	Same as ①
Biaxial tension (discrete spectra)	91 k (-297 F) to 366 k (200 F)	Parent metal, low Welds, high	Yes ⁽⁴⁾	Completely accessible	Interior surface accessible Access to exterior surface is very difficult	Same as ①	Same as ①	Same as ①	Same as ①
Biaxial tension (discrete spectra)	289 k (60 F) to 311 k (100 F)	Low	Yes	Completely accessible	Limited access to interior and exterior surfaces	Visual, penetrant	Visual	Visual, pressure decay, leak check	Visual, pressure decay, leak check
Axial tension/compression (random spectra)	273 k (0 F) to 422 k (300 F)	Low	No	Limited access through inspection panels, ABES cavities	Limited access through inspection panels, ABES cavities	Visual, penetrant, ultrasonic (raw material)	Visual, penetrant, (local web/plate weld regions)		Visual, aided by fiber optics
Bending plus axial load (random spectra)	143 k (-200 F) to 366 k (200 F)	Moderate	Very difficult	Completely accessible	Accessible by removal of TPS	Visual, penetrant	Visual, penetrant		Visual, penetrant
Axial tension/compression (random spectra)	273 k (0 F) to 522 k (480 F)	Moderate	Very difficult	Exterior surface accessible, limited access to interior surface	Exterior surface accessible, limited access to interior surface	Visual, penetrant	Visual, aided by fiber optics		Visual, aided by fiber optics
Axial tension/compression (random spectra)	111 k (-250 F) to 422 k (300 F)	Moderate	Yes	Completely accessible	Limited access to interior surface, exterior surface accessible by removal of TPS	Visual, penetrant, ultrasonic (raw material)	Visual, penetrant	Visual, penetrant	Visual, penetrant

Section code:
 elements for study
 elements for study

FOLDOUT FRAME

2

5.0 FATIGUE AND FRACTURE PROPERTIES

Summarized in this section are fatigue and fracture properties of materials that have been selected or are alternate candidates of interest for the chosen structural elements. Properties have been established from wide-spread literature survey, supplemented by in-house data derived from test programs conducted under other contracts.

5.1 FATIGUE PROPERTIES

5.1.1 2219 Aluminum Alloy

S-N curves for 2219-aluminum alloy are plotted in Figure 5-1. A family of curves are plotted for various values of stress ratio (maximum stress in cycle divided by minimum stress in cycle). The data (solid curves) are for a theoretical stress concentration factor (K_t) of 4.4, which is considered to be representative or slightly conservative for average design practice as applied to structural assemblies and joints of the propellant tanks. Data are also given (dashed curves) for a K_t of 3.0. The S-N curves are expressed in terms of percent of material ultimate tensile strength, and are considered to be applicable to both the -T851 and -T878 tempers of the alloy. The curves are based on room temperature data, but may be applied over the temperature range of -300 F to +300 F with only small error.

The curves are based primarily on the data of Reference 8; however, other sources, such as Reference 9, have been examined to compare and validate the data.

5.1.2 6Al-4V Titanium Alloy

S-N curves for 6Al-4V titanium alloy are plotted in Figure 5-2 ($K_t = 3.0$) and Figure 5.3 ($K_t = 4.5$). Again, a family of curves is plotted for various values of stress ratio, and the allowable maximum stress is expressed as a percentage of material ultimate tensile strength. The curves are based on room temperature test data for the annealed material and will be slightly conservative if applied to elevated temperature up to +650 F. Using the allowable stress values determined from these curves with annealed material properties for material in the solution treated and aged (STA) temper should also be conservative.

The S-N curves are based on the data presented in Reference 8 for titanium which was subjected to a diffusion bond thermal cycle. This is equivalent to a mill anneal temper insofar as strength and fatigue properties are concerned. Data on material in this condition were obtained by extensive testing at the NR Los Angeles Division. Data from other sources, such as References 10 and 11, were also reviewed to verify the validity of the S-N curves.

The S-N curves for $K_t = 4.5$ are considered to be representative of average design practice applied to joints and attachments; those for $K_t = 3.0$ representative of design practice where rather extensive care is taken to minimize stress concentrations and to employ other methods to retard fatigue crack initiation. An interesting comparison is presented in the modified Goodman diagram of Figure 3-4. Superimposed on the constant life curves for $K_t = 3.0$ and $K_t = 4.5$ are discrete points representing the results of fatigue tests on structural joints. Spotwelded joint data is taken from Reference 11, riveted joint data from Reference 12. It can be seen that the spotwelded joint and the Hi-Shear rivet joint were approximately comparable to a $K_t = 4.5$ in the higher cycle range; the riveted joint using Taper-Lok fasteners exhibited better fatigue life than notched specimens with $K_t = 3.0$. It also can be seen that the allowable stress determined from notched specimens becomes progressively more conservative compared to joint tests as the fatigue life is reduced below 10^5 cycles.

5.2 FRACTURE PROPERTIES

5.2.1 Fracture Toughness

The plane-strain fracture toughness (K_{Ic}) is the most common of the fracture properties of interest for engineering materials. It represents the resistance to fracture of a material containing cracks or crack-like defects and subjected to a monotonic tension loading. Ideally, it may be taken as a basic material property which is not affected by the detail design configuration. However, a number of different types of test specimens and test techniques have been used by various investigators to attempt to measure this property. Unfortunately, the results from those various approaches are not necessarily compatible and caution must be exercised in evaluating and interpreting the data. The compact tension (CT) and notch-bend (NB) type of test specimens have been standardized by ASTM committee for plane-strain fracture toughness testing in an attempt to provide a more uniform basis for comparison of data from various sources. However, there are a number of rules or tests that must be satisfied for each set of test data to qualify the validity of plane-strain fracture toughness results. One of the more significant rules involves the required minimum thickness of the test specimen to insure that plane-strain conditions exist. Some investigators prefer the surface flawed, or part-through-crack (PTC) type of specimen because it more closely simulates the type of defect and loading conditions encountered on actual structures in service. However, no ASTM standards have been established for this type of specimen.

A survey has been made of fracture toughness data for materials of interest from a number of sources; the results are summarized in Tables 5-1 and 5-2 for Ti-6Al-4V and 2219 aluminum alloys, respectively. The type and thickness of test specimen and the relative orientation of test loading and direction of crack extension is listed, as well as the range and average values of apparent fracture toughness. The nomenclature for test specimen orientation is illustrated in Figure 5-5.

FIG. 34: 610 DIETZEN - RAIN FACER
SEM - 1000000
5 CYCLES X 10 DIVISIONS PER INCH
EUGEN: DIETZEN CO.

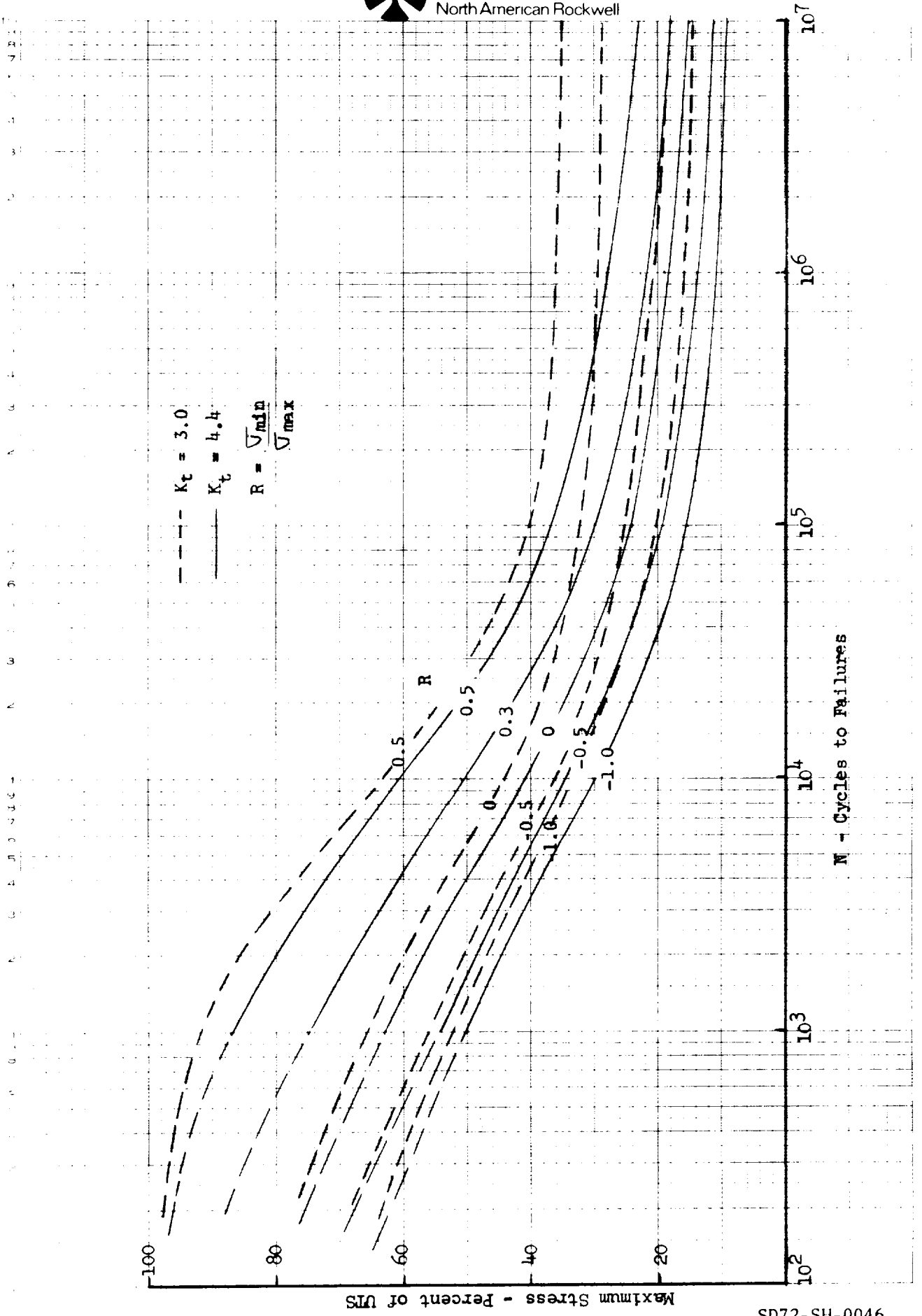


Figure 5-1 S-N Curves for 2219 Aluminum

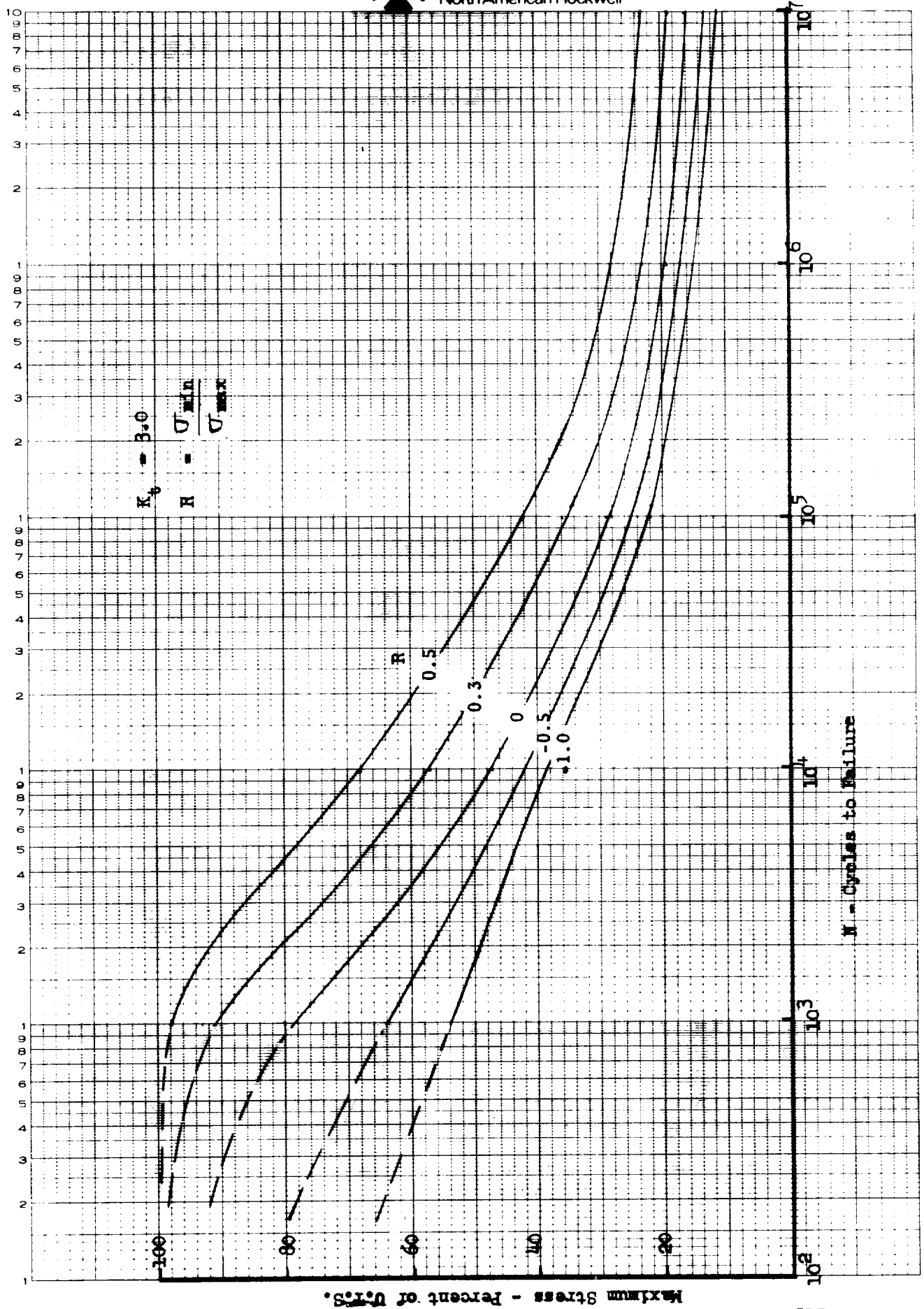


Figure 5-2 S-N Curves for TH-6Al-tV ($K_t = 3.0$)

EUGENE DIETZGEN CO.

MADE IN U.S.A.

NO. 340-LS-10 DIETZGEN GRAPH PAPER
SEMI LOGARITHMIC
5 CYCLES X 10 DIVISIONS PER INCH

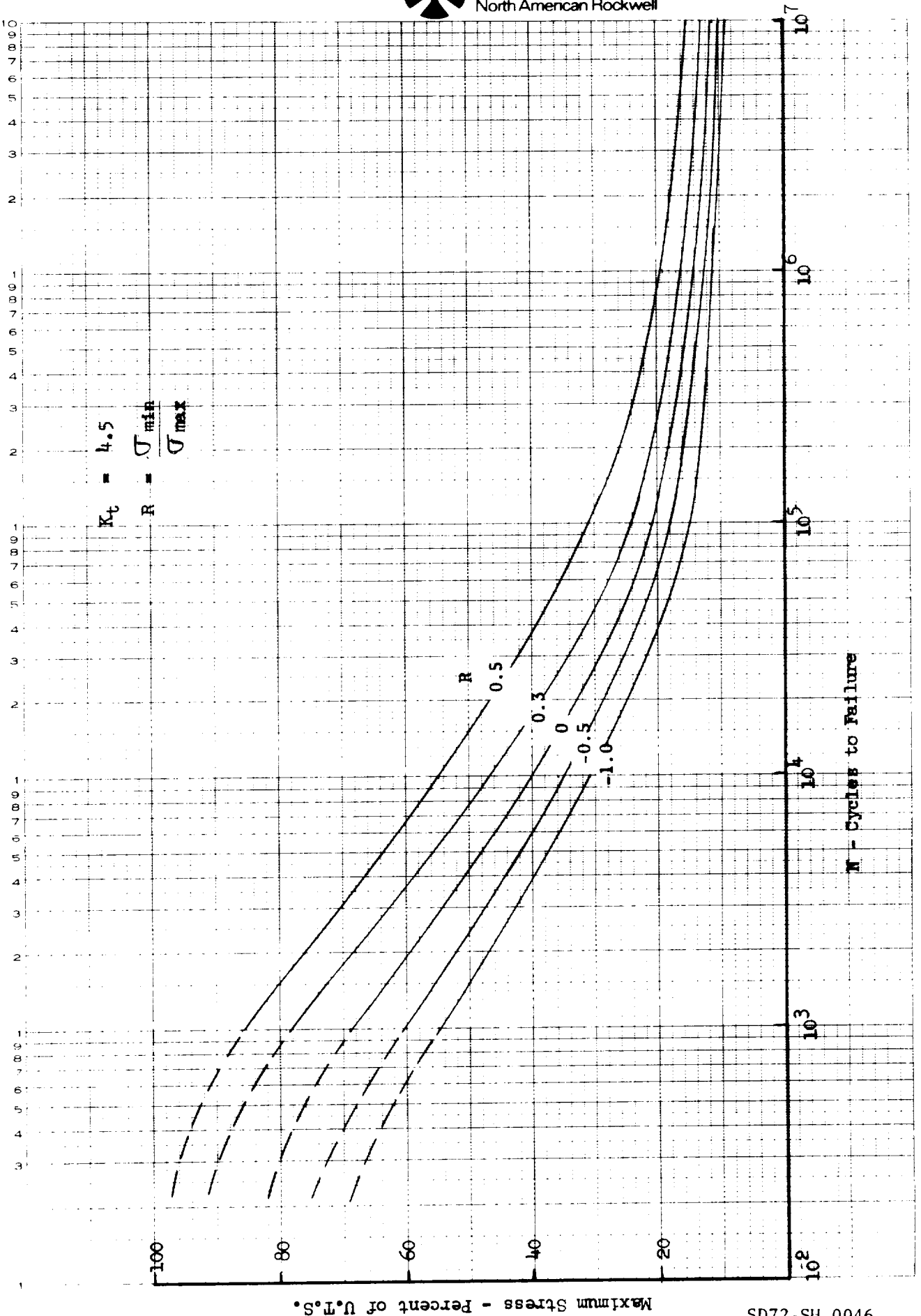


Figure 5-3 S-N Curves for TI-6Al-4V ($K_t = 4.5$)

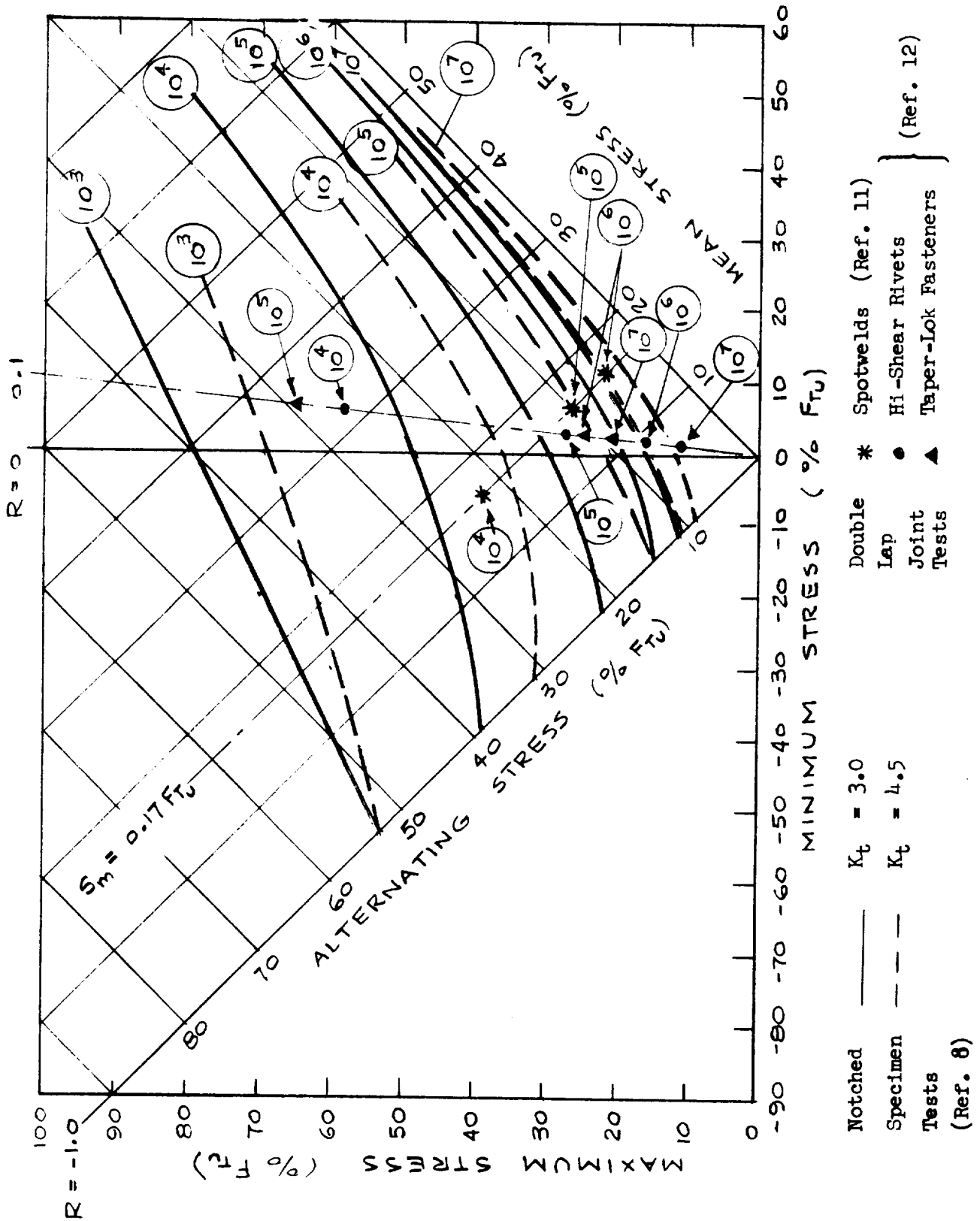


Figure 5-4 Modified Goodman Diagram for TH-6Al-4V (Annealed)

A considerable amount of fracture toughness test data for Ti-6Al-4V alloy in the annealed condition has been obtained by NR/Los Angeles Division on current production programs. This data is plotted versus specimen thickness in Figures 5-6 and 5-7. An estimated lower bound curve also is indicated, which defines an effective fracture toughness (K_{Ic}) of $87.6 \text{ MN}/(\text{m})^{3/2}$ ($80 \text{ ksi } \sqrt{\text{in.}}$) for thicknesses up to 0.51 cm (0.20 in.), decreasing to a value of $66 \text{ MN}/(\text{m})^{3/2}$ ($60 \text{ ksi } \sqrt{\text{in.}}$) for thicknesses of 1.9 cm (0.75 in.) and greater. This value for K_{Ic} also appears to be in reasonable agreement with data from other sources indicated in Table 5-1. A fracture toughness (K_{Ic}) of $38.4 \text{ MN}/(\text{m})^{3/2}$ ($35 \text{ ksi } \sqrt{\text{in.}}$) is estimated as a design value for this alloy in the solution treated and aged condition (STA) from other data presented in Table 5-1.

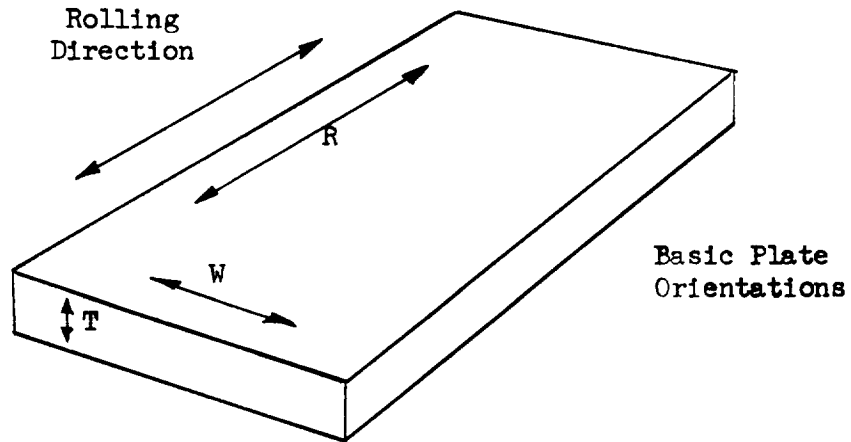
Design values for plane-strain fracture toughness (K_{Ic}) of 2219 aluminum parent metal and welds have been estimated from the data listed in Table 5-2, and are summarized below. The effective fracture toughness also is dependent on material thickness, but this influence will be accounted for by use of empirical test data currently being developed through in-house test programs.

2219-T87 Aluminum Alloy Material Form and Orientation	K_{Ic}			
	70 F		-320 F	
	$\text{MN}/(\text{m})^{3/2}$	$\text{ksi } \sqrt{\text{in.}}$	$\text{MN}/(\text{m})^{3/2}$	$\text{ksi } \sqrt{\text{in.}}$
Base metal - long. (RW)	36	33	39.5	36
Base metal - trans. (WR)	33	30	36	33
Weld (2319 filler alloy)	17.5	16	21	19

5.2.2 Crack Growth Rate-Cyclic Load

Crack growth under cyclic tension stresses is commonly characterized as da/dN ; i.e., the amount of crack extension (increase of half-length for a through crack, increase in depth for a surface crack) per cycle of applied loading. Most investigators agree that the crack growth rate is primarily dependent on the stress intensity range during the load cycle ($\Delta K = K_{min}/K_{max}$) and the associated maximum stress intensity achieved. In contrast to conventional fatigue practice, a negative value of load ratio has no meaning, because it is assumed that the crack will close under compression stresses and these stresses will be transferred by bearing along the crack surfaces with no further change in stress intensity at the tip of the crack. Therefore, a load ratio of zero is the minimum value encountered in crack growth analysis.

Extensive testing to determine crack growth rates for Ti-6Al-4V has been accomplished by NR/Los Angeles Division as part of current production programs. Current data from this source is plotted in Figure 5-8. This data represents production material lots with relatively low fracture toughness and crack growth rates somewhat higher than average. Therefore, it is considered to represent a reasonable design boundary for use in this study. The data points represent tests on five specimens, three at a load ratio of 0.3 and two at a load ratio of zero. An empirical equation has been proposed by R. Forman to



First symbol - direction of load

Second (third) symbol(s) - direction(s) of crack extension

Examples:

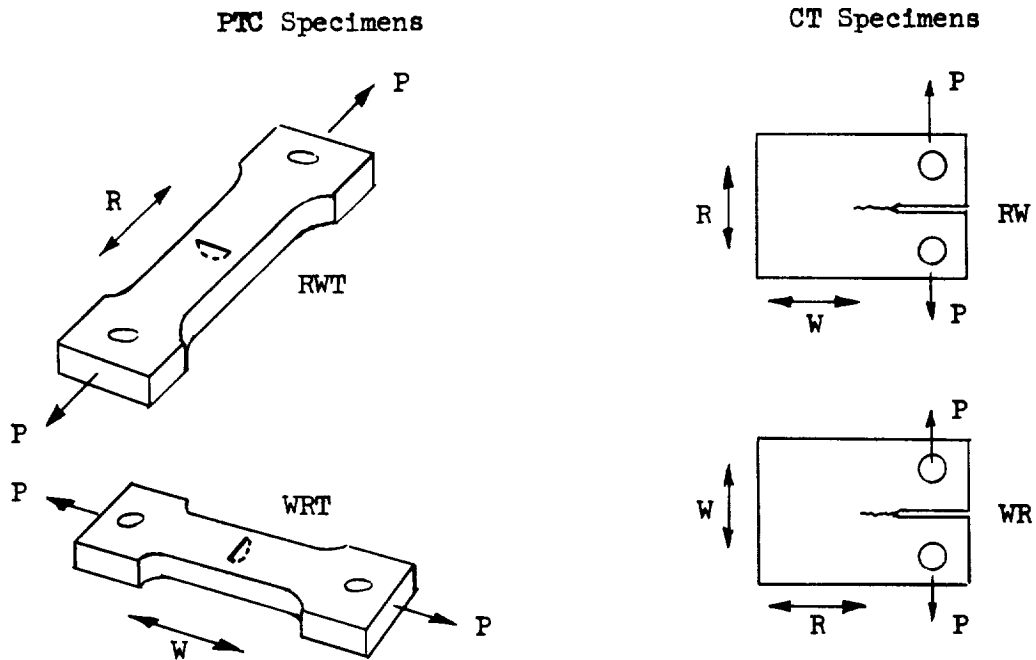


Figure 5-5 Orientation of Fracture Properties Test Specimens

Table 5-1. Fracture Toughness Test Data for Ti-6Al-4V

Material Form and Temper	Temp. and Environ.	Ref.	Type of Spec. (1)	Thickness cm in.	Orientation (2)	No. of Tests	Apparent Fracture Toughness			
							Range		Average	
							MN/(m) ^{3/2}	ksi.√in.	MN/(m) ^{3/2} ksi.√in.	
Sheet & Plate	70 F	13	Not Identified	2.54	RW	3			50.9	46.3
				2.28	RW	3			51.8	47.1
				2.54	WR	3	Not Listed		46.4	42.2
				2.28	WR	3			40.9	37.2
Solution Treated and Aged (STA)	Lab Air	14	PTC	.254	RWT	3	49.6-51.3	45.1-46.7	50.4	45.8
				.142	RWT	7	43.9-53.9	39.9-49.0	49.6	45.2
				.165	RWT	1	---	---	52.0	47.3
				.165	RWT	1	---	---	47.3	43.0
(STA)	-100 F Dry N ₂	17	CT	.508	RW	8	36.8-54.5	33.5-49.6	43.5	39.6
				.508	WR	7	38.2-49.3	34.8-44.9	43.5	39.6
				2.54	RW	3	Not Listed		50.7	46.2
				2.28	RW	3			46.5	42.3
Sheet & Plate Annealed	70 F	17	PTC	.508	RWT	8	63.2-70.3	57.5-64.0	67.0	61.0
				.508	RW	6	60.0-72.5	54.6-66.0	66.5	60.5
				1.27	RW	3	87.6-88.3	79.7-80.3	88.0	80.0
				2.03	RW	3	71.9-78.2	65.4-71.1	74.2	67.5
Sheet & Plate Annealed	Lab Air	19	CT	5.08	RW	10	67.2-99.7	61.1-90.8	83.6	76.2
				10.2	WR	10	66.1-100.2	60.2-91.1	82.8	75.4

(1) Specimen Type

- PTC - Part-thru crack
- CT - Compact tension
- CC - Center crack
- NB - Notch-bend
- SEN - Single edge notch

(2) Orientation

- R - Rolling direction
- W - Width direction
- T - Thickness direction
- First symbol - direction of load application
- Second/third symbols - direction/s of crack propagation

Table 5-2. Fracture Toughness Test Data for 2219 Aluminum Alloy

Material Form and Temper	Temp. and Environ.	Ref.	Type of Spec.	Thickness		Orientation	No. of Tests	Apparent Fracture Toughness			
				cm	in.			Range		Average	
								MN/(m) ^{3/2}	ksi.√in.		MN/(m) ^{3/2}
2219-T851 Plate	70 F Lab Air	13	NB	3.56	1.4		2			39.0	35.5
			SEN	2.54	1.0		4			39.5	36.0
			NB	3.56	1.4	Not Listed	4			36.6	33.3
			NB	2.54	1.0		4			39.0	35.5
2219-T87 Plate	70 F Lab Air	9	CN	2.54	1.0		12	40.0-52.2	36.4-47.5	45.4	41.4
				2.54	1.0		12	36.6-44.5	33.4-40.5	40.7	37.1
		15	PTC	2.54	1.0		3	54.8-56.4	49.9-51.3	55.9	50.8
				2.54	1.0		3	42.5-47.8	38.7-43.5	46.1	42.0
		16	PTC	1.55	0.61		1	---	---	37.1	33.8
				3.15	1.24		1	---	---	38.4	35.0
2219-T87 Plate	-320 F LN ₂	15	PTC	2.54	1.0		2	59.5-61.1	54.2-55.6	60.3	54.9
				2.54	1.0		2	49.1-51.9	44.7-47.2	50.5	46.0
		16	PTC	1.55	0.61		1	---	---	41.3	37.6
				3.12	1.23		1	---	---	41.6	37.9
2219-T87 Welds	70 F Lab Air	15	PTC	0.63	0.25		3	19.8-24.5	18.0-22.3	22.4	20.4
				1.27	0.50		3	17.0-21.7	15.5-19.7	19.4	17.7
2219-T87 Welds	-320 F LN ₂	15	PTC	0.63	0.25		3	23.1-28.5	21.0-25.9	26.4	24.0
				1.27	0.50		3	20.4-26.0	18.6-23.7	23.6	21.5

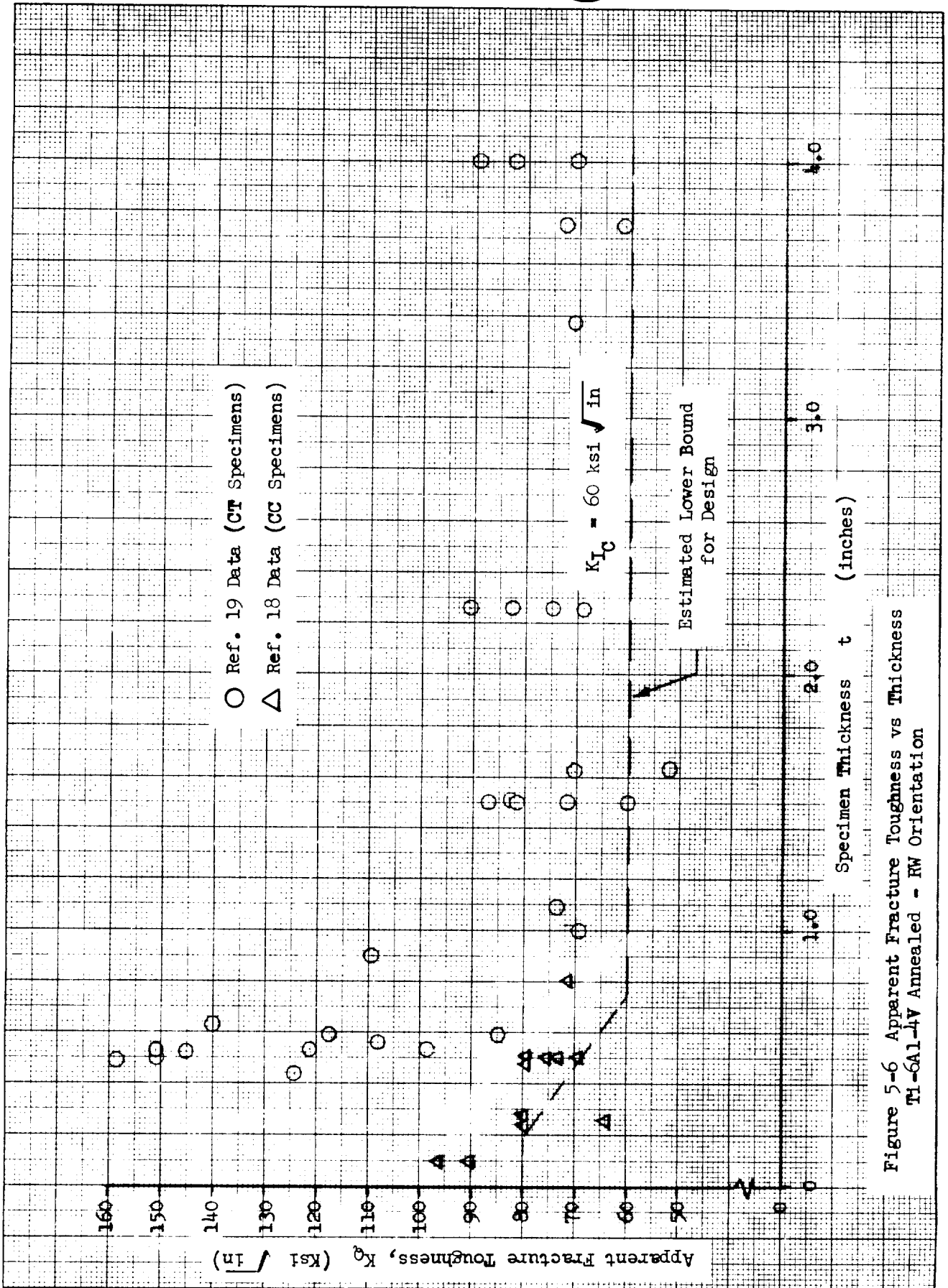


Figure 5-6 Apparent Fracture Toughness vs Thickness
 TH-6Al-4V Annealed - RW Orientation

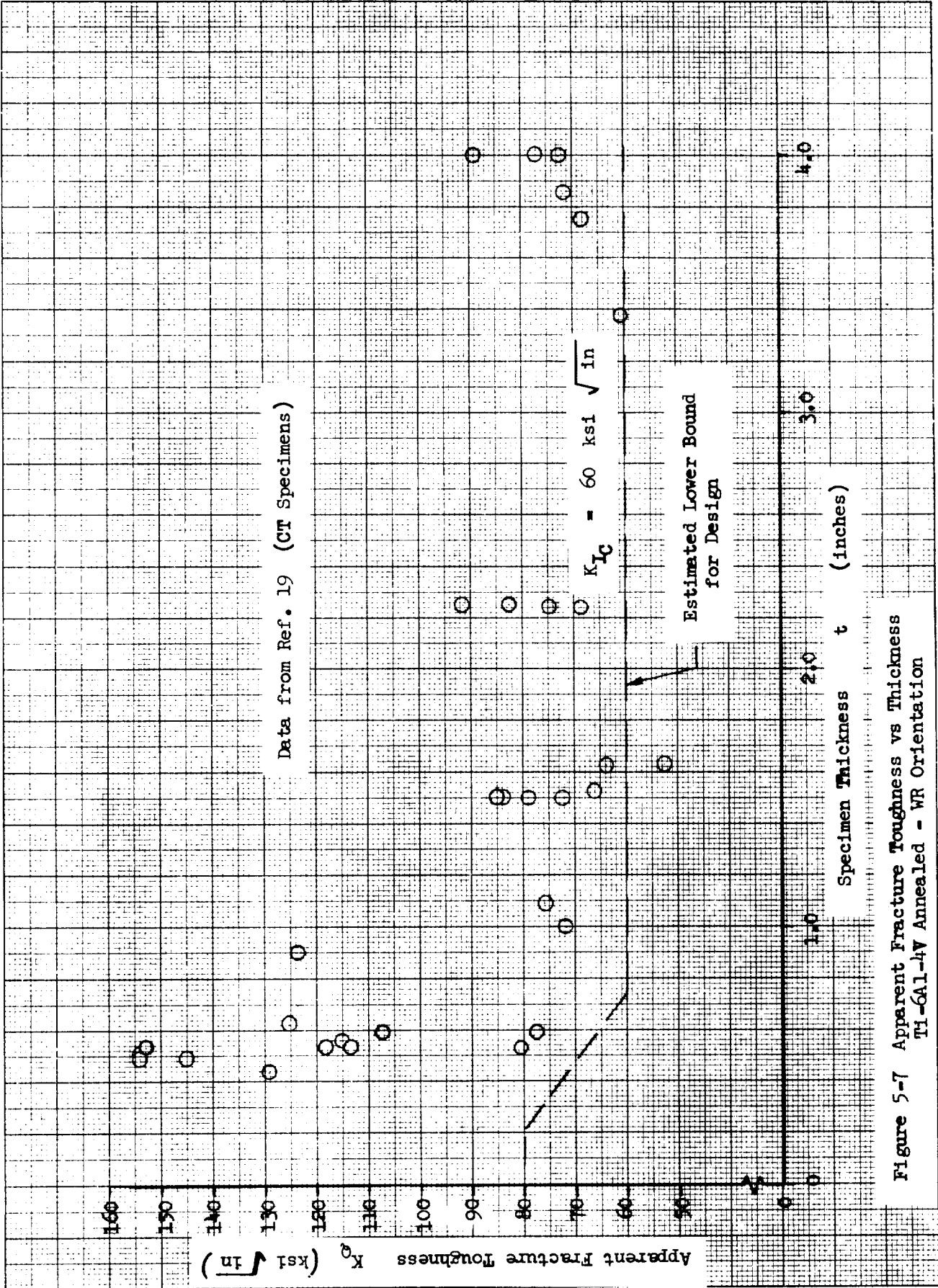


Figure 5-7 Apparent Fracture Toughness vs Thickness
 Ti-6Al-4V Annealed - WR Orientation

provide a mathematical expression which approximates typical crack growth rate characteristics for engineering materials. This equation is expressed as:

$$\frac{da}{dN} = \frac{c (\Delta K)^n}{(1-R)K_c - \Delta K}$$

where:

$$\frac{da}{dN} = \text{crack growth rate - in./cycle}$$

$$\Delta K = \text{range of stress intensity in load cycle} \\ (\Delta K = K_{\max} - K_{\min}) - \text{psi } \sqrt{\text{in.}}$$

$$R = \text{load ratio in cycle } (R = \frac{K_{\min}}{K_{\max}})$$

$$K_c = \text{critical stress intensity for fracture - psi } \sqrt{\text{in.}}$$

$$\left. \begin{matrix} c \\ n \end{matrix} \right\} \text{coefficients determined empirically to provide best fit to test data.}$$

The Forman equation will generally provide a satisfactory approximation to the upper transition of crack growth rate with ΔK , but will not account for the lower transition which may occur at low values of ΔK . Therefore, in some cases it may be desirable to define a second equation of the Forman type to approximate crack growth characteristics in the region of low ΔK .

Coefficients for the Forman equation have been determined to approximate the crack growth rate test data for Ti-6Al-4V (annealed) and are indicated on Figure 5-8 along with the corresponding curves. A lower transition in the slope of the crack growth curve appears to occur at a ΔK of approximately 10 ksi $\sqrt{\text{in.}}$. Therefore, a second set of coefficients have been determined to approximate the growth rate characteristics for ΔK less than 10 ksi $\sqrt{\text{in.}}$; these are also indicated on Figure 5-8.

Crack growth rates for 2219-T87 aluminum alloy have been determined by investigators using both PTC and CT specimens; these data are plotted in Figures 5-9 and 5-10 respectively. A curve representing the Forman equation with indicated coefficients is also plotted on each curve. These coefficients were established by Forman in Ref. 20. It can be seen that correlation of data between the two different investigators and types of specimens is generally excellent. The empirical curve proposed by Forman provides a good fit to the CT data for longitudinal specimens (RW orientation) over the complete range of ΔK investigated. However, crack growth rates for CT transverse specimens (WR orientation) appear to be somewhat greater in the range of high ΔK ; modified coefficients have been determined as indicated on Figure 5-10 to provide a better fit to this data. Crack growth rates

determined by Forman on PTC specimens at -320 F are plotted in Figure 5-11, along with the empirical fit curve and corresponding coefficients recommended by him.

Stress intensities calculated by Forman in reduction of crack growth rate test data include a deep-flaw magnification factor, with resulting expression:

$$\Delta K = 1.1 \Delta \sigma \sqrt{\pi(a/Q)} M_k$$

The variation of M_k with crack depth/thickness ratio and crack aspect ratio used by Forman is plotted in Figure 5-12.

One limitation of the Forman type equation is the difficulty of accurately representing the experimental data for crack growth in the low stress intensity range. This can be partially overcome by the use of a dual definition of Forman curves, as previously mentioned. However, it appears that a threshold stress intensity will exist for most materials below which no crack growth will occur. Even the use of two separate Forman type curves to represent test data will not accommodate a threshold stress intensity concept. A recent development at Space Division was the pursuit of a generalized growth rate expression that accommodates both a lower threshold and an upper limit of critical stress intensity. The equation developed to achieve this goal is presented below.

$$\frac{da}{dN} = \text{EXP} \left[n \cdot \frac{\ln K_c - \ln \Delta K_o}{2} \cdot \operatorname{arctanh} \left\{ \frac{\ln \Delta K - \frac{\ln K_c (1-R) + \ln \Delta K_o}{2}}{\frac{\ln K_c (1-R) - \ln \Delta K_o}{2}} \right\} + \ln \left\{ C \cdot \text{EXP} \left(\frac{\ln K_c + \ln \Delta K_o}{2} \cdot n \right) \right\} \right]$$

where material constants

n = Paris equation exponent

C = Paris equation coefficient

K_c = stress intensity for fracture

K_o = threshold stress intensity range for growth

and input variables

K = cyclic range of stress intensity (constant amplitude)

R = load ratio $\frac{P_{\min}}{P_{\max}}$

This equation may appear to be cumbersome to use for manual calculations, however, once programmed for computer analysis it is simple to apply because of the limited number of material constants and input variables that must be specified. Initial evaluations of the capability of this expression to provide a good fit to experimental data have been encouraging. A comparison of fit to experimental growth rate data determined by SD on two aluminum alloys is given in Figure 5-13.

This expression has been programmed for use in crack-growth analyses on the Hewlett-Packard Model 9810 computer/plotter and was applied to the propellant tank crack growth analyses presented in subsequent sections of this report. The growth rate curves used in these analyses are presented in Figure 5-14. Crack growth analyses for other structural components were performed using the EFFGRO computer program (IBM 360) with Forman equation(s) describing crack growth rates.

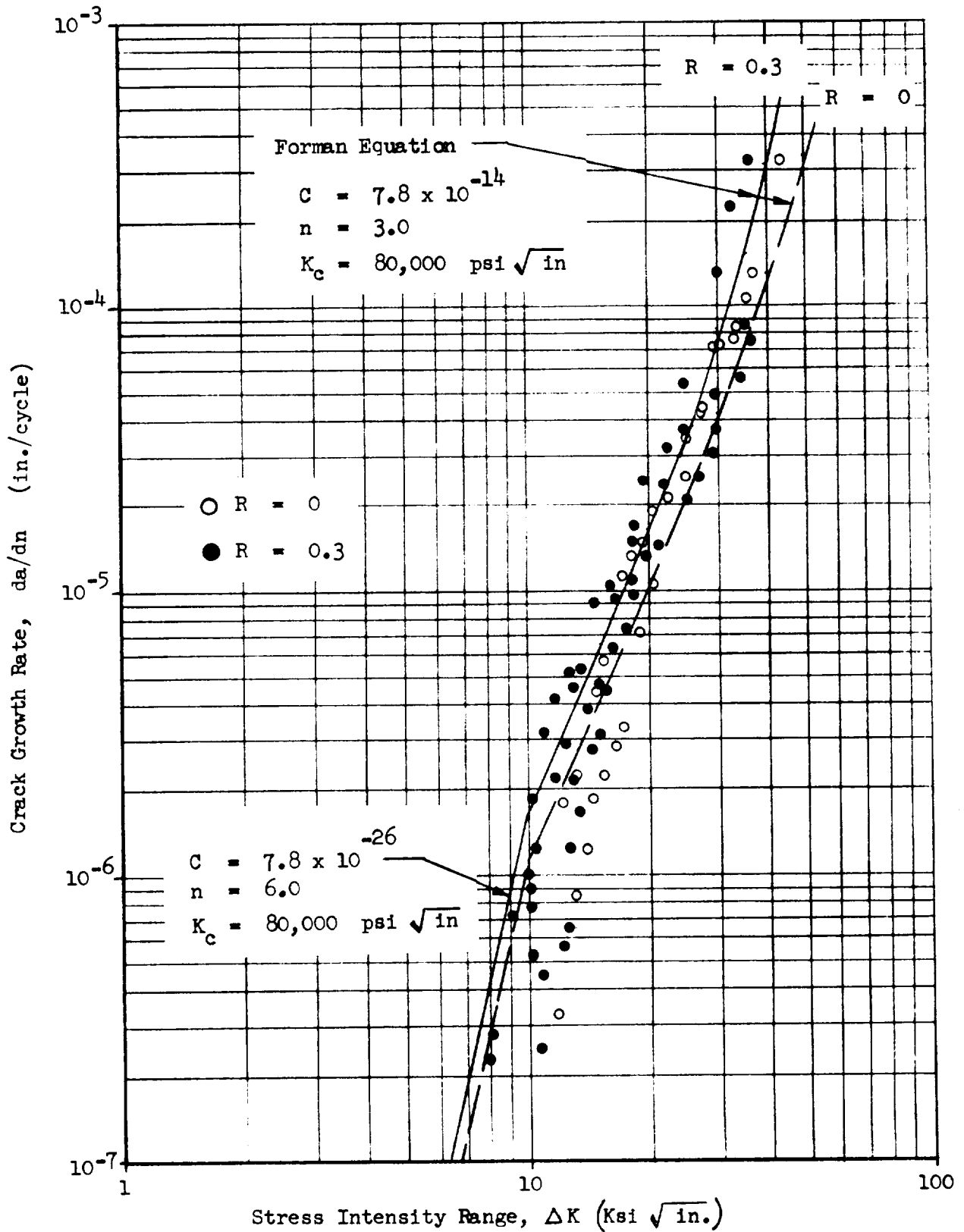


Figure 5-8. Crack Growth Rate for Ti-6Al-4V Under Cyclic Loading

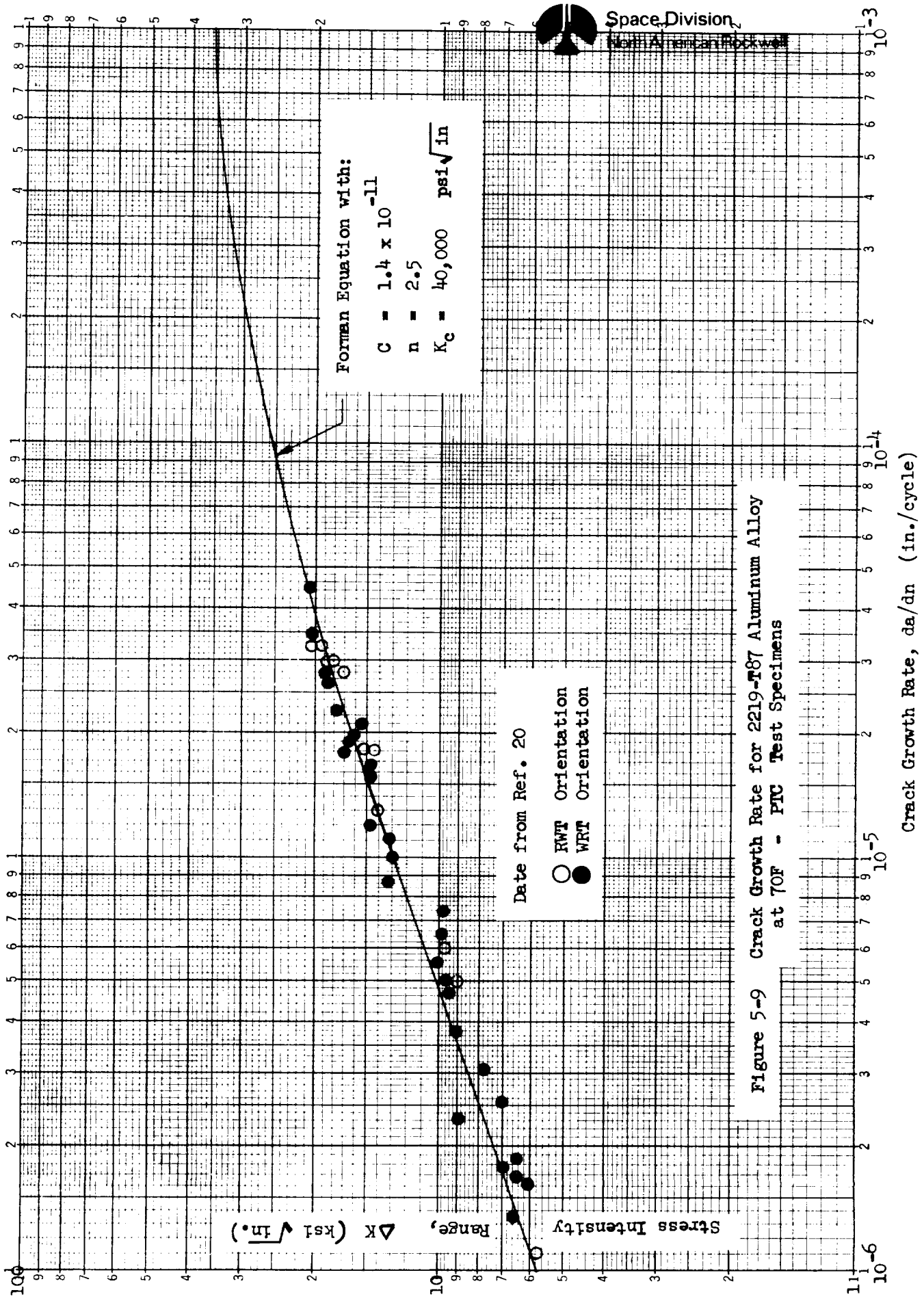
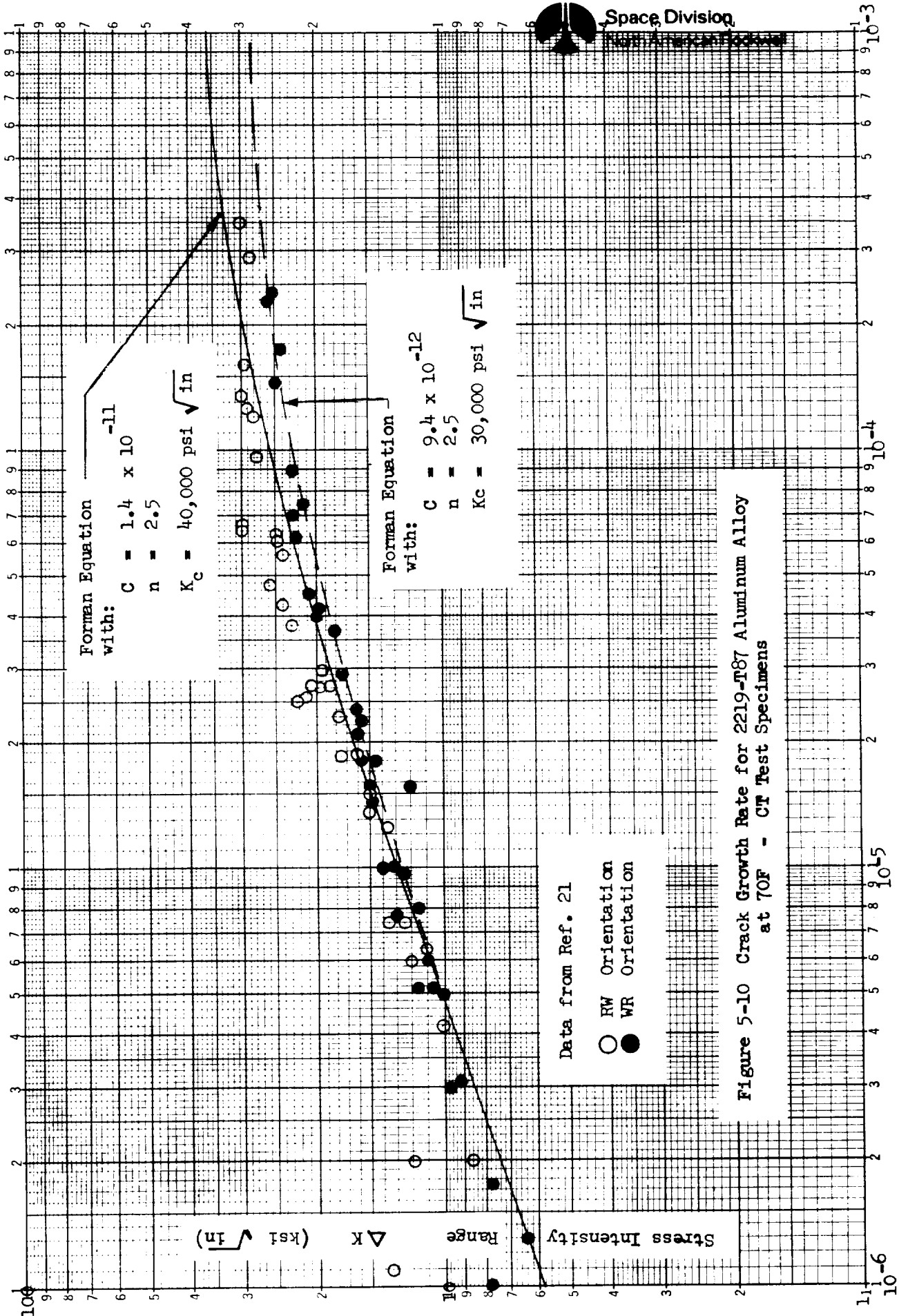


Figure 5-9 Crack Growth Rate for 2219-T87 Aluminum Alloy at 70F - PIC Test Specimens



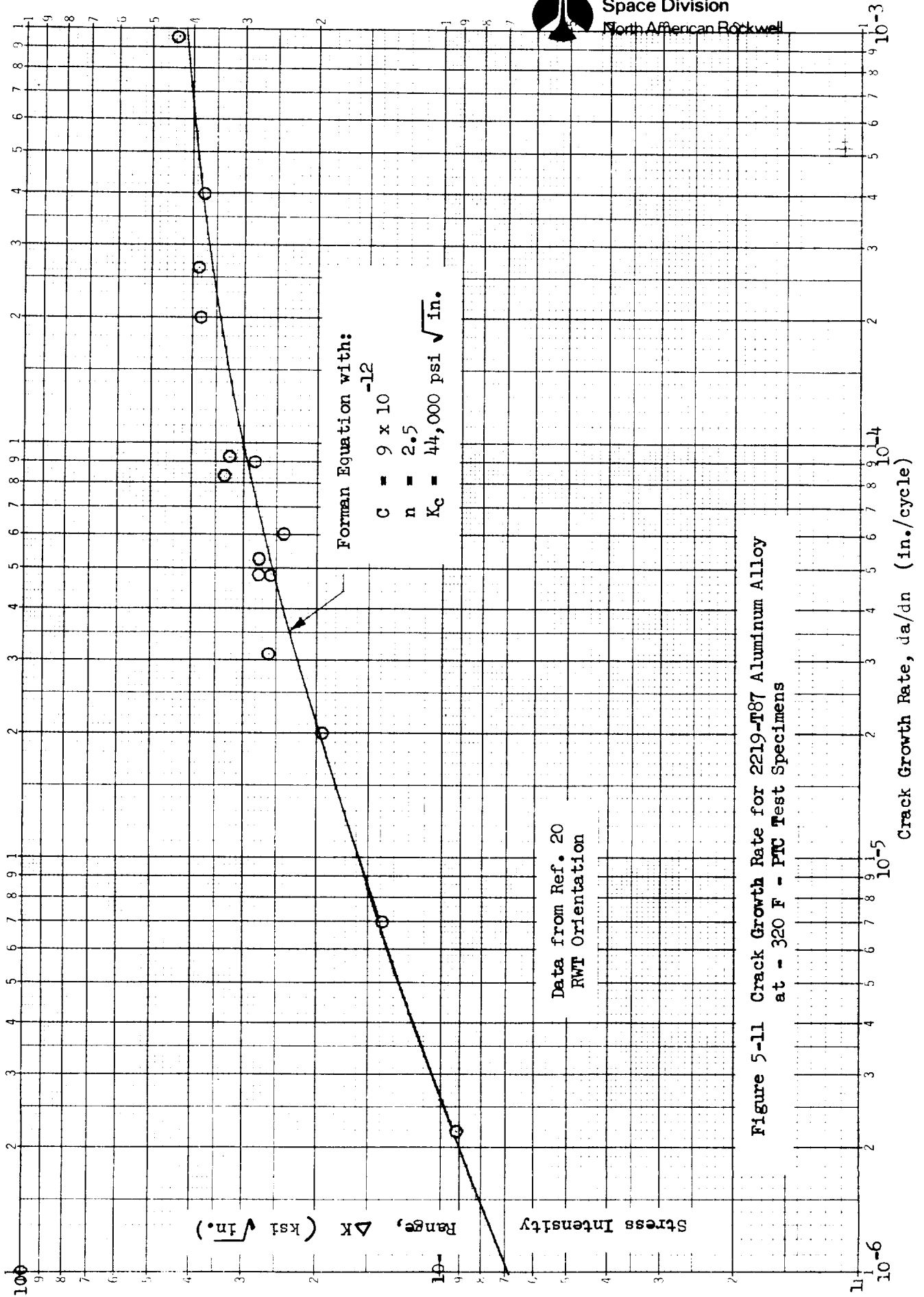
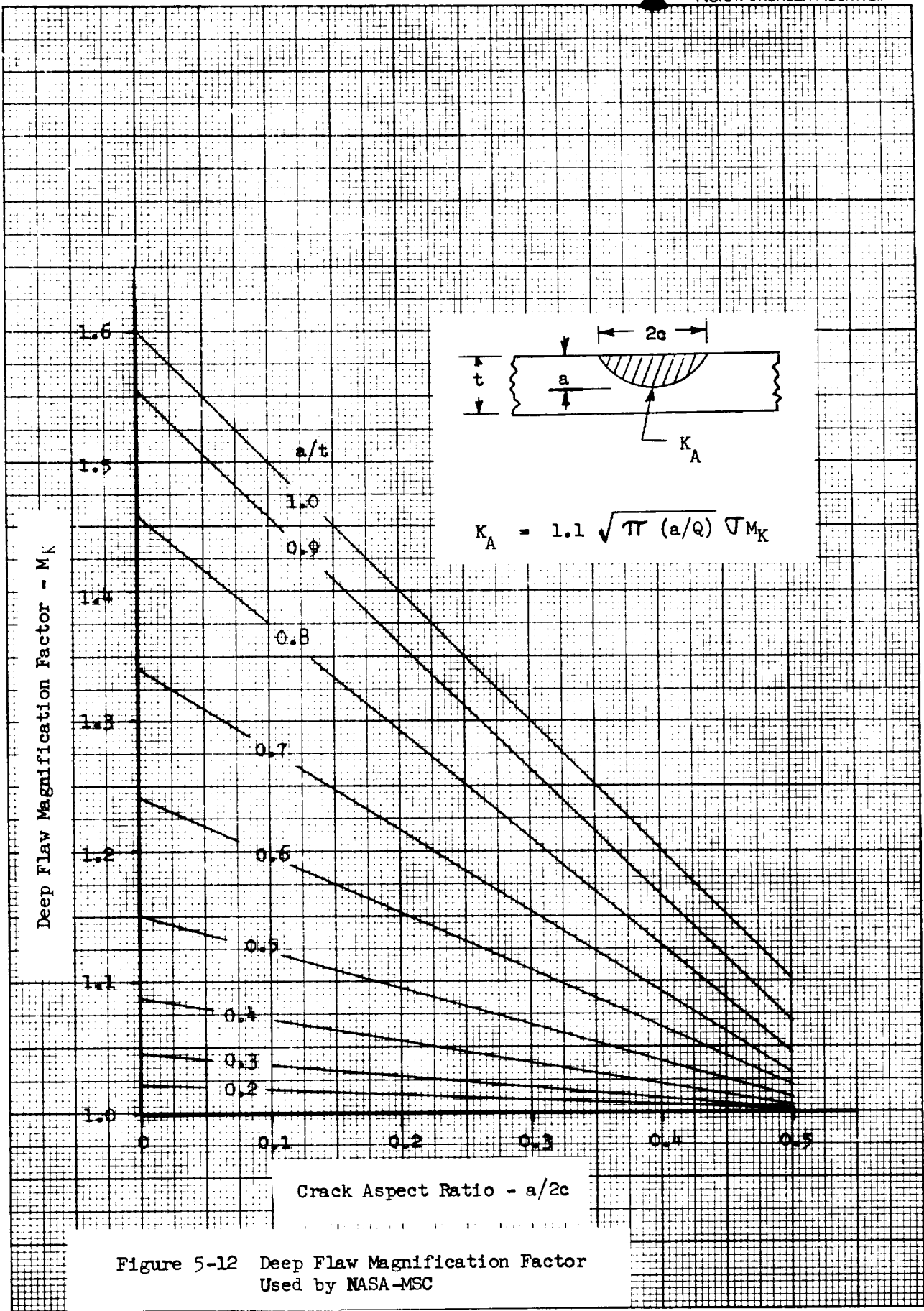


Figure 5-11 Crack Growth Rate for 2219-T87 Aluminum Alloy
 at - 320 F - PTC Test Specimens



10 X 10 TO THE 1/2 INCH 359T-11
 KEUFFEL & ESSER CO. PART NO. 1-A
 ALBANY, N.Y.

Figure 5-12 Deep Flaw Magnification Factor
Used by NASA-MSFC

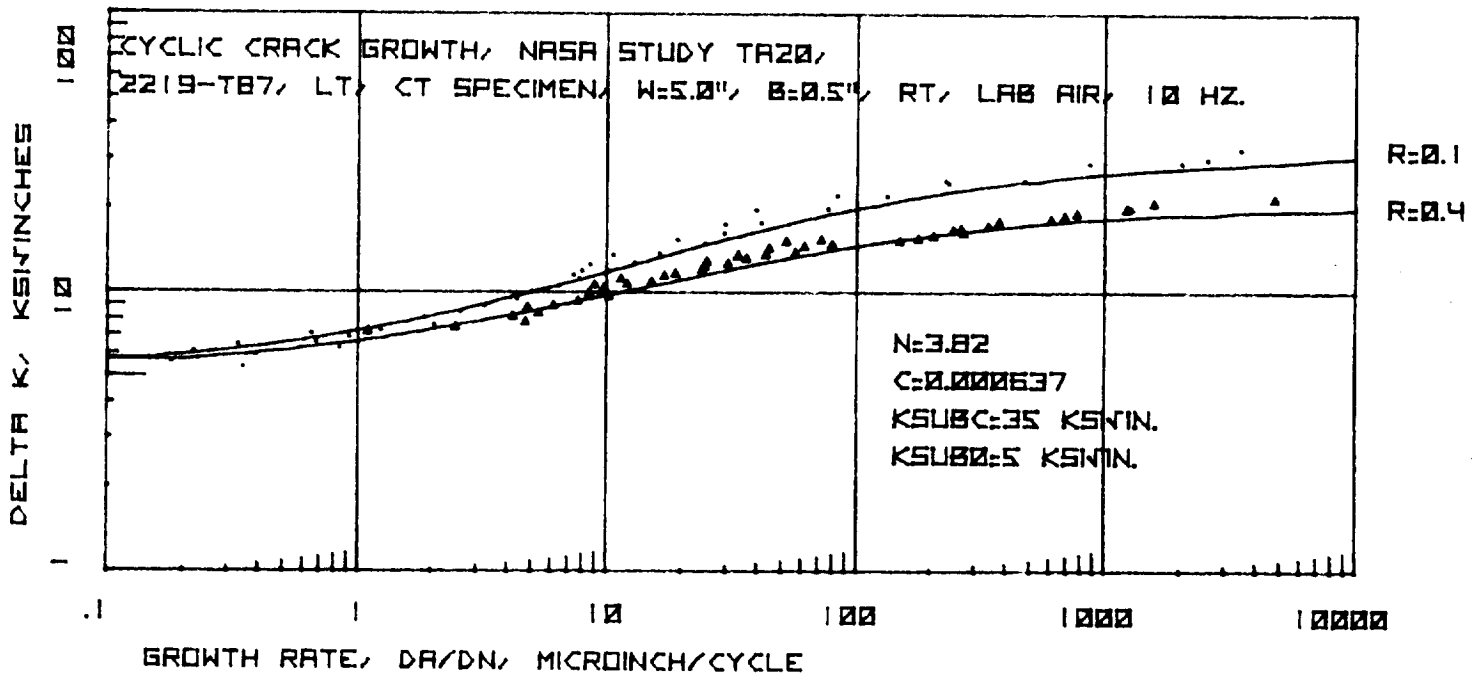
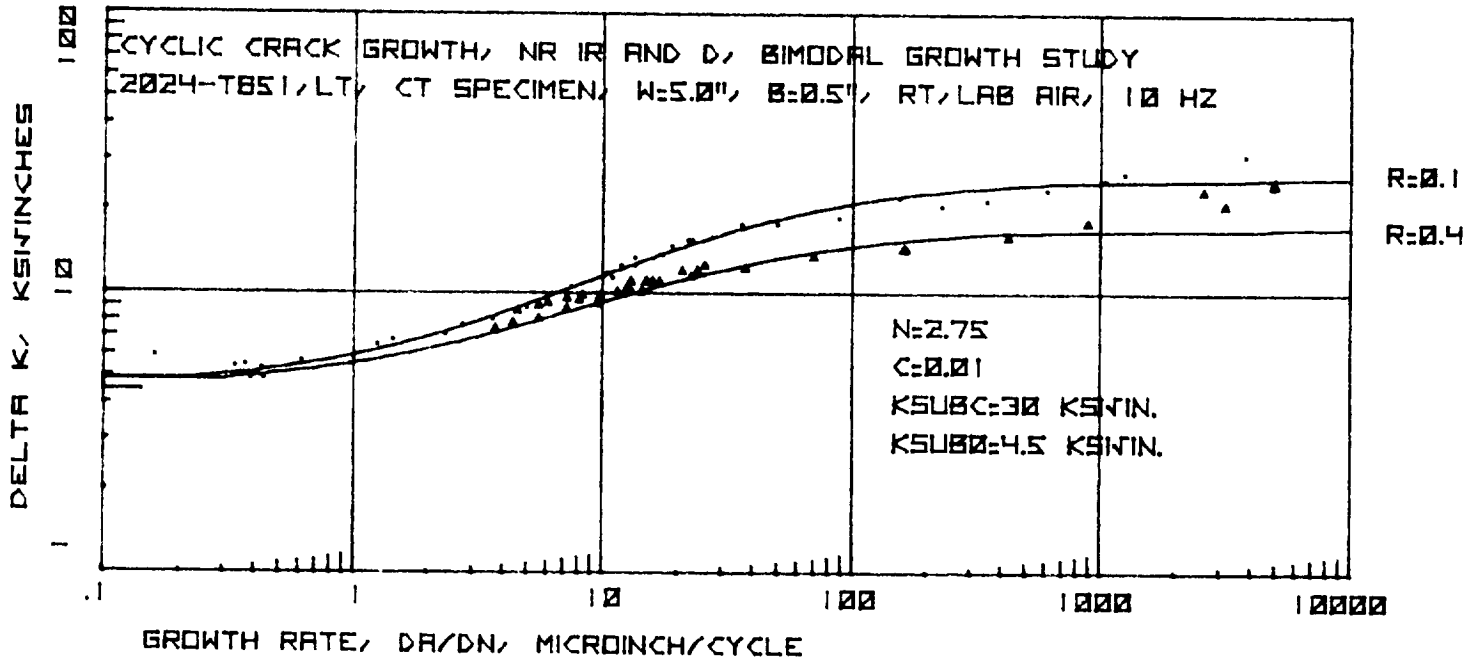


Figure 5-13. Generalized Crack Growth Rate Equation Compared to SD Experimental Data for 2024 and 2219 Aluminum

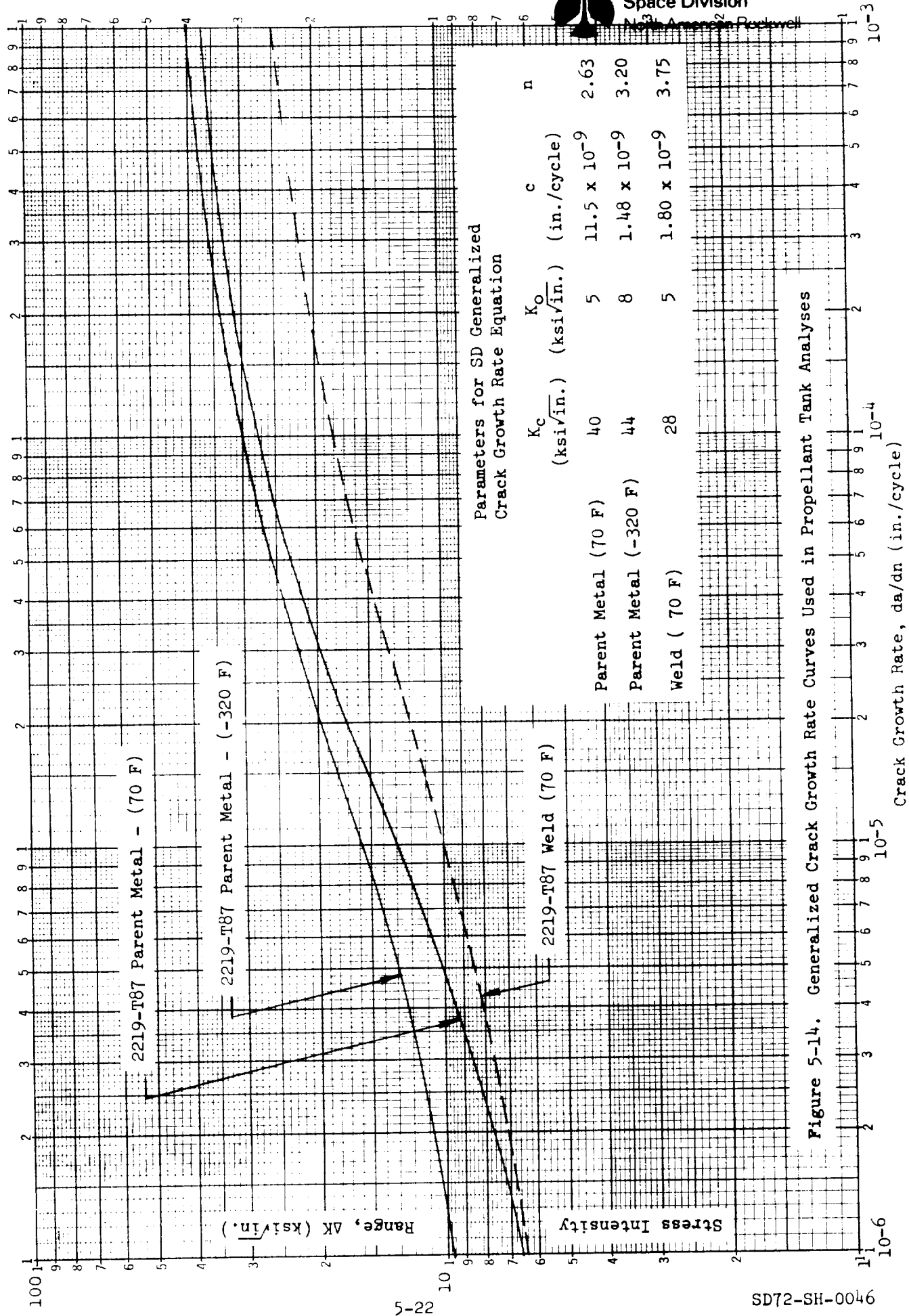


Figure 5-14. Generalized Crack Growth Rate Curves Used in Propellant Tank Analyses

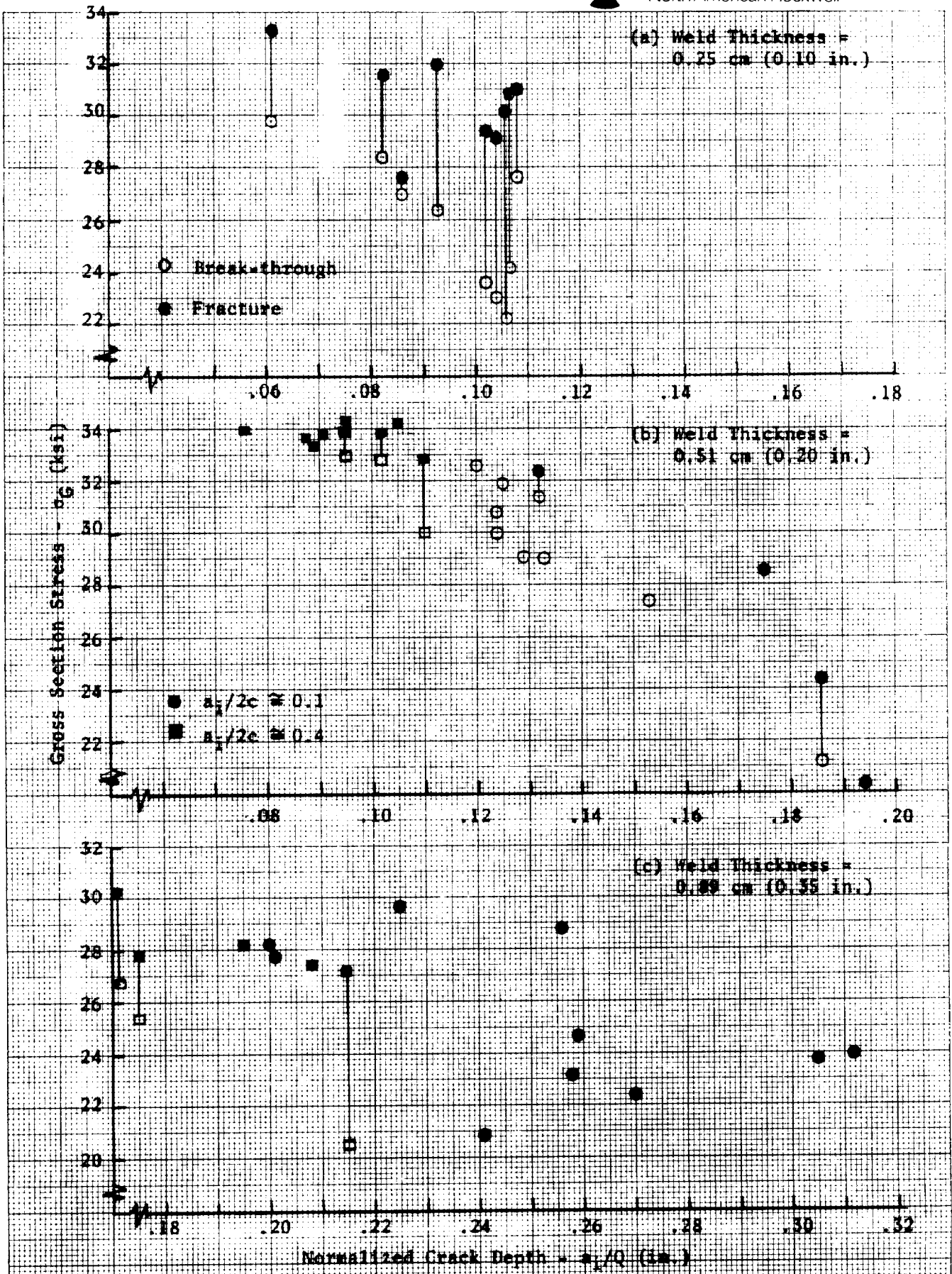
5.2.3 Empirical Fracture Data - 2219-T87 Welds

Fracture and flaw growth tests were performed on 2219-T87 weld joint specimens as part of the fracture mechanics experimental program conducted by Space Division under Contract NAS7-200, Supplemental Agreement 2026, TA-20. Crack growth rate data, determined from part-through crack specimens, are reflected in the curve of Figure 5-14.

Weld specimens were also tested under monotonic load to failure. The specimens were instrumented with crack opening displacement gauges and also with a vacuum cup mounted on the back surface to detect and record crack break-through. Tests were conducted on weld joints of 0.25 cm (0.10 in.), 0.51 cm (0.20 in.) and 0.89 cm (0.35 in.) thickness. Results of the static load tests are summarized in Figure 5-15; data for the individual weld thicknesses are plotted separately. The data are plotted as gross section stress versus normalized initial flaw depth (a_i/Q). The stress at which break-through occurred is indicated by open symbols, the stress at fracture by solid symbols. Pre-flawing was controlled to produce aspect ratios of initial flaws approximating $a/2c = 0.1$ and 0.4 ; these are indicated by circle and square symbols, respectively. It can be seen that for all specimens of 0.25 cm (0.1 in.) thickness, crack break-through occurred prior to fracture; in most cases the stress at fracture was considerably greater than the stress at break-through. The majority of specimens of 0.51 cm (0.2 in.) thickness also exhibited break-through prior to fracture, but only a few of the 0.89 cm (0.35 in.) thick specimens showed this characteristic. Mechanical properties tests on representative weld specimens showed a typical yield strength for the weld of about 138 MN/m^2 (20 ksi). It can be seen that the break-through or fracture phenomena of interest occurred at gross section stresses considerably above the weld yield strength in almost all cases. Therefore, fracture behavior is not expected to follow trends predictable by elastic fracture mechanics theory, and empirical description of crack growth and fracture characteristics is required.

The above data have been reduced to an apparent fracture toughness for either fracture or break-through by using the standard solution for stress intensity at the tip of a part-through crack with a deep flaw magnification factor determined from Figure 5-12. These results are plotted in Figure 5-16 as a function of flaw depth to thickness ratio (a_i/t). It can be seen that, although considerable scatter is present, the deep flaw magnification factor appears to normalize the data reasonably well with respect to flaw depth/thickness ratio. It can also be seen that the break-through phenomenon is not confined to only those specimens in which initial flaw depth approaches the thickness, but is distributed over a range of a_i/t from 0.5 to 0.95. Estimated lower and upper bounds of apparent fracture toughness when break-through occurs (or fracture for the 0.89 cm thick specimens) are indicated by dashed lines on these plots. The group of data points for $a_i/2c = 0.4$ in Figure 5-16b which fall below the estimated lower bound are excluded because they represent relatively small values of a_i/Q in which the fracture stress approaches the ultimate strength of an unflawed weld. This constraint results in artificially low values for apparent fracture toughness. These estimated

lower and upper bounds are used to construct the plot of Figure 5-17, which approximates the range of apparent fracture toughness as a function of weld thickness. This range is used in subsequent studies of critical flaw sizes and proof test requirements for the propellant tanks.



KEUFEFF & ESSER CO.
 KEUFEFF & ESSER CO.
 10 X 10 TO THE CENTIMETER 46 1517
 18 X 25 CM. ALBANY, N.Y. MADE IN U.S.A.

Figure 5-15. Gross Stress for Fracture or Break-through of 2219-T87 Weld Specimens

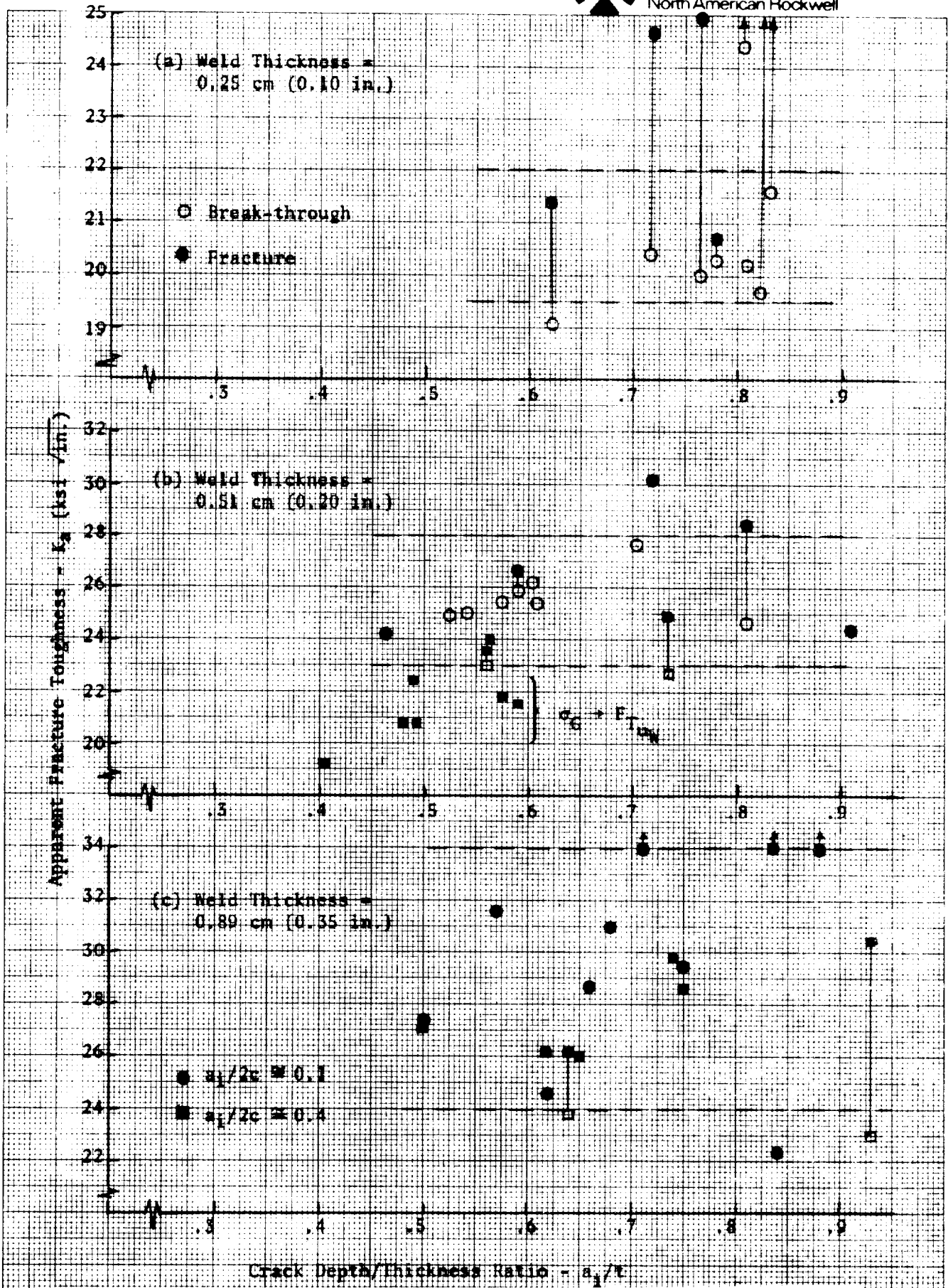


Figure 5-16. Apparent Fracture Toughness for Fracture or Break-through of 2219-T87 Weld Specimens

Note:

Boundaries of apparent fracture toughness refer to break-through of a surface crack or to fracture, whichever occurs first.

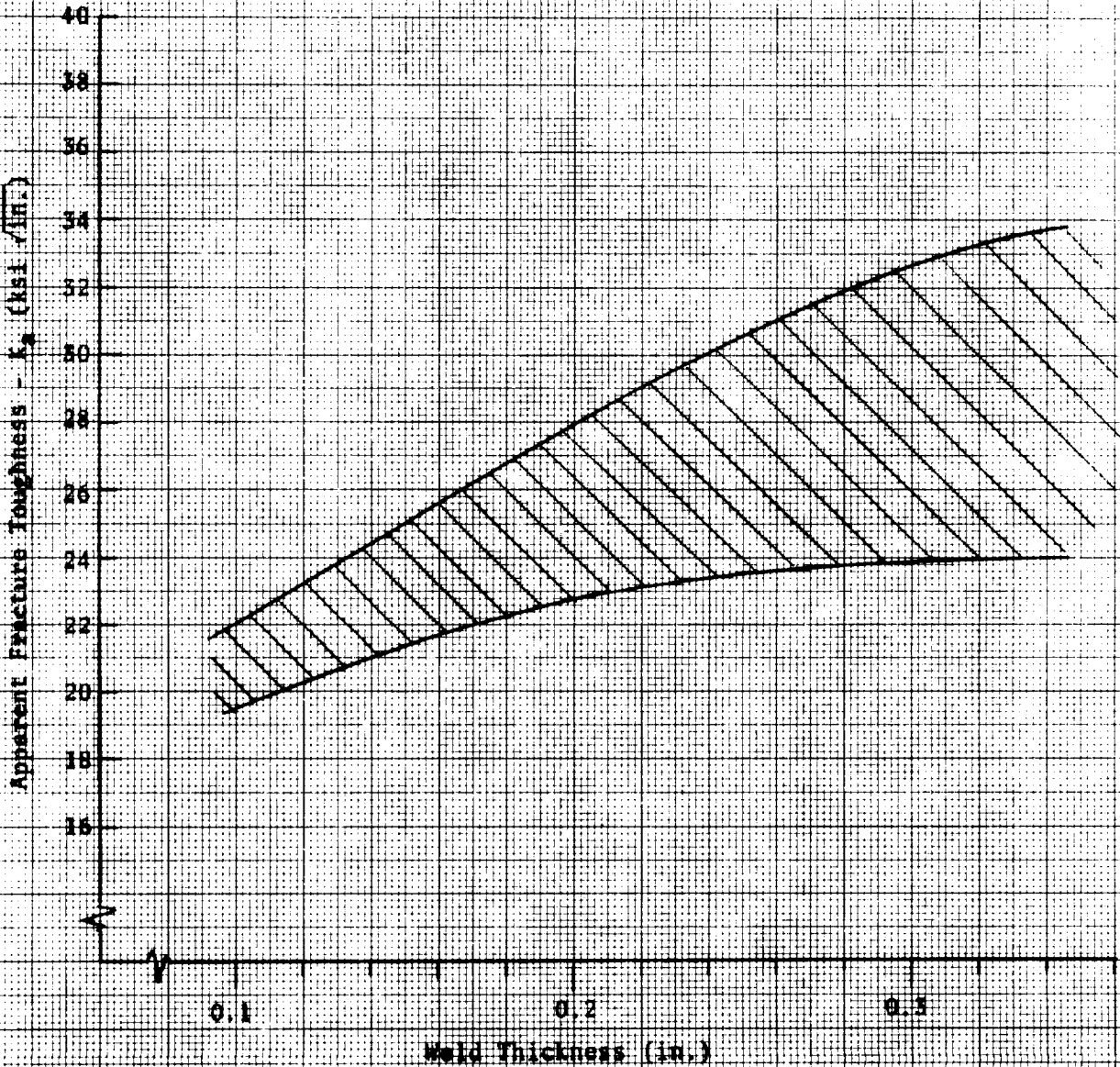


Figure 5-17. Range of Apparent Fracture Toughness vs. Thickness for 2219-T87 Weld Specimens

6.0 FATIGUE LIFE ANALYSIS

Summarized in this section are detailed fatigue damage analyses for the selected structural elements and the resulting safe-life predictions. Variations to the basic structural configuration and/or design stress levels defined for the selected structural elements in the Phase B studies are also investigated where appropriate.

6.1 ANALYSIS METHODS AND SUMMARY OF RESULTS

The linear cumulative damage theory (Miner's Law) is used as the basic analysis approach to predict fatigue damage due to the cyclic loading spectra and the resulting safe-life for a given structural element. The loading spectra presented in Section 3 of this report form the basis for this analysis. Random load spectra, such as bending moment on wing, vertical stabilizer, and fuselage are divided into regular increments of number of load exceedances. The difference between successive exceedances at each increment is the number of load occurrences within that increment. An average value of loading within that increment is used to represent all load cycles that occur over that increment. For structural elements with a more discrete loading spectra, such as propellant tank pressures, the load spectra are defined directly. The maximum and minimum stresses associated with load cycles for a given increment are determined from the Phase B definition of limit design stresses (modified where appropriate) and are used with the applicable S-N curves from Section 5 to determine the allowable number of cycles for these stress conditions. The ratio of number of applied load cycles to allowable load cycles is the fatigue damage for that increment of the loading spectra. The fatigue damage increments are then summed to find the total damage incurred by a given structural element for each major mission phase and for the entire mission profile. The safe-life is predicted by dividing the nominal calculated fatigue life by a factor of four. The above procedure can be represented by the following equations:

$$D = \sum \frac{\eta}{N}$$

$$L_s = \frac{100}{4D}$$

where:

D = Fatigue damage for 100 missions

η = Number of applied load cycles for specified stress conditions over 100 missions

N = Number of load cycles to cause fatigue failure under specified stress conditions

L_s = Safe-life in terms of number of missions

The results of the fatigue life analyses are summarized in Table 6-1. Fatigue damage is listed for each major mission phase and for the total mission profile, based on 100 mission exposure. The resulting predicted safe-life is also summarized. It can be seen that the predicted safe-lives for the vertical stabilizer and the intertanks adapter shell structure are very large (greater than 1000 missions) because of the low tension stresses under design conditions. Fatigue damage on the vertical stabilizer due to thermal stresses cycles is of the same order of magnitude as the damage due to airload cycles during the ascent phase.

Modest fatigue damage is indicated for the fuselage shell at Sta. 2600, the orbiter aft attachment support frame, and the crew compartment. The corresponding predicted safe-lives range from 480 missions to 960 missions. A relatively conservative theoretical stress concentration factor ($K_t = 4.4$) is assumed in these calculations. Therefore, normal good design practice should be adequate to provide satisfactory fatigue life for these structural components. Fatigue damage for the fuselage shell at Sta. 2600 is compared for two analytical models: (1) longitudinal membrane loading in the cylindrical shell due to bending moment, axial load, and internal pressure, and (2) membrane loading plus secondary bending stresses due to the discontinuity effects of fuselage ring frames restraining the free expansion of the skin-stringer shell under internal pressure loading. It can be seen that these secondary stresses may have a significant influence on fatigue damage; the predicted safe life is reduced from 960 missions to 520 missions for the example case.

Safe-life predicted for the LOX tank aft bulkhead is 185 missions. This represents a relatively small margin over the required service life of 100 missions and indicates that close attention to detail design of propellant tanks is desirable to assure satisfactory fatigue life. Development tests to determine fatigue life characteristics of typical welded and mechanical joints will be of particular importance.

Fatigue damage predicted for the wing spar cap in the root region is extremely high; a safe-life of only 6 missions is indicated for an assumed theoretical stress concentration factor of 4.4. The predicted safe-life is increased to 20 missions if S-N curves based on $K_t = 3.0$ are used in the damage analysis. This indicates that refined design practices to minimize fatigue effects will not be adequate by themselves to provide satisfactory fatigue life because of the severity of the loading spectra and the high tension stresses in the wing spars under limit design conditions of 600 MN/m^2 (88 ksi). It was determined by iteration that a reduction in limit design tension stress to approximately 450 MN/m^2 (65 ksi) is necessary to provide adequate fatigue life, assuming $K_t = 3.0$. This modification is also summarized in Table 6-1; a predicted safe-life of 135 missions is indicated.

Table 6-1. Fatigue Life of Selected Structural Elements - B-9U Booster

Structural Element	K _T ⁽¹⁾	Fatigue Damage ($\Sigma n/N$)							Safe-Life ⁽²⁾ (No. of Missions)
		Ascent	Entry	Cruise/ Landing	Taxi and Ground Operations	GAG ⁽³⁾	Total		
Vertical stabilizer	4.5	9.42×10^{-5}	1.90×10^{-5}	1.08×10^{-2}	0	$5.0 \times 10^{-5(6)}$	0.011	2270	
Fuselage Sta. 2600 (basic)	4.4	4.8×10^{-4}	1.2×10^{-4}	0	0	0.025	0.026	960	
Fuselage ⁽⁴⁾ Sta. 2600 (discontinuity)	4.4	0.0026	3.1×10^{-4}	0	0	0.045	0.048	520	
Intertank shell	4.4	0.0232	0	0	0	-	0.0232	1080	
Orbiter aft attach	4.4	0.0065	-	-	-	0.0455	0.052	480	
LO ₂ tank aft bulkhead	4.4	0.010	-	-	0.030 ⁽⁷⁾	0.095	0.135	185	
Crew compartment	4.4	-	-	-	-	0.037	0.037	675	
Wing	4.5	2.07	0.42	1.77	0	2.1×10^{-4}	4.26	6	
Wing	3.0	0.563	0.165	0.500	0	0	1.23	20	
Wing ⁽⁵⁾ (modified)	3.0	0.064	0.022	0.100	0	0	0.186	135	

(1) K_T = Theoretical stress concentration factor on material test specimens to establish S-N curves.
 (2) Safe-life = 0.25 x predicted life.
 (3) GAG = Ground-air-ground cycle.
 (4) Includes discontinuity bending stresses of fuselage shell due to restraint of ring frames.
 (5) Wing spar limit design stress reduced to 450 MN/m² (65 ksi).
 (6) Thermal stress cycles at separation and entry.
 (7) Damage due to ground checkout fueling and pressurization.

6.2 FATIGUE ANALYSIS - WING

6.2.1 Structural Configuration and Loading

Basic structural geometry, internal loadings and member sizing for major structural elements of the wing are given in Reference 22. Review of these data indicates that the wing spar caps on the lower wing surface in the root region are the most highly stressed tension members. Spar No. 4 at Span Sta. 0 is the most highly loaded member and this section is taken as the reference for the fatigue damage analysis. A sketch of the spar cap and adjacent geometry at this section is given in Figure 6-1.

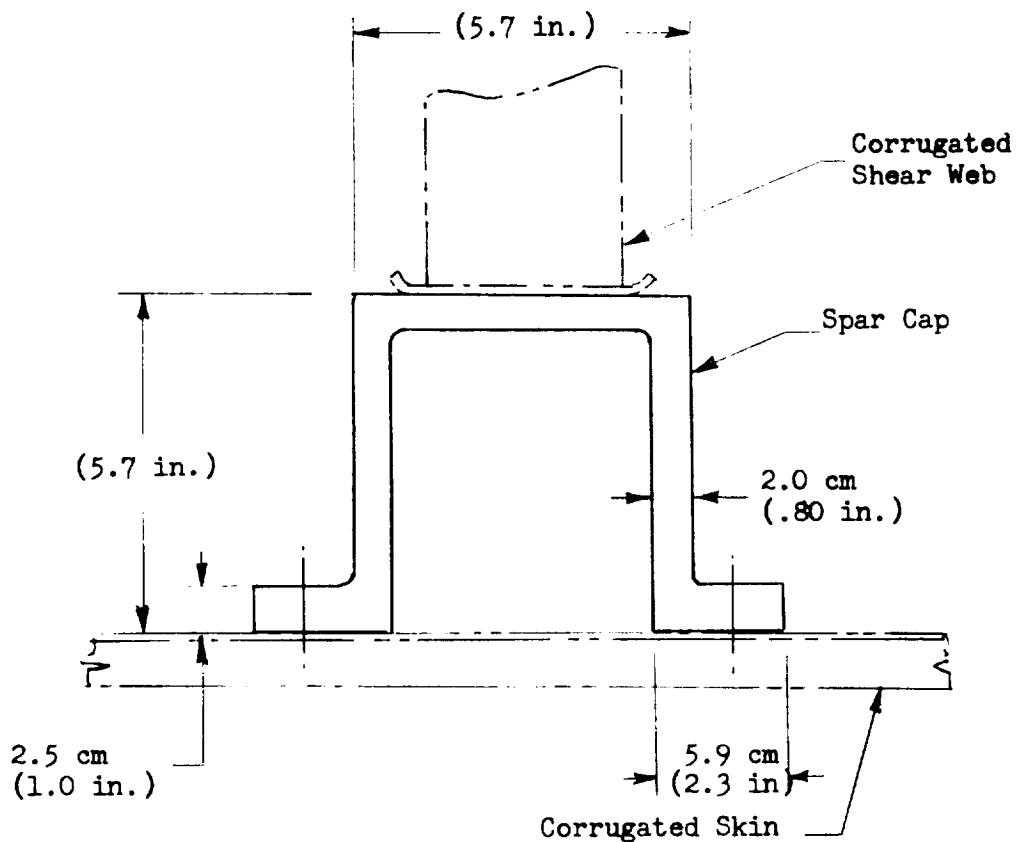


Figure 6-1. Wing Spar Cap Geometry

The spar cap area is sized on the basis of tension stress in the max q_u ultimate design condition; a 5 percent allowance is made for area lost due to fastener holes. The critical design condition is a room temperature case so that the gross section stress may be expressed as:

$$\sigma_{ult} = 0.95 F_{tu} = 850 \text{ MN/m}^2 \text{ (123 ksi)}$$

$$\sigma_{lim} = \frac{\sigma_{ult}}{1.4} = 570 \text{ MN/m}^2 \text{ (88 ksi)}$$

6.2.2 Damage Analysis

Detailed calculations of fatigue damage are presented in Table 6-2. The amplitude of alternating stress cycles and mean stress are based on the limit design stress defined above and the wing load spectra given in Figure 3-11. Allowable number of load cycles for given stress conditions are determined from S-N curves based on $K_t = 4.5$, presented in Figure 5-3. The calculated fatigue damage due to cruise/landing and taxi mission phases is doubled to approximate the effect of ferry missions over the operational life. It can be seen that the total damage factor for 100 missions is significantly greater than unity ($D = 4.26$); the corresponding safe-life is 6 missions. Atmospheric turbulence during the ascent and cruise/landing mission phases contributes the major portion of the damage; fatigue damage due to ground-air-ground (GAG) cycles is insignificant.

Because the safe-life predicted above is much less than the design requirement of 100 missions, a supplementary damage analysis was performed using S-N curves based on a lower theoretical stress concentration factor ($K_t = 3.0$) and given in Figure 5.2. It is considered that this corresponds, in an approximate manner, to employing extensive measures in design and fabrication to reduce effects detrimental to fatigue performance. These measures may include such things as generous fillet radii, tapered joints, interference fit fasteners, shot peening, coining, etc. Detailed calculations for this condition are presented in Table 6-3. It can be seen that significant improvement is indicated with a total damage factor of 1.23, however the corresponding safe-life of 20 missions is still far below the design requirements.

A final evaluation was performed to determine the reduction in limit design stress level required to meet design requirements for fatigue life. By iteration, it was determined that a limit tension stress of approximately 450 MN/m^2 (65 ksi) will satisfy the design requirement of 100 mission life, based on $K_t = 3.0$. Damage calculations for this case are presented in Table 6-4. A total damage factor of 0.186 is indicated, with corresponding safe-life of 135 missions.

Prepared By: RWW
 Checked By:
 Date: 9-25-71

SPACE DIVISION
 NORTH AMERICAN ROCKWELL CORPORATION

Page No. 6-6 of
 Report No. SD72-SH-0046
 Model No. E-9J

1	2	3	4	5	6	7	8	9	10	11	12	13	14	15
MISSION PHASE	T _{MAX} (G)	M _{MEAN} (% DESIGN)	N _e	MALT (% DESIGN)	N	MALT (% DESIGN)	T _{MEAN} (KSI)	T _{ALT} (KSI)	T _{MAX} (KSI)	Σ M _i (KSI)	R	T _{MAX} / F _{TU}	N	n / N
ASCENT	130F	0	100,000	1.0	90,000	1.5	0	1.1	.9	-1.9	-1.0	.007	∞	0
↑	↑	↑	10,000	2.0	9,000	2.1	↑	1.2	1.9	-1.9	↑	.015	↑	↑
			1,000	2.2	900	2.7	↓	2.4	2.4	-2.4	↓	.019	↓	↓
			100	3.2	90	3.6	↑	2.2	3.2	-3.2	↑	.025	↑	↑
			10	4	9	4.5	0	4.4	4.4	-4.4	0	.024	∞	0
	130F	0	1	5									Z	0
	130F	0	100,000	4.2	90,000	6.0	0	5.2	5.2	-5.2	-1.0	.041	∞	0
↑	↑	↑	10,000	7.8	9,000	9.3	↑	8.2	8.2	-8.2	↑	.063	∞	0
			1,000	10.8	900	12.3	↓	10.8	10.8	-10.8	↓	.083	∞	0
			100	13.8	90	15.2	↑	13.4	13.4	-13.4	↑	.103	2.5 × 10 ⁶	3.6 × 10 ⁻⁵
			10	16.6	9	18.3	0	16.1	16.1	-16.1	0	.124	2.8 × 10 ⁵	3.2 × 10 ⁻⁵
	130F	0	1	20									Σ	6.8 × 10 ⁻⁵
	130F	15	100,000	2.8	90,000	3.4	13.2	3.2	10.2	10.2	.63	.125	∞	0
↑	↑	↑	10,000	4.0	9,000	4.7	↑	4.1	11.3	9.1	.53	.133	∞	0
			1,000	5.4	900	6.2	↓	5.5	18.7	7.7	.41	.144	8 × 10 ⁶	11.2 × 10 ⁻³
			100	7.0	90	7.7	↑	6.8	20.0	6.4	.32	.154	2.3 × 10 ⁶	3.8 × 10 ⁻⁵
			10	8.4	9	9.2	0	8.1	21.3	5.1	.24	.164	6.5 × 10 ⁵	1.4 × 10 ⁻⁵
ASCENT	130F	15	1	10.0									Σ	16.4 × 10 ⁻⁵

1	2	3	4	5	6	7	8	9	10	11	12	13	14	15
MISSION PHASE	T _{MAX} (DEF. F)	M _{MEPV} (% DESIGN)	n _e	MALT (% DESIGN)	n	MALT (% DESIGN)	S _{MEAN} (KSI)	S _{ALT} (KSI)	S _{MAX} (KSI)	S _{MIN} (KSI)	R	S _{MAX} / F _{TU}	N	n / N
ASCENT	130 F	10	100,000	6.0	70,000	8.1	8.8	7.1	15.9	1.7	.11	.13	2.5 X 10 ⁶	2.8 X 10 ⁻²
			30,000	10.5	20,000	12.0		10.6	19.4	-1.8	-.09	.16	40 X 10 ⁵	5.0 X 10 ⁻²
			10,000	13.8	7,000	15.8		13.4	22.7	-5.1	-.22	.18	15 X 10 ⁵	4.7 X 10 ⁻²
			3,000	17.3	2,000	21.0		17.6	25.4	-8.8	-.33	.22	5.6 X 10 ⁴	3.6 X 10 ⁻²
			1,000	22.2	700	25.6		22.6	30.4		-.44	.26	3.0 X 10 ⁴	2.3 X 10 ⁻²
			300	29.0	300	32.5		29.1	35.4	-19.8	-.53	.30	1.6 X 10 ⁴	1.2 X 10 ⁻²
			100	36.0	70	39.7		35.1	43.7	-26.3	-.60	.36	8.0 X 10 ³	9 X 10 ⁻³
			30	43.8	20	47.4		41.6	50.4	-2.8	-.65	.41	5.0 X 10 ³	4 X 10 ⁻²
			10	51.0	7	55.0		48.4	54.5	-37.6	-.69	.46	3.0 X 10 ³	2 X 10 ⁻²
			3	59.0	2	62.5		55.0	65.2	-46.2	-.72	.52	1.6 X 10 ³	1 X 10 ⁻²
	130 F	10	1	66.0										
													Σ	21.2 X 10 ⁻²
	130 F	15	100,000	8.0	70,000	10.5	13.2	7.2	22.4	4.0	.18	.18	3.4 X 10 ⁵	20.6 X 10 ⁻²
			30,000	13.0	20,000	15.2		13.4	26.6	-0.2	-.007	.22	8.0 X 10 ⁴	25.0 X 10 ⁻²
			10,000	17.5	7,000	20.2		17.8	31.0	-4.6	-.15	.25	4.4 X 10 ⁴	15.9 X 10 ⁻²
			3,000	23.0	2,000	26.5		23.3	36.5	-10.1	-.28	.30	2.4 X 10 ⁴	8.3 X 10 ⁻²
			1,000	30.0	700	35.2		31.0	44.2	-17.0	-.40	.36	1.0 X 10 ⁴	7.0 X 10 ⁻²
			300	40.5	200	45.2		39.8	53.0	-26.6	-.50	.43	4.5 X 10 ³	4.4 X 10 ⁻²
			100	49.8	70	54.7		48.5	61.7	-35.0	-.57	.50	2.2 X 10 ³	3.2 X 10 ⁻²
			30	60.0	20	64.8		57.0	70.2	-43.8	-.62	.57	1.2 X 10 ³	1.7 X 10 ⁻²
			10	69.5	7	74.5		65.5	75.7	-52.3	-.66	.64	6.6 X 10 ²	1.1 X 10 ⁻²
			3	79.5	2	84.3		77.2	85.4	-61.6	-.70	.71	2.5 X 10 ²	7 X 10 ⁻²
ASCENT	130 F	15	1	89.0										
													Σ	87.9 X 10 ⁻²

		SPACE DIVISION NORTH AMERICAN ROCKWELL CORPORATION												
1	2	3	4	5	6	7	8	9	10	11	12	13	14	15
MISSION PHASE	T (DES. F)	M _{MEAN} (% DESIGN)	n _e	M _{MALT} (% DESIGN)	n	M _{MALT} (% DESIGN)	σ _{MEAN} (A ₁)	σ _{MALT} (A ₁)	σ _{MAX} (A ₁)	σ _{MIN} (A ₁)	R	σ _{MAX} / F _{TU}	N	n / N
ASCENT	130 F	40	100,000	5.5	70,000	7.0	35.2	6.2	41.4	29.0	70	.34	1.5 x 10 ⁵	46.7 x 10 ²
			30,000	8.5	20,000	9.8		8.6	43.8	26.6	61	.36	8.5 x 10 ⁴	235 x 10 ²
			10,000	11.0	4,000	12.8		11.3	41.5	23.7	51	.38	5.0 x 10 ⁴	140 x 10 ²
			3,000	14.5	2,000	15.8		13.9	41.1	21.3	43	.40	2.9 x 10 ⁴	6.9 x 10 ²
			1,000	17.0	1,000	18.8		16.0	51.8	12.6	36	.42	1.8 x 10 ⁴	3.9 x 10 ²
			300	20.5	200	21.2		19.2	54.4	16.0	21	.44	1.2 x 10 ⁴	1.7 x 10 ²
			100	23.0	70	24.8		21.8	51.0	13.4	24	.46	9.5 x 10 ³	7 x 10 ²
			30	26.5	20	27.8		24.4	57.6	10.8	18	.49	7.0 x 10 ³	3 x 10 ²
			10	29.0	7	30.8		27.1	62.3	8.1	13	.51	5.0 x 10 ³	1 x 10 ²
			3	32.5	2	33.8		29.8	65.0	5.4	8	.53	4.0 x 10 ³	0.8 x 10 ²
ASCENT	130 F	40	1	35.0									Σ	97.8 x 10 ²
ENTRY	300 F		100,000	9.5	70,000	12.8	0	11.3	11.3	0	0	.10	∞	0
			30,000	15.0	20,000	17.2		15.2	15.2			.14	1.0 x 10 ⁶	1.0 x 10 ²
			10,000	19.5	2,000	22.8		21.1	20.1			.18	2.2 x 10 ⁵	3.2 x 10 ²
			3,000	26.0	2,000	30.0		26.4	26.4			.24	5.7 x 10 ⁴	3.5 x 10 ²
			1,000	34.0	700	41.2		35.2	36.2			.33	2.0 x 10 ⁴	3.5 x 10 ²
			300	48.5	200	71.8		62.2	63.2			.58	2.2 x 10 ³	9.1 x 10 ²
			100	95.0	70	95.0		83.5	83.5			.77	4.5 x 10 ²	15.6 x 10 ²
			30	95.0	20	95.0		83.5	83.5			.77	4.5 x 10 ²	4.5 x 10 ²
			10	95.0	7	95.0		83.5	83.5			.77	4.5 x 10 ²	1.6 x 10 ²
			3	95.0	2	95.0		83.5	83.5			.77	4.5 x 10 ²	4.4 x 10 ²
ENTRY	300 F		1	95.0									Σ	42.4 x 10 ²

TABLE 6-2 WING FATIGUE (SHEET 4)		SPACE DIVISION NORTH AMERICAN ROCKWELL CORPORATION									Page No. 6-9 of Report No. SD72-SH-0042 Model No. B-97			
DAMAGE (K _T = 4.5)		Prepared By: JPS Checked By: Date: 10.10.71												
1	2	3	4	5	6	7	8	9	10	11	12	13	14	15
MISSION PHASE	T _{MAX} (DEG F)	M _{MEAN} (%DESIGN)	n _e	M _{ALT} (%DESIGN)	n	M _{ALT} (%DESIGN)	σ _{MEAN} (KSI)	σ _{ALT} (KSI)	σ _{MAX} (KSI)	σ _{MIN} (KSI)	R	σ _{MAX} / F _Y	N	$\frac{n}{N}$
CRUISE	300	35	100,000	1.5	70,000	4.0	30.8	3.5	34.3	2.73	.80	.31	4.0 x 10 ⁵	17.5 x 10 ²
LNDG			30,000	6.5	20,000	8.8		7.8	38.6	2.30	.60	.35	9.4 x 10 ⁴	21.3 x 10 ²
			10,000	11.0	7,000	13.8		12.2	43.0	1.86	.43	.39	3.7 x 10 ⁴	19.0 x 10 ²
			3,000	16.5	2,000	18.8		16.6	47.4	1.42	.30	.43	1.4 x 10 ⁴	14.3 x 10 ²
			1,000	21.0	700	23.5		20.7	51.5	1.01	.20	.47	8.5 x 10 ³	8.2 x 10 ²
			300	26.0	200	28.5		25.1	55.9	5.7	.10	.51	4.7 x 10 ³	4.2 x 10 ²
			100	31.0	70	33.5		29.5	60.3	1.3	.02	.55	2.8 x 10 ³	2.5 x 10 ²
			30	36.0	20	38.2		33.6	64.4	-2.8	-.04	.59	2.1 x 10 ³	1.0 x 10 ²
			10	40.5	7	41.8		36.8	67.6	-6.0	-.09	.62	1.5 x 10 ³	.5 x 10 ²
CRUISE			3	43.0	2	44.5	30.8	39.2	70.0	-8.4	-.12	.64	1.3 x 10 ³	2 x 10 ²
LNDG	300	35	1	46.0									2 x 10 ²	1.77
TAXI	300	-4	100,000	4	90,000	4.5	-3.5	7.0	0.5	-7.5	-.15	0	∞	0
			10,000	5	9,000	6.0		5.3	1.8	-8.8	-.5	.02	∞	0
			1,000	7	900	8.0		7.0	3.5	-10.5	-.3	.03	∞	0
			100	9	90	10.0		8.8	4.3	-12.3	-.29	.5	∞	0
			10	11	9	11.5	-3.5	10.1	6.6	-13.6	-.2	.09	1 x 10 ⁷	0
TAXI	300	-4	1	12									2 x 10 ²	0
GAG	130				200				17.6	-3.5	-.2	.135	9.5 x 10 ⁵	2.1 x 10 ⁴
TOTAL													D =	4.26

TABLE 6-3 WING FATIGUE (SHEET 1)
DAMAGE (K_r = 3.0)

TABLE 6-3 WING FATIGUE (SHEET 1)					SPACE DIVISION NORTH AMERICAN ROCKWELL CORPORATION						Prepared By: JFS	Page No. 6-10 of		
DAMAGE (K _r = 3.0)											Checked By:	Report N. SD72-34-0046		
1	2	3	4	5	6	7	8	9	10	11	12	13	14	15
MISSION PHASE	T (DEG F)	M MEAN (% DESIG)	N _e	N	σ _{MAX} (KSI)	σ _{MIN} (KSI)	R	$\frac{\sigma_{MAX}}{\sigma_{-1}}$	N	$\frac{1}{N}$				
ASSENT	130 F	0	100,000	90,000	9	-9	-1.0	.007	∞	0				
			10,000	9,000	1.9	-1.9		.015	↑	↑				
			1,000	900	2.1	-5.4		.019	↓	↓				
			100	70	3.2	-5.2		.025	↓	↓				
			10	9	4.4	-4.4	-1.0	.034	∞	0				
	130 F	0	1						Σ	0				
	130 F	0	100,000	90,000	5.3	-5.3	-1.0	.041	∞	0				
			10,000	9,000	8.2	-8.2		.063	∞	0				
			1,000	900	10.8	-10.8		.083	∞	0				
			100	70	13.4	-13.4		.103	1.0 × 10 ⁹	7.0 × 10 ⁶				
			10	7	16.1	-16.1	-1.0	.124	3.7 × 10 ⁶	2.4 × 10 ⁶				
	130 F	0	1						Σ	11.4 × 10 ⁶				
	130 F	15	100,000	90,000	16.2	10.2	.63	.125	∞	0				
			10,000	9,000	17.3	9.1	.53	.133	↑	↑				
			1,000	900	18.7	2.7	.41	.144	↓	↓				
			100	90	20.0	6.4	.32	.154	↓	↓				
			10	9	21.3	5.1	.24	.164	∞	0				
	130 F	15	1						Σ	0				

Prepared By: JPS
 Checked By:
 Date: 10-1-71

TABLE 6-3 WING FATIGUE (SHEET 2)
 DAMAGE (A; = 3.0)

1	2	3	4	5	6	7	8	9	10	11	12	13	14	15
MISSION PHASE	T (DEG F)	M _{MEAN} (% DESIGN)	N _C	n	σ _{MAX} (KSI)	σ _{MIN} (KSI)	R	σ _{MAX} / F _{TU}	N	$\frac{n}{N}$				
ASCENT	130 F	10	100,000	70,000	15.9	1.7	.11	.13	∞	0				
			30,000	20,000	19.4	-1.8	-.09	.16	4.5 X 10 ⁶	4.4 X 10 ⁻³				
			20,000	2,000	22.7	-5.1	-.22	.18	4.0 X 10 ⁵	17.5 X 10 ⁻³				
			3,000	2,000	26.4	-8.8	-.33	.22	2.0 X 10 ⁴	22.2 X 10 ⁻³				
			1,000	700	31.4	-13.8	-.44	.26	3.5 X 10 ⁴	23.3 X 10 ⁻³				
			300	200	37.4	-19.8	-.53	.30	1.6 X 10 ⁴	12.5 X 10 ⁻³				
			100	70	43.9	-26.3	-.60	.36	7.6 X 10 ³	9.2 X 10 ⁻³				
			30	20	50.4	-32.8	-.65	.41	4.0 X 10 ³	5.0 X 10 ⁻³				
			10	7	57.2	-39.6	-.69	.46	2.3 X 10 ³	3.0 X 10 ⁻³				
			3	2	63.8	-46.2	-.72	.52	1.0 X 10 ³	2.0 X 10 ⁻³				
	130 F	10	1						Σ	95.3 X 10 ⁻³				
	130 F	15	100,000	70,000	22.4	4.0	.18	.18	6.4 X 10 ⁶	1.1 X 10 ⁻²				
			30,000	20,000	26.6	-0.2	-.007	.22	4.0 X 10 ⁵	5.0 X 10 ⁻²				
			10,000	7,000	31.0	-4.6	-.15	.25	1.8 X 10 ⁵	3.9 X 10 ⁻²				
			3,000	2,000	36.5	-10.1	-.28	.30	5.8 X 10 ⁴	3.4 X 10 ⁻²				
			1,000	700	44.2	-17.8	-.40	.36	2.3 X 10 ⁴	3.0 X 10 ⁻²				
			300	200	53.0	-26.6	-.50	.43	9.0 X 10 ³	2.2 X 10 ⁻²				
			100	70	61.7	-35.3	-.57	.50	3.8 X 10 ³	1.8 X 10 ⁻²				
			30	20	70.2	-43.8	-.62	.57	1.6 X 10 ³	1.2 X 10 ⁻²				
			10	7	78.7	-52.3	-.66	.64	7.0 X 10 ²	1.0 X 10 ⁻²				
			3	2	87.4	-61.0	-.70	.71	2.3 X 10 ²	9 X 10 ⁻³				
ASCENT	130 F	15	1						Σ	13.5 X 10 ⁻²				

1	2	3	4	5	6	7	8	9	10	11	12	13	14	15
MISSION PHASE	T _{MAX} (DEG.F)	MEAN (% DESIGN)	N _C	n	σ _{MAX} (KSI)	σ _{MIN} (KSI)	R	σ _{MAX} / F _{TU}	N (KT=3.0)	n / N				
CRUISE/	300	35	100,000	70,000	34.3	27.3	.80	.31	1.0 X 10 ⁹	.7 X 10 ⁻²				
LNDG	↑	↑	30,000	20,000	38.6	23.0	.60	.35	4.0 X 10 ⁵	5.0 X 10 ⁻²				
↑			10,000	7,000	43.0	18.6	.43	.39	1.1 X 10 ⁵	6.4 X 10 ⁻²				
			3,000	2,000	47.4	14.2	.30	.43	4.0 X 10 ⁴	5.0 X 10 ⁻²				
			1,000	700	51.5	10.1	.20	.47	2.0 X 10 ⁴	3.5 X 10 ⁻²				
			300	200	55.9	5.7	.10	.51	1.0 X 10 ⁴	2.0 X 10 ⁻²				
			100	70	60.3	1.3	.02	.55	5.2 X 10 ³	1.3 X 10 ⁻²				
			30	20	64.4	-2.8	-.04	.59	3.5 X 10 ³	6 X 10 ⁻²				
↓			10	7	67.6	-6.0	-.09	.62	2.7 X 10 ³	3 X 10 ⁻²				
CRUISE/	↑	↑	3	2	70.0	-8.4	-.12	.64	2.2 X 10 ³	1 X 10 ⁻²				
LNDG	300	35	1						2 x Σ	0.50				
TAXI	300	-4	100,000	90,000	0.5	-7.5	-.15	0	∞	0				
↑	↑	↑	10,000	7,000	1.8	-8.8	-.5	.02	∞	0				
↑	↑	↑	1,000	900	3.5	-10.5	-.3	.03	∞	0				
↑	↑	↑	100	90	4.3	-12.3	-.29	.08	∞	0				
↑	↑	↑	10	9	6.6	-13.6	-.2	.09	∞	0				
TAXI	300	-4	1						2 x Σ	0				
GAG	130			200	17.6	-3.5	-.2	.135	7 X 10 ⁷	0				
TOTAL										D = 1.23				

SPACE DIVISION
 NORTH AMERICAN ROCKWELL CORPORATION

1	2	3	4	5	6	7	8	9	10	11	12	13	14	15
MISSION PHASE	(DEG F)	M _{MEAN} (% DESIGN)	n _e	n	σ _{MEAN} (KSI)	σ _{ALT} (KSI)	σ _{MAX} (KSI)	σ _{MIN} (KSI)	R	σ _{MAX} / F _{TU}	N (K _T = 3.0)	D		
ASCENT	130 F	0	100,000	90,000	0	1.0	1.0	-1.0	-1.0	.008	∞	0		
			10,000	7,000		1.4	1.4	-1.4		.011				
			1,000	900		1.8	1.8	-1.8		.015				
			100	70		2.3	2.3	-2.3		.019				
			10	9		2.9	2.9	-2.9	-1.0	.024	∞	0		
	130 F	0	1		0						Σ	0		
	130 F	0	100,000	90,000	0	3.9	3.9	-3.9	-1.0	.032	∞	0		
			10,000	7,000		6.0	6.0	-6.0		.049				
			1,000	900		8.0	8.0	-8.0		.065				
			100	70		9.9	9.9	-9.9		.080				
			10	9		11.9	11.9	-11.9	-1.0	.097	∞	0		
	130 F	0	1		0						Σ	0		
	130 F	15	100,000	90,000	9.8	2.2	12.0	7.6	.63	.018	∞	0		
			10,000	7,000		3.0	12.8	6.8	.53	.104				
			1,000	900		4.0	13.8	5.8	.42	.112				
			100	90		5.0	14.8	4.8	.32	.120				
			10	9		6.0	15.8	3.8	.24	.128	∞	0		
ASCENT	130 F	15	1								Σ	0		

SPACE DIVISION
 NORTH AMERICAN ROCKWELL CORPORATION

1	2	3	4	5	6	7	8	9	10	11	12	13	14	15
MISSION PHASE	T (DEG F)	M _{MEAN} (% DESIGN)	N _E	N	σ _{MEAN} (KSI)	σ _{ALT} (KSI)	σ _{MAX} (KSI)	σ _{MIN} (KSI)	A	$\frac{\sigma_{MAX}}{F_u}$	N (K=3.0)	$\frac{1}{N}$		
ASCENT	130 F	10	100,000	70,000	6.5	5.3	11.8	1.2	.10	.10	∞	0		
			50,000	20,000		7.8	14.3	-1.3	-.09	.12	∞	0		
			10,000	7,000		10.3	16.8	-3.8	-.23	.14	∞	0		
			3,000	2,000		13.0	19.5	-6.5	-.33	.16	2.7 X 10 ⁶	7.4 X 10 ⁻⁴		
			1,000	700		16.7	23.2	-10.2	-.44	.19	6.0 X 10 ⁵	1.7 X 10 ⁻⁴		
			300	200		21.2	27.7	-14.7	-.53	.23	1.4 X 10 ⁵	4.3 X 10 ⁻⁴		
			100	70		26.0	32.5	-19.5	-.60	.26	7.6 X 10 ⁴	7.2 X 10 ⁻⁴		
			30	20		30.8	37.3	-24.3	-.65	.30	4.0 X 10 ⁴	5.0 X 10 ⁻⁴		
			10	7		35.8	42.3	-29.3	-.70	.34	2.3 X 10 ⁴	3.0 X 10 ⁻⁴		
			3	2		40.6	47.1	-34.1	-.72	.38	1.4 X 10 ⁴	1.4 X 10 ⁻⁴		
	150 F	10	1								Σ	5.2 X 10 ⁻³		
	130 F	15	100,000	70,000	9.8	6.8	16.6	3.0	.18	.14	∞	0		
			30,000	20,000		9.9	19.7	-0.1	-.005	.16	1.0 X 10 ⁷	2.0 X 10 ⁻³		
			10,000	7,000		13.2	23.0	-3.4	-.15	.19	1.0 X 10 ⁶	7.0 X 10 ⁻³		
			3,000	2,000		17.3	27.1	-7.5	-.28	.22	2.7 X 10 ⁵	7.4 X 10 ⁻³		
			1,000	700		22.9	32.7	-13.1	-.40	.27	7.6 X 10 ⁴	9.2 X 10 ⁻³		
			300	200		29.4	39.2	-19.6	-.50	.32	3.5 X 10 ⁴	5.7 X 10 ⁻³		
			100	70		35.7	45.5	-25.9	-.57	.37	1.7 X 10 ⁴	4.1 X 10 ⁻³		
			30	20		42.0	51.8	-32.2	-.62	.42	7.0 X 10 ³	2.2 X 10 ⁻³		
			10	7		48.5	58.3	-38.7	-.67	.47	5.0 X 10 ³	1.4 X 10 ⁻³		
			3	2		55.0	64.8	-45.2	-.70	.53	2.1 X 10 ³	0.1 X 10 ⁻³		
ASCENT	130 F	15	1								Σ	3.1 X 10 ⁻²		

Prepared By: JPS
Checked By:
Date: 10-19-71

SPACE DIVISION NORTH AMERICAN ROCKWELL CORPORATION														
1	2	3	4	5	6	7	8	9	10	11	12	13	14	15
MISSION PHASE	T (DEG F)	M MEAN (% DESIGN)	n_e	n	σ_{MEAN} (KSI)	σ_{ALT} (KSI)	σ_{MAX} (KSI)	σ_{MIN} (KSI)	R	σ_{MAX} F_{70}	N ($k_T = 3.0$)	n		
ASCENT	130 F	40	100,000	70,000	26	4.7	30.7	21.3	69	25	∞	0		
			30,000	20,000	↑	6.4	32.4	19.6	.60	.26	6.0×10^6	3.3×10^3		
			10,000	7,000		8.3	34.3	17.7	51	.28	1.1×10^6	6.4×10^3		
			3,000	2,000		10.3	36.3	15.7	43	.30	4.0×10^5	5.0×10^3		
			1,000	700		12.2	38.2	13.8	36	.31	2.5×10^5	2.8×10^3		
			300	200		14.2	40.2	11.8	29	.33	1.2×10^5	1.7×10^3		
			100	70		16.1	42.1	9.9	24	.34	7.0×10^4	0.8×10^3		
			30	20		18.0	44.0	8.0	.18	.36	6.2×10^4	0.3×10^3		
			10	7		20.0	46.0	6.0	.13	.37	4.8×10^4	0.1×10^3		
			3	2		22.0	48.0	4.0	.08	.39	3.2×10^4	0.1×10^3		
ASCENT	130 F	40	1		26							Σ	2.0×10^2	
ENTRY	300 F		100,000	70,000	0	8.3	8.3	0	0	.07	∞	0		
			30,000	20,000	↑	11.2	11.2	↑	↑	.09	∞	0		
			10,000	7,000		14.8	14.8			.12	∞	0		
			3,000	2,000		19.5	19.5			.16	1.0×10^7	0.2×10^3		
			1,000	700		26.8	26.8			.22	4.2×10^5	1.7×10^3		
			300	200		46.7	46.7	↑	↑	.38	2.8×10^4	7.0×10^3		
			100	100		61.6	61.6	0	0	.50	9.8×10^3	1.28×10^3		
ENTRY	300 F		1		0							Σ	2.2×10^2	

TABLE 6-4 WING FATIGUE
 DAMAGE ($K_T = 3.0, \sigma_{LIM} = 65 \text{ ksi}$) (SHEET 4)

		SPACE DIVISION NORTH AMERICAN ROCKWELL CORPORATION												
1	2	3	4	5	6	7	8	9	10	11	12	13	14	15
MISSION PHASE	T (DEG F)	MMEAN (% DESIGN)	n_c	n	σ_{MEAN} (KSI)	σ_{ALT} (KSI)	σ_{MAX} (KSI)	σ_{MIN} (KSI)	R	$\frac{\sigma_{MAX}}{F_u}$	N ($K_T = 3.0$)	$\frac{n}{N}$		
CRUISE	300 F	35	100,000	70,000	22.8	2.6	25.4	20.2	80	.23	∞	0		
/LNDG			30,000	10,000		5.7	28.5	17.1	.60	.26	60×10^6	3.3×10^{-3}		
			10,000	7,000		9.0	31.8	13.8	.43	.29	50×10^5	14.0×10^{-3}		
			3,000	2,000		12.2	35.0	10.6	.30	.32	1.5×10^5	13.0×10^{-3}		
			1,000	700		15.3	39.1	7.5	.20	.35	7.6×10^4	9.2×10^{-3}		
			300	200		18.5	41.3	4.3	.10	.58	3.7×10^4	5.4×10^{-3}		
			100	70		21.8	44.6	1.0	.02	.41	2.2×10^4	3.2×10^{-3}		
			30	20		24.8	47.6	-2.0	-.04	.44	1.3×10^4	1.5×10^{-3}		
			10	7		27.3	50.1	-4.5	-.09	.46	1.0×10^4	$.7 \times 10^{-3}$		
CRUISE			3	2	22.8	29.0	51.8	-6.2	-.12	.48	8.0×10^3	$.2 \times 10^{-3}$		
/LNDG	300 F	35	1								2×10^2	10.0×10^{-2}		
TAXI	300 F	-4	100,000	90,000	-2.6	2.9	0.3	-5.5	-18.3	.003	∞	0		
			10,000	9,000		3.9	1.3	-6.5	-5.0	.012				
			1,000	700		5.2	2.6	-7.8	-3.0	.024				
			100	90		6.5	3.9	-9.1	-2.3	.036				
			10	9		7.5	4.9	-10.1	-2.0	.045	∞	0		
TAXI	300 F	-4	1											
GAG	130 F			200										
TOTAL														D = .186

6.3 FATIGUE ANALYSIS - VERTICAL STABILIZER

6.3.1 Structural Configuration and Loading

The vertical stabilizer main box is a 3-spar structure with integral stiffened cover skins of 6AL-4V titanium alloy. In contrast to the wing, in which spanwise bending is carried by concentrated spar caps, spanwise bending loads on the vertical stabilizer are resisted primarily by the distributed cover skins. The assembly is designed as a heat-sink structure, without an external thermal protection system, and therefore is subjected to higher temperatures and temperature gradients than the wing spar caps. Maximum stresses in the cover skins occur at the canted rib near the root; this section is selected for fatigue analysis as indicated in Figure 6-2.

The cover skin structural geometry and limit design stress requires considerable redefinition from the data presented in Reference 22 because of subsequent changes in design loads. The cover skin geometry developed in Reference 22 is shown in Figure 6-3(a). This was based on a critical limit root bending moment for the surface of 8.9×10^6 Nm (79×10^6 in-lb) imposed by the max $q\beta$ condition during the ascent phase. Subsequent final loads analyses showed a large reduction in max $q\beta$ loads to a limit root bending moment of 4.88×10^6 Nm (43.2×10^6 in-lb); the subsonic side gust condition became critical with a limit root moment of 7.1×10^6 Nm (63.0×10^6 in-lb). Time did not permit incorporation of these load changes into the structural sizing reported in Reference 22 as part of the Phase B study effort. Therefore, an approximate re-optimization of skin and integral stiffener dimensions has been performed in this study to reflect the revised design loads. Stability under spanwise compression loading is the critical design requirement; the skin thickness and rib spacing were taken the same as defined in Reference 22 and stiffener spacing, depth and thickness were varied to achieve simultaneous skin panel and wide column buckling at ultimate design load. The resulting cover skin configuration is illustrated in Figure 6-3(b).

The spanwise loading at the selected section due to current design loads is determined by applying the ratio of design bending moments and applicable ultimate factors of safety to the data reported in Reference 22. This results in an ultimate loading of 0.85 MN/m (4900 lb-in); with corresponding limit design stresses of 180 MN/m² (26 ksi) for the subsonic side gust condition and 124 MN/m² (18 ksi) for the max $q\beta$ condition, using the revised cover skin section indicated in Figure 6-3(b).

6.3.2 Damage Analysis

Detailed calculations of fatigue damage on the selected section are presented in Table 6-5. Allowable load cycles are determined from S-N curves based on $K_t = 4.5$, presented in Figure 5-3. The amplitude of applied stress cycles is based on the vertical stabilizer load spectra presented in Figure 3-12; however, some interpretation is required in the application of these load spectra because of the change in design loads. The load spectra are based on the original set of design loads, in which max $q\beta$ was the critical design condition. The curves for ascent phase are used directly

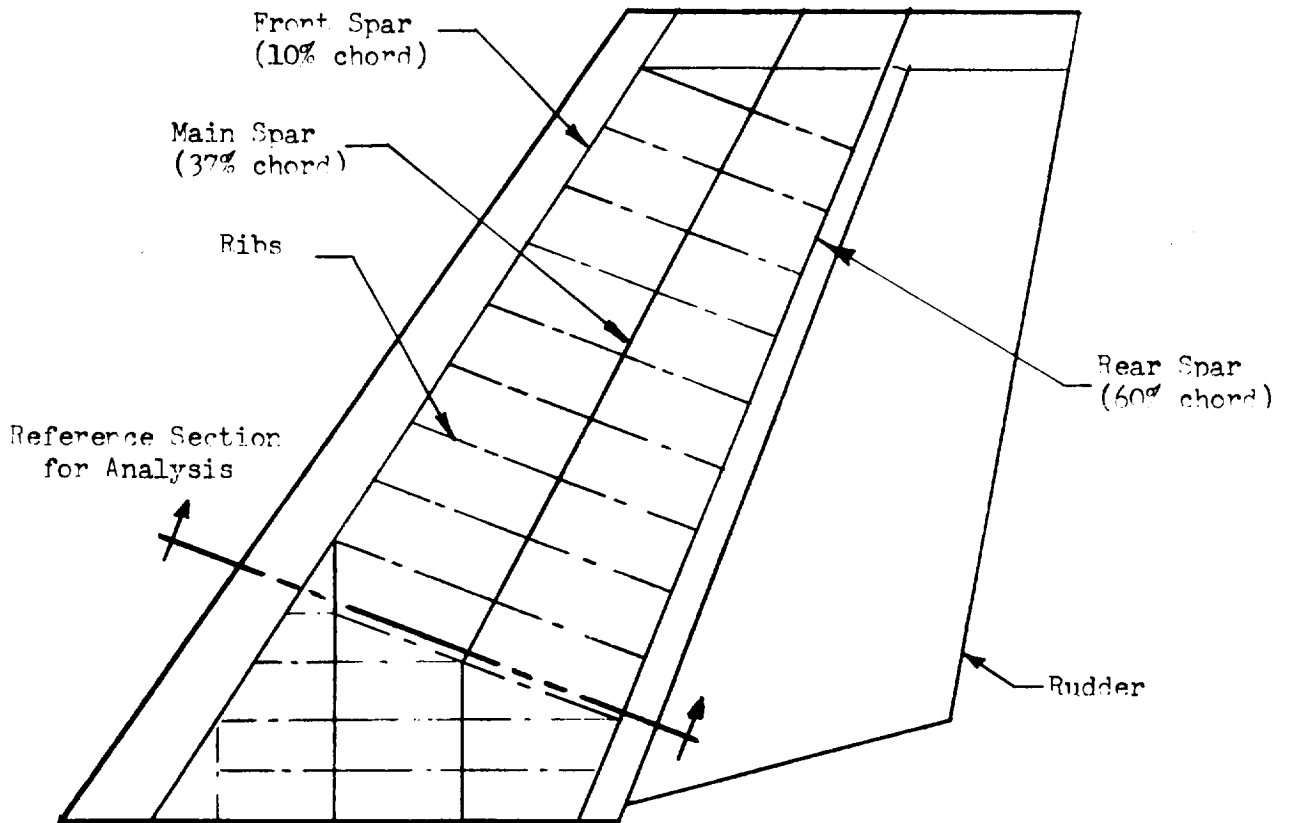


Figure 6-2. Vertical Stabilizer Planform

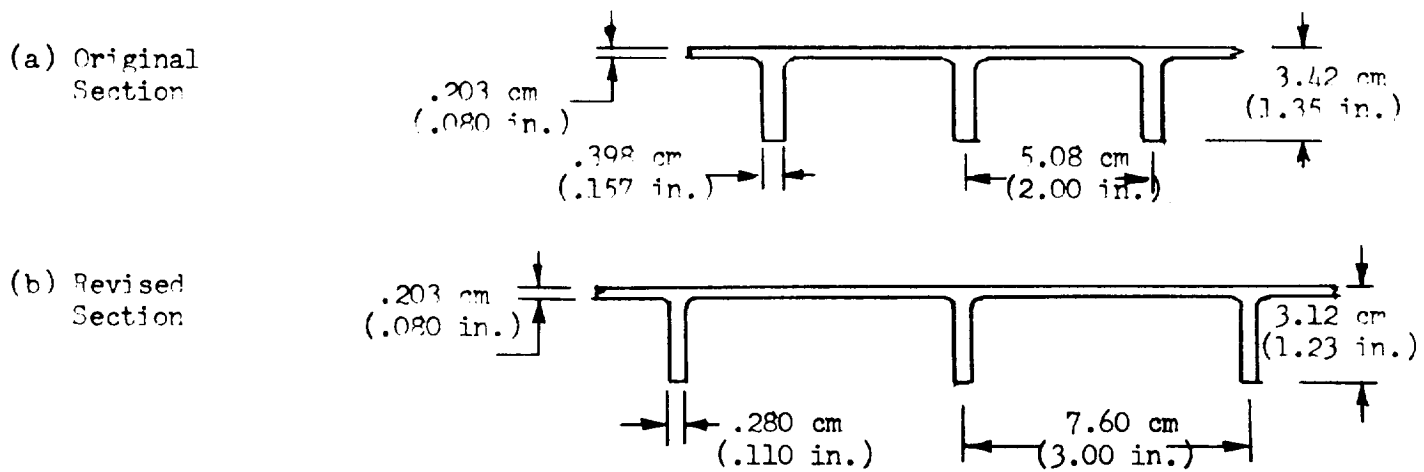


Figure 6-3. Vertical Stabilizer Cover Skin Configuration

with an associated limit design stress of 124 MN/m² (18 ksi). Cruise/landing phase now contains the critical design condition and it is assumed that limit load will be experienced once during 100 missions. The amplitude of this curve is increased by a factor of 2.17 to conform with this assumption, and is used with a limit design stress of 180 MN/m² (26 ksi) appropriate for the subsonic gust condition. The amplitude of the exceedance curve for the entry phase is increased by the ratio of the original to the revised root bending moments for the max q_β condition (k = 1.83) and is used with the current limit design stress for the max q_β condition.

Significant temperature gradients exist between the skin and integral stiffener elements, so an evaluation of the effect of thermal stresses on the fatigue damage is included in the analysis. Skin and stiffener temperature profiles are illustrated in Figure 3-17. These temperatures are based on the analysis of the original cover skin section shown in Figure 6-2(a) and will be slightly conservative for the current configuration because the smaller thickness and mass of the integral stiffener will reduce the temperature gradient between skin and stiffener. It can be seen that two distinct thermal pulses occur during the mission; the first is due to impingement of the orbiter main engine plumes during separation, and the second is due to entry heating. As a conservative simplification, these will be treated as two discrete stress cycles with the thermal stress assumed to return to zero between the two pulses. Elastic behavior will prevail during conditions of interest, so that the thermal stresses may be determined from the elementary equations:

$$\sigma_{1..} = \frac{-E_1 [\alpha_1 \Delta T_1 - \alpha_2 \Delta T_2]}{1 + (EA)_1 / (EA)_2}$$

$$\sigma_{2..} = E_2 [\alpha_1 \Delta T_1 - \alpha_2 \Delta T_2] \left[1 - \frac{A_2}{A_2 + \left(\frac{E_1}{E_2}\right) A_1} \right]$$

where:

σ = thermal stress

E = elastic modulus

A = cross-section area

α = coefficient of thermal expansion

ΔT = temperature change from room temperature

subscripts:

1 = skin

2 = integral stiffener

The values of the above parameters, and resulting thermal stresses, are summarized below for the two thermal pulses:

PULSE 1	PULSE 2
$T_1 = 460\text{K (370 F)}$	$T_1 = 516\text{K (470 F)}$
$\Delta T_1 = 167\text{C (300 F)}$	$\Delta T_2 = 222\text{C (400 F)}$
$T_2 = 310\text{K (100 F)}$	$T_2 = 390\text{K (245 F)}$
$\Delta T_2 = 17\text{C (30 F)}$	$\Delta T_2 = 97\text{C (175 F)}$
$\alpha_1 = 10.2 \times 10^{-6} \text{cm/cm-deg C}$ $(5.68 \times 10^{-6} \text{in/in-deg F})$	$\alpha_1 = 10.4 \times 10^{-6} \text{cm/cm-deg C}$ $(5.80 \times 10^{-6} \text{in/in-deg F})$
$\alpha_2 = 9.1 \times 10^{-6} \text{cm/cm-deg C}$ $(5.05 \times 10^{-6} \text{in/in-deg F})$	$\alpha_2 = 9.7 \times 10^{-6} \text{cm/cm-deg C}$ $(5.40 \times 10^{-6} \text{in/in-deg F})$
$E_1 = 1.03 \times 10^5 \text{MN/m}^2 (14.9 \times 10^6 \text{psi})$	$E_1 = .994 \times 10^5 \text{MN/m}^2 (14.4 \times 10^6 \text{psi})$
$E_2 = 1.12 \times 10^5 \text{MN/m}^2 (16.2 \times 10^6 \text{psi})$	$E_2 = 1.07 \times 10^5 \text{MN/m}^2 (15.5 \times 10^6 \text{psi})$
$A_1 = 1.55 \text{cm}^2 (0.240 \text{ in.}^2)$	$A_1 = 1.55 \text{cm}^2 (0.240 \text{ in.}^2)$
$A_2 = .865 \text{cm}^2 (0.134 \text{ in.}^2)$	$A_2 = .865 \text{cm}^2 (0.134 \text{ in.}^2)$
$\sigma_1 = -58.5 \text{MN/m}^2 (-8.5 \text{ ksi})$	$\sigma_1 = -51 \text{MN/m}^2 (-7.4 \text{ ksi})$
$\sigma_2 = 107 \text{MN/m}^2 (15.6 \text{ ksi})$	$\sigma_2 = 91.5 \text{MN/m}^2 (13.3 \text{ ksi})$

It can be seen from Table 6-1 that the fatigue damage at the selected section is small, with corresponding predicted safe-life of 2270 missions. This is the result of the low tension design stresses associated with this configuration in which stability under compression loading is the overriding design requirement. Almost all of the fatigue damage is incurred during the cruise/landing mission phase. As for the wing, the indicated damage for this phase is doubled to account for ferry missions over the operational life. The damage due to thermal stress, while not significant compared to the total, is about half the damage due to airload cycles during ascent and entry mission phases.

TABLE 6-5 VERTICAL STABILIZER		SPACE DIVISION NORTH AMERICAN ROCKWELL CORPORATION										Page No. 6-22 of		
FATIGUE DAMAGE ($K_T = 4.5$) (SHEET 1)												Report No. SD72-5H-0046		
												Model No. 5-9U		
1	2	3	4	5	6	7	8	9	10	11	12	13	14	15
MISSION PHASE	T (DEG F)	M_{MEAN} (% DESIGN)	η_c	MALT (% DESIGN)	η	M_{ALT} (% DESIGN)	σ_{MEAN} (KSI)	σ_{ALT} (KSI)	σ_{MAX} (KSI)	σ_{MIN} (KSI)	R	$\frac{\sigma_{MAX}}{F_{TU}}$	N	$\frac{\eta}{N}$
ASCENT	130 F	0	100,000	2.5	70,000	7.2	0	0.75	0.75	-0.75	-1.0	.006	∞	0
(1)	↑	↑	10,000	5.8	9,000	7.6	↑	1.37	1.37	-1.37	↑	.011	↑	↑
↑	↑	↑	4,000	9.0	900	11.0	↑	1.98	1.98	-1.98	↑	.016	↑	↑
↑	↑	↑	100	13.0	90	14.6	↑	2.63	2.63	-2.63	↑	.021	↑	↑
ASCENT	↑	↑	10	16.2	9	18.1	0	3.26	3.26	-3.26	-1.0	.027	∞	0
(1)	130 F	0	1	20.0									Σ	0
ASCENT	130 F	0	100,000	6.0	70,000	8.8	0	1.59	1.59	-1.59	-1.0	.013	∞	0
(2)	↑	↑	30,000	11.5	20,000	13.8	↑	2.48	2.48	-2.48	↑	.020	↑	↑
↑	↑	↑	10,000	16.2	7,000	19.2	↑	3.44	3.44	-3.44	↑	.028	↑	↑
↑	↑	↑	3,000	22.2	2,000	24.8	↑	4.46	4.46	-4.46	↑	.036	↑	↑
↑	↑	↑	1,000	27.5	700	30.2	↑	5.44	5.44	-5.44	↑	.044	↑	↑
↑	↑	↑	300	33.0	200	35.5	↑	6.38	6.38	-6.38	↑	.052	↑	↑
↑	↑	↑	100	38.0	70	40.9	↑	7.35	7.35	-7.35	↑	.060	↑	↑
↑	↑	↑	30	43.8	20	46.4	↑	8.35	8.35	-8.35	↑	.068	↑	↑
↑	↑	↑	10	48.0	7	51.8	↑	9.35	9.35	-9.35	↑	.076	↑	↑
ASCENT	↑	↑	3	54.5	2	57.2	0	10.30	10.30	-10.30	-1.0	.084	∞	0
(2)	130 F	0	1	60.0									Σ	0

TABLE 6-5 VERTICAL STABILIZER		SPACE DIVISION NORTH AMERICAN ROCKWELL CORPORATION										Prepared By: TPS			Page No. 6-23 of		
FATIGUE DAMAGE ($K_T = 4.5$) (SHEET 2)												Checked By:			Report No. SD72-SH-0046		
												Date: 10-2-77			Model No. R-14		
1	2	3	4	5	6	7	8	9	10	11	12	13	14	15			
MISSION PHASE	T (DEG F)	M _{MEAN} (% DESIGN)	τ_e	M _{ALT} (% DESIGN)	η	M _{ALT} (% DESIGN)	σ_{MEAN} (KSI)	σ_{ALT} (KSI)	σ_{MAX} (KSI)	F_{MIN} (KSI)	R	$\frac{\sigma_{MAX}}{F_{TU}}$	N	$\frac{\tau}{N}$			
ASCENT	130 F	0	100,000	7.5	70,000	14.2	0	2.6	2.6	-2.6	-1.0	.021	∞	0			
(3)	↑	↑	30,000	19.0	20,000	23.5	↑	4.2	4.2	-4.2	↑	.034	↑	↑			
			10,000	28.0	9,000	32.5		5.8	5.8	-5.8		.047					
			3,000	37.0	2,000	41.5		9.5	7.5	-7.5		.061					
			1,000	46.0	700	50.5		9.1	9.1	-9.1		.074					
			500	55.0	200	59.5		10.7	10.7	-10.7		.087	∞	0			
			100	64.0	70	68.5		12.3	12.3	-12.3		.100	3.0×10^6	2.3×10^{-5}			
			30	73.0	20	77.5		14.0	14.0	-14.0		.114	7.0×10^5	2.8×10^{-5}			
			10	82.0	7	86.5		15.6	15.6	-15.6		.127	2.5×10^5	2.8×10^{-5}			
ASCENT	↑	↑	3	91.0	2	95.5	0	17.2	17.2	-17.2	-1.0	.140	1.4×10^5	1.4×10^{-5}			
(3)	130 F	0	1	100.0									Σ	9.3×10^5			
ASCENT	130 F	0	100,000	7.0	70,000	10.2	0	1.8	1.8	-1.8	-1.0	.015	∞	0			
(4)	↑	↑	30,000	13.5	20,000	16.8	↑	3.0	3.0	-3.0	↑	.024	↑	↑			
			10,000	20.0	7,000	23.2		4.2	4.2	-4.2		.034					
			3,000	26.5	2,000	27.5		5.3	5.3	-5.3		.043					
			1,000	32.5	700	35.8		6.4	6.4	-6.4		.052					
			300	39.0	200	42.0		7.6	7.6	-7.6		.062					
			100	45.0	70	48.2		8.6	8.6	-8.6		.070					
			30	51.5	20	54.5		9.8	9.8	-9.8		.080	∞	0			
			10	57.5	7	61.0		11.0	11.0	-11.0		.090	1.0×10^7	7.0×10^{-7}			
ASCENT	↑	↑	3	64.5	2	67.2	0	12.1	12.1	-12.1	-1.0	.098	4.0×10^6	5.0×10^{-7}			
(4)	130 F	0	1	70.0									Σ	1.2×10^6			

TABLE 6-5 VERTICAL STABILIZER		SPACE DIVISION NORTH AMERICAN ROCKWELL CORPORATION										Prepared By: JPS		Page No. 6-24 of				
FATIGUE DAMAGE ($K_f = 4.5$) (SHEET 3)												Checked By:		Report No. SD72-SH-0046				
1	2	3	4	5	6	7	8	9	10	11	12	13	14	15	Date: 10-8-71		Model No. B-11	
MISSION PHASE	T (DEG F)	M MEAN (% DESIGN)	σ_e	MALT (% DESIGN)	N	MALT (% DESIGN)	σ_{MEAN} (KSI)	σ_{ALT} (KSI)	σ_{AMA} (KSI)	J_{MIN} (SSI)	R	σ_{MAX} (SSI)	N (K _f = 4.5)	$\frac{71}{N}$				
ASCENT (5)	130	0	100,000	5.5	70,000	7.5	0	1.4	1.4	-1.4	-1.0	.011	∞	0				
			30,000	9.5	20,000	11.5	↑	2.1	2.1	-2.1	↑	.017	↑	↑				
			10,000	13.5	7,000	16.0		2.1	2.1	-2.9		.024						
			3,000	18.5	2,000	20.5		3.7	3.7	-3.7		.030						
			1,000	22.5	1,000	25.0		4.5	4.5	-4.5		.037						
			300	27.5	200	29.5		5.3	5.3	-5.3		.043						
			100	31.5	70	34.0		6.1	6.1	-6.1		.050						
			30	36.5	20	38.8		7.0	7.0	-7.0		.057						
			10	41.0	7	43.2		7.8	7.8	-7.8		.063						
ASCENT (5)	130 F	0	3	45.5	2	47.8	0	8.6	8.6	-8.6	-1.0	.070	∞	0				
			1	50.0									∞	0				
ASCENT (6)	130 F	0	100,000	3.0	70,000	7.5	0	0.8	0.8	-0.8	-1.0	.006	∞	0				
			30,000	6.0	20,000	7.2	↑	1.3	1.3	-1.3	↑	.011	↑	↑				
			10,000	8.5	7,000	10.0		1.8	1.8	-1.8		.015						
			3,000	11.5	2,000	12.8		2.3	2.3	-2.3		.019						
			1,000	14.0	700	15.2		2.7	2.7	-2.7		.022						
			300	16.5	200	17.8		3.2	3.2	-3.2		.026						
			100	19.0	70	20.5		3.7	3.7	-3.7		.030						
			30	22.0	20	23.2		4.1	4.1	-4.1		.033						
			10	24.5	7	26.0		4.7	4.7	-4.7		.038						
ASCENT (6)	130 F	0	3	27.5	2	28.8	0	5.2	5.2	-5.2	-1.0	.042	∞	0				
			1	30.0									∞	0				

1	2	3	4	5	6	7	8	9	10	11	12	13	14	15
MISSION PHASE (DE. F.)	T (DE. F.)	M _{MEAN} (DESIGN)	R_e	M _{ALT} (DESIGN)	\bar{M} (DESIGN)	\bar{M}_{AV} (DESIGN)	F _{ALT} (DESIGN)	F _{AV} (DESIGN)	σ_{TENS} (DESIGN)	σ_{TENS} (DESIGN)	σ_{TENS} (DESIGN)	σ_{TENS} (DESIGN)	σ_{TENS} (DESIGN)	σ_{TENS} (DESIGN)
ASCENT	30 F	0	100,000	1.0	72,000	1.8	0	52	32	-32	-1.0	.003	∞	0
	↑	↑	10,000	2.5	7,000	3.2	↑	58	58	-58	↑	.005	↑	↑
	↑	↑	1,000	4.0	100	4.9	↑	86	86	-86	↑	.007	↑	↑
	↑	↑	100	5.5	10	6.2	↑	112	112	-112	↑	.007	↑	↑
ASCENT				7.0		9.0	0	143	143	-143	1.0	.02	∞	0
	130 F	0	1	7.0									Σ	0
ENTRY	480 F	0	100,000	8.2	70,000	11.4	0	2.0	2.0	-2.0	-1.0	.020	∞	0
	↑	↑	30,000	14.6	20,000	17.4	↑	3.1	3.1	-3.1	↑	.030	↑	↑
			10,000	20.1	7,000	23.8		4.3	4.3	-4.3		.042		
			3,000	27.4	2,000	30.2		5.4	5.4	-5.4		.053		
			1,000	32.7	700	36.6		6.6	6.6	-6.6		.065		
			300	40.3	400	43.4		7.8	7.8	-7.8		.076		
			100	46.6	20	49.8		9.0	1.0	-9.0		.088	∞	0
			30	53.0	50	56.2	↓	10.0	10.0	-10.0		.098	4.0 x 10 ⁶	5.0 x 10 ⁶
			10	59.5	7	63.0		11.3	11.3	-11.3	↑	.110	1.0 x 10 ⁶	7.0 x 10 ⁶
			3	66.6	2	69.8	0	12.6	12.6	-12.6		.124	3.0 x 10 ⁵	6.7 x 10 ⁶
ENTRY	480 F	0	1	73.0									Σ	1.9 x 10 ⁵
Thermal	100 F	0	-	-	100	-	0	-	15.6	0		.124	3.0 x 10 ⁶	3.3 x 10 ⁵
Stress	295 F	0	-	-	100	-	0	-	13.3	0	0	.118	6.0 x 10 ⁵	1.7 x 10 ⁵
													Σ	5.0 x 10 ⁵

6.4 FATIGUE ANALYSIS - INTERTANK ADAPTER

6.4.1 Structural Configuration and Loading

The intertank adapter is a cylindrical shell structure with integral stiffened 2219-T87 aluminum skins and internal ring frames. Maximum longitudinal tension loading in the cylindrical shell occurs on the bottom centerline near Body Sta. 2180. The limit design compression loading of 6.1×10^5 N/m (3500 lb/in) is considerably greater than limit design tension loading of 5.05×10^5 N/m (2900 lb/in) for this region (see Figure 3-5) so that the skin stringer shell will be critical for compression buckling mode of failure. It is assumed that the shell is designed to an allowable ultimate compression stress of 276 MN/m² (40 ksi); the resulting effective shell thickness is 0.31cm (0.122 in).

Conditions producing tension loading on the adapter lower surface and the resulting longitudinal tension stresses are summarized below:

Load Condition	Longitudinal Loading (N_x)		Longitudinal Stress (σ_x)	
	(N/m)	(lb/in)	(MN/m ²)	(ksi)
(11) Burnout	5.05×10^5	2900	164	23.8
(12) Entry	1.22×10^5	700	39	5.6
(13) Subsonic Gust	2.1×10^4	120	6.9	1.0
(16) 2-g Taxi	3.5×10^4	200	11	1.6

6.4.2 Damage Analysis

It is apparent that only the burnout case produces stress levels high enough to cause potential fatigue damage. Therefore, the loading spectra can be simplified to the basic GAG cycle which varies from -5.05×10^5 N/m (-2900 lb/in) at lift off to 5.05×10^5 N/m (2900 lb/in) at burnout. The structure is essentially at room temperature for these significant fatigue stresses. For these conditions:

$$R = -1.0$$

$$\sigma_{\max}/F_{tu} = \frac{23.8}{62.0} = 0.38$$

$$N = 4300 \text{ cycles (Figure 5-1)}$$

$$D = \frac{100}{4300} = .0232$$

$$L_s = \frac{100}{4(.0232)} = 1080 \text{ missions (Safe-life)}$$

6.5 FATIGUE ANALYSIS - FUSELAGE STA. 2600

6.5.1 Structural Configuration and Loading

Fuselage Sta. 2600 is in the LH₂ tank adjacent to the orbiter aft attachment. This section represents the region of maximum body bending during the ascent flight phase. The LH₂ tank is an integral stiffened cylindrical shell of 2219-T87 aluminum alloy. Ring frames are spaced at approximately 1.73 m (68 in.) to provide shell stability or to accept major external loads. Maximum tension stresses occur on the bottom center-line; therefore this region will be critical for fatigue life evaluation. The shell properties in this region are obtained from Reference 5 as follows:

$$t_s = 0.310 \text{ cm (0.122 in.)} \quad (\text{skin thickness})$$

$$\bar{t} = 0.445 \text{ cm (0.175 in.)} \quad (\text{effective thickness of skin and integral stringers})$$

Longitudinal loading in the LH₂ tank shell is produced by external bending moments and axial loads and by internal tank pressures. Longitudinal stresses due to applied moment are determined from the equation:

$$\sigma_{X_M} = \frac{M}{\pi R^2 \bar{t}}$$

and due to external axial load by the expression:

$$\sigma_{X_A} = \frac{F_X}{2\pi R \bar{t}}$$

where:

- M = applied bending moment
- R = shell radius = 5.05m (198 in.)
- \bar{t} = effective shell thickness
- F_X = applied external axial load

The tank ullage pressure (p_u) produces an average longitudinal tensile stress equal to:

$$\sigma_{X_P} = \frac{p_u R}{2\bar{t}}$$

However, because of Poisson effects associated with hoop stresses in the tank skin due to internal pressure, the actual longitudinal tension stress in the skin will be higher than in the integral stringers to maintain strain compatibility. The following equations for longitudinal stresses are derived on the basis of maintaining equal longitudinal strains between the skin and the integral stringers:

$$\sigma_{X_{str}} = \frac{P_u R}{2\bar{t}} (1-2\mu) \quad (\text{integral stringer stress})$$

$$\sigma_{X_{sk}} = \frac{P_u R}{2\bar{t}} \left[1+2\mu\left(\frac{\bar{t}}{t_s} - 1\right) \right] \quad (\text{skin stress})$$

6.5.2 Damage Analysis - Membrane Loading

Exceedance of alternating bending moment and associated values of mean bending moment are defined in Figure 3-13 for ascent, entry, cruise/landing and taxi mission phases. The effective GAG cycle to maximum thrust on every mission is also indicated. It is also necessary to define axial loads and tank pressures associated with these mission phases to determine the net mean and alternating stresses in the tank shell. The majority of significant alternating moment cycles during the ascent phase will occur near the max q^a condition, so axial load and tank pressures associated with this design condition are used for the ascent phase. Axial loads and tank pressures for all mission phases are summarized below:

Condition	Axial Load		Ullage Pressure	
	(MN)	(lb)	(MN/m ²)	(psi)
Ascent (max q^a)	-22.5	-5.05×10^6	.125	18.2
Ascent (burnout)	-1.51	-3.40×10^6	.143	20.8
Entry	-.55	-1.24×10^5	.119	17.2
Cruise/Landing	-.39	-8.8×10^4	.062	9.0
Taxi	0	0	.021	3.0

Stress spectra for the various mission phases are derived from the loading spectra presented in Figure 3-13 and the previously defined equations to convert loading to stress. Detailed stress spectra and corresponding fatigue damage calculations are presented in Table 6-6. The burnout (maximum thrust) condition is treated as an effective ground-air-ground (GAG) cycle, with total tension stress increasing from zero at prelaunch to a maximum at burnout once per mission. Tension stresses listed in the table refer to the skin element, because of Poisson's effect on tank pressure stresses, the net skin stress is higher than the integral stringer stress. Allowable number of load cycles for given stress conditions are obtained from the S-N curves of Figure 5-1.

It can be seen from the results of Table 6-6 that the calculated fatigue damage is moderate, with corresponding predicted safe-life of 960 missions. Almost all of the damage is due to the effective GAG cycles of maximum stress at burnout; the damage due to airload fluctuations during ascent and entry is relatively small. The assumed theoretical stress concentration factor of $K_t = 4.4$ that is the basis for the S-N curves used in the damage analysis is

Prepared By: JPS
 Checked By:
 Date: 10-11-91

SPACE DIVISION
 NORTH AMERICAN ROCKWELL CORPORATION

Page No. 6-30 of
 Report No. SD72-SH-0046
 Model No. B-9U

1	2	3	4	5	6	7	8	9	10	11	12	13	14	15
MISSION PHASE (DEG F)	T	M _{MEAN} (IN-LB X 10 ⁵)	γ_e	M _{ALT} (IN-LB X 10 ⁵)	γ	\bar{M}_{ALT} (IN-LB X 10 ⁵)	σ_{MEAN} (KSI)	σ_{ALT} (KSI)	σ_{MAX} (KSI)	σ_{MIN} (KSI)	R	$\frac{\sigma_{MAX}}{F_{TU}}$	N (K-74)	$\frac{\gamma}{N}$
ASCENT	-100 F	-348	100,000	28	70,000	36	6.1	168	778	442	0.57	.12	∞	0
			30,000	44	20,000	52		2.44	9.54	3.66	0.43	.13		
			10,000	60	7,000	69.5		3.18	1.28	2.92	0.31	.15		
			3,000	77	2,000	85		3.15	10.7	2.15	0.22	.16	∞	0
(BASIC CASE)			1,000	93	700	101.5		4.72	1082	1.38	0.13	.17	6.0×10^6	1.2×10^{-4}
			300	110	200	117.5		5.46	11.56	0.64	0.06	.18	1.5×10^6	1.3×10^{-4}
			100	125	70	133.5		6.27	12.30	-1.0	-0.008	.19	7.0×10^5	1.0×10^{-4}
			30	142	20	147.5		6.95	13.00	-85	-0.07	.20	3.4×10^5	6×10^{-4}
			10	157	7	165.5		7.70	13.80	-1.60	-0.12	.22	1.4×10^5	5×10^{-4}
			3	174	2	182		8.45	14.55	-2.35	-0.16	.23	1.2×10^5	2×10^{-4}
ASCENT -100 F -348			1	190									Σ	4.8×10^{-4}
MAX. THRUST - (BASIC CASE)	-100 F	0	100	680	100	680			31.0	0	0	.50	4.0×10^3	2.5×10^{-2}
													Σ	2.5×10^{-2}

TABLE 6-6 FUSELAGE STATION 2600		MEMBRANE DAMAGE -		MEMBRANE LOADING		SPACE DIVISION NORTH AMERICAN ROCKWELL CORPORATION										Page No. 6-31 of	
MISSION PHASE		T (DEG F)	M MEAN (IN-LB X 10 ³)	n _e	MALT (IN-LB X 10 ⁶)	n	MALT (IN-LB X 10 ⁶)	M MEAN (AS)	σ ALI (AS)	σ MAX (AS)	σ MIN (AS)	R	σ MAX / F _{TU}	N	N (K = 4.4)	n	
MEMBRANE PHASE		300 F	—	100,000	19	70,000	22.5	—	1.05	12.85	11.8	.92	.26	∞	∞	0	
	↑		↑	30,000	26	20,000	29	—	1.35	13.15	1	.90	.27	↑	↑	↑	
			↑	10,000	32	7,000	35.5	—	1.65	13.45		.88	.28	↑	↑		
	(BASIC CASE)		↑	3,000	39	2,000	42.5	—	1.98	13.78		.86	.28	↑	↑		
			↑	1,000	46	700	56.5	—	2.63	14.43		.82	.30	∞	∞	0	
			↑	300	61	200	95.5	—	4.45	16.25	↑	.73	.33	7×10^6	$.3 \times 10^{-4}$		
	↑		↑	100	124	100	124	—	5.75	17.55	11.8	.69	.36	1.1×10^6	$.9 \times 10^{-4}$		
	ENTRY 300 F	—	—	1	124											Σ 1.2 x 10 ⁻⁹	
	CRUISE 300 F	-10	↑	100,000	16	70,000	20.5	6.6	0.15	7.55	5.45	.75	.15	∞	∞	0	
	↑		↑	10,000	25	7,000	29.5	↑	1.37	8.21	5.23	.66	.16	↑	↑	↑	
	↑		↑	4,000	34	3,000	38.5	↑	1.79	8.39	4.81	.58	.17	↑	↑	↑	
	↑		↑	100	43	90	47.5	↑	2.21	8.81	4.39	.50	.18	↑	↑	↑	
	CRUISE		↑	10	52	7	56.5	6.6	2.63	9.23	3.41	.43	.11	∞	∞	0	
	↑		↑	1	61												
	LANDG 300 F	-10	↑	1													
	↑		↑														
	(BASIC CASE)																
	TOTAL																D = .026

probably conservative for the type of structure and welded joints associated with the skin element.

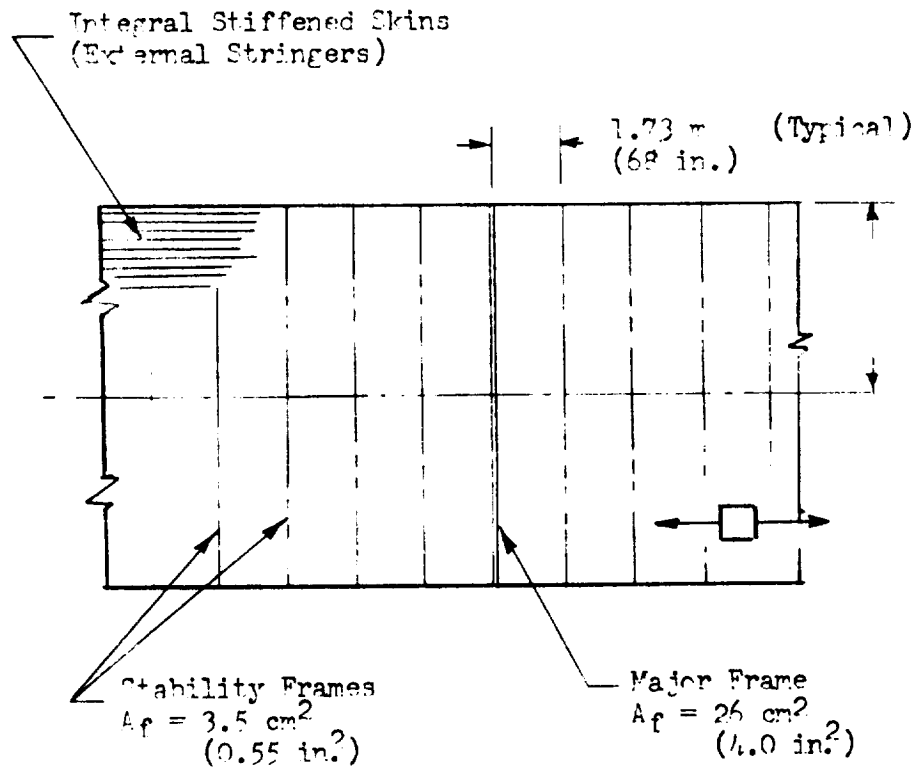
6.5.3 Damage Analysis - Membrane Plus Discontinuity Loading

The preceding fatigue damage analysis is based on an idealized structural model in which the tank is assumed to remain a pure cylinder and only elementary membrane loadings exist in the tank shell structure. In the actual structure, significant secondary stresses may be induced because of the restraint of the fuselage ring frames preventing free radial deflection of the skin/stringer shell under tank pressure or external axial loads. Therefore, it is considered desirable to perform a supplementary analysis which considers these effects and provides a comparison with the basic solution to evaluate the significance of such discontinuity stresses on the fatigue life of the tank shell.

Analysis of the secondary bending stresses due to the interaction of fuselage ring frames and the skin/stringer shell is accomplished by the use of "Shell of Revolution" computer program which was developed for and extensively applied to the analysis of the Saturn S-II stage. The idealized structural shell and a typical skin/stringer section are indicated in Figure 6-4. The influence of both a typical stability frame and a major load-carrying frame, such as the orbiter attach support frame at Sta. 2666, on secondary bending stresses in skin and stringers is considered. A tank ullage pressure of $.143 \text{ MN/m}^2$ (20.8 psig) is taken for the analysis, and three values of external longitudinal loading intensity are considered. The distribution of secondary bending moment on the skin/stringer beam element per unit shell width is plotted in Figure 6-5. The resulting secondary bending stresses are summarized in Table 6-7.

It can be seen that discontinuity effects adjacent to a major load-carrying frame are much greater than for a stability frame. Because the stringers are external to the tank, the flange element of stringer is loaded in compression by the secondary bending moment at the frame station. This will not aggravate the fatigue damage and therefore the skin element, which is loaded in tension by secondary bending, will be more critical. Secondary bending stresses on the skin vary from about 34 MN/m^2 (5 ksi) for $N_x = .49 \text{ MN/m}$ (2800 lb/in) to 55 MN/m^2 (3 ksi) for $N_x = -.61 \text{ MN/m}$ (-3500 lb/in). These secondary bending effects are incorporated in the fatigue damage calculations summarized in Table 6-8. The secondary bending stresses for a given mission phase are approximated by interpolation between the results summarized in Table 6-7 for the values of tank pressure and external longitudinal loading applicable to each mission phase. The secondary bending stress is included as an increase in the mean stress for each applicable mission phase.

The secondary bending moment midway between frames produces tension on the stringer flange element and compression on the skin. However, the secondary bending stress on flange at this location is less than the difference in stress between skin and stringer due to Poisson's effect on skin hoop stresses. Therefore, the skin remains as the critical element for fatigue life analysis.



Properties of
Typical Section

$A = 4.65 \text{ cm}^2 \text{ (.721 in.}^2\text{)}$

$I = 33.2 \text{ cm}^4 \text{ (.800 in.}^4\text{)}$

$\bar{t} = .457 \text{ cm (.180 in.)}$

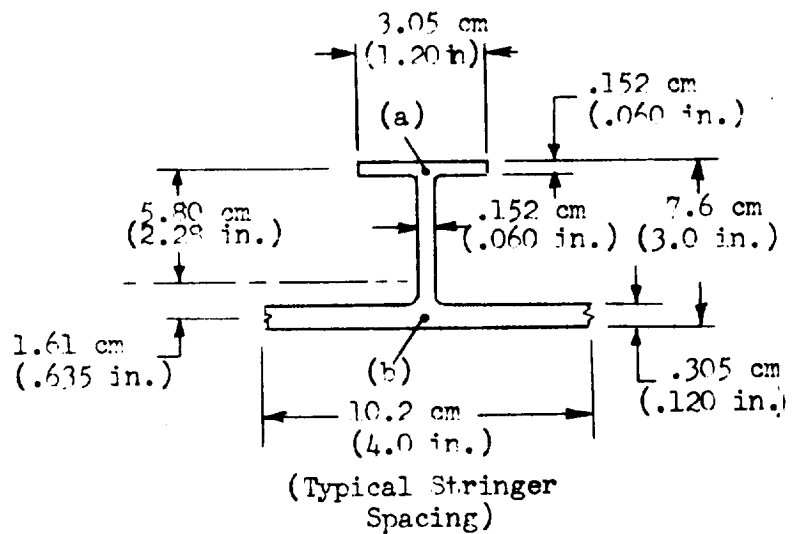


Figure 6-4. LH₂ Tank Shell Model for Discontinuity Analysis

Load Case	Longitudinal (MN/m)	Loading - N_x (lb/in.)
1	0	0
2	.485	2800
3	-.610	-3500

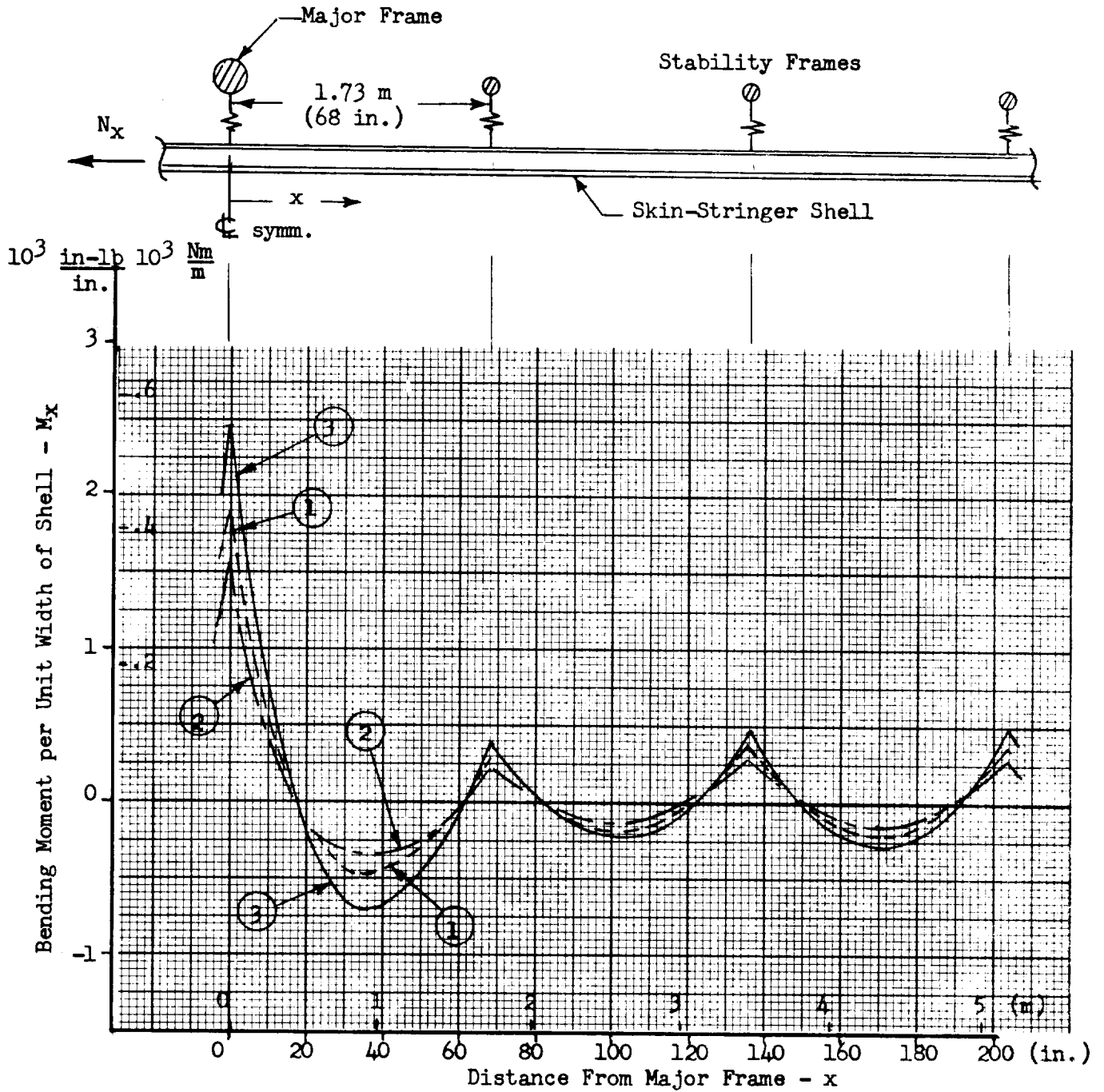


Figure 6-5. LH₂ Tank Secondary Bending Moment Distribution

Table 6-7. LH₂ Tank Secondary Bending Stresses

Distance From Major Frame (x) (m)	Section (1) Location	Secondary Bending Stress (σ_x) (3)					
		Case 1 $N_x = 0$ (2)	Case 2 $N_x = 2800$ lb/in.	Case 3 $N_x = -3500$ lb/in.			
		(MN/m ²) (ksi)	(MN/m ²) (ksi)	(MN/m ²) (ksi)			
0	(a)	-151	-21.9	-121	-17.5	-194	-28.2
	(b)	42	6.1	33	4.8	54	7.8
.86	(a)	36	5.2	26	3.8	52	7.5
	(b)	-9.7	-1.4	-7.6	-1.1	-14	-2.1
4.31	(a)	12	1.8	9.0	1.3	18	2.6
	(b)	-3.5	-0.5	-2.8	-0.4	-4.8	-0.7
5.18	(a)	-30	-4.3	-23	-3.3	-39	-5.7
	(b)	8.3	1.2	6.2	0.9	11	1.6

(1) (a) - stringer flange) (See Fig. 6-4)
(b) - skin

(2) N_x is longitudinal loading from external axial load and bending moment (does not include loading due to tank ullage pressure)

(3) Tank ullage pressure = .143 MN/m² (20.8 psig)

Prepared By: JFS
 Checked By: F.W.S.
 Date: 10/11/71

SPACE DIVISION
 NORTH AMERICAN ROCKWELL CORPORATION

1	2	3	4	5	6	7	8	9	10	11	12	13	14	15
MISSION PHASE (DEG F)	M ^{MEAN} (IN-LB X 10 ⁶)	%	M ^{ALT} (IN-LB X 10 ⁶)	N	M ^{ALT} (IN-LB X 10 ⁶)	M ^{MEAN} (KSI)	S ^{ALT} (KSI)	J ^{MAX} (KSI)	S ^{MIN} (KSI)	R	S ^{MAX} / F _{2U}	N	N	N
TAXI 300 F	-10	100,000	12	90,000	15	2.6	0.70	3.30	1.10	.58	.067	∞	∞	0
(BASIC CASE)		10,000	18	9,000	21		0.98	5.58	1.62	45	.073	↑	↑	↑
		1,000	24	900	26.5		1.23	3.83	1.37	36	.078	↑	↑	↑
		100	29	90	32		1.49	4.09	1.11	20	.084	↑	↑	↑
		10	35	9	37.5		1.75	7.35	0.85	20	.089	∞	∞	0
TAXI 300 F	-10	1	40									Σ	Σ	0
ASCENT -100 F	-348	100,000	28	70,000	36	12.2	1.68	13.88	10.52	76	.22	∞	∞	0
		30,000	44	20,000	52		2.44	14.64	9.76	67	.23	∞	∞	0
		10,000	60	7,000	68.5		3.18	15.38	9.02	59	.24	∞	∞	0
		3,000	77	2,000	85		3.95	16.15	8.25	51	.25	40 X 10 ⁶	40 X 10 ⁶	50 X 10 ⁴
2nd BNDG		1,000	93	700	101.5		4.72	16.92	7.48	44	.26	12 X 10 ⁶	12 X 10 ⁶	58 X 10 ⁴
BNDG		300	110	200	117.5		5.46	17.66	6.74	38	.28	3.0 X 10 ⁵	3.0 X 10 ⁵	6.7 X 10 ⁴
STRESS		100	125	70	133.5		6.20	18.40	6.00	33	.29	1.5 X 10 ⁵	1.5 X 10 ⁵	4.7 X 10 ⁴
		50	142	20	149.5		6.95	19.15	5.25	27	.30	7.5 X 10 ⁴	7.5 X 10 ⁴	2.7 X 10 ⁴
		10	157	7	165.5		7.70	19.90	4.50	23	.31	6.5 X 10 ⁴	6.5 X 10 ⁴	1.1 X 10 ⁴
		3	174	2	182		8.45	20.60	3.75	18	.32	4.5 X 10 ⁴	4.5 X 10 ⁴	4 X 10 ⁴
ASCENT -100 F	-348	1	190									Σ	Σ	26.4 X 10 ⁴
MAX THRUST	-100 F	0	100	680	100	680		35.8	0	0	.56	2.2 X 10 ³	2.2 X 10 ³	4.5 X 10 ²
		(2nd BNDG STRESS)												

Prepared By: RWN
 Checked By:
 Date: 10-5-71

SPACE DIVISION
 NORTH AMERICAN ROCKWELL CORPORATION

1	2	3	4	5	6	7	8	9	10	11	12	13	14	15
MISSION PHASE	T (DEG F)	M _{MEAN} (IN-LB X 10 ⁶)	N _e	M _{ALT} (IN-LB X 10 ⁶)	n	M _{ALT} (IN-LB X 10 ⁶)	V _{MEAN} (KSI)	V _{ALT} (KSI)	V _{MAX} (KSI)	σ _{MIN} (KSI)	R	σ _{MAX} / F _{TU}	N (K _T =4.4)	n / N
ENTRY	300		100,000	19	70,000	22.5	—	1.05	17.5	16.5	.94	.36	∞	0
↑			30,000	26	20,000	29.0	—	1.35	17.9	↑	.92	.36	↑	↑
			10,000	32	7,000	35.5	—	1.65	18.1		.91	.37	↓	↓
			3,000	37	2,000	42.5	—	1.98	18.5		.89	.38	↓	↓
			1,000	46	700	56.5	—	2.63	19.1		.86	.39	∞	0
			300	67	200	95.5	—	4.45	21.0	16.5	.79	.43	3.5 x 10 ⁶	.57 x 10 ⁻⁴
↓			100	124	100	124	—	5.75	22.9	17.1	.74	.47	4 x 10 ⁵	2.5 x 10 ⁻⁴
ENTRY	300		1	124									Σ	3.1 x 10 ⁻⁴
CRUISE/	300		100,000	16	90,000	20.5	9.1	1.0	10.1	8.1	.80	.20	∞	0
LANDING	↑		10,000	25	9,000	29.5	↑	1.4	10.5	7.7	.73	.21	↑	↑
			1,000	34	900	38.5	↓	1.8	10.9	7.3	.67	.22	↓	↓
			100	43	90	47.5		2.2	11.3	6.9	.61	.23	∞	0
↓			10	52	9	56.5	9.1	2.6	11.7	6.5	.55	.24	1.0 x 10 ⁷	9 x 10 ⁻⁷
↓	300		1	61									Σ	9 x 10 ⁻⁷
TOTAL														D = .048

The total fatigue damage indicated from Table 6-8 is still moderate, but a significant increase is noted over the basic case. The predicted safe-life is 520 missions as compared with 960 missions for the solution considering only membrane stresses. This illustrates that discontinuity effects and associated secondary stresses must be carefully considered in the design development and fatigue evaluation of actual vehicle structure.

6.6 FATIGUE ANALYSIS - ORBITER AFT ATTACH SUPPORT FRAME

6.6.1 Structural Configuration and Loading

The orbiter aft attach support structure is a major fuselage ring frame of 2219 aluminum alloy. The frame extends from the LH₂ tank wall to the external mold line defined by the contour of the thermal protection system. The inboard cap of the frame is an integral part of the LH₂ tank wall. A sketch showing the idealized structural geometry and identification of individual members used by GDC in the Phase B study analysis is given in Figure 6-6.

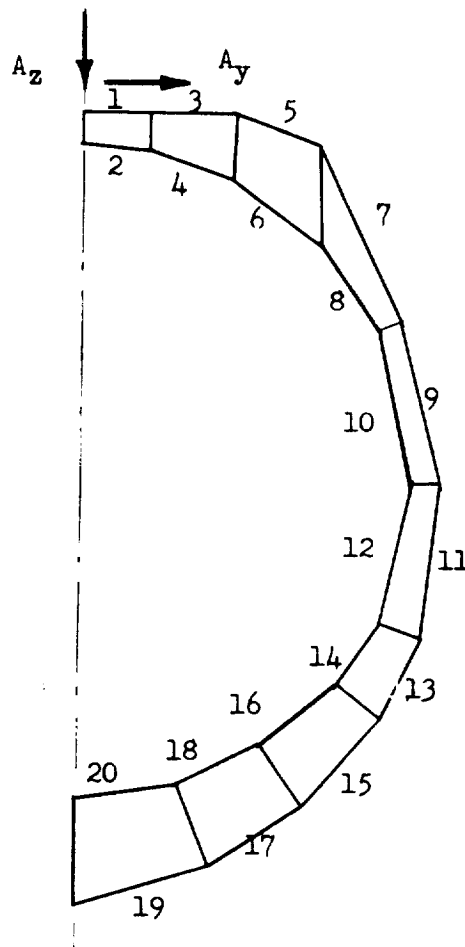


Figure 6-6. Orbiter Aft Attach Support Frame

From Reference 7, the critical member in the idealized frame configuration is indicated as bar #6 (inboard cap). This member is designed by tension load in the inboard cap, whereas the other members generally have larger compression design loads than tension, with consequent reduction in the operating tension stresses. The frame experiences internal bending moment, shear and axial loads due to the external normal and lateral loads applied at the orbiter aft attachment. Unit stress solutions for bar #6 are given in Reference 7 as follows:

$$A_z = 1000 \text{ kips}, \quad \sigma_6 = 24.7 \text{ ksi}$$

$$A_y = 1000 \text{ kips}, \quad \sigma_6 = 68.0 \text{ ksi}$$

Because the frame is an integral part of the LH₂ tank, it is also loaded in hoop tension due to the radial deflection tendency of the tank shell under internal pressure and longitudinal compression loading. The discontinuity solution described in Section 6.5.3 also provides the net radial deflection at frame locations, from which the effective hoop stress in the frame is calculated. The frame cross-section area assumed in the discontinuity analysis is 26 cm² (4.0 in.²); this value is a reasonable overall average for this frame and also for the local section which includes bar #6. The frame hoop stresses calculated from the discontinuity solution for a tank ullage pressure of 0.143 MN/in.² (20.8 psig) are:

Case	External Longitudinal Loading (N _x)	Frame Hoop Stress	
		(MN/m ²)	(ksi)
1	0	124	18.0
2	2800 lb/in.	106	15.4
3	-3500 lb/in.	145	21.1

In this case, the reference values of longitudinal loading are related to the external axial load, without regard to external bending moment, because the influence on frame hoop stress is associated with Poisson's effect on the hoop strains in the tank skin.

Critical design loads on the frame occur in the max q_α and max q_β conditions; limit design values and corresponding limit stresses in bar #6 are:

<u>max q_α</u>	<u>max q_β</u>
A _z = 4.21 MN (950 kips)	A _z = 2.90 MN (654 kips)
A _y = 0	A _y = 0.74 MN (167 kips)
σ ₆ = 163 MN/m ² (23.6 ksi)	σ ₆ = 190 MN/m ² (27.5 ksi)

For this flight condition, the limit design axial loading and tank pressure are:

$$F_x = 22.2 \text{ MN } (-5.05 \times 10^6 \text{ lb})$$

$$N_x = -0.705 \text{ MN/m } (-4050 \text{ lb/in.})$$

$$p_u = 0.136 \text{ MN/m}^2 \text{ (19.7 psig)}$$

By interpolation of discontinuity solution values, the resulting hoop stress in the frame is determined to be

$$\sigma_{\text{hoop}} = 138 \text{ MN/m}^2 \text{ (20 ksi) (limit)}$$

The total tension stress in bar #6 for the max q β condition is then:

$$\sigma_{6_{\text{tot}}} = 327 \text{ MN/m}^2 \text{ (47.5 ksi) (limit)}$$

$$= 457 \text{ MN/m}^2 \text{ (66.5 ksi) (ultimate)}$$

This total ultimate stress is somewhat greater than the ultimate tensile strength of the material, if room temperature properties are assumed. Therefore, it is assumed that the area of bar #6 is increased so that the ultimate applied stress does not exceed $0.95 F_t^u$ for 2219-T87 aluminum alloy at room temperature. This allows a 5 percent local reduction in net section area due to fastener holes. It is further assumed that the local increase in area of bar #6 will not significantly change the frame hoop stress due to internal pressure. The stress coefficients for unit normal and lateral frame loads are then ratioed down to maintain acceptable stresses from this loading source, as follows:

$$k = \frac{0.95(62.0) - 1.4(20)}{1.4(27.5)} = 0.805$$

The stress coefficients for bar #6 due to unit normal and lateral external loads applied to the frame then become:

$$A_z = 1000 \text{ kips,} \quad \sigma_6 = 20 \text{ ksi}$$

$$A_y = 1000 \text{ kips,} \quad \sigma_6 = 55 \text{ ksi}$$

6.6.2 Damage Analysis

Fatigue damage calculations are summarized in Table 6-9. The loading spectra is derived from the exceedance curves of Fig. 3-14 and the limit design loads for max q α and max q β conditions listed in the preceding section. These are converted to stress spectra for bar #6 by applying the unit load/stress coefficients defined above. The influence of tank pressure and axial load on the mean stress is included in the same manner as described in the preceding section. Because the major cyclic loads will occur in the vicinity of max q α flight time, the axial load and nominal tank ullage pressure of $.125 \text{ MN/in}^2$ (18.2 psig) associated with this condition are used to determine this contribution to the mean stress. This increment is found to be 127 MN/in^2 (18.5 ksi).

Prepared By: RWW
 Checked By:
 Date: 12-6-71

SPACE DIVISION
 NORTH AMERICAN ROCKWELL CORPORATION

TABLE 6-9. ORBITER AFT ATTACH FRAME FATIGUE DAMAGE		SPACE DIVISION NORTH AMERICAN ROCKWELL CORPORATION														
1	2	3	4	5	6	7	8	9	10	11	12	13	14	15		
MISSION PHASE	T (DEG F)	Az MEAN (% DESIGN)	Ne	ΔA (% DESIGN)	n	ΔA (% DESIGN)	σ MEAN (KSI)	σ ALT (KSI)	σ MAX (KSI)	σ MIN (KSI)	R	σ MAX / FTU	N	n / N		
↑	70F	.63	100,000	3.0	70,000	3.8	30.5	0.7	31.2	29.8	.96	.50	∞	0		
ASCENT	↑	↑	30,000	4.5	20,000	5.2	↑	1.0	31.5	29.5	.94	.51	↑	↑		
NORMAL			10,000	6.0	7000	6.5		1.2	31.7	29.3	.92	.51				
LOAD			3,000	7.0	2000	7.8		1.5	32.0	29.0	.90	.52				
EXCURS			1000	8.5	700	10.5		2.0	32.5	28.5	.88	.53	∞	0		
(ΔAz)			300	12.5	200	14.8		2.8	33.3	27.7	.85	.54	3 x 10 ⁶	.07 x 10 ⁻³		
			100	17.0	70	19.8		3.8	34.3	26.7	.78	.55	2.5 x 10 ⁵	.29 x 10 ⁻³		
			30	22.0	20	24.8		4.7	35.2	25.8	.73	.57	7.6 x 10 ⁴	.26 x 10 ⁻³		
			10	27.0	7	29.8		5.6	36.1	24.9	.69	.58	4.0 x 10 ⁴	.18 x 10 ⁻³		
			3	32.5	2	34.8	30.5	6.6	37.1	23.9	.64	.60	2.7 x 10 ⁴	.07 x 10 ⁻³		
↓		.63	1	37.0									Σ	.87 x 10 ⁻³		
↑		.63	100,000	8.0	70,000	10.5	30.5	1.0	31.5	29.5	.94	.51	∞	0		
ASCENT	↑	↑	30,000	13.0	20,000	15.2	↑	1.4	31.9	29.1	.91	.52	∞	0		
LATERAL			10,000	17.5	7000	20.0		1.8	32.3	28.7	.89	.52	∞	0		
LOAD			3000	22.5	2000	25.0		2.3	32.8	28.2	.86	.53	5.0 x 10 ⁶	.40 x 10 ⁻³		
EXCURS.			1000	27.5	700	33.2		3.1	33.6	27.4	.82	.54	7.0 x 10 ⁵	1.0 x 10 ⁻³		
(ΔAz)			300	39.0	200	45.0		4.2	34.7	26.3	.76	.56	1.4 x 10 ⁵	1.43 x 10 ⁻³		
			100	51.0	70	57.2		5.3	35.8	25.2	.70	.58	4.5 x 10 ⁴	1.55 x 10 ⁻³		
			30	63.5	20	69.5		6.4	36.9	24.1	.65	.60	2.7 x 10 ⁴	.74 x 10 ⁻³		
			10	75.5	7	81.8		7.5	38.0	23.0	.60	.61	2.0 x 10 ⁴	.35 x 10 ⁻³		
			3	88.0	2	94.0	30.5	8.7	39.2	21.8	.55	.63	1.1 x 10 ⁴	.18 x 10 ⁻³		
↓	70F	.63	1	100									Σ	5.65 x 10 ⁻³		
GAG	70F	-		.63	100	-	-	-	34.5	0	0	.56	2.2 x 10 ³	45.5 x 10 ⁻³		
				(Az)												

In addition, the frame stress resulting from the combination of tank ullage pressure and the mean normal load at orbiter attach is treated as an effective GAG cycle, with the stress building from zero to the maximum value once per mission.

The total fatigue damage indicated in Table 6-9 is moderate, with a corresponding predicted safe life of 480 missions. This indicates that no fatigue problems should be expected for this type of structural element on the shuttle vehicle if normal good design practices are followed. It should be noted that the major share of fatigue damage (approximately 90 percent) is due to the effective GAG cycle of stress due to tank pressure and mean normal load at the orbiter attachment. The remainder of the damage is primarily due to alternating lateral loads at the orbiter attachment.

6.7 FATIGUE ANALYSIS - LOX TANK AFT BULKHEAD

6.7.1 Structural Configuration and Loading

The LOX tank aft bulkhead is a membrane dome of ellipsoidal contour having an aspect ratio of $\sqrt{2}$. The dome is a welded assembly employing formed gore sections of 2219-T87 aluminum alloy. The gore skin thickness is tapered from the maximum value at the apex of the dome to maintain approximately constant stresses in the meridian direction over the bulkhead surface. Weld lands are assumed to be twice the thickness of the basic skin. The basic skin in the region of the bulkhead apex is selected as the element for fatigue life analysis.

The maximum limit pressure of 0.30 MN/in^2 (43.5 psig) at the apex of the bulkhead occurs 100 sec. after liftoff with longitudinal load factor of 2.05 g. This limit design pressure assumes a pressure regulator malfunction, so that tank ullage pressure is at the top of the relief valve range. The total pressure for this flight condition with nominal tank ullage pressure is 0.286 MN/in^2 (41.5 psig).

Total pressure at the apex of the bulkhead during prelaunch (tank fully fueled) is 0.183 MN/in^2 (26.5 psig).

6.7.2 Damage Analysis

The primary fatigue load spectrum on the bulkhead is essentially a GAG cycle with the pressure increasing from zero at prelaunch, prior to fueling, to a maximum value during boost once per mission. However, the influence of engine thrust oscillations and corresponding inertia head pressures; ground checkout fueling and pressurizations; and pressure regulator malfunctions also will be evaluated. Two basic bulkhead configurations will be considered, one based on ultimate strength design requirements and the other based on the proof factor established by GDC during the Phase B study.

Ultimate Strength Design

Skin thickness at bulkhead apex is assumed to be sized so that applied stress under ultimate design pressure loading is equal to the uniaxial

ultimate tensile strength of the material. Then fatigue stress spectrum may be obtained as:

Boost:

$$\frac{\sigma_{\max}}{F_{tu}} = \left(\frac{1}{1.4}\right)\left(\frac{P_{\text{nom}}}{P_{\text{lim}}}\right) = \left(\frac{1}{1.4}\right)\left(\frac{41.5}{43.5}\right) = 0.68$$

$$\sigma_{\min} = 0$$

$$R = 0$$

$$N = 550 \text{ cycles (Fig. 5-1, } K_T = 4.4)$$

$$\Delta D = \frac{100}{550} = 0.182$$

Ground checkout:

Assume three ground fueling and pressurization cycles per operational mission

$$\frac{\sigma_{\max}}{F_{tu}} = \left(\frac{1}{1.4}\right)\left(\frac{26.5}{43.5}\right) = 0.435$$

$$\sigma_{\min} = 0$$

$$R = 0$$

$$N = 7600 \text{ cycles (Fig. 5-1)}$$

$$\Delta D = \frac{300}{7600} = 0.040$$

Thrust Excursion:

The maximum thrust excursion indicated in Fig. 3-15 is ± 3.2 percent of steady state value. At the time of maximum pressure on bulkhead the LOX head is approximately 7.65 m (300 in.) and the corresponding inertia head pressure is 0.175 MN/in^2 (25.3 psig). The oscillating pressure is then:

$$\Delta p = \pm .032(25.3) = \pm 0.81 \text{ psi}$$

$$p_{\max} = 41.5 + 0.81 = 42.31 \text{ psi}$$

$$p_{\min} = 41.5 - 0.81 = 40.69 \text{ psi}$$

$$R = \frac{40.69}{42.31} = 0.96$$

SPACE DIVISION NORTH AMERICAN ROCKWELL CORPORATION										11	12	13	14	15
2	3	4	5	6	7	8	9	10	11	12	13	14	15	
T _{MAX} (DEG F)	M _{MEAN} (% DESIGN)	N _e	N	C _{MAX} (KSI)	C _{MIN} (KSI)	R	C _{MAX} F ₂₀	N (K.S.I.)	N					
130 F	10	100,000	70,000	6.3	0.7	.11	.10	∞	0					
		30,000	20,000	7.7	-0.7	-.09	.13	↑	↑					
		10,000	7,000	9.0	-2.0	-.22	.15	↑	↑					
		3,000	2,000	10.5	-3.5	-.33	.18	∞	0					
		1,000	700	12.2	-5.2	-.43	.21	1.8X10 ⁶	.39X10 ³					
		500	200	14.9	-7.9	-.53	.25	8.0X10 ⁴	2.5X10 ³					
		100	100	17.5	-10.5	-.60	.30	2.0X10 ⁴	3.5X10 ³					
		50	20	20.1	-13.1	-.65	.34	1.1X10 ⁴	1.82X10 ³					
		10	7	22.8	-15.8	-.69	.39	4.8X10 ³	1.21X10 ³					
		3	2	25.4	-18.4	-.72	.43	3.5X10 ³	.57X10 ³					
130 F	10	1							Σ .010					
130 F	15	100,000	70,000	8.9	1.6	.176	.15	∞	0					
		30,000	20,000	10.6	-.09	-.008	.18	∞	0					
		10,000	7,000	12.3	-1.9	-.15	.21	∞	0					
		3,000	2,000	14.5	-4.0	-.28	.24	1.5X10 ⁶	.13X10 ²					
		1,000	700	17.6	-7.1	-.40	.30	3.5X10 ⁴	2.0X10 ²					
		300	200	21.1	-10.6	-.50	.36	9.4X10 ³	2.13X10 ²					
		100	70	24.5	-14.0	-.57	.42	4.2X10 ³	1.67X10 ²					
		30	20	27.9	-17.4	-.62	.47	2.3X10 ³	.87X10 ²					
		10	7	31.3	-20.8	-.66	.53	1.0X10 ³	.7X10 ²					
		3	2	34.7	-24.2	-.70	.59	4.0X10 ²	.5X10 ²					
130 F	15	1							Σ .08					

ultimate tensile strength of the material. Then fatigue stress spectrum may be obtained as:

Boost:

$$\frac{\sigma_{\max}}{F_{tu}} = \left(\frac{1}{1.4}\right) \left(\frac{P_{\text{nom}}}{P_{\text{lim}}}\right) = \left(\frac{1}{1.4}\right) \left(\frac{41.5}{43.5}\right) = 0.68$$

$$\sigma_{\min} = 0$$

$$R = 0$$

$$N = 550 \text{ cycles (Fig. 5-1, } K_T = 4.4)$$

$$\Delta D = \frac{100}{550} = 0.182$$

Ground checkout:

Assume three ground fueling and pressurization cycles per operational mission

$$\frac{\sigma_{\max}}{F_{tu}} = \left(\frac{1}{1.4}\right) \left(\frac{26.5}{43.5}\right) = 0.435$$

$$\sigma_{\min} = 0$$

$$R = 0$$

$$N = 7600 \text{ cycles (Fig. 5-1)}$$

$$\Delta D = \frac{300}{7600} = 0.040$$

Thrust Excursion:

The maximum thrust excursion indicated in Fig. 3-15 is ± 3.2 percent of steady state value. At the time of maximum pressure on bulkhead the LOX head is approximately 7.65 m (300 in.) and the corresponding inertia head pressure is 0.175 MN/in^2 (25.3 psig). The oscillating pressure is then:

$$\Delta p = \pm .032(25.3) = \pm 0.81 \text{ psi}$$

$$p_{\max} = 41.5 + 0.81 = 42.31 \text{ psi}$$

$$p_{\min} = 41.5 - 0.81 = 40.69 \text{ psi}$$

$$R = \frac{40.69}{42.31} = 0.96$$

$$\frac{\sigma_{\max}}{F_{tu}} = 0.69$$

$$N \approx 10^6 \text{ cycles}$$

Assuming 100 occurrences per flight of this magnitude transient, which is very conservative:

$$\Delta D \approx \frac{100 (100)}{10^6} \approx .010$$

Total damage is then:

$$D = 0.182 + 0.040 + 0.010 = 0.232$$

and corresponding safe life is:

$$L_s = \frac{100}{4(.232)} = 108 \text{ missions}$$

If a pressure regulator malfunction is assumed to occur on 10 percent of the flights, which is probably highly conservative, the fatigue damage due to boost pressure cycles becomes:

Nominal Pressure: (90 percent of flights)

$$\Delta D = \frac{90}{550} = 0.163$$

Limit Pressure: (10 percent of flights)

$$\frac{\sigma_{\max}}{F_{tu}} = \frac{1}{1.4} = 0.715$$

$$\sigma_{\min} = 0$$

$$R = 0$$

$$N = 350 \text{ cycles}$$

$$\Delta D_2 = \frac{10}{350} = 0.029$$

$$\Delta D = 0.163 + 0.029 = 0.192$$

$$D = 0.192 + 0.040 + 0.010 = 0.242$$

$$L_s = \frac{100}{4(.242)} = 103 \text{ missions}$$

Proof Test Design

A proof factor for the lower LOX tank of 1.23 was determined by GDC during the Phase B Study; this was based on the assumption that the proof test would be performed with liquid nitrogen and was derived by application of plane-strain fracture mechanics theory and test data. This value may not agree with proof factors that will be subsequently determined in this study using empirical data from current fracture mechanics test programs; however, it will be used for the present to illustrate the potential effect of proof test requirements on fatigue life. This proof factor required an increase in bulkhead skin thickness in the apex region from 0.292 cm (0.115 in.) to 0.318 cm (0.125 in.) to avoid exceeding material yield stress under proof test conditions. Therefore, the stress spectra for this configuration is determined by applying the inverse ratio of the appropriate skin thicknesses to the preceding values.

Boost:

$$\frac{\sigma_{\max}}{F_{tu}} = \frac{0.115}{0.125} (0.68) = 0.92 (0.68) = 0.625$$

$$\sigma_{\min} = 0$$

$$R = 0$$

$$N = 1050 \text{ cycles (Fig. 5-1)}$$

$$\Delta D = \frac{100}{1050} = 0.0955$$

Ground checkout:

$$\frac{\sigma_{\max}}{F_{tu}} = 0.92 (0.435) = 0.400$$

$$\sigma_{\min} = 0$$

$$R = 0$$

$$N = 10,100 \text{ (Fig. 5-1)}$$

$$\Delta D = \frac{300}{10,100} = 0.0297$$

Thrust Excursion:

$$\Delta D = 0.010$$

Total Damage:

$$D = 0.0955 + 0.0297 + 0.010 = 0.135$$

$$L_s = \frac{100}{4(.135)} = 185 \text{ missions}$$

Discussion of Results

The S-N curves used in this analysis, based on $K_T = 4.4$, are probably conservative for the type of structure and weld joint details of the bulkhead, particularly in the high stress-low cycle range of interest. However, the very marginal safe fatigue life indicated by these analyses shows that close attention to detail design and adequate fatigue life development and qualification tests will be of vital importance to assure satisfactory fatigue performance of the reusable propellant tanks for space shuttle. It also can be seen that fatigue damage due to ground checkout tanking and pressurization and due to thrust excursions is relatively minor. Reductions in operating stress due to proof test requirements may provide significant improvement in fatigue life.

6.8 FATIGUE ANALYSIS - CREW COMPARTMENT

6.8.1 Structural Configuration and Loading

The structural configuration of the crew compartment was not defined to the depth of detail in the Phase B Study as for other structural elements presently considered; therefore, it is necessary to make several assumptions. The mid-portion of the crew compartment is idealized as a pressurized, semi-monocoque cylindrical shell of 3.05 m (120 in.) diameter, constructed of 2219-T87 aluminum alloy. Minimum skin thickness is assumed to be 0.076 cm (0.030 in.). The crew compartment is mounted from the nose TPS shell structure and does not experience primary body loads. The major loading source is due to compartment internal pressure with a maximum value of 0.103 MN/m^2 (15 psia).

$$\sigma = \frac{pR}{t} = \frac{(15.0)(60)}{0.030} = 30,000 \text{ psi}$$

$$(206 \text{ MN/m}^2)$$

6.8.2 Damage Analysis

The stress spectrum for operational missions is a simple 6A6 cycle from zero to maximum pressure differential once per mission.

$$\frac{\sigma_{\max}}{F_{tu}} = \frac{30}{62} = 0.48$$

$$\sigma_{\min} = 0$$

$$R = 0$$

$$N = 5,000 \text{ cycles (Fig. 5-1, } K_T = 4.4)$$

$$\Delta D = \frac{100}{5000} = 0.020$$

It is also necessary to consider the fatigue damage that may be incurred during ferry missions. It is conservatively assumed that one complete transcontinental ferry mission is performed for each operational mission, as a worst case situation. The typical transcontinental route involves 10 flight segments; an ascent from sea level to maximum cruise altitude of 6.1 km (20,000 ft) is assumed for each segment. Ambient pressure at that altitude is .046 MN/m² (6.7 psia) so the maximum pressure differential is:

$$\Delta p = 15.0 - 6.7 = 8.3 \text{ psi}$$

$$\sigma_{\text{max}} = \frac{8.3(60)}{.030} = 16,600 \text{ psi}$$

$$\frac{\sigma_{\text{max}}}{F_{\text{tu}}} = \frac{16.6}{62.0} = 0.27$$

$$\sigma_{\text{min}} = 0$$

$$R = 0$$

$$N = 60,000 \text{ cycles (Fig. 5-1)}$$

$$\Delta D = \frac{10(100)}{60,000} = 0.017$$

Total damage:

$$D = 0.020 + 0.017 = 0.037$$

$$L_s = \frac{100}{4(.037)} = 675 \text{ missions}$$

These results indicate that no fatigue problems should be expected for the crew compartment, even with very extensive ferry mission utilization.

6.9 FATIGUE ANALYSIS - WING - ALTERNATE MATERIAL

6.9.1 Structural Configuration and Loading

The use of 2219-T87 aluminum alloy for wing spar caps will be evaluated from fatigue and fracture mechanics considerations to determine relative merits compared to the primary selection of 6Al-4V titanium alloy. The general configuration and shape of the aluminum spar caps is assumed to be similar to the titanium members, however the section dimensions and thickness are increased to provide additional area consistent with the reduced allowable stresses for the aluminum material. The basic loading spectra are the same as employed for fatigue analysis of the titanium structure. The stress levels for individual load cycles are reduced in proportion to the limit operating stresses of aluminum versus titanium material. A maximum structural temperature of 370 K (200 F) is assumed for the aluminum spar caps during entry and subsequent cruise flight. A corresponding limit operating stress of 275 MN/m² (40 ksi) is approximated for the max qa design condition.

6.9.2 Damage Analysis

Detailed calculations of fatigue damage for the reference limit stress of 275 MN/m² (40 ksi) are presented in Table 6-10. Damage analysis is based on S-N curves with a theoretical stress concentration factor of 3.0 to be consistent with the final approach selected for the basic wing configuration with titanium alloy. A total damage factor of 0.66 is calculated; this corresponds to a safe-life of 38 missions with a scatter factor of 4.0 included. This is not satisfactory, so the limit operating stress must be reduced to achieve adequate fatigue life--a limit stress of approximately 240 MN/m² (35 ksi) was determined by iteration. Fatigue damage analysis for this reduced limit stress is summarized in Table 6-11. A total damage factor of 0.238 is calculated for this case; this corresponds to a safe-life of 105 missions. A comparison of structural weight between aluminum and titanium material for the wing spar caps is performed in a subsequent section of this report dealing with safe-life analyses assuming an initial crack-like flaw to be present in the structure.

Prepared By: JPS
 Checked By:
 Date: 4-12-72

SPACE DIVISION
 NORTH AMERICAN ROCKWELL CORPORATION

1	2	3	4	5	6	7	8	9	10	11	12	13	14	15
MISSION PHASE	T _{MAX} (DEG F)	M _{MEAN} (% DESIGN)	n _e	M _{ALT} (% DESIGN)	n	M _{ALT} (% DESIGN)	σ _{MEAN} (KSI)	σ _{ALT} (KSI)	σ _{MAX} (KSI)	σ _{MIN} (KSI)	R	σ _{MAX} / F _{TU}	N (K _T =3.0)	n / N
ASCENT	130 F	10	100,000	6.0	70,000	8.1	4.0	3.2	7.2	0.8	.11	.12	∞	0
	↑	↑	30,000	10.2	20,000	12.0	↑	4.8	8.8	-0.8	-.09	.15	∞	0
			10,000	13.8	7,000	15.8		6.3	10.3	-2.3	-.22	.17	∞	0
			3,000	17.8	2,000	20.0		8.0	12.0	-4.0	-.33	.20	10 ⁷	2 X 10 ⁻³
			1,000	22.2	700	25.6		10.0	14.0	-6.0	-.43	.24	2.5 X 10 ⁵	2.8 X 10 ⁻³
			300	29.0	200	32.5		13.0	17.0	-9.0	-.53	.29	2.5 X 10 ⁴	8.0 X 10 ⁻³
			100	36.0	70	39.9		16.0	20.0	-12.0	-.60	.34	1.1 X 10 ⁴	6.4 X 10 ⁻³
			30	43.8	20	49.4	↓	19.0	23.0	-15.0	-.65	.39	6.0 X 10 ³	3.3 X 10 ⁻³
			10	51.0	7	55.0		22.0	26.0	-18.0	-.69	.44	3.2 X 10 ³	2.2 X 10 ⁻³
			3	59.0	2	62.5	4.0	25.0	29.0	-21.0	-.72	.49	1.6 X 10 ³	1.2 X 10 ⁻³
	130 F	10	1	66.0									Σ	.0241
	130 F	15	100,000	8.0	70,000	10.5	6.0	4.2	10.2	1.8	.176	.17	∞	0
	↑	↑	30,000	13.0	20,000	15.2	↑	6.1	12.1	-0.1	-.008	.20	∞	0
			10,000	17.5	3,000	20.2		8.1	14.1	-2.1	-.15	.24	10 ⁷	.07 X 10 ⁻²
			3,000	23.0	2,000	26.5		10.6	16.6	-4.6	-.28	.28	10 ⁵	2.0 X 10 ⁻²
			1,000	30.0	700	35.2		14.1	20.1	-8.1	-.40	.34	1.5 X 10 ⁴	4.7 X 10 ⁻²
			300	40.5	200	45.2		18.1	24.1	-12.1	-.50	.41	5.0 X 10 ³	4.0 X 10 ⁻²
			100	49.8	70	54.9		22.0	28.0	-16.0	-.57	.48	2.1 X 10 ³	3.3 X 10 ⁻²
			30	60.0	20	64.8	↓	25.9	31.9	-19.9	-.62	.54	9.0 X 10 ²	2.2 X 10 ⁻²
			10	69.5	7	74.5		29.8	35.8	-23.8	-.66	.61	3.0 X 10 ²	2.3 X 10 ⁻²
			3	79.5	2	84.3	6.0	33.7	39.7	-27.7	-.70	.67	10 ²	2.0 X 10 ⁻²
ASCENT	130 F	15	1	89.0									Σ	.2057

TABLE 6-10 WING FATIGUE DAMAGE - ALUMINUM SPAR CAPS (KT = 3.0, $\sigma_{lim} = 40 \text{ KSI}$) (SHEET 2)														
SPACE DIVISION NORTH AMERICAN ROCKWELL CORPORATION														
Prepared By: JPS														
Page No. 6-50 of Report No. SD 72-54-0046														
Checked By:														
Date: 4-8-62 Model No. B-1U														
1	2	3	4	5	6	7	8	9	10	11	12	13	14	15
MISSION PHASE	T_{MAX} (DEG F)	M_{MEAN} (% DESIGN)	n_e	M_{ALT} (% DESIGN)	n	M_{ALT} (% DESIGN)	σ_{MEAN} (KSI)	σ_{ALT} (KSI)	σ_{MAX} (KSI)	σ_{MIN} (KSI)	R	$\frac{\sigma_{MAX}}{F_{T0}}$	N	$\frac{n}{N}$
ASCENT	130 F	40	100,000	5.5	70,000	7.0	16.0	2.8	18.8	13.2	0.70	32	∞	0
			30,000	8.5	20,000	9.8		3.9	19.9	12.1	0.51	34	∞	0
			10,000	11.0	7,000	12.8		5.1	21.1	10.9	0.52	36	10^7	$.01 \times 10^{-2}$
			3,000	14.5	2,000	15.8		6.3	22.3	9.7	0.44	38	1.1×10^5	1.82×10^{-2}
			1,000	17.0	700	18.8		7.5	23.5	8.5	0.36	40	6.0×10^4	1.17×10^{-2}
			300	20.5	200	21.8		8.7	24.7	7.3	0.30	42	7.3×10^4	4.6×10^{-2}
			100	23.0	70	24.8		9.9	25.9	6.1	0.24	44	2.5×10^4	2.8×10^{-2}
			30	26.5	20	27.8		11.1	27.1	4.9	0.18	46	1.5×10^4	$.13 \times 10^{-2}$
			10	29.0	7	30.8		12.3	28.3	3.7	0.13	48	1.0×10^4	$.07 \times 10^{-2}$
			3	32.5	2	33.8		13.5	29.5	2.5	0.08	50	5.0×10^3	$.04 \times 10^{-2}$
ASCENT	130 F	40	1	35.0										
													Σ	0.404
ENTRY	200 F		100,000	9.5	70,000	12.8	0	5.1	5.1	0	0	.09	∞	0
			30,000	15.0	20,000	17.2		6.9	6.9			12		
			10,000	19.5	7,000	22.8		9.1	7.1			16		
			3,000	26.0	2,000	30.0		12.0	12.0			21	∞	0
			1,000	34.0	700	41.2		16.5	16.5			30	3.0×10^5	.002
			300	48.5	200	71.8		28.8	28.8			51	4.5×10^3	.044
ENTRY	200 F		100	95.0	100	95.0	0	38.0	38.0	0	0	68	7.0×10^2	.143
													Σ	.189

TABLE 6-10 WING FATIGUE DAMAGE - ALUMINUM SPAR CAPS
 (KT = 3.0, $\sigma_{LIM} = 40$ KSI) (SHEET 3)

SPACE DIVISION
 NORTH AMERICAN ROCKWELL CORPORATION

Prepared By: JPS
 Checked By:
 Date: 4-13-72
 Page No. 6-51 of
 Report No. SD72-SH-0046
 Model No. B-9-U

1 MISSION PHASE	2 T_{MAX} (DEG F)	3 M_{MEAN} (% DESIGN)	4 n_e	5 MALT (% DESIGN)	6 n	7 \bar{M}_{ALT} (% DESIGN)	8 σ_{MEAN} (KSI)	9 σ_{ALT} (KSI)	10 σ_{TMAX} (KSI)	11 σ_{TMIN} (KSI)	12 R	13 $\frac{\sigma_{TMAX}}{F_{TU}}$	14 N ($K_T = 3.0$)	15 $\frac{n}{N}$
CRUISE /	200 F	35	100,000	1.5	70,000	4.0	14.0	1.6	15.6	12.4	.80	.28	∞	0
LNDG			30,000	6.5	20,000	8.8	↑	3.5	17.5	10.5	.60	.31	∞	0
			10,000	11.0	7,000	13.8		5.5	19.5	8.5	.44	.35	1.0×10^6	$.7 \times 10^{-2}$
			3,000	16.5	2,000	18.8		7.5	21.5	6.5	.30	.38	7.0×10^4	2.9×10^{-2}
			1,000	21.0	700	23.5		9.4	23.5	4.6	.20	.42	2.5×10^4	2.8×10^{-2}
			300	26.0	200	28.5		11.4	25.4	2.6	.10	.45	1.3×10^4	1.5×10^{-2}
			100	31.0	70	33.5		13.4	27.4	0.6	.02	.49	6.0×10^3	1.2×10^{-2}
			30	36.0	20	38.2		15.3	29.3	-1.3	-.04	.52	4.0×10^3	$.5 \times 10^{-2}$
			10	40.5	7	41.8		16.8	30.8	-2.8	-.09	.55	2.5×10^3	$.3 \times 10^{-2}$
			3	43.0	2	44.5	14.0	17.8	31.8	-3.8	-.12	.57	1.9×10^3	$.1 \times 10^{-2}$
CRUISE /	200 F	35	1	46.0										
LNDG													$2 \times \Sigma$.20
TOTAL														$D = 0.66$

SPACE DIVISION NORTH AMERICAN ROCKWELL CORPORATION										Prepared By: JPS		Page No. 6-52 of		
										Checked By:		Report No. SD 72-54-0046		
										Date: 4-14-72		Model No. B-7U		
1 MISSION PHASE	2 T _{MAX} (DEG F)	3 M _{MEAN} (% DESIGN)	4 N _e	5 N	6 σ _{TMAX} (KSI)	7 σ _{TMIN} (KSI)	8 R	9 σ _{TMAX} F ₂₁	10 N (A. S. S.)	11 N N	12	13	14	15
ASCENT	130 F	10	100,000	70,000	6.3	0.7	.11	.10	∞	0				
			30,000	20,000	7.7	-0.7	-.09	.13	↑	↑				
			10,000	7,000	9.0	-2.0	-.22	.15	↑	↑				
			3,000	2,000	10.5	-3.5	-.33	.18	∞	0				
			1,000	700	12.2	-5.2	-.43	.21	1.8X10 ⁶	.37X10 ³				
			500	200	14.9	-9.9	-.53	.25	8.0X10 ⁴	2.5X10 ³				
			100	100	17.5	-10.5	-.60	.30	2.0X10 ⁴	3.5X10 ⁻³				
			50	20	20.1	-13.1	-.65	.34	1.1X10 ⁴	1.82X10 ³				
			10	7	22.8	-15.8	-.69	.39	4.8X10 ³	1.21X10 ³				
			3	2	25.4	-18.4	-.72	.43	3.5X10 ³	.57X10 ³				
	130 F	10	1							Σ .010				
	130 F	15	100,000	70,000	8.9	1.6	.176	.15	∞	0				
			30,000	20,000	10.6	-.09	-.008	.18	∞	0				
			10,000	7,000	12.3	-1.9	-.15	.21	∞	0				
			3,000	2,000	14.5	-4.0	-.28	.24	1.5X10 ⁶	1.3X10 ²				
			1,000	700	17.6	-7.1	-.40	.30	3.5X10 ⁴	2.0X10 ²				
			300	200	21.1	-10.6	-.50	.36	9.4X10 ³	2.13X10 ²				
			100	70	24.5	-14.0	-.57	.42	4.2X10 ³	1.67X10 ²				
			30	20	27.9	-17.4	-.62	.47	2.3X10 ³	.87X10 ²				
			10	7	31.3	-20.8	-.66	.53	1.0X10 ³	.7X10 ²				
			3	2	34.7	-24.2	-.70	.59	4.0X10 ²	.5X10 ²				
ASCENT	130 F	15	1							Σ .08				

SPACE DIVISION NORTH AMERICAN ROCKWELL CORPORATION										13	14	15		
1	2	3	4	5	6	7	8	9	10	11	12	13	14	15
MISSION PHASE	T _{MAX} (DEG F)	M _{MEAN} (% DESIGN)	N _e	N	σ _{MAX} (KSI)	σ _{MIN} (KSI)	R	σ _{MAX} /F _U	N (K _T = 3.0)	N				
ASCENT	130 F	40	100,000	70,000	16.5	11.6	.70	.28	∞	0				
			30,000	20,000	17.4	10.6	.61	.30						
			10,000	7,000	18.5	9.5	.52	.32						
			3,000	2,000	19.5	8.5	.44	.33	∞	0				
			1,000	700	20.6	7.4	.36	.35	2.5X10 ⁵	2.8X10 ³				
			300	200	21.6	6.4	.30	.37	8.0X10 ⁴	2.5X10 ³				
			100	70	22.7	5.3	.24	.38	5.0X10 ⁴	1.4X10 ³				
			30	20	23.7	4.3	.18	.40	3.0X10 ⁴	.67X10 ³				
			10	7	24.8	3.2	.13	.42	2.0X10 ⁴	.35X10 ³				
			3	2	25.8	2.2	.08	.44	1.3X10 ⁴	.15X10 ³				
ASCENT	130 F	40	1											
										Σ	.0079			
ENTRY	200 F		100,000	70,000	4.5	0	0	.08	∞	0				
			30,000	20,000	6.0			.10						
			10,000	7,000	8.0			.14						
			3,000	2,000	10.5			.18						
			1,000	700	14.5			.26	∞	0				
			300	200	25.2			.45	8.6X10 ³	2.3X10 ²				
			100	100	33.2			.60	1.9X10 ³	5.3X10 ²				
ENTRY	200 F													
										Σ	.076			

Prepared By: JPS
 Checked By:
 Date: 4-17-72

SPACE DIVISION
 NORTH AMERICAN ROCKWELL CORPORATION

TABLE 6-11 WING FATIGUE DAMAGE -
 ALUMINUM SPAR CAPS (SHEET 3)
 (KT = 3.0) (VLM = 35 KSI)

1	2	3	4	5	6	7	8	9	10	11	12	13	14	15
MISSION PHASE	T _{MAX} (DEG F)	M _{MEAN} (% DESIGN)	n _e	n	σ _{MAX} (KSI)	σ _{MIN} (KSI)	R	$\frac{\sigma_{MAX}}{F_{TU}}$	N (K _T = 3.0)	$\frac{D}{N}$				
CRUISE/	200 F	35	100,000	70,000	13.6	10.9	.80	.24	∞	0				
LNDG	↑	↑	30,000	20,000	15.3	9.2	.60	.27	∞	0				
			10,000	7,000	17.1	7.4	.44	.30	∞	0				
			3,000	2,000	18.8	5.7	.30	.33	1.0 X 10 ⁶	2 X 10 ⁻²				
			1,000	700	20.6	4.0	.20	.37	6.0 X 10 ⁴	1.2 X 10 ⁻²				
			300	200	22.2	2.3	.10	.39	2.5 X 10 ⁴	8 X 10 ⁻²				
			100	70	24.0	0.5	.02	.43	1.2 X 10 ⁴	6 X 10 ⁻²				
			30	20	25.6	-1.1	-.04	.45	8.0 X 10 ³	2.5 X 10 ⁻²				
			10	7	27.0	-2.4	-.09	.48	5.4 X 10 ³	1.3 X 10 ⁻²				
			3	2	27.8	-3.3	-.12	.50	4.0 X 10 ³	.05 X 10 ⁻²				
CRUISE/	200 F	35	1											
LNDG									2 X 10 ⁶	.0646				
TOTAL									D =	.238				

7.0 SAFE-LIFE ANALYSIS

Summarized in this section are analyses that investigate the characteristics of crack growth in the selected structural elements to the point where critical dimensions are reached. In contrast to the preceding fatigue life analyses, in which an originally sound structure is assumed and the amount of service exposure to initiate a fatigue crack is determined, the safe-life analyses of this section assume a pre-existing flaw in the structure prior to the start of operational service. The crack growth under the applicable repeated load spectra is evaluated, and the safe-life in terms of number of missions is determined as the interval until the initial defect grows to a size that could cause failure under limit design conditions. The size of initial defect is arbitrarily selected; usually with regard to nondestructive evaluation (NDE) capabilities appropriate for the type of defect, material, and structural configuration. In some cases, the initial defect size is taken so that a parametric investigation of missions to failure (critical size) versus initial flaw size may be performed. The resulting influence of various initial defect sizes and various safe-life safety factors on the weight of a structure designed to achieve a safe-life of 100 missions is evaluated for appropriate structural elements.

7.1 ANALYSIS METHODS

7.1.1 Stress Intensity and Critical Flaw Size

Fracture mechanics theory uses the basic parameter of stress intensity as the key index to determine crack instability and crack growth behaviour. Stress intensity is a function of both the applied general stress level and the size, character, and location of the crack or crack-like defect. Stress intensity solutions and design curves are summarized in Reference 23 for a large number of practical cases. For convenience, the stress intensity equations for elementary cases considered in this study are summarized in Fig. 7-1.

The critical crack size that will cause abrupt instability under a prescribed stress level on the general section, or the critical stress for a given crack size, can be determined from the stress intensity equations by setting the applied stress intensity equal to the critical value. This critical value is customarily taken as the plane-strain fracture toughness (K_{Ic}) if the structural member in question is relatively thick. Higher values for critical stress intensity, approaching the plane-stress fracture toughness (K_{Ic}), may be justified for thin members. A discussion of fracture toughness trends, and values recommended for use in this study, is given in Section 5. Where empirical data are available from current in-house testing on fracture of 2219 aluminum alloy containing through or part-through cracks, these data are used directly to establish critical flaw sizes or critical stress levels.

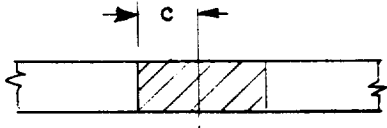
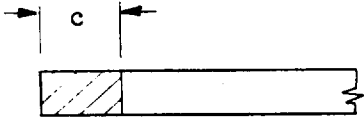
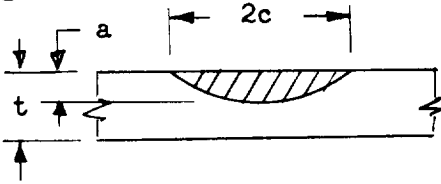
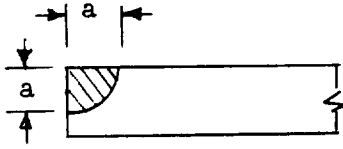
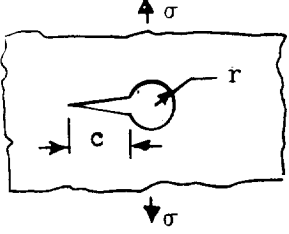
Crack Type	Stress Intensity
<p>Through Crack</p> 	$K_I = \sigma \sqrt{\pi c} \lambda$
<p>Edge Crack</p> 	$K_I = 1.12 \sigma \sqrt{\pi c} \lambda$
<p>Part-Through Crack</p> 	$K_{I_{\max}} = 1.1 M_K \sigma \sqrt{\pi(a/Q)}$ $Q = f(a/2c, \sigma/\sigma_y)$ <p>(See Figure 1, Reference 24)</p> $M_K = f(a/2c, a/t)$ <p>(See Figure 5-12)</p>
<p>Corner Crack</p> 	$K_{I_{\max}} = 0.705 \sigma \sqrt{\pi a}$
<p>Crack from Fastener Hole</p> 	$K_I = \sigma \sqrt{\pi c} f\left(\frac{c}{r}\right)$ <p>[See Reference 23, page 44 for $f(c/r)$]</p>
<p>λ = Finite width correction factor; significant if crack length > 0.2 plate width. (See Reference 23, pages 51-55 for specific values.)</p>	

Figure 7-1. Elementary Stress Intensity Solutions

In the application of the theoretical stress intensity equations to practical structures, it is generally necessary to make corrections for plasticity effects. In the case of a part-through crack, this plasticity correction is an inherent part of the design curves for the shape factor (Q) given in Figure 1 of Reference 24. For the cases of through cracks of various configurations, plasticity effects are commonly accounted for by adding an increment to the actual crack length equal to the radius of the plastic zone at the tip of the crack. This plastic zone radius can be approximated by the expressions:

$$r_p = \frac{1}{2\pi} \left(\frac{K_I}{\sigma_y} \right)^2 \quad (\text{plane-stress})$$

$$r_p = \frac{1}{6\pi} \left(\frac{K_I}{\sigma_y} \right)^2 \quad (\text{plane-strain})$$

7.1.2 Crack Growth Analysis

Crack growth under random spectra loading is accomplished by use of the EFFGRO computer program. This computer program was developed by NR's Los Angeles Division to expedite fracture mechanics analyses in support of the B-1 design effort. Crack growth analyses are accomplished by systematically increasing crack size in 0.1 percent increments, and finding the number of load cycles, or portion of the spectrum loading, required to grow through that increment. This approach eliminates the iterative procedures required by earlier crack growth analysis programs and greatly increases computing efficiency. Forman coefficients are input data for crack growth rates used to calculate total growth. The program accommodates a dual description of these coefficients so that crack growth rates at low stress intensity ranges may be approximated more accurately. Through crack, part-through crack, corner crack, and crack from fastener hole are configurations accommodated. The program provides the option to include retardation effects if desired; analysis of these effects is based on residual stress intensity theory (Ref. 26). The program continues crack growth analysis until instability is calculated or until a specified number of load blocks are consumed. Spectral load data are input as repeated blocks of the defined discrete load steps. Options to permit randomization of the load steps are being developed. Output data provide crack size, growth rate, and stress intensity for each load step of each block. The points at which transition from a part-through to a through crack and crack instability occur are defined. A sample printout of the computer solution is given in the Appendix.

The same general procedure is employed in manual calculations of crack growth under simple loading spectra, such as propellant tank pressures, where it is desired to introduce empirical descriptions of crack behaviour that are not amenable to the computer program input options.

7.1.3 Retardation Effects

A number of investigators have observed that the application of an overload will significantly reduce the crack growth rate under subsequent load cycles at a lower stress intensity, compared to the basic case of constant amplitude cyclic loading at the same stress intensity. This effect is generally attributed to the influence of a larger plastic zone and more severe local yielding at the crack tip due to the overload. A theory postulated by Elber, Reference 25, considers that the crack will close at a tensile stress greater than zero because of large residual tension strains imposed on the ligaments adjacent to the crack tip by the overload. This effectively reduces the range of stress intensity experienced at the crack tip during subsequent load cycles with corresponding reduction in the crack growth rate.

A somewhat similar theoretical concept has been pursued at NR's Los Angeles division to develop crack growth retardation analysis techniques for B-1 fracture mechanics evaluations (Reference 26). Semi-empirical equations have been derived and incorporated as an analysis option in the EFFGRO computer program. A residual tensile stress intensity is assumed to exist at the crack tip (with no load on the structure) due to the large plastic deformations and residual tensile strains imposed on ligaments adjacent to the crack tip by overloads. The surrounding elastic material attempts to close the crack as loading is removed, but complete crack closure is prevented by the residual tensile strains of these ligaments. The ligaments immediately adjacent to the crack tip are therefore loaded in residual compression and the adjacent material, still within the plastic zone region, is loaded in residual tension. This residual tension serves to reduce the range of stress intensity experienced at the crack tip during cyclic loading. As the crack tip grows through the region of residual compression stress, and begins to sever ligaments that are loaded in residual tension, the magnitude of retardation effects will decay because of decreasing restraint of the deformed material around the crack tip. The semi-empirical equations to predict retardation effects are summarized as follows:

$$K_{RES} = 0.25 K_{max} \left[\frac{a_{ol} + r_{p_{ol}} - a_i}{r_{p_{ol}}} \right]^{\frac{1}{2}} \left[1 + 0.25 \left(\frac{\sigma}{\sigma_y} \right)^3 \right]$$

$$\Delta K_{EFF} = 1.33 (\Delta K - K_{RES})$$

where:

K_{RES} = Residual stress intensity at crack tip subsequent to overload.

K_{MAX} = Applied stress intensity at crack tip due to overload

ΔK = Range of stress intensity, from minimum to maximum value over load cycle

K_{EFF} = Effective range of stress intensity over the load cycle considering the effect of residual stress intensity

a_{ol} = Crack size after application of overload

a_i = Crack size after application of given load cycles subsequent to overload

$r_{p_{ol}}$ = Size of plastic zone at crack tip formed by overload

σ = Applied Stress

σ_y = Yield Stress.

A comparison of predicted crack growth, using the retardation analysis methods described above, and values measured on a B-1 development test is given in Figure 7-2. This test simulated the random spectrum loading imposed on a reference fuselage station. It can be seen that correlation between analysis and test is quite good; predicted crack growth neglecting retardation effects is highly conservative. Somewhat greater deviations between theory and test have been observed in other comparisons of this type; however the analytical prediction of retardation is generally conservative, i.e., it predicts a more rapid growth than actually observed in test.

- TEST NO. 14 CORNER CRACK FROM BOLTHOLE
- 2024-T851 ALUMINUM
- FUSELAGE SPECTRUM
- 10 BLOCKS = 1 A / V LIFE

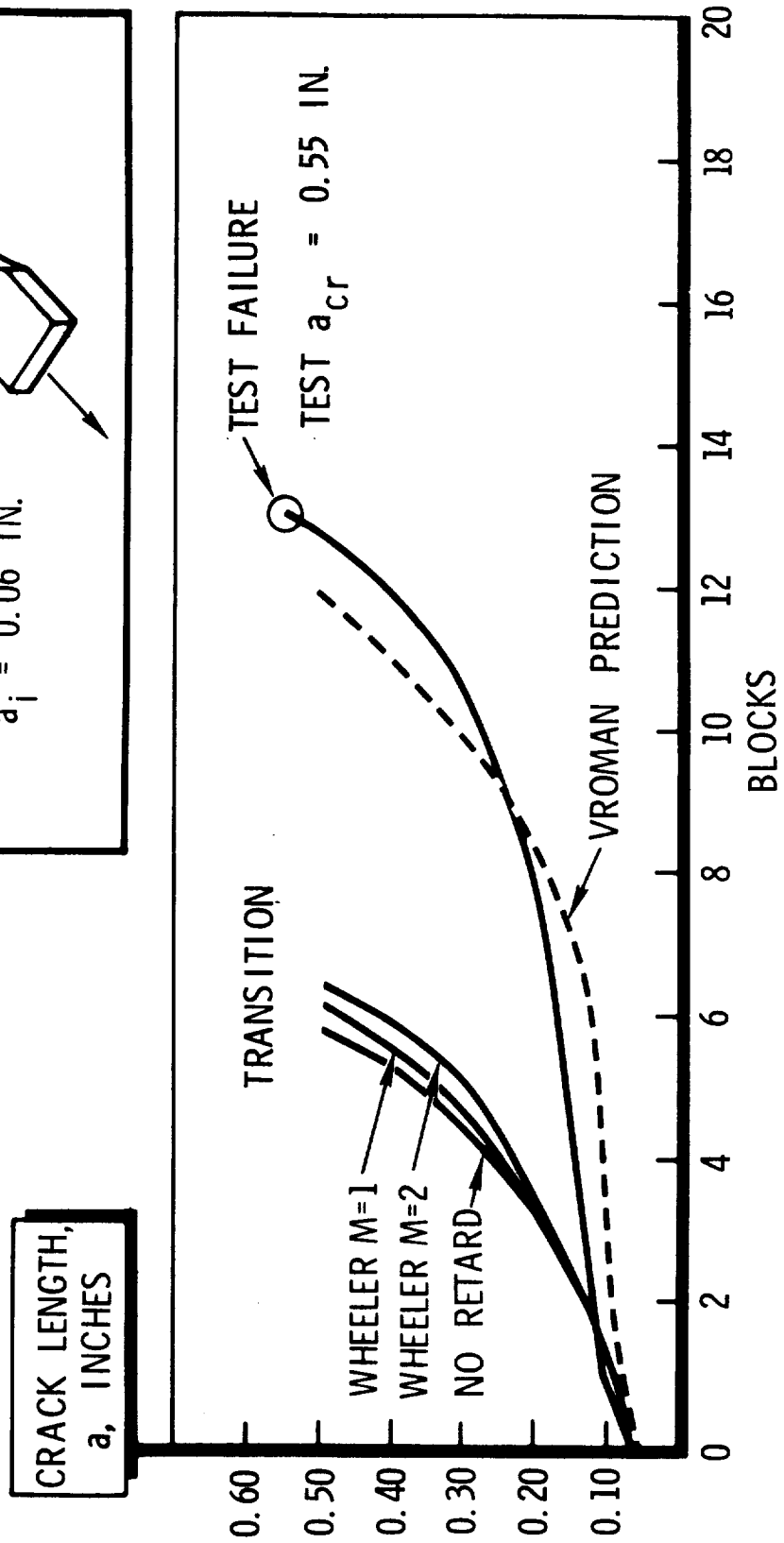
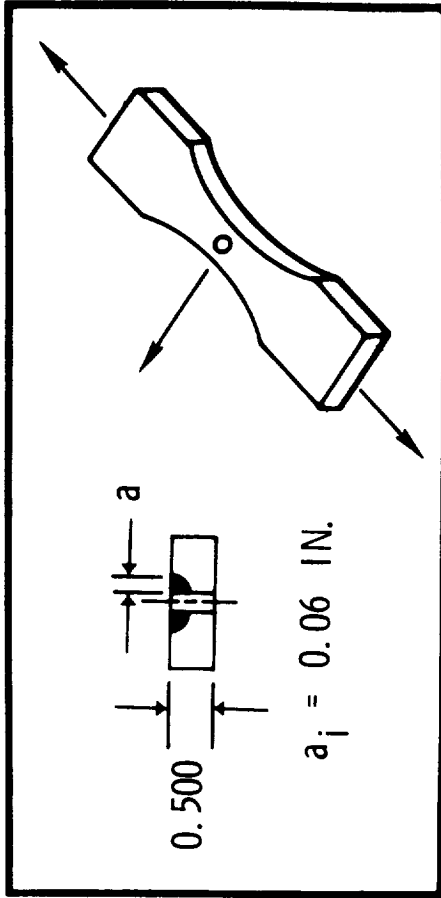


Figure 7-2. Comparison of Predicted vs. Measured Crack Growth - Random Spectra Loading - B-1 Development Tests

7.2 SAFE-LIFE ANALYSIS - WING

7.2.1 Structural Configuration and Loading

The lower spar cap of spar #4 in the root region is selected as the critical wing structural element for crack growth analysis. Sizing of this element at Span Sta. 0 is given as 103 cm^2 (15.8 in.^2) in Reference 22; the corresponding cross-section dimensions also are given in this reference. However, this sizing was based on ultimate strength design requirements with a corresponding limit operating stress of 605 MN/m^2 (88 ksi). Results of the fatigue life analysis for this member indicate that it is necessary to reduce the limit design stress to approximately 450 MN/m^2 (65 ksi) to achieve a satisfactory fatigue life. Therefore, the section area is increased to approximately 123 cm^2 (19 in.^2); this accounts for the desired reduction in stress level and also for a reduction in wing design bending loads from the values used in the sizing analysis presented in Reference 22. The general hat-section shape and proportions defined in this reference have been maintained and the section size increased to provide the desired additional area. A sketch of the resulting cross-section is given in Fig. 7-3. Adjacent structure and the assumed types of initial cracks also are indicated on the sketch.

A simplified stress spectrum for crack growth analysis is derived from the fatigue stress spectra given in Table 6-4 and is summarized in Table 7-1. This spectrum was established by combining cycles with similar maximum and minimum stresses from the various phases of the fatigue spectra to improve computational efficiency of the crack growth analysis. In contrast to the fatigue analysis, a negative value of minimum stress is not meaningful for crack growth analysis because it is assumed that the crack closes under compression loading and the compression is carried by bearing along the crack contact surfaces with no further change in stress intensity at the crack tip. Therefore, a stress of zero is the minimum value considered in the crack growth stress spectrum. The spectrum listed in Table 7-1 is based on a limit design stress of 450 MN/m^2 (65 ksi); smaller values of limit design stress are also considered in the parametric studies of wing spar crack growth, the indicated stress spectrum is reduced by the appropriate ratio of limit design stresses for these analyses.

7.2.2 Crack Growth Analysis

Crack growth for wing spar caps is evaluated in parametric form over a range of limit design stresses from 450 MN/m^2 (65 ksi) to 275 MN/m^2 (40 ksi). Critical flaw sizes, that would cause fracture under limit stress, have been calculated for the types of initial defects considered in this section using the appropriate equations from Fig. 7-1. A plot of these critical sizes is given in Fig. 7-4.

Crack growth analyses have been made for the various types of assumed initial defects using the EFFGRO computer program. The growth is expressed as flaw dimension (depth or length) versus number of missions until critical size is reached. Selection of initial flaw size is arbitrary, but in general

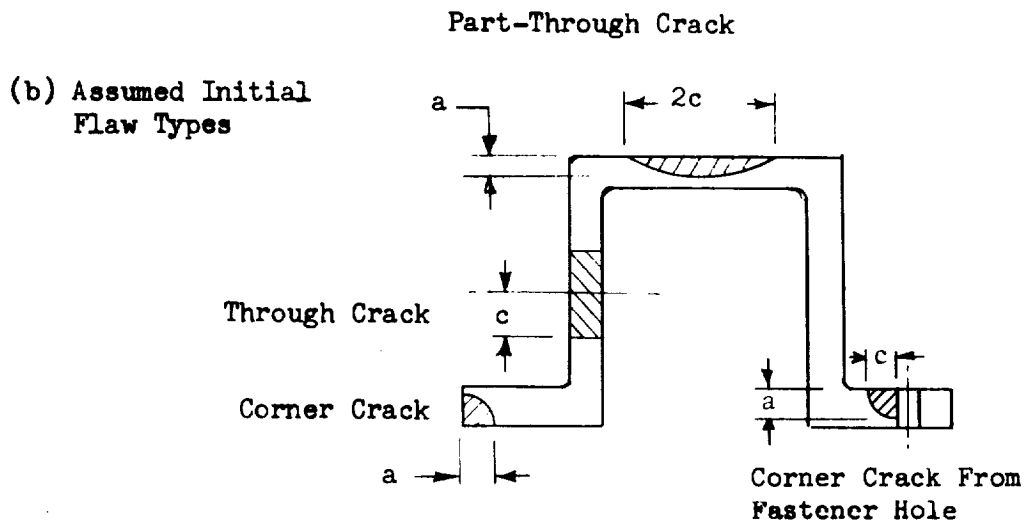
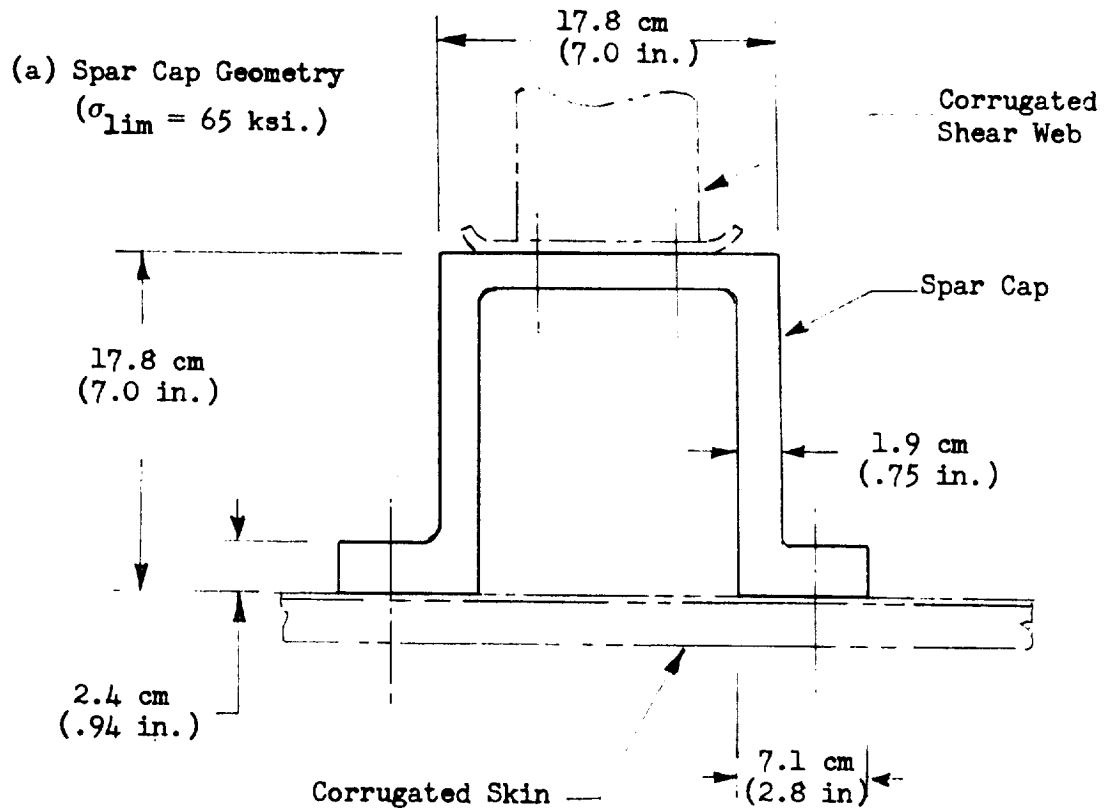


Figure 7-3. Wing Spar Cap Cross Section

Table 7-1. Wing Spar Cap Stress Spectrum

Load Step	Maximum Stress (ksi)	Minimum Stress (ksi)	Number of Cycles
1	13.6	0	9000.0
2	18.8	0	9900.0
3	25.9	0	990.0
4	37.2	0	100.0
5	49.9	0	10.0
6	62.8	0	1.0
7	32.3	20.4	9000.0
8	36.1	19.4	900.0
9	40.0	12.8	90.0
10	43.9	9.0	9.0
11	46.0	6.0	1.0
12	10.3	0	9000.0
13	18.2	0	900.0
14	26.8	0	70.0
15	46.7	0	20.0
16	61.6	0	10.0
17	28.5	17.1	4000.0
18	34.7	12.2	1800.0
19	41.0	5.9	180.0
20	46.4	0	18.0
21	51.3	0	2.0
22	22.8	0	20.0

Stress spectrum based on limit operating stress of 65.0 ksi.
This load block represents 10 operational missions.

PREPARED BY: D.M.F.	SPACE DIVISION NORTH AMERICAN ROCKWELL CORPORATION 12214 LAKEWOOD BOULEVARD • DOWNEY, CALIFORNIA 90241	PAGE NO. 7-10 OF
CHECKED BY:		REPORT NO. SD72-SH-0046
DATE: 12-1-77	WING SPAR CAPS	MODEL NO. 7-10

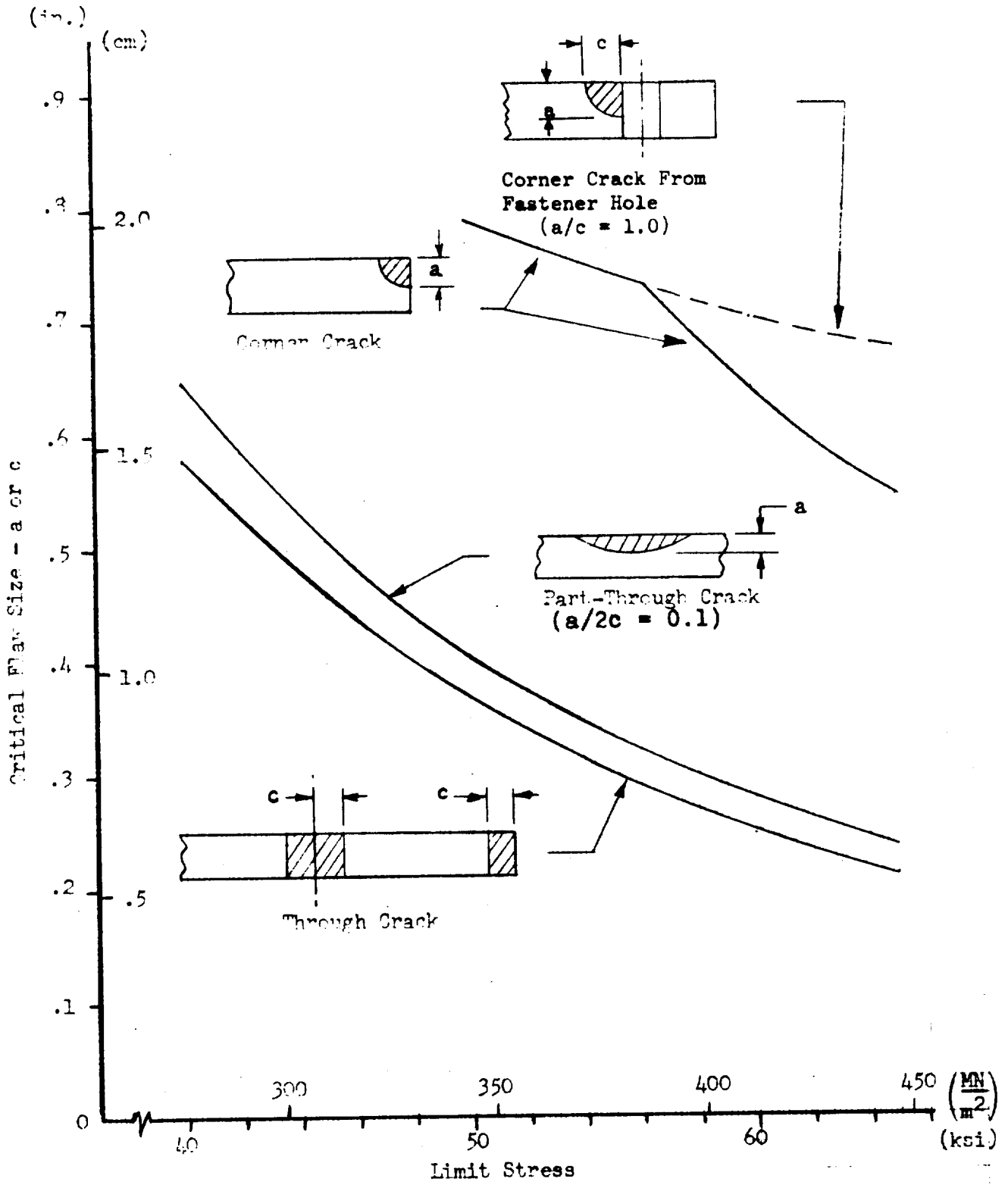


Figure 7-4. Wing Spar Cap Critical Flaw Sizes



has been taken to represent a flaw that could not be reliably detected by NDE. Results of these growth analyses are plotted in Figures 7-5 through 7-8. The growth curves are primarily for the basic case in which retardation effects are not considered; however, examples of crack growth in which retardation due to occasional high stresses in the loading spectrum are considered are also superimposed on these figures to facilitate comparison. It can be seen that crack growth retardation is very significant for this type of loading spectrum; the safe-life is increased by a factor of 5 or greater for the examples considered here.

The crack growth to failure plots are used to construct curves showing the number of safe-life missions as a function of initial flaw size; this form of data presentation is more convenient for subsequent analysis and evaluation. Curves of this type are given in Figures 7-9 through 7-12 for the types of flaws and the range of limit design stresses considered. These curves are for the basic analysis case in which crack growth retardation effects are not considered. These data can then be used to construct cross-plots that define the allowable limit design stress as a function of the number of safe-life missions required. Plots of this type are presented in Fig. 7-13 for 100, 150 and 200 safe-life missions, so that the effect of applying a safety factor to the required service life can be readily evaluated.

Similar crack growth to failure analyses have been performed in which retardation effects are considered. Allowable number of missions versus initial flaw size have been derived from the crack growth curves and are plotted in Figures 7-14 through 7-16. It can be seen that the calculated retardation effect greatly increases the number of safe-life missions for a given initial flaw size. However, this indicated improvement should be treated rather cautiously for two major reasons: (1) the early stage of retardation theory and test development at this time, and (2) the simplified loading spectrum assumes that high stress cycles will be encountered in the initial missions, with the result that crack growth retardation is considered to be effective over almost all of the service life. Therefore, it is recommended that the data of Figures 7-14 through 7-16 be considered as an upper bound of the potential improvement that may be gained by considering crack growth retardation.

7.2.3 Design Implications

The fatigue analysis of wing spar caps indicated that the limit design stress should be reduced to approximately 450 MN/m^2 (65 ksi) to achieve a satisfactory fatigue life. However, the results of crack growth analyses summarized in the preceding section show that even this stress level may result in critical initial flaw sizes that are too small to reliably detect by present day NDE techniques. Therefore, it is desirable to determine the actual weight penalty involved for various sizes of initial defects to help establish design criteria and NDE development requirements.

Not all of the wing spar cap structure is designed to operate at the same maximum stress level as the section selected for crack growth analysis. This is due to other design requirements, practical limitations on minimum

PREPARED BY: *D.W.P.*
 CHECKED BY:
 DATE: 12-1-71



Space Division
 North American Rockwell

PAGE NO. 7-12 OF
 REPORT NO. SD72-SH-0046
 MODEL NO. P-01

WTNG SPAR CAPS

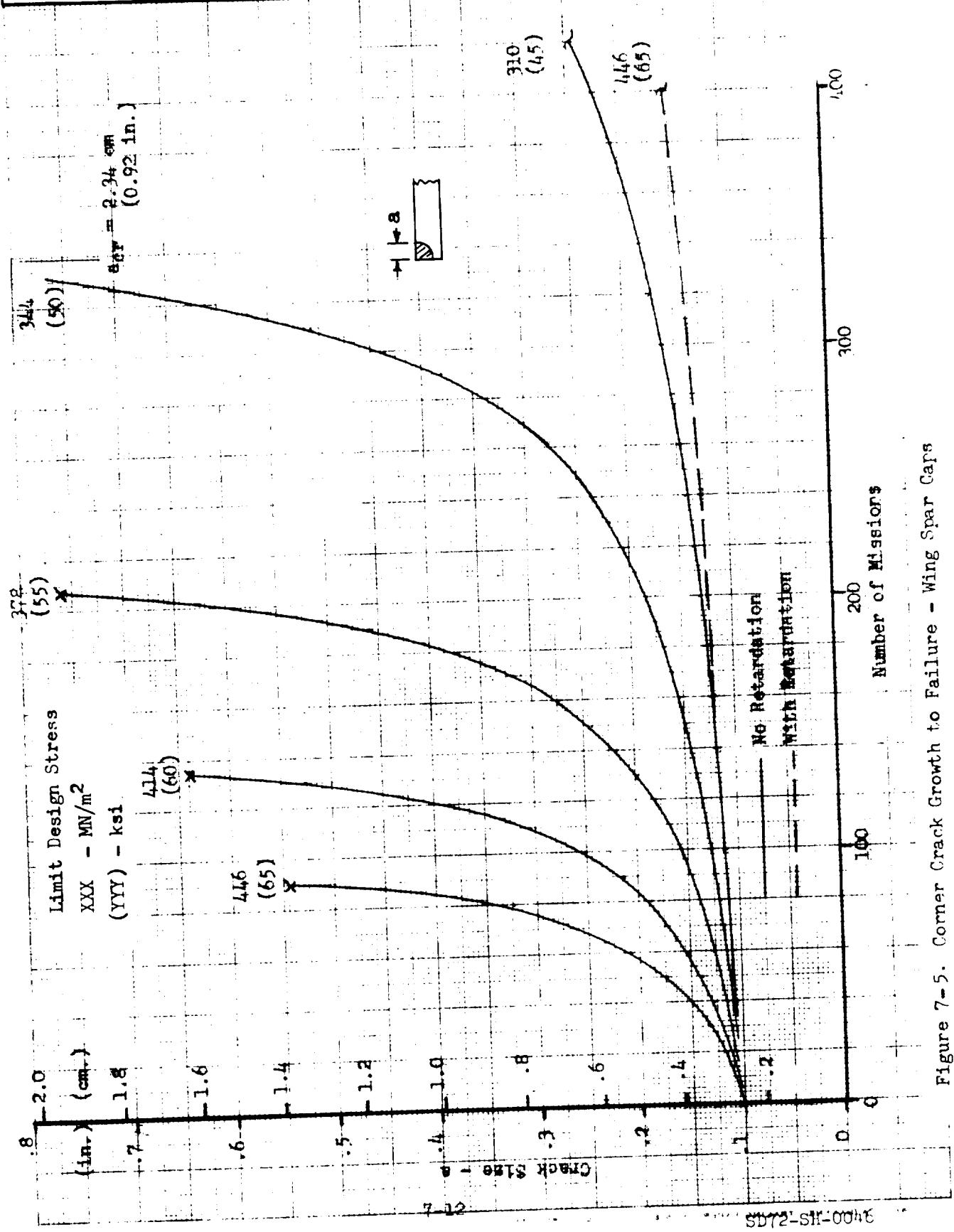



Figure 7-5. Corner Crack Growth to Failure - Wing Spar Caps

SD72-SH-0046

PREPARED BY: DLM	 Space Division North American Rockwell	PAGE NO. 7-13 OF
CHECKED BY:		REPORT NO. SD72-SH-0046
DATE: 12-1-77	WING SPAR CAP	MODEL NO. P-01

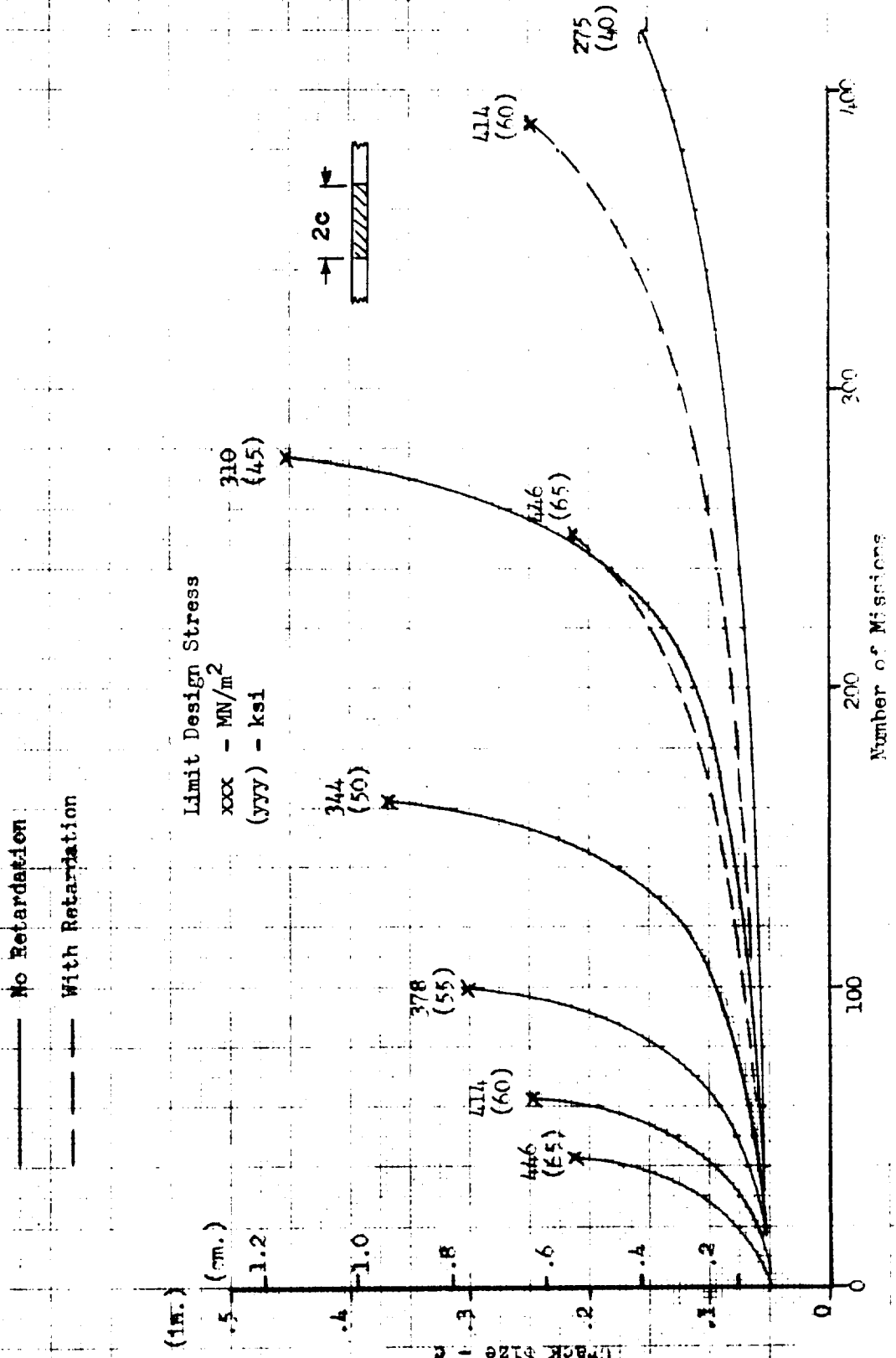


Figure 7-6. Through Crack Growth to Failure - Wing Spar Caps

7-13
 SD72-SH-0046

PREPARED BY: DLT	 Space Division North American Rockwell	PAGE NO. 7-14 of
CHECKED BY:		REPORT NO. SD72-SH-0046
DATE: 12-1-72	WING SPAR CAPS	MODEL NO. R-01

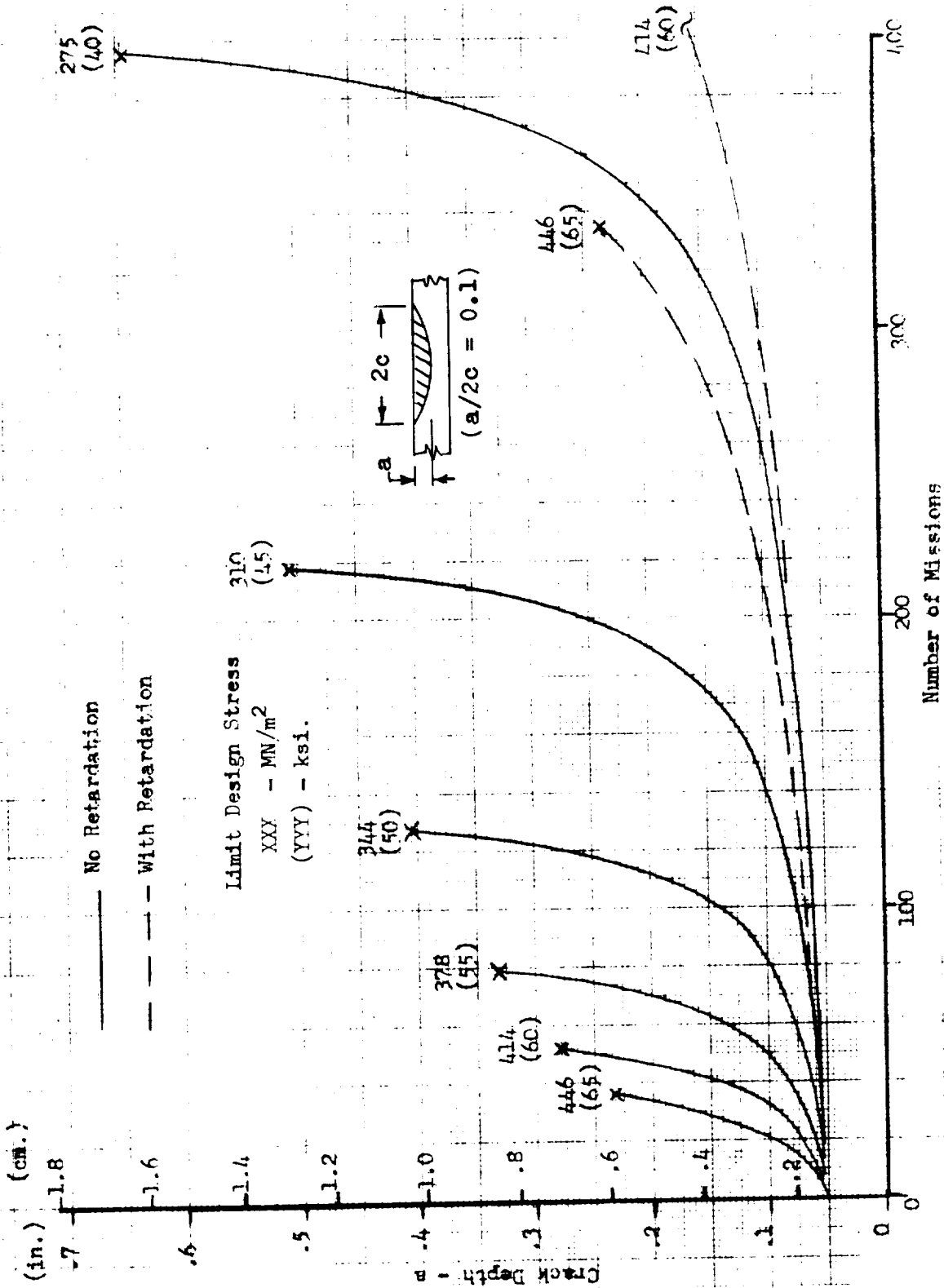


Figure 7-7. Part-Through Crack Growth to Failure - Wing Spar Caps

PREPARED BY: JS	NORTH AMERICAN AVIATION, INC. SPACE and INFORMATION SYSTEMS DIVISION	PAGE NO 7-15 of
CHECKED BY:		REPORT NO SD72-SH-0046
DATE: 3-15-72	WING SPAR CAPS	MODEL NO B-90

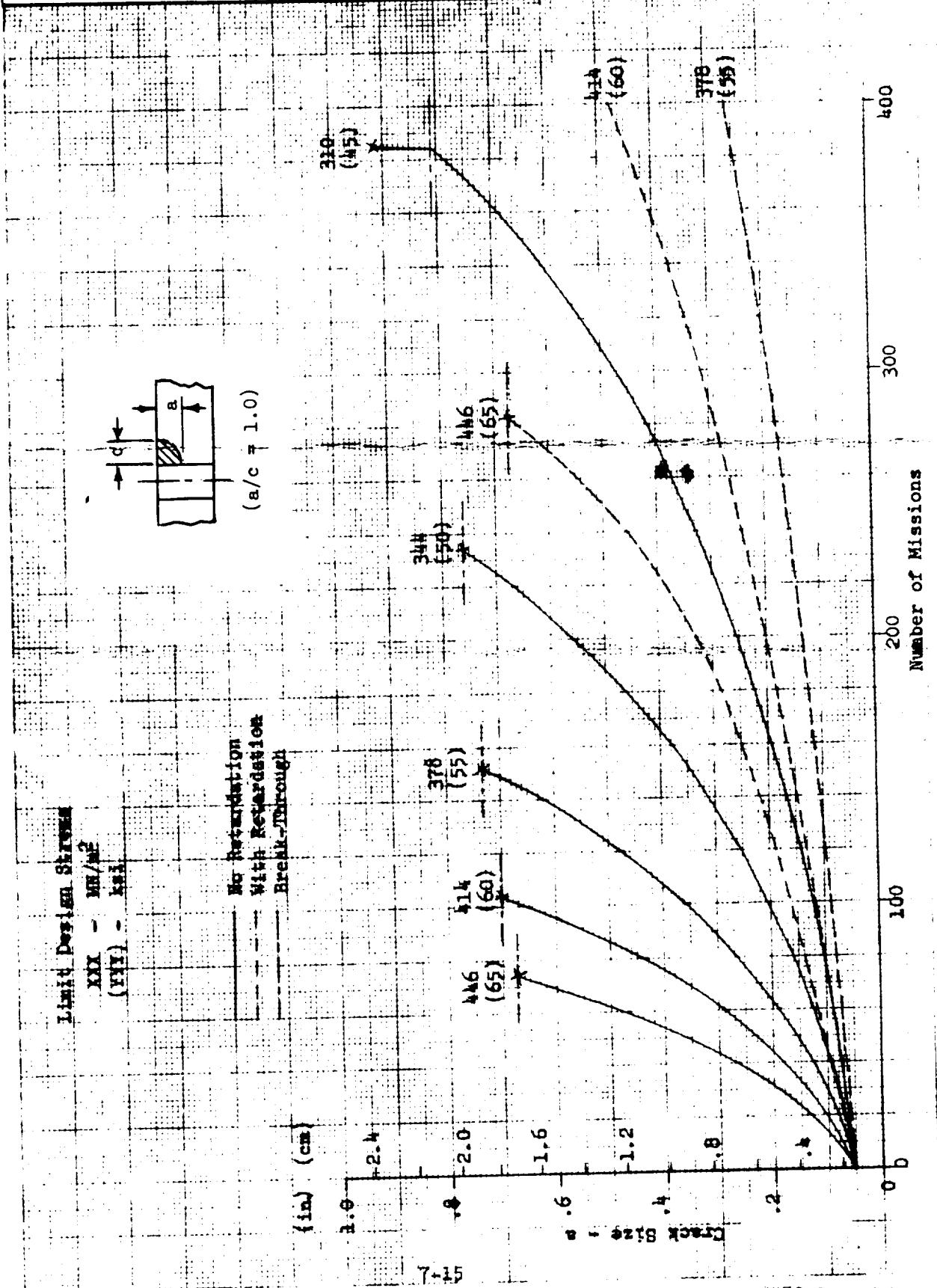


Figure 7-8. Corner Crack From Fastener Hole - Growth to Failure - Wing Spar Caps

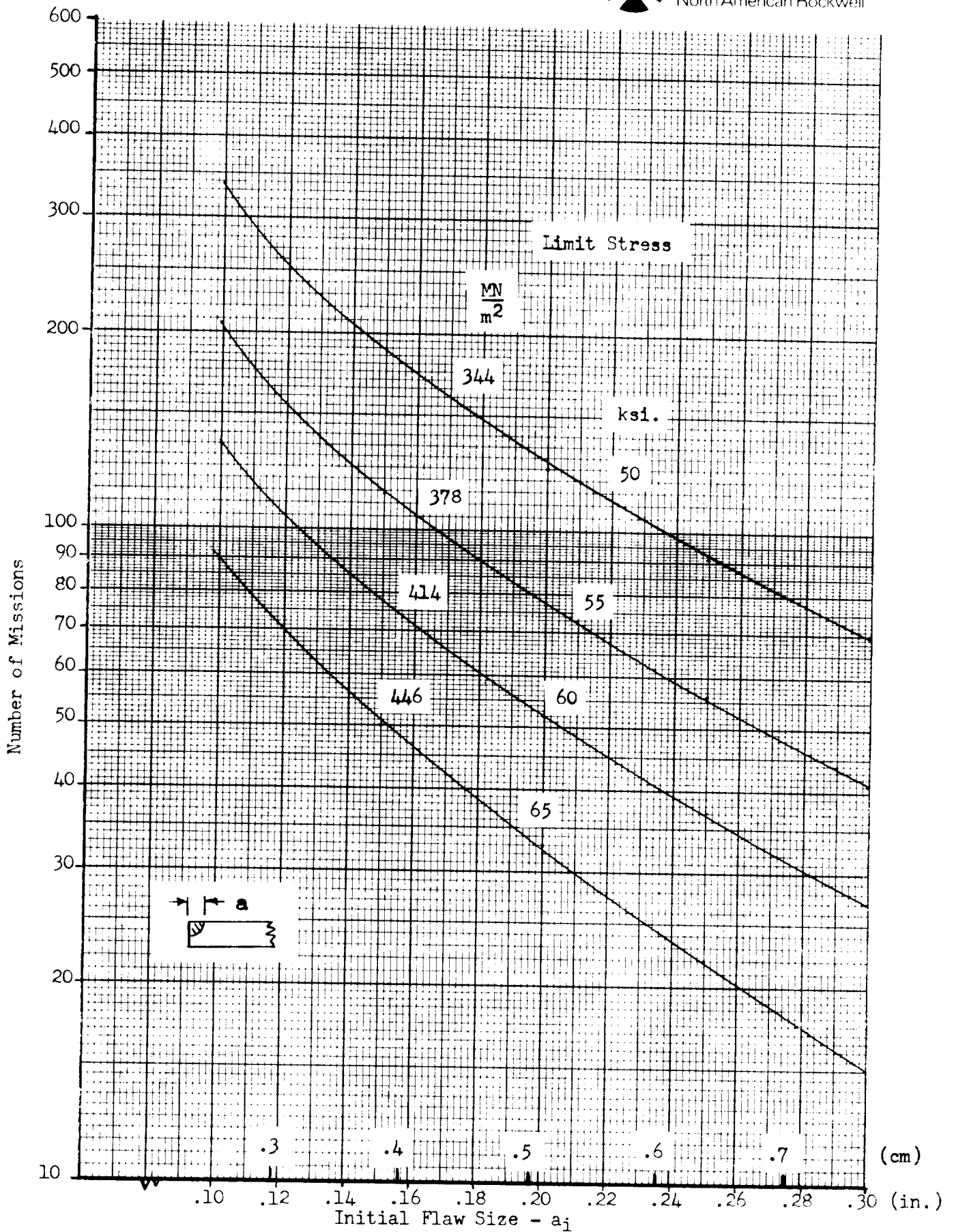


Figure 7-9. Missions to Failure - Corner Crack in Wing Spar Caps
(Retardation Not Considered)

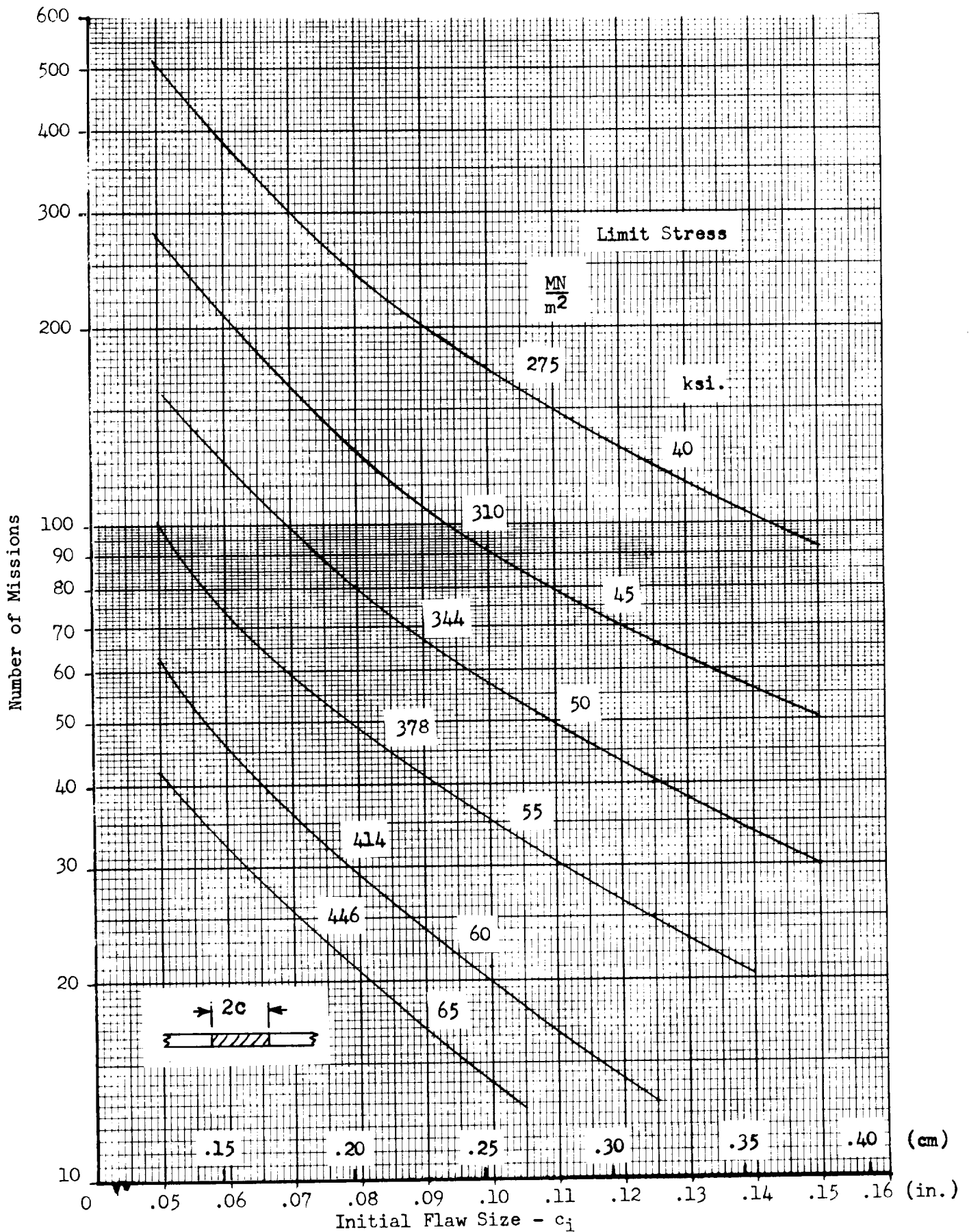


Figure 7-10. Missions to Failure - Through Crack in Wing Spar Caps
(Retardation Not Considered)

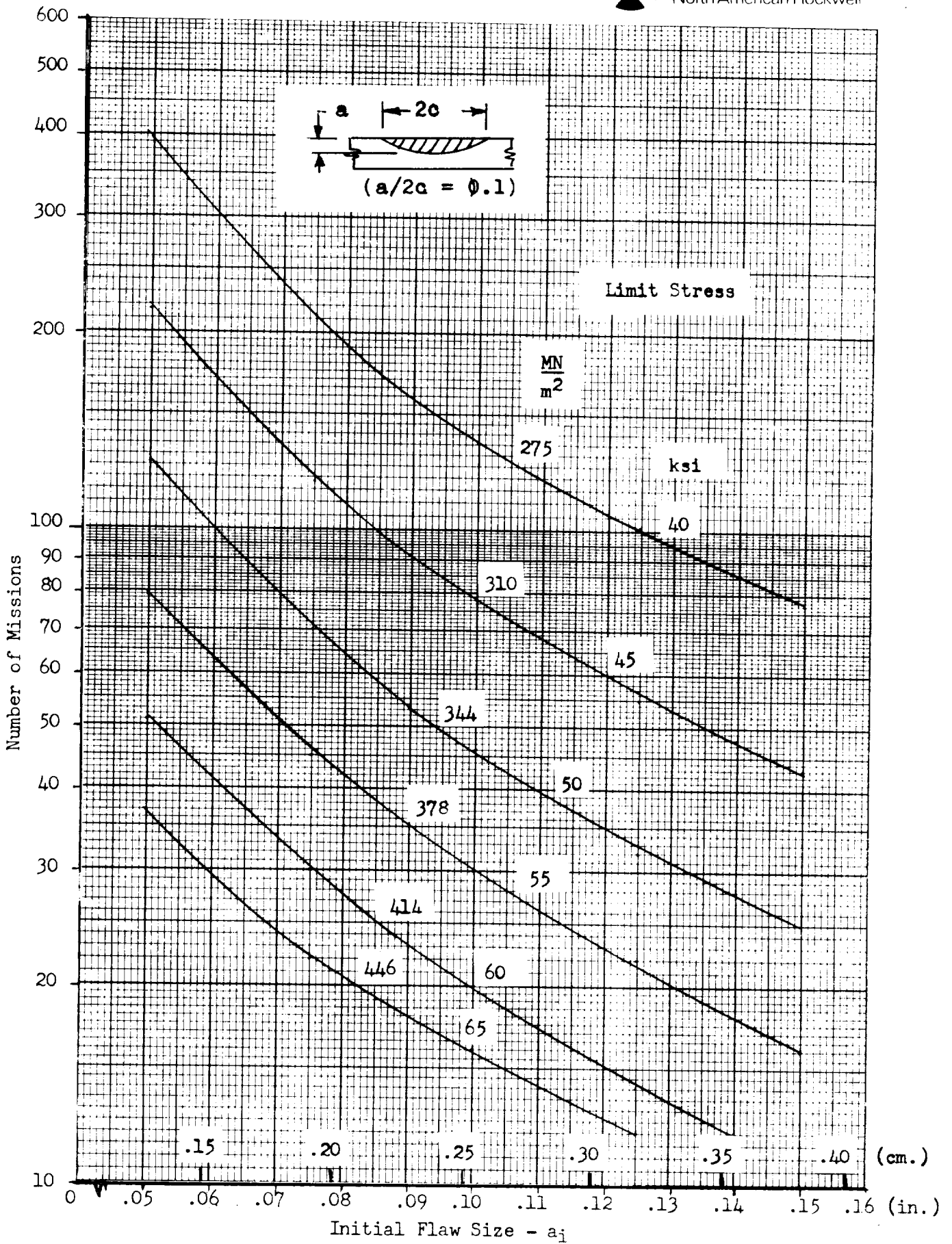


Figure 7-11. Missions to Failure - Part-Through Crack in Wing Spar Caps (Retardation Not Considered)

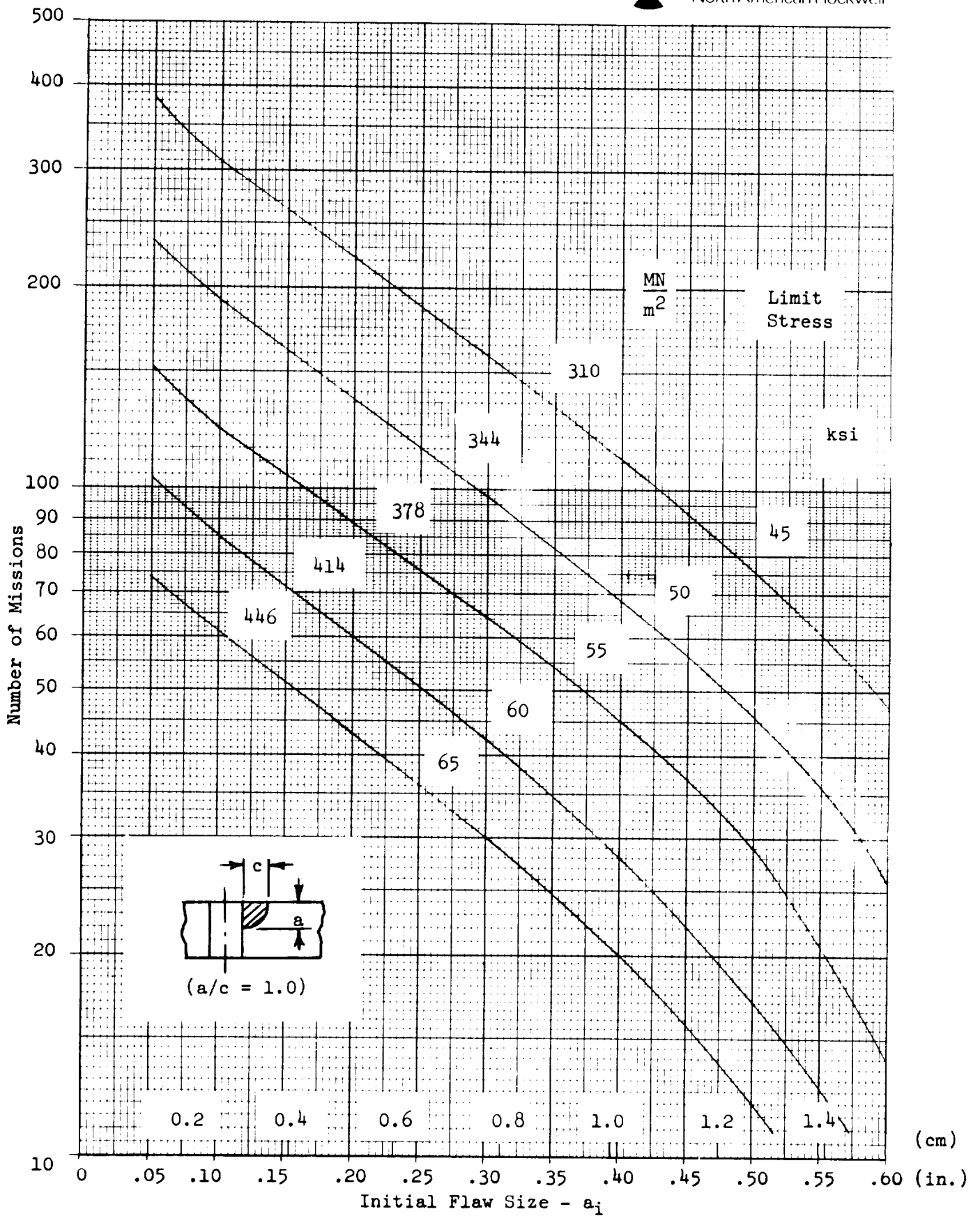


Figure 7-12. Missions to Failure - Corner Crack From Fastener Hole in Wing Spar Caps (Retardation Not Considered)

PREPARED BY: D.M.J.	 Space Division North American Rockwell	PAGE NO. 7-20 OF
CHECKED BY:		REPORT NO. SD72-SH-0046
DATE: 12-1-71	WING SPAR CAPS	MODEL NO. P-01

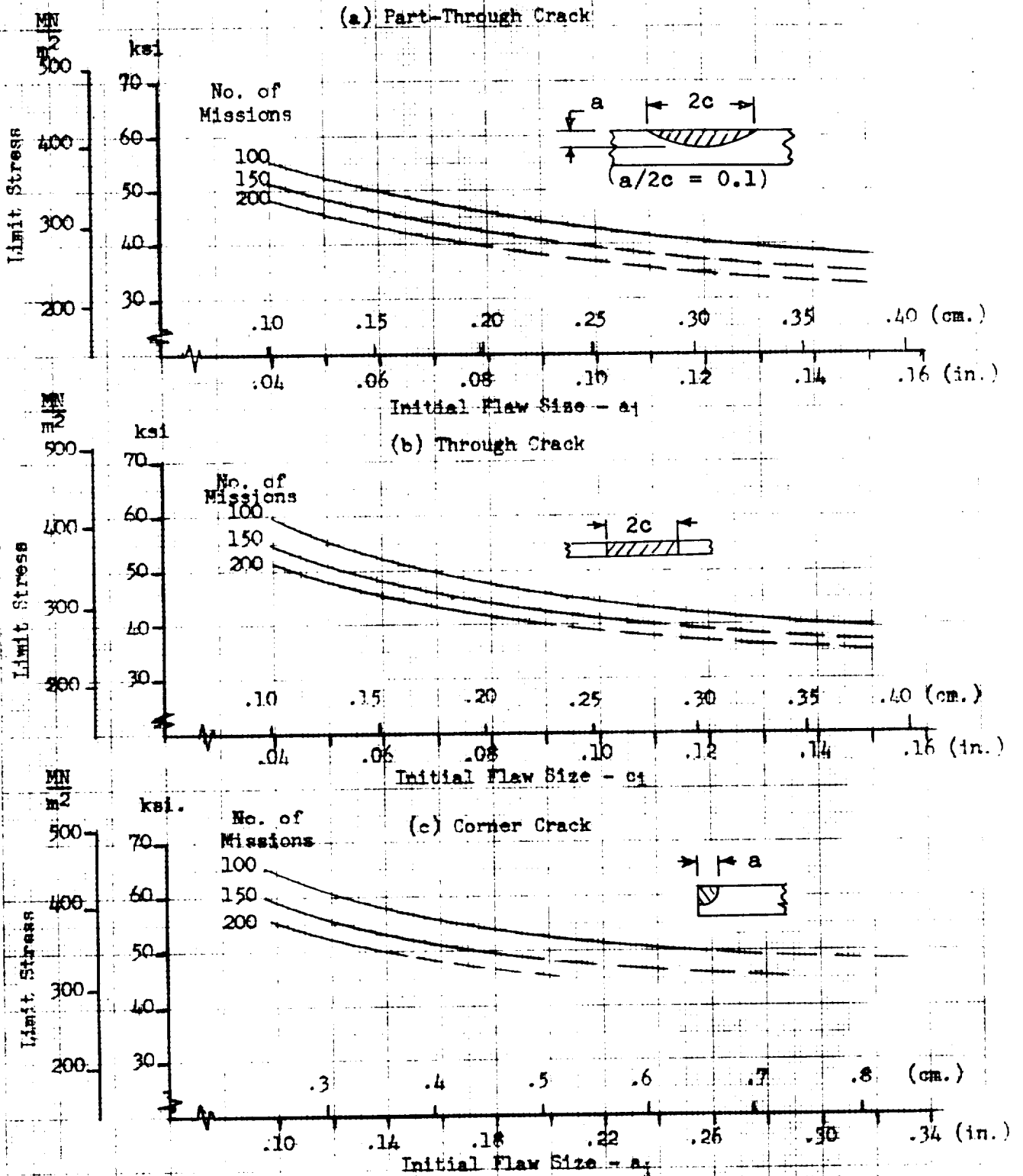


Figure 7-13. Effect of Initial Flaw Size on Allowable Limit Stress for Safe-Life - Wing Spar Caps - (Crack Growth Retardation Not Considered)

PREPARED BY: JS	 Space Division North American Rockwell	PAGE NO. 7-21 OF
CHECKED BY:		REPORT NO. SD72-SH-0046
DATE: 3-15-72	WING SPAR CAPS	MODEL NO. B-9U

(d) Corner Crack From Fastener Hole

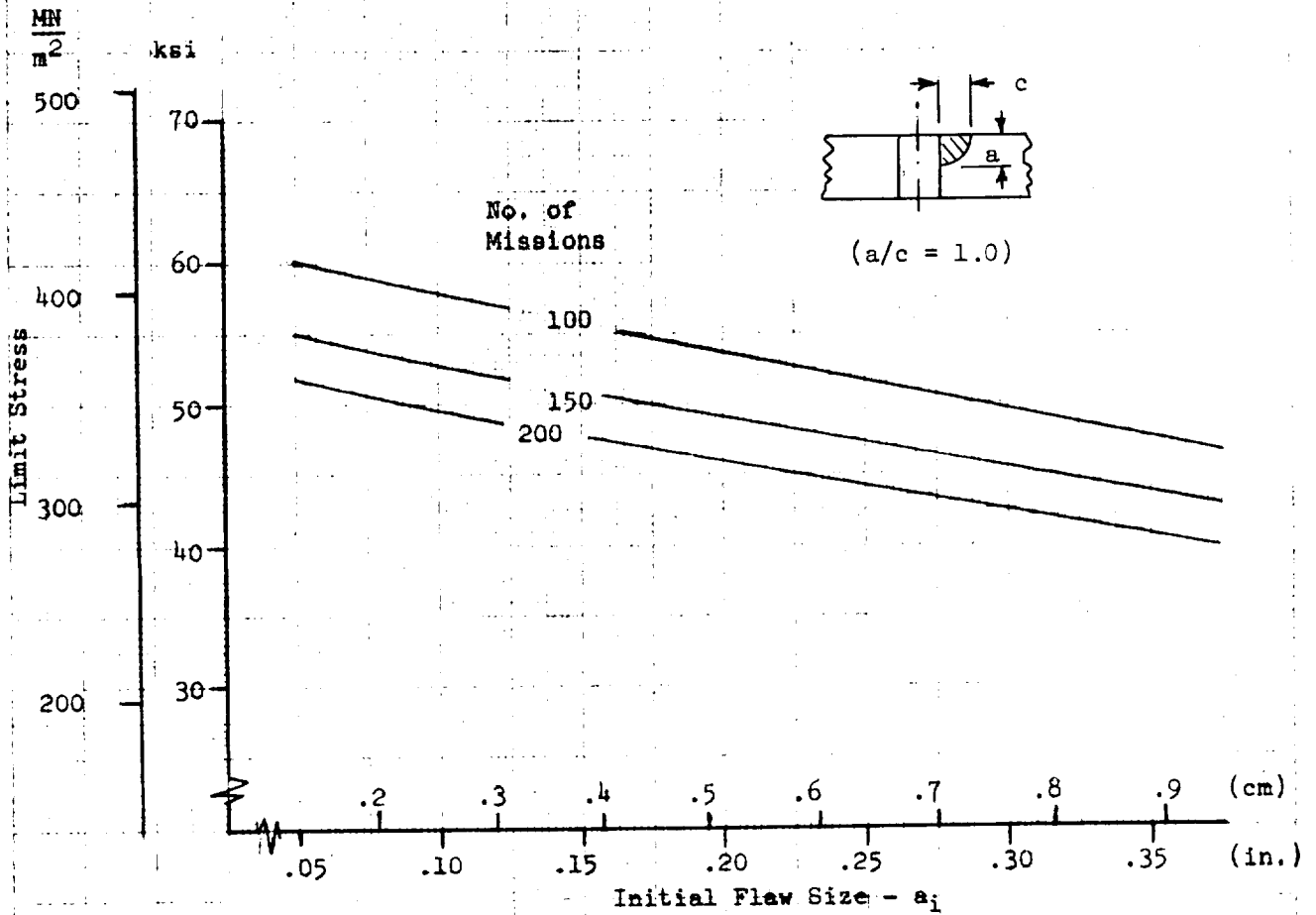


Figure 7-13. Effect of Initial Flaw Size on Allowable Limit Stress for Safe-Life - Wing Spar Caps (continued) (Crack Growth Retardation Not Considered)

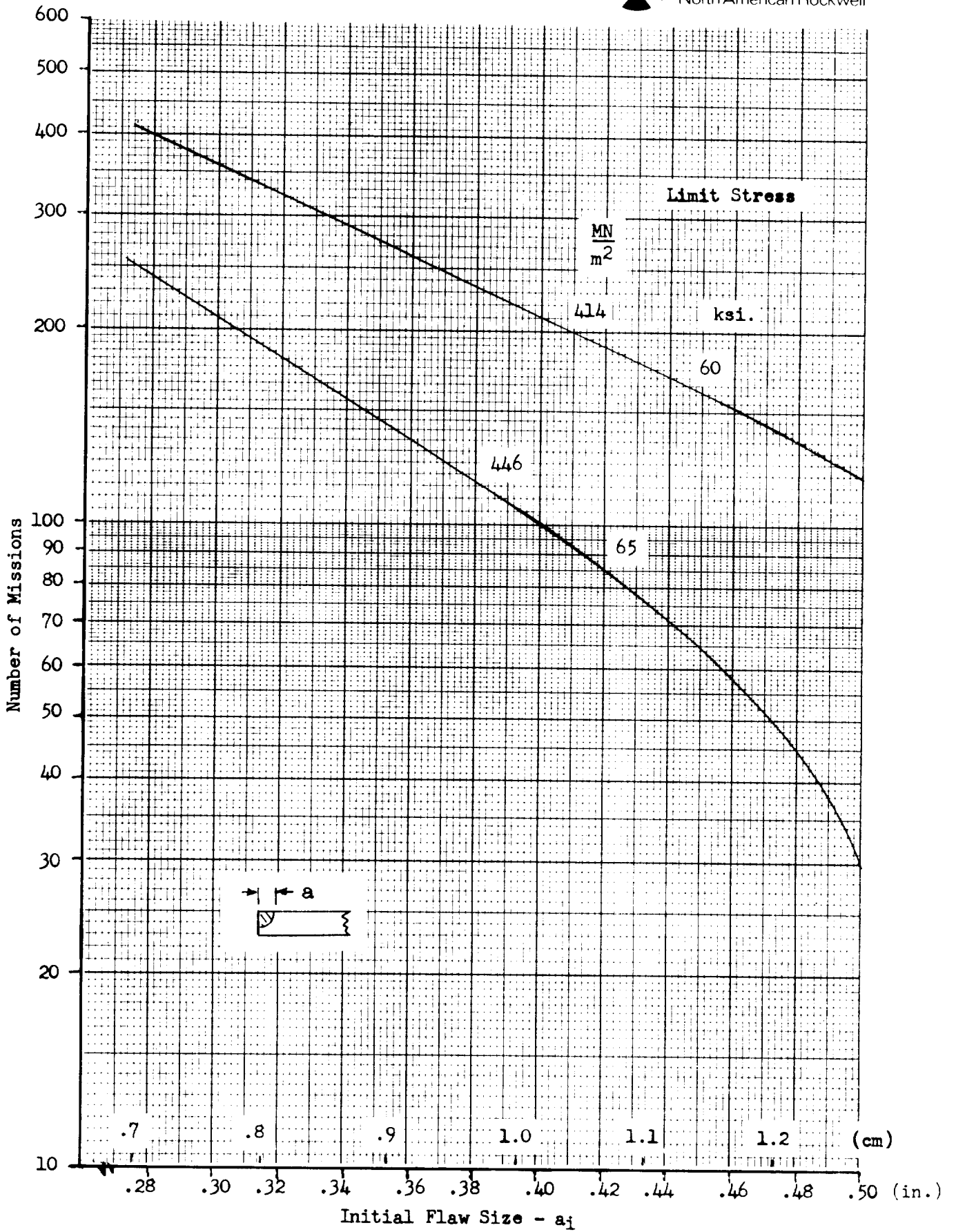


Figure 7-14. Missions to Failure - Corner Crack in Wing Spar Caps (Retardation Included)

SD72-SH-0046

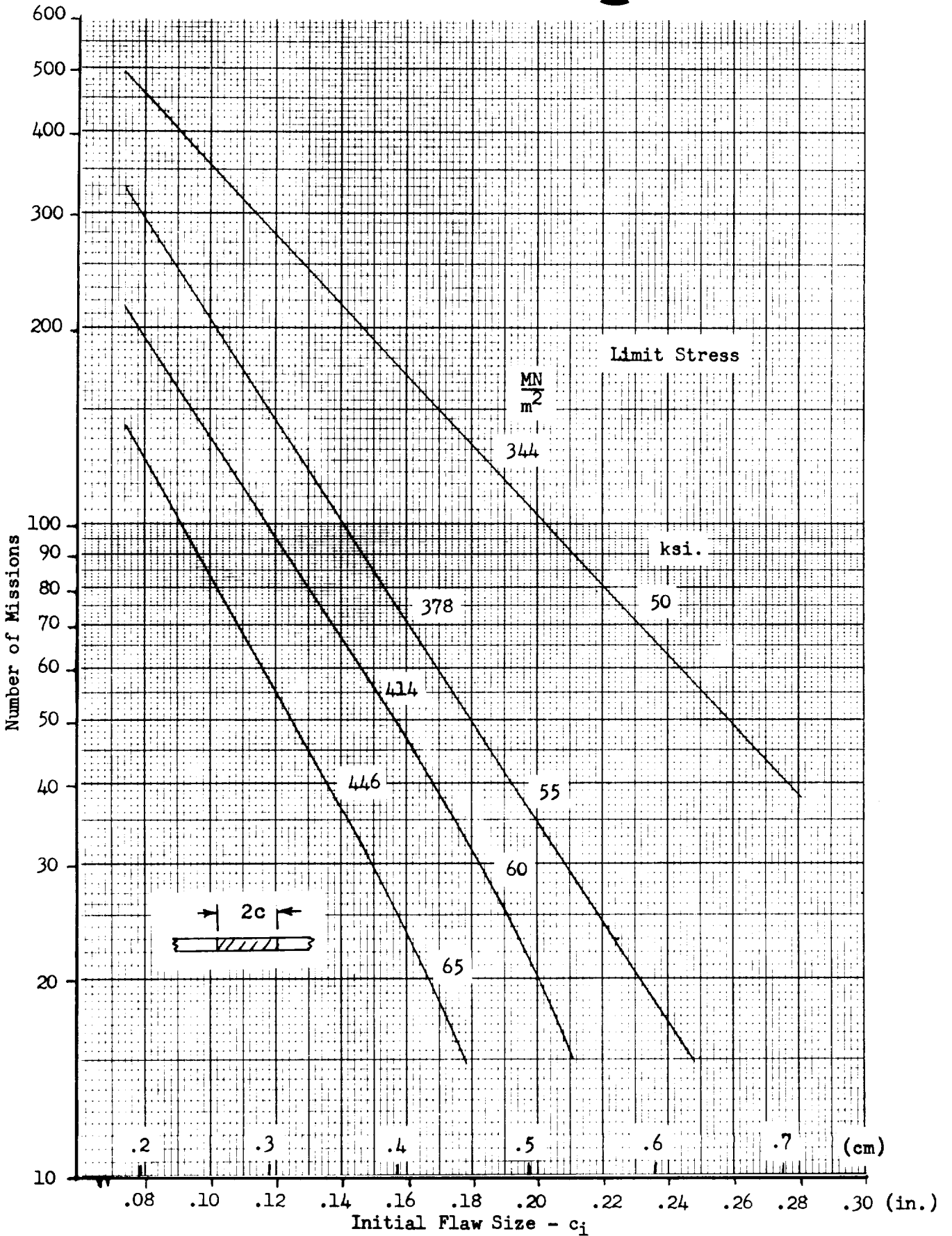


Figure 7-15. Missions to Failure - Through Crack in Wing Spar Caps (Retardation Included)

SD72-SH-0046

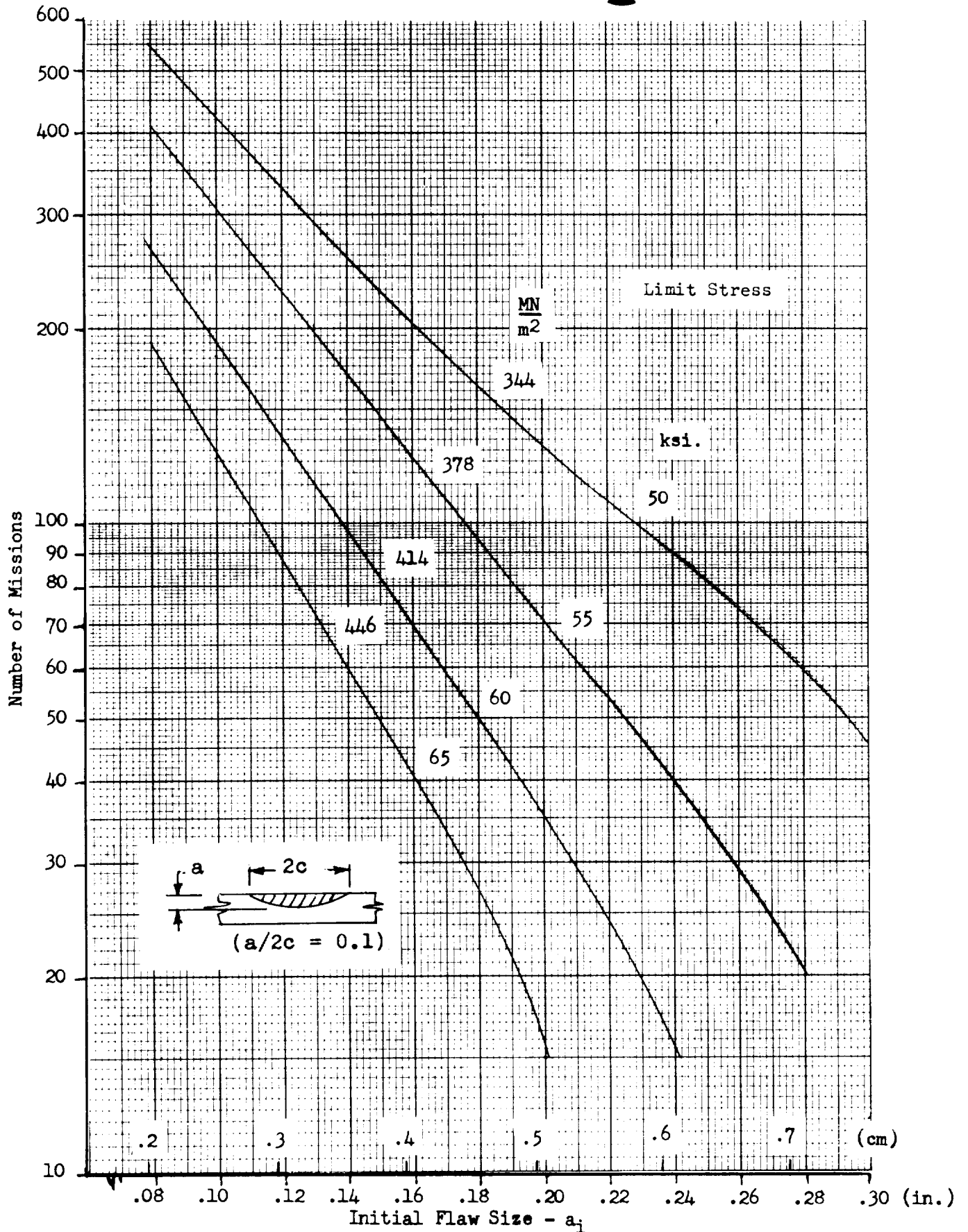


Figure 7-16. Missions to Failure - Part-Through Crack in Wing Spar Caps (Retardation Included)

area, etc. This situation is illustrated in Figure 7-17, wing spar cap iso-stress contours are plotted for upper and lower surfaces. These curves represent the structural sizing and operating stress levels determined by GDC during the Phase B Study, and reported in Reference 22. These data have been used to determine the increase in wing spar cap weight that would result from restricting the limit operating stress to various values over the range of 275 MN/m^2 (40 ksi) to 450 MN/m^2 (65 ksi). The weight increase was evaluated by numerical integration of the increments to spar cap area required for each stress level; the integration was based on average properties over increments of length defined by sixteen stations over the semi-span. The results of this evaluation are plotted in Figure 7-18. It is of interest to note that decreasing the limit operating stress to 450 MN/m^2 (65 ksi) to satisfy fatigue life requirements causes a relatively small increase in wing weight. A weight penalty of only about 450 kg. (1000 lb) is indicated from Figure 7-18. This is about 1.5 percent of total wing weight.

The above data are used with the previously defined variation of critical initial flaw size versus limit operating stress to define summary curves that depict wing weight increase as a function of assumed initial flaw size and the number of safe-life missions required. These summary curves are plotted in Figures 7-19 and 7-20 for the types of cracks considered in this analysis. The weight trend curves of Figure 7-19 are for the basic analysis case in which crack growth retardation is not considered. It can be seen that weight increase is very sensitive to the size of initial flaw assumed to exist in the structure, and that a very significant weight penalty is involved for flaw sizes that might practically be considered as a lower limit of reliable detection under present NDE capabilities. Similar curves are plotted in Figure 7-19 for the case in which crack growth retardation is included in the analysis. Comparison with the preceding curves illustrates that consideration of retardation effects may provide appreciable benefit to minimize the weight penalty associated with achieving safe life for a practical initial flaw size criteria. However, caution should be exercised at this time in the use of predicted crack growth retardation for Space Shuttle design and development. The basic theories and analytical methods to predict this phenomenon are in an early stage of development and only limited test verification has been achieved. Recent experimental results, obtained by investigators at NR SD and elsewhere, have indicated that the beneficial effects of retardation may be eliminated or greatly reduced if the structure is periodically exposed to elevated temperatures at points interspersed throughout the random load spectra. Therefore, unless comprehensive test data become available regarding this interaction, it appears unlikely that crack growth retardation predictions can be used with confidence for Space Shuttle structure that is subjected to elevated temperatures from ascent or entry heating.

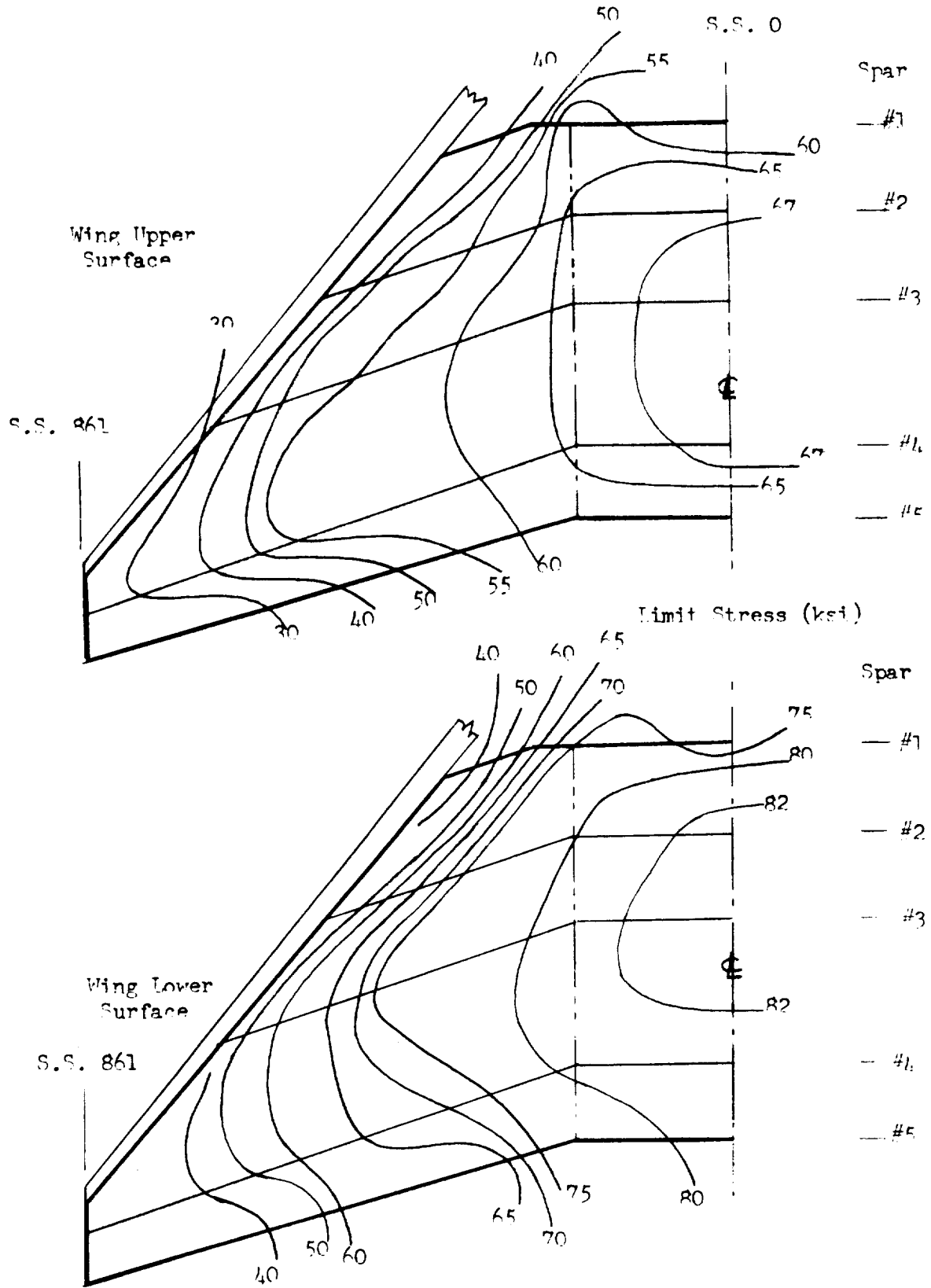


Figure 7-27. Wing Spar Ca. Two-stress Contours

PREPARED BY: RWT	 Space Division North American Rockwell	PAGE NO. 7-27 OF
CHECKED BY:		REPORT NO. SD72-SH-0046
DATE: 12-1-67	WING SPAR CAPS	MODEL NO. P-1

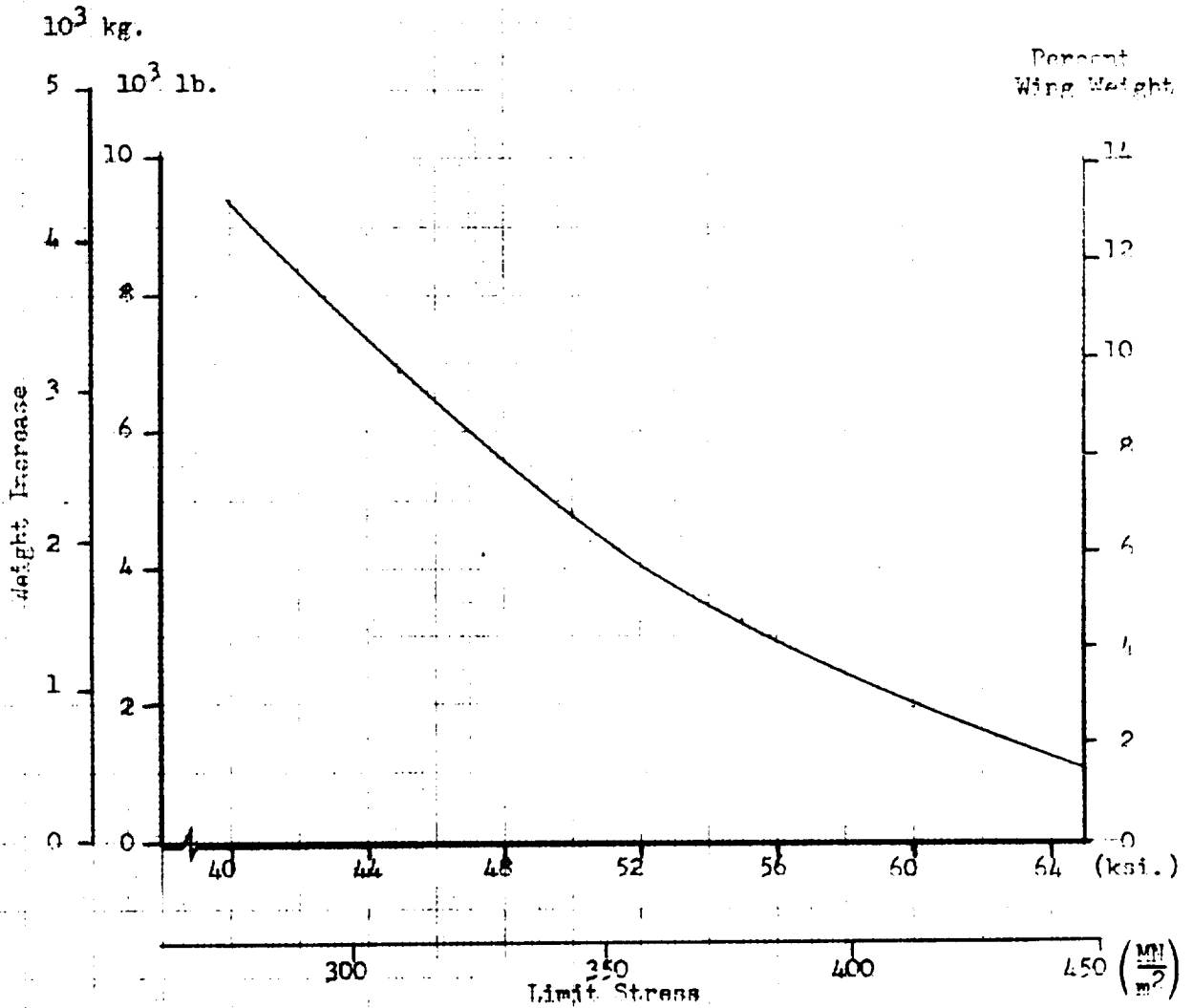


Figure 7-18. Effect of Spar Cap Limit Design Stress on Wing Weight

PREPARED BY: R/W	 Space Division North American Rockwell	PAGE NO. 7-28 OF
CHECKED BY:		REPORT NO. SD72-SH-0046
DATE: 12-1-71		MODEL NO. R-011
WING SPAR CAPS		

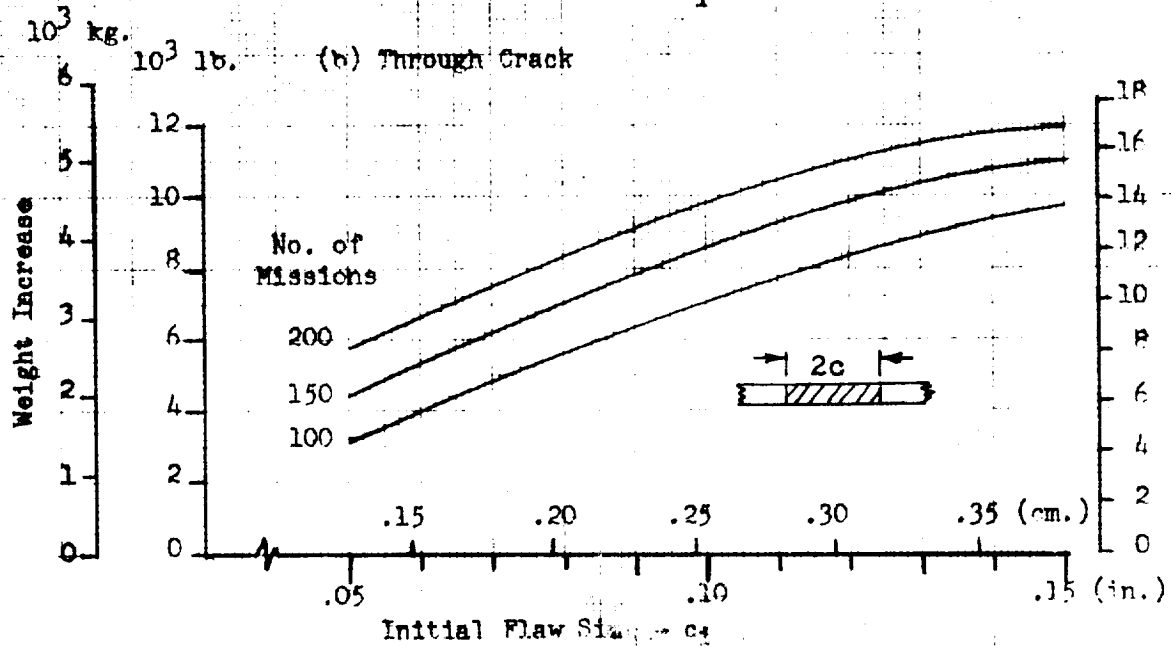
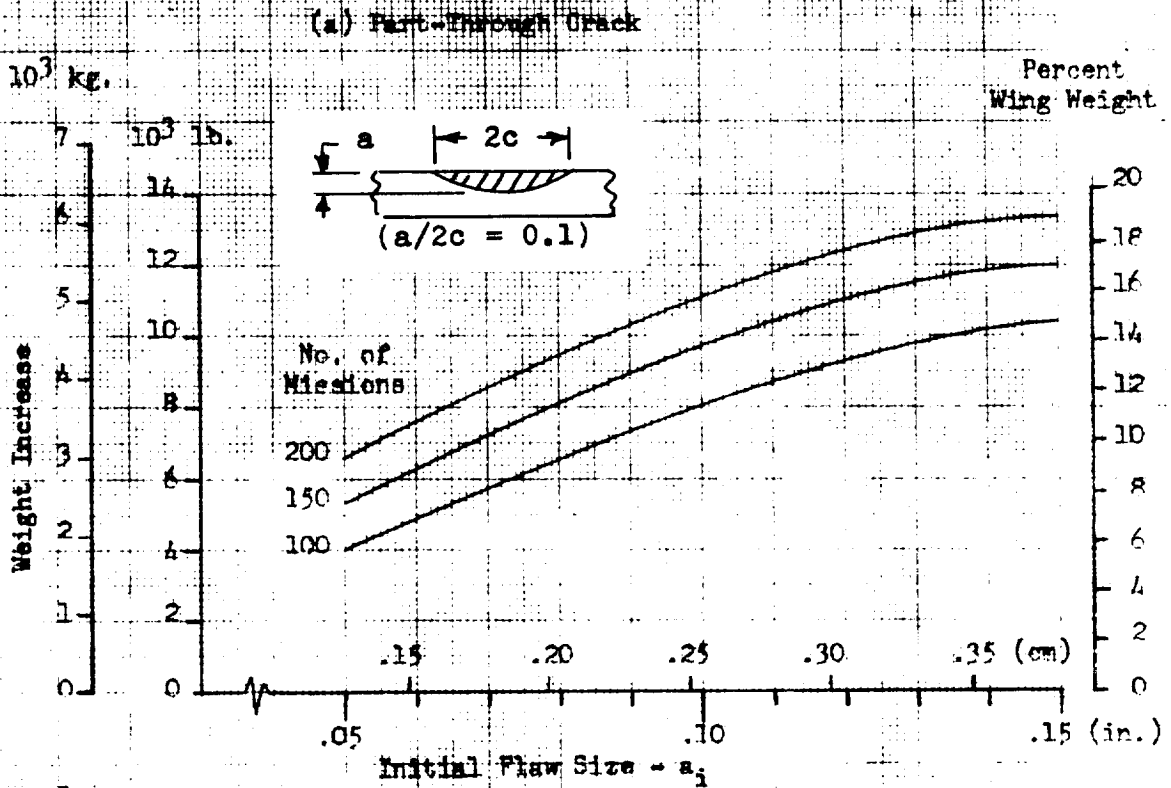


Figure 7-19. Effect of Initial Flaw Size on Wing Weight for Safe-Life - (Crack Growth Retardation Not Considered)

PREPARED BY: RFW	 Space Division North American Rockwell	PAGE NO. 7-29 OF
CHECKED BY:		REPORT NO. SD72-SH-0046
DATE: 12-1-71	WING SPAR CAPS	MODEL NO. R-111

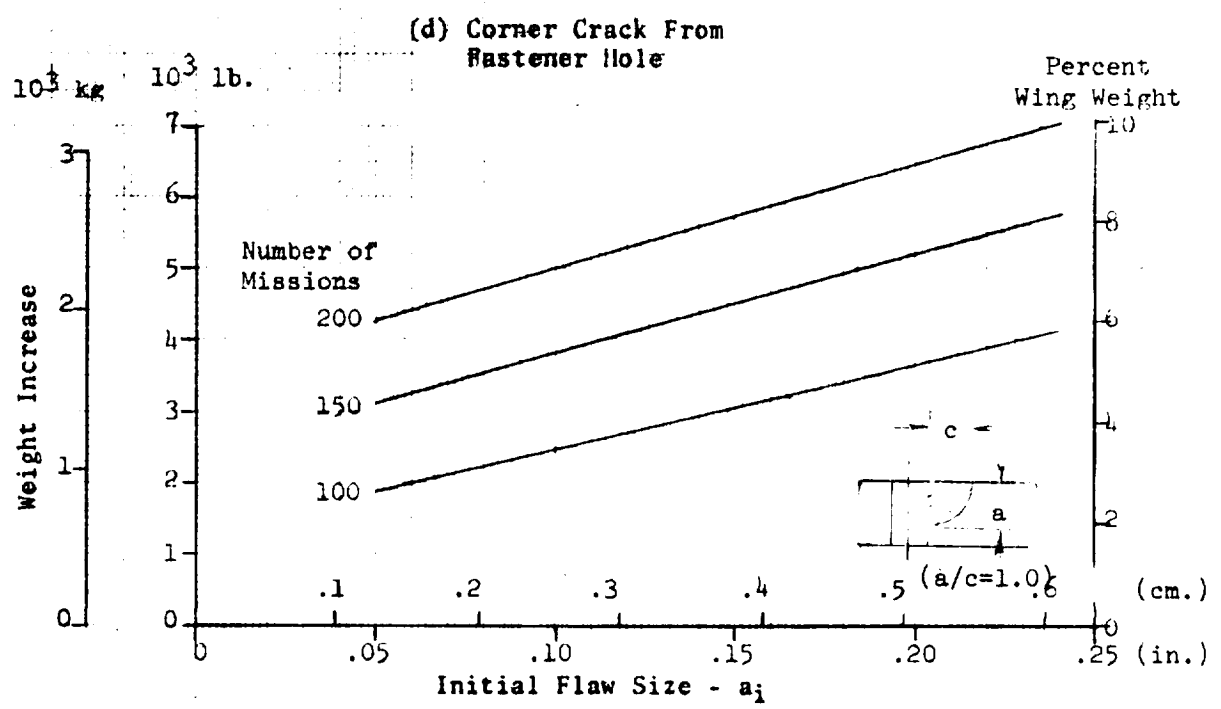
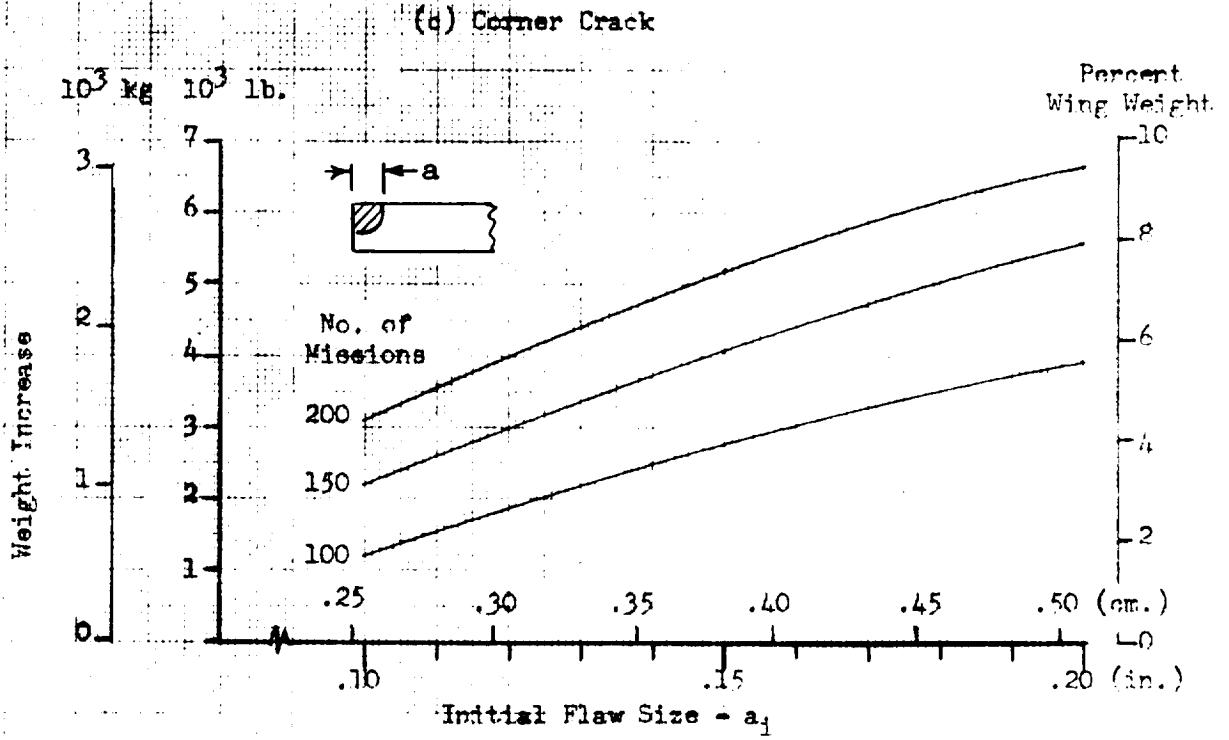
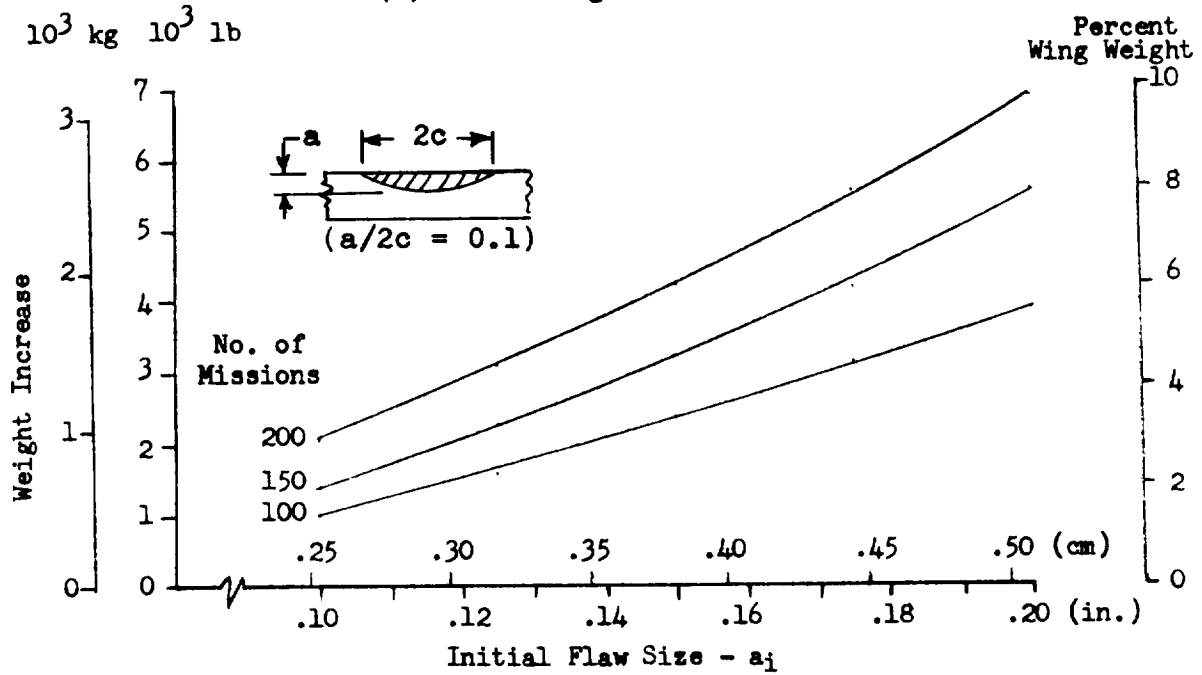


Figure 7-19. Effect of Initial Flaw Size on Wing Weight for Safe-Life - Crack Growth Retardation Not Considered (continued)

PREPARED BY: RWW	SPACE DIVISION NORTH AMERICAN ROCKWELL CORPORATION 12214 LAKEWOOD BOULEVARD • DOWNEY, CALIFORNIA 90241	PAGE NO. 7-30 OF
CHECKED BY:		REPORT NO. SD72-SH-0046
DATE: 12-10-71	WING SPAR CAPS	MODEL NO. B-9U

(a) Part-Through Crack



(b) Through Crack

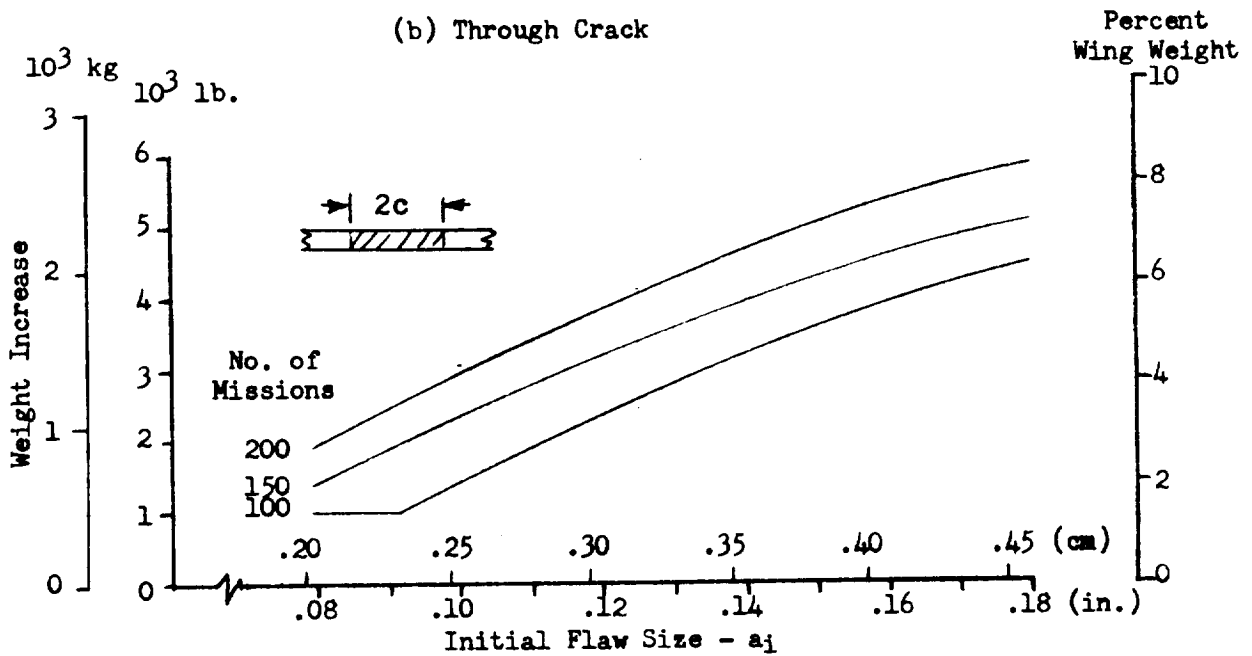


Figure 7-20. Effect of Initial Flaw Size on Wing Weight for Safe Life (Crack Growth Retardation Included)

7.3 SAFE-LIFE ANALYSIS - VERTICAL STABILIZER

7.3.1 Structural Configuration and Loading

The critical section on vertical stabilizer main box selected for crack growth analysis is the same as that selected for fatigue analysis, and is illustrated in Figure 6-3(b).

A simplified stress spectrum for crack growth analysis is derived from the fatigue stress spectra given in Table 6-5. The procedure is similar to that described for the wing crack growth analysis, and the results are summarized in Table 7-2. Thermal stress cycles are not included in this stress spectrum because the predominant thermal transients produce tension on the integral stiffeners and compression on the skin. The skin is the critical element for crack growth evaluation; analysis indicates that complete fracture of an integral stiffener is not a critical situation.

7.3.2 Crack Growth Analysis

Because of the thin skin and relatively low operating stresses of the stabilizer main box, a part-through crack cannot become critical before growing through the thickness. Therefore, a through crack is the only type of initial defect of practical interest for this structural element. A critical crack size (half-length) of 7.5 cm (2.95 in.) is calculated for this type of crack at a limit stress of 180 MN/m^2 (26 ksi). This result is based on a value for critical stress intensity of $87.6 \text{ MN/m}^{3/2}$ (80 ksi $\sqrt{\text{in.}}$) and a size of plastic zone based on plane stress theory.

Because of the relatively low operating stresses of the vertical stabilizer skins, it is expected that flaw growth will be slow and readily detectable before critical size is reached. To verify this premise, an initial flaw size (half-length) of 1.27 cm (0.5 in.) is selected as the basis for growth analysis. Flaw growth is calculated by computer program in the same manner as described for the wing spar caps. Results are plotted in Figure 7-21, crack growth retardation is not considered. The crack growth curve is used to derive the plot of number of missions to reach critical crack length as a function of initial crack size, presented in Figure 7-22.

7.3.3 Design Implications

From Figure 7-22 it is apparent that a relatively large initial crack can be tolerated in the vertical stabilizer skins. If a design requirement of 200 missions is assumed (a safety factor of 2 on safe-life), the corresponding maximum tolerable initial crack length is 4.8 cm (1.9 in.). Retardation effects would further increase this allowable initial size. The skins are accessible for direct visual inspection throughout the service life because no external TPS is employed on this structural assembly. Therefore, it is considered that a crack of this size would not escape detection and that no further design provisions are required to ensure safe life.

Table 7-2. Vertical Stabilizer Stress Spectrum

Load Step	Maximum Stress (ksi)	Minimum Stress (ksi)	Number of Cycles
1	3.0	0	64700.0
2	5.0	0	3900.0
3	7.0	0	1100.0
4	8.0	0	230.0
5	9.0	0	80.0
6	12.0	0	30.0
7	14.0	0	2.0
8	15.6	0	1.0
9	3.0	0	9000.0
10	5.0	0	900.0
11	6.6	0	70.0
12	7.8	0	20.0
13	9.0	0	10.0
14	5.0	0	18000.0
15	10.0	0	1800.0
16	12.6	0	140.0
17	15.0	0	40.0
18	17.5	0	14.0
19	19.8	0	4.0
20	26.0	0	2.0

This load block represents 10 operational missions.

PREPARED BY: JPS	 Space Division North American Rockwell	PAGE NO. 7-33
CHECKED BY:		REPORT NO. SD72-SH-0046
DATE: 12-13-71	VERTICAL STABILIZER	MODEL NO. 13-71

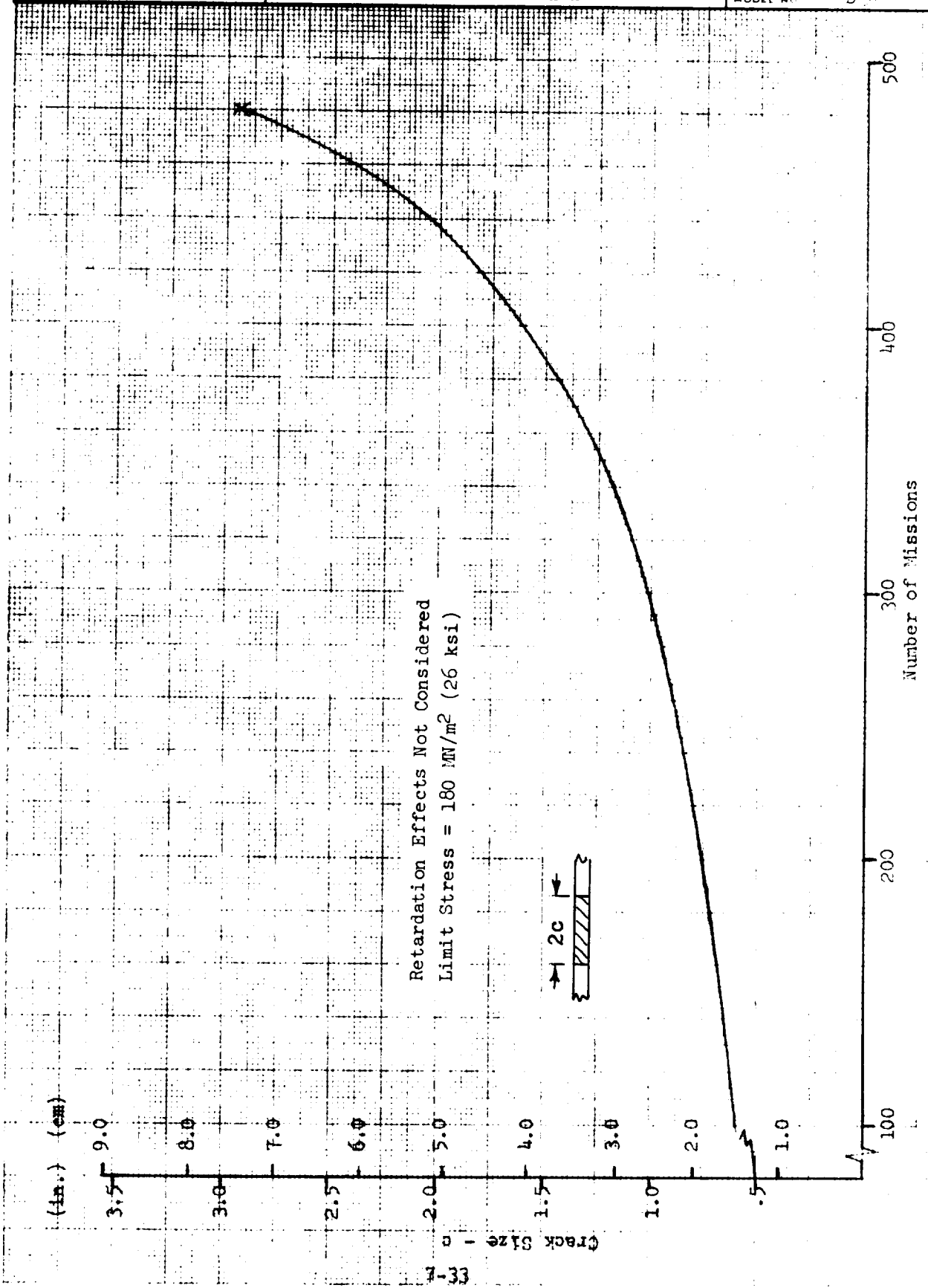


Figure 7-21. Through Crack Growth to Failure - Vertical Stabilizer Skin

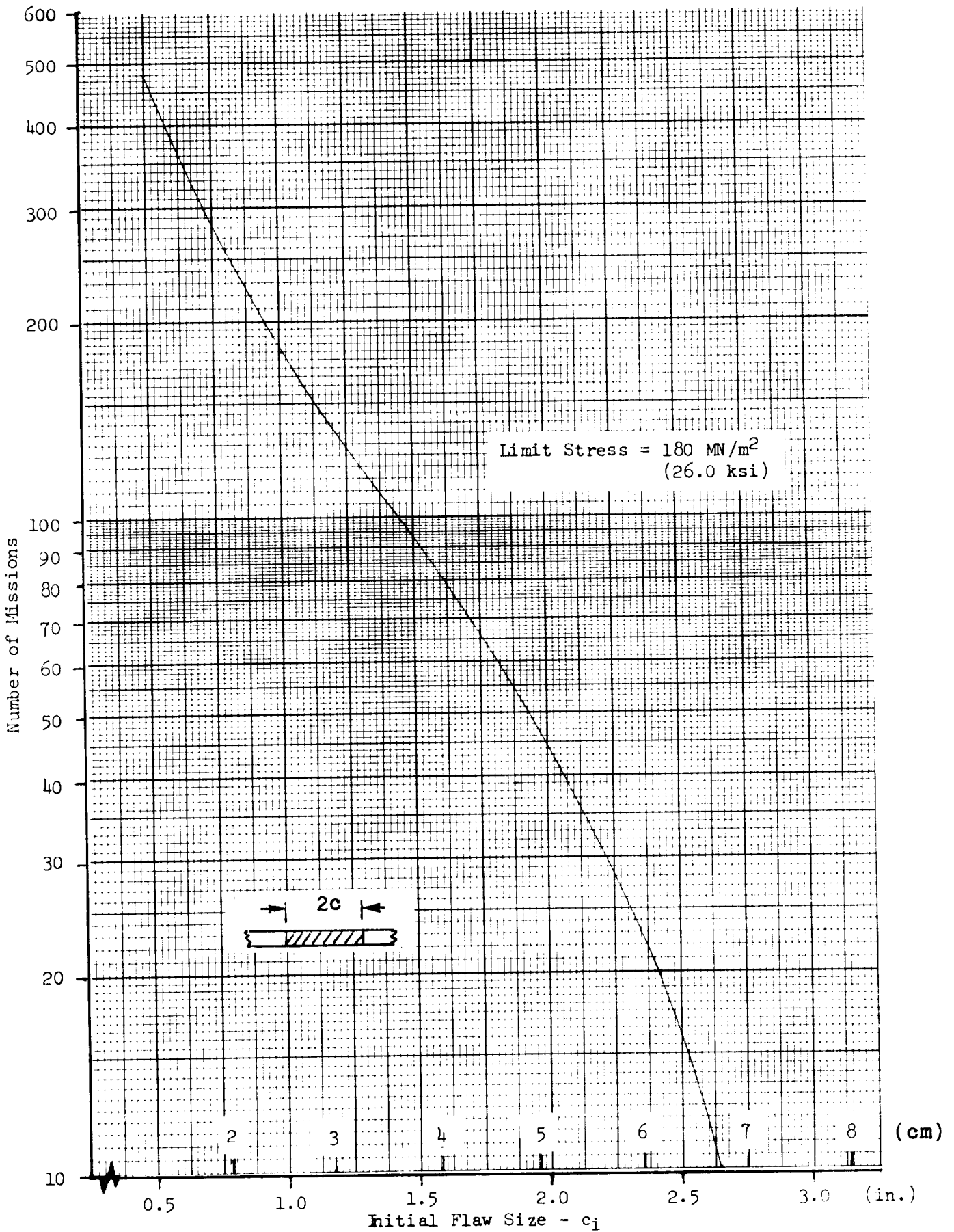


Figure 7-22. Missions to Failure - Through Crack in Vertical Stabilizer Skin

7.4 SAFE-LIFE ANALYSIS - CREW COMPARTMENT

7.4.1 Structural Configuration and Loading

The structural configuration and loading employed in the fatigue analysis (Section 6.8.1) is used directly in the crack growth evaluation. The stress spectrum is derived from repeated compartment pressurization cycles imposed during operational missions and a conservative estimate of associated ferry missions. Because of the simplicity of the loading spectrum, a mission-by-mission stress spectrum is established for crack growth analysis. This spectrum consists of alternate applications of one cycle of 207 MN/m^2 (30 ksi) stress due to the operational mission and 10 cycles of 115 MN/m^2 (16.6 ksi) stress from the ferry mission.

7.4.2 Crack Growth Analysis

Because the crew compartment skins are thin, a through crack is the only type of defect of practical interest. A critical crack size (half length) of 0.81 cm (0.32 in.) is calculated for the limit design stress of 207 MN/m^2 (30 ksi). This prediction is based on a critical stress intensity of $36 \text{ MN/m}^{3/2}$ (33 ksi $\sqrt{\text{in.}}$), which is probably somewhat conservative for the thin skins involved. A plastic zone size based on plane-stress theory is included in the prediction of critical size.

Crack growth characteristics are calculated for initial crack sizes (half-length) of 0.38 cm (0.15 in.) and 0.64 cm (0.25 in.); results are plotted in Figure 7-23. Growth both with and without retardation effects is presented. It can be seen that the predicted retardation is relatively much less than for the wing spar caps. This is due to the difference in the stress spectra associated with each structural element; the spectrum for crew compartment approaches a constant amplitude situation whereas the wing spectrum is highly random.

7.4.3 Design Implications

From Figure 7-23 it can be seen that a maximum initial crack length of approximately 1.27 cm (0.5 in.) can be tolerated within the safe-life design requirements. A through crack of this size should be reliably detected during fabrication and final inspection of the structure. However, a crack of this size caused by accidental damage during the service life might go undetected because of restricted accessibility due to external TPS, internal equipment, etc. Therefore, a fail-safe design concept may be highly desirable to protect against this eventuality.

PREPARED BY: JPS	 Space Division North American Rockwell	PAGE NO. 7-36 of
CHECKED BY:		REPORT NO. SD72-SH-0046
DATE: 12-15-71	CREW COMPARTMENT	MODEL NO. B-9U

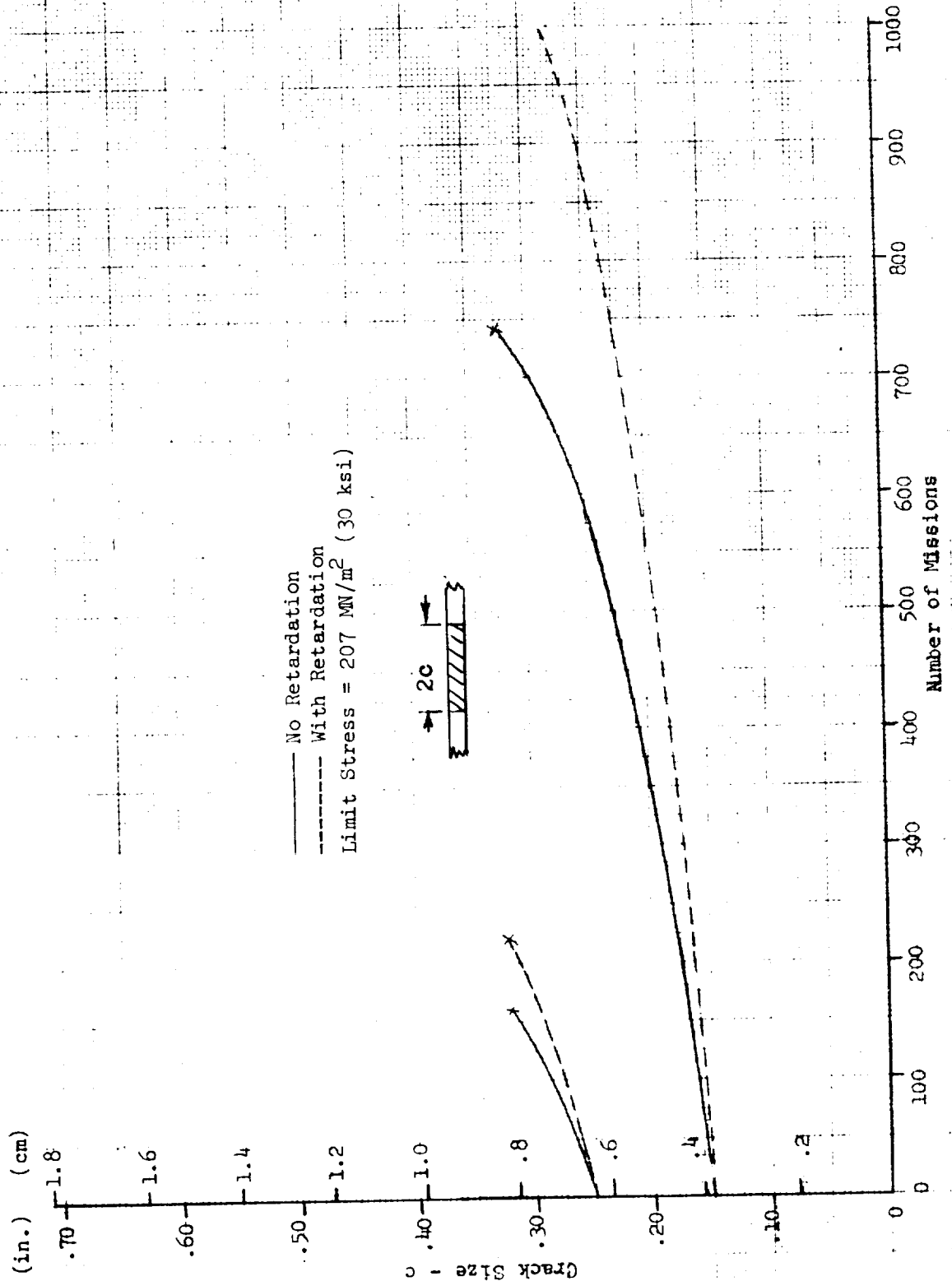


Figure 7-23. Through Crack Growth to Failure - Crew Compartment Skin

7.5 SAFE-LIFE ANALYSIS - ORBITER AFT ATTACH SUPPORT FRAME

7.5.1 Structural Configuration and Loading

A general description of the frame and major loadings is given in the discussion of fatigue analysis (Section 6.6.1). A detailed description of the areas and design loads for frame cap segments is given in Reference 27. A limit design tension load of .246 MN (53 kips) and corresponding area of 9.0 cm² (1.4 in.²) are listed for the critical tension element, bar #6. However, this sizing did not account for the hoop tension stress induced in the frame by tank internal pressure; a cap area of 15.5 cm² (2.4 in.²) is found to be required when this effect is considered. The data of Reference 27 also shows that the required inboard cap area is much less over the lower portion of the frame circumference. Therefore, it is concluded that it is not desirable to incorporate the required area for element #6 as an integral part of the LH₂ tank wall because it would be very difficult to taper it to the smaller area required over much of the frame. An assumed frame cap configuration that provides the required area and is practical to fabricate is shown in Figure 7-24. A simplified stress spectrum is derived from the fatigue analysis stress spectra presented in Table 6-9, and is summarized in Table 7-3 below.

Table 7-3. Orbiter Aft Attach Frame Stress Spectrum

Load Step	Max. Stress (ksi)	Min. Stress (ksi)	Number of Cycles
1	31.5	29.5	16,000
2	31.9	29.1	2,700
3	32.3	28.7	900
4	32.8	28.2	270
5	33.6	27.4	90
6	34.7	26.3	27
7	36.1	24.9	10
8	36.9	24.1	2
9	38.0	23.0	1
10	34.5	0	10

The load block described in Table 7-3 represents 10 flight missions and corresponds to a limit design stress of 290 MN/m² (42 ksi). Crack growth is also investigated for assumed limit stresses of 240 MN/m² (35 ksi) and 207 MN/m² (30 ksi). The stress spectrum for these cases is obtained by applying the appropriate ratio of limit stresses to the values given in Table 7-3.

7.5.2 Crack Growth Analysis

The growth characteristics of a through crack in the flange of the frame cap are evaluated for the limit stress values indicated above and a corresponding assumption of initial flaw size. Growth with and without consideration of retardation effects is calculated; results are plotted in Figure 7-25.

These data are used to construct curves of number of safe-life missions versus initial flaw size, presented in Figure 7-26.

7.5.3 Design Implications

Design loads in the frame cap elements must be expressed in terms of envelopes of maximum tension and compression values resulting from the several potentially critical conditions of external loading applied at the orbiter attachment points. Therefore, a detailed analysis is necessary to determine the effect of imposing safe crack growth limitations on structural weight. The envelope of maximum tension and compression design loads for each cap segment (bar) is given in Reference 27, and is listed in Table 7-4. However, these loads are based on consideration of loads applied to the frame at the orbiter attachment points only. Therefore, a revised envelope of design loads is calculated which includes the effects of tank internal pressure. A frame tensile axial load of 0.36 MN (80,000 lb) has been determined from the discontinuity analysis (see Section 6.6.1) for a tank internal pressure corresponding to the max q_x condition. This force is divided between the inboard and outboard caps in proportion to their respective cross section areas. Revised envelopes of design loads, including this effect, are listed in Table 7-4. Reference areas of cap segments are calculated on the basis of these revised loads and allowable limit stresses as follows:

$$\text{Tension:} \quad \sigma_{\text{allow}} = \frac{0.95 F_{tu}}{1.4} = 42 \text{ ksi.}$$

$$\text{Compression:} \quad \sigma_{\text{allow}} = \frac{F_{cy}}{1.4} = 36 \text{ ksi.}$$

The 5 percent reduction in tensile ultimate strength is an allowance for fastener holes or other local reductions in net section area. The change in area of each cap segment to limit the maximum tension stress to 35 ksi and 30 ksi, respectively, and corresponding weight increases are summarized in Table 7-4. The resulting frame weight increase as a function of maximum tension stress is plotted in Figure 7-27. These data are used with the safe-life curves of Figure 7-26 to develop curves of frame weight increase versus initial flaw size presented in Figure 7-28.

It can be seen that the frame weight increase is relatively small for significant increases in initial flaw size. For example, an initial through crack of approximately 0.76 cm (0.3 in.) length can be tolerated in the caps of a frame designed to static strength requirements. If this initial size is increased to a length of 1.27 cm (0.5 in.) the weight increase is 24 kg (53 lb) for 100 mission life and 31 kg (69 lb) for 200 mission life. This is in the range of 4 percent of the frame basic structural weight. Therefore, it is concluded that safe-life requirements are feasible and will not impose a significant weight penalty on the design of the booster major frames.

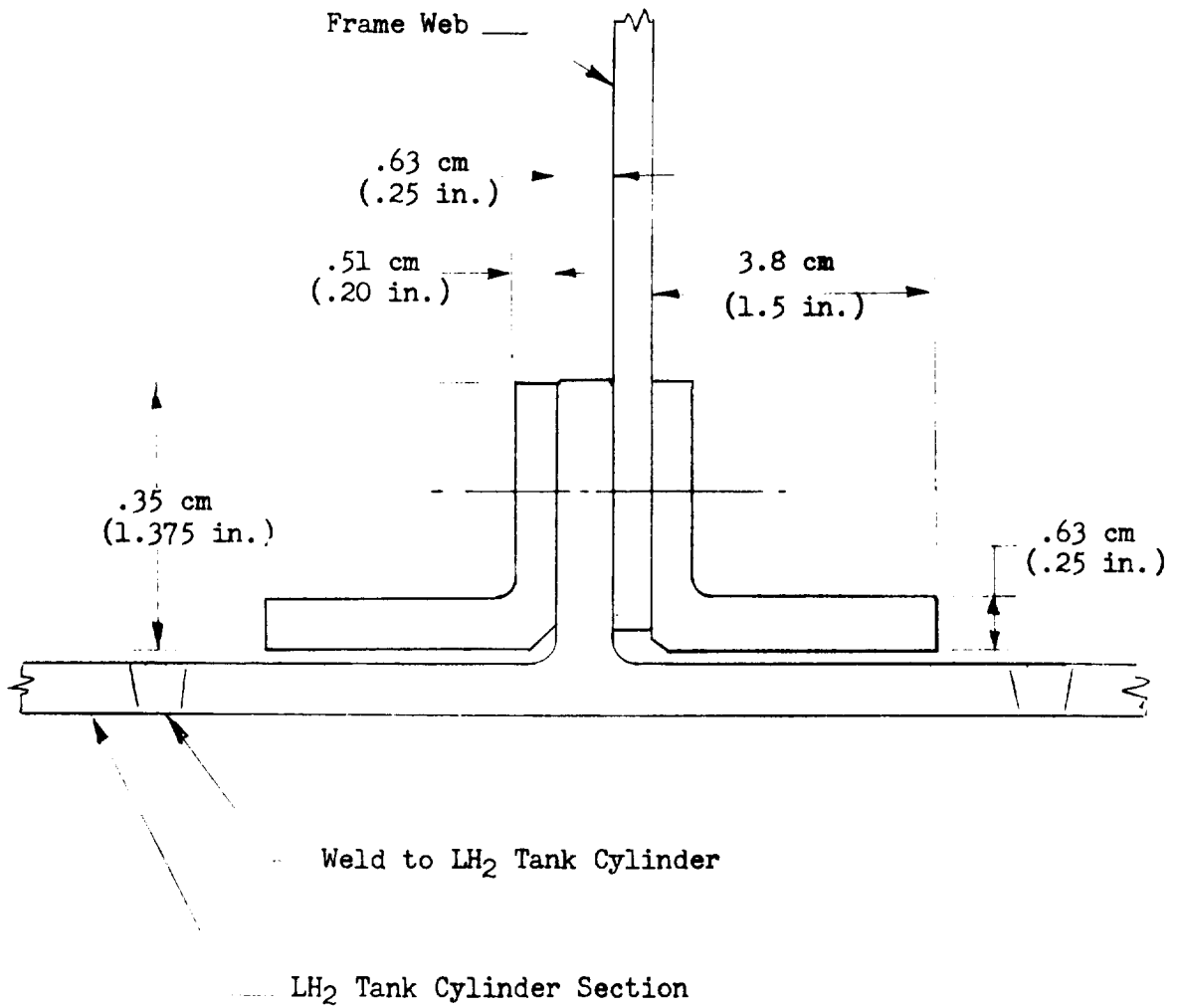



Figure 7-24. Frame Cap Configuration - Orbiter Aft Attach

PREPARED BY: JPS	 Space Division North American Rockwell	PAGE NO 7-40 OF
CHECKED BY:		REPORT NO SD72-SH-0046
DATE: 12-15-71	ORBITER AFT ATTACH FRAME	MODEL NO B-9U

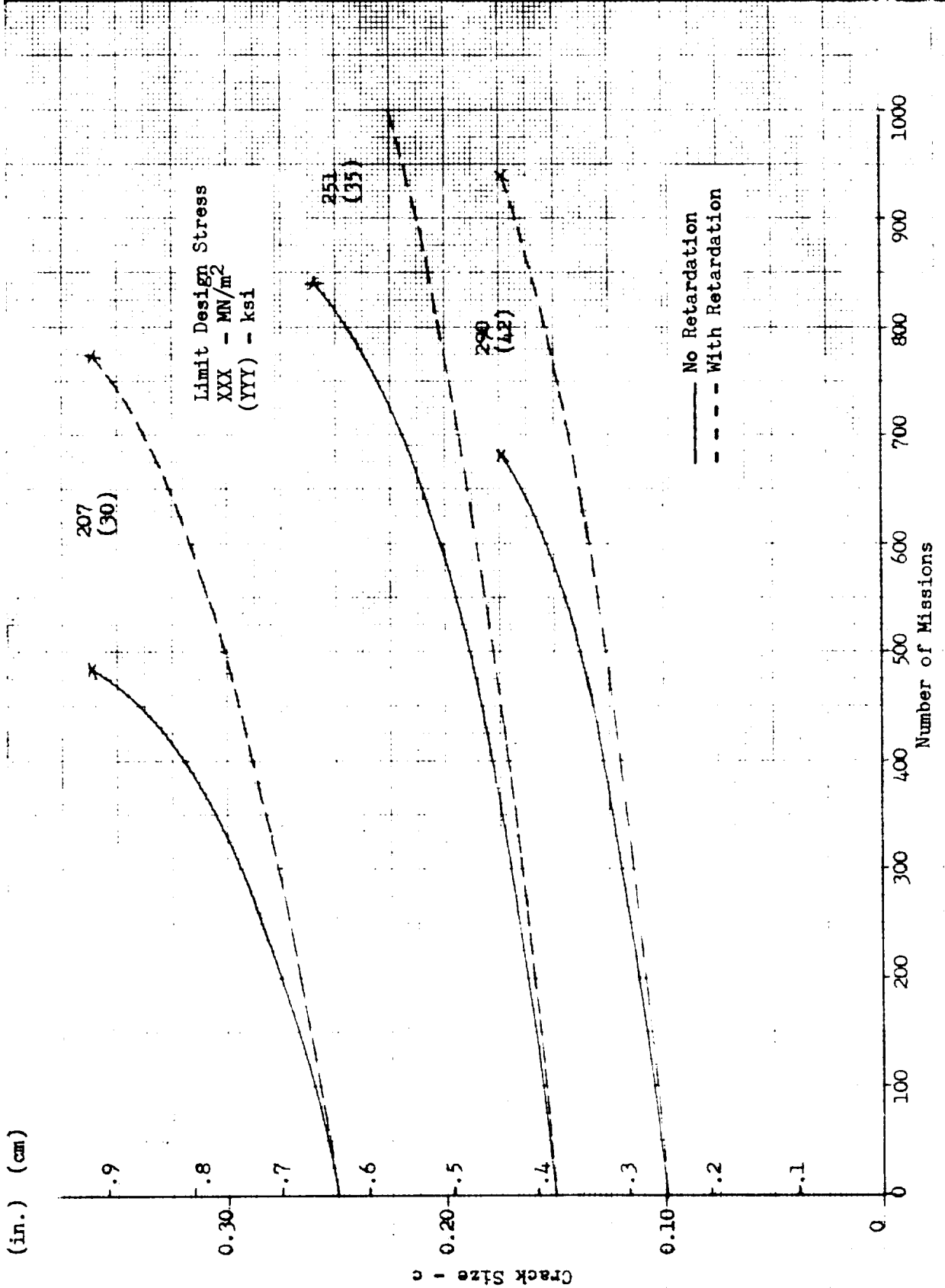


Figure 7-25. Through Crack Growth to Failure - Orbiter Aft Attach Frame Cap

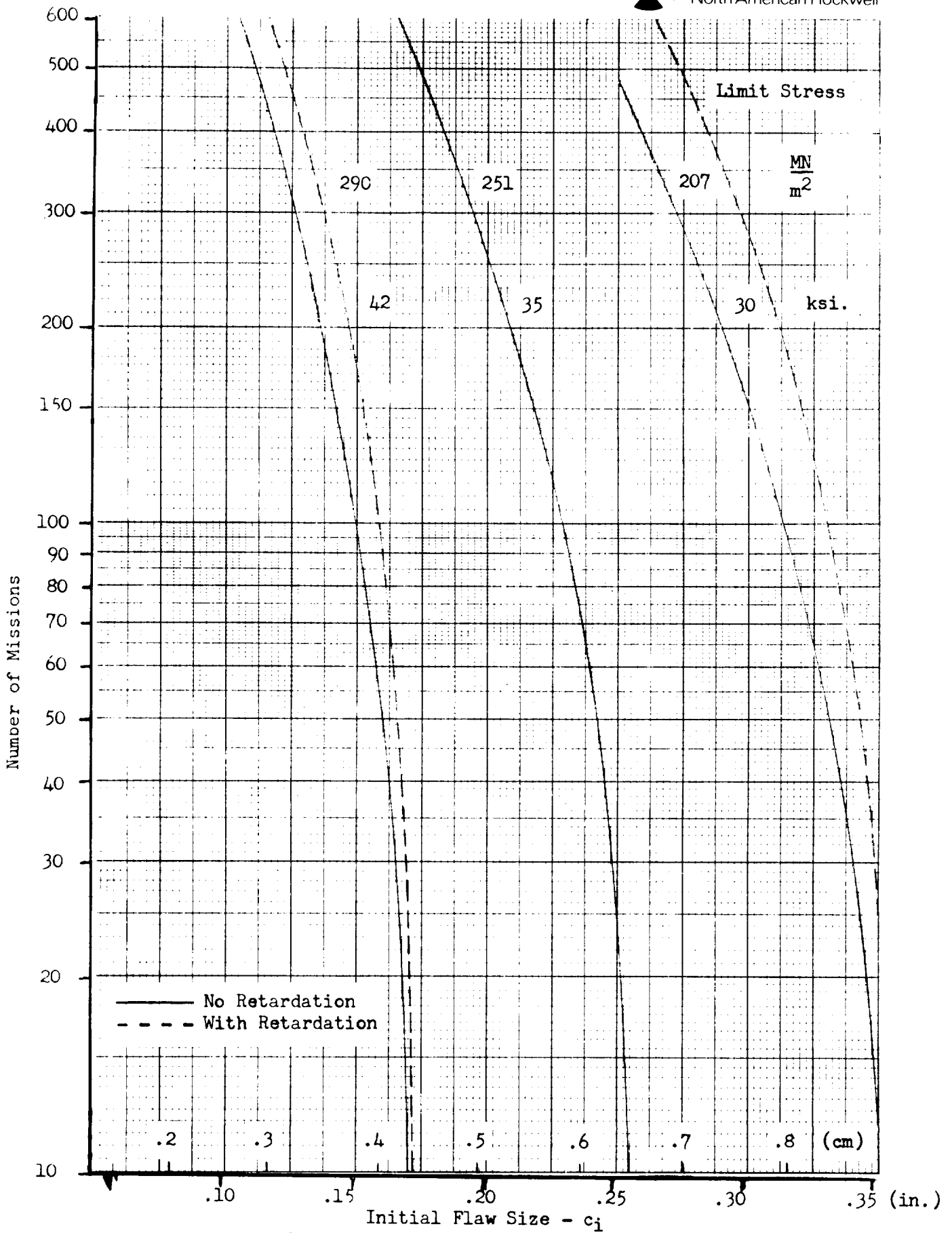


Figure 7-26. Missions to Failure - Through Crack in Orbiter Aft Attach Frame Cap

Table 7-4. Cap Areas and Weight Increases -
 Orbiter Aft Attach Support Frame

Bar no.	(1) Original Design Load (kips)		(2) Revised Design Load (kips)		(3) A_0 (in. ²)	$\sigma_{tens} = 35 \text{ ksi}$		$\sigma_{tens} = 30 \text{ ksi}$	
	Tens.	Comp.	Tens.	Comp.		ΔA (in. ²)	ΔW (lb)	ΔA (in. ²)	ΔW (lb.)
1	216	268	266	218	6.3	1.3	5.3	2.6	10.6
2	---	167	30	137	3.8	0	0	0	0
3	157	269	211	215	6.0	0	0	1.0	5.1
4	62	129	88	103	2.9	0	0	0	0
5	---	186	62	124	3.7	0	0	0	0
6	53	---	71	---	1.7	0.3	1.9	0.7	4.4
7	---	303	58	245	6.8	0	0	0	0
8	62	115	84	93	2.6	0	0	0.2	1.3
9	---	79	30	49	1.6	0	0	0	0
10	18	132	68	82	2.6	0	0	0	0
11	24	4	42	---	1.0	0.2	2.1	0.4	4.2
12	---	62	62	---	1.5	0.3	2.8	0.6	5.6
13	1	---	41	---	1.0	0.2	1.1	0.4	2.2
14	9	5	49	---	1.2	0.2	1.0	0.4	1.9
15	0	4	40	---	1.0	0.1	0.7	0.3	2.1
16	16	0	56	---	1.3	0.3	1.7	0.6	3.5
17	---	5	40	---	1.0	0.1	0.7	0.3	2.1
18	10	---	50	---	1.2	0.2	1.1	0.5	2.7
19	---	4	40	---	1.0	0.1	0.8	0.3	2.5
20	4	---	44	---	1.1	0.2	1.3	0.4	2.5
						$2 \times \Sigma$	41.0		101
(1) Limit loads due to orbiter attach forces. (2) Limit loads including effects of tank internal pressure. (3) Reference cap areas based on allowable limit stresses: Tension $\sigma_{allow} = 42 \text{ ksi.}$ Compression $\sigma_{allow} = 36 \text{ ksi.}$									

PREPARED BY: JPS



Space Division
North American Rockwell

PAGE NO 7-43 OF

CHECKED BY:

REPORT NO SD72-SH-0046

DATE: 1-6-72

ORBITER AFT ATTACH FRAME

MODEL NO B-9U

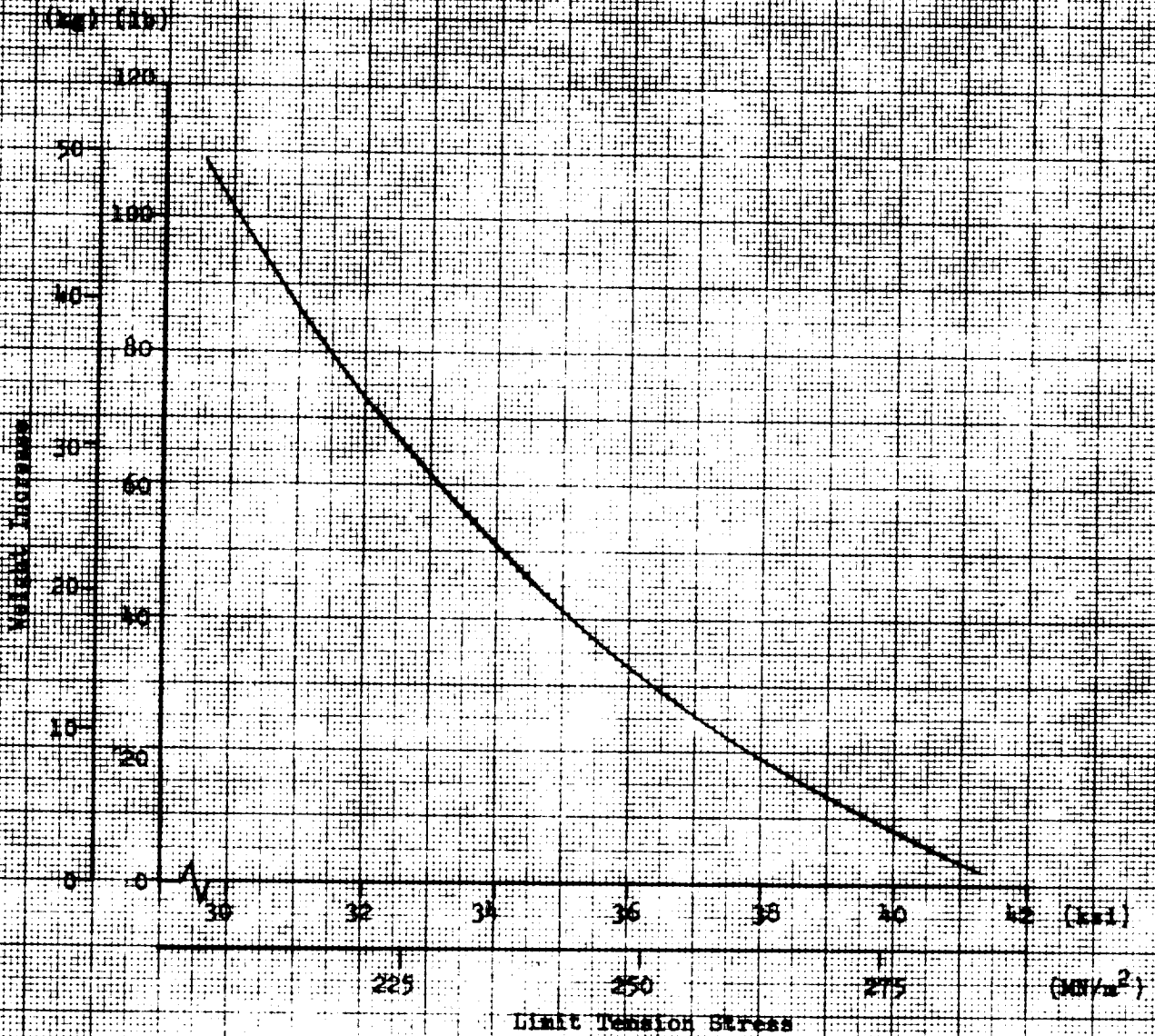


Figure 7-27. Effect of Frame Cap Limit Stress on Weight of Orbiter Aft Attach Bulkhead

PREPARED BY: JPS	 Space Division North American Rockwell	PAGE NO. 7-44 OF
CHECKED BY:		REPORT NO. SD72-SH-0046
DATE: 1-6-72	ORBITER AFT ATTACH FRAME	MODEL NO. B-9U

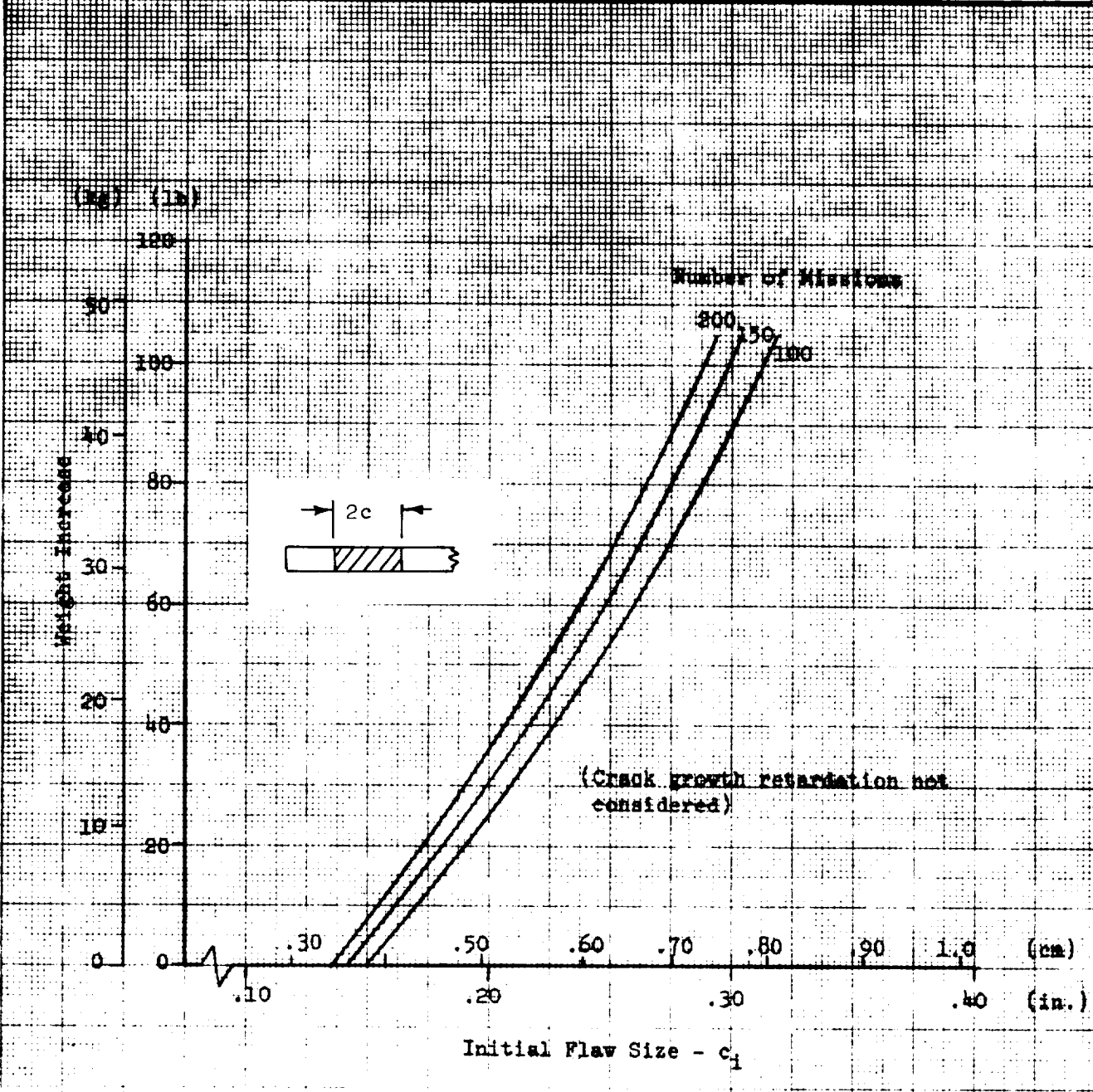


Figure 7-28. Effect of Initial Flaw Size on Structural Weight for Safe Life-Orbiter Aft Attach Bulkhead

7.6 SAFE-LIFE ANALYSIS - FUSELAGE STA. 2600

7.6.1 Structural Configuration and Loading

A general description of the LH₂ tank shell and major loadings in the region of fuselage Sta. 2600 is given in the discussion of fatigue analysis (Section 6.5). Maximum limit design stress occurs at the burnout condition with internal tank pressure of 0.154 MN/m² (22.3 psi), and is comprised of the following elements:

Body axial load and bending moment	- 110 MN/m ² (16.0 ksi)
Membrane stress due to tank pressure	- 111 MN/m ² (16.1 ksi)
Discontinuity bending stress	- 36 MN/m ² (5.2 ksi)
Total	257 MN/m² (37.3 ksi)

A simplified stress spectrum for crack growth analysis is derived from the fatigue stress spectra given in Table 6-8. The procedure is similar to that described for the wing crack growth analysis, and the results are summarized in Table 7-5. This spectrum includes the effects of discontinuity bending stresses and is based on nominal tank pressures.

Table 7-5. Fuselage Sta. 2600 Stress Spectrum

Load Step	Max. Stress (ksi)	Min. Stress (ksi)	Number of Cycles
1	3.8	1.4	9990
2	4.4	0.8	11
3	13.9	10.5	7000
4	14.6	9.8	2000
5	15.4	9.0	700
6	16.9	7.5	270
7	17.7	6.2	20
8	18.4	6.0	10
9	19.9	4.5	3
10	35.8	0	10
11	17.5	16.5	7000
12	18.1	16.5	2700
13	18.5	16.5	200
14	19.1	16.5	70
15	21.0	16.5	20
16	22.9	17.1	10
17	10.9	7.3	9990
18	11.3	6.9	10
19	11.7	6.5	1

The load block described in Table 7-5 represents 10 flight missions and corresponds to the limit design stress of 257 MN/m² (37 ksi). Load step 10 represents the effective GAG cycle in which the total tension stress increases from zero at prelaunch to a maximum at burnout once per mission.

7.6.2 Crack Growth Analysis

A surface crack is the only type of initial defect of interest for the propellant tanks; a through crack would presumably be detected by leak tests prior to the mission. Therefore, a part-through crack with aspect ratio (a/2c) of 0.10 is selected as the basic model for this study. Critical size is based on transition to a through crack, rather than instability. For this study, transition is assumed to occur when the remaining ligament thickness is equal to the plastic zone size. Because of the relatively thin material, the plastic zone size is assumed to be given by the plane stress equation:

$$r_p = \frac{1}{2\pi} \left(\frac{K_I}{\sigma_y} \right)^2$$

Substituting the equation for stress intensity of a part-through crack, and rearranging terms yields the expression:

$$r_p = t-a = \frac{1}{2\pi} \left[\frac{1.95 M_K \sigma}{\sigma_y} \right]^2 \left(\frac{a}{Q} \right)$$

which can be put in the form:

$$\frac{a}{t} = \frac{1}{1 + \frac{1}{2\pi Q} \left(\frac{1.95 M_K \sigma}{\sigma_y} \right)^2}$$

This equation is solved by iteration using limit applied stress and a deep flaw magnification factor as given by Figure 5-12; a value of a/t = 0.668 at crack break-through is determined. The critical crack depth is therefore:

$$a_{cr} = 0.668 (0.120) = 0.080 \text{ in.}$$

Crack growth to critical size is calculated for several assumed initial flaw depths, both with and without retardation effects included. Results are plotted in Figure 7-29. These data are used to construct curves of number of safe-life missions versus initial flaw size, presented in Figure 7-30.

7.6.3 Design Implications

It can be seen from Figures 7-29 and 7-30 that crack growth is relatively small, even without retardation effects considered. For a safe life of 100 missions, an initial flaw depth of 0.19 cm (0.075 in.) can be tolerated; for 200 missions the allowable initial size is reduced to 0.18 cm (0.070 in.).

These initial flaw depths are in the order of 60 percent of the skin thickness, with corresponding surface length of about 1.8 cm (0.70 in.). Flaws of this character should be reliably detected by existing inspection practices and NDE techniques. Therefore, it is concluded that no special design provisions are required to assure safe life for the case of part-through cracks oriented in the circumferential direction in propellant tank skins.

Examination of the detailed computer output of crack growth analysis indicated that about 94 percent of the total growth was due to the effective GAG cycles of load step 10. This shows that alternating load cycles due to atmospheric turbulence and entry maneuvers have relatively small effect on the total crack growth.

PREPARED BY: JPS	 Space Division North American Rockwell	PAGE NO. 7-48 OF
CHECKED BY:		REPORT NO. SD72-SH-0046
DATE: 1-5-72	FUSELAGE STA. 2600	MODEL NO. B-9U

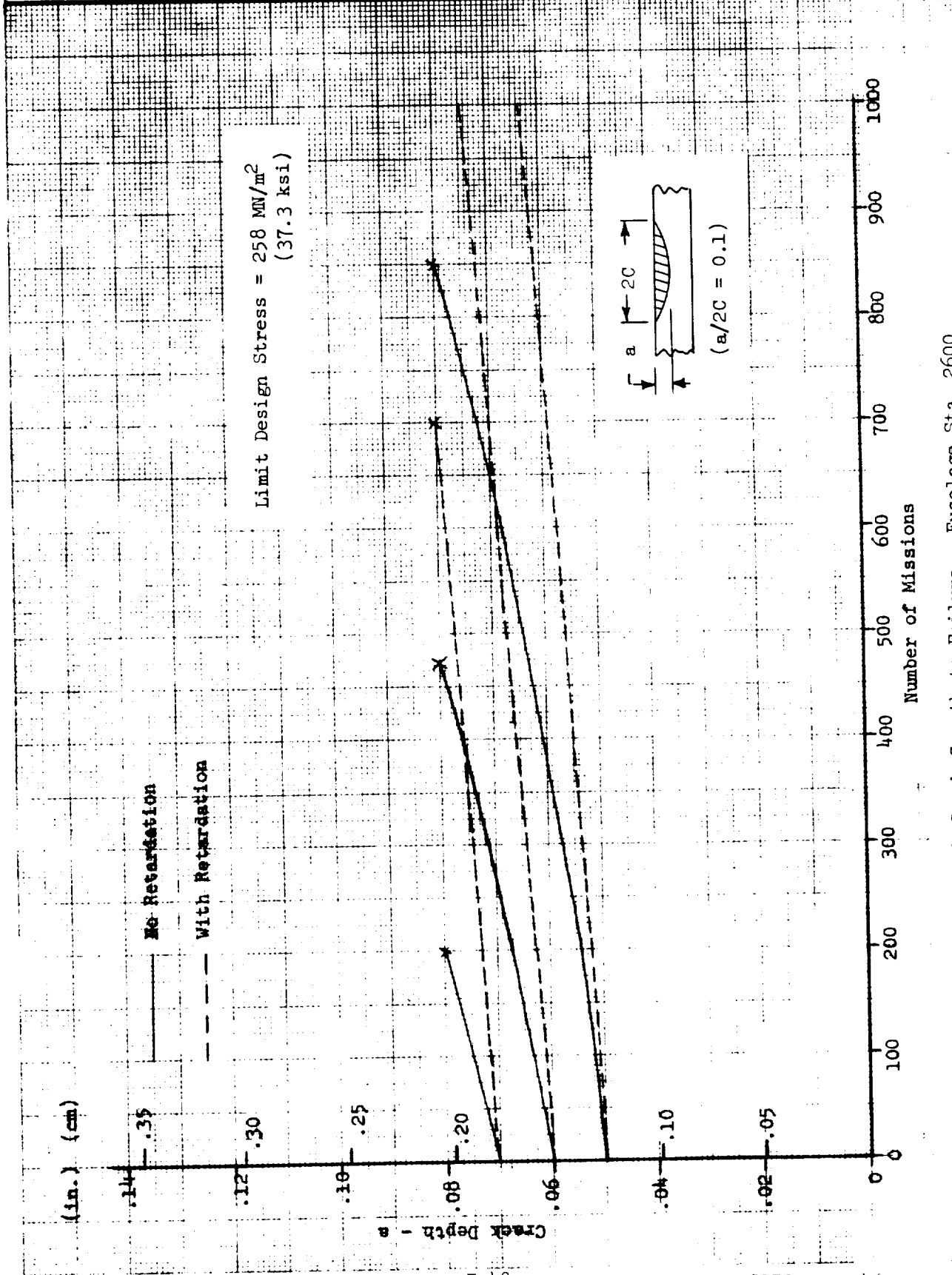


Figure 7-29. Part-Through Crack Growth to Failure - Fuselage Sta. 2600

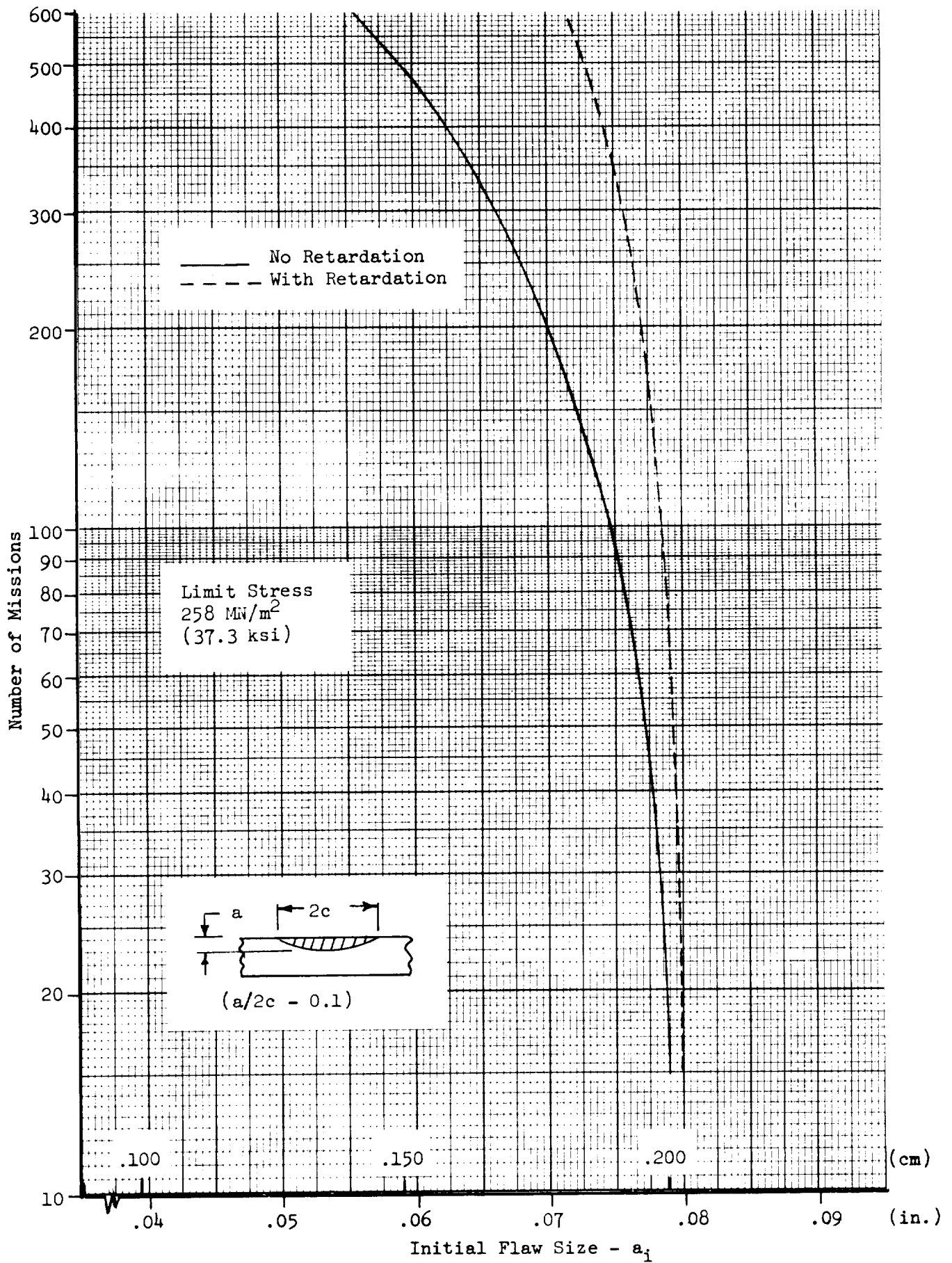


Figure 7-30. Missions to Failure - Part-Through Crack in LH₂ Tank Skin (Sta. 2600) - Circumferential Orientation
7-49 SD72-SH-0046

7.7 SAFE-LIFE ANALYSIS - PROPELLANT TANKS

7.7.1 Structural Configuration and Loading

Crack growth and fracture analyses are presented in this section for parent metal and weld joint in the aft region of the LH₂ tank cylinder and for parent metal at the apex of the LO₂ tank aft bulkhead. Propellant tanks are of 2219-T87 aluminum alloy. The general structural configurations for these tank elements are described in the appropriate portions of the fatigue analysis (Sections 6.5.1 and 6.7.1). Crack orientation is assumed to be normal to the maximum principal stress direction in these tank elements. This principal stress is not significantly affected by loadings other than tank internal pressure, so simple load spectra, derived from ground test and flight pressurizations, are applicable for these elements. A baseline reference thickness and corresponding stress level for parent metal is established from ultimate strength design requirements and the ultimate factor of safety of 1.4. Weld land thickness is assumed to be twice the corresponding thickness of parent metal. The limit stresses, material thicknesses, and alternating stress spectra for the reference propellant tank elements are given in Table 7-6. The limit tank pressures are established by maximum relief valve settings; the alternating stresses in the service load spectra are based on normal pressure regulator ranges.

Table 7-6. Propellant Tank Stress Spectra

Parameter		LH ₂ Tank Cylinder - Aft Region		LO ₂ Tank Aft Bulkhead (Parent Metal)
		Parent Metal	Weld	
Design Temperature		70 F	70 F	-297 F
Limit Design Stress (ksi)		44.4	22.2	53.0
Minimum Thickness (in.)		0.114	0.228	0.117
Ground Test	σ_{\max} (ksi)	33.8	16.9	32.4
Pressure	σ_{\min} (ksi)	0	0	0
Cycles	N ⁽¹⁾	3	3	3
Flight	σ_{\max} (ksi)	41.6	20.8	50.5
Pressure	σ_{\min} (ksi)	0	0	0
Cycles	N ⁽¹⁾	1	1	1
(1) Number of stress cycles per mission				



In addition to the limit stresses defined above, which are based on static strength design requirements, arbitrary values of reduced limit operating stresses are also investigated to evaluate parametric trends of crack growth, critical flaw sizes, and proof test requirements as a function of operating stress. The material thickness and spectral stress levels are adjusted to correspond to these revised values of limit stress. The selected limit stresses (parent metal) are 44.4 ksi, 40.0 ksi and 35.0 ksi for the LH₂ tank; 53.0 ksi, 50.0 ksi and 45.0 ksi for the LO₂ tank.

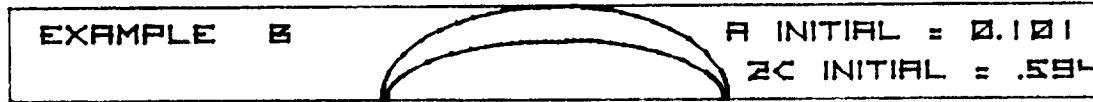
7.7.2 Crack Growth Analysis

Because of the structural configuration and service application involved, a part-through crack is the only type of initial defect of practical interest. Crack growth characteristics are calculated, assuming various arbitrary initial flaw sizes, to determine the number of missions until fracture or break-through (leakage) occurs. Aspect ratios of both $a/2c = 0.1$ and 0.4 are considered, so as to bound the practical range of interest.

Growth analyses are accomplished using a computer program recently developed at NR SD for use on the Hewlett-Packard Model 9810 computer/plotter. This program accommodates the NR SD generalized growth rate expression and also calculates the growth of a surface crack in both the length and depth direction, thus accounting for the effect of changing aspect ratio during crack propagation on the stress intensity and corresponding growth rate. Basic growth rate data represented by Figure 5-14 are used with deep flaw magnification factors corresponding to Figure 5-12 in the crack growth analyses. Break-through is assumed to occur when the crack depth is equal to the material thickness. Fracture is predicted when the applied stress intensity is equal to the critical value (K_C) for the appropriate case listed in Figure 5-14. Retardation effects are not considered.

Excellent agreement has been obtained between theoretical predictions, using the methods described above, and experimental data for cycles to break-through on 2219-T87 aluminum specimens of representative thickness. Examples of this predictive analysis for a range of initial aspect ratios are given in the computer drawn plots of Figure 7-31. Crack growth to breakthrough is plotted for three selected specimens and cross section sketches of the corresponding initial and predicted final crack configurations are indicated. A comparison of predicted cycles to breakthrough with experimental results is given in Figure 7-32. Test data reflected in this plot were generated by Lockheed under NASA MSC Contract NAS9-11722. The predictive analyses used as a starting point the actual initial flaw geometry of the test specimens (determined by post-test examination of the fracture surface).

Results of the crack growth analyses are summarized in the computer drawn plots presented in Figures 7-33 through 7-41. These data are used to construct curves of number of safe life missions versus initial flaw size, presented in Figures 7-42 through 7-44.



CRACK GROWTH PREDICTION FOR 2219-T87 ALUMINUM
 THICKNESS = 0.16 INCH
 SIGMA MAX = 28 KSI, SIGMA MIN = 0.58 KSI
 KSUBC = 40 KSI $\sqrt{\text{IN.}}$, K SUB 0 = 5 KSI $\sqrt{\text{IN.}}$
 C = 0.0115, N = 2.63, RT, LAB AIR

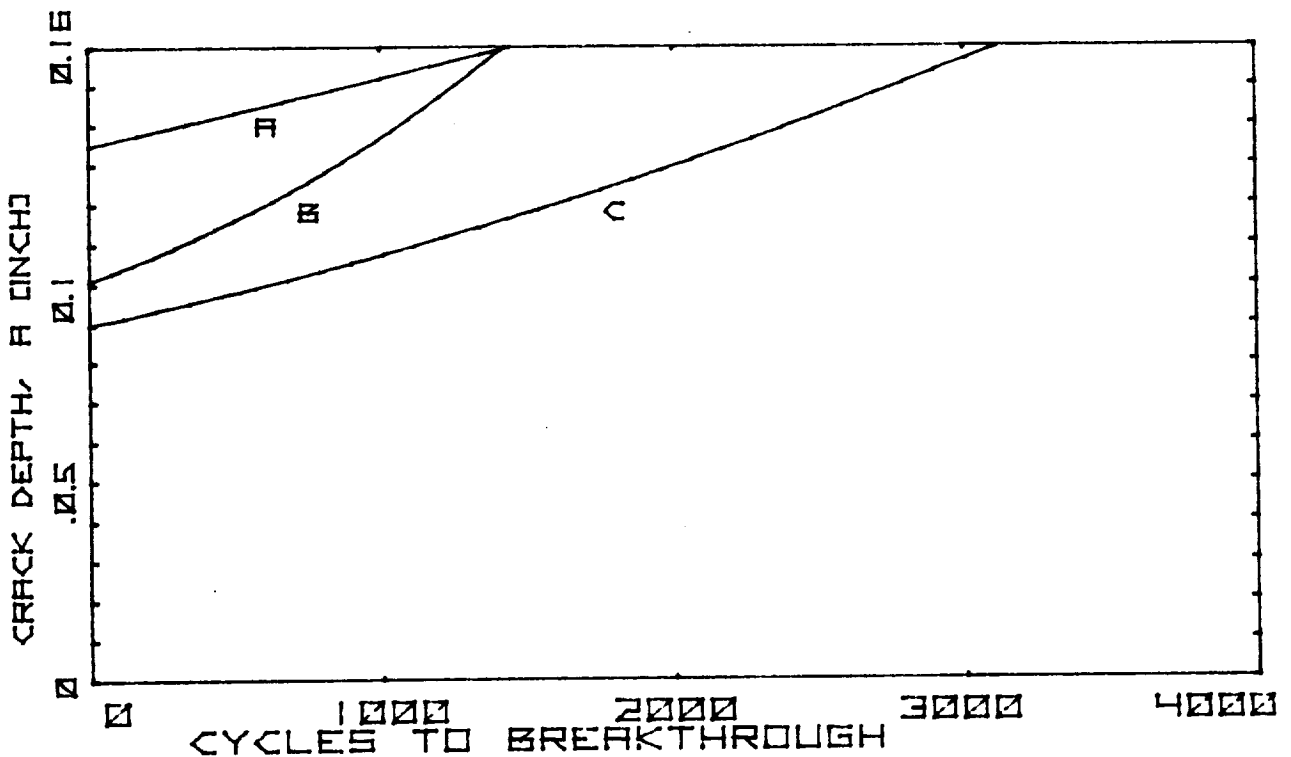


Figure 7-31. Predicted Two-Dimensional Growth for Part-Through Cracks

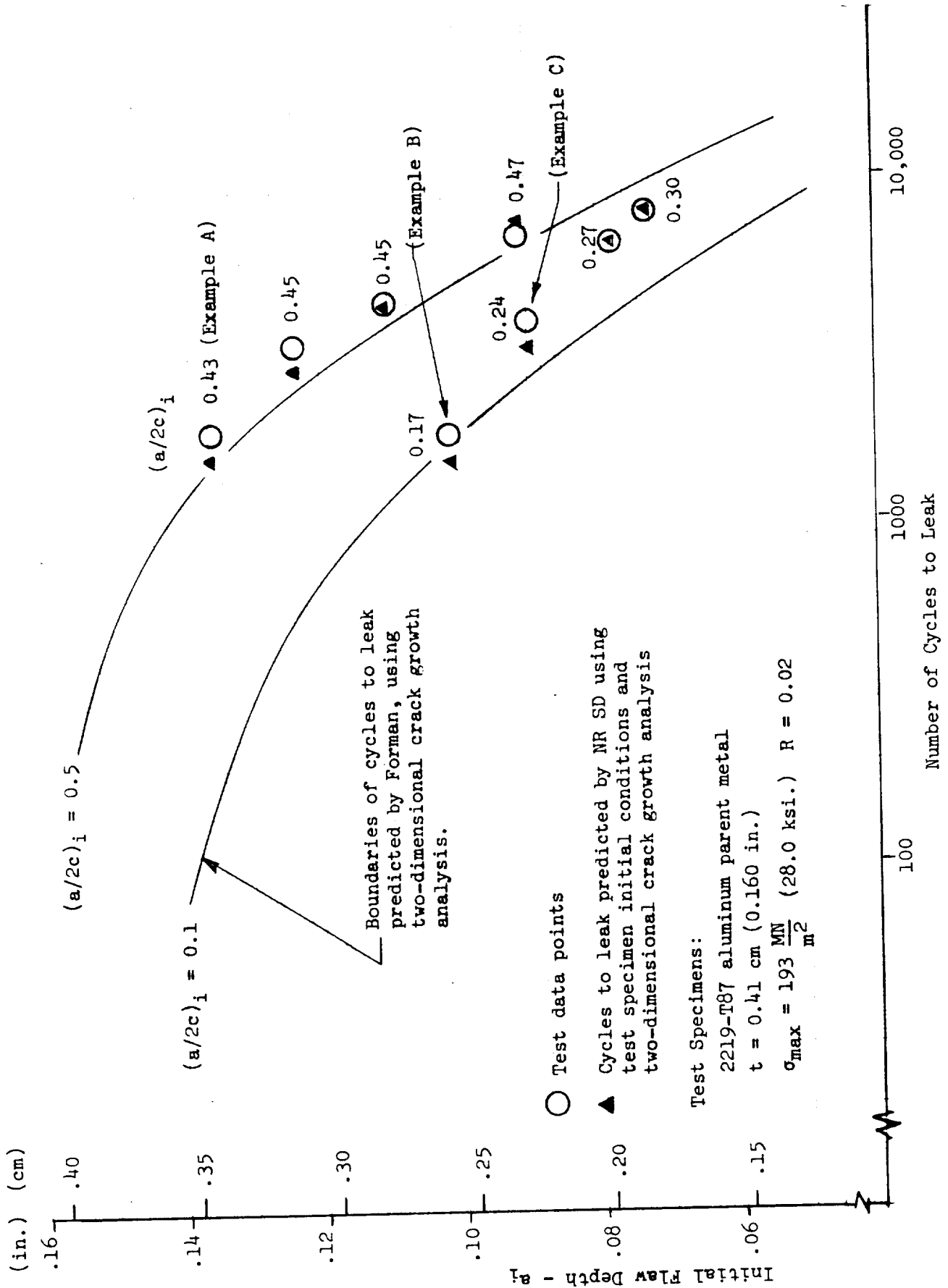


Figure 7-32. Comparison of Predicted Load Cycles to Leak With Experimental Results

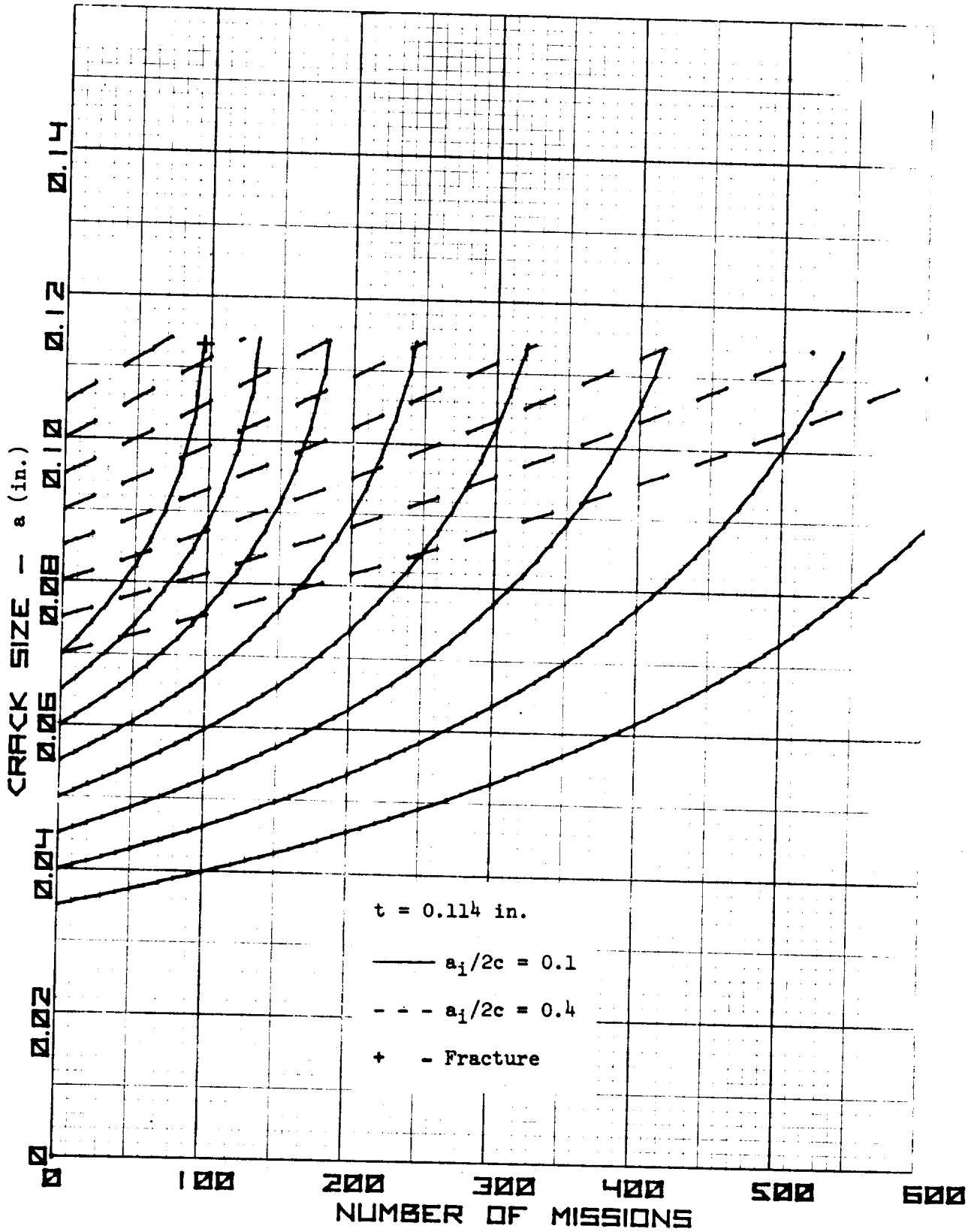


Figure 7-33. Crack Growth to Failure - LH₂ Tank Parent Metal
($\sigma_{lim} = 44.4$ ksi)

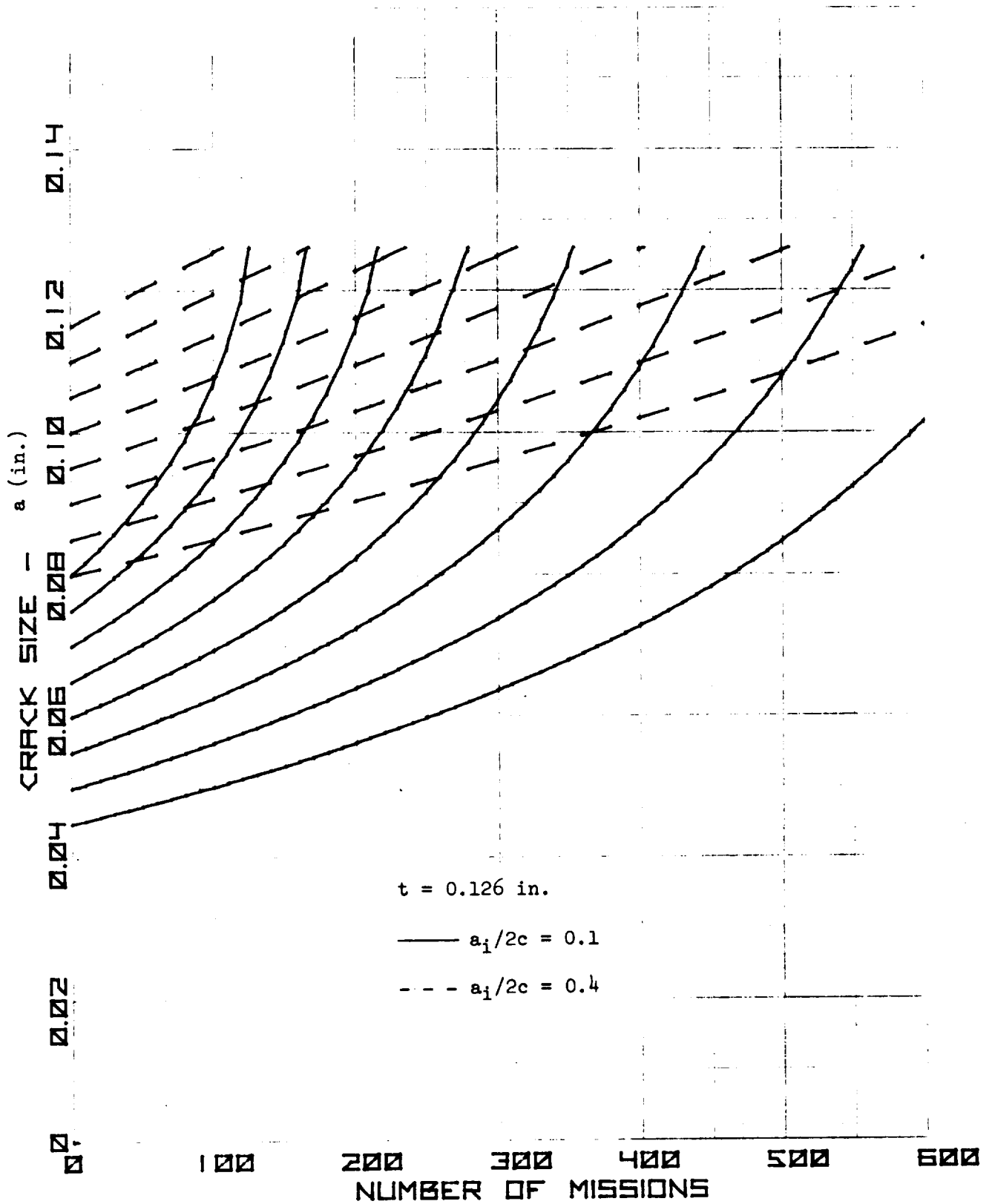


Figure 7-34. Crack Growth to Failure - LH₂ Tank Parent Metal
($\sigma_{lim} = 40.0$ ksi)

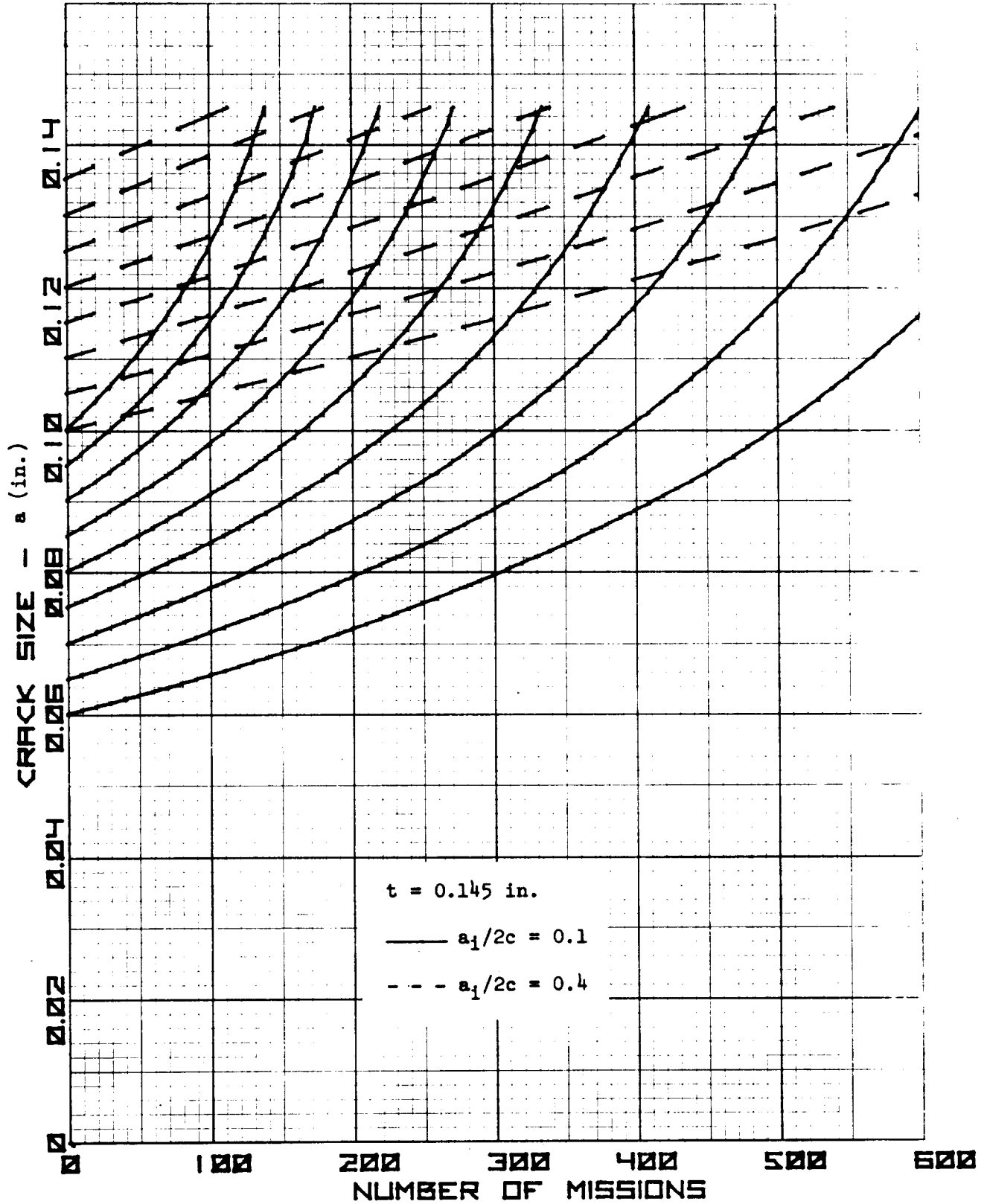


Figure 7-35. Crack Growth to Failure - LH₂ Tank Parent Metal
($\sigma_{lim} = 35.0$ ksi)

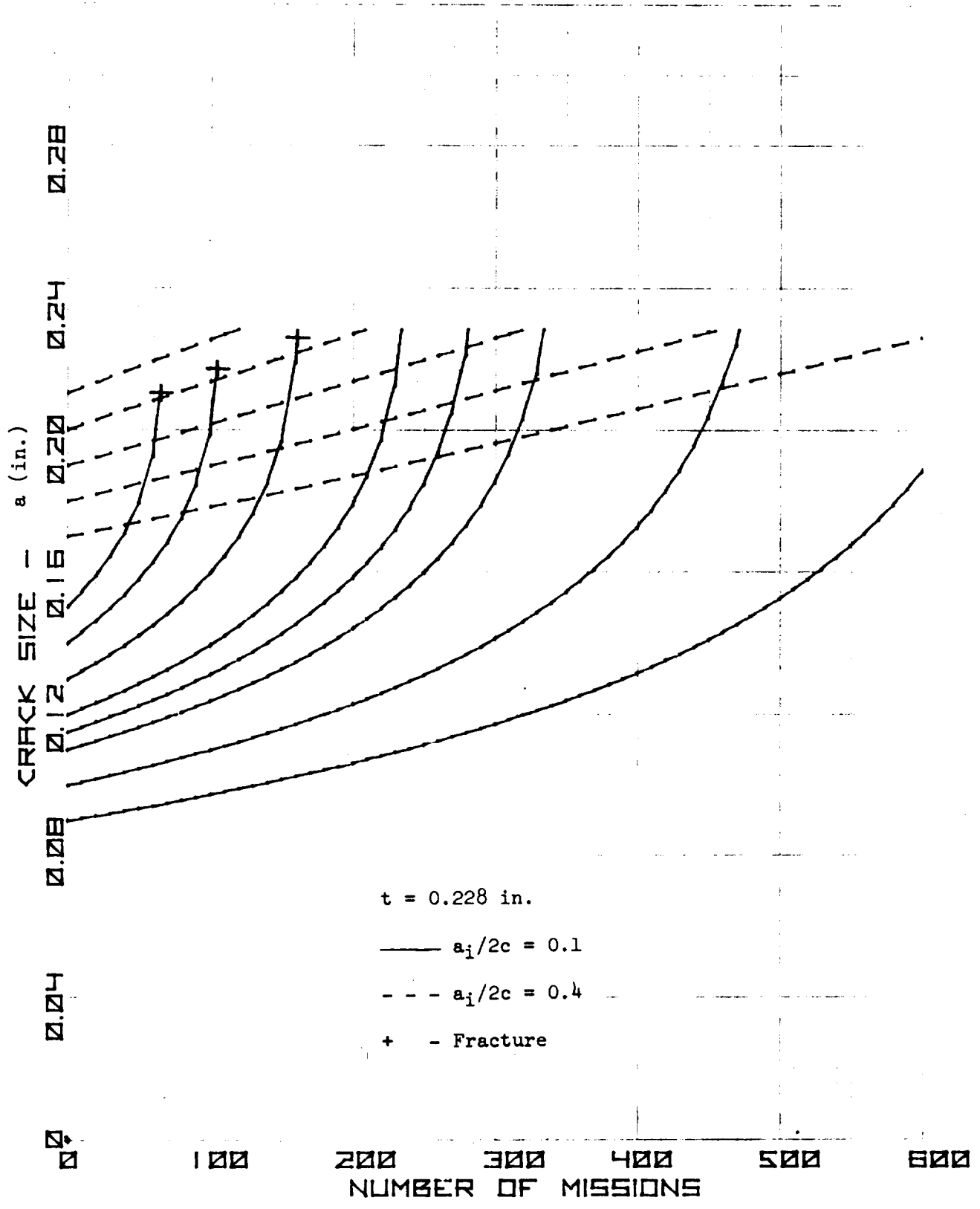


Figure 7-36. Crack Growth to Failure - LH₂ Tank Welds
($\sigma_{lim} = 22.2$ ksi)

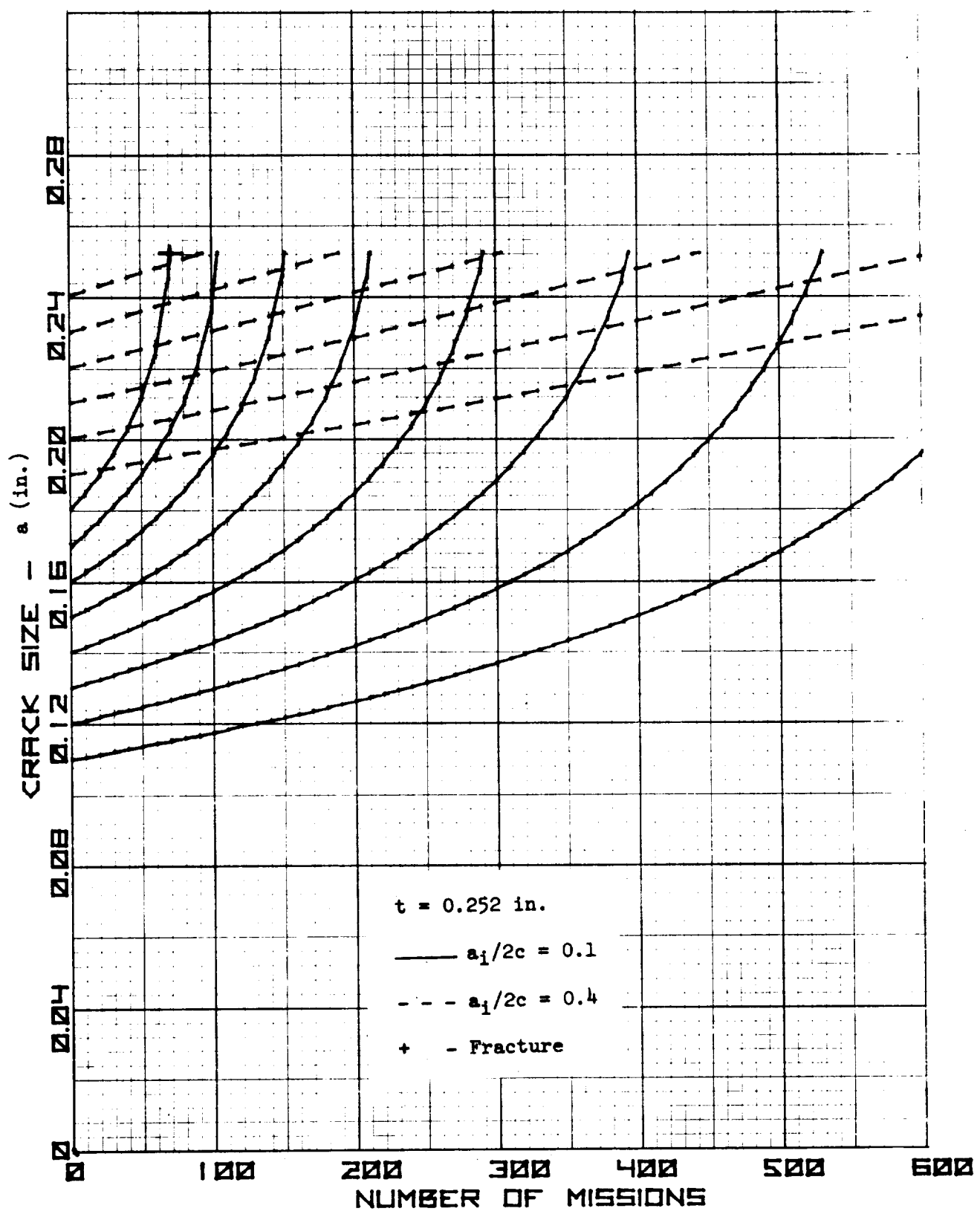


Figure 7-37. Crack Growth to Failure - LH₂ Tank Welds
($\sigma_{lim} = 20.0 \text{ ksi}$)

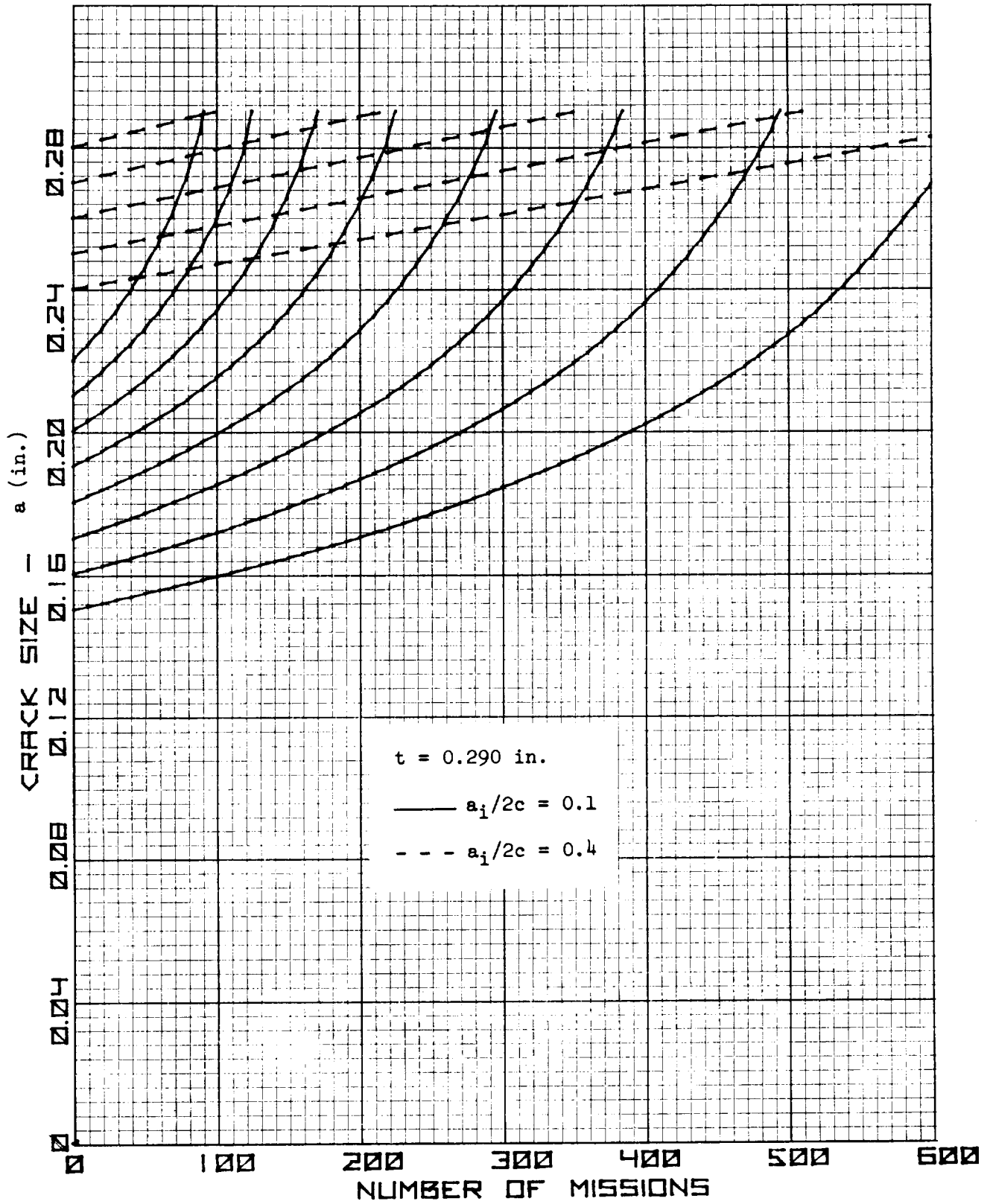


Figure 7-38. Crack Growth to Failure - LH₂ Tank Welds
($\sigma_{lim} = 17.5$ ksi)

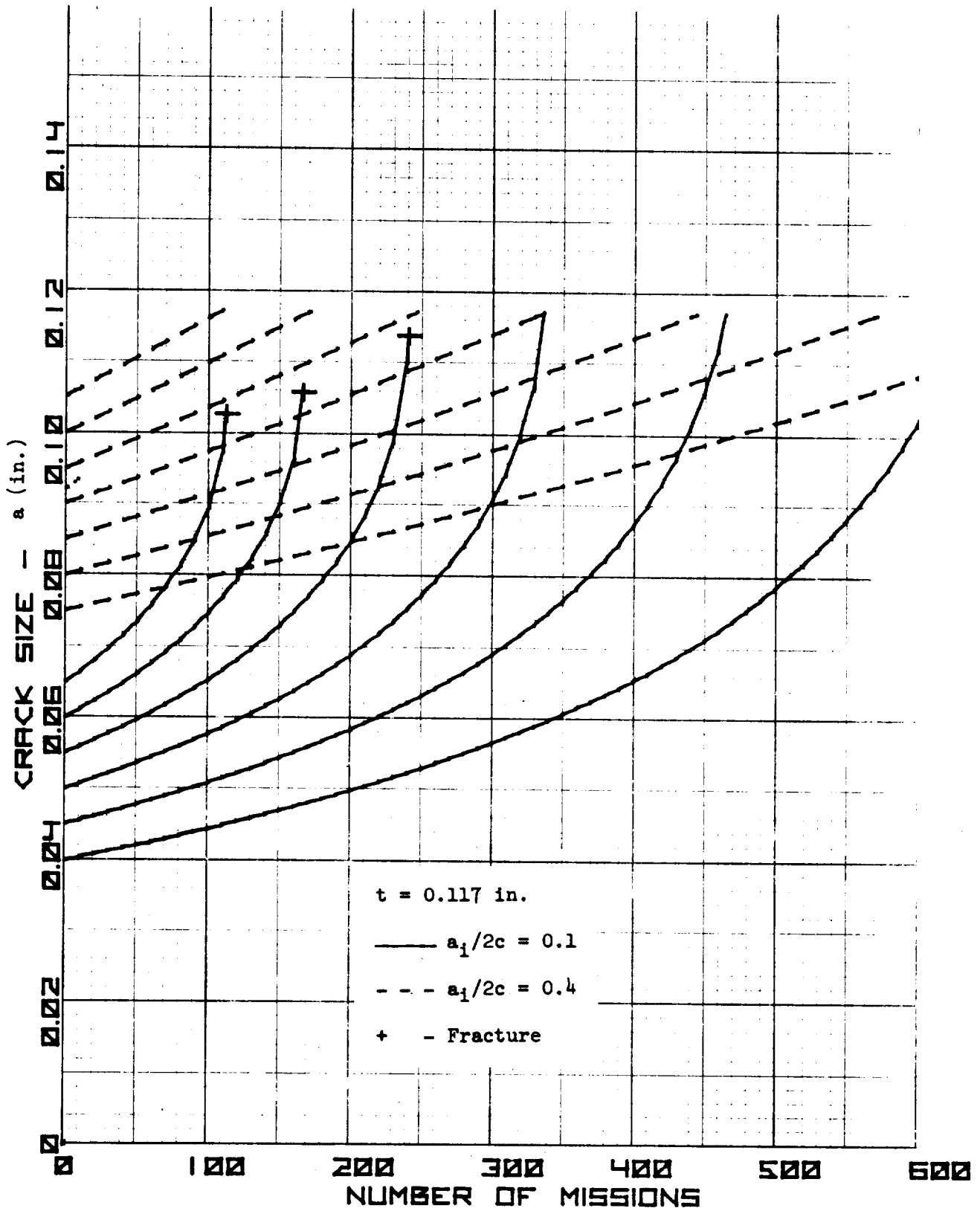


Figure 7-39. Crack Growth to Failure - LO₂ Tank Parent Metal
($\sigma_{lim} = 53.0$ ksi)

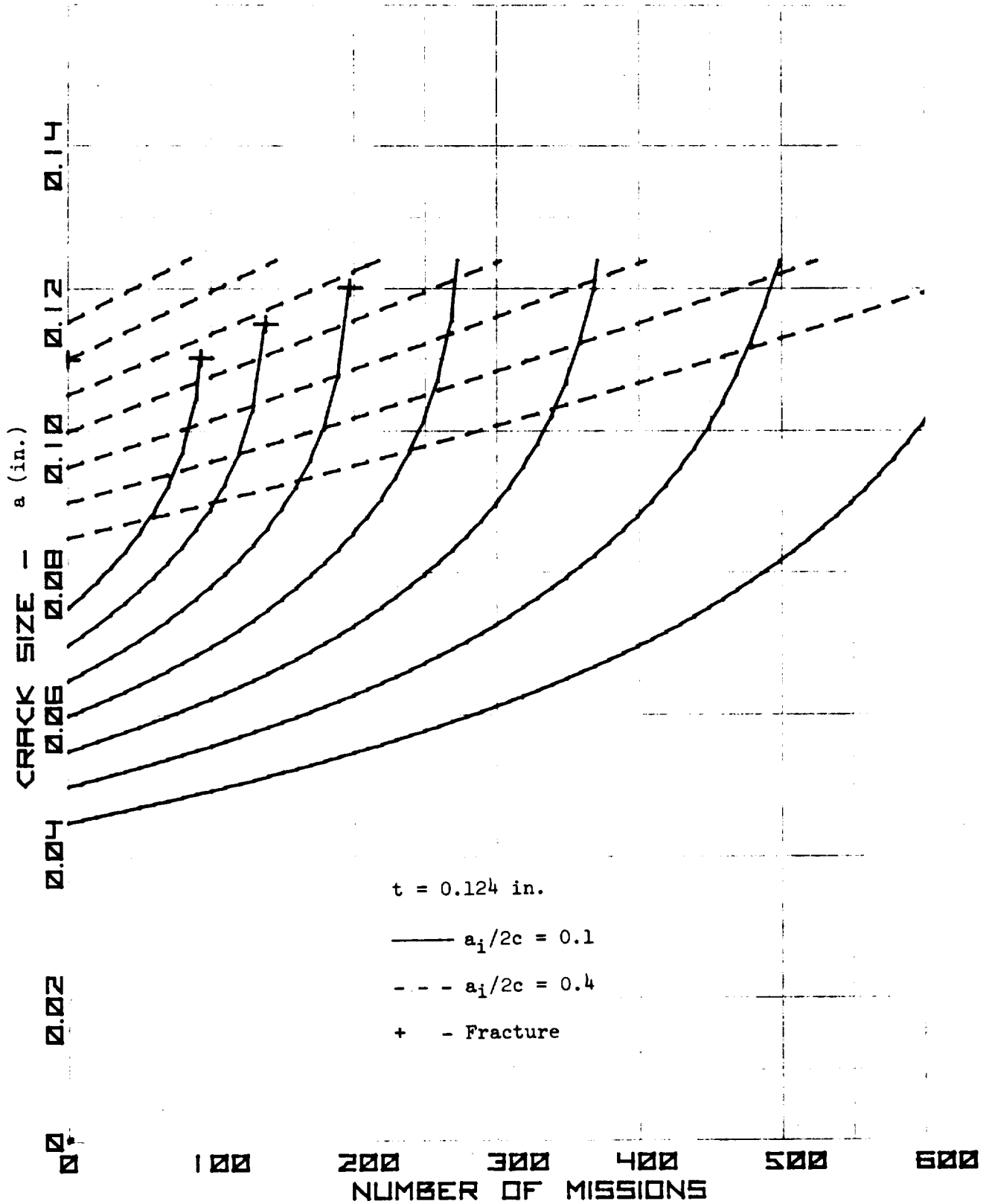


Figure 7-40. Crack Growth to Failure - LO₂ Tank Parent Metal
($\sigma_{lim} = 50.0$ ksi)

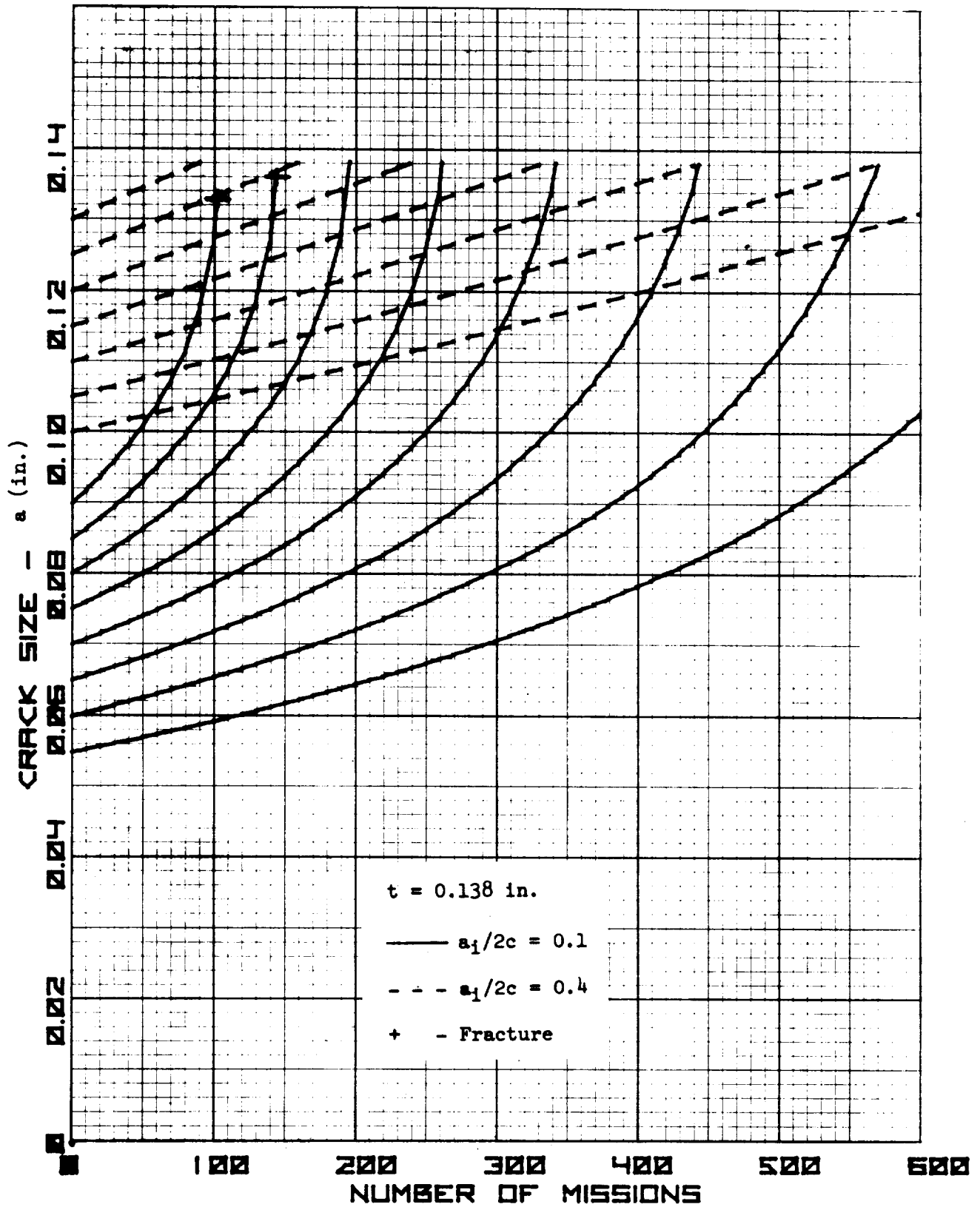


Figure 7-41. Crack Growth to Failure - LO₂ Tank Parent Metal ($\sigma_{lim} = 45.0$ ksi)

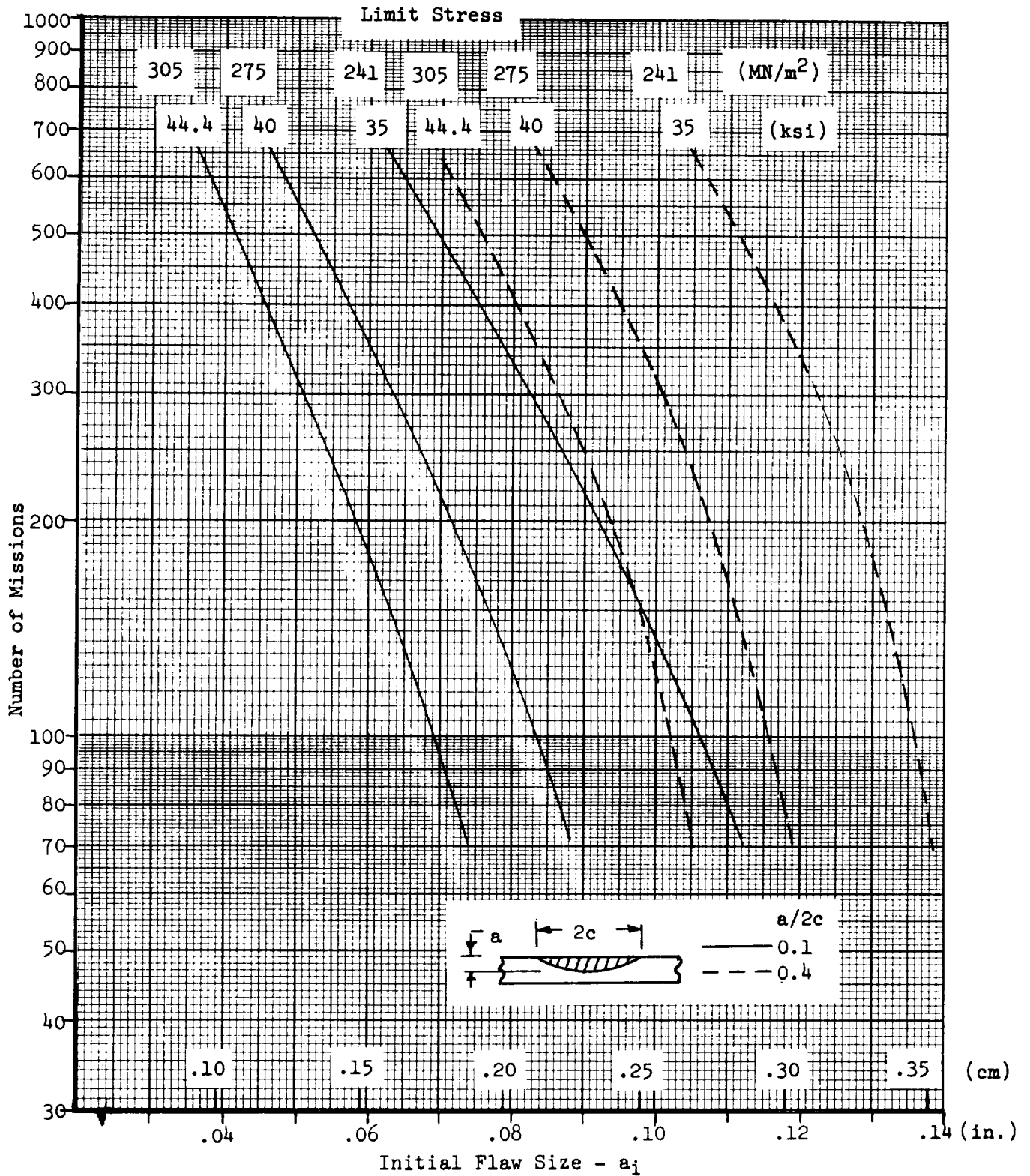


Figure 7-42. Missions to Failure - Part-Through Crack in LH₂ Tank Parent Metal

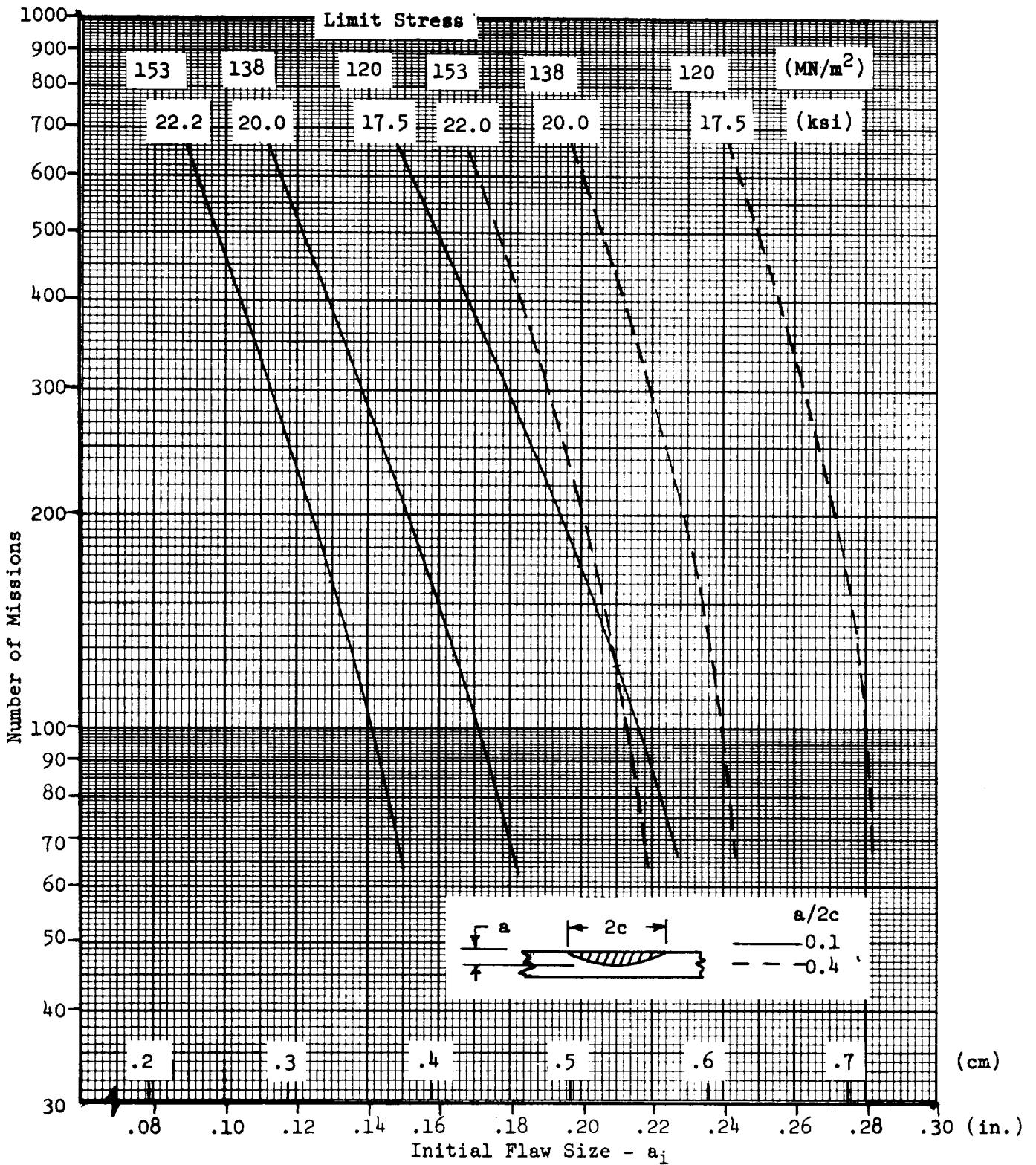


Figure 7-43. Missions to Failure - Part-Through Crack in LH₂ Tank Welds

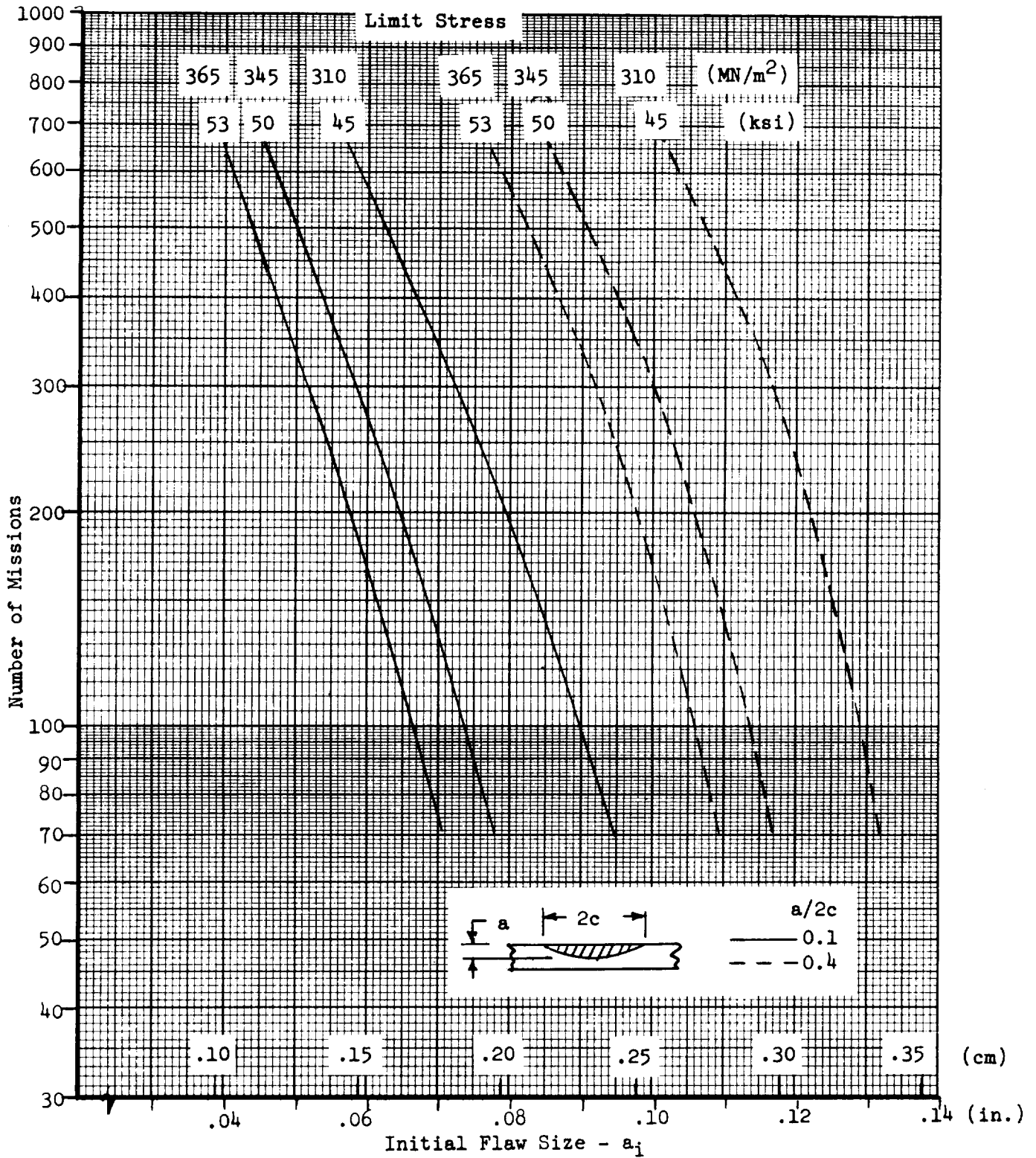


Figure 7-44. Missions to Failure - Part-Through Crack in LO_2 Tank Parent Metal

7.7.3 Design and Proof Test Implications

A review of the crack growth to failure curves (Figures 7-33 through 7-41) shows that leakage will be the critical failure mode (crack propagates to break-through prior to fracture) in all cases for aspect ratio of $a/2c = 0.4$. The same situation is true for most cases of aspect ratio $a/2c = 0.1$ investigated for the LH₂ tank. Initial cracks of this aspect ratio ($a/2c = 0.1$) in the LO₂ tank bulkhead generally result in a predicted fracture failure mode for service lives up to about 200 missions and leakage for greater service usage. The difference between LH₂ and LO₂ tank failure mode characteristics is due to the relative increase of tensile strength compared to fracture toughness for 2219-T87 aluminum at the cryogenic design temperature of the LO₂ tank. However, as the service life requirement is increased, and the corresponding allowable initial flaw becomes smaller, a greater change in crack aspect ratio takes place during growth to critical conditions and leakage rather than fracture becomes the predicted failure mode. For most practical cases of interest, the aspect ratio of initial part-through cracks will lie somewhere between $a/2c = 0.1$ and 0.4 , and probably closer to the latter value. Therefore, it is concluded that leakage rather than fracture is the most probable failure mode for the major portion of the integral propellant tanks. This offers some potential design advantages if a small amount of leakage can be tolerated by incorporating suitable purge and vent provisions in the vehicle design to eliminate potential hazards. Detection of such leakage should be possible by either an onboard monitoring system or during pre-flight checkout. This failure mode thus offers the potential advantage of facilitating detection of defects and accomplishing repair before catastrophic failure occurs. However, as discussed below, this failure mode also complicates the task of establishing proof test conditions that will verify that fracture or leakage will not occur over the service life.

Data presented in Figures 7-42 through 7-44 are summarized in Table 7-7 to describe the characteristics of the most severe initial flaws that can be tolerated in the propellant tank sections investigated in this study. The data summary is for the basic case in which thicknesses and operating stresses are based on ultimate strength design requirements. This reference case represents the smallest values of allowable initial flaws. Service life requirements of both 100 and 200 missions and initial flaw aspect ratios of $a/2c = 0.1$ and 0.4 are considered. It can be seen from this summary table that in all cases the initial flaw characteristics are such that reliable detection by current state-of-the-art NDE techniques should be possible. The minimum flaw depth is approximately 0.15 cm (0.06 in.); the minimum flaw surface length about 0.5 cm (0.2 in.), and minimum flaw depth/thickness ratio is 0.4. Therefore, it is concluded that safe-life characteristics of propellant tanks designed to conventional ultimate strength requirements (UFS = 1.4) are compatible with current NDE capabilities for detection of initial flaws.

Proof testing of pressure vessels, including integral propellant tanks, is standard practice to verify the as-fabricated strength of each article. Proof testing of all booster stages of the Saturn V vehicle was accomplished; a proof factor of 1.05 times limit design pressure constituted the minimum

Table 7-7. Summary of Characteristics of Allowable Initial Flaws in Propellant Tanks⁽¹⁾

Component	Parameter	Required Service Life			
		100 Missions		200 Missions	
		a/2c = .1	a/2c = .4	a/2c = .1	a/2c = .4
LH ₂ Tank Parent Metal	a _i (cm) (in.)	.15 (.059)	.23 (.092)	.12 (.048)	.21 (.084)
	c _i (cm) (in.)	1.5 (.59)	.63 (.25)	1.2 (.48)	.53 (.21)
	a _i /t	.52	.81	.42	.74
LH ₂ Tank Welds	a _i (cm) (in.)	.36 (.141)	.54 (.213)	.31 (.124)	.51 (.200)
	c _i (cm) (in.)	3.6 (1.41)	1.4 (.55)	3.1 (1.24)	1.3 (.50)
	a _i /t	.62	.93	.54	.87
LO ₂ Tank Parent Metal	a _i (cm) (in.)	.17 (.067)	.26 (.106)	.15 (.058)	.25 (.098)
	c _i (cm) (in.)	1.7 (.67)	.66 (.26)	1.5 (.58)	.61 (.24)
	a _i /t	.57	.90	.49	.84
(1) Propellant tank wall thicknesses and operating stresses based on ultimate strength design requirements (UFS = 1.4).					

requirements for this program. The feasibility of establishing proof test requirements on a fracture mechanics basis, so as to verify that fracture or leakage due to growth of initial crack-like defects will not occur during the service life, is of great interest to provide higher confidence in structural integrity than can be gained by application of NDE only. This feasibility will therefore be investigated, using the specific propellant tank sections analyzed in this study as representative of the general tank characteristics. A number of proof test approaches could be considered in practical application to simulate the design pressure and temperature profiles over the tank. For purposes of this study, the possible options will be simplified to the following presumed approach:

1. The LH₂ tank will be tested as a complete assembly at room temperature, using pneumatic pressurization.
2. The LO₂ tank will be tested in sub-assembly increments, per the following sequence. Sub-assemblies will be in the vertical attitude during cryogenic tests.
 - (a) Aft bulkhead - LN₂ pressurization
 - (b) Aft bulkhead
+ aft cylinder section - LN₂ pressurization
 - (c) Complete tank - pneumatic pressurization

Proof test requirements predicated on fracture mechanics theory are established so that flaws which are more severe than allowable limits will be revealed by causing rupture or leakage during proof test. In practice, some simplifying assumptions appear to be required to be able to apply present fracture mechanics technology. For example, the proof stress required to cause fracture with an initial flaw present can be approximated from the basic equation:

$$K_I = 1.1 \sigma \sqrt{\pi(a/Q)} M_K$$

where the stress intensity (K_I) is set equal to a critical value appropriate for the material, thickness, and proof test environment, and the flaw size (a) is the maximum allowable initial flaw determined from the crack growth analyses. This approach has been used to determine required proof stresses for each operating stress and flaw aspect ratio considered in the study at service life requirements of 100, 150, and 200 missions. Results are plotted (Figures 7-45 through 7-47) as curves of required proof stress versus limit design stress for a given service life requirement. Proof stresses for parent metal (Figures 7-45 and 7-46) are based on a lower bound estimate of critical stress intensity (K_C) consistent with the value used to predict flaw growth and fracture under service operation. Specific values used in the analysis are $K_C = 44 \text{ MN/m}^{3/2}$ (40 ksi $\sqrt{\text{in.}}$) at room temperature and $48.5 \text{ MN/m}^{3/2}$ (44 ksi $\sqrt{\text{in.}}$) at 77 K (-320 F). The normalizing parameter Q is determined for the appropriate initial flaw aspect ratio ($a/2c$) with the assumption that proof stress is equal to the yield strength of the material. This latter condition represents the upper bound of what

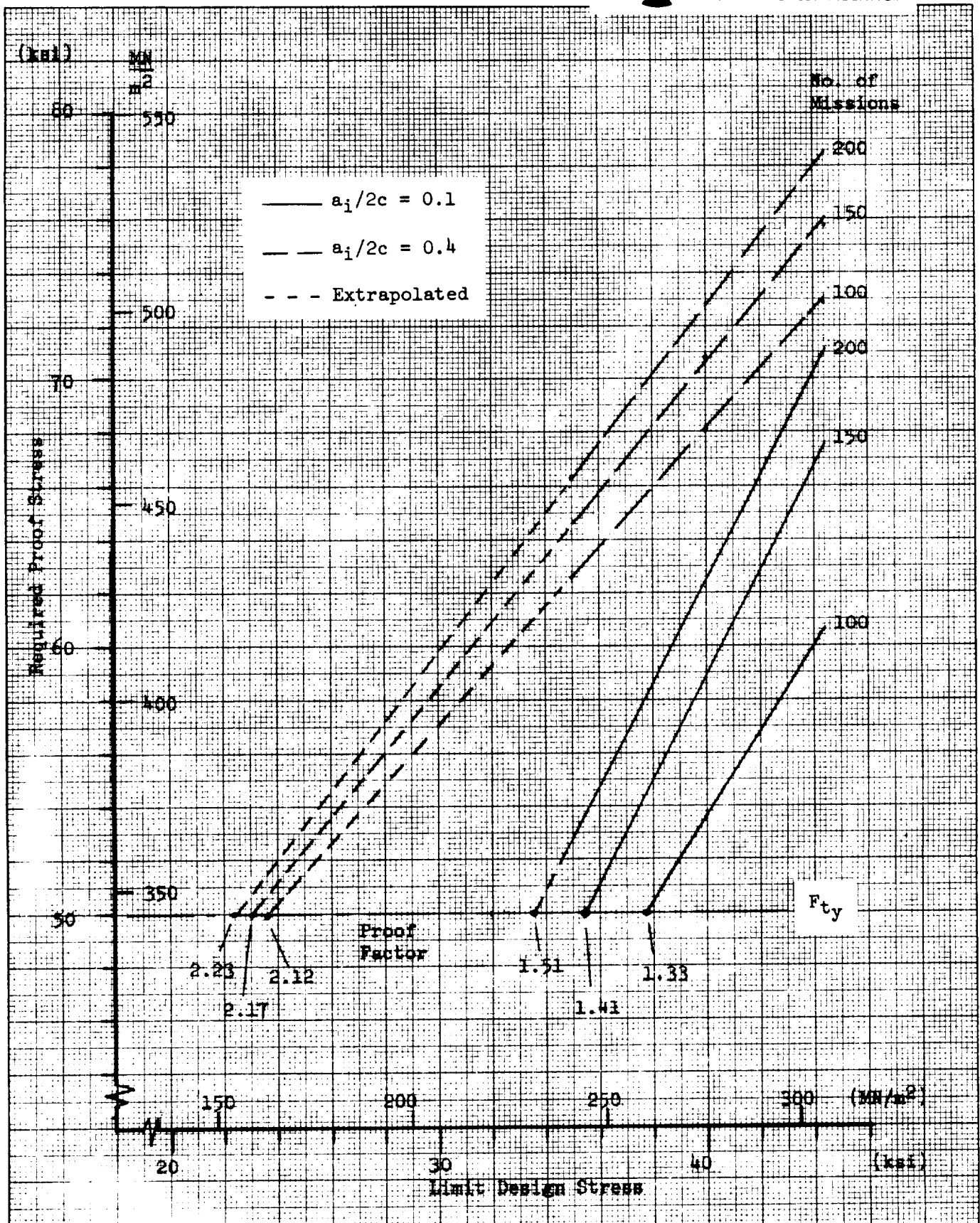


Figure 7-45. Required Proof Test Stresses - LH₂ Tank Parent Metal

KE 10 X 10 TO THE CENTIMETER 46 1517
 MADE IN U.S.A.
 KEUFFEL & ESSER CO.

KEUFEFF & ESSER CO.
 18 X 25 CM. • ALBANY, N.Y.
 48 1511
 MADE IN U.S.A.

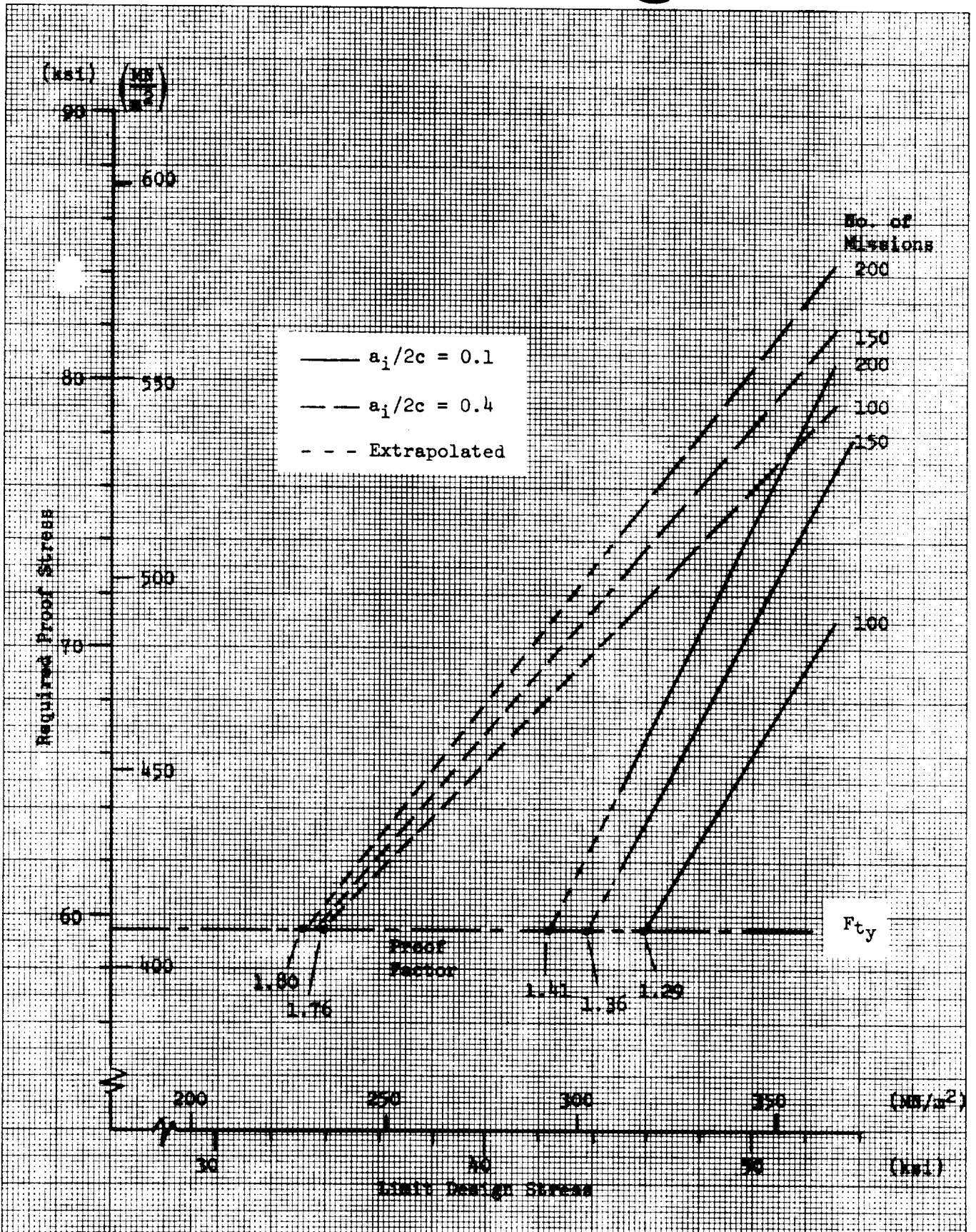


Figure 7-46. Required Proof Test Stresses - LO₂ Tank Parent Metal

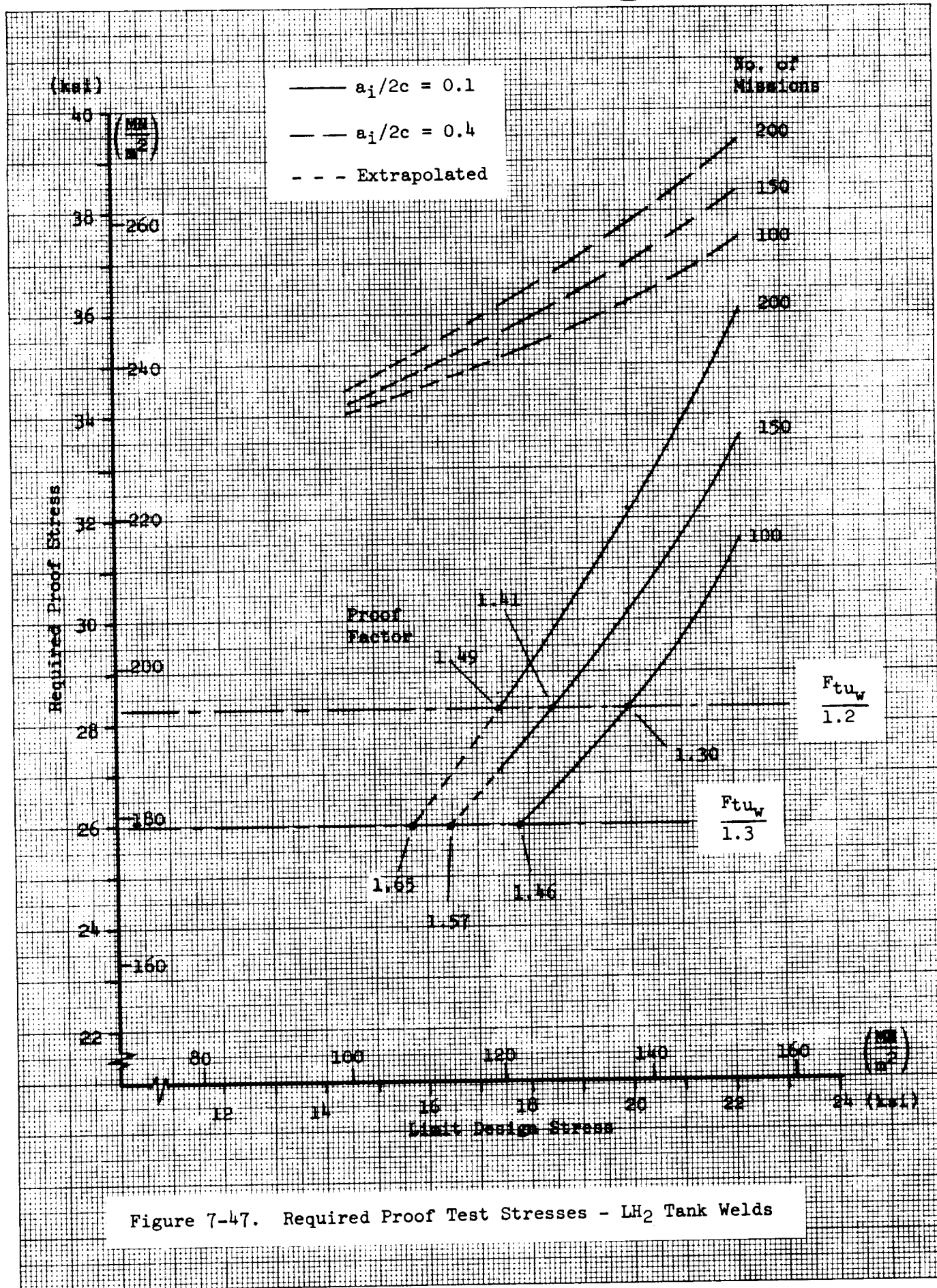


Figure 7-47. Required Proof Test Stresses - LH₂ Tank Welds

may be considered an acceptable proof test stress. Therefore, the parent metal yield strength appropriate for the proof test temperature is also indicated on Figures 7-45 and 7-46 and is taken as the maximum permissible proof test stress. The curves of required proof test stress are extrapolated to the point of intersection with this boundary. This intersection defines the maximum allowable limit design stress that will be compatible with practical proof test verification. The ratio of proof stress to limit design stress is designated as the proof factor. However, it is important to note that the proof factors determined in this manner represent the best possible situation, or the minimum value of proof factor that may satisfy the fracture mechanics requirements for proof test. The logic of using a lower bound estimate of critical stress intensity to establish required proof stress has some validity when the operational failure mode is fracture and the corresponding critical flaw size is also determined on the basis of lower bound fracture properties. However, when the critical operational failure mode is leakage, then upper bounds of critical stress intensity may be required to establish proof stresses that will provide high confidence of screening initial flaws that could cause leakage during operational service. A realistic definition of such an upper bound will require extensive test data applicable to the specific material, thickness, and flaw aspect ratios of interest. Available empirical data for 2219-T87 parent metal were insufficient to permit investigation of the effect of an "upper bound" requirement on proof factors.

The same general approach is used to determine required proof stresses for the reference LH₂ tank weld joint, except that in this case an upper bound of apparent fracture toughness is used for those cases where leakage is the predicted failure mode. This upper bound represents either crack break-through or fracture (whichever occurs first) and is approximated from the empirical test data presented in Figure 5-16. The variation of both upper and lower bounds of apparent fracture toughness with weld joint thickness is estimated in Figure 5-17. The required proof stress is plotted in Figure 7-47 as a function of limit design stress in the weld joint for service life requirements of 100, 150 and 200 missions. It is necessary to define a maximum permissible proof stress on the weld joint to determine the allowable limit design stress and the corresponding proof factor. Typical yield strength for the 2219 welds is in the order of 140 MN/m² (20 ksi). It can be seen that if the proof stress is limited to the weld yield strength, similar to the parent metal approach, proof test verification does not appear to be practical. It can also be questioned whether this limitation is even a desirable requirement. The localized yielding that may occur in a weld joint will not produce a measurable change in tank dimensions. Also, yielding of the weld metal during proof test may actually be beneficial by reducing and redistributing residual weld stresses and by improving geometric alignment of the joint. However, the proof stress should obviously not be set at a level where a significant risk of proof test failure is encountered due to scatter in weld strength properties. The fracture strength data presented in Figure 5-15 show that an ultimate strength greater than 234 MN/m² (34 ksi) should be obtained in welds which do not have significant crack-like defects. Proof safety factors of 1.2 and 1.3 are estimated as reasonable bounds of the safety margin that should be provided in proof test. Allowable proof stresses,



based on these safety factors and the weld joint ultimate strength defined above, are also indicated on Figure 7-47. Intersection of the required proof stress curves with these limiting values defines the allowable limit design stresses and corresponding proof test factors for the weld joints. It can be seen that reasonable results are obtained for an initial flaw aspect ratio $a_i/2c = 0.1$; however, proof test verification that no leakage will occur in weld joints for an assumed initial flaw of aspect ratio $a_i/2c = 0.4$ does not appear to be feasible. The investigation of proof stress requirements for welds is more conservative than that performed for parent metal, because upper bound rather than lower bound values were used for critical stress intensity. However, the weld test data presented in Figures 5-15 and 5-16 illustrate another factor that complicates the task of defining proof test requirements on a rigorous fracture mechanics basis. A significant amount of subcritical flaw growth under monotonic loading is indicated for many of the specimens. This raises the possibility that flaws may exist of a size such that break-through or fracture does not occur but that significant subcritical growth during proof test increases their dimensions to a point where propagation to leakage may result under the subsequent service load spectra. This possible complication also exists for the parent metal behavior.

A summary of proof factors derived from the curves of Figures 7-45 through 7-47 is presented in Table 7-8. Because of the simplifying assumptions and uncertainties discussed above, these factors must be considered as tentative, and possibly lower bound, values. Considerably more research in this area, beyond the scope of the present study, will be required to clarify procedures for and practical limitations of the application of fracture mechanics principles to define proof test requirements. This is particularly true for thin wall pressure vessels such as the B-9U integral propellant tanks. It can be seen from the summary table that the proof factors associated with flaw aspect ratio $a_i/2c = 0.4$ are very high-- in the range of 1.8 for the LO_2 tank and 2.2 for the LH_2 tank. Also, there is very little difference in proof factor between service life requirements of 100 and 200 missions. This situation results because the stress intensity at break-through for a flaw of this aspect ratio is much less than the critical value to cause fracture. Therefore, the fracture mechanics theory predicts a very high proof stress required to screen out flaws of this character by producing fracture during proof test. Because the permissible proof stress is limited to the material yield strength, the net effect of the fracture mechanics rationale is to require a significant decrease in operating stress and corresponding increase in tank wall thickness such that a crack of depth approaching the thickness will be critical under proof loading to yield stress level. In this regime, the crack growth due to the service load spectra is very small compared with initial assumed flaw dimensions, and little difference can be seen between 100 mission and 200 mission service life requirements. Thus, it would appear that establishing proof test requirements to ensure no leakage during operational service will not be practical for flaws approaching a semi-circular shape. However, the development of empirical data regarding flaw growth to break-through under monotonic loading should be considered to obtain a more realistic assessment of potential proof test capabilities.

Table 7-8. Proof Factors and Associated Weight Increases for B-9U Propellant Tanks

Parameter	LH ₂ Tank ⁽³⁾ Parent Metal			LH ₂ Tank ⁽³⁾ Welds			LO ₂ Tank ⁽⁴⁾ (Parent Metal)		
	100	150	200	100	150	200	100	150	200
Number of Missions	100	150	200	100	150	200	100	150	200
Proof ⁽¹⁾ Factor	$a_i/2c = 0.1$	1.33	1.41	1.51	1.46	1.57	1.65	1.36	1.41
	$a_i/2c = 0.4$	2.12	2.17	2.23	Large	Large	Large	1.78	1.80
Weight ⁽²⁾ Increase	Kilograms	1080	1560	1990	---	---	---	780	950
	Pounds	2380	3440	4380	---	---	---	1720	2080
	Percent of Tank Structural Wt.	4.2	6.1	7.8	---	---	---	12.8	15.5

(1) Proof factor = Proof stress/Limit design stress
(2) Weight increase is with respect to baseline established by ultimate strength design requirements. Increase is based on proof factors determined for initial flaw aspect ratio $a_i/2c = 0.1$.
(3) Proof factors and weight increases are based on pneumatic proof test at room temperature.
(4) Proof factors and weight increases are based on cryogenic (LN ₂) proof test of aft bulkhead and cylinder sub-assemblies.

The approximate weight increase of the tanks necessary to achieve the indicated proof factors ($a/2c = 0.1$) is also indicated in Table 7-8. This increase is with respect to a baseline design predicated on conventional ultimate strength requirements ($UFS = 1.4$). These weight increments also account for the practical limitations of matching proof pressure and flight design pressure profiles over the length of a tank. These weights should be considered as only approximate indications, and probably lower limits, of the performance penalty associated with proof test based on fracture mechanics rationale. As previously discussed, the effects of simplifying assumptions, uncertainties, and flaw aspect ratios greater than $a/2c = 0.1$ may all tend to increase the indicated weight values.

The weight increases calculated for tank bulkheads are obtained directly from the relative limit design stresses associated with ultimate strength design versus required proof factor. However, the weight increments for tank cylindrical sections do not increase directly with proof factor because, as the tank skin thickness is increased, some reduction can be made in the weight of integral stringers required to provide shell stability under compressive loading. The following approximate relationships, derived from skin/stringer optimization curves presented in Reference 6, are used in calculation of weight increase for tank cylindrical sections:

$$\text{LH}_2 \text{ tank: } \bar{\Delta t} = 0.50 \Delta t_s$$

$$\text{LO}_2 \text{ tank: } \bar{\Delta t} = 0.80 \Delta t_s$$

where:

$\bar{\Delta t}$ = increment of effective tank wall thickness (skin + distributed stringers)

$$\Delta t_s = t_s - t_{s_0}$$

t_s = tank skin thickness required to meet specified proof factor

t_{s_0} = tank skin thickness to meet ultimate strength design requirements ($UFS = 1.4$)

7.8 SAFE-LIFE ANALYSIS - WING SPAR CAPS - ALTERNATE MATERIAL

A limited investigation of flaw growth and fracture characteristics of 2219-T87 aluminum alloy wing spar caps is summarized in this section. Results of this investigation and the fatigue analyses of Section 6.9 are used to compare relative merits of the aluminum alloy with the primary selection of 6Al-4V titanium alloy.

7.8.1 Structural Configuration and Loading

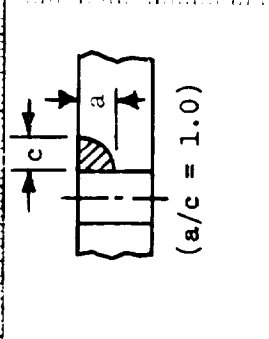
The general configuration and shape of the aluminum spar caps is assumed to be similar to the titanium members, however the section dimensions and thickness are increased to provide additional area consistent with the reduced allowable stresses for the aluminum material. Limit design stress levels of 275, 240 and 207 MN/m² (40, 35 and 30 ksi) are selected as the basis for parametric analyses. Simplified service load spectra for crack growth analyses are obtained by applying the appropriate ratio of limit design stresses to the load spectrum of Table 7-1.

7.8.2 Crack Growth Analysis

A review of the crack growth analysis results for the titanium spar caps indicates that a corner crack from a fastener hole is one of the more critical types of initial defects. It is also a realistic type of defect for the materials and design configuration of the spar caps, and is therefore selected as the basic analytical model for comparison between the aluminum and titanium material options. Crack growth to critical size is calculated for an assumed initial flaw depth of .13 cm (0.050 in.) and an assumed aspect ratio of corner crack ($a/c = 1.0$). Results are summarized in Figure 7-48 for the selected limit design stress levels. These data are used to construct curves of number of safe-life missions versus initial flaw size, presented in Figure 7-49.

7.8.3 Design Implications

It can be seen from Figure 7-49 that the allowable limit design stress will be greater than 240 MN/m² (35 ksi) for all initial flaw sizes up to 0.63 cm (0.25 in.) and up to 200 safe-life missions. These limits should cover the practical range of interest for both assumed initial flaw dimensions based on NDE detection capabilities and a specified safety factor to be applied to service life used in flaw growth analyses. A maximum limit design stress of 240 MN/m² (35 ksi) was previously determined (Section 6.9) to satisfy basic fatigue life requirements, which include a scatter factor of 4.0 on required service life. Therefore, it is concluded that the basic fatigue life requirement will govern the design of aluminum spar caps over the practical range of interest. The basic structural weight of aluminum spar caps was evaluated by numerical integration of spar cap areas over the wing surface; the integration was based on average properties over increments of length defined by sixteen stations over the semi-span. Spar caps on the upper wing surface are critical under compression loading during the max q₀ flight condition. Required areas were determined assuming the ultimate allowable compression stress to be equal to the material yield strength of



Limit Design Stress

$MAX = 607/1.2$
 $(F17) = 506$

No Retention
Stress Intensity

(K_{1c}) (ksi)

210
(35)

235
(40)

275
(40)

100 200 300 400 500 600 700 800 900 1000
Cycles of Loading

Figure 7-48. Corner Crack From Fastener Hole - Growth to Failure - 2219-T87 Aluminum Wing Spar Caps

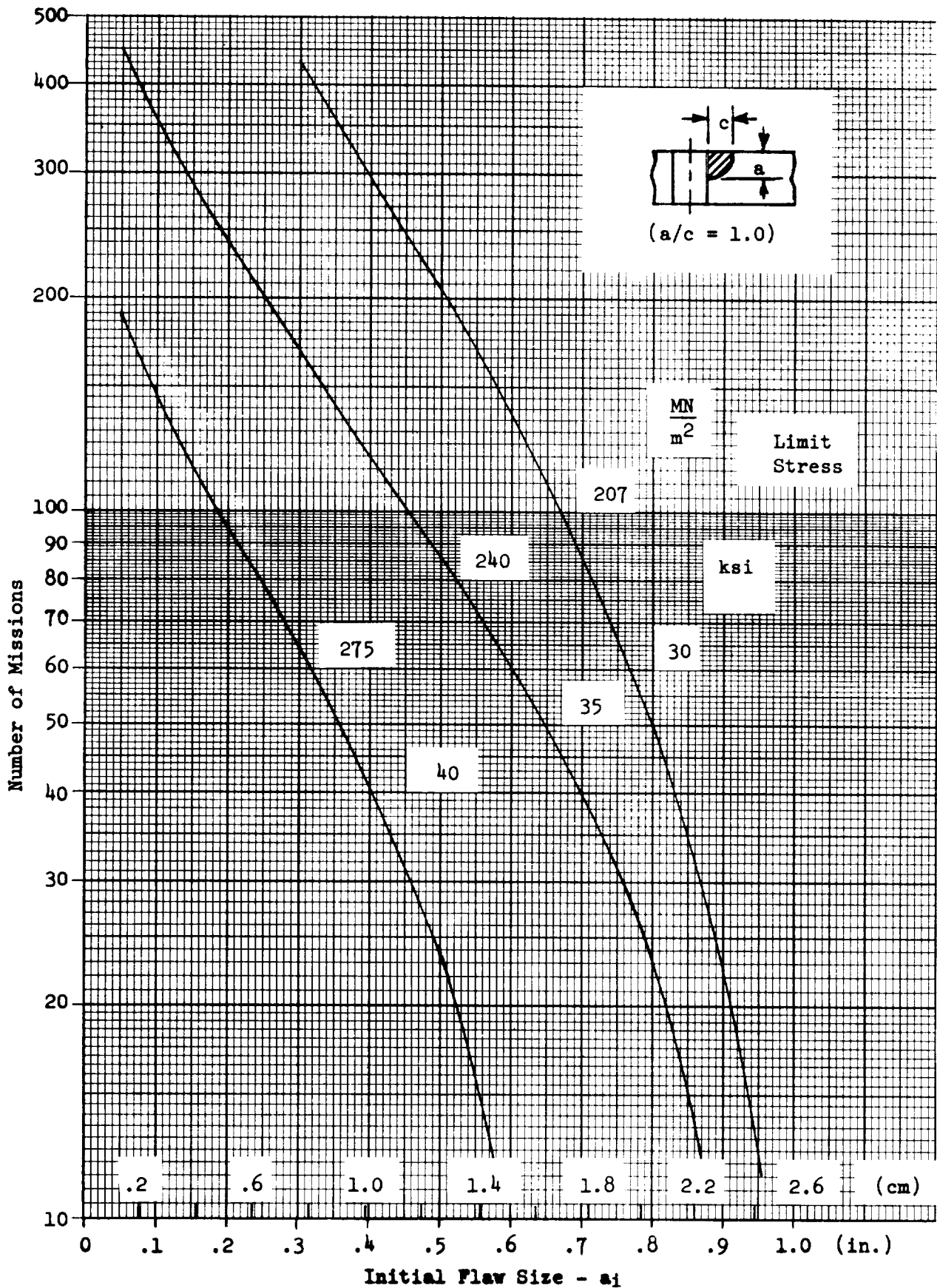


Figure 7-49 . Missions to Failure - Corner Crack From Fastener Hole in 2219-T87 Aluminum Wing Spar Caps (Retardation Not Considered)

345 MN/m² (50 ksi). Spar caps on the lower wing surface are critical under tension loading in the same flight condition, required areas were determined on the basis of the fatigue limited ultimate allowable stress of 338 MN/m² (49 ksi). A basic structural weight of 8200 kg (18,100 lb) was calculated in this manner for the 2219-T87 aluminum spar caps.

The use of aluminum spar caps will also impose more severe requirements on the thermal protection system (TPS) because of the reduction in structural temperature that can be tolerated. The basic TPS for the B-9U is sized to limit the temperature of the titanium substructure to 590 K (600 F). A temperature of approximately 420 K (300 F) is estimated as a maximum practical limit for the aluminum structure. (A corresponding temperature of 370 K (200 F) is estimated for critical spar sections in wing root region because of heat-sink capacity.) Estimated weight increases required in the TPS to achieve this reduced structural temperature are summarized in Table 7-9. A total increase of 1810 kg (4000 lb) is estimated, which must be added to the basic structural weight of aluminum spar caps to permit a valid comparison between aluminum and titanium material.

Table 7-9. Estimated Weight Increase of TPS to Accommodate Aluminum Wing Spar Caps

Description of Change	Weight Increase	
	(kg)	(lb)
Increase thickness of Dynaflex insulation (lower wing surface) from 1.4 cm (0.55 in.) to 2.5 cm (1.0 in.).	1280	2830
Provide local insulation and insulating spacers between upper wing skin and spar, rib, and former caps.	195	430
Increase thickness of selected panels of wing lower structural skin to accommodate increased differential thermal strain.	335	740
TOTAL	1810	4000

A summary weight comparison between the aluminum and titanium alloys for wing spar caps is given in Figure 7-50. The total wing spar cap weight for Ti-6Al-4V alloy is plotted as a function of initial flaw size and number of safe-life missions required in the crack growth analysis. These curves are developed from the data of Figures 7-13 and 7-18. The weight of aluminum

spar caps plus the TPS weight increase are superimposed on the same plot. It can be seen that the titanium structure is considerably lighter than the aluminum over most of the range of practical interest. The titanium weight approaches that of the aluminum if initial flaw size is taken in the order of 0.63 cm (0.25 in.) and a factor of safety of 2.0 is applied to the crack growth prediction.

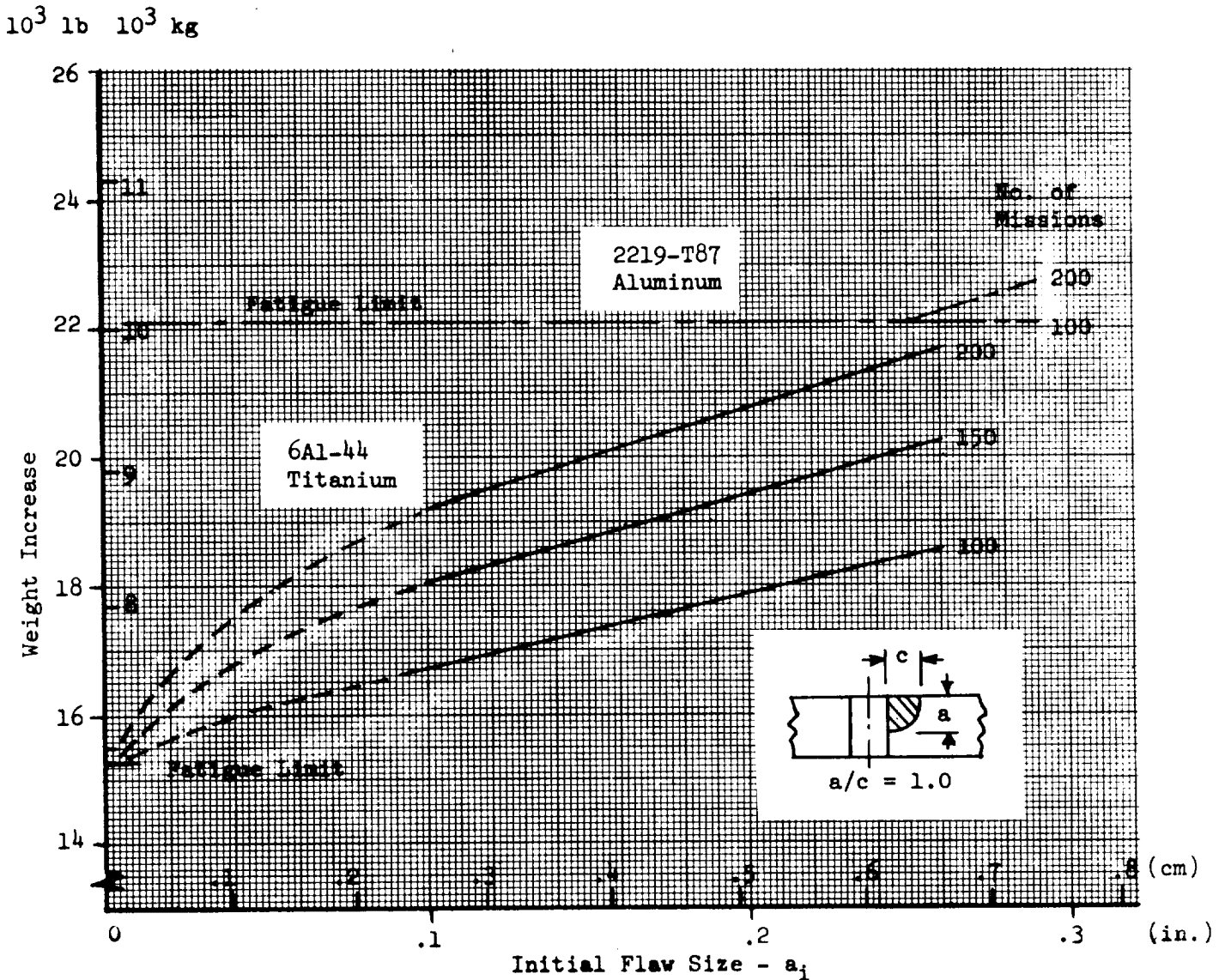


Figure 7-50. Summary Weight Comparison - Aluminum and Titanium Alloys for Wing Spar Caps

7.9 SAFE-LIFE ANALYSIS - EXTERNAL TANK

A brief fracture mechanics evaluation is made of the external tank associated with the current Space Shuttle configuration concept. This tank supplies all of the propellant for the orbiter main engines during the ascent phase. The tank is separated from the orbiter after burnout (in orbit) and is expended with each mission. Because of this one-use application, there is no significant flaw growth to consider prior to the final operational usage. The fracture mechanics evaluation is therefore limited to prediction of critical flaw sizes for various regions of the tank and determining the corresponding proof test requirements. An overall evaluation is then made of a practical proof test approach to determine what design penalties will be imposed on the tank structure to accommodate proof test.

7.9.1 Structural Configuration and Loading

A view of the overall external tank configuration is given in Figure 7-51. The total assembly is comprised of an LO₂ tank subassembly and an LH₂ tank subassembly, separated by a skirt. The LO₂ tank is located at the forward end and is shaped to provide an aerodynamic conical nose contour. The tanks are primarily monocoque shells of revolution, local stiffening is employed only in regions of concentrated longitudinal loading introduced by the attachments of the orbiter or the solid rocket motors. This configuration concept was selected to achieve design simplicity and manufacturing economy. The cylindrical and conical walls of the tanks are 2219-T87 aluminum alloy; 2219-T81 aluminum alloy is used for the end bulkheads to allow stretch forming of the gore panels. All pressure-carrying structural joints between tank components are fusion welded, using the DC-TIG process. A preliminary definition of tank skin and weld land thicknesses, based on flight design requirements, is given in Figure 7-51.

The preliminary structural analyses of the external tank indicate that hoop stresses due to tank internal pressure will be the critical factor for both static strength design and for consideration of failure due to crack-like defects. Body loads due to aerodynamic, thrust, and inertia forces during ascent are not expected to modify significantly the critical principal stresses for most regions of the tank. Therefore, consideration of design loadings can be simplified to the variation of total pressure over the length of the tanks. These pressure profiles are plotted in Figures 7-52 and 7-53 for the LO₂ and LH₂ tanks, respectively. Three time points during the ascent trajectory are considered to ensure bounding an envelope of maximum design pressures.

7.9.2 Critical Flaw Sizes and Proof Test Requirements

Critical sizes for an assumed initial surface flaw are calculated for several locations in both the LO₂ and LH₂ tanks. The fundamental equation for a part-through crack (Figure 7-1) and a far surface magnification factor determined from Figure 5-12 are used in these calculations. Assumed initial flaw aspect ratios of $a/2c = 0.1$ and 0.4 are investigated. Results of these investigations are summarized in Table 7-10. The skin thickness, limit design stress, and corresponding design temperature are listed for the selected

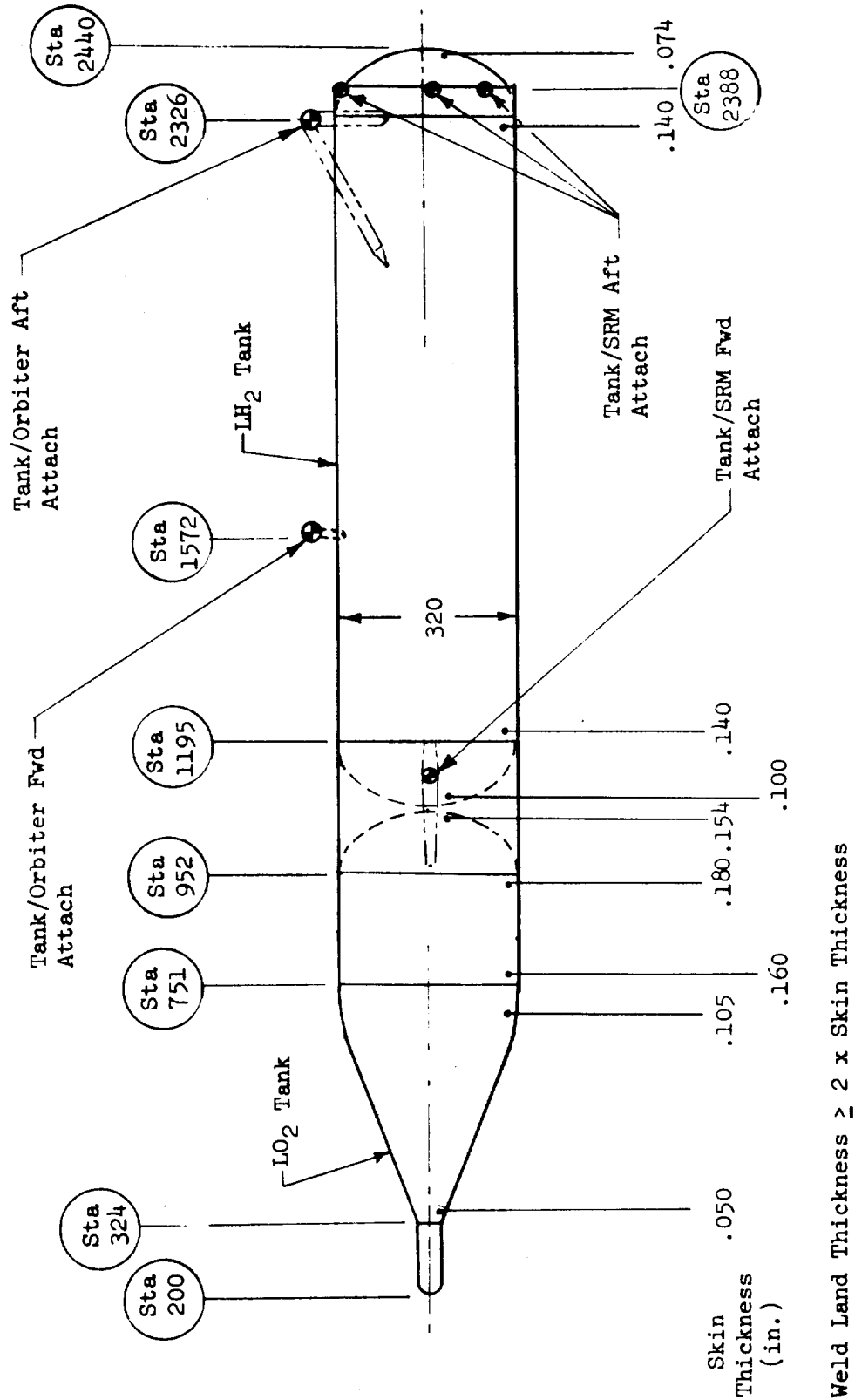


Figure 7-51. External Tank Configuration



REPLACES 9-52823
18 X 22 CM. • AFFINITY
10 X 10 TO THE CENTIMETER •
NO. 1211

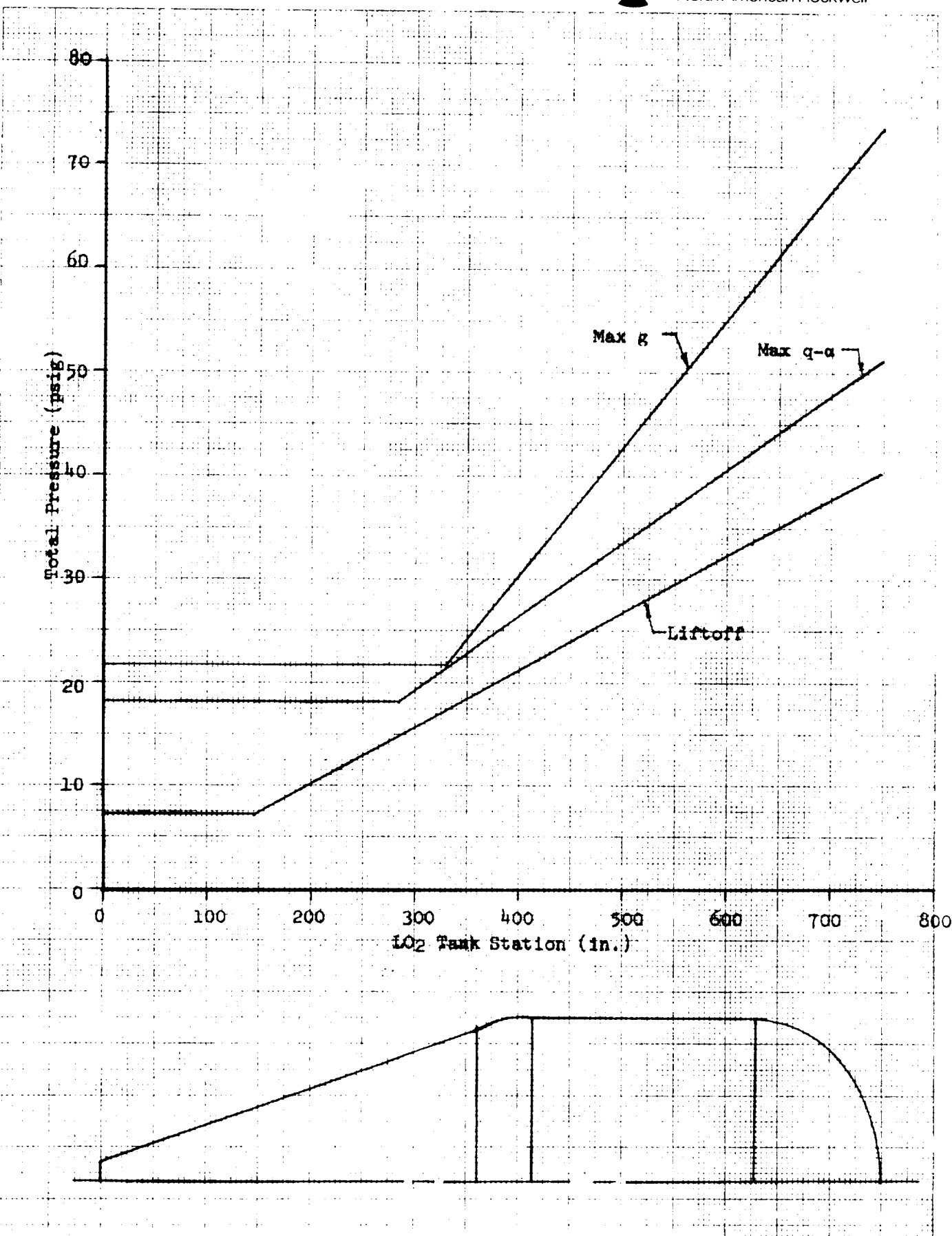


Figure 7-52. External Tank LO₂ Limit Pressure Profiles

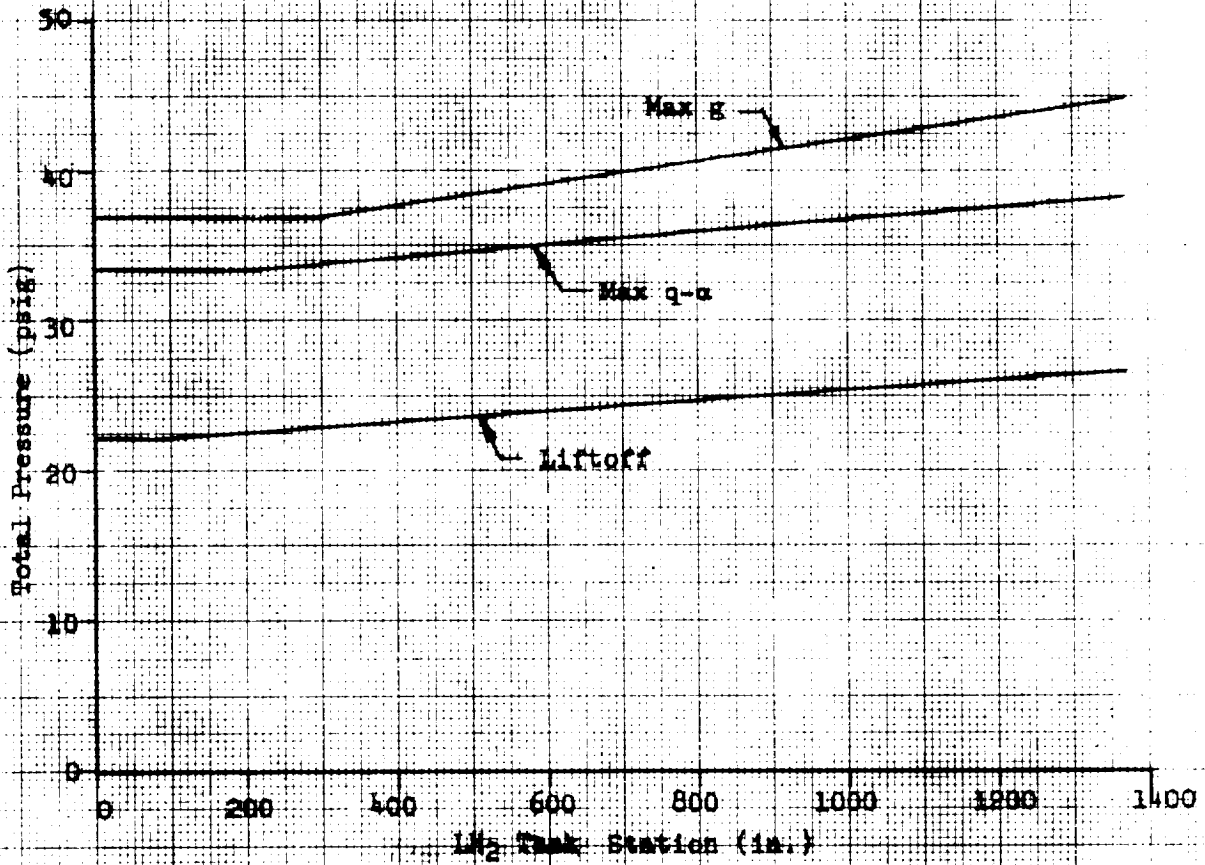


Figure 7-53. External Tank LH₂ Limit Pressure Profiles

FULLER & SAUNDERS
 18 X 22 CM. & AVAILABLE
 10 X 10. THE CENTIMETER
 48 1213
 1961

Table 7-10. Summary of Critical Flaw Sizes for External Tank Components

Tank Component	Wall Thickness cm (in.)	Limit Stress MN/m ² (ksi)	Design Temp. °K (°F)	K _c MN/m ^{3/2} (ksi√in.)	a/2c = 0.1		a/2c = 0.4	
					(2) a _{cr} cm (in.)	(3) K _{trans} MN/m ^{3/2} (ksi√in.)	(2) a _{cr} cm (in.)	(3) K _{trans} MN/m ^{3/2} (ksi√in.)
LO ₂ Fwd Cylinder	.406 (.160)	224 (32.5)	91 (-297)	48.0 (44.0)	PTC → TC	56.3 (51.6)	PTC → TC	28.2 (25.8)
LO ₂ Aft Cylinder	.457 (.180)	358 (52.0)	91 (-297)	48.0 (44.0)	.302 (.119)	--	PTC → TC	47.2 (43.3)
LO ₂ Aft Bulkhead	.391 (.154)	352 (51.0)	91 (-297)	48.0 (44.0)	.277 (.109)	--	PTC → TC	43.3 (39.7)
LH ₂ Fwd Bulkhead	.254 (.100)	271 (39.3)	367 (200)	39.8 (36.5)	.241 (.095)	--	PTC → TC	26.8 (24.6)
LH ₂ Fwd Cylinder	.355 (.140)	288 (41.8)	311 (100)	43.0 (39.4)	.290 (.114)	--	PTC → TC	33.8 (31.0)
LH ₂ Aft Cylinder	.355 (.140)	345 (50.0)	20 (-423)	48.5 (44.5)	.280 (.110)	--	PTC → TC	40.4 (37.0)
LH ₂ Aft Bulkhead	.188 (.074)	448 (65.0)	20 (-423)	48.5 (44.5)	.149 (.058)	--	PTC → TC	38.2 (35.1)

(1) K_c - Critical stress intensity used in fracture analysis
 (2) Critical depth for part-through crack (PTC)
 (3) Stress intensity for through crack (TC) at point of transition from PTC to TC

points in each tank. The fracture toughness is dependent on temperature, so the values of critical stress intensity (K_C) used in the analyses are also indicated in the table. The resulting critical flaw sizes (depth) are given for the two assumed aspect ratios; in cases where the crack breaks through to leakage prior to fracture, the stress intensity at transition is also given. This stress intensity is calculated for a through crack of length $2c$. It can be seen that for the extreme aspect ratio $a/2c = 0.1$, fracture as a part-through crack is predicted for almost all cases. In the one case where break-through is predicted, the stress intensity for a through crack of the original surface crack length is well above critical value, so that break-through and fracture would occur simultaneously. For aspect ratio $a/2c = 0.4$ break-through to leakage prior to fracture is predicted for all cases. The stress intensities for a through crack of length equal to thickness/0.4 are all less than critical value; therefore, the crack would remain stable and fracture would not occur without an increase in stress level. These results indicate that current inspection techniques should be adequate to provide high confidence in structural integrity. For the assumed flaw of $a/2c = 0.1$, the minimum flaw depth to thickness ratio is about 0.65 and the surface length of critical flaws is in the range of 2.5 cm (1.0 in.) to 4.0 cm (1.6 in.). As the assumed initial flaw approaches a semicircular shape, the surface length decreases, but the flaw would have to be almost completely through the thickness of material such that the plastic zone induced by loading could cause break-through to leakage. In addition to the inspection capabilities for detection, this condition should be revealed during proof test by flaw break-through and consequent leakage.

A preliminary evaluation of proof test requirements under various possible proof test environments is performed using the relative fracture properties of tank parent metal as the primary correction factor. Empirical data obtained during the Saturn S-II program supported the adequacy of a proof factor of 1.05 to verify structural integrity for a one-use article such as the S-II stage or the Shuttle external tank assembly. Therefore, the required proof stresses for the external tank components are determined by multiplying the limit design stress by the proof factor of 1.05 and by the ratio of critical stress intensity for the parent metal at proof test temperature to that at flight design temperature. Proof test practical limitations with regard to matching flight design pressure profiles are also investigated to determine effects on tank design. Some regions of the tank cylindrical shells are sized by monocoque stability requirements, so that some reserve capability is present to accommodate proof pressures that exceed theoretical requirements. On the other hand, the tank bulkheads are designed by the flight pressure/temperature conditions and no reserve strength is inherently provided by other design requirements. The maximum allowable proof stress is assumed to be equal to the parent metal yield stress at proof test temperature. The specific proof test approaches investigated are summarized below:

LH₂ Tank

A pneumatic proof test of the entire tank at room temperature is assumed. Required proof pressure is determined to be 0.292 MN/m² (42.5 psi).

LO₂ Tank

It is assumed that proof test of the LO₂ tank will be accomplished by incremental tests as the assembly progresses. The aft bulkhead will be tested as a separate component; a second proof test, to a lower pressure appropriate for the aft cylinder region, will then be performed after assembly of the complete tank. The tank is in the vertical attitude during this test. Both a room temperature test using water and a cryogenic test using LN₂ as the pressurizing medium are investigated for this general proof test approach.

A summary of the results of the investigation of proof test requirements is given in Table 7-11. The required proof stress and the actual proof stresses resulting from the practical proof test approaches considered are listed for each of the selected tank components. The wall thicknesses of the components, as determined by either flight or proof test requirements, are also listed. Values are underlined where the proof test approach results in an increase in thickness above flight design requirements. It can be seen that the room temperature proof test on the LH₂ tank requires a small increase in thickness of the forward bulkhead and a significant thickness increase for the aft bulkhead. The resulting weight increase is estimated to be approximately 90 kg (200 lb). No increase in thickness is required on the cylindrical walls of the LH₂ tank. The data of Table 7-11 also indicate that a cryogenic proof test of the LO₂ tank will not result in any thickness increase of tank components above the flight design requirements. A room temperature hydrostatic proof test sequence requires increasing the thickness of the aft bulkhead; a weight penalty of approximately 45 kg (100 lb) is estimated for this approach.

The total tank weight penalty associated with room temperature proof testing is not considered to be excessive, and program costs will be much less than for cryogenic proof test. Therefore, the room temperature tests are recommended as the preferred primary approach. However, this approach will require careful laboratory evaluation of the fracture properties of both parent metal and welds at room temperature and at the flight design temperatures to assure that proper proof stress correction factors are determined.



Table 7-11. External Tank Stresses and Wall Thicknesses for Flight Design and Proof Test Conditions

Tank Component and Material	Flight Design Condition			Room Temperature Proof Test			Cryogenic Proof Test		
	Limit Stress MN/m ² (ksi)	Temp. °K (°F)	Thick- ness cm (in.)	Required Proof Stress MN/m ² (ksi)	Actual (1) Proof Stress MN/m ² (ksi)	Thick- ness cm (in.)	Required Proof Stress MN/m ² (ksi)	Actual (1) Proof Stress MN/m ² (ksi)	Thick- ness cm (in.)
L02 Fwd Cylinder (2219-T87)	224 (32.5)	91 (-297)	.406 (.160)	214 (31.0)	324 (47.0)	.406 (.160)	236 (34.2)	374 (54.3)	.406 (.160)
L02 Aft Cylinder (2219-T87)	358 (52.0)	91 (-297)	.457 (.180)	342 (49.6)	342 (49.6)	.457 (.180)	377 (54.6)	377 (54.6)	.457 (.180)
L02 Aft Bulkhead (2219-T81)	352 (51.0)	91 (-297)	.391 (.154)	303 (44.0)	303 (44.0)	.435 (.171)	369 (53.5)	369 (53.5)	.391 (.154)
LH ₂ Fwd Bulkhead (2219-T81)	271 (39.3)	367 (200)	.254 (.100)	303 (44.0)	303 (44.0)	.262 (.103)			
LH ₂ Fwd Cylinder (2219-T87)	288 (41.8)	311 (100)	.355 (.140)	303 (44.0)	331 (48.0)	.355 (.140)			
LH ₂ Aft Cylinder (2219-T87)	345 (50.0)	20 (-423)	.355 (.140)	327 (47.2)	332 (48.1)	.355 (.140)			
LH ₂ Aft Bulkhead (2219-T81)	448 (65.0)	20 (-423)	.188 (.074)	303 (44.0)	303 (44.0)	.264 (.104)			

(1) Stress resulting from selected practical proof test approach

8.0 FAIL-SAFE ANALYSIS

"Fail-safe" structure involves a damage tolerant design philosophy under which failure of a structural element can be temporarily tolerated by providing sufficient residual strength or alternate load paths to avoid catastrophic failure under subsequent exposure to a limited period of service operation. Successful application of this design approach depends on three major considerations:

- (1) The fail-safe structure must be accessible for regular and effective in-service inspection so that a damaged condition will be reliably detected.
- (2) The residual strength and stiffness after initial failure must be adequate to provide an acceptably low probability of catastrophic failure under subsequent normal service operation. Limit load is most commonly taken as the required residual strength level.
- (3) The fatigue life of the remaining structure, after failure of a single principal element, must be adequate to prevent any significant additional damage from occurring prior to the next regular inspection period.

Typical fail-safe designs involve multielement or redundant structural arrangements with crack arrest provisions in the form of geometric boundaries or stiffening elements. Many of the typical stiffened panels employed in conventional aircraft wing and fuselage structure possess an inherent fail-safe capability of significant magnitude. It is obviously desirable to make use of such inherent fail-safe characteristics and enhance them to the extent required to comply with the fail-safe design requirements to obtain maximum efficiency in applying this design concept.

Analyses presented in this section investigate the inherent fail-safe capabilities of selected structural elements and determine the structural modifications or reinforcement, and the associated weight increase, to meet a specified level of residual strength. In most cases this residual strength level has been varied over the range from 1.0 to 1.2 times limit load, so that a parametric evaluation can be made of design impact resulting from various levels of residual strength requirement. The following structural components are considered to be reasonable candidates for a fail-safe design approach, and are investigated in this section:

- Wing spar caps
- Vertical stabilizer main box
- Crew compartment
- LH₂ tank cylinder sections

8.1 FAIL-SAFE ANALYSIS - WING

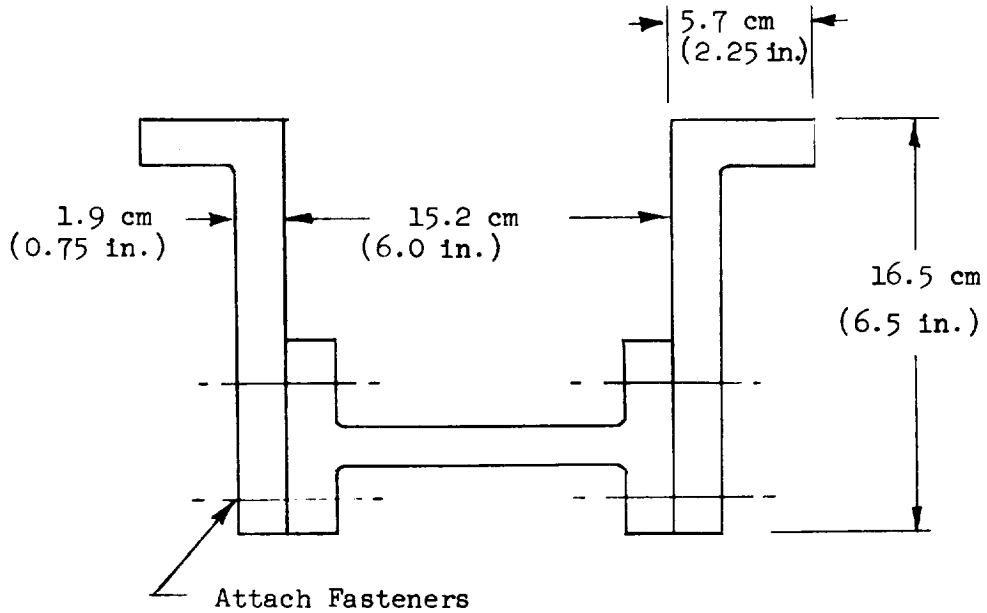
8.1.1 Structural Configuration and Loading

The maximum tension loading on the wing upper surface (down bending) is only about 70 percent of the tension loading on the lower surface (up bending); therefore, only the wing lower surface is considered for evaluation of fail-safe design concepts. Also, it can be seen from the iso-stress contours of Figure 7-15 that operating stresses in the wing spar caps decrease rapidly in the tip region. For this reason, the fail-safe investigation is not extended beyond Wing Sta. 500. Because of the multispar arrangement of the wing structure, it is apparent that a significant residual strength would remain, even if one spar cap were completely fractured. Therefore, the first fail-safe design approach that is investigated assumes monolithic spar caps of the configuration described in Section 7.2, and that any one spar cap may be fractured at any point along its span. It is further assumed that spar cap areas have been increased as necessary to reduce the limit operating stress to 446 MN/m^2 (65 ksi.) so that a satisfactory fatigue life is achieved. The critical loading condition for fail-safe requirements is max q_α , which produces maximum tension loading on the wing lower surface. The distribution of spar cap loads for this condition, assuming an undamaged structure, is taken from Reference 22. These loads are summarized in Table 8-1.

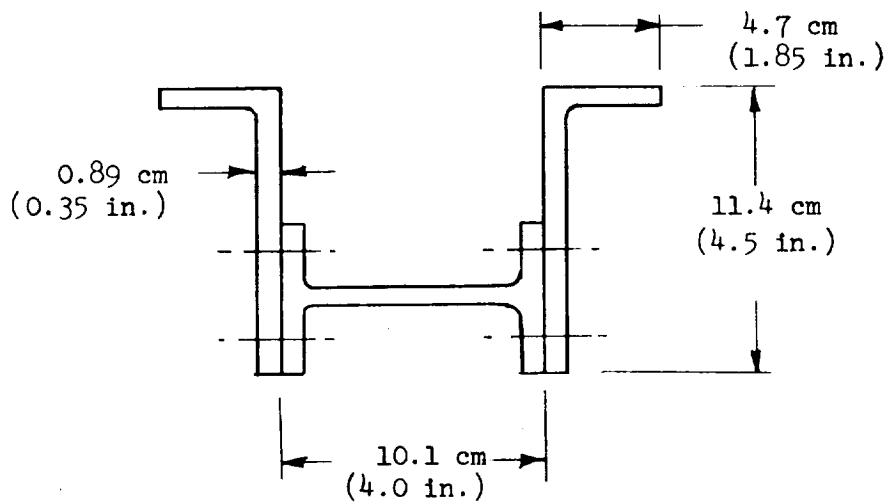
An alternate fail-safe design approach is also investigated; this alternate approach assumes that each spar cap is built up of a number of separate elements that are joined by mechanical fasteners. Complete fracture of any one element is presumed; the remaining elements are required to carry the total load in that spar cap. An example of this design concept is illustrated in Figure 8-1.

8.1.2 Residual Strength and Sizing Analysis - Monolithic Spar Cap

Basic fail-safe analyses of the B-9U wing structure were performed by General Dynamics Convair and are documented in Reference 27. These analyses utilized computer solution of finite element representation of the redundant wing structure to evaluate the revised distribution of internal loading associated with failure of various members. Failure of spar cap, spar cap and spar web, and spar truss diagonal was considered in these analyses. However, failures were presumed to be located at selected discrete points over the surface of the wing. For present purposes, it is believed that attention can be concentrated on spar cap failure, but it is desirable to include the generalization that such failure can occur at any point along the span of the spar cap. Therefore, the data in Reference 27 have been used to determine approximate "load addition factors" to account for the effect of failure of one spar cap on the resulting loads in the adjacent spar caps. These factors are summarized below.



(2) Spar Cap No. 4 - Wing Sta. 0 - $A = 120 \text{ cm}^2$ (18.5 in.²)



(b) Spar Cap No. 4 - Wing Sta. 450 - $A = 42 \text{ cm}^2$ (6.5 in.²)

Figure 8-1 Wing Spar Cap - Multi-Element Fail-Safe Design Concept

Spar Cap	Critical Failure Location (Adjacent Spar)	Additional Load (Percent of Original Load in Failed Member)
1	2	30%
2	3	60%
3	2	65%
4	5	90%
5	4	55%

These factors are used with the basic design limit loads summarized in Table 8-1 to obtain the fail-safe design loads listed in Table 8-2. These loads are based on limit applied wing bending moment and the assumption that an adjacent spar cap has fractured at the most adverse location. The spar cap area required to satisfy applicable design requirements are determined as follows:

- (1) For an intact structure, the spar cap areas must satisfy the ultimate strength design requirement in conjunction with the loads of Table 8-1 and a safety factor of 1.4 appropriate for the critical design condition and also satisfy the requirement for satisfactory fatigue life. In this case, the fatigue life requirement has been determined more critical and will establish the baseline spar cap areas. These areas are calculated using the loads of Table 8-1 and a limit operating stress of 446 MN/m^2 (65 ksi.), which has been previously determined as the maximum limit operating stress that will provide satisfactory fatigue life.
- (2) For a damaged structure, assuming one spar cap completely fractured, the remaining structure must withstand a specified percentage of limit load. The allowable stress for this case is taken as $0.95 F_{tu}$ to allow for local reductions in area due to fastener holes, etc. The spar cap areas required to meet this condition are therefore calculated using the loads of Table 8-2 and an allowable stress of 875 MN/m^2 (123 ksi.); required areas have been determined for a residual strength of 1.0, 1.1 and 1.2 times limit load.

The difference between baseline spar cap areas, based on fatigue life requirements, and the areas needed to satisfy the varying levels of fail-safe requirements is then used to determine the weight increase associated with the fail-safe design by numerical integration over the portion of the wing considered. A further allowance of 20 percent of the indicated spar cap weight increase is made to account for increased weight of cover skin and spar truss diagonals. This factor is estimated from the results summarized in Reference 27. The resulting weight increases are:

Table 8-1. Limit Design Loads for Wing Lower Surface Spar Caps (Undamaged Structure) (Kips)

Wing Span Station	Spar Cap Number				
	1	2	3	4	5
0	222	393	910	1260	365
60	215	386	880	1250	372
120	208	372	815	1210	343
163	200	365	794	1180	343
207	193	336	730	1150	322
267	150	293	650	1060	264
327	79	271	565	880	150
387	---	228	465	636	150
447	---	157	380	422	150
507	---	71	286	250	128

Table 8-2. Fail-Safe Design Loads⁽¹⁾ For Wing Lower Surface Spar Caps (Kips)

Wing Span Station	Spar Cap Number				
	1	2	3	4	5
0	340	938	1166	1590	1060
60	331	914	1130	1585	1062
120	320	862	1057	1520	1008
163	310	840	1032	1490	993
207	293	776	948	1440	955
267	238	683	840	1298	849
327	160	611	741	1015	635
387	---	508	613	771	500
447	---	385	482	557	382
507	---	243	332	365	266

(1) Based on limit applied bending moment

Residual Strength Level (Percent Limit Load)	Wing Weight Increase	
	(kg)	(lb)
100	365	805
110	495	1090
120	710	1570

8.1.3 Residual Strength and Sizing Analysis - Multi-Element Spar Cap

As an alternate fail-safe design approach, it appears practical to build up the spar cap of three separate elements of approximately equal area and also accommodate the desired spanwise taper in cap area. This design concept is illustrated in Figure 8-1, which shows cross sections of spar cap No. 4 at Wing Sta. 0 and 450. The section dimensions are based on a maximum limit stress of 446 MN/m² (65 ksi.) to satisfy fatigue life requirements. The section elements are arranged so that each is accessible for visual inspection from inside the wing, so that extensive cracking or fracture of any one element can be reliably detected.

The fail-safe design criteria requires that adequate residual strength be available if one of the elements is assumed to be completely fractured. This residual strength can be approximated assuming the spar cap load is carried by a uniform tension stress distributed over the remaining cross section area. This approximation is considered to be justified because bending stresses due to local eccentricities from failure of one element will tend to be dissipated by restraint of skin and web and by plastic deformations as ultimate strength capability is approached. For the example case, the gross stress on the remaining section is then 1.5 times the original gross stress on the spar cap, so that at limit load:

$$\sigma_{\text{gross}} = 1.5(446) = 670 \text{ MN/m}^2 (97.5 \text{ ksi.})$$

The indicated fastener pattern, which is discussed below, reduces the net section area by 12.5 percent, so that:

$$\sigma_{\text{net}} = \frac{670}{.875} = 765 \text{ MN/m}^2 (111 \text{ ksi.})$$

The ultimate tension strength is 895 MN/m² (130 ksi.), so the inherent fail-safe capability of this design approach can be determined as:

$$R = \frac{895}{765} = 1.17 \text{ x limit load}$$

This result shows that the basic spar cap of three section elements has an inherent residual strength capability adequate to satisfy fail-safe design requirements. Weight increase associated with this design concept will be

due to the weight of additional fasteners to join the individual elements and possibly due to practical limitations on achieving an idealized taper of spar cap area in the spanwise direction.

The fasteners selected for this design concept are 5/32 inch diameter Hi-Shear rivets of A-286 steel with aluminum collars. A double row of fasteners at 4D spacing is used at each element joint, as indicated in Figure 8-1. This fastener pattern was selected to provide capability to transfer the load from a failed element to the remaining elements over a reasonable length. The estimated weight increase for this design concept over the portion of the wing considered (lower surface to Wing Sta. 500) is:

Fasteners to assemble spar cap elements	220 kg	(485 lb)
Allowance for "non-optimum" taper (estimated as 10 percent of change in area from root to W.S. 500)	180 kg	(400 lb)
Total estimated weight increase	400 kg	(885 lb)

8.1.4 Residual Fatigue Life

The fail-safe design approach must provide adequate fatigue life, in addition to adequate residual static strength, after failure of a single principal element so that structural integrity is maintained until the next regularly scheduled major structural inspection. The element failure would be detected at this time and repair or replacement accomplished to restore full structural capabilities. In the case of the present study, no firm major inspection periods have been established. Therefore, the residual fatigue life (after failure of one spar cap) for wing spar caps using the monolithic design approach are investigated for three arbitrary levels of residual strength (1.0, 1.1 and 1.2 x limit load) and the required inspection intervals determined for these cases. Calculations are carried out in Table 8-3; the fatigue load spectrum is the same as that used for the basic wing fatigue evaluation (Table 6-3) except that some fatigue blocks that contributed negligible damage have been eliminated. The reference limit stress for the case where residual strength is equal to limit load is 850 MN/m² (123 ksi). The cyclic stresses listed in Table 6-3 are increased by the ratio of the relative limit operating stresses to obtain the fatigue stress spectrum for the fail-safe condition. This approach may be somewhat conservative because it inherently assumes that the fractured spar cap is ineffective under compression as well as tension loading. A rather extensive investigation of an actual hardware design, including some test evaluation, would be required to determine compression load effectiveness more accurately.

The total fatigue damage calculated in Table 8-3 is based on 100 operational missions, so that the nominal fatigue life (number of missions) is determined by dividing 100 by the accumulated damage. This nominal life

Prepared By: RWW
Checked By:
Date: 3-1-72

Space Division
North American Rockwell

TABLE 8-3 WING RESIDUAL
FATIGUE LIFE (KT=3.0) (SHEET 1)

1	2	3	4	5	6(1)	7	8	9	10	11	12	13	14	15
MISSION PHASE	M _{MEAN} (% DESIGN)	N	σ _{MAX} (KSI)	σ _{MIN} (KSI)	R	σ _{MAX} / F _{TU}	N	n / N	σ _{MAX} / F _{TU}	F.S. x 1.1	n / N	σ _{MAX} / F _{TU}	N	n / N
ASCENT	0	90,000	7.4	-7.4	-1.0	.057	∞	0	.052	∞	0	.047	∞	0
	↑	9,000	11.5	-11.5	↑	.088	∞	0	.080	∞	0	.073	∞	0
	↓	900	15.1	-15.1	↓	.116	8 x 10 ⁶	11.3 x 10 ⁻⁵	.105	1 x 10 ⁷	9.0 x 10 ⁻⁵	.097	∞	0
	↓	90	18.7	-18.7	↓	.144	1.2 x 10 ⁶	7.5 x 10 ⁻⁵	.131	2.7 x 10 ⁶	3.3 x 10 ⁻⁵	.120	5.0 x 10 ⁶	1.8 x 10 ⁻⁵
	0	9	22.5	-22.5	-1.0	.173	4.2 x 10 ⁶	2.1 x 10 ⁻⁵	.157	7.9 x 10 ⁵	1.2 x 10 ⁻⁵	.145	1.3 x 10 ⁶	.7 x 10 ⁻⁵
							Σ	2.1 x 10 ⁻⁴		Σ	1.3 x 10 ⁻⁷		Σ	2.5 x 10 ⁻⁵
	15	90,000	22.6	14.3	.63	.175	∞	0	.160	∞	0	.146	∞	0
	↑	9,000	24.2	12.7	.53	.186	∞	0	.170	∞	0	.155	∞	0
	↓	900	26.2	10.8	.41	.202	1 x 10 ⁷	9 x 10 ⁻⁵	.184	∞	0	.168	∞	0
	↓	90	28.0	8.9	.32	.215	3.0 x 10 ⁶	3 x 10 ⁻⁵	.195	9.0 x 10 ⁶	1 x 10 ⁻⁵	.180	∞	0
	15	9	29.8	7.1	.24	.230	8.4 x 10 ⁵	1.1 x 10 ⁻⁵	.210	1.7 x 10 ⁶	.5 x 10 ⁻⁵	.192	5.0 x 10 ⁶	.2 x 10 ⁻⁵
							Σ	1.3 x 10 ⁻⁴		Σ	1.5 x 10 ⁻⁵		Σ	.2 x 10 ⁻⁵
	10	79,000	22.2	2.4	.11	.18	3.8 x 10 ⁶	1.0 x 10 ⁻⁴	.164	1 x 10 ⁷	1.0 x 10 ⁻⁵	.15	∞	0
	↑	20,000	27.2	-2.5	-.09	.22	3.5 x 10 ⁶	1.0 x 10 ⁻⁵	.20	6.2 x 10 ⁵	1.0 x 10 ⁻⁵	.183	1.2 x 10 ⁶	1.0 x 10 ⁻⁵
		7,000	31.8	-7.1	-.22	.25	1.3 x 10 ⁵	1.0 x 10 ⁻⁵	.23	2.0 x 10 ⁶	1.0 x 10 ⁻⁵	.21	3.5 x 10 ⁵	1.0 x 10 ⁻⁵
		1,000	36.0	-12.3	-.33	.31	4.8 x 10 ⁴	1.0 x 10 ⁻⁴	.28	7.5 x 10 ⁴	1.0 x 10 ⁻⁴	.26	1 x 10 ⁵	1.0 x 10 ⁻⁵
		700	44.0	-19.3	-.44	.36	2.2 x 10 ⁴	1.0 x 10 ⁻⁴	.33	3.2 x 10 ⁴	1.0 x 10 ⁻⁴	.30	5.0 x 10 ⁴	1.0 x 10 ⁻⁴
		200	52.4	-27.7	-.53	.42	9500	1.0 x 10 ⁻⁴	.38	1.0 x 10 ⁵	1.0 x 10 ⁻⁴	.35	2.0 x 10 ⁵	1.0 x 10 ⁻⁴
		70	61.4	-36.8	-.60	.50	3500	1.0 x 10 ⁻⁴	.46	5250	1.0 x 10 ⁻⁴	.42	9000	1.0 x 10 ⁻⁴
		20	70.5	-46.0	-.65	.57	1550	1.0 x 10 ⁻⁴	.52	2700	1.0 x 10 ⁻⁴	.47	4600	1.0 x 10 ⁻⁴
	↓	7	80.0	-55.5	-.69	.64	660	1.0 x 10 ⁻⁴	.58	1260	1.0 x 10 ⁻⁴	.53	2200	1.0 x 10 ⁻⁴
ASCENT	10	2	89.3	-64.5	-.72	.73	210	1.0 x 10 ⁻⁴	.67	430	1.0 x 10 ⁻⁴	.61	800	1.0 x 10 ⁻⁴
							Σ	.277		Σ	.173		Σ	.0983

(1) FACTOR OF SAFETY ON LIMIT LOAD FOR REQUIRED RESIDUAL STRENGTH LEVEL

TABLE 8-3 WING RESIDUAL FATIGUE LIFE ($K_T=3.0$) (SHEET 3)														
1	2	3	4	5	6	7	8	9	10	11	12	13	14	15
MISSION PHASE	M_{MEAN} (% DESIGN)	N	σ_{MAX} (KSI)	σ_{MIN} (KSI)	R	$\frac{\sigma_{MAX}}{\sigma_{FTU}}$	N	$\frac{N}{N}$	$\frac{\sigma_{MAX}}{\sigma_{FTU}}$	N	$\frac{N}{N}$	$\frac{\sigma_{MAX}}{\sigma_{FTU}}$	N	$\frac{N}{N}$
ENTRY		70,000	15.8	0	0	.12	∞	0	.11	∞	0	.10	∞	0
↑		20,000	21.3	↑	↑	.16	1×10^7	.002	.145	∞	0	.133	∞	0
		7,000	28.1			.22	4.2×10^5	.017	.20	8.0×10^5	1,009	.18	2.1×10^6	.0033
		2,000	37.0			.28	1.1×10^5	.018	.254	1.8×10^5	.011	.23	3.1×10^5	.0065
		700	50.7			.39	2.5×10^4	.028	.355	3.9×10^4	.018	.32	6.1×10^4	.0115
		200	88.5	↓	↓	.68	2×10^3	.100	.62	3×10^3	.067	.57	4.5×10^3	.0945
ENTRY		100	117	0	0	.90	115	.870	.82	500	.200	.75	1.3×10^3	.0770
							Σ	1.035		Σ	.305		Σ	.193
CRUISE/	35	70,000	18.0	38.2	.80	.42	8×10^5	.0875	.38	1.6×10^6	.0438	.35	4×10^6	.0175
LANDG	↑	20,000	54.0	32.2	.60	.47	1.1×10^5	.1820	.43	1.6×10^5	.1250	.39	2.6×10^6	.0770
		7,000	60.0	26.0	.43	.53	2.7×10^4	.2600	.48	4.4×10^4	.1590	.44	6.5×10^4	.1080
		2,000	66.2	19.8	.30	.58	9.5×10^3	.2100	.53	1.5×10^4	.1330	.48	2.4×10^4	.0835
		700	72.0	14.1	.20	.63	4.8×10^3	.1455	.57	7.6×10^3	.0920	.53	1×10^4	.0700
		200	78.0	8.0	.10	.69	2.4×10^3	.0835	.63	3.6×10^3	.0556	.57	5.8×10^3	.0345
		70	84.4	1.8	.02	.74	1.4×10^3	.0500	.67	2.2×10^3	.0318	.62	3.1×10^3	.0225
		20	90.0	-3.9	-.04	.80	620	.0322	.78	1.4×10^3	.0143	.67	2.1×10^3	.0095
CRUISE/	↓	7	94.6	-8.4	-.09	.84	290	.0241	.76	700	.0100	.70	1.5×10^3	.0047
LANDG	35	2	98.0	-11.8	-.12	.86	180	.0111	.78	500	.0040	.72	1.2×10^3	.0017
							Σ	1.086		Σ	.668		Σ	.429
GAG		200	84.6	-4.8	-.20	.19	8×10^5	.0002	.17	1.6×10^6	.0001	.16	3.5×10^6	.0001
TOTAL DAMAGE								6.821			3.070			1.751
NOMINAL FATIGUE LIFE (NUMBER OF MISSIONS)								14			32			57
"SAFE" FATIGUE LIFE (NUMBER OF MISSIONS)								3			8			14

is then divided by a scatter factor of 4.0 to obtain "safe" fatigue life, which is indicated at the bottom of Table 8-3. These lives are 3, 8 and 14 missions for residual strength factors of 1.0, 1.1, and 1.2, respectively.

The safe fatigue life for the multi-element spar cap design concept can be approximated by interpolation of the above results. This concept provides an inherent residual strength factor of 1.17, so that the corresponding safe fatigue life is approximately 12 missions after failure of one element in the spar cap assembly. It should be noted that this analytical prediction may be unconservative, because it is based on the assumption of a uniform tension stress over the remaining spar cap elements. It is possible that bending stresses due to the local eccentricities resulting from failure of one element may significantly reduce fatigue life, even though these bending stresses may be alleviated by plastic deformation as ultimate load capability is approached. Therefore, test evaluation of residual fatigue life should be obtained for this type of fail-safe concept in an actual design application.

8.1.5 Design Evaluation

A comparison of the relative structural weight increase between the safe-life and fail-safe design approaches is, of course, of primary interest. However, the weight increase curves for the safe-life approach, summarized in Section 7, are baselined to the original preliminary design sizing which considered only static strength requirements. Therefore, a weight increment of approximately 450 kg (1000 lb) must be added to the fail-safe weight requirements determined in this section to put them on a common basis for comparison. This weight increment accounts for the reduction in maximum limit tension stress to 446 MN/m^2 (165 ksi) to provide adequate fatigue life. With this adjustment, the weight increase for the fail-safe approach employing multi-element spar caps is 850 kg (1885 lbs) and for monolithic spar caps would range from 815 kg (1805 lbs) to 1160 kg (2570 lbs), depending on the level of residual strength required. Examination of Figure 7-18 shows that these weights are in the same order as weight increases for the safe-life approach based on a reasonable estimate of maximum initial flaw size that may exist in the structure. It would be necessary to precisely define the types and sizes of initial flaws and service life to be used as design requirements for the safe-life approach to permit a more specific comparison. However, it can be concluded that fail-safe is a practical and viable alternate design approach in terms of impact on structural weight. The fail-safe approach should result in greater safety because of decreased dependence on inspection reliability to detect small flaws, and is considered to be the preferred design approach for this application. However, it should be noted that the evaluation of residual fatigue life indicates a safe-life, after failure of a major structural element, of only 3 to 14 missions, depending on the fail-safe design concept and residual strength level provided. This is a relatively high frequency for major structural inspections, and may be an important factor in the selection of the most appropriate design approach.

Several aspects need to be considered in a comparison of the relative merits between the two types of fail-safe design approaches investigated in this study. The monolithic spar cap offers the advantages of lower

manufacturing costs and fewer fastener holes which may serve as fatigue crack initiation sites. The multi-element spar cap is significantly lighter for the same level of residual strength; failure of one element would result in much less severe perturbations of wing stiffness and general internal loading distributions than for monolithic design; and the multi-element design is much more amenable to test verification of residual strength capability than the monolithic approach. This last point may be a very significant factor in evaluation of the two design concepts; the practical difficulties in testing a full-scale wing structure employing monolithic spar caps to verify satisfactory residual strength and fatigue life of remaining structure can be seen to be very formidable, particularly when consideration is given to all the potentially critical locations in which a failure may occur. On the other hand, this type of testing may be accomplished quite readily using component specimens representative of the multi-element spar cap designs. A specific evaluation of the relative test costs, relative manufacturing costs, and level of confidence in fail-safe integrity would be required to select the most appropriate design concept for an actual hardware application.

8.2 FAIL-SAFE ANALYSIS - VERTICAL STABILIZER

The preceding evaluation of safe-life characteristics of the cover skins of the vertical stabilizer (Section 7.3) indicated a satisfactory condition; an initial through crack of almost 2 inch length can exist without growing to failure during the service life. This should be quite detectable by ordinary inspection if the outer surface of the vertical stabilizer is not covered by a thermal protection system. However, a fail-safe investigation will also be conducted on this assembly to provide some insight as to the inherent fail-safe characteristics of this type of distributed integral-stiffened structure and to evaluate what improvement in fail-safe capability may be readily accomplished.

8.2.1 Structural Configuration and Loading

The vertical stabilizer main box is a three-spar structure, with the spanwise bending resisted primarily by integral stiffened cover skins of Ti-6Al-4V. The typical skin-stringer configuration is illustrated in Figure 6-3b. The total cover skin assembly is fabricated from spanwise planks machined to this integral stiffened configuration. Ten such planks are joined to cover the chord of the main box structure. The basic design concept from the Phase B study employed fusion welding for the spanwise joints between planks. An alternate design, involving splice straps and mechanical fasteners, will be investigated to evaluate crack arrest and residual strength characteristics of this approach. The two joint configurations are illustrated in Figure 8-2.

Critical bending on the vertical stabilizer is due to lateral gust during subsonic flight; a limit spanwise bending stress of 180 MN/m^2 (26 ksi) results for the selected design configuration in the critical root region (see Figure 6-2). This applied stress may be either tension or compression, and is assumed to be uniform over the chord of the reference section for the purposes of this study.

8.2.2 Inherent Residual Strength

The welded spanwise joints between skin planks of the basic design configuration provide no crack arrest capability; therefore, the inherent crack arrest and residual strength characteristics are dependent on the integral stiffeners. An approximate solution for the stress intensity at the tip of a crack through the skin thickness is obtained as the crack approaches, and then extends through, the integral stiffeners.

The initial model for this study assumes a through crack, of length $2a$, originating midway between integral stiffeners, as indicated in sketch below.

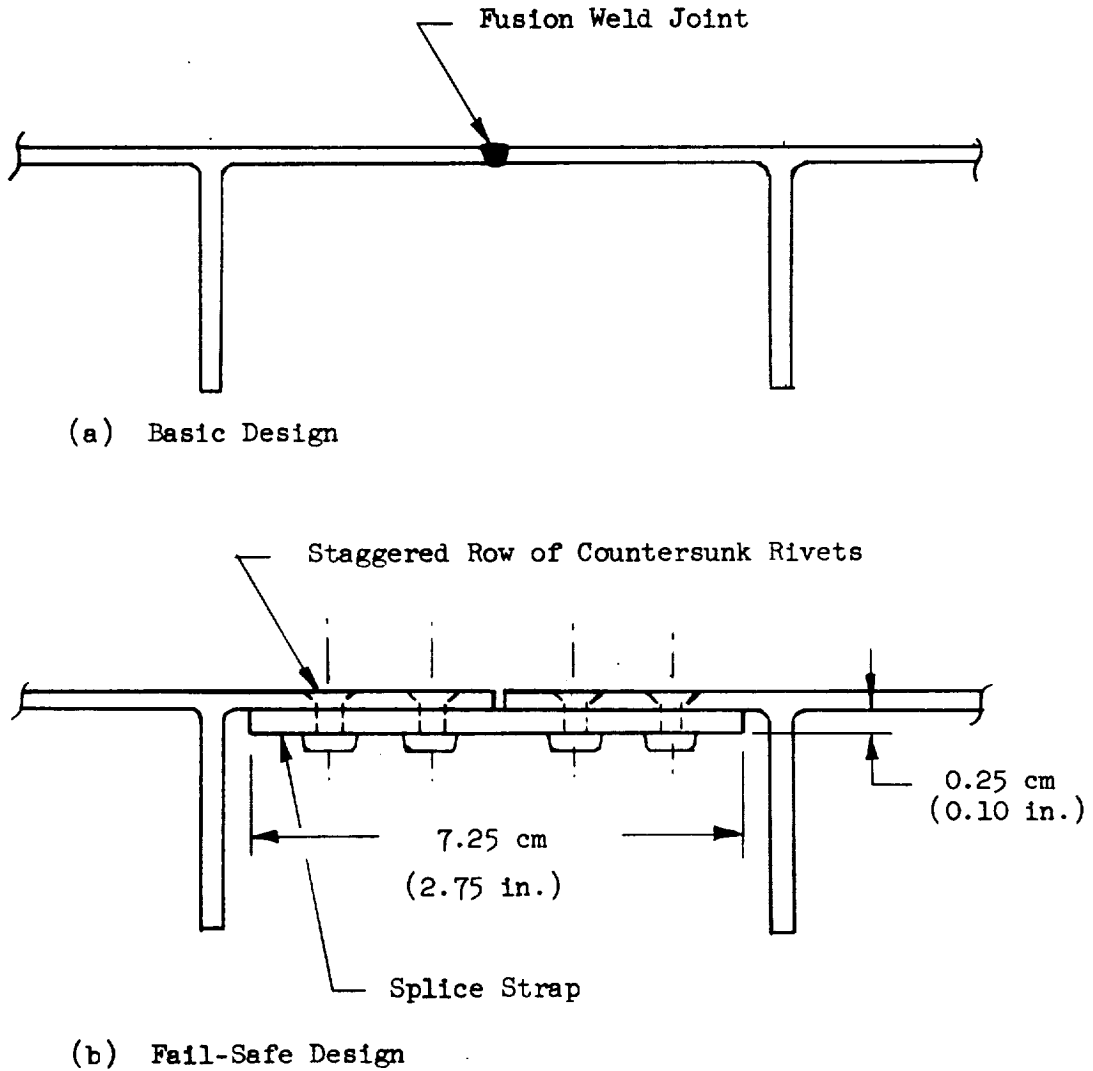
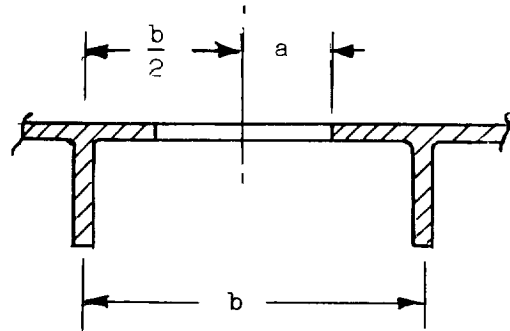


Figure 8-2 Vertical Stabilizer Skin Plank Joint Configurations

If no stiffeners were present, the stress intensity would be given by the elementary equation:

$$K_I = \sigma \sqrt{\pi a} \quad (1)$$



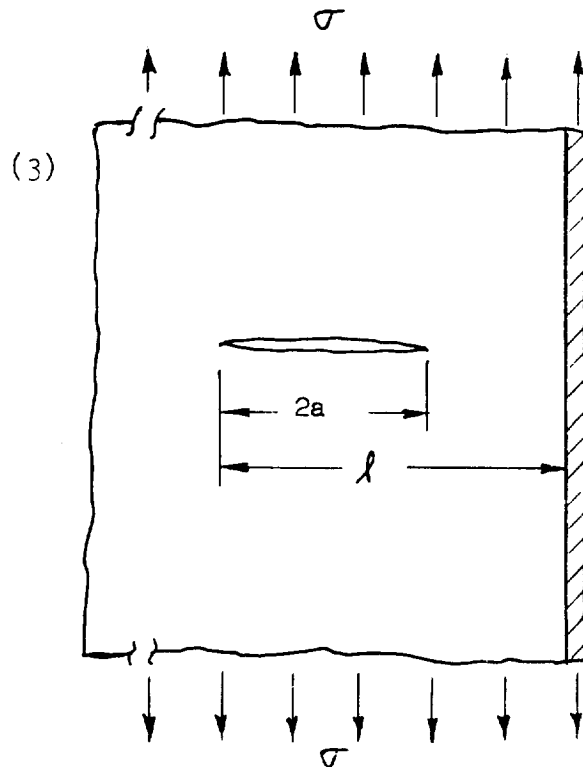
As the crack approaches an integral stiffener, the stress intensity is reduced because of the restraint provided by the stiffener. The resulting stress intensity can be expressed as:

$$K_I = \lambda \sigma \sqrt{\pi a} \quad (2)$$

where λ is a correction factor depending on crack size, proximity of crack tip to stiffener, and the relative stiffness of that member. An approximate solution may be obtained from Figure 46 of Reference 23, where for the parameters indicated in the sketch below:

$$\lambda = f \left(S, \frac{l - 2a}{l} \right)$$

$$S = \frac{4 E_{sk} t_{sk} l}{A_{str} E_{str} (1 + \nu)(3 - \nu)}$$



In this case:

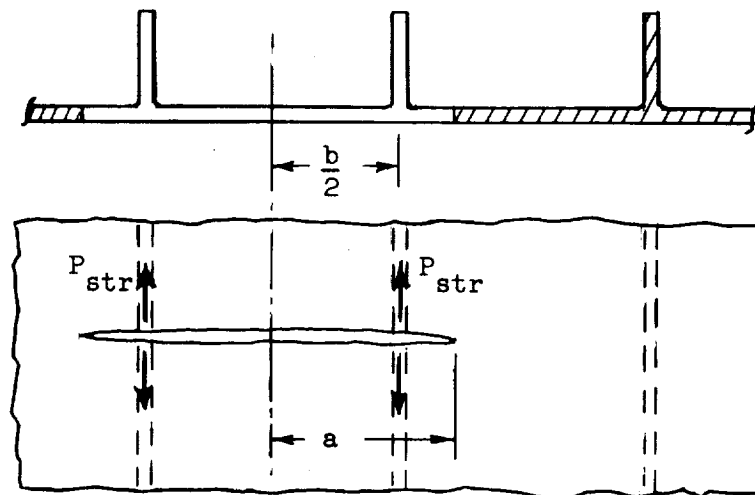
$$s = \frac{4 (0.080) l}{(0.127)(1.3)(2.7)} = 0.72 l$$

$$K_I = \lambda(26.0) \sqrt{3.14 a} = 46.0 \lambda \sqrt{a} \quad (\text{ksi } \sqrt{\text{in.}})$$

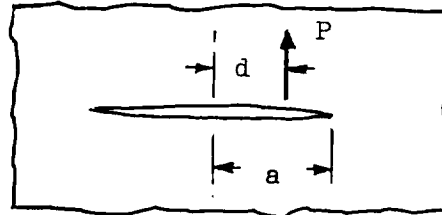
Stress intensity is calculated in the table below as the crack grows from 80 percent to 100 percent of the panel width.

$\frac{2a}{b}$	2 a (in.)	$l-2a$ (in.)	l (in.)	$\frac{l-2a}{l}$	s	λ	\sqrt{a}	K_I (ksi $\sqrt{\text{in.}}$)
0.70	2.10	0.450	2.550	0.177	1.85	0.95	1.02	44.5
0.80	2.40	0.300	2.700	0.111	1.95	0.90	1.09	45.0
0.85	2.55	0.225	2.775	0.081	2.00	0.88	1.13	45.5
0.90	2.70	0.150	2.850	0.052	2.05	0.81	1.16	43.1
0.95	2.85	0.075	2.925	0.026	2.12	0.75	1.19	41.1
1.00	3.00	0	3.000	0	2.16	0.72	1.22	40.5

As the crack grows through the first set of integral stiffeners, a stress intensity magnification will be imposed. This is due to the effect of loading in the severed stiffener, remote from the crack, to apply additional crack opening forces. This is illustrated in the diagram below.



The increase in stress intensity can be approximated from the basic crack loading model sketched below, and the expression:



$$K_I = \frac{P}{2\sqrt{\pi a}} \sqrt{\frac{a+d}{a-d}} \quad (4)$$

where:

P = Load per unit thickness

A correction factor of 1.25 is applied to the above expression to account for the actual case of colinear and opposite forces; this correction provides close agreement with the solution of C.C. Poe for a somewhat different geometric configuration that is presented in Reference 23, and is based on a more exact general analysis.

Equation (4) can be expanded to cover the present problem by accounting for the symmetric stiffener forces near each end of the crack and converting stiffener force to a stress function, with the result:

$$K_I = \frac{1.25 \sigma_{Astr}}{2 t_{sk} \sqrt{\pi a}} \left[\left(\frac{a+d}{a-d} \right)^{\frac{1}{2}} + \left(\frac{a-d}{a+d} \right)^{\frac{1}{2}} \right] \quad (5)$$

It is convenient to put this expression in a coefficient form such that:

$$K_I = \lambda' \sigma \sqrt{\pi a} \quad (6)$$

and

$$K_I = (\lambda' + 1) \sigma \sqrt{\pi a} \quad (7)$$

where:

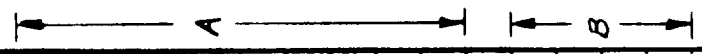
$$\lambda' = \frac{1.25 A_{str}}{2 \pi a t_{sk}} \left[\left(\frac{a+d}{a-d} \right)^{\frac{1}{2}} + \left(\frac{a-d}{a+d} \right)^{\frac{1}{2}} \right] \quad (8)$$

Prepared By: **RWW**
 Checked By:
 Date: **2-10-72**

Space Division
 North American Rockwell

TABLE B-4 STRESS INTENSITY VS. CRACK LENGTH - VERT. STAB. SKIN

1	2	3	4	5	6	7	8	9	10	11	12	13	14	15
a (in.)	a+d ₁ (in.)	a-d ₁ (in.)	a+d ₂ (in.)	a-d ₂ (in.)	$\sqrt{\frac{2}{3}} + \sqrt{\frac{4}{5}}$	$\sqrt{\frac{3}{2}} + \sqrt{\frac{5}{4}}$	λ'	ρ	$\frac{\rho-2a}{\rho}$	S	λ	$\lambda(1+\lambda')$	\sqrt{a}	K _I (KSI/√in.)
1.7	3.2	0.2			4.00	.25	.80	6.2	.45	4.5	1.0	1.80	1.30	107
2.0	3.5	0.5			2.64	.38	.48	6.5	.38	4.7	1.0	1.48	1.41	96
2.5	4.0	1.0			2.00	.50	.31	7.0	.29	5.0	.99	1.30	1.58	95
3.0	4.5	1.5			1.73	.58	.25	7.5	.20	5.4	.98	1.23	1.73	98
3.5	5.0	2.0			1.58	.63	.20	8.0	.125	5.7	.95	1.14	1.87	98
3.9	5.4	2.4			1.50	.67	.18	8.4	.072	6.0	.91	1.07	1.97	97
4.1	5.6	2.6			1.47	.68	.17	8.6	.046	6.2	.87	1.02	2.02	95
4.3	5.8	2.8			1.44	.69	.16	8.8	.023	6.3	.83	.96	2.08	92
4.4	5.9	2.9			1.43	.70	.15	8.9	.011	6.4	.81	.93	2.10	90
4.5	6.0	3.0			1.41	.71	.15	9.0	0	6.5	.78	.90	2.12	88
4.7	6.2	3.2			8.17	.87	.61	12.2	.23	8.8	1.0	1.61	2.17	160
5.0	6.5	3.5			5.72	.97	.42	12.5	.20	9.0	.99	1.40	2.24	144
5.5	7.0	4.0			4.48	1.07	.32	13.0	.15	9.4	.98	1.29	2.35	140
6.0	7.5	4.5			3.93	1.15	.27	13.5	.11	9.7	.96	1.22	2.45	138
A - TWO STIFFENERS SEVERED (d = 1.5 in.)														
B - FOUR STIFFENERS SEVERED (d ₁ = 4.5 in., d ₂ = 1.5 in.)														





in this case:

$$\lambda' = \frac{1.25 (0.127)}{2(3.14)(0.080) a} \left[\left(\frac{a+d}{a-d} \right)^{\frac{1}{2}} + \left(\frac{a-d}{a+d} \right)^{\frac{1}{2}} \right]$$

$$= \frac{0.318}{a} \left[\left(\frac{a+d}{a-d} \right)^{\frac{1}{2}} + \left(\frac{a-d}{a+d} \right)^{\frac{1}{2}} \right] \quad (9)$$

As the crack tip approaches the next set of stiffeners, a reduction in stress intensity will be caused by the restraint of these members, as indicated by Equation 2 and subsequent evaluation. After the crack progresses through the second set of stiffeners, the stress intensity can be determined using the above procedures by superimposing the additional stress intensity from crack-opening forces associated with both sets of severed stiffeners. The resulting distribution of stress intensity as a function of crack length is calculated in Table 8-4, using Equations 2, 3, 7 and 9 and a limit applied stress of 180 MN/m² (26 ksi). The results are plotted in Figure 8-3. Both the stress intensity and the net stress intensity correction factor, $\lambda(1+\lambda')$, are plotted in this diagram. A critical stress intensity of 87.6 MN/m^{3/2} (80 ksi√in) is also superimposed on this plot.

It can be seen that integral stiffeners are relatively ineffective in providing fail-safe capability. As the crack tip approaches the first stiffener, the stress intensity is reduced approximately 30 percent by the restraint of this member. However, as the crack progresses through the stiffener, the stress intensity is significantly increased because of additional crack-opening forces associated with the severed stiffener. If the stiffener is severed abruptly, the stress intensity will jump to a value in the order of 120 MN/m^{3/2} (110 ksi√in.). If the crack is assumed to progress through the stiffener element at the same rate as through the skin (suggested by the theoretical and experimental work of Reference 28), the stress intensity will increase more gradually to a value of about 107 MN/m^{3/2} (98 ksi√in.). As the crack tip approaches the second stiffener, the stress intensity is again reduced because of the restraint of this member. However, the minimum stress intensity achieved, adjacent to this stiffener, is 92 MN/m^{3/2} (84 ksi√in.). This is slightly above the design value for allowable stress intensity, so that crack arrest at the second stiffener is not assured. Therefore, the inherent fail-safe capability of the vertical stabilizer skin is limited to a crack of 7.6 cm (3 in.) length, which will be arrested by the adjacent integral stiffeners.

8.2.3 Residual Strength of Planked Skins

The use of mechanically fastened spanwise joints for wing skin planks will be investigated as a possible improved fail-safe design concept. The total chord of the main box is comprised of ten skin planks, and the width of each plank is about 56 cm (22 in.) in the critical root region. The residual strength of the structure is determined assuming that a crack extends completely across the width of one skin plank. Because the riveted splice joint provides a geometric discontinuity to accomplish crack arrest, it is

An estimated 5 in. of adjacent panel is combined with splice member as an effective coaming stringer, so that:

$$A_2 \cong 0.275 + 5 (0.122) = 0.89 \text{ in.}^2$$

$$A_3 = 11 (0.122) = 1.34 \text{ in.}^2$$

$$A_1 \cong 40 (0.122) = 4.88 \text{ in.}^2$$

(at least two intact planks assumed on either side of fractured plank)

The distances to centroids of areas

A_1 and A_3 are:

$$b_{c1} = 25 \text{ in.}$$

$$b_{c2} = 5.5 \text{ in.}$$

and the effective distance to lumped areas is approximately 0.65 • distance to centroids (empirical relationship developed in Reference 29) so that:

$$b_1 \cong 0.65 (25) = 14.3 \text{ in.}$$

$$b_2 \cong 0.65 (5.5) = 3.6 \text{ in.}$$

The relative stiffness parameters and resulting stress distributions are then given by:

$$\beta_1^2 = \frac{Gt}{Eb_1} \left[\frac{1}{A_1} + \frac{1}{A_2} \right] = \frac{0.4 (0.080)}{14.3} \left[\frac{1}{4.88} + \frac{1}{0.89} \right] = 0.00296$$

$$\beta_1 = 0.0545$$

$$\beta_2^2 = \frac{Gt}{Eb_2} \left[\frac{1}{A_2} + \frac{1}{A_3} \right] = \frac{0.4 (0.080)}{3.6} \left[\frac{1}{0.89} + \frac{1}{1.39} \right] = 0.0165$$

$$\beta_2 = 0.128$$

$$\beta_3 = \frac{Gt}{Eb_1 A_2} = \frac{0.4(0.080)}{14.3 (0.89)} = 0.00252$$

$$\beta_4 = \frac{Gt}{Eb_2 A_2} = \frac{0.4 (0.080)}{3.6 (0.89)} = 0.0100$$

in this case:

$$\begin{aligned} \lambda' &= \frac{1.25 (0.127)}{2(3.14)(0.080) a} \left[\left(\frac{a+d}{a-d} \right)^{\frac{1}{2}} + \left(\frac{a-d}{a+d} \right)^{\frac{1}{2}} \right] \\ &= \frac{0.318}{a} \left[\left(\frac{a+d}{a-d} \right)^{\frac{1}{2}} + \left(\frac{a-d}{a+d} \right)^{\frac{1}{2}} \right] \end{aligned} \quad (9)$$

As the crack tip approaches the next set of stiffeners, a reduction in stress intensity will be caused by the restraint of these members, as indicated by Equation 2 and subsequent evaluation. After the crack progresses through the second set of stiffeners, the stress intensity can be determined using the above procedures by superimposing the additional stress intensity from crack-opening forces associated with both sets of severed stiffeners. The resulting distribution of stress intensity as a function of crack length is calculated in Table 8-4, using Equations 2, 3, 7 and 9 and a limit applied stress of 180 MN/m^2 (26 ksi). The results are plotted in Figure 8-3. Both the stress intensity and the net stress intensity correction factor, $\lambda(1+\lambda')$, are plotted in this diagram. A critical stress intensity of $87.6 \text{ MN/m}^{3/2}$ (80 ksi $\sqrt{\text{in}}$) is also superimposed on this plot.

It can be seen that integral stiffeners are relatively ineffective in providing fail-safe capability. As the crack tip approaches the first stiffener, the stress intensity is reduced approximately 30 percent by the restraint of this member. However, as the crack progresses through the stiffener, the stress intensity is significantly increased because of additional crack-opening forces associated with the severed stiffener. If the stiffener is severed abruptly, the stress intensity will jump to a value in the order of $120 \text{ MN/m}^{3/2}$ (110 ksi $\sqrt{\text{in}}$). If the crack is assumed to progress through the stiffener element at the same rate as through the skin (suggested by the theoretical and experimental work of Reference 28), the stress intensity will increase more gradually to a value of about $107 \text{ MN/m}^{3/2}$ (98 ksi $\sqrt{\text{in}}$). As the crack tip approaches the second stiffener, the stress intensity is again reduced because of the restraint of this member. However, the minimum stress intensity achieved, adjacent to this stiffener, is $92 \text{ MN/m}^{3/2}$ (84 ksi $\sqrt{\text{in}}$). This is slightly above the design value for allowable stress intensity, so that crack arrest at the second stiffener is not assured. Therefore, the inherent fail-safe capability of the vertical stabilizer skin is limited to a crack of 7.6 cm (3 in.) length, which will be arrested by the adjacent integral stiffeners.

8.2.3 Residual Strength of Planked Skins

The use of mechanically fastened spanwise joints for wing skin planks will be investigated as a possible improved fail-safe design concept. The total chord of the main box is comprised of ten skin planks, and the width of each plank is about 56 cm (22 in.) in the critical root region. The residual strength of the structure is determined assuming that a crack extends completely across the width of one skin plank. Because the riveted splice joint provides a geometric discontinuity to accomplish crack arrest, it is

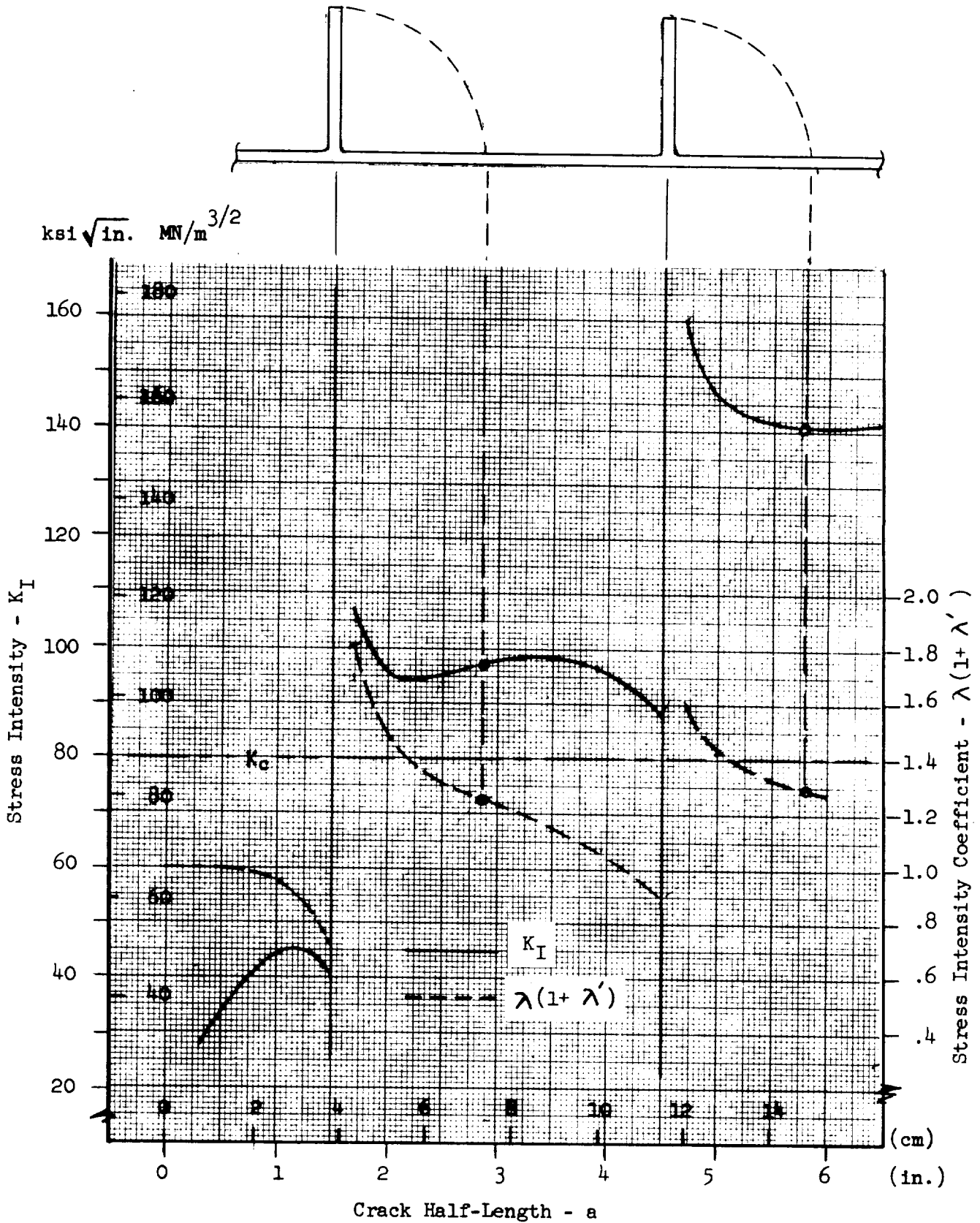


Figure 8-3 Stress Intensity vs. Crack-Length - Vertical Stabilizer Skins

not necessary or appropriate to apply fracture mechanics theory to predict residual strength. However, the failure of one skin plank will cause an elastic concentration of loading in the adjacent planks, that must be accounted for. This is basically a load redistribution or "shear lag" problem, and an approximate solution is obtained employing the "three-stringer method" for rectangular cutouts in stiffened panels that is presented in Reference 29. The vertical stabilizer design provides ribs at 1.27 (50 in.) spacing with intermediate stiffeners midway between the ribs. Therefore, a crack completely across a skin plank creates an effective "cut-out" bay of 56 cm (22 in.) width and 63 cm (25 in.) length before redistribution of the longitudinal loading can be accomplished by skin shear flows.

The idealized model of the structure containing this equivalent cut-out, and the analysis equations from Reference 29 are summarized below. (To avoid confusion with stress intensity designation, the coefficients K_1, K_2 etc. defined in Ref. 29 are identified as β_1, β_2 etc. in the present text.)

$$\sigma_1 = \bar{\sigma} \left[\frac{1 - R C_o A_2 \cosh \beta_1 X}{A_1 \cosh \beta_1 d} \right]$$

$$\sigma_2 = \bar{\sigma} \left[\frac{1 + R C_o \cosh \beta_1 X}{\cosh \beta_1 d} \right]$$

where: $\bar{\sigma}$ = average stress in net section, which has the area $A_1 + A_2$

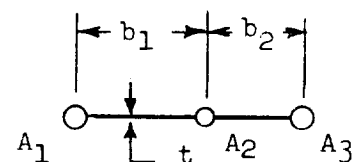
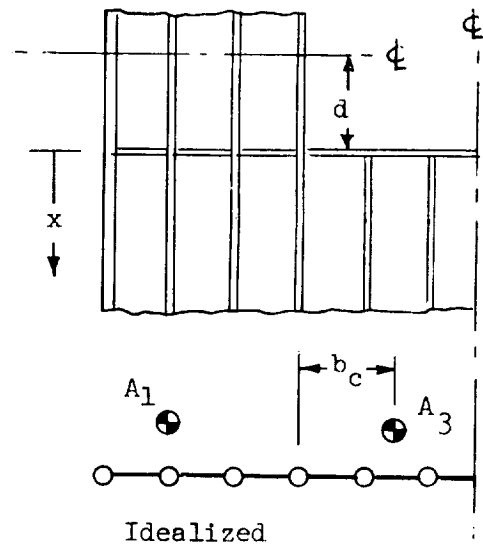
C_o, R are stress redistribution factors, dependant on relative axial and shear stiffness.

In this case:

$t = 0.080$ in. (skin thickness)

$\bar{t} = 0.122$ in. (equivalent thickness of skin and stiffeners)

$A_{sp} = 0.275$ in.² (area of splice strap)



An estimated 5 in. of adjacent panel is combined with splice member as an effective coaming stringer, so that:

$$A_2 \cong 0.275 + 5 (0.122) = 0.89 \text{ in.}^2$$

$$A_3 = 11 (0.122) = 1.34 \text{ in.}^2$$

$$A_1 \cong 40 (0.122) = 4.88 \text{ in.}^2 \quad (\text{at least two intact planks assumed on either side of fractured plank})$$

The distances to centroids of areas

A_1 and A_3 are:

$$b_{c1} = 25 \text{ in.}$$

$$b_{c2} = 5.5 \text{ in.}$$

and the effective distance to lumped areas is approximately 0.65 • distance to centroids (empirical relationship developed in Reference 29) so that:

$$b_1 \cong 0.65 (25) = 14.3 \text{ in.}$$

$$b_2 \cong 0.65 (5.5) = 3.6 \text{ in.}$$

The relative stiffness parameters and resulting stress distributions are then given by:

$$\beta_1^2 = \frac{Gt}{Eb_1} \left[\frac{1}{A_1} + \frac{1}{A_2} \right] = \frac{0.4 (0.080)}{14.3} \left[\frac{1}{4.88} + \frac{1}{0.89} \right] = 0.00296$$

$$\beta_1 = 0.0545$$

$$\beta_2^2 = \frac{Gt}{Eb_2} \left[\frac{1}{A_2} + \frac{1}{A_3} \right] = \frac{0.4 (0.080)}{3.6} \left[\frac{1}{0.89} + \frac{1}{1.39} \right] = 0.0165$$

$$\beta_2 = 0.128$$

$$\beta_3 = \frac{Gt}{Eb_1 A_2} = \frac{0.4 (0.080)}{14.3 (0.89)} = 0.00252$$

$$\beta_4 = \frac{Gt}{Eb_2 A_2} = \frac{0.4 (0.080)}{3.6 (0.89)} = 0.0100$$

$$\bar{\beta}^2 = \beta_1^2 \beta_2^2 - \beta_3 \beta_4 = (.00296)(.0165) - (.00252)(.0100) \\ = 0.236 \times 10^{-4}$$

$$\bar{\beta} = 0.00486$$

$$C_0 = \frac{\beta_3 \beta_4}{\beta_1^2 \bar{\beta} + \bar{\beta}^2} = \frac{(.00252)(.0100)}{(.00296)(.00486) + .236 \times 10^{-4}} = 0.665$$

$$R \cong \frac{1}{1 + \tanh \beta_1 d} = \frac{1}{1 + \tanh (.0545)(12)} = 0.635$$

$$\sigma_2 = \bar{\sigma} \left[1 + (0.635)(0.665) \frac{\cosh \beta_1 X}{\cosh \beta_1 d} \right]$$

The maximum stress in the net section will occur at the edge of the cut-out, where $x = d$, so that:

$$\sigma_{2_{\max}} = \bar{\sigma} [1 + 0.42] = 1.42 \bar{\sigma}$$

However, $\bar{\sigma}$ is the average stress in the net section, and is related to the gross stress by the ratio of original to remaining area after fracture of one skin plank, so that:

$$\bar{\sigma} = \frac{10}{9} \sigma_0 = 1.11 \sigma_0$$

$$\sigma_{2_{\max}} = 1.11 (1.42) \sigma_0 = 1.58 \sigma_0$$

For this case, with σ_0 equal to limit stress of 180 MN/m^2 (26 ksi):

$$\sigma_{2_{\max}} = 1.58 (180) = 280 \text{ MN/m}^2 (41 \text{ ksi})$$

For tension loading, the allowable stress is estimated at $0.90 F_{T_u}$, to account for local area reductions due to fastener holes, etc. This gives an allowable stress of 810 MN/m^2 (117 ksi), and the corresponding residual strength factor is:

$$\text{F.S.} = \frac{810}{280} = 2.9$$

This shows a residual strength capability approximately three times limit load under tension loading, so obviously the fail-safe capability is adequate for this failure mode. However, if the cracked skin plank is assumed to be

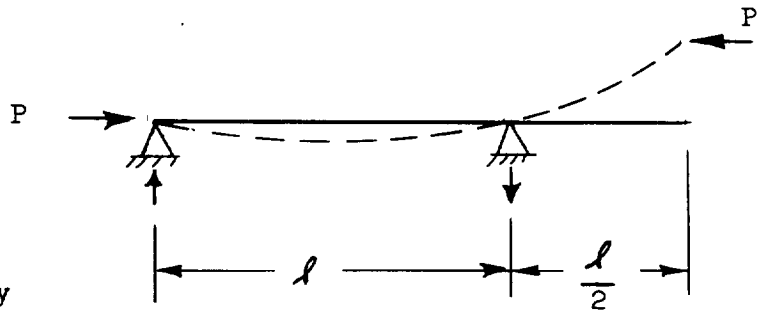
completely ineffective under compression loading as well as tension, then the previously determined stress concentration factor is also applicable to the adjacent skin planks under compression loading. Because the design loads on the vertical stabilizer are completely reversible, the maximum compression stress would also be 280 MN/m^2 (41 ksi). The allowable compression stress, as governed by panel buckling, is 270 MN/m^2 (39.4 ksi). Therefore, the fail-safe factor of safety under compression loading would be:

$$\text{F.S.} = \frac{270}{280} = 0.96$$

This indicates that slightly less than limit load capability would be provided if the cracked skin plank is completely ineffective under compression loading. Therefore, it is considered desirable to undertake an approximate evaluation of the compression load carrying capability of the cracked skin plank.

Compression loading can be transmitted by bearing pressure on the crack surfaces unless severe misalignment of the panels on each side of the crack has occurred. However, the effective bending stiffness will be reduced or eliminated at the crack section. Assume, as a worst case, that the crack occurs midway between chordwise stiffeners and that the bending stiffness of skin-stringer panels is completely eliminated at this point. The structural model on each side of the cracks can then be idealized as a simply supported column with an overhanging free end of length equal to one half the support spacing. This is indicated in the sketch below:

The critical load can be determined by writing the appropriate differential equations for each section of the model (between the supports, and overhang region), imposing the requirement for compatible slope at the common junction, and solving for coefficients by imposing appropriate boundary conditions.



The resulting combined equation is:

$$\frac{k l}{\tan k l} - 1 = \frac{\left[\cos \frac{k l}{2} \quad -2 \right]}{\sin \frac{k l}{2}} k l$$

where:

$$k = \sqrt{P/EI}$$

l = column length between supports

$$kl = \pi \sqrt{P/P_e}$$

P_e = Euler critical load for simply supported column.

The above equation was solved by iteration to obtain the value of kl , and an effective column end fixity coefficient of 0.64 was determined. However, some misalignment or imperfect bearing may exist between the crack surfaces, so the effective end fixity coefficient is arbitrarily reduced to 0.40 to allow for these possible effects. The allowable compression stress across the cracked skin plank then becomes:

$$\sigma_{cr} = 0.40 (39.4) = 15.8 \text{ ksi.}$$

The previously determined load redistribution factors are then applied to the difference between the gross applied stress and the allowable stress of the cracked plank. This results in the following expression for the maximum stress in adjacent skin planks.

$$\begin{aligned} \sigma &= 15.8 + 1.58 (\sigma_o - 15.8) \\ &= 1.58 \sigma_o - 9.2 \end{aligned}$$

Equating this applied stress to the panel buckling allowable:

$$39.4 = 1.58 \sigma_o - 9.2$$

$$\sigma_o = 30.8 \text{ ksi. (allowable gross stress)}$$

and the fail-safe factor of safety is:

$$\text{F.S.} = \frac{30.8}{26.0} = 1.18$$

This indicates that, based on the preceding assumptions, the residual strength under compression loading is approximately 20 percent above limit load level. Because of this relatively small margin, and the gross nature of some of the required assumptions, test verification of the residual strength would be highly desirable for an actual design application.

8.2.4 Design Evaluation

The preceding evaluation showed that the inherent fail-safe capability of the basic design for vertical stabilizer cover skins is relatively low; a through crack of 7.6 cm (3.0 in.) length is the maximum that will be arrested by integral stiffeners. However, by replacing the welded spanwise

joints between skin planks with riveted splices, the fail-safe capability can be greatly improved. With this configuration, a crack completely across the width of a skin plank (crack length = 22 in.) will be arrested and the residual strength of the remaining structure is greater than limit load for both tension and compression loading. The maximum stress on the remaining structure is approximately 280 MN/m^2 (41 ksi) at limit load, so that the safe fatigue life of the remaining structure should exceed one service lifetime (100 missions), by comparison to the wing spar fatigue analysis. Therefore, it is of interest to determine the approximate weight increase associated with the riveted splices. This weight increase is estimated on the basis of the following assumptions:

- 1) Splice straps are 7.0 cm (2.75 in.) wide and taper in thickness from 0.254 cm (0.100 in.) at the root to 0.127 cm (0.050 in.) at the tip.
- 2) A staggered double row of counter sunk head titanium fasteners are used on each side of the splice. Fasteners are $3/16$ in. diameter and the pattern is equivalent to a single row at $5/8$ inch spacing.
- 3) Nine full-span splices are provided on each surface of the vertical stabilizer main box.

The average length of spanwise splices is 11.2 m (440 in.), the resulting calculated weight of splice straps is 118 kg (260 lb). However, if these splice members are accounted for as effective spanwise bending material in the original design, the gauge of basic skin and stringers may be reduced slightly. Therefore, it is estimated that 50 percent of the indicated splice weight is an actual increase to the vertical stabilizer structure.

The total length of splices involves approximately 25,000 fasteners with an estimated weight of 20 kg (40 lb). The total weight increase is the sum of fastener weight and effective splice strap weight:

$$20 + 0.5 (118) = 79 \text{ kg (170 lb)}$$

This represents 1.8 percent of the stabilizer main box structural weight.

For the specific case of the B-9U vertical stabilizer, it is probable that the additional fail-safe capabilities of riveted splices between skin planks is not required. A through crack of 7.6 cm (3.0 in.) length should be readily detected by visual inspection during pre-flight checks. However, if this type of structure were used in an application that was not readily inspectable, the additional fail-safe capability could be highly desirable. For example, if the outer surface were covered with a thermal protection system, direct visual inspection would not be possible. Radiographic inspection, shooting completely through the structure, should reliably detect a crack 56 cm (22 in.) long, but might not ensure detection of a crack only 7.6 cm (3 in.) long.

8.3 FAIL-SAFE ANALYSIS - CREW COMPARTMENT

The safe-life analysis of crew compartment indicated that an initial crack of approximately 1.27 cm (0.5 in.) length through the compartment skin can exist without growing to failure during the service life. An initial flaw of these characteristics should be reliably detected during fabrication and final inspection of the structure. However, a crack of this size caused by accidental damage during the service life might go undetected because of restricted accessibility due to external TPS, internal equipment, etc. Therefore, because of the extreme importance of compartment structural integrity to crew safety, an investigation of fail-safe design concepts is also performed. Particular attention is given to the problem of maintaining a cabin atmosphere adequate for crew survival in the event that a crack propagates to significant size before being arrested by the fail-safe design provisions.

8.3.1 Structural Configuration and Loading

For purposes of the fail-safe study, the crew compartment is idealized as a cylindrical shell of 3.05 m (120 in.) diameter and 4.6 m (180 in.) length. The skin is of 2219-T87 aluminum alloy with integral longitudinal stiffeners. Minimum skin thickness is 0.076 cm (0.030 in.). The fail-safe design concept to be investigated assumes the use of circumferential "tear straps" of annealed 6AL-4V titanium alloy riveted to the aluminum shell. These straps serve as crack arrest members to prevent longitudinal cracks in the basic skin from extending beyond the straps. Titanium is selected for these members because of its high strength and toughness and the satisfactory performance demonstrated on jet transport aircraft cabins. The strap spacing is considered a variable in the study, and the structural and cabin pressure systems weight is evaluated as a function of strap spacing, considering both structural integrity and cabin atmosphere requirements.

The crew compartment is loaded primarily by internal pressure; maximum differential pressure is 14.7 psi. The limit hoop stress in basic skin is 206 MN/m^2 (30 ksi).

8.3.2 Residual Strength and Sizing Analysis

In keeping with common practice employed in the design of jet transport aircraft cabins, it is assumed that a longitudinal crack may initiate in the skin at the point of attachment of a tear strap and proceed in both directions from this origin. The adjacent tear straps must then be adequate to arrest the crack and confine it to a two-bay length. The effectiveness of the tear straps may be expressed as a stress intensity reduction factor applied to the crack tip. Theoretical and experimental investigations have shown that this reduction is dependent on the relative stiffness of the strap to the basic skin and the spacing of rivets in the strap attachment pattern. Design curves have been developed in Reference 30 and are reproduced in Figure 8-4. In this figure, a family of stress intensity coefficient curves are plotted over three bays of a stiffened panel for various values of relative stiffness and rivet spacing. In the present case it is desired to confine the crack half-length to one bay, so the stress intensity conditions in the vicinity

of the first strap away from the crack origin are of primary interest. It can be seen that the maximum reduction in crack tip stress intensity occurs at a value of $a/b \cong 1.05$. The stress intensity coefficients at this location are cross-plotted as a function of relative stiffness parameter (μ) in Figure 8-5; this presents the data in a form more easily used for determining strap sizing requirements. In determining these requirements, it is assumed that the maximum stress intensity at crack tip will be limited to 90 percent of the critical value to ensure crack arrest. For thin sections of 2219-T87 aluminum alloy sheet, a critical stress intensity (K_c) of $71 \text{ MN/m}^{3/2}$ ($65 \text{ ksi } \sqrt{\text{in.}}$) is estimated from literature sources. The governing relationship can then be written as:

$$K_I = \lambda \sigma \sqrt{\pi a} = 0.90 K_c$$

where:

$$\sigma = 30 \text{ ksi} \quad (\text{limit hoop stress in skin})$$

$$a = 1.05 b \quad (\text{point of max reduction in stress intensity})$$

$$K_c = 65 \text{ ksi } \sqrt{\text{in.}}$$

$$\lambda = f \left(\mu, \frac{p}{b} \right)$$

therefore :

$$0.90 (65.0) = \lambda (30.0) \sqrt{(3.14) (1.05) b} \quad (10)$$

$$\lambda = \frac{1.07}{\sqrt{b}}$$

Rivets are assumed to be at $3/4$ in. spacing, so the rivet parameter (p/b) is defined for a given value of strap spacing, b . The data plotted in Figure 8-5 is then used to determine the strap sizing required to achieve a given value of λ , from the relationship:

$$\mu = \frac{1}{1 + \frac{A_{sk} E_{sk}}{A_{st} E_{st}}}$$

where:

$$A_{sk} = bt_{sk} \quad (\text{cross-section area of skin over one bay length})$$

$$A_{st} = \text{cross-section area of reinforcing strap}$$

$$E_{sk} = \text{modulus of elasticity of skin material}$$

$$E_{st} = \text{modulus of elasticity of strap material}$$

In this case:

$$\mu = \frac{1}{1 + \frac{A_{sk} (10.5)(10^6)}{A_{st} (16.0)(10^6)}} = \frac{1}{1 + \frac{0.665 A_{sk}}{A_{st}}}$$

$$A_{st} = 0.665 \left[\frac{\mu}{1 - \mu} \right] A_{sk} \quad (11)$$

The increased structural weight due to the addition of crack arrest straps is calculated from the following relationships:

$$\text{Number of straps: } n = \frac{180}{b} \quad (\text{use next higher integer})$$

$$\text{Circumference: } S = 3.14 (120) = 375 \text{ in.}$$

$$W_{st} = n (375) A_{st} (0.160) = 60 n A_{st} \quad (12)$$

In addition to this weight, some allowance is made for the practical requirements of attaching the straps to the basic shell. The basic skin thickness (0.030 in.) would limit the effectiveness of the riveted attachment because of high bearing stresses on the skin. Therefore, it is assumed that an integral reinforcing land, 1 in. wide and 0.060 in. thick is provided under each strap to improve the joint allowable. These contributions to structural weight increase are estimated using the following relationships:

Additional skin weight:

$$W_{sk} = n (375)(1)(.030)(0.10) = 1.13 n \quad (13)$$

Fastener weight:

$$\text{Additional weight per fastener} \cong 0.0043 \text{ lb}$$

$$\text{Number of fasteners} = \frac{375}{0.75} n = 500 n$$

$$W_f = (500 n)(.0043) = 2.15 n$$

The strap area required and the resulting increase in structural weight are calculated for a range of strap spacings from 4 in. to 20 in., employing Equations 10, 11, 12, 13 and 14; calculations are summarized in Table 8-5. A plot of the resulting structural weight increase is given in Figure 8-6. It can be seen that minimum structural weight occurs at a strap spacing of about 20 cm (8 in.); however, the curve is relatively flat and spacing can be increased to the range of 30 cm (12 in.) to 36 cm (14 in.) with only a modest penalty.

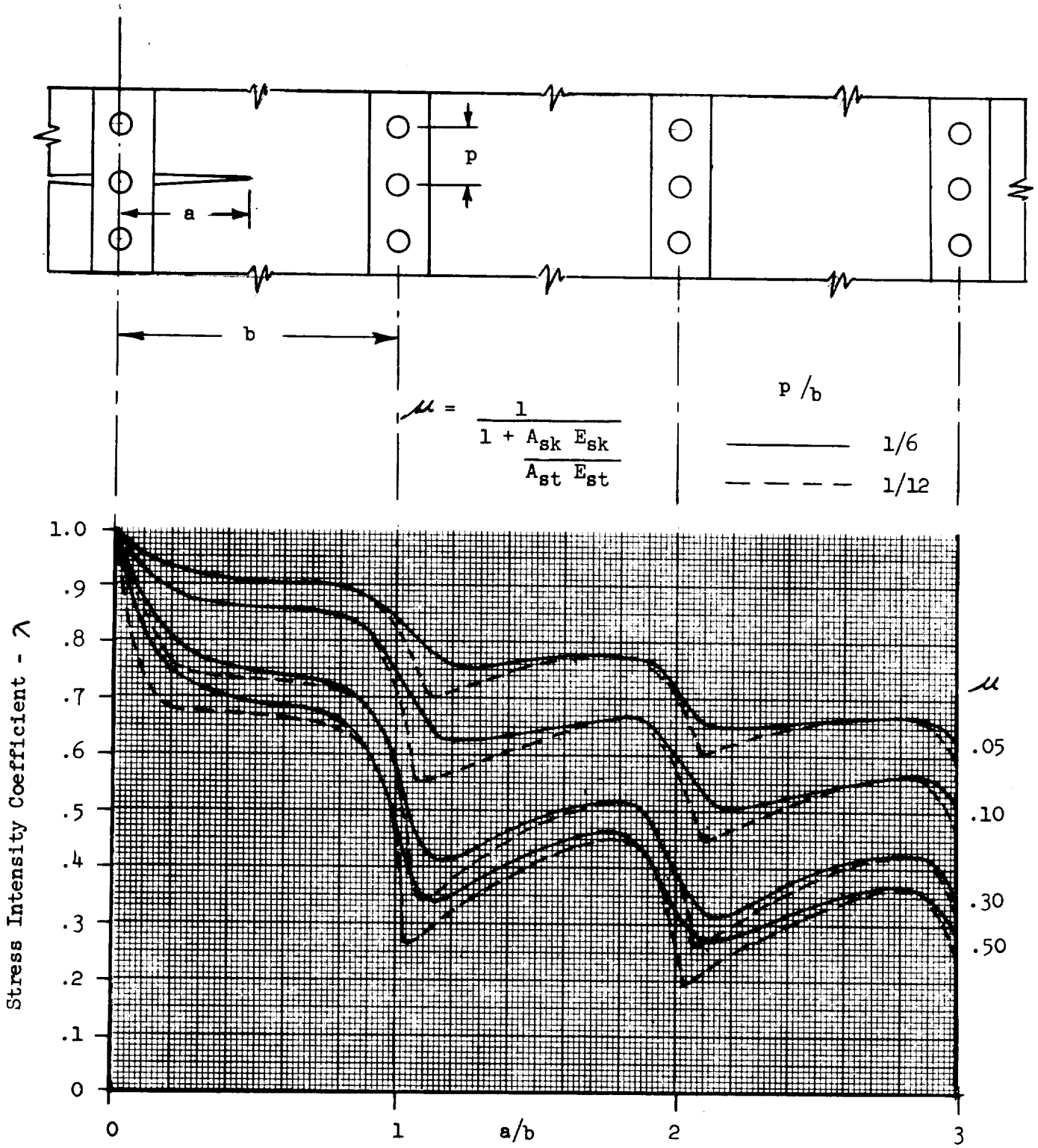


Figure 8-4 Stress Intensity Coefficients for Cracked Panel with Riveted Reinforcing Straps

$$K_I = \lambda \sqrt{\pi a} \sigma$$

p = rivet pitch

$$\mu = \frac{1}{\frac{1 + A_{sk} E_{sk}}{A_{st} E_{st}}}$$

b = stiffener spacing

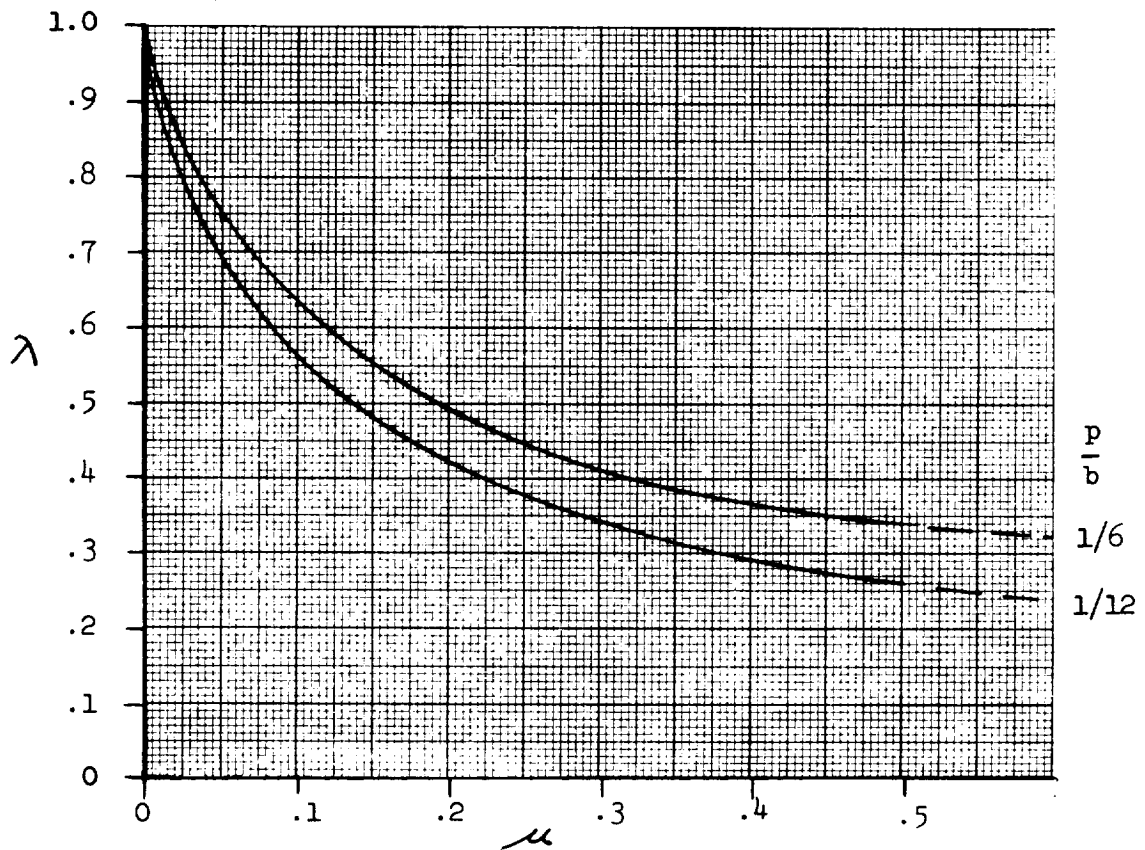


Figure 8-5 Stress Intensity Coefficient vs Relative Stiffness of Reinforcing Member

Table 8-5 Crack-Arrest Strap Sizing and Structural Weight Increase - Crew Compartment

Strap Spacing b (in.)	No of Straps n	(1) $\lambda = \frac{1.07}{\sqrt{b}}$	(2) P/b	(3) μ	$\frac{\mu}{1-\mu}$	A _{sk} (in. ²)	A _{st} (in. ²)	W _{st} (lb)	W _{sk} (lb)	W _f (lb)	W _{tot} (lb)
4	45	.535	.19	.175	.212	.120	.017	46	51	97	194
8	22	.390	.094	.255	.342	.240	.054	72	25	47	144
10	18	.340	.075	.300	.430	.300	.086	93	20	39	152
12	15	.310	.062	.360	.563	.360	.135	121	17	32	170
14	13	.286	.054	.420	.725	.420	.203	158	15	28	201
16	11	.267	.047	.475	.905	.480	.290	192	12	24	228
18	10	.250	.042	.540	1.17	.540	.420	252	11	22	285
20	9	.240	.038	.630	1.70	.600	.680	367	10	20	397

(1) λ = Stress intensity reduction factor

(2) P/b = Rivet pitch/strap spacing

(3) μ = Skin/strap relative stiffness parameter

The above evaluation considers only the requirement of maintaining structural integrity, i.e., preventing complete rupture of the crew compartment with a significant crack present in the skin. This requirement is adequate for conventional aircraft, which can quickly descend to a safe altitude if such an event occurs and significant cabin leakage results. However, the B-9U booster is constrained to follow a programmed flight path, so that the problem of loss of cabin atmosphere may be equally as important as preventing rupture of the compartment. This aspect of fail-safe design requirements is investigated in the following sections.

8.3.3 Cabin Atmosphere Leakage

Experimental data on a specific configuration is probably required to accurately define a relationship between crack length and effective leakage area; however, for purposes of this study approximate relationships will be developed using analysis and experimentally derived crack-opening displacement.

Normalized compliance expressions for center-cracked panels have been developed as part of NR/SD fracture mechanics test effort. For panels of infinite width, the compliance equation can be simplified to:

$$\text{COD} \left(\frac{AE}{P} \right) = \left[\frac{G}{1 + \frac{2a}{G}} + 4a \right]$$

where:

- COD = measured opening displacement at center of crack
- P/A = applied tension stress
- E = modulus of elasticity of panel material
- G = gauge length over which displacement is measured
- a = crack half-length

The actual opening of the crack faces is desired, so the gauge length approaches zero for this case, and the above equation may be simplified to:

$$\delta \left[\frac{E}{\sigma} \right] = 4a = 2\ell$$

where:

- δ = maximum crack opening, at center of crack.

If the crack faces are assumed to follow a sine wave deflection pattern, the incremental area may be integrated with the following result for total area of the crack opening:

$$A = 0.64 \delta \ell$$

However, the crack faces probably tend to remain relatively parallel over the mid-region, so the following estimated expression is used for crack opening area:

$$A = 0.80 \delta l = 1.60 \left[\frac{\sigma}{E} \right] l^2$$

In this case:

$$\sigma = 30,000 \text{ psi}$$

$$E = 10.5 \times 10^6 \text{ psi}$$

$$l = b \text{ (crack length assumed equal to strap spacing)}$$

so that the expression for total crack opening area, considering that the reference model is equivalent to two cracks of length b emanating from a tear strap, may be written as:

$$A_0 = 2 \frac{(1.60)(30,000)}{(10.5)(10^6)} b^2 = 0.0092 b^2 \text{ (in.}^2\text{)} \quad (15)$$

The above expression is based on linear displacement of a flat panel under the action of in-plane tensile stresses. Because the actual model is a portion of a cylindrical shell, which is subject to normal pressure loading in addition to hoop stresses, it is possible that out-of-plane deflections may occur which increase the effective leakage area. Deflections normal to the shell have been approximated for the case of a relatively long crack ($l = 20$ in.) by applying beam theory to a typical panel of skin with integral stiffeners. The additional component of deflection in the opening mode was found to be negligibly small ($\delta' \cong 0.002$ in.) for integral stiffeners sized to carry the normal pressure loading by beam action over the length of the crack. However, the pressure loading on segments of the skin between the crack face and the first longitudinal stiffener may cause local skin distortions which could increase the effective leakage area but which cannot be accurately predicted by theoretical analysis. Therefore, an uncertainty factor, which varies linearly from 1.0 for small cracks ($l \cong 4$ in.) to 1.5 for long cracks ($l \cong 20$ in.) is applied to the crack-opening area given by Equation 15.

The following basic assumptions are made to establish the framework for detailed investigation of the impact of cabin atmosphere leakage on fail-safe design requirements:

- (1) The crew compartment is initially pressurized with air to standard sea level conditions. A pressurized volume of 1200 cu ft is assumed.



- (2) The minimum cabin pressure for crew survival and adequate performance is 7 psi; this is a cabin altitude of approximately 20,000 ft. It is assumed that the crew will don oxygen masks during this emergency period.
- (3) The period of time between the point in the ascent trajectory at which a cabin skin failure could reasonably occur, and the point at which the booster has descended to an altitude of 20,000 ft after entry is 600 sec. Cabin atmosphere leakage will be considered over this maximum time period.
- (4) Ambient pressure external to the crew compartment is assumed to be zero for the entire time period defined above.
- (5) An emergency pressurization system will be employed as required to maintain a minimum cabin pressure of 7 psia.

With the simplifying assumption that cabin leakage is always to vacuum conditions over the period of interest, the flow through the crack opening area will be sonic, and the pressure at the orifice is related to the compartment pressure by the constant relationship:

$$P_o = 0.528 P_c \quad (16)$$

where:

P_o = pressure in free stream at orifice

P_c = compartment pressure

The gas temperatures in the orifice stream and the compartment are related by the adiabatic equation:

$$\begin{aligned} T_o &= T_c \left[\frac{P_o}{P_c} \right]^{\frac{k-1}{k}} = T_c \left[\frac{P_o}{P_c} \right]^{0.286} \\ &= T_c (0.528)^{0.286} = 0.84 T_c \end{aligned} \quad (17)$$

The sonic velocity at the orifice is a function of free-stream temperature and is given by the equation:

$$C_o = k g R T \quad (18)$$

where:

C_o = sonic velocity at orifice - ft/sec

k = gas constant = 1.4 for air

g = gravitational acceleration - 32.2 ft/sec²

R = universal gas constant = 53.3

T = absolute temperature - deg Rankine

so for this case:

$$C_o = 49 \sqrt{T_o} \quad (19)$$

The free-stream gas density at the orifice is obtained from the fundamental relationship:

$$w_o = \frac{P_o}{RT_o} \quad (20)$$

The normalized flow rate (mass flow per unit area) is then obtained as the product of velocity and density:

$$G/A = C_o w_o \quad (21)$$

where:

G = mass flow - lb/sec

A = effective crack-opening orifice area - ft²

C_o = flow velocity - ft/sec

w_o = flow density - lb/ft³

However, as leakage occurs, the air remaining in the compartment will expand by adiabatic processes, which changes the initial reservoir conditions used to find the free-stream properties at the orifice. The key relationships are expressed by:

$$T_{c_2} = T_{c_1} \left[\frac{P_{c_2}}{P_{c_1}} \right]^{\frac{k-1}{k}} = T_{c_2} \left[\frac{P_{c_2}}{P_{c_1}} \right]^{0.286} \quad (22)$$

$$w_{c_2} = \frac{P_{c_2}}{RT_{c_2}} \quad (23)$$

The cabin atmosphere properties and resulting normalized mass flow rates are calculated using Equations 16 through 23, for several values of cabin pressure over the range of 14.7 psia to 7.0 psia, in Table 8-6. The time required to depressurize from 14.7 psia to 7.0 psia can then be determined in normalized form by numerical integration considering the change in cabin atmosphere weight and the average normalized mass flow rate between each of the pressure increments considered in Table 8-6. However, as the cabin pressure decreases, the effective orifice area of the crack opening will also decrease because of the reduced hoop stress. As indicated earlier in this section, crack opening deflection is a linear function of applied stress, so

this relationship can be used to correct for the change in orifice area at each cabin pressure level. This procedure can be represented by the equations:

$$\phi = \frac{1}{A_o} \sum_{i=0}^{i=n} \frac{\Delta W_i}{\left(\frac{G}{A}\right)_i \left(\frac{A_i}{A_o}\right)} \quad (24)$$

$$\frac{A_i}{A_o} = \frac{P_i}{14.7} \quad (25)$$

where:

- ϕ = depressurization time (sec.)
- ΔW = increment of change in cabin atmosphere weight (lb)
- $\frac{G}{A}$ = normalized mass flow rate (lb/ft² - sec)
- A_i = effective orifice area for increment considered
- A_o = original orifice area at full cabin pressure

These calculations are also conducted in Table 8-6; numerical integration of Equation 24 yields a normalized depressurization time (14.7 psia to 7.0 psia) of 1.52 ft²-sec. The actual time to depressurize is obtained by dividing this value by the original orifice area. This area is a function of the strap spacing and is obtained from Equation 15 and the estimated factor to account for local skin distortion. If the depressurization time is greater than 600 sec, no pressure make-up system is required. If the time is less than this value, the required weight of pressurization gas can be obtained by multiplying the mass flow rate at 7.0 psia cabin pressure by the time over which pressurization must be provided. A total system weight of 2.8 x weight of stored gas has been estimated from preliminary analyses. This factor is based on a 2000 psi stored gas system using T₁-6A1-4V receivers designed to a burst factor of 2.0. Depressurization times, weights of make-up gas, and total pressurization system weights are calculated in Table 8-7 for crack-arrest strap spacings of 4 in. to 20 in. The resulting pressurization system weight (including weight of stored gas) and the total of structural and system weight increase is plotted in Figure 8-6.

8.3.4 Design Evaluation

It can be seen from Figure 8-6 that a cabin pressure make-up system is required for strap spacings greater than about 15 cm (6 in.), and the weight of this system increases rapidly for strap spacings beyond 25 cm (10 in.) to 30 cm (12 in.). For a strap spacing of 25 cm (10 in.), a total weight increase of 120 kg (260 lb) is calculated for the structural reinforcements

Table 8-6 Normalized Flow Rates and Depressurization Time -
 Crew Compartment Atmosphere Leakage

P_c (psi)	P_{c_n} (psf)	$\frac{P_{c_n}}{P_{c_l}}$	T_c (°R)	w_c (lb/ft ³)	P_o (psf)	T_o (°R)	w_o (lb/ft ³)	C_o (ft/sec)	$\frac{G}{A}$ (lb/ft ² -sec)	w_c (lb)	Δw_c (lb)	$\left(\frac{\bar{G}}{A}\right)$	$\frac{\Delta w}{(G/A)}$	$\frac{A}{A_o}$	$\frac{\Delta w}{(G/A_o)}$
14.7	2120	1.0	530	.0750	1120	442	.0475	1030	49.0	90.0	12.0	45.2	.265	.90	.294
12.0	1730	0.815	500	.0650	915	416	.0413	1000	41.3	78.0	9.5	38.5	.247	.75	.328
10.0	1440	0.680	475	.0570	761	396	.0362	975	35.4	68.5	10.2	32.5	.313	.61	.514
8.0	1150	0.545	445	.0485	608	370	.0308	945	29.1	58.3	5.4	27.5	.196	.51	.385
7.0	1010	0.476	430	.0440	531	359	.0278	926	25.8	52.9					

Σ 1.52

Table 8-7 Depressurization Time and Pressure System
Weight - Crew Compartment Atmosphere Leakage

Strap Spacing b (in.)	(1)	.0092b ² (in. ²)	A _o (2)		ϕ ⁽³⁾ (sec)	Δϕ (sec)	G ⁽⁴⁾ (lb/sec)	W _{gas} ⁽⁵⁾ (lb)	W _{sys} (lb)
	k _o		(in. ²)	(ft ²)					
4	1.0	.147	.147	.00102	1470	0	-	0	0
6	1.05	.332	.350	.00242	625	0	-	0	0
7	1.07	.450	.480	.00334	455	145	.041	6	17
8	1.1	.590	.650	.00450	338	262	.055	14.5	41
10	1.2	.920	1.12	.0078	195	405	.096	39	109
12	1.3	1.33	1.73	.0120	126	474	.148	70	196
14	1.4	1.80	2.52	.0175	87	513	.215	110	308
16	1.5	2.36	3.54	.0246	62	538	.302	162	454
18	1.5	2.96	4.44	.0308	50	550	.378	208	582
20	1.5	3.68	5.50	.0382	40	560	.470	263	737

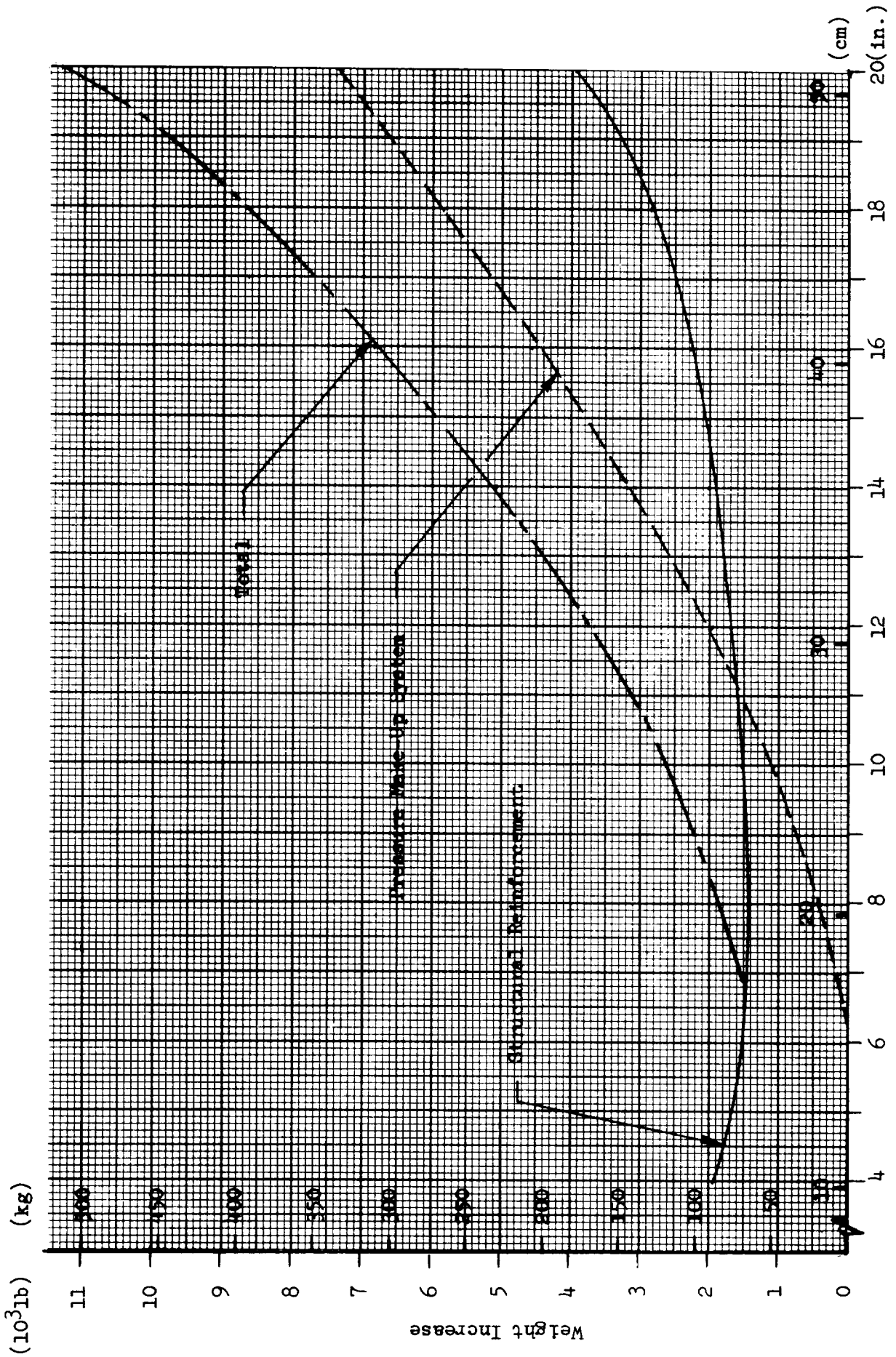
(1) Estimated factor for increased orifice area due to local skin distortions

(2) Orifice area under maximum cabin pressure

(3) Time to depressurize from 14.7 psia to 7.0 psia

$$(4) \quad G = \left[\frac{G}{A} \right]_{p=7.0} \cdot \left[\frac{A}{A_o} \right] A_o = 25.8 \left[\frac{7.0}{14.7} \right] A_o = 12.3 A_o$$

(5) Weight of make-up gas to maintain cabin pressure of 7.0 psia.



Crack-Arrest Strap Spacing
Figure 8-6 Structure and System Weight Increase vs. Crack-Arrest Strap Spacing - Crew Compartment



and pressure make-up system. This indicates that fail-safe design concepts, including consideration of cabin atmosphere leakage, are feasible for the crew compartment, but the associated weight increase may be in the order of 15 percent of the basic structural weight for this assembly.

More detailed investigation would be required to determine, for an actual design application, if strap spacing should be selected to eliminate the need for a make-up pressurization system. The additional manufacturing costs for the structure would have to be weighed against cost and reliability considerations of the emergency pressurization system. In any event, representative tests should be performed to more accurately determine effective orifice area as a function of crack length. The study has shown this to be a very critical parameter, and it was necessary to make a number of assumptions to approximate this relationship for the present evaluation.

Another factor of possible concern is that the riveted attachment of the crack-arrest straps to the compartment skins introduces several thousand potential leak sources. However, it is believed that good design practice, perhaps supplemented by auxiliary sealing provisions, can maintain normal compartment leakage within acceptable limits. For example, on several S-II stages mechanical joints were introduced in the LH₂ tank because of rework or repair requirements. These joints were covered by aluminum foil seals bonded to the structure with a suitable cryogenic adhesive. Leakage during tanking, static firing, and prelaunch was monitored. Leakage was within acceptable limits, and negligible in most cases. Sealing against liquid hydrogen leakage is obviously a much more difficult problem than that of sealing a compartment against leakage of air at normal environmental temperatures.

8.4 FAIL-SAFE ANALYSIS - LH₂ TANK

Application of fail-safe design approach to large, welded integral propellant tanks, such as the B-9U liquid hydrogen tank, intuitively appears to be impractical. A limited fail-safe capability may be possible by developing a "leak-before-break" failure mode for initial surface flaws of reasonable aspect ratio. The larger task of providing crack-arrest reinforcement to contain a through crack of significant length without rupture would appear to be prohibitively heavy. This intuitive appraisal has been verified in analyses conducted by General Dynamics Convair and reported in Reference 31. The following section presents a brief summary of these results.

There is, however, one detail aspect of fail-safe design that is believed to have practical significance for this type of application. This concerns the design of circumferential weld lands on a pressure vessel so as to preclude the propagation of a transverse crack in the weld nugget through the adjacent parent metal. Detailed investigation of this subject is presented in Section 8.4.2.

8.4.1 Cylindrical Shell

The analyses of Reference 31 investigated the use of graphite/epoxy crack-arrest straps bonded to the aluminum skin of both LOX and LH₂ tanks of the B-9U booster. A strap cross-section 2.5 cm (1.0 in.) thick X 7.6 cm (3.0 in.) was assumed for the LH₂ tank. Strap spacings of 46 cm (18 in.) and 92 cm (36 in.) were investigated. The straps were treated as integral stiffeners and stress intensity reduction factors determined from appropriate curves of Reference 23 were used in the analyses. Results showed that for a strap spacing of 46 cm (18 in.), and assuming a through crack of that length, the allowable hoop stress in the skin was only about 110 MN/m² (16 ksi) and the corresponding additional strap weight was approximately 7700 kg (17,000 lb). The additional skin weight required to reduce the stress level from 300 MN/m² (44 ksi) to 110 MN/m² (16 ksi) would be approximately 16,000 kg (35,000 lb). Therefore, the total weight penalty would be in the order of 23,700 kg (52,000 lb). This is obviously not a tolerable weight increase. Another factor of practical concern is that the leakage of a cryogenic propellant from a through crack of the size considered would probably be a disastrous situation in itself.

8.4.2 Circumferential Weld Lands

Transverse cracks across a weld suggest, due to weld shrinkage strains, are one of the most common forms of weld defect. Because of the high incidence of this type of flaw it would be desirable to design the weld joint to prevent such a crack from propagating through the adjacent parent metal of the weld land at limit stress. The feasibility and potential weight penalty of this approach is investigated in this section.

For a cylindrical pressure vessel, the circumferential welds are most highly stressed in a direction parallel to the weld and hence are the most critical regions in which to consider the presence of transverse cracks.

Weld lands with about twice the thickness of basic skin are typically selected for aluminum alloy pressure vessels. For the present example of the B-9U LH₂ tank, the basic skin thickness is 0.305 cm (0.120 in.) and a weld land thickness of 0.635 cm (0.250 in.) is assumed. The other properties of the LH₂ tank shell are illustrated in Figure 6-4.

The fail-safe design of the weld joint may involve adjustment of two variables, (1) controlling the width of weld bead to limit the length of transverse crack and (2) adjusting the width of the weld land to modify the net hoop stress applied to the crack tip. Therefore, a parametric investigation is conducted to define the net hoop stress as a function of tank pressure and weld land width and to define critical stress as a function of weld bead width. The transverse crack is assumed to be completely through the thickness and across the width of the weld bead for purposes of this study.

The circumferential weld land acts as a small ring frame in the tank shell and tends to reduce the hoop stress below the general stress field for the skin because of the additional area. The variation of net hoop stress at the center of the weld land with weld land width is investigated using the "Shell of Revolution" computer program. A range of weld land widths from 7.6 cm (3.0 in.) to 25.4 cm (10 in.) is considered. The weld land is assumed to be located midway between typical stability frames (see Figure 6-4). Applied loading and tank pressure used in the analysis are:

$$p = .172 \text{ MN/m}^2 \text{ (25.0 psig)}$$

$$N_x = -.870 \text{ MN/m (-5000 lb/in.)}$$

The compression axial load case is the most critical because of Poisson effects which tend to increase the hoop stress in the weld land compared to the skin. Results for the above loading condition and the previously described shell geometry are summarized below:

Weld Land Width		Hoop Stress	
(cm)	(in.)	(MN/m ²)	(ksi)
7.6	3.0	262	38.0
12.7	5.0	249	36.1
17.8	7.0	237	34.4
25.4	10.0	222	32.3

The limit design pressure varies from about 0.152 MN/m² (22 psig) to 0.172 MN/m² (25 psig) over the length of the LH₂ tank. The hoop stresses at other pressures for a given weld land width are approximated from the following equation, which provides allowance for Poisson effects:

$$\sigma_i = \sigma_o - \left[0.80 \frac{1 - \frac{p_i}{p_o}}{p_o} \right] \sigma_o$$

where:

P_0 = reference pressure used in analysis

σ_0 = hoop stress determined in analysis for reference conditions

σ_i = hoop stress resulting from tank pressure p_i

This relationship is used to define the family of curves showing the relationship between hoop stress and weld land width for various values of tank pressure, plotted in Figure 8-7.

Critical stress for the transverse crack is determined from the basic equation for stress intensity at the tip of a through crack:

$$K_I = \sigma \sqrt{\pi a}$$

where:

$$K_I \cong K_{Ic} = 32.6 \text{ MN/m}^{3/2} \quad (30 \text{ ksi } \sqrt{\text{in.}})$$

a = 0.5 x weld bead width.

Critical hoop stress for a range of weld bead widths is also plotted in Figure 8-7. It can be seen that the critical stress, and the resulting required weld land width, is quite sensitive to the width of the weld bead. For conventional MIG or TIG welds in aluminum alloys, the weld bead width is typically about 1.5 x material thickness. A current NR/SD welding specification permits a maximum weld bead width of 2.5 t for t = 0.20 in., reducing to 2.0 t for t = 0.50 in.

Considering the maximum limit pressure of 0.172 MN/m² (25 psig) and a minimum practical weld land width of 7.6 cm (3.0 in.), the applied hoop stress is 262 MN/m² (38 ksi) and a weld bead width of 1.07 cm (0.42 in.) is fail-safe. This width is about 1.7 x thickness, so the nominal case ($b_w \cong 1.5 t$) is satisfactory with minimum weld land width.

To further explore the potential impact of this fail-safe requirement on tank weight and/or welding specification limits on bead width, a maximum bead width of 1.27 cm (0.5 in.), which is twice the weld land thickness, is assumed and the effect of various residual strength factors on weld land weight are evaluated. It is assumed that the LH₂ tank will be fabricated from 15 cylindrical segments, so that 14 circumferential weld lands exist over the length of the tank. Of this total, eight weld lands are subjected to a tank pressure of 0.154 MN/m² (22.4 psig) and six are assumed to be loaded by an average tank pressure of 0.165 MN/m² (24.0 psig). A minimum practical weld land width of 7.6 cm (3.0 in.) is taken as the reference from which to evaluate weight increase. A range of residual strength factors from 1.0 to 1.2 times limit load is investigated and results are summarized in Table 8-8.

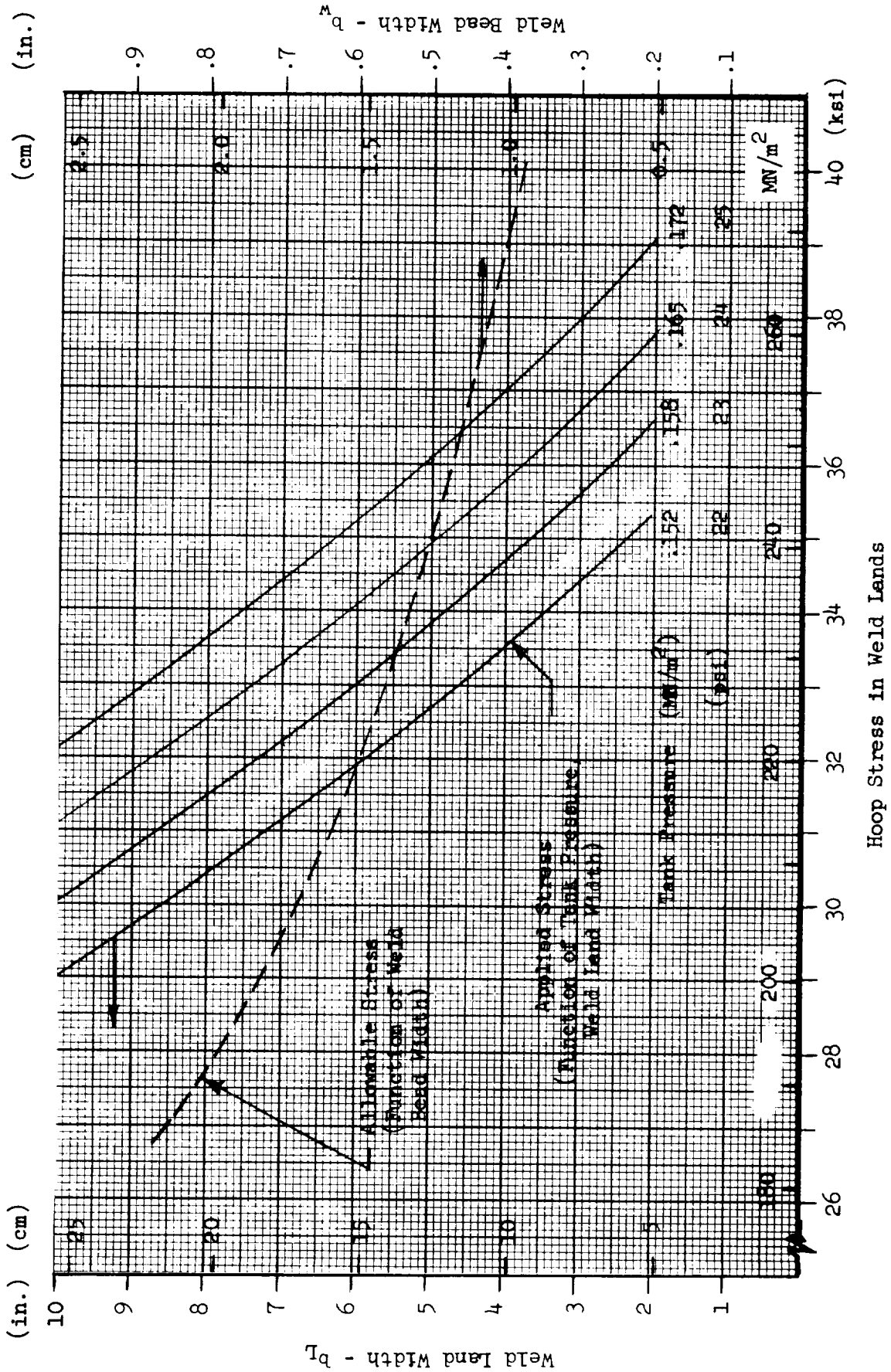


Figure 8-7 Applied and Allowable Hoop Stresses for Circumferential Weld Lands - LH₂ Tank

Table 8-8 LH₂ Tank Circumferential Weld Land
 Fail-Safe Requirements

Parameter		Residual Strength Factor				
		1.0	1.05	1.10	1.15	1.20
Critical Stress (ksi) ($b_w = 0.5$ in.)		35.0	33.4	31.8	30.4	29.2
p = 24 psig (6 welds)	b_L (in.)	4.90	6.80	9.00	10.9	12.8
	ΔW_L (lb)	354	710	1120	1470	1830
p = 22.4 psig (8 welds)	b_L (in.)	3.0	4.7	6.8	8.7	10.4
	ΔW_L (lb)	0	420	940	1410	1830
Total Weight Increase	(lb)	354	1120	2060	2880	3660
	% Cyl. Shell	0.53	1.6	3.1	4.3	5.5

- b_w - width of weld bead
- b_L - width of weld land
- ΔW_L - additional weight of weld lands due to increased width

8.4.3 Design Evaluation

It has been shown that it is completely impractical to apply the type of fail-safe design approach commonly used for jet transport aircraft fuselage structure to a large, welded, integral propellant tank, such as the B-9U LH₂ tank. However, it does appear feasible to incorporate limited fail-safe provisions in the design of welded joints. Proper design can prevent unstable propagation of a transverse crack in the weld nugget across the adjacent parent metal of the weld land under limit loading conditions. This design approach may involve adjusting the width of weld land, limiting the maximum width of weld bead, or a combination of these factors. Because of the high incidence of this type of defect in typical welded structures, it is recommended that this fail-safe design approach be applied wherever practicable.



A review of the results summarized in Table 8-8, for the specific example of LH₂ tank circumferential welds, indicates a small weight penalty for residual strength equal to limit load. However, the weight penalty increases greatly as residual strength factor is increased. This suggests that representative tests should be conducted for an actual design application to verify what factor, if any, is required for reliable performance. Also, modest reductions in allowable weld bead width will significantly increase allowable hoop stresses and decrease the indicated weight penalty. This illustrates the importance of reviewing welding processes and welding specifications to ensure that efficient, but realistic, requirements are specified.

The example analyzed in this study is for a tank designed to conventional ultimate strength requirements. If proof test requirements cause an increase in tank skin gauge, with corresponding reduction in limit operating stress, the task of meeting present fail-safe requirements may be considerably less difficult.

9.0 CRITERIA EVALUATION AND RECOMMENDATIONS

Presented in this section are candidate design criteria that are formulated to meet the objective of assuring the structural integrity of Space Shuttle vehicles over their service lives. These criteria include consideration of basic fatigue life assurance and both fail-safe and safe-life approaches in damage tolerant design. A discussion of the rationale leading to the candidate criteria is given, and the effects of these criteria on the reference vehicle are evaluated. The evaluation covers a range of service life requirements from 100 missions to 500 missions. The recommended criteria selected on the basis of these evaluations are summarized as an integrated package. A comparison is made of the relative merits between fail-safe and safe-life design approaches for applicable structural elements.

Factors considered in the evaluation of candidate criteria include the effect on structural weight, in-service inspection frequency, and the type of NDE techniques required for both production line and in-service inspections. To make a quantitative evaluation of the effects of candidate safe-life criteria on structural weight, it is necessary to establish an initial flaw size to serve as the starting point for the crack growth analyses. This assumed flaw size is dependent on the specific NDE techniques applied during production line or in-service inspections and their associated capabilities for reliable detection of flaws of the type and location of interest. In actual practice during a hardware program this will require very close scrutiny of all pertinent aspects of inspection of a given structural component to define specific flaw detection capabilities. These aspects will include the type of NDE technique selected, the detail structural configuration and material, surface condition of the part, the possible type and location of defects, and the accessibility for inspection. In many cases the actual flaw detection capability will have to be verified by representative tests. This depth of investigation is obviously beyond the scope of the present study; however, it is necessary to define representative capabilities for flaw detection to permit a realistic assessment of the effect of safe-life criteria on the reference vehicle. Therefore, the first portion of this section is concerned with a review of NDE techniques that are within present state-of-the-art and are applicable to Space Shuttle structure. The NDE techniques, equipment and facilities required, and limitations on application are described. A preliminary selection of the most appropriate techniques and inspection points for the reference structural elements is discussed. Generalized flaw detection capabilities for the primary techniques are summarized; this definition is based on a combination of literature survey, prior SD experience, and results to date of verification tests being accomplished by NR LAD under the B-1 program.

9.1 NDE TECHNIQUES AND CAPABILITIES

Presented in the following sections are brief summaries describing the types of currently available NDE methods applicable to Space Shuttle elements; the facilities and supporting equipment required to apply these methods; and a preliminary assessment of the flaw detection capabilities of the various NDE techniques. This evaluation of detection capabilities is used as the basis to evaluate the impact of safe-life design requirements on the selected structural elements of the B-9U booster and to compare safe-life and fail-safe design approaches.

9.1.1 Basic NDE Techniques and Associated Equipment and Facility Requirements

The basic types of NDE methods applicable to Space Shuttle structural elements are described below. A summary of the equipment and facilities required to apply these methods is given in Table 9-1. Additional considerations for application of these methods to in-service inspection of Space Shuttle are also summarized in this table.

Visual/Optical Inspection

Visual inspection, the most elementary method for detecting surface cracks, relies on the illumination of the object and the examination of the surface with the eye. To improve visual inspection, optical aids such as mirrors, microscopes, and borescopes (fiber and rod optics) can be utilized to provide magnification and direct viewing conditions.

Penetrant Inspection

As an extension of visual inspection, the liquid penetrant method is capable of detecting smaller surface cracks beyond the scope of the visual technique. The penetrant method depends on the ability of an applied low viscosity, low surface tension liquid to penetrate the surface crack by capillary action. Excess penetrant is removed and an absorbent material developer is applied to enhance the indications. Penetrants containing fluorescent dyes are generally viewed with black light to find surface cracks.

Ultrasonic Inspection

Ultrasonic methods use low energy, high frequency mechanical vibrations (sound waves) which are produced by a transducer (piezoelectric element) and transmitted into the part by a couplant material at the transducer part interface. A change in acoustic properties is detectable due to cracks (surface or internal) which reflect and/or scatter the sound energy. The reflected waves generate a received signal which is amplified and displayed on a cathode ray tube.

Eddy Current Inspection

The eddy current method involves a coil carrying a high frequency alternating current, which is brought into the vicinity of an electrical conductor and thereby induces eddy currents in the conductor. The magnetic

Table 9-1. NDE Techniques and Associated Facility and

Type of NDE Technique	Facilities and Equipment Required
Optical	<p>Portable Test Equipment: Borescope, rod optics, flexible fiber optics, cold light source, camera and viewing adapter.</p>
Fluorescent Penetrant	<p>Permanent Stationary Test Equipment: Dip tanks; drain, rinse, developer, dryer and black-light inspection stations. Large parts may require spray booth facilities for penetrant and developer application.</p> <p>Portable Test Equipment: Applicator kits, spray cans of penetrant and developer, portable black-light source, pre-inspection etching and neutralizing materials and applicators, post-inspection cleaning and drying materials.</p>
Ultrasonic	<p>Permanent Stationary Test Equipment: Immersion tank or couplant spray facility, bridge, turntable, ultrasonic transducer and recorder. Cleaning and drying facility.</p> <p>Portable Test Equipment: Portable ultrasonic transducers, couplant and applicator, signal display and/or recorder, power and instrumentation cables, post-inspection cleaning and drying materials.</p>
Eddy Current	<p>Portable Test Equipment: Eddy current probe (test coils), signal display and/or recorder, calibration test blocks.</p>
Radiographic	<p>Permanent Stationary Test Equipment: Lead-lined room, dark room facilities, film processing unit, X-ray unit (X-ray generator, 150 KV, 300 KV tubes, headstand)</p> <p>Portable Test Equipment: 150 KV X-ray tube, X-ray generator, headstand 150 KV rod anode tube, isotope and source guide.</p> <p>Miscellaneous Support Equipment: Collimators, cones, film cassettes, positioning devices, penetrameters, identification and orientation markers, shielding materials, safety monitoring equipment (film badges, dosimeters, etc.), high intensity film viewer.</p>



Equipment Requirements

Application to In-Service Inspection

Applicability limited only by accessibility for inspection. Permanent fiber optics installations may be considered for local critical regions.

Most inspections will be performed in place (on board vehicle) and will utilize portable test equipment.

Some inspections on removed components may be conducted using permanent maintenance base facilities.

Adequate post-inspection cleaning and drying must be accomplished. Limited access and potential entrapment of fluids in joints may curtail usage.

Limited access may curtail usage. Fasteners must be removed to detect cracks from edge of fastener holes unless they extend beyond head of fastener.

In-place (on board vehicle) inspections will utilize portable radiographic equipment. Because of high cost, inspection time, and necessary safety precautions, such inspections will probably be limited to selected local areas.

Radiographic inspection of removed components may be conducted using permanent maintenance base facilities.

field generated by the flow of the eddy current will be interrupted or changed by cracks. This change, which affects the induced currents and magnetic field produced, is detectable. An indicating device (ammeter or oscilloscope) across the test coil or probe is utilized to measure the magnetic field variations. Instrument sensitivity to small cracks requires frequent calibration to maximize response and minimize the effect of lift-off or any variations between the probe and surface of the part.

Radiographic Inspection

The radiographic method is based on the ability of X-ray, gamma, beta or neutron radiation sources to penetrate a material, with the intensity of transmitted radiation proportional to the effective density of the material. Internal cracks or voids are revealed because of the local change in effective density they cause and consequent image they produce on the radiographic film. The detectable size of defects is directly influenced by material thickness. Maximum sensitivity is obtained when the crack orientation (longest dimension) is parallel to the direction of radiation.

Acoustic Emission

The acoustic emission method involves the observation of a sound pulse or elastic wave generated in a solid material when the material deforms. The audible and inaudible (ultrasonic) signals or acoustic signatures are detected by high sensitivity sensors, amplified, and recorded. Although the technique is not applicable to static detection of cracks, crack growth during structural loading generally involves sufficient release of energy to produce detectable signals. The primary application of this method would be during proof test of items such as propellant tanks and pressure vessels. Acoustic emissions would be monitored during the test to identify any indications of crack propagation and to obtain approximate locations of acoustic emission sources. This concept also has the potential for development as a continuous monitoring system for selected structural regions during operational service.

It is believed that considerably more development and application experience is required before this type of system can be used as a primary inspection method, replacing more conventional NDE techniques. Therefore, it is not included in the baseline of NDE techniques and capabilities used to establish specific safe-life design requirements. However, it is recommended that strong consideration be given to the use of such a system as a supplementary inspection approach during proof testing of Space Shuttle pressure vessels.

9.1.2 Application of NDE Techniques to Reference Structural Elements

Summarized in the following sections are the results of a preliminary assessment to determine which NDE techniques are most suitable for inspection of each of the reference structural elements, considering the individual characteristics of material, design configuration and associated fabrication processes. The most appropriate in-process inspection points during the fabrication and assembly phase are identified in general terms. Possible

methods for periodic inspection of the structural members during operational service are discussed and limitations or constraints on the application of these methods are described.

Fabrication and Assembly

Ultrasonic inspection will be performed on raw material of thick product form, such as extrusions for wing spar caps and plates for propellant tank skin/stringer panels, to detect internal voids or cracks.

Visual and penetrant inspection will be used to detect surface cracks on detail parts after significant machining or forming operations. Wing spar caps, frame caps, and integral stiffened skin panels for the propellant tanks will be inspected in this manner.

Fastener holes in critical regions of thick sections, such as wing spar and fuselage frame caps, will be inspected after drilling. Visual and penetrant inspection will be used for those parts which are "destacked" and individually accessible after the drilling operation.

For joints which must remain assembled after the drilling operations, and penetrant entrapment or contamination becomes a problem, the eddy current method will be used for inspection of the fastener holes.

A combination of visual, penetrant, and radiographic inspection will be made of the fusion weld joints in the propellant tank and crew compartment assembly. Visual inspection is made immediately after welding and is primarily to verify that the weld bead is properly centered on the joint and that lack of fusion does not exist. Penetrant and radiographic inspection will be performed after the weld bead build-up is machined flush with the surrounding parent metal of the weld joint. Surface etching will precede the penetrant inspection to remove any smeared metal that may obscure detection of surface cracks. These operations are normally performed before the assembly is removed from the weld tooling, so that any required weld repairs may be readily accomplished. It is anticipated that penetrant and radiographic inspection of welds will also be performed after proof test of the crew compartment or propellant tank assemblies.

Post-assembly inspection of mechanical joints will rely primarily on visual/optical methods; borescope and rod and fiber optics will be used in close-out areas which limited access for visual inspection. Penetrant and ultrasonic methods, using portable equipment, may be used on a limited basis for selected areas.

Operational Service

During operational service, the application of nondestructive evaluation methods will rely on the accessibility of the structural element. To expose the critical location and surface of some of the reference structural elements, some disassembly may be required and in other areas removal of the thermal protective system will be necessary.

In the wing area, limited access through inspection panels and engine cavities restricts primary nondestructive evaluation to visual examination of spar caps using rod and flexible fiber optics, with optical magnification and cold light source. Any unusual deformation of spar cap structure, fastener damage, and the existence of visible cracks in the spar caps, or in the vicinity of fastener holes, will be ascertained. Ultrasonic or eddy current methods may be used to evaluate or verify the structural condition in a suspect region. Removal of fasteners is required for use of eddy current methods to detect cracks which do not extend beyond the fastener head.

These methods are of value for inspection of local critical or suspect areas, but are probably too costly and time-consuming to be considered for application to entire structural areas during periodic in-service inspection.

The preceding description is also applicable to inspection of major fuselage frames, but it will generally be necessary to remove external TPS panels to obtain access for application of NDE techniques. It is obviously desirable to avoid imposing a requirement for frequent removal and replacement of TPS panels; therefore, a safe-life equal to the entire service life appears to be an appropriate design requirement for these members.

In-service inspection of the LH₂ tank is difficult because of lack of accessibility. The interior surface is covered with foam type insulation and the exterior surface of cylindrical walls is shrouded by the TPS. Therefore, in-service inspection will probably be limited to local regions that are suspect problem areas. Local removal of internal insulation or TPS panels is required for visual, penetrant, ultrasonic, or radiographic inspection. The LO₂ tank is considerably more accessible because internal insulation is not required. Penetrant and ultrasonic inspection can be performed directly on the interior surface. Local removal of TPS panels may be necessary for placement of film or radiation source to accomplish radiographic inspection.

Limited access is available to the external and internal surfaces of the crew compartment. In-service inspection will depend primarily on visual methods, supplemented by periodic leak checks. Penetrant and ultrasonic methods, using portable equipment, may be used to good advantage in local areas. Access is generally available for radiographic inspection of welds, but because of cost, inspection time, and necessary safety precautions, this method would not be recommended for regular periodic inspection.

The critical flaw size in vertical stabilizer skins is sufficiently large that visual inspection methods should be adequate. Limited inspection of stabilizer root fittings and attachments is possible by rod and fiber optics through access holes and inspection ports.

9.1.3 NDE Capabilities

The flaw detection capabilities of any given NDE technique are, at best, difficult to define precisely. Capabilities and reliability may be influenced by many detail factors such as material, surface finish, protective coatings,

geometric complexity, etc. Detail considerations of this nature are obviously beyond the scope of the present study; however, it is necessary to establish some general bounds that will serve as a realistic basis to evaluate the effect of candidate safe-life criteria on design configuration, operating stresses, and associated structural weight. A review of currently available literature regarding NDE capabilities (References 32, 33 and 34) and of the results to date of NR LAD qualification tests on NDE techniques to be applied to the B-1 program has been made. Results of this review are reflected in the estimated curves of "design values" for reliable detection of crack-like flaws summarized in Figure 9-1. Individual curves are given for the NDE techniques of interest. The curves are applicable to the most common case of a crack partially through the thickness of material, and attempt to provide a reasonable estimate of interaction between crack length and crack depth as it affects detectability. For example, if crack depth increases, the minimum detectable length probably decreases. On the other

structure and equal to the entire aircraft service life for structure that is not inspectable. A suitable safety factor to account for fatigue scatter is applied.

Maintenance, refurbishment, and pre-flight checkout plans for Space Shuttle are not presently developed to a level of detail that permits defining a specific inspection interval for use as part of the fail-safe design criteria. It is probable that this interval may be adjusted somewhat to avoid undue structural weight penalties, but it is postulated that inspection intervals more frequent than every 10 missions would be undesirable. The primary factor to consider in setting fail-safe design requirements for Space Shuttle is the level of residual strength required after failure of a single principal element. The current Air Force approach requires that the residual strength be equal to or more than limit load or maximum spectrum load, whichever is greater. This approach is rational if very high confidence is held that any given structure will exhibit at least the design strength level, or if the basic design loads are considered to be rather conservative, such that some allowance for strength variations is inherently provided. However, if the premise is adopted that realistic limit loads will be defined for Space Shuttle, then some factor of safety applied to limit load to define the required residual strength level appears to be desirable. A number of the potential critical design conditions for shuttle structure result from planned operation of the vehicle within rather narrowly controlled limits. Examples are thrust and inertia forces and tank pressures during ascent, entry maneuvers, etc. Therefore, the probability of encountering flight conditions that approach limit design cases is considerably higher for Space Shuttle than for conventional aircraft.

Selection of a structural factor of safety is always somewhat arbitrary and subject to individual judgment--validation of the selection usually depends on demonstration by satisfactory service experience. A basic factor of safety of 1.1 is proposed to account for possible variation in strength between vehicles due to material properties, workmanship and prior service experience. However, it is also necessary to consider the potential inaccuracies associated with the basic structural design and analysis. Fail-

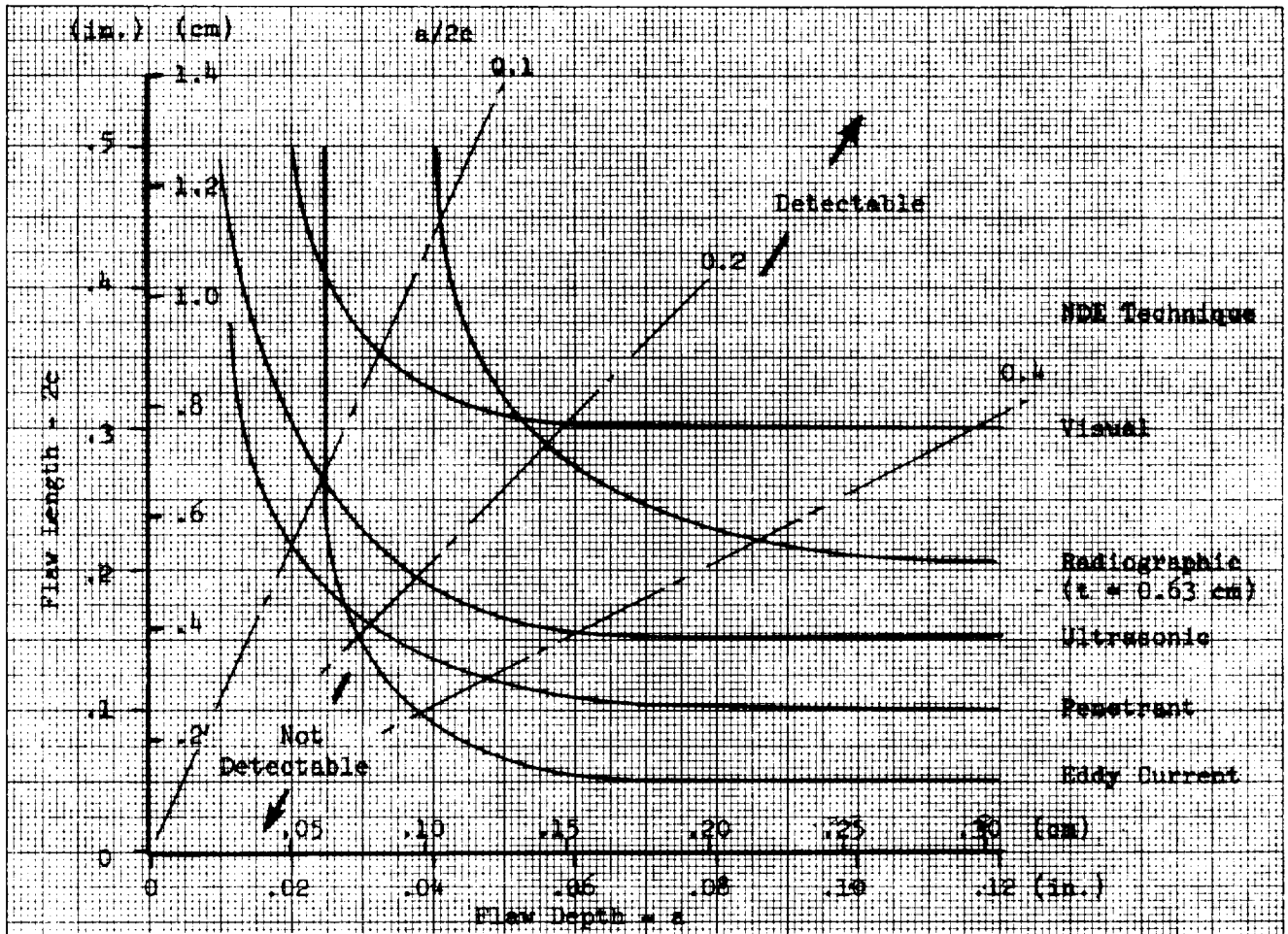


Figure 9-1. Estimated NDE Capabilities for Flaw Detection

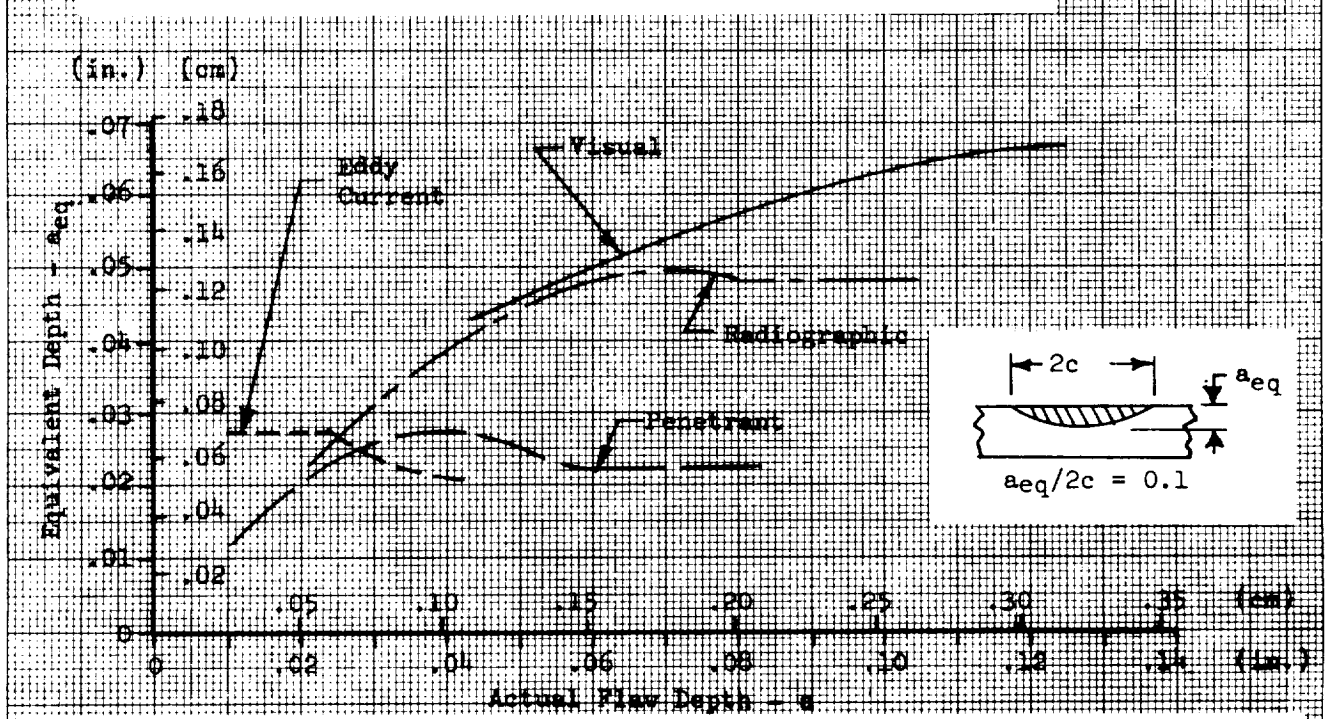


Figure 9-2. Equivalent Depth of Detectable Cracks for Various NDE Techniques

9.2 EVALUATION OF DESIGN CRITERIA

9.2.1 Fatigue Life Criteria

The current Air Force approach to ensure adequate fatigue life of operational aircraft involves a scatter factor of 4.0 to be used in analysis and test if an average service load spectrum is employed. Typical or "best-fit" S-N data are used in the fatigue analysis. The scatter factor of 4.0 is probably somewhat arbitrary and, at best, only an approximate allowance for the variability in specimen and component fatigue test results. However, it is beyond the scope of the present study to attempt a more rigorous evaluation of fatigue life criteria. The Air Force approach has become widely accepted and appears to provide generally satisfactory results. Therefore, it is recommended that it be adopted as the basic fatigue life criteria to be applied to all primary structure of the Space Shuttle.

The results of the fatigue analyses conducted in this study indicate that the above fatigue life design criteria should not result in significant weight increase to Space Shuttle structure. The wing spar caps are the only structural elements of the reference group in which fatigue life requirements dictated a reduction in operating stresses below the level established by static strength design requirements. For the basic 100 mission service life requirement used as a ground rule in this study, the increase in structural weight was about 450 kg (1000 lb). This is only about 0.4 percent of the structural weight of the total vehicle. It should be noted that the current Space Shuttle Phase C RFP indicates a 500 mission service life to be a design objective. This will, of course, increase the significance of fatigue considerations in the design and development of Space Shuttle structure. Detailed fatigue analyses based on a 500 mission service life requirement have not been performed in this study; however, an approximate evaluation can be made by considering the characteristics of the S-N curves in the stress and load ratio ranges where greatest damage is incurred. A reduction in limit design stress to 360 MN/m^2 (52 ksi) is estimated in this manner to satisfy a 500 mission fatigue life for the wing spar caps. The corresponding weight increase is about 1800 kg (4000 lb), which represents 1.5 percent of the dry weight of the reference vehicle. Of course, the actual impact of the fatigue life requirements will be strongly influenced by the detail structural configuration of the selected design. The wing design for the B-9U reference vehicle involves concentrated spar caps which carry all of the spanwise bending loads. The cover skins are corrugated in the chordwise direction and are ineffective as bending material for spanwise loading. The spar caps are heavy, compact sections with allowable ultimate static strength approaching the material tensile ultimate or compressive yield stresses. Therefore, an efficient static strength design requires relatively high operating stresses in the spar caps. On the other hand, if the wing structural box were designed with distributed, stiffened covers as the primary elements to resist spanwise bending loads, the allowable static stresses would generally be significantly reduced by plate and column buckling considerations. Because of the inherent lower operating stresses for this type of structure, the effect of fatigue life requirements on the design would be significantly reduced. This is illustrated by the fatigue analysis results for the B-9U vertical stabilizer, which represents the latter type of

design configuration. The analysis predicts a safe fatigue life of approximately 2200 missions for the static strength design; it is apparent that a 500 mission service life requirement will not impose any significant weight increase on the vertical stabilizer.

The fatigue analyses also indicate that the integral propellant tanks, based on static strength design, would not have a 500 mission safe fatigue life. However, the estimated effective stress concentration factor used in these analyses is quite conservative for the general tank structure. The 500 mission service life requirement will necessitate closer attention to detail design of joints, attachments, and integral reinforcements in the tank walls to ensure satisfactory fatigue life, but the resulting weight increase should be relatively minor.

The preceding discussions lead to the conclusion that the B-9U reference vehicle represents a conservative baseline from which to evaluate the effects of fatigue life requirements on Space Shuttle structural design. It is further concluded that the proposed safe fatigue life criteria can be accommodated without unacceptable weight increase; weight increases of approximately 0.5 percent and 1.5 percent of the vehicle total structural weight are estimated for the 100 mission and 500 mission service life requirements, respectively.

9.2.2 Fail-Safe Design Criteria

Recent experience with new operational aircraft has rather dramatically illustrated that conventional fatigue design requirements and verification test programs may not be adequate by themselves to prevent premature fracture of aircraft primary structure. It is recognized that, despite fatigue life assurance efforts, undetected flaws or damage can exist in primary structure at some time during the life of the aircraft. The Air Force is currently attempting to cope with this problem by requiring damage tolerant design concepts to be applied in critical areas of the primary structure. The damage tolerance concepts may be of either the "fail-safe" or "safe-life" (slow crack growth) categories. Application of these design approaches, in conjunction with an overall fracture control program which will provide assurance of adequate material fracture properties, inspection techniques, development and verification tests, and operational practices, is first being implemented from the inception of an aircraft design on the B-1 program. Historical experience shows that such design approaches and controls are necessary precautions to assure the structural integrity of Space Shuttle vehicles. Therefore, the question is not whether such approaches should be applied, but rather what specific criteria is appropriate for Space Shuttle.

Current criteria for fail-safe design on the B-1 program requires that complete failure of a single principal structural element will not result in catastrophic failure or inability to operate the airplane under limit load conditions before a suitable inspection is performed. The inspection interval compatible with this approach is based on the degree of inspectability of the structure. In specific application to the B-1, a fatigue life of remaining structure (after failure of a single principal element) equal to one-fourth of the aircraft service life is required for readily inspectable



structure and equal to the entire aircraft service life for structure that is not inspectable. A suitable safety factor to account for fatigue scatter is applied.

Maintenance, refurbishment, and pre-flight checkout plans for Space Shuttle are not presently developed to a level of detail that permits defining a specific inspection interval for use as part of the fail-safe design criteria. It is probable that this interval may be adjusted somewhat to avoid undue structural weight penalties, but it is postulated that inspection intervals more frequent than every 10 missions would be undesirable. The primary factor to consider in setting fail-safe design requirements for Space Shuttle is the level of residual strength required after failure of a single principal element. The current Air Force approach requires that the residual strength be equal to or more than limit load or maximum spectrum load, whichever is greater. This approach is rational if very high confidence is held that any given structure will exhibit at least the design strength level, or if the basic design loads are considered to be rather conservative, such that some allowance for strength variations is inherently provided. However, if the premise is adopted that realistic limit loads will be defined for Space Shuttle, then some factor of safety applied to limit load to define the required residual strength level appears to be desirable. A number of the potential critical design conditions for shuttle structure result from planned operation of the vehicle within rather narrowly controlled limits. Examples are thrust and inertia forces and tank pressures during ascent, entry maneuvers, etc. Therefore, the probability of encountering flight conditions that approach limit design cases is considerably higher for Space Shuttle than for conventional aircraft.

Selection of a structural factor of safety is always somewhat arbitrary and subject to individual judgment--validation of the selection usually depends on demonstration by satisfactory service experience. A basic factor of safety of 1.1 is proposed to account for possible variation in strength between vehicles due to material properties, workmanship and prior service experience. However, it is also necessary to consider the potential inaccuracies associated with the basic structural design and analysis. Fail-safe investigations conducted in this study have illustrated that complete verification of fail-safe capabilities by test may not always be practical. For example, consider the case of a fail-safe wing design in which complete failure of an individual spar cap is tolerated by providing sufficient redundancy and strength in the remaining spars to carry the specified loadings without failure. Design of the spars to accomplish this goal depends on rather complex analyses to predict the influence of failure of one spar cap on the internal load distributions and resulting design loads in adjacent spars. The presumed initial failure may reasonably occur at many possible locations along each of the spar caps. Under these conditions it may not be practical to completely verify by test that the required fail-safe capability exists in the structure because of the multiplicity of possible damage situations that must be considered. Therefore, it is recommended that the residual strength criteria for fail-safe design be specified in two categories, depending on whether test verification of residual strength is accomplished. A factor of safety of 1.2 is proposed for the case in which crack arrest and residual strength is not verified by test, so as to

provide additional allowance for uncertainties and inaccuracies that may be present in the analysis and design procedures. A summary of structural weight increase as a function of residual strength factor of safety is given in Table 9-2 for those elements where a fail-safe design approach is feasible and of practical interest. It can be seen that for the elements considered

Table 9-2. Structural Weight Increases for Fail-Safe Design Approach

Structural Element	Weight Increase ⁽¹⁾					
	F.S. = 1.0		F.S. = 1.1		F.S. = 1.2	
	(kg)	(lb)	(kg)	(lb)	(kg)	(lb)
Wing spar caps	365	805	495	1090	710	1570
Vertical stabilizer skins	77	170	77	170	90	200
Crew compartment skin ⁽²⁾	77	170	82	180	88	195
Total	519	1145	654	1440	888	1965
Percent of total vehicle structural weight	0.42		0.53		0.73	
<p>(1) Increase above structural weight required to satisfy basic static strength or fatigue life requirements.</p> <p>(2) Based on crack-arrest strap spacing of 30 cm (12 in.).</p>						

the total difference in weight between a residual strength factor of safety of 1.0 and 1.2 is less than 400 kg (800 lb). If all of the indicated fail-safe options are incorporated on the B-9U vehicle, the increase in weight is approximately 0.7 percent of the total vehicle structural weight for a factor of safety of 1.2 on residual strength. (The potential weight increase of propellant tanks to provide fail-safe design of weld lands is not included in this summary because the actual weight penalty, if any, will be highly dependent on the proof test approach and proof factors selected for the tanks. Also, this fail-safe concept is really an optional consideration that may be pursued in addition to the basic safe-life design requirements for the tanks.) There are undoubtedly additional structural elements beyond those considered in this study for which the fail-safe design approach would be applicable and may contribute to a total structural weight increase. On the other hand,

test verification of fail-safe capability may be feasible, or the inherent residual strength may approach 120 percent of limit load in a number of cases (the multi-element fail-safe concept for wing spar caps is an example). Therefore, it is estimated that fail-safe design to the proposed criteria will result in less than one percent increase in structural weight of the Space Shuttle vehicle. This is considered to be an acceptable performance compromise to achieve the additional confidence in structural integrity provided by the fail-safe design approach and associated criteria.

Another factor which merits specific attention in the fail-safe design approach is the potential effect of failure of a single principal structural element on the performance of other systems. There are some aspects of Space Shuttle that impose additional restrictions beyond what would be encountered in a conventional aircraft. For example, the integrity of the thermal protection system is of critical importance to assure safe entry. The TPS for the B-9U reference vehicle is basically an outer metallic shell supported from the primary structure in a manner to minimize restraint to differential thermal expansion. Failure of a single principal element of primary structure would probably have little effect on the integrity of this type of TPS. However, a thermal protection system employing reusable external insulation bonded to the primary structure, such as is presently considered for shuttle orbiter, might be much more seriously affected by a failure in the substructure. Cracking or debonding of a portion of insulation as a result of spar cap or skin plank fracture could have catastrophic consequences during entry. Therefore, development and verification tests would be required in this type of situation to assure that failure of a single principal element of primary structure would not impair the functional integrity of the TPS. Another example of this type of potential interaction is given by the investigation of fail-safe design applied to the crew compartment. Results of this study showed that the effects of cabin atmosphere leakage and resulting pressure make-up system requirements overshadowed the basic problem of providing structural reinforcement to prevent catastrophic rupture of the compartment.

9.2.3 Safe-Life Design Criteria

The safe-life design concept to achieve damage tolerance involves the selection of materials, stress levels, and detail structural configurations such that the largest undetected flaw at a given inspection will not propagate to critical dimensions prior to its discovery at a subsequent inspection or, alternatively, during the service life of the vehicle. The major elements of specific criteria to be considered in the application of this design approach to Space Shuttle are:

- The safe-life period to be provided. (The total service life or a portion thereof based on periodic inspection.)
- Factors of safety to be applied to limit load to define the residual strength required at the end of the safe-life period, and the associated critical flaw size.

- Factors of safety to be applied to the required safe-life period to provide for uncertainties in the flaw growth predictions.
- Requirements for statistical definition of fracture properties and initial detectable flaw sizes used in the design analyses.

The detailed evaluations of this section involve a postulation of proposed criteria for each of these major aspects, a discussion of the purpose and rationality of the criteria, and an evaluation of the effect of the proposed criteria on structural design, structural weight, and other factors for the reference vehicle. In making such an evaluation, it is necessary to establish a baseline of the types and sizes of initial flaws that will be considered in the safe-life analyses. The selection of the most appropriate NDE techniques and realistic definition of associated flaw detection capabilities is therefore of fundamental importance in the evaluation process. The flaw detectability threshold curves given in Figures 9-1 and 9-2 are taken as a "best estimate" of NDE capabilities that will be available for reliable detection of crack-like flaws in Space Shuttle structure. A summary of the types of initial flaws of practical interest, the minimum detectable sizes for applicable NDE techniques, and the resulting weight increases for safe-life periods of 100 to 200 missions is given in Table 9-3 for the reference structural elements of this study. The weight increases listed in this table are obtained directly from the safe-life analyses of Section 7. The values do not include allowance for the effects of factors of safety on residual strength or crack growth predictions, but are intended to serve as a guide to identify the most critical types of initial flaws and to select the most appropriate NDE techniques for individual cases. These selections, indicated by underlining in Table 9-3, are used as the basis for subsequent evaluation of proposed criteria. The weight increases reflected in this table and in the following detailed evaluations are based on crack growth analyses in which retardation effects are not considered. As previously discussed, the uncertainties associated with prediction of retardation effects for Space Shuttle structure--particularly the influence of periodic exposure to elevated temperature--prevent taking advantage of the potential benefit in design evaluations at the present time.

Residual Strength

It is probable that structures subject to fracture failure due to pre-existing flaws will exhibit as much scatter in strength properties as is the case for more conventional modes of failure. Certainly, the uncertainties in strength analysis prediction are no less than for conventional failure modes. Therefore, it would appear to be prudent to include a factor of safety in the definition of required residual strength to provide some allowance for these uncertainties. For simplicity and uniformity of criteria, it is desirable to establish the same definition of residual strength requirements for both the fail-safe and safe-life design approaches. The recommended criteria are as follows:

Residual strength shall be equal to or greater than 1.1 x limit load for cases where this capability is verified by representative structural tests.

Table 9-3. Structural Weight Increases for Safe-Life Design Approaches and Various NDE Techniques

Structural Element	Type of Crack	a/2c	NDE Technique	Detectable Flaw Size (1)		Weight Increase (2)					
						100 Missions		150 Missions		200 Missions	
				(cm)	(in.)	(kg)	(lb)	(kg)	(lb)	(kg)	(lb)
Wing Spar Caps	PTC	0.1	Visual	.17	.066	2500	5500	3140	6900	3770	8300
	PTC	0.1	Penetrant	.069	.027	950	2100	1410	3100	1860	4100
	CC-FH	0.5	Penetrant	.25	.10	1180	2600	1720	3800	2270	5000
	CC-FH	0.5	Eddy Current	.13	.05	860	1900	1410	3100	1950	4300
Vert. stab. skin	TC	---	Visual	.76	.30	0	0	0	0	0	0
Crew comp't. skin	TC	---	Visual	.76	.30	0	0	0	0	0	0
LH ₂ tank skin	PTC	0.4	Visual	.30	.12	820	1800	1090	2400	1320	2900
	PTC	0.4	Penetrant	.10	.04	0	0	0	0	0	0
LO ₂ tank skin	PTC	0.4	Visual	.30	.12	320	700	500	1100	860	1900
	PTC	0.4	Penetrant	.10	.04	0	0	0	0	0	0
Orbiter aft support frame	TC(3)	---	Visual	.76	.3	410	90	450	100	50	110
	TC(3)	---	Penetrant	.25	.1	0	0	0	0	0	0

(1) Size is flaw depth for part-through crack and flaw length for through crack.

(2) Increase in structural weight above that required to satisfy conventional static strength requirements

(3) Assumed to be at edge of frame cap flange

Legend: PTC - Part-through crack

TC - Through crack

CC-FH - Corner crack from fastener hole

Residual strength determined by design analyses shall be equal to or greater than 1.2 x limit load for cases where test verification is not accomplished.

Test verification of residual strength would generally involve element or small component tests in which an initial flaw is artificially induced, the flaw is grown under fatigue loading to predicted critical size, and the specimen is then loaded to failure to determine the actual residual strength level. Care must be taken to properly model the structural geometry and internal load distributions of the full-scale structure in the specimen tests. Actual fracture properties of the test specimen would be determined and used to reduce the test results to a residual strength based on design fracture properties. Because of the cost and time associated with these type of tests and the multiplicity of potentially critical structural elements, and flaw types, sizes and locations, it will probably not be practical to provide complete test verification of all critical structural elements for which the safe-life design approach is selected. Therefore, it is considered appropriate and probably necessary to define the dual design criteria.

The effect of the proposed criteria regarding residual strength on structural design will vary widely, depending on the nature of the structural element and the service load spectrum. Two example cases are illustrated in the sketch below. Case A

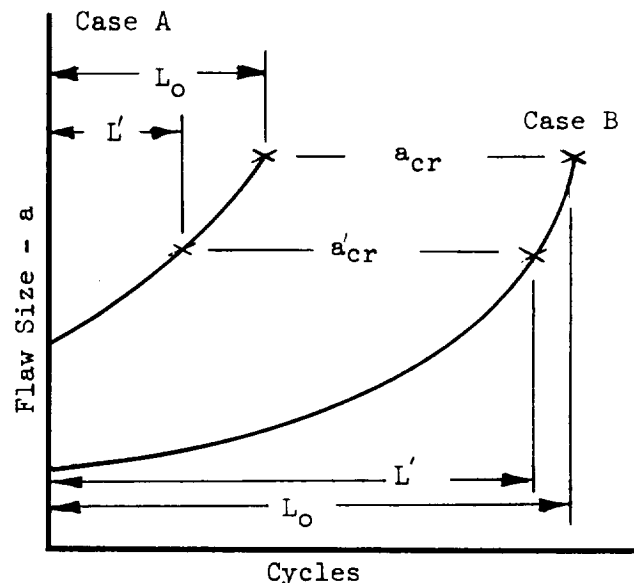
represents an element subjected to a limited, discrete loading spectrum such that the crack growth over the service life from initial to critical size is relatively small. The basic critical size a_{CR} corresponds to unstable growth or fracture at limit stress level. If this size is reduced to a'_{CR} because of the factor of safety specified for residual strength, a significant reduction in crack growth life is observed. (The reduction in critical flaw size is proportional to the residual strength safety factor squared.) An appreciable decrease in operating stress level may be necessary to meet the safe-life requirements for this type of situation. Case B is an example of the opposite situation, in which a structural element is subjected to an extensive

L = Safe-life

a_{cr} = Critical flaw size at limit stress

a'_{cr} = Critical flaw size for required residual strength

$$\cong a_{cr}/(F.S.)^2$$



random load spectrum over the safe-life period and a large amount of crack growth is involved from initial to critical size. In this case, the reduction in crack growth life associated with a residual strength safety factor is small and the influence on design of the element may be negligible. More specific evaluations are presented in the curves of missions to failure versus initial flaw size given in Figures 9-3 and 9-4 for the wing spar caps and the orbiter aft support frame caps, respectively. Curves are plotted for residual strength factors of safety of 1.0, 1.1 and 1.2, and cover the range from 100 to 1000 missions. Consideration is given to this expanded range for service life because of the current interest in a 500 mission useful life and to allow evaluation of the combined effects of factors of safety on both residual strength and on safe crack growth life. It can be seen that the wing spar caps correspond to example Case B, with only a small effect noted of residual strength safety factor on allowable safe-life missions for a given initial flaw size. This effect also decreases as the number of missions increases. The resulting weight increases for various mission life requirements are also compared in Figure 9-5. It can be seen that the difference in weight between a factor of safety of 1.0 and 1.2 on residual strength is in the order of 230 kg (500 lb). This is a very small proportion of total wing weight. The orbiter aft support frame corresponds more closely to example Case A. The major portion of crack growth is due to the repeated pressure cycles imposed on the LH₂ tank. The influence of random spectra loads induced at the orbiter attach points is relatively small. The pressure loading represents a limited, discrete spectrum over the service life and the crack growth from initial to critical size is small. Therefore, the application of a factor of safety to the required residual strength has relatively much more significance than for the wing spar caps. However, in this case the weight of affected structure is comparatively small, so that the net effect on total vehicle structure weight is not large. A weight increase of 18 kg (40 lb) is calculated for the extreme of 1000 mission service life and factor of safety of 1.2 on residual strength; this represents about 2.3 percent of the weight of the basic frame. If this same percentage increase is estimated for all major fuselage frames, a maximum weight increase of 240 kg (530 lb) is projected for this portion of the vehicle structure.

A review of the effect of this proposed criteria on the other reference structural elements indicates that no significant weight increases would be incurred. The vertical stabilizer skins are not affected, because of the inherent large margin on crack growth to critical size, even for a 1000 mission service life. The deepest initial flaws in propellant tank skins that could escape detection by penetrant inspection will tend to approach a semicircular shape ($a/2c = 0.4$ was used as a reference in this study). This type of flaw will break through to leakage before failure and the stress intensity in this condition is considerably less than critical value. Therefore, an inherent margin on residual strength exists for the propellant tank skins and the proposed safety factors will not cause a weight increase. Evaluation of crew compartment skins indicates that a slight reduction in operating stress, from 207 MN/m² (30 ksi) to 193 MN/m² (28 ksi) would be required to achieve a safe-life of 1000 missions based on residual strength safety factor of 1.2. However, the associated weight increase is negligible.

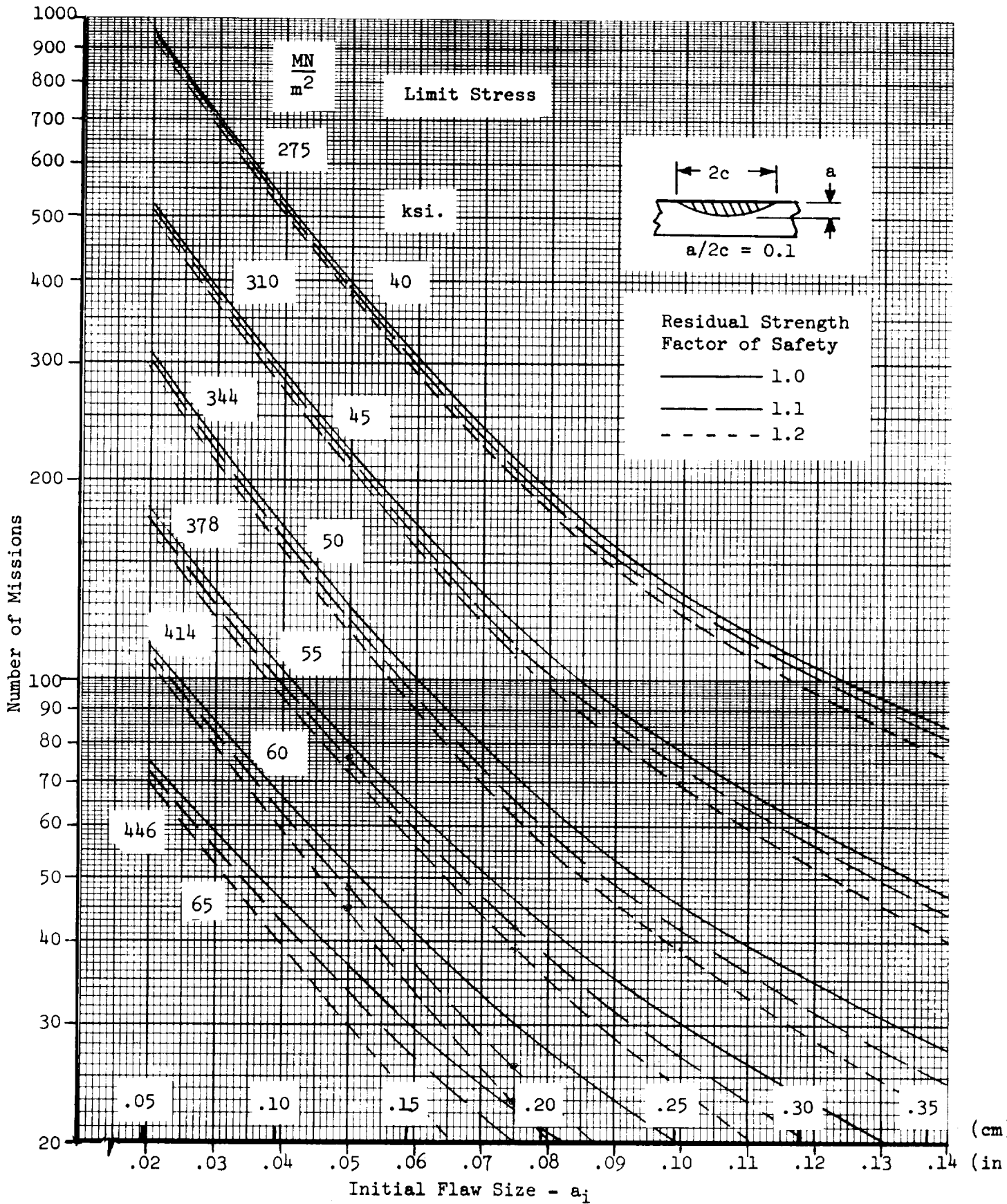


Figure 9-3. Missions to Failure for Various Residual Strength Safety Factors - Part-Through Crack in Wing Spar Caps

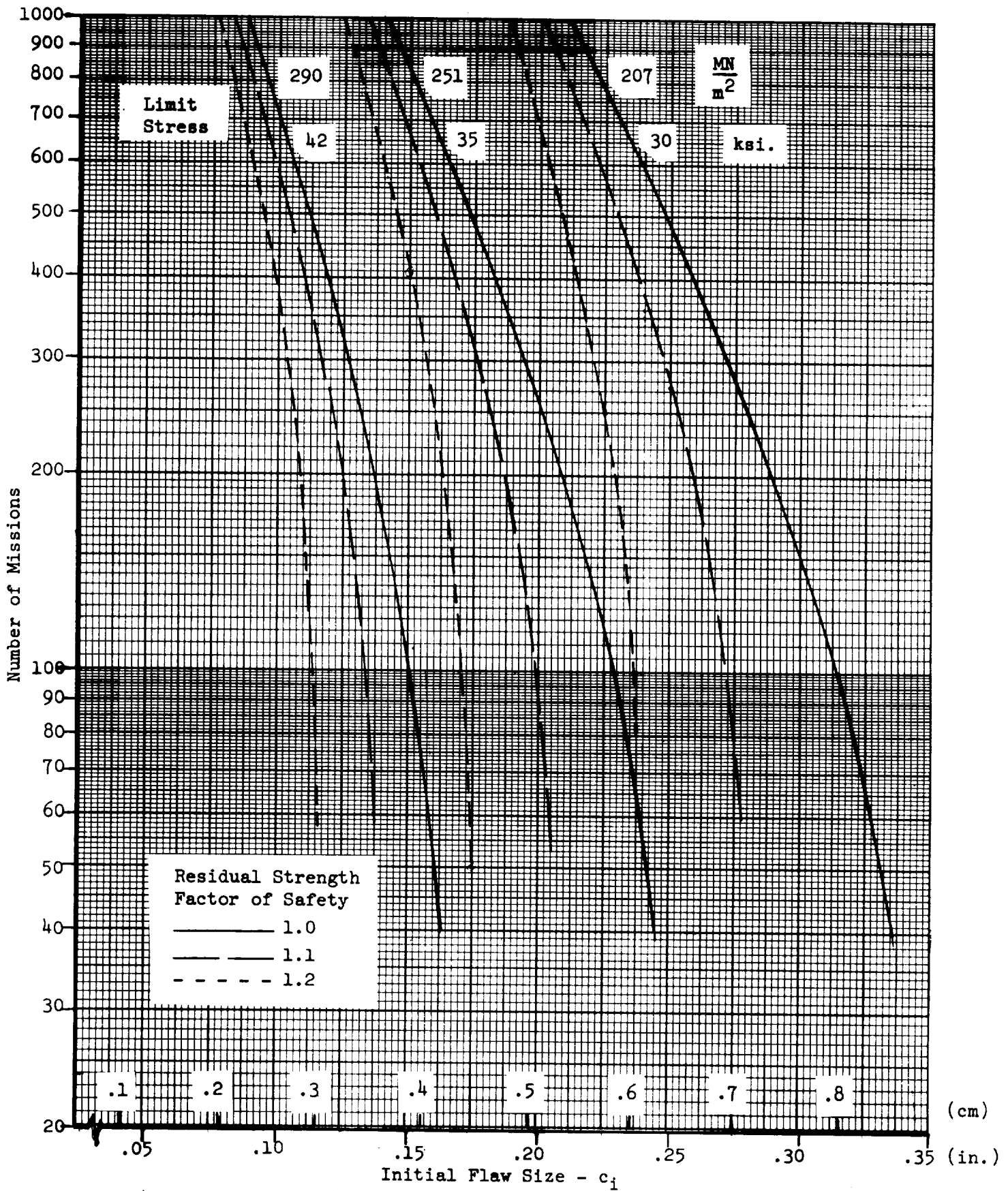


Figure 9-4. Missions to Failure for Various Residual Strength Safety Factors - Through Crack in Orbiter Aft Attach Frame Cap

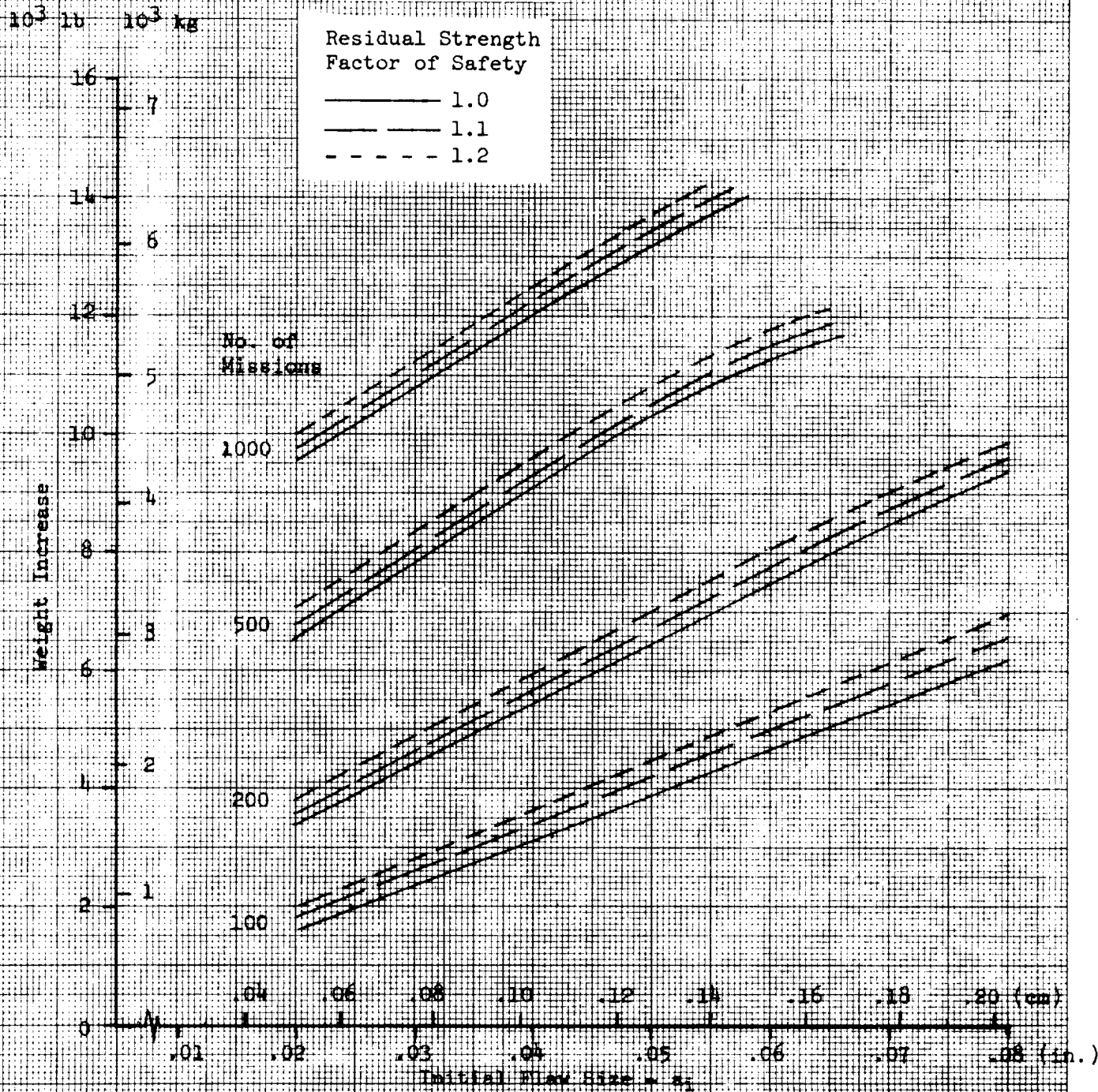
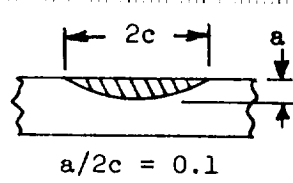


Figure 9-5. Structural Weight Increases for Various Residual Strength Safety Factors and Initial Flaw Sizes - Part-Through Crack in Wing Spar Caps

KE 10 X 10 TO THE CENTIMETER 46 1517
 18 X 25 CM. • ALBANENEO
 MADE IN U.S.A.
 KEUFFEL & ESSER CO.

A detailed listing of calculated weight increases for each of the structural elements over a range of residual strength safety factor of 1.0 to 1.2 and safe-life requirements of 100 to 1000 missions is given in Table 9-4.

Statistical Definition of Fracture Parameters

It seems apparent that some approach is necessary to assure that the numerical values of fracture parameters used in the structural design and analysis will conservatively represent actual conditions for any of the flight vehicles. Fracture parameters of interest include fracture properties such as toughness and crack growth rate and the definition of detectable initial flaw sizes. The dispersion in values for a given parameter may be quite different for various materials, structural configurations, and environmental exposure. Therefore, it is considered to be more logical to establish design values for the key fracture parameters on the basis of statistical probability rather than by applying an arbitrary factor of safety to typical properties. It is proposed that a statistical criteria equivalent to "B" properties in MIL-HDBK-5--90 percent probability with 95 percent confidence level--be used as the basis to establish design fracture properties. This specific criteria is currently being applied by the Air Force to the demonstration of NDE capabilities for flaw detection as applied to the B-1 program.

Considerable care must be exercised in obtaining and selecting the basic data used in statistical definition of fracture properties. Differences in type of test specimens, instrumentation, test techniques, and test environments may result in dispersion of test data that is not truly representative of the variability of fracture properties being tested. These precautions are particularly important if the test results from several investigators are to be combined to form the data base for statistical treatment. In the event that excessive data scatter or other circumstances make the application of statistical criteria impractical for a given case, conservative design values for fracture parameters should be estimated on a rational basis and submitted to the procuring agency for review and approval.

It is of interest to examine the effect of the proposed criteria on the structural design and weight of the reference structural elements considered in this study. The values of fracture toughness or critical stress intensity used in the study investigations have been selected as conservative "lower-bound" estimates. Although the values were not determined by rigorous statistical methods, it is believed that they are reasonably compatible with the proposed criteria and that no further adjustment of study results is required. The crack growth rate data used in the study generally conforms to typical or average characteristics, particularly for the 2219-T87 aluminum alloy. An approximate statistical evaluation was made of the crack growth rate data shown in Figure 5-9 to define a 90 percent probability of non-exceedance design curve. This was accomplished by taking the deviation of each individual data point (ΔK) from the nominal Forman curve, finding the standard deviation of the total data array, and displacing the nominal Forman curve by an increment of stress intensity compatible with 90 percent probability of nonexceedance at 95 percent confidence level. A comparison

of nominal and design curves for crack growth rate is given in Figure 9-6. It can be seen that over the stress intensity range of interest, the design growth rate is greater than nominal by a factor of approximately 1.5. The effect of this criteria on structural weight can be estimated by applying this factor to the required service life in the various comparisons summarized in Table 9-4.

The curves of detectable flaw sizes for various NDE techniques, presented in Figure 9-1, are intended to be compatible with the proposed statistical criteria. However, an evaluation has also been made of the effect of arbitrarily increasing those initial flaw sizes by a factor of 2, and results are also summarized in Table 9-4. These results certainly represent a conservative upper-bound of the possible effect of the proposed criteria regarding demonstration of NDE capabilities. Comparison of the two cases also provides insight regarding the sensitivity of structural weight to the criteria for initial flaw size.

Crack Growth Life

In addition to the effect of dispersion in material fracture properties on crack growth rate and consequent safe-life from initial to critical flaw size, the possible influence of uncertainties and inaccuracies in the predictive analysis must also be considered. From typical growth rate data, such as Figure 5-9, it can be seen that an error of 10 percent in predicting the applied stress intensity may change the growth rate by 30 percent to 60 percent, or more, depending on the stress intensity range involved. Some verification of crack growth predictions may be obtained from element or small component tests, but it will seldom be feasible to verify growth characteristics in full-scale structural tests. Therefore, a factor of safety applied to the required safe life is considered desirable to provide some allowance for uncertainties or inaccuracies in the analysis methods and data. A predicted safe life of twice the required period of service operation is recommended for general application. However, it is also appropriate to distinguish between structures that are accessible for periodic inspection during operational service and those that are not. The inspectable structure is certainly a more comfortable situation because the opportunity exists to detect actual crack growth that may be greater than predicted levels and accomplish repair before critical size is reached. Therefore, it is proposed that in this case no factor would be applied to the overall service life requirement; however, the life safety factor of 2.0 would be used, in conjunction with a maximum undetected flaw size appropriate for the in-service inspection technique, to determine the required inspection interval. The effect of this criteria on the weight of the reference structural elements can be approximated from the comparisons summarized in Table 9-4 for the various service lives.

Combined Criteria

Several elements of the proposed design criteria have additive effects on the structural weight, so it is desirable to evaluate the overall effect of the composite criteria on the reference vehicle. In applying the criteria, it is conservatively assumed that residual strength is not verified by test

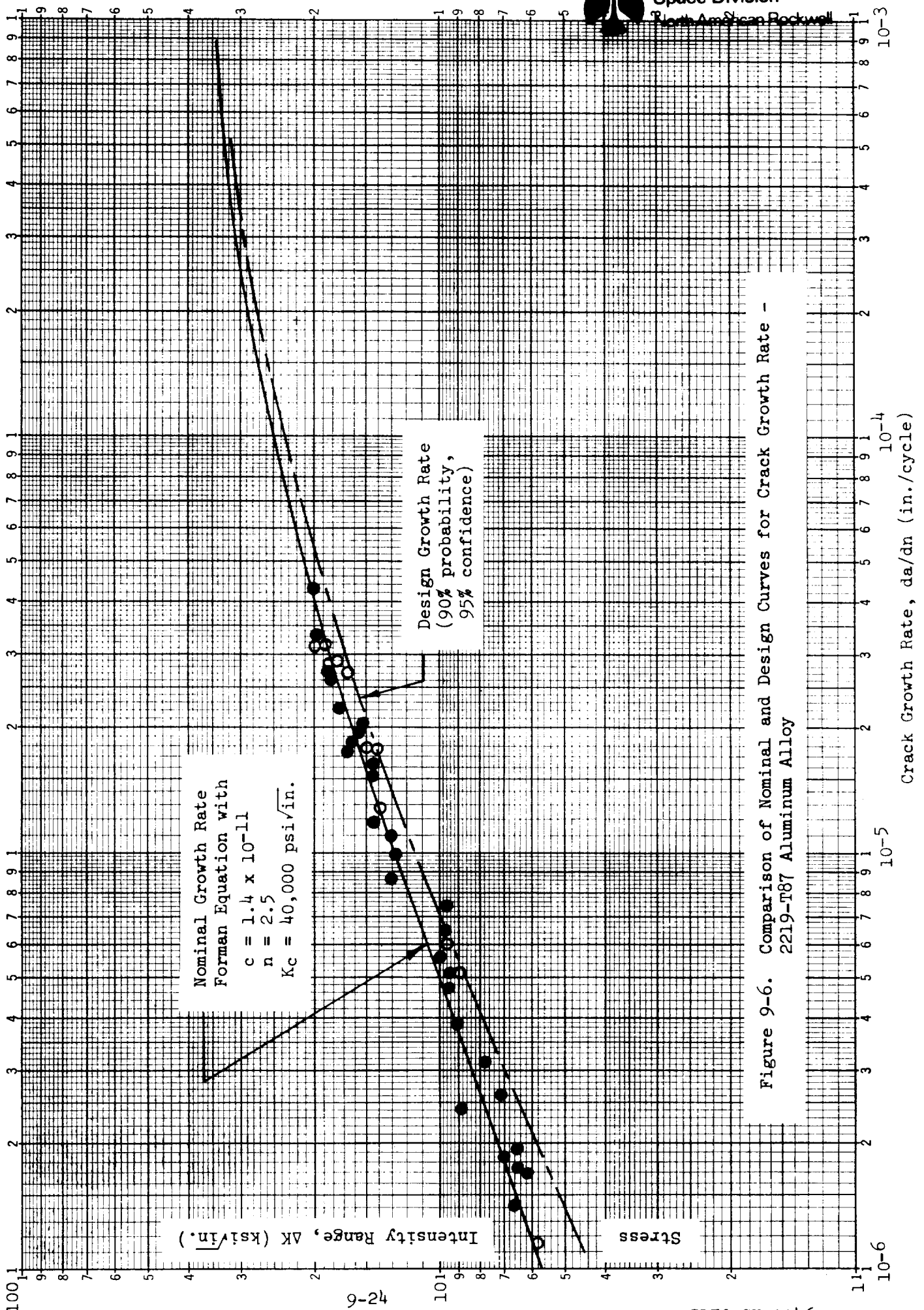


Figure 9-6. Comparison of Nominal and Design Curves for Crack Growth Rate - 2219-T87 Aluminum Alloy



Table 9-4. Structural Weight Increases for Various Residual Strength Safety Factors and Safe-Life Periods

Number of Missions Residual Strength Safety Factor	100						200						500						1000						
	1.0		1.1		1.2		1.0		1.1		1.2		1.0		1.1		1.2		1.0		1.1		1.2		
	Weight Increase	Initial Flaw Size	Weight Increase	Initial Flaw Size	Weight Increase	Initial Flaw Size	Weight Increase	Initial Flaw Size	Weight Increase	Initial Flaw Size	Weight Increase	Initial Flaw Size	Weight Increase	Initial Flaw Size	Weight Increase	Initial Flaw Size	Weight Increase	Initial Flaw Size	Weight Increase	Initial Flaw Size	Weight Increase	Initial Flaw Size	Weight Increase	Initial Flaw Size	
INITIAL FLAW SIZE CORRESPONDING TO BASELINE NDE CAPABILITY (FIGURE 9-1)																									
Wing spar caps (kg) (lb)	950 (2100)	1080 (2380)	1160 (2550)	1950 (4300)	2040 (4500)	2160 (4760)	3900 (8600)	4040 (8900)	4190 (9220)	5550 (12200)	5650 (12450)	5750 (12700)													
Fuselage frames (kg) (lb)	0	0	20 (50)	0	0	40 (90)	30 (60)	50 (110)	100 (230)	130 (280)	170 (370)	240 (530)													
LH2 tank skin	0	0	0	0	0	0	0	0	0	0	0	0													
LO2 tank skin	0	0	0	0	0	0	0	0	0	0	0	0													
Vert. stab. skin	0	0	0	0	0	0	0	0	0	0	0	0													
Crew compt. skin	0	0	0	0	0	0	0	0	0	0	0	0													
Total	950 (2100)	1080 (2380)	1180 (2600)	1950 (4300)	2040 (4500)	2200 (4850)	3930 (8660)	4090 (9010)	4290 (9450)	5680 (12480)	5820 (12820)	5990 (13230)													
Percent total veh. structural weight	0.78	0.88	0.96	1.60	1.67	1.80	3.20	3.33	3.50	4.61	4.75	4.90													
INITIAL FLAW SIZE = 2 x BASELINE VALUES																									
Wing spar caps (kg) (lb)	1900 (4200)	2040 (4500)	2180 (4800)	3120 (6860)	3240 (7150)	3380 (7450)	4870 (10720)	4960 (10950)	5100 (11250)	6160 (13600)	6300 (13900)	6450 (14200)													
Fuselage frames (kg) (lb)	300 (660)	430 (940)	650 (1420)	390 (850)	470 (1140)	730 (1600)	590 (1300)	720 (1580)	930 (2040)	850 (1870)	940 (2080)	1080 (2380)													
LH2 tank skin	0	0	0	0	0	0	0	0	0	0	0	0													
LO2 tank skin	0	0	0	0	0	0	0	0	0	0	0	0													
Vert. stab. skin	0	0	0	0	0	0	0	0	0	0	0	0													
Crew compt. skin	0	0	0	0	0	0	0	0	0	0	0	0													
Total	2200 (4860)	2470 (5440)	2830 (6220)	3510 (7710)	3710 (8290)	4110 (9050)	7410 (16320)	7630 (16830)	7980 (17590)	10830 (23870)	11060 (24380)	11350 (24980)													
Percent total veh. structural weight	1.80	2.0	2.30	2.86	3.07	3.35	6.05	6.23	6.50	8.85	9.0	9.25													

for any of the reference structural elements, and that a safety factor of 1.2 is therefore applied. The wing spar caps, crew compartment skin and vertical stabilizer skin are assumed to be inspectable during operational service by ultrasonic and/or visual techniques. The major fuselage frames and propellant tank skins are assumed to be not readily inspectable. The corresponding weight increases for the reference structural elements and for the total vehicle are listed in Table 9-5 for service life requirements of 100, 200 and 500 missions. The weight increments are with respect to a structural design based on conventional static strength requirements only. The basic comparison is predicated on the flaw detection capabilities of applicable NDE techniques as given in Figure 9-1. A comparison is also summarized for the case where the initial flaw sizes are taken as twice the baseline values.

It can be seen that for the basic case the total weight increase is approximately 1.5 percent of the vehicle structural weight for a 100 mission service life; this increases to about 4.5 percent for a 500 mission life. The latter value is still considered to be tolerable, although it does represent a significant performance penalty. It should be noted that almost all of the weight increase is contributed by the wing spar caps. Consideration of the fail-safe design approach for these members is obviously warranted; this would satisfy the fracture control criteria and impose a much smaller weight penalty, particularly for the longer service life requirements.

If the baseline values for size of maximum undetected initial flaws are doubled, the corresponding structural weight increases are about 3.5 percent of the vehicle structural weight for 100 missions and 10 percent for 500 missions. The wing spar caps are still the largest single weight item, but the fuselage frames and propellant tank skins contribute about one-half of the total weight increase. This comparison illustrates the importance to structural efficiency and to an effective fracture control program of selecting the most appropriate NDE techniques and obtaining an accurate definition of their flaw detection capabilities.

The preceding evaluations are based on safe-life analyses using initial flaw sizes derived from inspection procedures and associated NDE capabilities as a starting point. If proof testing of the propellant tanks is considered as a primary technique to screen out initial flaws that could cause failure during operational service, then some additional weight increase must be combined with the previous summaries. However, as discussed under the propellant tank safe-life investigations (Section 7.7.3), it is difficult to establish a practical and effective proof test approach for the tanks because of the prevalence of the leak-before-break failure mode. Weight increases resulting from proof test requirements were estimated for assumed initial flaws of $a/2c = 0.1$ and service life requirements of 100 to 200 missions. However, these estimates must be considered as "lower bound"; the weight penalty may increase greatly as the assumed initial flaw approaches a semicircular shape and other complicating factors regarding flaw growth or fracture during proof test are considered. This "minimum" weight increase associated with proof test is calculated to be 1660 kg (3680 lb) for both tanks and a required service life of 100 missions;

Table 9-5. Summary of Structural Weight Increases* Resulting From Application** of Proposed Safe-Life Design Criteria to the Reference Vehicle

Required Safe-Life (Number of Missions)		100	200	500	
INITIAL FLAW SIZE CORRESPONDING TO BASELINE NDE CAPABILITY (FIGURE 9-1)					
Weight Increase	Wing spar caps	(kg) (lb)	1700 (3750)	3000 (6600)	5100 (11,250)
	Fuselage frames	(kg) (lb)	60 (140)	150 (320)	340 (740)
	LH ₂ tank skin		0	0	0
	LO ₂ tank skin		0	0	0
	Vertical stabilizer skin		0	0	0
	Crew compartment skin		0	0	0
	Total	(kg) (lb)	1760 (3890)	3150 (6920)	5440 (11,990)
Percent total vehicle structural weight			1.44	2.57	4.35
INITIAL FLAW SIZE = 2 x BASELINE VALUES					
Weight Increase	Wing spar caps	(kg) (lb)	3000 (6600)	4310 (9500)	6050 (13,300)
	Fuselage frames	(kg) (lb)	770 (1700)	950 (2100)	1270 (2800)
	LH ₂ tank skin	(kg) (lb)	550 (1200)	1950 (4300)	3770 (8300)
	LO ₂ tank skin	(kg) (lb)	90 (200)	500 (1100)	1040 (2300)
	Vertical stabilizer skin		0	0	0
	Crew compartment skin		0	0	0
	Total	(kg) (lb)	4410 (9700)	7710 (17,000)	12,130 (26,700)
Percent total vehicle structural weight			3.60	6.30	9.90
<p>*Increases are with respect to a vehicle designed to conventional static strength requirements.</p> <p>**Assumptions made in application of criteria:</p> <ol style="list-style-type: none"> (1) Wing spar caps, crew compartment and vertical stabilizer skins are inspectable during operational service. (2) Fuselage frames, propellant tank skins are not inspectable during operational service. (3) Test verification of residual strength not accomplished for any of the structural elements (residual strength safety factor = 1.2). 					

if a factor of safety of 2.0 is applied to the required service life the weight increase becomes 2900 kg (6460 lb). This is almost twice the value of the weight increase from the other structural elements; the total increase would be about 4 percent of the vehicle structural weight for a 100 mission service life requirement. This is a rather significant performance penalty and it is associated with a proof test that does not provide, under present knowledge, a rigorous fracture mechanics verification of tank integrity. The weight penalty would probably be much greater for a test that would provide a rigorous verification, if indeed such a test is technically feasible at all. Therefore, the use of proof test to screen out, by direct demonstration, all flaws that could propagate to failure during operational service does not appear to be an attractive option for this application. However, a proof test of the tanks to provide a conventional strength demonstration is certainly desirable, and if this is followed by a thorough post-test inspection it will provide a significant contribution to the overall fracture control program.

In summary, this review has indicated that the basic safe-life design criteria proposed in this section are reasonable and will not result in unacceptable weight increase of the reference vehicle. However, the feasibility of proof testing the propellant tanks to verify that no flaws exist which could subsequently grow to failure during operational service appears to be questionable, and therefore the requirement for such a proof test should not be a mandatory part of the safe-life criteria.

9.3 COMPARISON OF SAFE-LIFE VS. FAIL-SAFE DESIGN APPROACHES

A comparison between safe-life and fail-safe design approaches for the wing spar caps and the vertical stabilizer and crew compartment skins is summarized in Table 9-6. Factors considered in this comparison are weight increase, required in-service inspection interval and the type of NDE techniques required for both production line and in-service inspections. Both 100 mission and 500 mission service life requirements are considered.

The structural weight increases for wing spar caps designed for safe-life are obtained from the results summarized in Table 9-5. The weight increases for fail-safe design are based on the monolithic spar cap approach (Section 8.1.2) and a residual strength safety factor of 1.2. The weight increase for 100 mission service life is taken directly from the results of the fail-safe analyses summarized in Section 8.1. The weight increase for 500 mission service life is approximated from consideration of the required reduction in general stress level to achieve satisfactory fatigue life plus any additional increment necessary to meet residual strength requirements. This increment was determined to be small, only spar cap #5 required additional reinforcement above the fatigue design requirements. It can be seen that the fail-safe approach is somewhat lighter than safe-life for a 100 mission service life requirement and a great deal lighter for a 500 mission life.

The required inspection interval for the fail-safe design is based on safe fatigue life of the remaining structure, after fracture of one spar cap. This life was determined in the analyses summarized in Section 8.1. The required inspection interval is the same for the 500 mission service life as for 100 missions, because at least one spar (No. 5) can be operating at the same stress level after failure of an adjacent spar in both cases. The wing spar caps designed for safe-life are assumed to be inspectable during operational service and therefore no scatter factor is applied to crack growth predictions from which structural weight increases are determined. The required inspection intervals for this case are approximated in the following manner:

- (a) It is assumed that a corner crack from a fastener hole is the most likely and the most critical type of defect to be detected, and that a portable ultrasonic unit will be used as the primary NDE technique for in-service inspection.
- (b) The baseline flaw size for ultrasonic inspection is 0.38 cm (0.150 in.); however, it is assumed that a crack may be completely masked until it propagates beyond the fastener head. Therefore, an additional allowance of 0.25 cm (0.1 in.) is added to the baseline value. This results in a reference flaw size of 0.63 cm (0.25 in.) for in-service inspection.

Table 9-6. Comparison of Safe-Life vs. Fail-Safe Design Approaches for Selected Structural Elements

Structural Element	Parameter	Safe-Life		Fail-Safe	
		100 Missions	500 Missions	100 Missions	500 Missions
Wing Spar	Structural weight increase (kg) (lb)	1700 (3750)	5100 (11,250)	1160 (2570)	1950 (4300)
	In-service inspection interval (missions)	13	110	14	14
	Production inspection - NDE techniques	Penetrant, eddy current		Visual	
Caps	In-service inspection - NDE techniques	Visual, ultrasonic		Visual	
	Structural weight increase (kg) (lb)	0	0	79 (170)	79 (170)
Vertical Stabilizer	Production inspection - NDE techniques	Visual		Visual	
	In-service inspection - NDE techniques	Visual		Visual	
Crew Compartment	Structure & system weight increase (kg) (lb)	0	0	118 (260)	118 (260)
	Production inspection - NDE techniques	Visual, penetrant		Visual	
Skins	In-service inspection - NDE techniques	Visual, ultrasonic, penetrant		Visual	

- Notes: (1) Weight increases are with respect to a vehicle designed to conventional static strength requirements.
 (2) A residual strength safety factor = 1.2 is provided in both safe-life and fail-safe design approaches.

- (c) The predicted number of safe-life missions for this flaw size and an operating stress corresponding to safe-life design for either 100 missions or 500 missions is determined from the appropriate parametric plots of Figure 7-12. This predicted life is then divided by a scatter factor of 2.0 to determine the required inspection interval.

The safe-life inspection interval determined by this approach is about the same as for the fail-safe design under a 100 mission service life requirement and considerably longer (less frequent inspection) for the 500 mission case. This is due to the reduction in spar cap stress level required to provide safe-life for 500 missions.

The types of NDE techniques required for both production line and in-service inspection are also compared. Obviously, the fail-safe design approach permits the use of much less sophisticated NDE techniques. However, if advantage is taken of this to reduce production costs and schedules, the probability of having a failure in service will be much higher for the fail-safe design than for the safe-life approach. Such a failure would not be catastrophic, but it could result in significant "down time" and repair costs for the vehicle during operational service. Therefore, the final decision regarding the quality of NDE to be employed during production of the fail-safe design must weigh these opposing factors.

It appears that the fail-safe design is advantageous for both the 100 mission and 500 mission service life requirements. However, for the 100 mission case, the weight difference is not large and the relative importance of other factors may be decisive.

A comparison between fail-safe and safe-life design approaches for the vertical stabilizer and crew compartment skins is not truly a valid trade study because these structures inherently possess adequate safe-life characteristics without requiring structural weight increase or the use of extraordinary NDE techniques. Therefore, the decision involved is whether an "add-on" of fail-safe provisions is warranted to achieve additional structural reliability at the expense of some increase in production costs and/or weight. This is a program management type of decision which transcends the scope of this study.

The above discussion and comparisons lead to the conclusion that it is not possible, or proper, to establish rigid and all-encompassing rules regarding the selection between fail-safe and safe-life design approaches. In most cases a specific trade study evaluation will be required between the two approaches, with consideration given to the types of factors illustrated in this section. The weighting of relative importance between these factors will depend on the philosophy, goals, constraints and financial/performance circumstances of the Space Shuttle Phase C/D Program.

9.4 SUMMARY OF RECOMMENDED DESIGN CRITERIA

The following recommended criteria are intended to supplement and not replace the conventional criteria regarding ultimate strength, yield strength, stiffness, etc. The primary intent of the criteria is to provide assurance that the service life requirements of Space Shuttle vehicles will be achieved and that catastrophic failure of shuttle primary structure due to the propagation of undetected crack-like flaws will be prevented.

Basic Approach

Safe fatigue life design shall be provided for all elements of the primary structure and pressurized components of Space Shuttle vehicles. In addition, damage tolerance shall be provided for critical components of structure or systems that are susceptible to the fracture mode of failure and that such failure could cause loss of the vehicle or jeopardize crew safety. Damage tolerance is commonly provided by either the fail-safe or safe-life (safe crack growth) design approach, as described below.

(a) Fail-Safe Approach

This approach requires that the complete failure of a principal structural element will not result in catastrophic failure or inability to operate the vehicle under limit load conditions before a suitable inspection is performed. Fail-safe designs generally provide crack arrest features and sufficient redundancy to maintain the required residual strength in the damaged condition.

(b) Safe-Life Approach

This approach requires that the largest undetected flaw at a given inspection (production line, in-service, etc.) will not propagate to critical dimensions prior to its discovery at a subsequent inspection or, alternatively, during the service life of the vehicle. Critical crack dimensions are based on the required level of residual strength. Safe-life can be achieved through selection of materials, stress levels, detail structural configurations, etc., without necessarily incurring fail-safe features.

The choice of fail-safe or safe-life design approaches should be based on results of trade study evaluations that consider the effects of each design approach on vehicle weight, structural reliability, cost, inspection requirements and other pertinent program factors. In general, the selected approach should exploit the inherent fail-safe or safe-life features of the vehicle and structure configuration.

Fatigue Life Criteria

The nominal fatigue life of unflawed structure shall be determined by analysis and test to be at least four times the required service life for Space Shuttle. The predicted nominal fatigue life is based on average S-N characteristics for the materials and structural assemblies and an average service load/environment spectrum.

Development tests shall be performed as required to support the structural design and provide assurance of meeting the fatigue life requirements. Full-scale fatigue life verification tests shall be performed for fatigue-critical regions of the structure, as agreed to by the contractor and the procuring agency.

The effects of periodic exposure to elevated temperature, thermal stresses resulting from temperature gradients, and local discontinuity stresses such as encountered in stiffened pressure vessels shall be accounted for in the fatigue analyses and development and verification tests.

Fail-Safe Design Criteria

Fail-safe designs shall provide adequate fracture-arrest capability and residual strength after failure of a principal structural element. All fail-safe structure shall be accessible for periodic inspection during operational service. The residual strength provided by the design shall be at least 1.1 x limit load if this capability is verified by structural test. If test verification is not accomplished, the design and supporting analyses shall be based on a residual strength at least 1.2 x limit load.

The residual strength evaluation shall account for critical compression design loads, and the possible reduction in stability due to failure of a principal structural element, in addition to the critical tension design load cases.

For fail-safe designs in which fracture arrest is provided by geometric boundaries, such that no crack front exists in the remaining structure, the nominal fatigue life of the remaining structure shall be at least four times the interval between regularly scheduled inspections.

For fail-safe designs in which fracture arrest is provided by structural reinforcement, such that a crack front remains in the load-carrying structure, the safe-life (safe crack growth) of the remaining structure shall be at least two times the interval between regularly scheduled inspections. Critical crack sizes used in determining safe-life characteristics shall be based on the required level of residual strength, as previously specified. Material fracture properties used in residual strength and crack growth analyses shall be derived from applicable test data to correspond with MIL-HDBK-5 "B" design properties (90 percent probability at 95 percent confidence level).

The above safe-life requirements may be waived in cases where failure of a principal structural element would become immediately obvious by virtue of fluid leakage, loss of pressure, etc.

The effect of failure of a principal structural element on the performance and integrity of other systems shall be considered where applicable. Where the fail-safe provisions involve a "leak-before-break" concept for pressure vessels the consequences and potential hazards associated with leakage of the contained fluid shall be critically examined. Verification tests shall be performed as required to provide assurance that the structural design concept provides acceptable failure modes that will not critically impair the performance or integrity of other systems. Examples of specific concern for Space Shuttle are the integrity of the thermal protection system, loss of cabin atmosphere, leakage of propellants or cryogenics from internal storage vessels.

Safe-Life Design Criteria

Critical primary structure and pressure vessels that are not fail-safe shall be designed so that initial flaws will not propagate to critical size during the specified service life of the vehicle. The critical flaw sizes shall be based on the required level of residual strength, as specified below. The critical flaw size for pressure vessels is defined as the point of fracture or of break-through (leakage), whichever occurs first.

The residual strength at the end of the service life shall be at least $1.1 \times$ limit load if this capability is verified by applicable structural component tests. If test verification is not accomplished, the design and supporting analyses shall be based on a residual strength at least $1.2 \times$ limit load.

The crack growth life from initial to critical size shall be determined on the basis of a realistic and typical service load/environment spectrum and design values of fracture properties for the material. This safe crack growth life determined in this manner, using initial flaw sizes compatible with the detection capabilities of production-line inspection methods, shall meet one of the following requirements, as applicable:

- (1) For structure that is subjected to regular inspections during operational service, the safe crack growth life shall be equal to or greater than the specified vehicle service life.
- (2) For structure that is not subjected to regular inspections during operational service, the safe crack growth life shall be at least two times the vehicle service life.

Required inspection intervals shall be established for the first case considering safe crack growth from an initial size that is compatible with the detection capabilities of in-service inspection techniques; the safe life shall be at least two times the regular inspection interval. Accessibility for regular in-service inspection may require removal of access panels, doors, etc. If removal of permanent type skins and fasteners is required to perform an adequate inspection, the structure should be classified as noninspectable.

The character and location of initial flaws used as the basis of safe-life analyses and verification tests shall be realistic selections consistent with the material product form, processing history, thickness, and detail design configuration. The assumed size of such initial flaws shall be consistent with capabilities for reliable detection by the NDE techniques that will be used during production line or in-service inspections. It shall be demonstrated by representative tests that the selected NDE techniques will provide at least 90 percent probability of detection, at 95 percent confidence level, of flaws equal to or larger than the assumed initial sizes.

In defining the assumed characteristics of initial flaws that extend only part way through the thickness of material, the following criteria shall be observed:

- (a) If the selected NDE technique interrogates only flaw length, the depth of flaw shall be assumed to be a maximum of one-half the flaw length.
- (b) If the selected NDE technique interrogates only flaw depth, the length of flaw shall be assumed to be a maximum of five times the flaw depth.

Fracture properties data for the selected structural materials will be obtained from approved sources or generated by test as required. The data shall include evaluation of the effects of applicable temperature and chemical environments and of variations in material product forms and processing parameters. The fracture properties (toughness, growth rate, threshold stress intensity, etc.) used in residual strength and crack growth analyses shall correspond to MIL-HDBK-5 "B" design properties (90 percent probability at 95 percent confidence level). In cases where valid statistical definition of fracture properties is not possible because of data limitations or other reasons, conservative design values shall be established on a rational basis and shall be approved by the procuring agency.

If predicted effects of crack growth retardation due to peak loads in a random load spectrum are used in design verification analyses, these predictions shall be substantiated by tests of flawed specimens. These tests shall employ a flight-by-flight loading spectrum which includes exposure to elevated and/or depressed temperatures in the proper sequence and relative duration with respect to the applied loads.

All Space Shuttle pressure vessels, including integral propellant tanks, shall be proof tested. The minimum requirements for proof test are as defined by proof factors listed in applicable contract specifications. In addition, the contractor shall assess the feasibility of proof test to detect initial flaws that could grow to failure during operational service. Empirical data regarding flaw growth and fracture characteristics, appropriate for the material, thickness, and environments of the intended application, shall be generated as necessary to make this assessment. Proof testing based on this approach shall be conducted as agreed to by the contractor and the procuring agency. Structural design of the pressure vessels shall be developed to accommodate a practical proof test to the appropriate requirements.

APPENDIX

Sample Computer Print-Out
for Crack Growth Analysis.

WING SPAR CAP CRACK GROWTH ANALYSIS, LIMIT STRESS = 65.0 KSI.

TI-6AL-4V, PART THRU CRACK, W=25 IN.

YIELD STRESS = 120000.0 KSUBIC FOR A = 80000.0 KSUBC FOR C = 80000.0

FORMAN'S COEFF C (LOW SEGM) = 0.780E-25 EXP SMALN (LOW SEGM) = 6.000
(HIGH SEGM) = 0.780E-13 (HIGH SEGM) = 3.000

DELTA K AT TRANSITION POINT = 10000.0

TYPE = 1 (PART THROUGH CRACK=1, THROUGH CRACK=2)

RETARD = 0 (NO RETARDATION=0, WITH RETARDATION=1)

INIT. CRACK DEPTH (A) = 0.050 ASPECT RATIO (A/2C) = 0.100000 PHI SQUARED = 1.100
INIT. HALF CRACK LENGTH (C) = 0.0 THICKNESS = 0.750 HALF WIDTH = 12.500

NUMBER OF LOAD STEPS IN LOAD BLOCK = 22
MAX. NUMBER TO REPEAT LOAD BLOCK = 50
MAX. STRESS IN LOAD BLOCK = 62800.0

A 2



Space Division
North American Rockwell



LOAD BLOCK'S	STEP NO.	MAX. STRESS	MIN. STRESS	NUMBER OF CYCLES
	1	13600.0	0.0	9000.0
	2	18800.0	0.0	9900.0
	3	25900.0	0.0	990.0
	4	37200.0	0.0	100.0
	5	49900.0	0.0	10.0
	6	62800.0	0.0	1.0
	7	32300.0	20400.0	9000.0
	8	36100.0	19400.0	900.0
	9	40000.0	12800.0	90.0
	10	43900.0	9000.0	9.0
	11	46000.0	6000.0	1.0
	12	10300.0	0.0	9000.0
	13	18200.0	0.0	900.0
	14	26800.0	0.0	70.0
	15	46700.0	0.0	20.0
	16	61600.0	0.0	10.0
	17	28500.0	17100.0	4000.0
	18	34700.0	12200.0	1800.0
	19	41000.0	5900.0	180.0
	20	46400.0	0.0	18.0
	21	51300.0	0.0	2.0
	22	22800.0	0.0	20.0

CRACK LENGTH AT BEGINNING OF BLOCK 1 IS 0.050000

ANALYSIS BY G. VROMAN'S CRACK PROPAGATION METHOD

STEP	CYCLES	A	C	DADN	(B E F O R E)	DELTA K	KMAX
1	9000.0	0.050313	(AFTER CYCLES)	0.351918E-07	5678.6	5678.6	
2	9900.0	0.053044		0.298765E-06	8066.7	8066.7	
3	990.0	0.054630		0.164024E-05	11304.4	11304.4	
4	100.0	0.055166		0.540187E-05	16392.8	16392.8	
5	10.0	0.055313		0.147369E-04	22187.7	22187.7	
6	1.0	0.055347		0.338457E-04	28218.3	28218.3	
7	9000.0	0.055958		0.689251E-07	5268.6	14300.6	
8	900.0	0.056355		0.446091E-06	7436.5	16075.3	
9	90.0	0.056653		0.332689E-05	12167.4	17893.3	
10	9.0	0.056709		0.623408E-05	15649.1	19684.7	
11	1.0	0.056717		0.876947E-05	17968.1	20663.4	
12	9000.0	0.056802		0.937852E-08	4566.7	4566.7	
13	900.0	0.057076		0.306303E-06	8099.6	8099.6	
14	70.0	0.057213		0.196896E-05	11974.9	11974.9	
15	20.0	0.057462		0.124848E-04	21122.5	21122.5	
16	10.0	0.057800		0.339907E-04	28252.3	28252.3	
17	4000.0	0.058011		0.530271E-07	5131.9	12829.6	
18	1800.0	0.061719		0.216446E-05	10473.3	16152.2	
19	180.0	0.062926		0.681630E-05	16556.2	19339.2	
20	18.0	0.063183		0.143316E-04	22005.4	22005.4	
21	2.0	0.063224		0.204105E-04	24410.9	24410.9	
22	20.0	0.063251		0.137769E-05	10697.2	10697.2	

CRACK LENGTH AT END OF BLOCK 1 IS 0.063251



Space Division
North American Rockwell

CRACK LENGTH AT BEGINNING OF BLOCK 2 IS 0.063251

ANALYSIS BY G.VROMAN'S CRACK PROPAGATION METHOD

STEP	CYCLES	A	C	DADN	DELTA K	KMAX
		(AFTER CYCLES)				
1	9000.0	0.063896		0.728074E-07	6399.7	6399.7
2	9900.0	0.069890		0.695173E-06	9260.0	9260.0
3	990.0	0.072358		0.256292E-05	13008.3	13008.3
4	100.0	0.073209		0.859565E-05	18884.8	18884.8
5	10.0	0.073448		0.239659E-04	25572.5	25572.5
6	1.0	0.073504		0.564756E-04	32516.5	32516.5
7	9000.0	0.075005		0.172290E-06	6102.1	16562.7
8	900.0	0.076008		0.113994E-05	8635.4	18666.9
9	90.0	0.076498		0.547444E-05	14137.8	20790.9
10	9.0	0.076591		0.103455E-04	18193.7	22885.5
11	1.0	0.076606		0.145886E-04	20881.8	24014.0
12	9000.0	0.076816		0.234080E-07	5309.9	5309.9
13	900.0	0.077510		0.783628E-06	9442.6	9442.6
14	70.0	0.077734		0.320941E-05	13954.8	13954.8
15	20.0	0.078153		0.210573E-04	24633.1	24633.1
16	10.0	0.078744		0.595154E-04	32981.4	32981.4
17	4000.0	0.079298		0.140236E-06	6001.9	15004.6
18	1800.0	0.085554		0.369833E-05	12330.8	19016.9
19	180.0	0.087649		0.118914E-04	19541.3	22826.1
20	18.0	0.088102		0.253325E-04	25983.9	25983.9
21	2.0	0.088175		0.365062E-04	28825.5	28825.5
22	20.0	0.088222		0.233431E-05	12632.9	12632.9

CRACK LENGTH AT END OF BLOCK 2 IS 0.088222

CRACK LENGTH AT BEGINNING OF BLOCK 3 IS 0.088222

ANALYSIS BY G. VROMAN'S CRACK PROPAGATION METHOD

STEP	CYCLES	A	C	DADN	(B E F O R E (AFTER CYCLES)	DELTA K	KMAX
1	9000.0	0.090025		0.206935E-06	7596.0	7596.0	7596.0
2	9900.0	0.104551		0.165020E-05	11326.1	11326.1	11326.1
3	990.0	0.109307		0.498186E-05	15990.0	15990.0	15990.0
4	100.0	0.111013		0.172929E-04	23257.4	23257.4	23257.4
5	10.0	0.111514		0.503026E-04	31506.2	31506.2	31506.2
6	1.0	0.111640		0.125881E-03	40086.4	40086.4	40086.4
7	9000.0	0.117515		0.709004E-06	7637.6	20730.6	20730.6
8	900.0	0.120902		0.385717E-05	10890.3	23541.3	23541.3
9	90.0	0.121987		0.121337E-04	17848.5	26247.8	26247.8
10	9.0	0.122196		0.232845E-04	22974.8	28899.6	28899.6
11	1.0	0.122229		0.331385E-04	26375.8	30332.2	30332.2
12	9000.0	0.123103		0.983827E-07	6724.1	6724.1	6724.1
13	900.0	0.124858		0.197354E-05	11983.6	11983.6	11983.6
14	70.0	0.125345		0.696884E-05	17720.3	17720.3	17720.3
15	20.0	0.126322		0.491773E-04	31311.3	31311.3	31311.3
16	10.0	0.127827		0.152296E-03	42015.0	42015.0	42015.0
17	4000.0	0.130408		0.667245E-06	7696.8	19241.9	19241.9
18	1800.0	0.145245		0.903707E-05	16068.0	24780.4	24780.4
19	180.0	0.150568		0.305761E-04	25614.8	29920.4	29920.4
20	18.0	0.151772		0.673105E-04	34090.4	34090.4	34090.4
21	2.0	0.151972		0.100371E-03	37852.6	37852.6	37852.6
22	20.0	0.152084		0.561091E-05	16584.9	16584.9	16584.9

CRACK LENGTH AT END OF BLOCK 3 IS 0.152084



Space Division
North American Rockwell

CRACK LENGTH AT BEGINNING OF BLOCK 4 IS 0.152084

ANALYSIS BY G. VROMAN'S CRACK PROPAGATION METHOD

STEP	CYCLES	A	C	DADN	(B E F O R E (AFTER CYCLES)	DELTA K	KMAX
1	9000.0	0.162129		0.118404E-05	10195.0	10195.0	10195.0
2	9900.0	0.201331		0.471091E-05	15717.0	15717.0	15717.0
3	990.0	0.215678		0.153513E-04	22456.9	22456.9	22456.9
4	100.0	0.221398		0.586394E-04	32849.4	32849.4	32849.4
5	10.0	0.223332		0.195148E-03	44582.4	44582.4	44582.4
6	1.0	0.223944		0.613598E-03	56757.6	56757.6	56757.6
7	9000.0	0.276464		0.705454E-05	11711.8	11711.8	31789.1
8	900.0	0.292571		0.188899E-04	16939.1	16939.1	36616.8
9	90.0	0.298224		0.640931E-04	27918.3	27918.3	41056.3
10	9.0	0.299401		0.131206E-03	35958.6	35958.6	45231.5
11	1.0	0.299595		0.194107E-03	41286.2	41286.2	47479.1
12	9000.0	0.311611		0.137756E-05	10696.9	10696.9	10696.9
13	900.0	0.319571		0.903498E-05	19171.1	19171.1	19171.1
14	70.0	0.321980		0.346528E-04	28406.3	28406.3	28406.3
15	20.0	0.328635		0.340865E-03	50510.8	50510.8	50510.8
16	10.0	0.350330		0.251164E-02	69551.5	69551.5	69551.5
17	4000.0	0.385583		0.961911E-05	13228.6	13228.6	33071.5

A-7

 TRANSITION TO A THROUGH CRACK. A = 0.45562 ATRANS= 0.45518 C= 2.27810
 AT 1083.9 CYCLES OF STEP 18

 KMAX= 94804.9 IS GREATER THEN KSUBC = 80000.0 FOR C= 2.278103
 THUS, PART BREAKS IN TRANSITION



